Mission-Oriented Seismic Research Program

Annual Report

2012

M-OSRP

University of Houston

Sponsors and Advisory Board representatives

April 29, 2013

Corporate Sponsors

Anadarko ..... Roger Reagan, Mark Chang
BHP ..... Corey Morgan
BP ..... Jingfeng Zhang, Imtíaz Ahmed
Chevron ..... Debbie Bones
ConocoPhillips ..... Haiyan Zhang, Robert Stolt
Devon Energy ..... Kenneth Beeney, Richard Brietzke
Encana ..... David Mackidd
ENI-Agip ..... Nicola Bienati
ExxonMobil ..... Peter Traynin
Hess ..... Scott Morton
IBM ..... Tom McClure
Ion ..... Jacques Leveille
Landmark ..... Dave Diller
Pemex ..... Pamela Diaz
Petrobras ..... Neiva Zago
PGS ..... Nizar Chemingui, Sverre Brandsberg-Dahl
Repsol ..... Gladys Gonzalez, Francisco Ortigosa
Saudi Aramco ..... Yi Luo
Shell ..... Jonathan Sheiman
Spectrum ..... Alex Wang
Statoil ..... Marianne Houbiers, Lasse Amundsen
Total ..... Wafik Beydoun
WesternGeco ..... Richard Coates

Federal Support

DOE Basic Sciences award DE-FG02-05ER15697 ..... Nick Woodward
NSF-CMG award DMS-0327778 ..... Henry A. Warchall

M-OSRP Personnel

Faculty

Hicham Ayadi ..... Research Scholar (Physics)
Lasse Amundsen (Statoil) ..... Adjunct Professor (Physics)
Douglas J. Foster (ConocoPhillips) ..... Adjunct Professor (Physics)
Wilberth Herrera ..... PostDoc Fellow (Physics)
Kristopher A. Innanen (Associate Professor, University of Calgary) .. Adjunct Professor (Physics)
Robert G. Keys (ConocoPhillips) ..... Adjunct Professor (Physics)
Jacques Leveille (Amerada Hess) ..... Adjunct Professor (Physics)
Fang Liu ..... Research Assistant Professor (Physics)
Ken H. Matson (Shell) ..... Adjunct Associate Professor (Physics)
Bogdan Nita (Assistant Professor, Montclair State U.) ..... Adjunct Assistant Professor (Physics)
Jon Sheiman (Shell) ..... Adjunct Professor (Physics)
Robert H. Stolt (ConocoPhillips) ..... Adjunct Professor (Physics)
T. Hing Tan (Shell) ..... Adjunct Professor (Physics)
Arthur B. Weglein ..... Cullen Professor (Physics)
Daniel Whitmore (PGS) ..... Adjunct Professor (Physics)

Graduate Students

Qiang Fu ..... Physics
Qi Huang ..... Physics
Hong Liang ..... Physics
Xinglu Lin ..... Geosciences
Chao Ma ..... Physics
Jim Mayhan ..... Physics
Lin Tang ..... Physics
Jing Wu ..... Physics
Jinlong Yang ..... Physics
Yanglei Zou ..... Physics

Recent Alumni

Andre Ferreira[2] ..... Geosciences
Zhiqiang Guo ..... Geosciences
Shih-Ying Hsu ..... Physics
Xu Li ..... Physics
Jose Eduardo Lira[2] ..... Geosciences
Fang Liu ..... Physics
Francisco Miranda ..... Physics
Mozhdeh Niazmand ..... Physics
Adriana Citlali Ramírez ..... Physics
Simon A. Shaw ..... Geosciences
Zhiqiang Wang ..... Physics
Haiyan Zhang ..... Physics
Jingfeng Zhang ..... Physics

Administrative Support

Jennifer Chin-Davis ..... Associate Director, Physics Department
Andrew Fortney ..... Computer/IT Support
Chris Watts ..... Webmaster/NSM IT

[2]Petrobras, Brazil

Table of Contents

Reports/Abstracts

M-OSRP 2012 Annual Report: INTRODUCTION AND SUMMARY

Arthur B. Weglein

April 29, 2013

The 2012-2013 Annual Report focuses on recent progress, developments and plans, and how changes and concomitant challenges within our sponsor's portfolios are influencing the introduction of new subtopics and allocation and distribution of resources within projects. Your feedback at the May 2012 M-OSRP Annual Technical Review and Meeting, in Austin, and at the Executive Summary Meeting at the 2012 SEG Conference and Convention in Las Vegas, was extremely positive, worthwhile, encouraging and very much appreciated — and your response galvanizes and energizes our research efforts and progress to reach our goals .

1 OVERVIEW

The main recent petroleum industry shift in sponsor portfolios for difficult on-shore (with near surface complexity and shale-oil/shale-gas objectives) and complex marine plays communicated what amounts to a new and heightened research interest and focus requiring a higher priority and pressing need for an increased capability in the area of multiple removal. The earlier trend (25 years ago) to deep water exploration caused many traditional multiple removal methods to bump up against their assumptions, with a concomitant rejuvenated interest in multiple attenuation. New methods were developed and delivered in response to that earlier challenge. At this time, we are once again experiencing a period of heightened industry interest with a yet higher demand and standard for multiple attenuation effectiveness. That priority translates into the need to be able to predict the amplitude and phase of free surface and especially internal multiples at all offsets, and of all orders, and along an arbitrary offset trajectory. The ability to predict multiples with phase and amplitude fidelity would allow the surgical removal of the multiple without damaging proximal primaries. The inverse scattering series communicates its potential to provide that capability, which is beyond what we have developed and delivered to-date for internal multiple attenuation. The frequent inability to provide adequate subsurface information for multiple removal, in these challenging on-shore and off-shore plays, once again points to the inverse scattering series as the place to find a solution. We felt that M-OSRP was particularly well-suited to respond to that new priority and pressing challenge. That decision resulted in a new focus and effort with significant fundamental research and practical aspects, with a reassessment and return to a problem we had considered mature, and, we viewed as basically "paying the rent." Multiple removal returned to center stage as a fundamental

research project within M-OSRP. The prerequisites that are needed to allow the inverse scattering series methods to reach their potential also needed an upgrade and increased attention and resource allocation within the group. That resulted in a heightened interest and examination of Green's theorem for wave-field separation applications, e.g., de-ghosting and determining the reference wave and the scattered wave-field. That focus also (inadvertently) led to a new wave-field prediction, as well, and the first wave theory for RTM. The Green's theorem wave-field separation methods were intentional projects within M-OSRP strategy and linked chain of processing methods. The Green's theorem for wave theory RTM was neither planned nor part of the M-OSRP global strategy. However, that wave theory RTM "spinoff" appears to have more significance than those of us who developed the method understood or anticipated.

2 SUMMARY

All projects within the program had significant progress to report since the 2012 Annual Meeting and Technical Review in May, 2012.

Below please find a succinct summary of the status, progress and plans within individual projects in the program.

3 Green's theorem delivered prerequisites for wavelet estimation and source and receiver de-ghosting

There has been a keen industry-wide interest in de-ghosting due to the need for low frequency within methods to iteratively model match update the velocity model at, e.g., the top salt and for shallow hazard detection.

Separately, inverse scattering series for multiple removal have a serious and non-linear interest in wavelet removal and source and receiver de-ghosting, to allow predictions with amplitude and phase fidelity. Green's theorem methods for de-ghosting have several practical advantages over the industry standard $P - V_z$ summation. In contrast to the latter, the former doesn't require: a 1D earth, Fourier transforms, or a horizontal measurement surface for sources and receivers (for ocean bottom or on-shore application). Tests on the Green's theorem methods were carried out with synthetic, SEAM and field data with encouraging results. The preprocessing impact on subsequent ISS processing (e.g., multiple elimination) have been tested and evaluated along with the accommodation of source and receiver arrays and other acquisition and preprocessing parameters, e.g., estimating near-surface effective properties for on-shore Green's theorem and ISS applications. $P-V_z$ (i.e., operating in the k_x, ω domain) wave separation methods have an advantage over Green's theorem methods (operating in the x, ω domain) when the interest is in having the source on the receiver measurement surface and the output on that surface, as well. The latter is an essential difference and advantage of (k_x, ω) methods for on-shore application.

4 Multiples: Encouraging news and new fundamental issues and practical challenges for on-shore and off-shore plays

We were very pleased to hear about and read (this past year) published papers and public reports from M-OSRP sponsor companies, further documenting stand-alone capability of the leading order inverse scattering series (ISS) internal multiple attenuator, compared to all other methods with the same purpose and objectives, and demonstrating their mettle under the most complex and daunting on-shore and offshore field data circumstances. However, the sponsor/industry trends to ever more complex offshore (e.g., targets beneath complex 3D salt and complicated and numerous salt layers) and on-shore plays (with e.g., challenges that arise with a large number of high contrast near surface internal multiple generators, and unconventional oil and gas plays) can often have multiples proximal to or intersecting primaries or multiples of different orders — and raises the bar and demand for yet more effective free surface and internal multiple removal. Surgical removal of multiples at all offsets will be the goal, with a demand for amplitude, phase and shape fidelity. The standard reliance on prediction and subtraction, with the latter based on different versions of "energy minimization" will not fit that new challenge and demand. The current leading order ISS internal multiple attenuation algorithm predicts the precise time and approximate amplitude of all first order internal multiples, including converted wave internal multiples. The ISS internal multiple prediction has to become significantly stronger to provide amplitude and phase fidelity, to allow the algorithm to go from an attenuator to an eliminator. Also, new issues arise for the leading order internal multiple algorithm (that has been delivered in 1D, 2D and 3D) when three or more strong reflectors generate the multiples, and when internal multiples are themselves treated as subevents in the leading order algorithm.

However, all of the shortcomings and limitations of the leading order internal multiple algorithm are anticipated by the inverse scattering series, and higher order ISS internal multiple removal terms directly address each and every one of them. The M-OSRP plan (and on-going activity) is to harvest all of the beyond leading order terms that will allow that surgical removal of multiples without damaging proximal or intersecting primaries — to meet the yet more daunting challenges our sponsors are currently facing, and will increasingly face. The inverse scattering series is the only candidate method with that potential and promise, and always achieves a processing goal without requiring subsurface information or interpreter intervention. We are also actively pursuing replacements for the "energy minimization" adaptive subtraction, with a criteria that always aligns with and is consistent with the multiple removal prediction the "subtraction" it is meant to serve. Another key project is continuing to deliver algorithms that reduce the run-times of the 3D internal multiple algorithm. Finally, and equally important is the delivery of ISS prerequisites like wavelet estimation and de-ghosting from Green's theorem to allow ISS free surface and internal multiple algorithms to reach their potential.

5 Green's theorem for RTM, direct depth imaging with a velocity model

First steps towards implementing a new wave-theory formulation for RTM from Green's theorem that doesn't require a PML is underway, with a parallel effort to implement asymptotic (and industry standard) RTM with PML. The purpose is to study and compare run times and cost benefit of both

approaches. At some point soon, we will connect with sponsors with RTM PML expertise to assure that our tests and comparisons are relevant and realistic. The Green's theorem method for RTM came about as a natural extension of our Green's theorem methods for wavelet estimation and de-ghosting. However, the Green's theorem wavelet estimation and de-ghosting are wave-field separation methods whereas the Green's theorem for RTM is wave-field prediction. Green's theorem for wave-field separation doesn't require subsurface information. Green's theorem for wave-field prediction and RTM is a linear depth imaging method, and, in common with all current industry best practice migration methods, requires a velocity model.

The asymptotic PML RTM and the new wave-theory Green's theorem RTM that we are developing and have begun to test are within current migration concepts. For clarity, wave theory migration in our communication refers to first predicting the wavefield for a source and receivers in the subsurface and then applying an imaging condition to locate structure. Traditional migration means a migration that requires subsurface information.

To understand the value of wave theory RTM, it's useful to think of the two ingredients: wave theory and RTM, and what does each separately bring on its own, and, e.g., under what circumstances wave theory migration provides value beyond asymptotic (e.g., Kirchhoff and Beam) migration methods, for one way migration. Then separately, consider when current industry standard RTM migration provides value beyond industry standard one way migration, and then to imagine when both of those values and differences/benefits (RTM and wavefield prediction and imaging migration) are called upon and would be simultaneously provided within a single algorithm as needed/required to address a challenging imaging problem requiring both wave theory propagation and imaging and RTM.

6 Migration history in a nutshell

We can think of migration theory history as first being formulated as a wave theory (Claerbout 1971, Stolt 1978, Schneider 1978) with a one way downward continuation of sources and receivers and a causality based imaging condition at depth to locate reflectors. Then for lack of adequate data (in line and especially cross line) the less complete and less demanding asymptotic ("ray") methods came into vogue (Kirchhoff) based on a less than wave theory travel time arguments for imaging, and a less complete picture of how waves actually passed through the overburden on their trip back into the subsurface and before imaging. Then with subsalt imaging the latter compromises were decided to be contra-indicated, and a return to the original wave theory propagation and imaging became the standard, and the strategy was to collect the data needed. Then a thought emerged that perhaps imaging the base salt by a going around the outside with a two way diving wave with a $v(z)$ medium in the sediments was useful, and that led to the recent increase in RTM activity today. However, the current RTM methods based on: (1) using the data as a boundary condition in a finite difference modeling run backwards in time, (2) together with a forward modeling of a shot record and (3) and then the latter two are linked for imaging with a ray theory travel time imaging condition. The latter single shot experiment RTM is not a wave theory for predicting a source and receiver at depth, nor is it calling on the original wave theory imaging conditions (small time for a predicted coincident source and receiver at depth) to locate reflectors. That is, RTM today is a an asymptotic ray theory migration, with all the benefits and drawbacks that implies. Current RTM allows two

way propagation, and that's a step forward — but it's a step back to Kirchhoff rather than wave theory. Asymptotic migration and travel-time imaging conditions can have problems with amplitude analysis at the target, even when the overburden can justify asymptotic propagation models.

7 Wave theory RTM

The Green's theorem RTM method that we have developed provides more than just a way to deal with incidental PML boundary issues impinging on the image space. It provides a wave theory for RTM, allowing for downward continuing receivers and sources and then a causality based imaging condition in a way consistent with what the original migration pioneers (Stolt 1978) as well as avoiding (sometimes) troublesome boundary conditions. We understand that perhaps for a simple $c(z)$ medium outside a salt body, that an asymptotic migration might be adequate for structure, however, it can be inadequate if you are interested in amplitude analysis at the target. If you are interested in amplitude analysis at the target or if you had a two way wave in a complex medium, wave theory RTM from Green's theorem would probably be indicated, even for structure. We plan to test and evaluate and report on these different approaches for RTM in terms of effectiveness and efficiency. Professor Fang Liu has recently produced the first wave theory RTM result in a 1D medium with rapid variation (i.e., reflectors), and his output predict the location of reflectors and the reflection coefficient at the reflector. That's very positive and encouraging.

8 Inverse scattering series for direct depth imaging without the velocity model

Weglein et al. (2012, JSE) provided the first field data examples of direct depth imaging without a velocity model. We were honored and enormously pleased to have had our SEG Abstract, on that subject, selected for the Recent Advances and Road Ahead session of the 2012 International SEG Convention and Conference. The paper and SEG Abstract explain in logical detail why the results on field data demonstrate that ISS direct depth imaging without the velocity model is working on that field data test and is viable. It is shown that when ISS depth imaging algorithms produce a flat common image gather, the image has moved until it stops and when it stops it's at the correct depth. For ISS direct depth imaging the flat CIG is a necessary and sufficient condition that depth has been found, in contrast with traditional velocity dependent imaging where CIG flatness is a necessary but not sufficient condition, and the correct and other velocity models can satisfy that criteria, with the correct and incorrect depth being produced. The presentation at the SEG described the three steps that will be needed to go from "working" to "adding value and a place in the seismic toolbox" with the goal of improving upon current best practice depth imaging with a velocity model. Those three steps are being pursued.

9 Summary

This past year produced good progress in each of the projects within the program. There has been a resource reallocation and focus on projects in response to sponsor communicated prioritized and

pressing fundamental challenges that M-OSRP is particularly well-suited to address. The 2012-2013 Report describes the goals, progress and plans in each project.

Thank you for your encouragement and support.

Best regards,

Art

Green's theorem de-ghosting algorithms in the k,ω (e.g., $P-V_z$ de-ghosting) as a special case of x,ω algorithms (based on Green's theorem) with: (1) significant practical advantages and disadvantages of algorithms in each domain, and (2) a new message, implication and opportunity for marine towed streamer, ocean bottom and on-shore acquisition and applications.

Arthur B. Weglein*, James D. Mayhan*, Lasse Amundsen†, and Hong Liang*

April 29, 2013

Abstract

This paper is examining the implication/differences of a Green's theorem method of deghosting in two domains: (x,ω) and (k_x,ω). Substituting V_z for P_n, in the (k_x,ω) domain, and benefits/limitations that arise from that substitution (while important) are not within the scope of this paper. We point out how $P-V_z$ deghosting (in $\vec{k},\omega$) can be derived from Green's theorem deghosting (in $\vec{r},\omega$). We discuss the advantages and disadvantages of each deghosting method. For example, Green's theorem deghosting is less sensitive to sampling and aperture and can handle an arbitrary measurement surface, whereas $P-V_z$ deghosting allows the source and field locations to be on the receiver measurement surface. We discuss the implications of each deghosting/wavefield separation method for towed-streamer, ocean-bottom and on-shore acquisition.

1 Introduction

We start with the meaning of deghosting, and the simplest up-down separation idea. Then, we show how those early simple ideas and thinking have evolved and advanced through methods based on Green's theorem. We then show explicitly how these recent advances reduce to the original, and readily accessible and understandable concepts and algorithms, and the advantages and disadvantages, and delivery that the original and more recent progress represent.

We will connect Green's theorem deghosting to the industry standard $P-V_z$. We will show a more direct way to derive that connection than appears in Appendix B of Mayhan and Weglein (2013). We start with what resides behind the industry standard type of deghosting algorithm, review the Green's theorem deghosting method, and then show how the industry standard is a special case of

*M-OSRP, University of Houston, 617 Science & Research Bldg. 1, Houston, TX, 77004-5005. E-mail: aweglein@central.uh.edu

†Statoil Research Centre, Norway, and The Norwegian University of Science and Technology, Department of Petroleum Engineering and Applied Geophysics, Norway. E-mail: lam@statoil.com

the more general Green's theorem approach. We point out how the $P - V_z$ form has advantages over Green's theorem for on-shore application where the source is on the receiver measurement surface and the interest is in deghosting the data you acquired on the cable. Green's theorem has advantages over $P - V_z$ with limited aperture and sparse sampling and when the receiver/source acquisition is not on a horizontal surface.

2 The processing flow (steps) that are followed before ISS processing

Let's assume that the actual medium consists of air, a free surface at the air/water boundary, a water column, and earth. The sources and receivers for the towed streamer experiment are located in the water column. For the purposes of ISS multiple removal, depth imaging and AVO, we suggest the steps and definitions below.

First step: Define the reference medium as air and water with an assumed free surface at the air/water boundary. The latter assumes the air-water boundary can be replaced by a vacuum-water boundary. The reference wave is the wavefield in the reference medium. The reference Green's function is the response due to a localized source in the reference medium. Second step: For the actual medium, the Green's function, G, is the wavefield due to an idealized source $(\delta(\vec{r}-\vec{r}_s)\delta(t-t_s))$. The scattered wavefield, ψ_s, for an idealized δ source is $G - G_0$. Third step: Deghost, i.e., remove events which have begun their history going up from the source and/or end their history travelling downward when they are measured. We express G_0 as $G_0 = G_0^d + G_0^{FS}$, where G_0^d is the whole space causal Green's function and G_0^{FS} is the extra term in G_0 due to the presence of the free-surface. In terms of G_0 and G_0^d, we can describe source and receiver deghosting of the scattered wavefield as follows:

$$G_0^d G_0^{-1} \psi_s G_0^{-1} G_0^d. \tag{1}$$

Equation 1 removes 3/4 of the events in the scattered wave, ψ_s. Events that go up (from the source) and down (from the free surface) can destructively interfere with non-ghosted events putting notches in the data, which are not in the source spectrum. Deghosting removes destructive interference and boosts low frequencies. Removing the downwave recorded by the receiver, we want to be left with an upwave, which is up/down separation. In addition to the traditional interests in deghosting described above, we prefer to deghost data prior to calling upon the inverse series to remove free surface multiples. Primaries, free surface multiples, and internal multiples are defined as events in the deghosted part of the measured scattered field. We want ghosts out first, because we want the free surface multiple prediction algorithm to focus on removing free surface multiples, not ghosts. If we don't deghost the data, then the role of G_0^{FS} inside each term of the free surface multiple prediction algorithm has to remove both free surface multiples and ghosts, which is a much more complicated task. G_0^{FS} in the forward series creates ghosts and free surface multiples, and G_0^{FS} in the inverse series removes ghosts and free surface multiples. The removal of ghosts in equation 1 involves $G_0^{-1} G_0^d = (G_0^d + G_0^{FS})^{-1} G_0^d$, and G_0^{FS} is the sole factor in that form that differentiate this deghosting operator from the unit operator. Hence, G_0^{FS} is responsible for creating and removing ghosts. It's more economical to get rid of ghosts first (before you start with the series for multiple removal).

Consider a simple 1D normal incidence example, where in the vicinity of the (towed streamer) cable the pressure field P satisfies:

$$\left[\frac{\partial^2}{\partial z^2} - \frac{1}{c_0^2}\frac{\partial^2}{\partial t^2}\right] P = 0, \tag{2}$$

where c_0 is the wave speed in water, and

$$\left[\frac{d^2}{dz^2} + \frac{\omega^2}{c_0^2}\right] P = 0 \tag{3}$$

is the temporal Fourier transform of equation 2. The solution of equation 3 is

$$P = \underbrace{A\exp(ikz)}_{down} + \underbrace{B\exp(-ikz)}_{up}, \tag{4}$$

where the convention $\exp(-i\omega t)$ is used for going from ω to t. For deghosting, we want to up-down separate P at the assumed measurement location $z = a$. That requires two pieces of information about P.

2.1 Two measurements at one depth

If we make the required two pieces of information about P measurements of the field and its derivative at one level, for a cable at $z = a$,

$$\begin{aligned} P(a) &= A\exp(ika) + B\exp(-ika) \\ P'(a) &= ik[A\exp(ika) - B\exp(-ika)], \end{aligned}$$

again with the convention $\exp(-i\omega t)$ is used for going from ω to t. Solve for B,

$$B = \frac{ikP(a) - P'(a)}{2ik}\exp(ika)$$

and the upgoing wave at $z = a$ is

$$\frac{ikP(a) - P'(a)}{2ik}.$$

If we extend the above to a multi-D world in the vicinity of the cable,

$$\left[\nabla^2 - \frac{1}{c_0^2}\partial_t^2\right] P(x, z, x_s, z_s, t) = 0.$$

In the temporal Fourier domain, this becomes

$$(\nabla^2 + k^2)P(x, z, x_s, z_s, \omega) = 0,$$

and then Fourier transforming over x we have

$$\left[\frac{d^2}{dz^2} + k^2 - k_x^2\right] P(k_x, z, x_s, z_s, \omega) = 0. \tag{5}$$

Equation 5 looks like equation 3 where $q^2 \equiv k^2 - k_x^2$. The solution is

$$P = A\exp(iqz) + B\exp(-iqz),$$

where A, B are functions of k_x and ω, whereas in equation 4, A, B are functions of ω. We get B the same way as before except that the role of k will be played by q, i.e., in the prestack form (equation 5) the deghosted data at the cable (at $z = a$) is

$$P_r(a, k_x, \omega) = \frac{iqP(a, k_x, \omega) - P'(a, k_x, \omega)}{2iq} \tag{6}$$

with $q = +\sqrt{(\omega/c_0)^2 - k_x^2}$.

When P' is substituted with $i\omega\rho V_z$ where ρ is the local mass density at the cable and V_z is the vertical component of velocity, equation 6 becomes

$$P_r(a, k_x, \omega) = \frac{iqP(a, k_x, \omega) - i\omega\rho\, V_z(a, k_x, \omega)}{2iq} \tag{7}$$

the receiver deghosted data on the cable at $z = a$. The latter formula is the proto-type industry standard $P - V_z$ summation for deghosting.

2.2 Two measurements at two depths

Another way to provide two pieces of information about P is to use P on the cable and P at the free surface (where $P = 0$). We get

$$P(0) = A + B \tag{8a}$$
$$P(a) = A\exp(ika) + B\exp(-ika). \tag{8b}$$

To solve for B, multiply equation 8a by $\exp(ika)$ and subtract equation 8b to get,

$$\begin{aligned}\exp(ika)P(0) - P(a) &= B[\exp(ika) - \exp(-ika)] \\ B &= \frac{\exp(ika)P(0) - P(a)}{\exp(ika) - \exp(-ika)} \\ &= \frac{\exp(ika)P(0) - P(a)}{2i\sin(ka)},\end{aligned} \tag{9}$$

which in principle is entirely equivalent to equation 7, but can have stability issues compared to equation 7 for small errors in the cable depth, especially in the vicinity of notches. This was noted in Mayhan and Weglein (2013). To illustrate, let's assume that the total wave is upgoing and it doesn't need deghosting. Then the measured wave is $P(z) = P(0)\exp(-ikz)$. Then put $P(a)$ into equation 9 to get

$$B = \frac{\exp(ika)P(0) - \overbrace{P(0)\exp(-ika)}^{P(a)}}{\exp(ika) - \exp(-ika)} = P(0),$$

the deghosted data at $z = 0$; if the depth is correct, then the exponentials $(\exp(ika) - exp(-ika))$ in the numerator and denominator cancel for any frequency and there's no problems. But, if you got the cable depth wrong (the cable is at a but you think it's at b), the exponentials don't cancel, and you can get zeros in the denominator.

There is no sensitivity in equation 7 to division. Equation 7 is the solution for B with two measurements at one depth, while equation 9 is the same formula for B with two measurements at two depths. In theory equations 7 and 9 are the same, but in practice equation 9 can have issues. Zhang (2007) shows that for small error in depth equation 7 is stable. For typical towed streamer data at 6m, the receiver notch occurs at 125Hz. This frequency is usually outside your data (say max 70Hz). But if you're collecting data to 250Hz, the notch is in your data. The zero is at $ka = \pi$, or $k = \pi/a$. If you make the cable deeper, the notch comes in quicker. At the ocean bottom, the notches can come at 5Hz. Deghosting is very serious for ocean bottom data, because the notches are inside your data. Equation 7 is two measurements (field and its derivative) at one level. That's what Green's theorem depends on, $(P\nabla' G_0 - G_0\nabla' P)$ on the measurement surface.

3 Green's theorem

Green's theorem has two applications for us: wave separation and wave prediction. Both come from the same equation. Wave separation comes from the following idea. The actual medium is the reference medium plus sources located on both sides of the measurement surface. In the reference medium plus source math-physics description, sources don't interact (unlike individual air guns in an array). On the left hand side of the differential equation, write the reference operator, and sources are the terms on the right hand side of the differential equation. The total field P cares about the reference medium and all sources. Consider

$$P_r(\vec{r}, \vec{r}_s, \omega) = \oint_S [P(\vec{r}', \vec{r}_s, \omega)\nabla' G_0^+(\vec{r}, \vec{r}', \omega) - G_0^+(\vec{r}, \vec{r}', \omega)\nabla' P(\vec{r}', \vec{r}_s, \omega)] \cdot \hat{n}\, dS'. \tag{10}$$

Make part of the closed surface S' on the measurement surface. This integral is a function (not a number). $\vec{r}'$ is on the measurement surface, and $\vec{r}$ is free. When you evaluate equation 10 for $\vec{r}$ inside a volume V, it gives the contribution due to sources outside V.

For deghosting, choose the reference medium as a whole space of water, and with that reference medium there are three sources. One source converts water to air, one source corresponds to the air guns, and one source converts water to earth. With this homogeneous reference medium, the causal whole-space Green's function from a source to the field point is always outgoing and straight away from the source. Once you're in this math-physics description, it doesn't make sense to talk about the wave emitted from the airguns bouncing off the free surface. For an alternative description, where the reference medium is vacuum/air-water, once a source (e.g., airguns) emits a wave, that outgoing wave interacts with the reference medium (the air-water boundary is a part of that reference medium). In a source description where the reference is a whole space of water, everything just goes off and outwards forever, with no bouncing between sources. In this whole space reference medium, the reference wave is just G_0^d, and outgoing everywhere from each source.

In the whole space reference picture, at a point $\vec{r}$ above the water bottom but below the air guns, the wave due to the earth is upgoing, whereas the waves from the air guns and air are downgoing. With

the description of three sources and the whole space reference medium, the integral in equation 10 gives the portion of the total wavefield due to the source ρ_{earth}. At that point, $\vec{r}$, the portions of the total wave due to the other two sources are downgoing. Hence, equation 10 removes the reference wave and receiver deghosts the scattered wave.

4 Derive $P - V_z$ from Green's theorem

We now start with equation 10 and derive equation 7, the latter being the basis of $P-V_z$ deghosting. We provide the derivation in 2D, and the 3D derivation is a straightforward generalization. Let x', z' be the receiver coordinates, i.e., x' runs along the cable and z' is the constant depth of the cable, x_s, z_s is the source location, and x, z is the prediction point, where we choose for deghosting $z_s < z < z'$. The integral (in equation 10) produces an upwave at x, z, which outputs the receiver deghosted field.

Equations 1 and 9 depend on measurements at two depths. The integral (in equation 10) relates to equation 7. Advances in acquisition have allowed equation 10 to be realized in practice. Writing equation 10 in 2D,

$$P_r(x, z, x_s, z_s, \omega) = \int dx' \times \left\{ P(x', z', x_s, z_s, \omega) \frac{\partial}{\partial z'} G_0(x, z, x', z', \omega) - G_0(x, z, x', z', \omega) \frac{\partial}{\partial z'} P(x', z', x_s, z_s, \omega) \right\}, \tag{11}$$

where the left hand side is the receiver deghosted portion of P. The next steps in this derivation benefit from the work of Corrigan et al. (1991), Amundsen (1993) and Weglein and Amundsen (2003). Fourier transforming equation 11 with respect to x gives

$$\int \exp(-ik_x x) dx \, P_r(x, z, x_s, z_s, \omega) = \int \exp(-ik_x x) dx \int dx' \times \left\{ P(x', z', x_s, z_s, \omega) \frac{\partial}{\partial z'} G_0(x, z, x', z', \omega) - G_0(x, z, x', z', \omega) \frac{\partial}{\partial z'} P(x', z', x_s, z_s, \omega) \right\}, \tag{12}$$

where G_0 satisfies

$$(\nabla^2 + k^2) G_0(\vec{r}, \vec{r}', \omega) = \delta(\vec{r} - \vec{r}'). \tag{13}$$

Substitute the bilinear form of the Green's function

$$G_0(\vec{r}, \vec{r}', \omega) = \int \frac{1}{(2\pi)^3} \frac{\exp(-i\vec{k}' \cdot \vec{r}')}{-|\vec{k}'|^2 + k^2 + i\varepsilon} \exp(i\vec{k}' \cdot \vec{r}) d\vec{k}', \tag{14}$$

This bilinear form is the plane wave decomposition of G_0. Equation 14 requires all wavenumbers to produce a single temporal frequency wave solution in a region that includes the source, because this form works where equation 13 is valid. With the source included in the region the solution is not a d'Alembert form. It takes a superposition of plane waves of every wavenumber to produce a single frequency response in the region that includes the source. Why does a single temporal

frequency solution, G_0, require all $\vec{k}'$? Because the Dirac delta does, the source or the driving function contains all wavenumbers, so the solution does as well. In 2D,

$$G_0(x,z,x',z',\omega) = \frac{1}{(2\pi)^2}\int \frac{\exp\left(ik'_x[x-x']\right)\exp\left(ik'_z[z-z']\right)}{-k'^2+k^2+i\epsilon}dk'_x\,dk'_z$$

Fourier transform G_0 with $\int \exp(-ik_x x)dx$,

$$\underbrace{\int dx \exp(-ik_x x)\exp(ik'_x x)}_{2\pi\delta(k_x-k'_x)}\exp(-ik'_x x')\exp(ik'_z(z-z'))$$

and the Dirac delta allows you to carry out $\int dk'_x$

$$\exp(-ik_x x')\int \frac{\exp(ik'_z(z-z'))}{-k_x^2-k_z'^2+k^2+i\varepsilon}\,dk'_z. \tag{15}$$

The integral looks like a 1D Green's function if we define $k^2-k_x^2 \equiv q^2$. The latter relation between q, k_x and k is not due to a dispersion relationship but by introducing and defining the quantity q.

The 1D causal solution to

$$\left(\frac{d^2}{dz^2}+k^2\right)G_0 = \delta$$

is

$$G_0^+ = \frac{\exp(ik|z-z'|)}{2ik}. \tag{16}$$

The integral in equation 15 then results in:

$$\frac{\exp(iq|z-z'|)}{2iq},$$

from equation 16, and equation 15 becomes

$$\exp(-ik_x x')\frac{\exp(iq|z-z'|)}{2iq}.$$

Now differentiate equation 15 with respect to z',

$$\frac{iq\,sgn(z'-z)}{2iq}\exp(iq|z-z'|)\exp(-ik_x x').$$

The other term (in equation 11) will have G_0 with no derivative. Performing the integral over x' we then find

$$P_r(k_x,z,x_s,z_s,\omega) \tag{17}$$

$$=P(k_x, z', x_s, z_s, \omega)\frac{sgn(z'-z)}{2}\exp\left(iq|z-z'|\right) - P'(k_x, z', x_s, z_s, \omega)\frac{\exp\left(iq|z-z'|\right)}{2iq}.$$

It's a combination of P and P' at z' (the measurement depth.) Note there is no sum and no integral. The output point is shallower than the cable, $z' > z$, so $sgn(z'-z) = 1$ and $|z-z'| = z'-z$, and we get the form equation 7. This is called $P - V_z$ deghosting.

The industry standard practise replaces P' with displacement using the idea sketched here. Start with a 1D Newton's second law:

$$F = ma$$

and in the frequency domain

$$F = mi\omega V_z,$$

where $a = i\omega V_z$ and V_z is the vertical component of velocity. This becomes

$$\frac{F}{A} = \frac{m}{A} i\omega V_z,$$

where A is "area".

$$P' \sim \frac{1}{l}\frac{F}{A} \sim \frac{\partial}{\partial z}\frac{F}{A} = \frac{m}{Al} i\omega V_z = \rho i\omega V_z, \tag{18}$$

where $\rho = m/(Al)$ is the mass density. The Fourier transform turns the integral into a single product (diagonalizes an integral equation into an algebra expression with single products of terms). Equation 17 with equation 18 for P' is the industry standard and called $P - V_z$ summation. Why are we interested in a Green's theorem solution equation 10 when equations 17 and 18 are available?

1. In equations 17 and 18 we have to be able to Fourier transform. In the crossline direction, it can be a challenge to perform a Fourier transform because crossline receivers are further apart than inline receivers and crossline aperture is limited compared to inline. Green's theorem allows you to directly input and integrate the data you have recorded. Green's theorem is less upset with missing data, whereas transforming has a more severe requirement (see, e.g., Wu et al. (2013)).

2. Green's theorem can perform a line or surface integral on the ocean bottom or onshore or for a non horizontal cable. Ghosts are particularly important at the ocean bottom because the notches arrive at lower frequencies and within the seismic bandwidth.

We have shown that Green's theorem relates to the industry standard when the measurement surface is horizontal and the data is adequate to perform Fourier transforms. Wu et al. (2013) compared Green's theorem and $P - V_z$ for different numbers of receivers and different distances between receivers. Green's theorem and $P - V_z$ are not the same for a curved boundary. Green's theorem is directly applicable to any shape or form of measurement surface whereas $P - V_z$ is not.

5 On-shore Green's theorem wave field separation: near surface properties

On shore multiple attenuation can be an outstanding issue and significant challenge. Among issues that contribute to this pressing and high priority challenge are: (1) complex and ill-defined near surface properties, (2) numerous and hard to identify multiple generators, and (3) interfering primaries and multiples. To address the latter issue, you need surgical removal of multiples so you don't damage the primaries, and that in turn requires capable delivery of the prerequisites required by ISS multiple removal. A set of Green's theorem procedures have been developed by Weglein et al. (2002), Jingfeng Zhang (Zhang and Weglein, 2005, 2006; Zhang, 2007), Jim Mayhan (Mayhan et al., 2011, 2012; Mayhan and Weglein, 2013), Lin Tang (Tang et al., 2013), and others to separate reference wave and deghost. These procedures have shown value in synthetic SEAM data and marine field data (Mayhan et al., 2012; Mayhan and Weglein, 2013). The biggest challenge is on land; how do we get the prerequisites on land?

On land, the measurement surface is right on the perturbation, and the source is on the same line as the measurements. We want to identify/remove the reference wave/surface wave. The reference wave now has surface waves, and Green's theorem can be a way to remove surface waves. Today the industry often uses a combination of filter methods and intervention by capable processors. Surface wave removal remains an open and important practical problem.

In the marine application of Green's theorem wavefield separation methods, we assume the source is above the cable and the output point is either above or below the measurement surface. For on-shore application the source can be on (or below) the measurement surface, and we might want the wave separation of the measured data itself. In Mayhan and Weglein (2013) it was shown that using the Green's theorem form (equation 10) that the output point must be more than $1/2\,\Delta x$ above the measurement surface, i.e., that $\Delta z \geq 1/2\,\Delta x$, where z is the output depth, z' is the cable depth, and Δx is the sampling interval. If it gets closer, the calculation becomes unstable, with empirically observed numerical issues. That numerical issue in the x, ω domain (Green's theorem) precludes the output point that is too close to the cable, let alone on the cable. $\Delta z \geq 1/2\,\Delta x$ holds for both Green's theorem deghosting and wavefield separation ($P = P_0 + P_s$) in the x, ω domain.

However, in the $P - V_z$, or k_x, ω domain, form of wave field separation (for deghosting or separating P_0 and P_s, see Weglein and Secrest (1990)), when you Fourier transform, it assumes you have sampling sufficient to do the integral correctly without error. If you assume $\Delta x = 0$ as in $P - V_z$ forms, you can accommodate proximal to and on the cable for both the source and output point.

The consequences of this difference between x, ω (Green's theorem) and k_x, ω ($P - V_z$) approaches are more significant than just wanting to deghost marine data on the cable. The difference between these two will allow us to deghost and wave separate on land. We will illustrate this using a simple example separating P_0 and P_s in a 1D earth with a normal incidence wave . In our example, we will further assume there is no earth, that P is P_0 and the scattered wave is zero. What if we want the source on the cable and the prediction point on the cable? Don't use equation 10 directly; instead put equation 10 (Weglein et al., 2002) in the Fourier domain. We will do it in 1D normal incidence which is the same as being in the k_x, ω domain, since there is no x and no integral over x. Another question is how do we get P' on land? There are a lot of ways for doing this . If you are in the Middle East, one uses Vibroseis. The base plate has a phone and you get something like a wavelet.

From the wavelet and the field you get the derivative. $A(\omega), P, P'$ are called the triangle; given two, the triangle will give you the third (Weglein and Amundsen, 2003).

Fourier transform equation 10 and you produce an algebra problem. In equation 10 the derivative is inside the integral, and you have to invert a Fredholm one integral equation, which is often unstable. Fourier transform and suddenly you have no integrals; the integrals have become products (the Fourier transform has diagonalized the problem). Once you have P', you can calculate P_0 (which is an effective reference wave with a source signature and a radiation pattern).

From Weglein and Secrest (1990) we know that

$$\Big|_a^b \left\{ P\frac{dG_0^+}{dz'} - G_0^+\frac{dP}{dz'} \right\} = \begin{cases} -P_s \\ {\scriptstyle above\ z=a} \\ P_0 \\ {\scriptstyle below\ z=a} \end{cases} \tag{19}$$

This is a 1D formula or the Fourier transform of the multi-D formula equation 10. Equation 10 in 1D normal incidence becomes equation 19, or Fourier transform equation 10 over x to get equation 19.

In the example, a is on the measurement surface on the surface of the earth, b is below a, and z_s is above a. The output point is above a or below a. Later in this example, we will make z_s on the surface of the earth, and our output point will be on a, as well. In the world of a whole space of water, the output point above a gives P_s and below a gives P_0. And in this simple world, separating P_0 and P_s is also deghosting, because it is the same $G_0^+ = G_0^{d+}$. (For deghosting pick $G_0^+ = G_0^{d+}$. In general, deghosting and wavefield separation are not the same.) There is no P_s because there is no up going wave anywhere, including above $z = a$. The source wave is moving down so deghosting gives zero.

When we want to compute something where: (1) the source is on the measurement surface, and (2) we want to calculate P_s and P_0 in the data/on the cable. But we can't do that in the $\vec{r}, \omega$ domain. Equation 10 makes you stay above the cable (by an amount that depends on sampling), whereas $P - V_z$ has in principle perfect sampling (Δx is zero).

For transparency we consider the 1D normal incidence example. In equation 19

$$P = \frac{\exp\left(ik|z' - z_s|\right)}{2ik}$$
$$\frac{dP}{dz'} = ik\frac{\exp\left(ik|z' - z_s|\right)}{2ik} sgn(z' - z_s)$$
$$G_0 = \frac{\exp\left(ik|z - z'|\right)}{2ik}$$
$$\frac{dG_0}{dz'} = \frac{ik\, sgn(z' - z)}{2ik} \exp\left(ik|z - z'|\right)$$
$$\Big|_a^b \left\{ \frac{\exp\left(ik|z' - z_s|\right)}{2ik} \left\{ \frac{sgn(z' - z)}{2} \exp\left(ik|z - z'|\right) \right\} - \frac{\exp\left(ik|z - z'|\right)}{2ik} \frac{1}{2} \exp\left(ik|z' - z_s|\right) sgn(z' - z_s) \right\}.$$

Evaluate at $a < z < b$. a will contribute and b won't contribute. This is shown below.

$$\frac{\exp\left(ik(b - z_s)\right)}{2ik} \overbrace{\frac{sgn(b - z)}{2}}^{1} \exp\left(ik(b - z)\right) - \frac{\exp\left(ik(b - z)\right)}{2ik} \frac{1}{2} \exp\left(ik(b - z_s)\right) \overbrace{sgn(b - z_s)}^{1}$$

$$-\left\{\frac{\exp\left(ik(a-z_s)\right)}{2ik}\overbrace{\frac{sgn(a-z)}{2}}^{-1}\exp\left(ik(z-a)\right)-\frac{\exp\left(ik(z-a)\right)}{2ik}\frac{1}{2}\exp\left(ik(a-z_s)\right)\overbrace{sgn(a-z_s)}^{1}\right\} \tag{20}$$

$$=\underbrace{\frac{\exp\left(ik(b-z_s)\right)}{2ik}\frac{1}{2}\exp\left(ik(b-z)\right)-\frac{\exp\left(ik(b-z)\right)}{2ik}\frac{1}{2}\exp\left(ik(b-z_s)\right)}_{=0}$$

$$-\left\{\frac{\exp\left(ik(a-z_s)\right)}{2ik}\frac{-1}{2}\exp\left(ik(z-a)\right)-\frac{\exp\left(ik(z-a)\right)}{2ik}\frac{1}{2}\exp\left(ik(a-z_s)\right)\right\}$$

$$=\frac{1}{2ik}\exp\left(ik(z-z_s)\right)=P=P_0$$

There is no contribution from b. The terms with b's cancel, and $P=P_0$ because the reference wave is the total wavefield. If we evaluate at $z_s<z<a$, the total contribution is zero because $P_0=P$ and $P_s=0$.

What do you do when you put the source on the cable? Fourier transforming into a k_x,ω form avoids the $\Delta z\geq 1/2\,\Delta x$ restriction because it begins with $P(k_x,z',x_s,z_s,\omega)$. No integral is left for x. The only question is where do you choose the output point, z? If you want to deghost on the cable, Fourier transform over x and use the $P-V_z$ forms. The Dirac delta function properties are:

$$\int_V \delta(\vec{r}-\vec{r}')f(\vec{r}')d\vec{r}'=\begin{cases} f(\vec{r}) & \vec{r}\text{ in V} \\ 0 & \vec{r}\text{ outside of V.}\end{cases}$$

The application of Green's theorem methods to either the source or output point on the surface (the measurement surface) boils down to the question of what is $\int_V \delta(\vec{r}-\vec{r}')f(\vec{r}')d\vec{r}'$ when $\vec{r}$ is on the surface enclosing V. You can choose whether it's in or out of V (Morse and Feshbach, 1953, page 805). In our example above, evaluate at a, when the source is on the cable ($sgn(z'-z_s)=sgn(0)$), and if you want the source on the cable to be treated as the source above the cable, then choose $sgn(a-z_s)=1$ with $z_s=a$. For the output point, when $z=a$ (predict at the cable), if we want the same sign as when $z>a$, choose $sgn(a-z)=-1$ when $z=a$. If you want the output point when it is on the surface (measurement surface) to be included with points above the cable choose $sgn(a-z)=+1$ when $z=a$.

So our choice of sgns will give P_0 or P_s on the cable, depending on whether you choose the cable to be included with the region below or above the cable, respectively. You're deciding whether the boundary is inside or outside the volume. You can't arrange this in equation 10 because you can't get to the boundary, at least not while keeping the algorithm stable.

The bottom line here is for land you can't get close enough (to the boundary) to make a decision in equation 10. This is not true if you go to the Fourier k_x,ω domain. But there is no free lunch. If Δx gets too big, $P(k_x,z,\omega)$ becomes inaccurate, and $P-V_z$ can have issues.

6 Summary

x,ω methods for wave separation have advantages compared to k_x,ω for limited data (sampling and aperture) and for non horizontal measurement surfaces (ocean bottom, dipping cable). For

applications where the interest is in wave separation on the cable itself and where the source is on the measurement surface (on-shore) k_x, ω would accommodate that interest whereas x, ω (Green's theorem) will not. This paper is examining the implication/differences of a Green's theorem method of deghosting in two domains: (x, ω) and (k_x, ω). Substituting V_z for P_n, in the (k_x, ω) domain, and benefits/limitations that arise from that substitution (while important) are not within the scope of this paper.

7 Acknowledgement

We thank the M-OSRP sponsors for their encouragement and support. We would like to thank Clark Trantham and Mamadou Diallo of ExxonMobil for stimulating discussions that motivated and encouraged this study.

References

Amundsen, Lasse. "Wavenumber-based filtering of marine point-source data." Geophysics 58 (1993): 1335–1348.

Amundsen, Lasse, Arthur B. Weglein, and Arne Reitan. "On seismic deghosting using integral representation for the wave equation: Use of Green's functions with Neumann or Dirichlet boundary conditions." accepted for publication 05-Apr-2013. Geophysics (2013).

Corrigan, D., A. B. Weglein, and D. D. Thompson. 1991 "Method and apparatus for seismic survey including using vertical gradient estimation to separate downgoing seismic wavefields.". US Patent number 5051961.

Mayhan, James D., Paolo Terenghi, Arthur B. Weglein, and Nizar Chemingui. "Green's theorem derived methods for preprocessing seismic data when the pressure P and its normal derivative are measured." 81st Annual International Meeting, SEG, Expanded Abstracts. Society of Exploration Geophysicists, 2011, 2722–2726.

Mayhan, James D. and Arthur B. Weglein. "First application of Green's theorem-derived source and receiver deghosting on deep-water Gulf of Mexico synthetic (SEAM) and field data." Geophysics 78 (March 2013): WA77–WA89.

Mayhan, James D., Arthur B. Weglein, and Paolo Terenghi. "First application of Green's theorem derived source and receiver deghosting on deep water Gulf of Mexico synthetic (SEAM) and field data." 82nd Annual International Meeting, SEG, Expanded Abstracts. Society of Exploration Geophysicists, 2012, 1–5.

Morse, P. M. and H. Feshbach. Methods of theoretical physics. New York: McGraw-Hill Book Co., 1953.

Tang, Lin, James D. Mayhan, Jinlong Yang, and Arthur B. Weglein. "Using GreenŠs theorem to satisfy data requirements of multiple removal methods: The impact of acquisition design." 83rd Annual International Meeting, SEG, Expanded Abstracts. Submitted April 3, 2013, Society of Exploration Geophysicists, 2013, TBD.

Weglein, A. B., F. V. Araújo, P. M. Carvalho, R. H. Stolt, K. H. Matson, R. T. Coates, D. Corrigan, D. J. Foster, S. A. Shaw, and H. Zhang. "Inverse Scattering Series and Seismic Exploration." Inverse Problems 19 (2003): R27–R83.

Weglein, Arthur B. and Lasse Amundsen. "Short note: G_0^{D0} and G_0^D integral equations relationships; The triangle relation is intact." M-OSRP 2002 Annual Report. 2003, 32–35.

Weglein, Arthur B. and Bruce G. Secrest. "Wavelet estimation for a multidimensional acoustic earth model." Geophysics 55 (July 1990): 902–913.

Weglein, Arthur B., S. A. Shaw, K. H. Matson, J. L. Sheiman, R. H. Stolt, T. H. Tan, A. Osen, G. P. Correa, K. A. Innanen, Z. Guo, and J. Zhang. "New approaches to deghosting towed-streamer and ocean-bottom pressure measurements." 72nd Annual International Meeting, SEG, Expanded Abstracts. Society of Exploration Geophysicists, 2002, 2114–2117.

Wu, Jing, Arthur B.Weglein, and James D. Mayhan. "Comparison and analysis of space and temporal frequency, and, spatial wave-number and temporal frequency (e.g., P-Vz) Green's theorem de-ghosting methods, with different receiver spacing and aperture: Implications for 3 D de-ghosting." M-OSRP 2012 Annual Report. 2013, 99–104.

Zhang, Jingfeng. Wave theory based data preparation for inverse scattering multiple removal, depth imaging and parameter estimation: analysis and numerical tests of Green's theorem deghosting theory. PhD thesis, University of Houston, 2007.

Zhang, Jingfeng and Arthur B. Weglein. "Extinction theorem deghosting method using towed streamer pressure data: analysis of the receiver array effect on deghosting and subsequent free surface multiple removal." 75th Annual International Meeting, SEG, Expanded Abstracts. Society of Exploration Geophysicists, 2005, 2095–2098.

Zhang, Jingfeng and Arthur B. Weglein. "Application of extinction theorem deghosting method on ocean bottom data." 76th Annual International Meeting, SEG, Expanded Abstracts. Society of Exploration Geophysicists, 2006, 2674–2678.

A new Green's theorem de-ghosting method that simultaneously: (1) avoids a finite difference approximation for the normal derivative of the pressure and, (2) avoids the need for replacing the normal derivative of pressure with the vertical component of particle velocity, thereby avoiding issues that can arise within each of those two assumptions/approaches: Theory and analytic and numeric examples.

Arthur B. Weglein, Hong Liang, Jing Wu, James D. Mayhan, and Lin Tang
April 28, 2013
M-OSRP/Physics Dept./UH

April 29, 2013

Abstract

Green's theorem deghosting requires the pressure and its normal derivative on a cable. Current marine dual measurement deghosting approaches can have issues caused by: (1) using over-under cable pressure measurements to provide a finite difference approximation to the normal derivative; or (2) using the pressure, P, and the vertical component of particle velocity, V_z, can have issues at low frequency, and with instrument response differences. The deghosting method provided in this paper avoids both of those issues. Analytic and numerical tests show encouraging results, in comparison with current approaches.

1 Theory

We show in Weglein et al. (2013) that a two way wavefield in a homogeneous medium can be written

$$P = A\exp(iqz) + B\exp(-iqz), \tag{1}$$

where $q = +\sqrt{(\omega/c_0)^2 - k_x^2}$ (2D) or $q = +\sqrt{(\omega/c_0)^2 - k_x^2 - k_y^2}$ (3D). If an over/under cable at depths a, b is used directly, the upwave (deghosted wave) is

$$P_r = B\exp(-iqz) = \frac{P(b)\exp(iqa) - P(a)\exp(iqb)}{2i\sin(q(a-b))}\exp(-iqz). \tag{2}$$

Equation 2 is found by using the cable measurements to solve for B in equation 1:

$$B = \frac{\begin{vmatrix}\exp(iqa) & P(a)\\ \exp(iqb) & P(b)\end{vmatrix}}{\begin{vmatrix}\exp(iqa) & \exp(-iqa)\\ \exp(iqb) & \exp(-iqb)\end{vmatrix}}$$

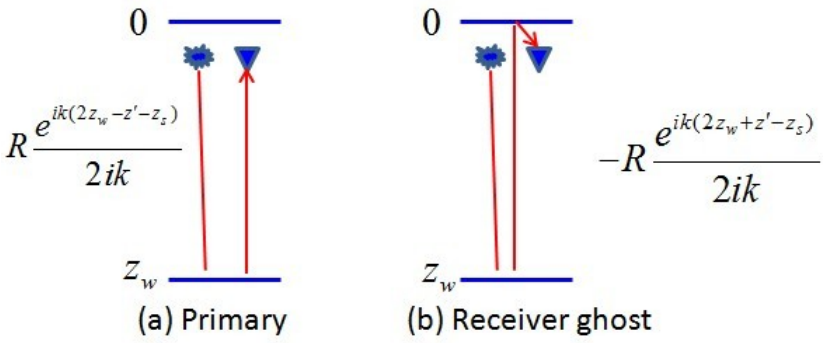

Figure 1: 1D normal incidence analytic data including one primary and one receiver ghost.

$$= \frac{P(b)\exp(iqa) - P(a)\exp(iqb)}{\exp(iq(a-b)) - \exp(-iq(a-b))}$$
$$= \frac{P(b)\exp(iqa) - P(a)\exp(iqb)}{2i\sin(q(a-b))}.$$

Equation 2 assumes sufficient inline and crossline sampling for a Fourier transform from $\vec{r}, \omega$ to $\vec{k}, \omega$. Equation 2 has ghost notches when $q(a-b) = n\pi$, where special care must be taken. On the other hand, $a-b$ may be smaller than the depth of a single cable, which means the ghost notches move out (to higher frequencies).

2 Analytic example

2.1 Analytic data including one primary and one receiver ghost

For a 1D normal incidence case, as shown in Figure 1, assume the recorded data at z' is

$$P(z', z_s, \omega) = R \times \frac{e^{ik(2z_w - z' - z_s)}}{2ik} - R \times \frac{e^{ik(2z_w + z' - z_s)}}{2ik}$$
$$= R\frac{e^{ik(2z_w - z_s)}}{2ik}(e^{-ikz'} - e^{ikz'}), \tag{3}$$

where z', z_s, and z_w are the depths of receiver, source and water bottom, respectively, and $k = \omega/c_0$. Therefore, the exact derivative of the wavefield at z' is

$$P'(z', z_s, \omega) = R\frac{e^{ik(2z_w - z_s)}}{2ik}(-ike^{-ikz'} - ike^{ikz'})$$
$$= -\frac{R}{2}e^{ik(2z_w - z_s)}(e^{-ikz'} + e^{ikz'}). \tag{4}$$

2.2 Up-down separation using two measurement at two depths

Consider a simple 1D normal incidence example, where in the vicinity of the (towed streamer) cable the pressure field P satisfies:

$$\left[\frac{\partial^2}{\partial z^2} - \frac{1}{c_0^2}\frac{\partial^2}{\partial t^2}\right] P = 0, \tag{5}$$

where c_0 is the wave speed in water, and

$$\left[\frac{d^2}{dz^2} + \frac{\omega^2}{c_0^2}\right] P = 0 \tag{6}$$

is the temporal Fourier transform of equation 5.

The solution of equation 6 is

$$P = \underbrace{Ae^{(ikz)}}_{down} + \underbrace{Be^{(-ikz)}}_{up}, \tag{7}$$

Using two measurement at two depths

$$P(a) = Ae^{ika} + Be^{-ika}, \tag{8a}$$
$$P(b) = Ae^{ikb} + Be^{-ikb}. \tag{8b}$$

By multiplying equation 8a with $e^{ik(b-a)}$ and subtracting equation 8b, we get

$$e^{ik(b-a)}P(a) - P(b) = Be^{ik(b-2a)} - Be^{-ikb}$$
$$B = \frac{e^{ik(b-a)}P(a) - P(b)}{e^{ik(b-2a)} - e^{-ikb}}. \tag{9}$$

Therefore, the upgoing wave at $z' = a$ is

$$P_r(a) = Be^{-ika}$$
$$= \frac{e^{ik(b-2a)}P(a) - e^{-ika}P(b)}{e^{ik(b-2a)} - e^{-ikb}}. \tag{10}$$

From equation 3, we can get the two measurements, i.e., $P(z' = a, z_s, \omega)$ and $P(z' = b, z_s, \omega)$, as follows:

$$P(a, z_s, \omega) = R\frac{e^{ik(2z_w - z_s)}}{2ik}(e^{-ika} - e^{ika}), \tag{11a}$$
$$P(b, z_s, \omega) = R\frac{e^{ik(2z_w - z_s)}}{2ik}(e^{-ikb} - e^{ikb}). \tag{11b}$$

and then substituting equations 11a and 11b into equation 10, we get

$$
\begin{aligned}
P_r(a) &= \frac{Re^{ik(2z_w-z_s)}[(e^{-ika}-e^{ika})\times e^{ik(b-2a)}-(e^{-ikb}-e^{ikb})\times e^{-ika}]}{2ik[e^{ik(b-2a)}-e^{-ikb}]} \\
&= \frac{Re^{ik(2z_w-z_s)}[e^{ik(b-3a)}-e^{ik(b-a)}-e^{-ik(b+a)}+e^{ik(b-a)}]}{2ik[e^{ik(b-2a)}-e^{-ikb}]} \\
&= \frac{Re^{ik(2z_w-z_s)}[e^{ik(b-3a)}-e^{-ik(b+a)}]}{2ik[e^{ik(b-2a)}-e^{-ikb}]} \\
&= \frac{Re^{ik(2z_w-z_s)}e^{-ika}[e^{ik(b-2a)}-e^{-ikb}]}{2ik[e^{ik(b-2a)}-e^{-ikb}]} \\
&= \frac{Re^{ik(2z_w-z_s)}e^{-ika}}{2ik} \\
&= R\frac{e^{ik(2z_w-a-z_s)}}{2ik}.
\end{aligned} \tag{12}
$$

This is exactly the upgoing wave recorded at $z' = a$ with source at z_s (in this case, is the primary).

2.3 Up-down separation using wave-field and the exact derivative of wave-field at one depth

For equation 7, if we have the wave-field and the exact derivative of the wave-field at one depth, then

$$P(a) = Ae^{ika} + Be^{-ika}, \tag{13a}$$

$$P'(a) = ikAe^{ika} - ikBe^{-ika}. \tag{13b}$$

By multiplying equation 13a with ik and subtracting equation 13b, we have

$$
\begin{aligned}
ikP(a) - P'(a) &= ikBe^{-ika} + ikBe^{-ika} \\
B &= \frac{ikP(a)-P'(a)}{2ik}e^{ika}.
\end{aligned} \tag{14}
$$

Therefore, the upgoing wave at $z' = a$ is

$$
\begin{aligned}
P_r(a) &= Be^{-ika} \\
&= \frac{ikP(a)-P'(a)}{2ik}.
\end{aligned} \tag{15}
$$

Substituting $P(a)$ and $P'(a)$ (using equations 3 and 4) into equation 15, we have

$$P_r(a) = \frac{ikP(a)-P'(a)}{2ik}$$

$$
\begin{aligned}
&= \frac{ikR\frac{e^{ik(2z_w-z_s)}}{2ik}(e^{-ika}-e^{ika}) - [-\frac{R}{2}e^{ik(2z_w-z_s)}(e^{-ika}+e^{ika})]}{2ik} \\
&= \frac{Re^{ik(2z_w-z_s)}e^{-ika}}{2ik} \\
&= \frac{Re^{ik(2z_w-a-z_s)}}{2ik},
\end{aligned} \tag{16}
$$

which is the same result as equation 12.

2.4 Up-down separation using wave-field and approximate derivative of wave-field at one depth

If we have two measurements at two depths, we can also get the approximate derivative of the wave-field using finite difference, for example,

$$
P'(a) = \frac{P(b)-P(a)}{b-a}. \tag{17}
$$

Substituting $P(b)$ in equation 11b and $P(a)$ in equation 11a into equation 17, we can have

$$
\begin{aligned}
P'(a,z_s,\omega) &= \frac{Re^{ik(2z_w-z_s)}}{2ik} \times \frac{(e^{-ikb}-e^{ikb})-(e^{-ika}-e^{ika})}{b-a} \\
&= \frac{Re^{ik(2z_w-z_s)}}{2ik} \times \frac{-2i\sin(kb)+2i\sin(ka)}{b-a} \\
&= -Re^{ik(2z_w-z_s)} \times \frac{\sin(kb)-\sin(ka)}{k(b-a)}.
\end{aligned} \tag{18}
$$

In comparison, the exact derivative of the wave-field in equation 4 at $z'=a$ can be rewritten as

$$
\begin{aligned}
P'(a,z_s,\omega) &= -\frac{R}{2}e^{ik(2z_w-z_s)}(e^{-ika}+e^{ika}) \\
&= -\frac{R}{2}e^{ik(2z_w-z_s)} \times 2\cos(ka) \\
&= -Re^{ik(2z_w-z_s)}\cos(ka) \\
&= -Re^{ik(2z_w-z_s)}\frac{d\sin(kz')}{kdz'}\bigg|_{z'=a}.
\end{aligned} \tag{19}
$$

And, we have

$$
\frac{d\sin(kz')}{kdz'} = \lim_{(b-a)\to 0}\frac{\sin(kb)-\sin(ka)}{k(b-a)}
$$

$$= \cos(ka). \tag{20}$$

Hence, if the two depths (b and a) are close enough, equation 18 will reduce to equation 19, and using wave-field and approximate derivative of wave-field at one depth in equation 15 can give a reasonable result; otherwise, using the approximate derivative in equation 15 can produce an error.

The method developed in this paper can be derived from Green's theorem, where the closed surface consists of the over/under cables and the Green's function is arranged to vanish at each cable. In the k_x, ω domain the Green's theorem method comes closest to the 1D analysis in this paper, and would allow deghosting on the cable.

3 Numerical examples

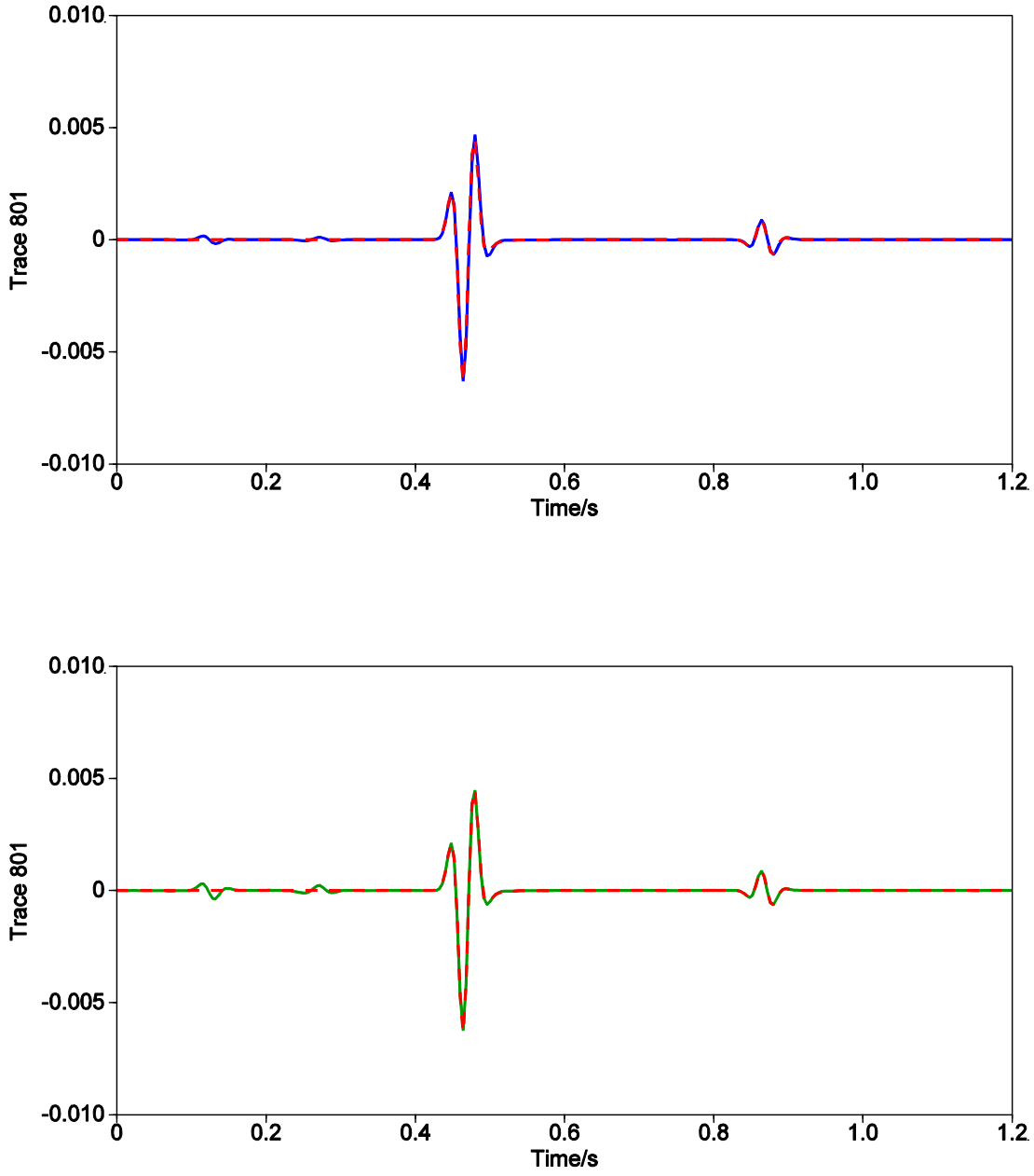

Figure 2: *Two cables: (a) source depth 7m receiver depth 11m, spatial sampling interval 3m, trace number 801 (zero offset trace). (b) source depth 7m receiver depth 9m, spatial sampling interval 3m, trace number 801. Using this two data get dp/dz and put it on 11m. Predicted depth is 11m. Red line represents the data generated by using Cagniard-de Hoop method, exact data without receiver side ghosts, depth is 11m. Blue line represents result using dp/dz. Green line represents result using the cables directly.*

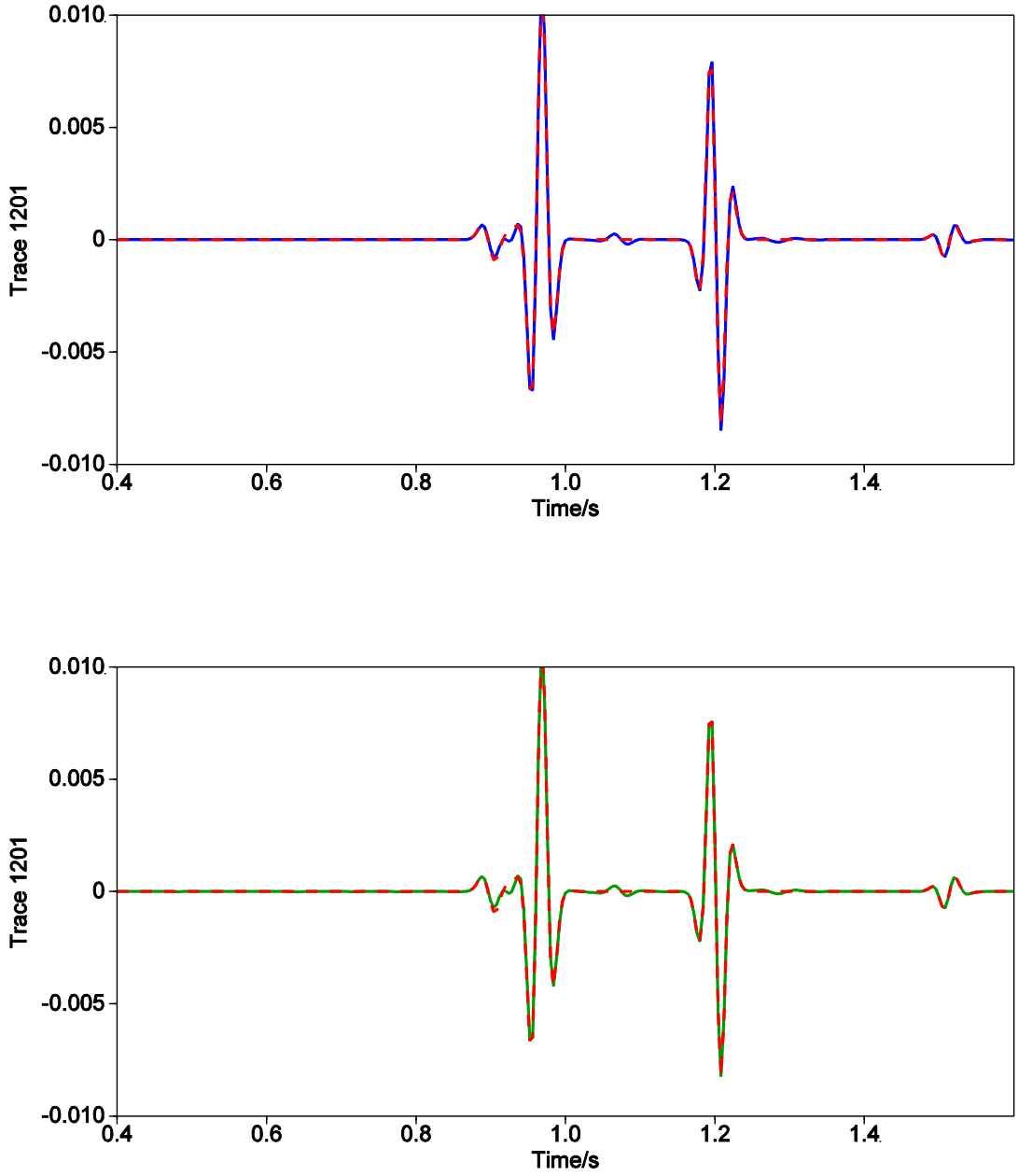

Figure 3: *Same as Figure 2 except trace 1201 (half way between zero offset trace and far offset trace).*

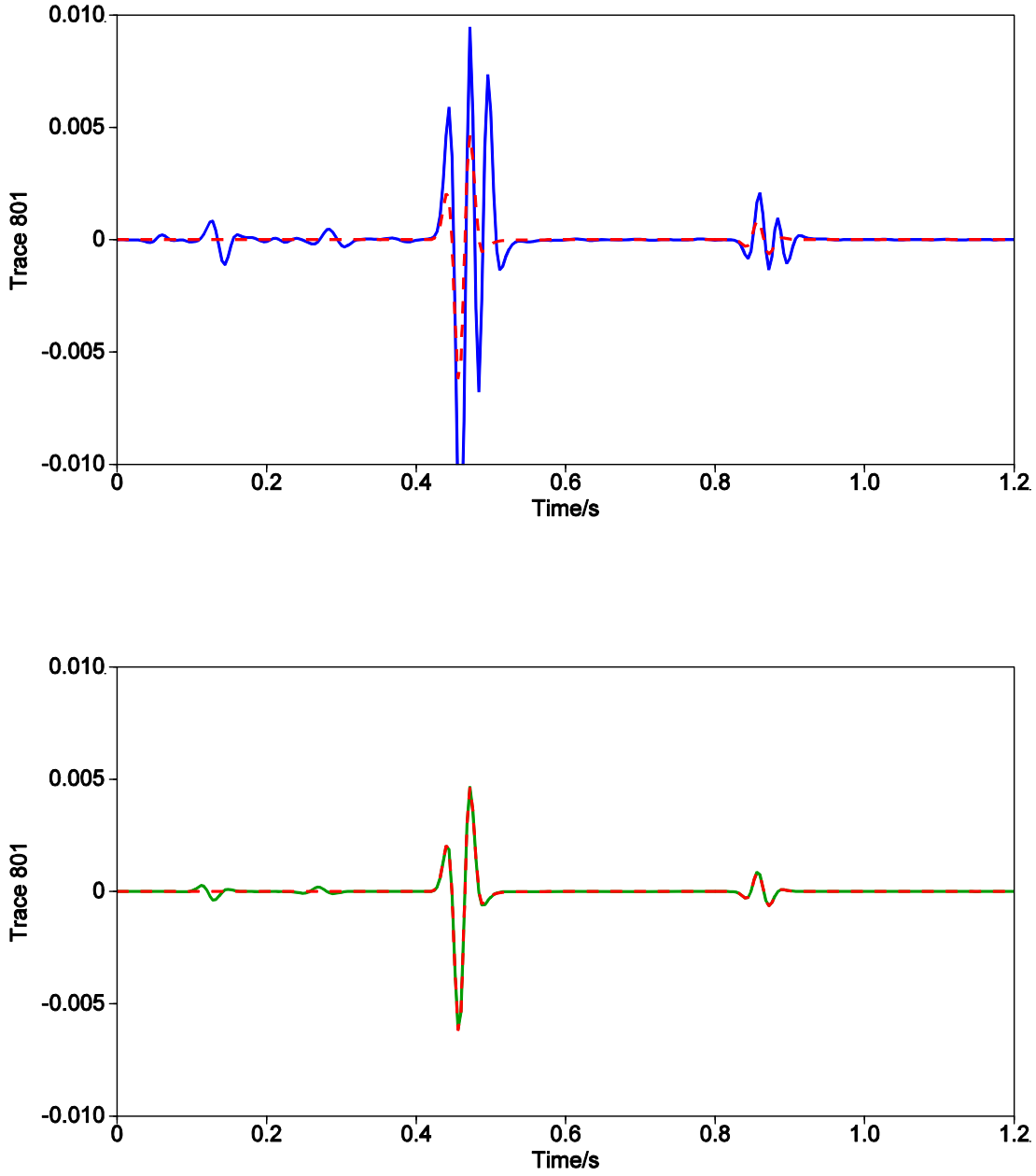

Figure 4: *Two cables: (a) source depth 7m receiver depth 21m, spatial sampling interval 3m, trace number 801 (zero offset trace). (b) source depth 7m receiver depth 11m, spatial sampling interval 3m, trace number 801. Using this two data get dp/dz and put it on 21m. Predicted depth is 21m. Red line represents the data generated by using Cagniard-de Hoop method, exact data without receiver side ghosts, depth is 21m. Blue line represents result using dp/dz Green line represents result using the cables directly.*

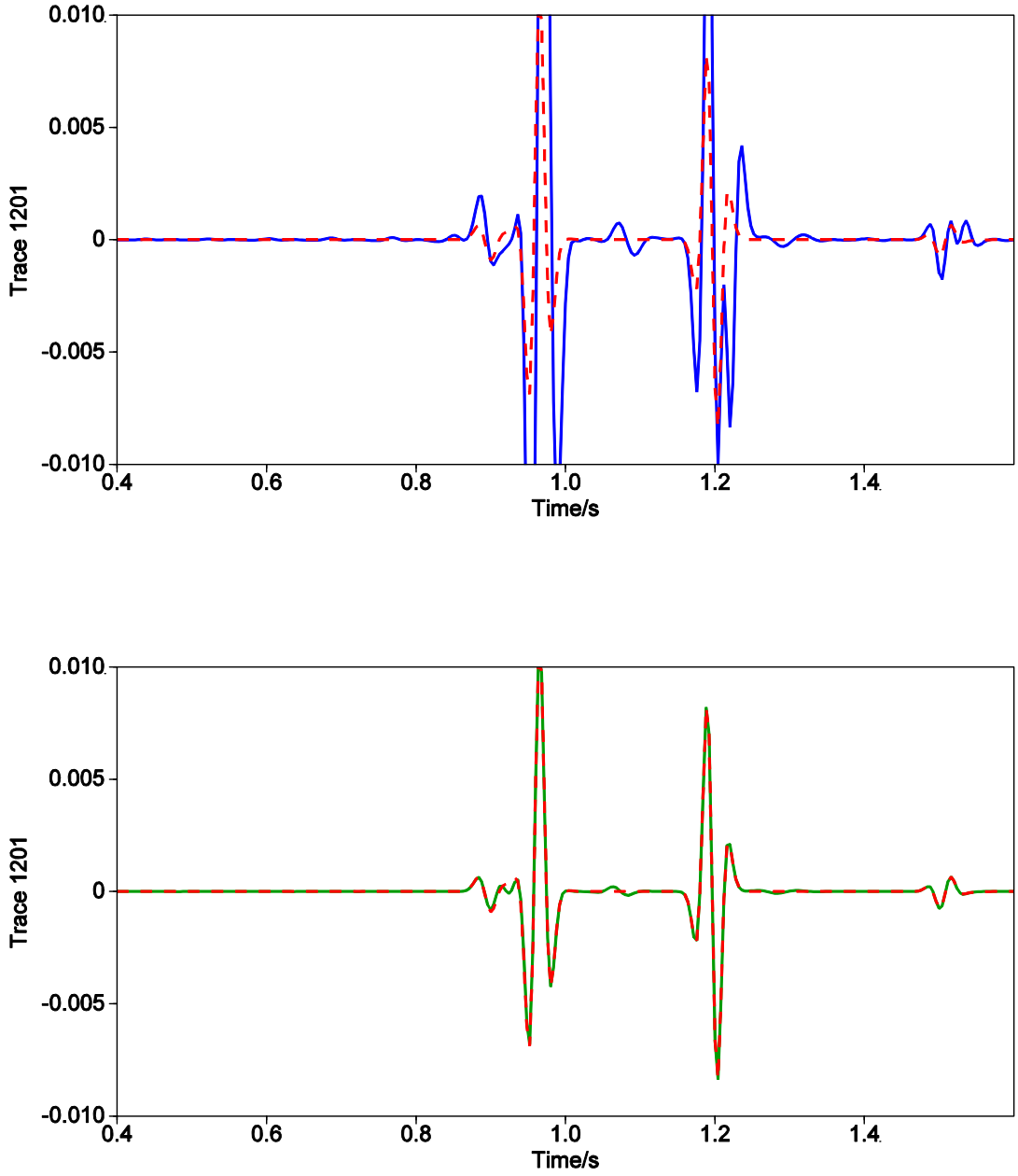

Figure 5: *Same as Figure 4 except trace 1201 (half way between zero offset trace and far offset trace).*

4 Summary

A new deghosting method is proposed, for dual cable measurements, that addresses shortcomings in current approaches. Analytic and numerical examples are encouraging, and further tests are planned.

References

Weglein, Arthur B., James D. Mayhan, Lasse Amundsen, and Hong Liang. "Green's theorem de-ghosting algorithms in the k, ω (e.g., $P-V_z$ de-ghosting) as a special case of x, ω algorithms (based on Green's theorem) with: (1) significant practical advantages and disadvantages of algorithms in each domain, and (2) a new message, implication and opportunity for marine towed streamer, ocean bottom and on-shore acquisition and applications.." M-OSRP 2012 Annual Report. 2013, 7–19.

Green's theorem for source and receiver de-ghosting with Cagniard-de Hoop, SEAM, and field data tests and impact on multiple attenuation

James D. Mayhan and Arthur B. Weglein

April 29, 2013

Abstract

Deghosting benefits traditional seismic processing and is a prerequisite to all inverse-scattering-series (ISS) based processing. The freedom of choosing a convenient reference medium (and associated Green's function) means Green's theorem offers a flexible framework for deriving a number of useful algorithms including deghosting. Among the advantages of GreenâĂŹs theorem deghosting over traditional deghosting methods are: (1) there is no need for Fourier transforms over receivers and sources, and (2) GreenâĂŹs theorem deghosting can accommodate a horizontal or non-horizontal measurement surface, the latter being of particular interest for ocean-bottom and on-shore applications. A brief tutorial is presented on the theory of Green's theorem-derived deghosting, and several properties of Green's theorem-derived deghosting are discussed. Deghosting is illustrated with images before and after receiver deghosting for separated data (where the source and receivers are deep enough to separate events and their ghosts), partially interfering events, and overlapping events. The advantages and disadvantages of each kind of cable configuration are listed. Green's theorem-derived deghosting is insensitive to cable depth, gives better results as the vertical distance between over and under cables decreases, and (for wavefield prediction) is sensitive to the presence of ghost notches in the data. Green's theorem-derived deghosting has fewer requirements than does wavenumber-based deghosting.

1 Introduction

Deghosting is a long-standing problem (see, e.g., Robinson and Treitel (2008)) and benefits both traditional seismic processing and all inverse-scattering-series (ISS)-based processing. The benefits of deghosting include the facts that: (1) removal of the downward component of the recorded pressure wavefield (receiver deghosting) enhances seismic resolution by removing ghost notches and boosting low frequencies, (2) deghosting is a prerequisite for many processing algorithms, including multiple elimination (ISS free-surface multiples, ISS internal multiples, and surface-related-multiple elimination (SRME)), and (3) model-matching full-wave inversion (FWI) benefits from enhanced low-frequency data.

While ISS methods are independent of subsurface velocity (and in fact of all subsurface properties), they make certain assumptions about their input data. Weglein et al. (2003) describe how every ISS isolated-task subseries requires (1) the removal of the reference wavefield, (2) an estimate of

the source signature and radiation pattern, and (3) source and receiver deghosting, and they also explain how the ISS has a nonlinear dependence on these preprocessing steps. The fact that the ISS is nonlinear places a higher premium on preprocessing requirements. An error in the input to a linear process creates a linear error in its output, but the same linear error in ISS input creates a combination of linear, quadratic, cubic, etc. errors in its output. The non-linear model matching FWI would share that interest.

The freedom of choosing a convenient reference medium (and associated Green's function) means that Green's theorem offers a flexible framework for deriving a number of useful algorithms. Green's theorem methods can be categorized as wavefield-prediction or wavefield-separation methods. In order to predict the wavefield anywhere in a volume V, Green's theorem-based wavefield prediction has the traditional need for (a) wavefield measurements on the boundary S enclosing V and (b) a knowledge of the medium throughout V. Examples of wavefield prediction based on Green's theorem include Schneider (1978), Clayton and Stolt (1981), Stolt and Weglein (2012), and reverse time migration (RTM) (Weglein et al., 2011a;b). In contrast, Green's theorem-based wavefield separation only assumes separate sources inside and outside V, and nothing about the character of those sources is called for or needed. Within wavefield separation, different applications (e.g., wavelet estimation and deghosting) call for different choices of reference media and sources. Examples of wavefield separation based on Green's theorem include source-wavelet estimation (Weglein and Secrest, 1990) and deghosting (Weglein et al., 2002; Zhang and Weglein, 2005; 2006; Zhang, 2007). In Green's theorem wavefield-separation methods, evaluation of the surface integral at a point inside V provides the contribution to the total field at a point inside V due to sources outside V, without needing or determining the nature or properties of any of the actual (active or passive) sources inside or outside V. Hence, Green's theorem-derived wavefield-separation preprocessing steps (e.g., for wavelet estimation and deghosting) are consistent with subsequent ISS processing methods that also do not assume knowledge of or require subsurface information. The Green's theorem wavefield-prediction and wavefield-separation methods are multidimensional and work in the $(\mathbf{r}, \omega)$ or $(\mathbf{r}, t)$ data spaces (and, hence, are simple to apply to irregularly spaced data).

Green's theorem-derived deghosting was developed in a series of papers (Weglein et al., 2002; Zhang and Weglein, 2005; 2006; Zhang, 2007) and has characteristics not shared by previous methods. For example, there is no need for Fourier transforms over receivers and sources, and it can accommodate a horizontal or non-horizontal measurement surface. In Mayhan et al. (2011), we reported the first use of Green's theorem-derived receiver deghosting on deep-water Gulf of Mexico synthetic (SEAM) and field data; in Mayhan et al. (2012), we reported the first use of Green's theorem-derived source deghosting on the same data; and in this paper we provide more detail on the algorithms used.

A brief aside on our terminology. (1) The total wavefield P measured by the hydrophones is considered as the sum of a reference wavefield P_0 (which for a homogeneous whole space reference medium (used in Green's theorem deghosting) is a direct wave from source to receiver) and the scattered wavefield P_s (which is $P - P_0$). (2) Ghosts begin their propagation moving upward from the source (source ghosts) or end their propagation moving downward to the receiver (receiver ghosts) or both (source/receiver ghosts) and have at least one upward reflection from the earth. After the reference wavefield and all ghosts have been removed, multiples and primaries are defined. (3) Free-surface multiples have at least one downward reflection from the air/water boundary and more than one upward reflection from the earth. (An nth-order free-surface multiple has n downward reflections from the air/water boundary.) (4) Internal multiples have no downward reflections from

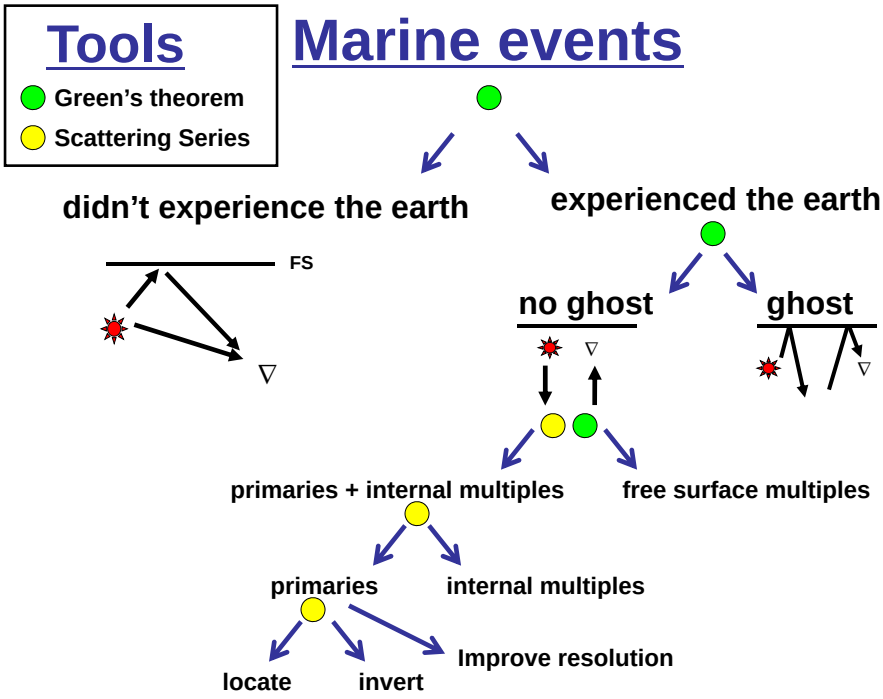

Figure 1: *Classification of marine events and how they are processed by M-OSRP's methodology.*

the air/water boundary, more than one upward reflection from the earth, and at least one downward reflection from inside the earth. (An nth-order internal multiple has n downward reflections from any reflector(s) inside the earth.) (5) Primaries have only one upward reflection from the earth. These marine events are summarized in Figure 1.

The source- and receiver-deghosting steps described below essentially follow the method described and exemplified in pages 33-39 of Zhang (2007). The difference is that for each shot we choose to input dual measurements of P and $\partial P/\partial z$ along the towed streamer, whereas Zhang chose to use the source wavelet and P along the cable for his numerical examples. (The theory in Zhang (2007) covers both cases.) The advantages of having the wavefield P and its normal derivative along the towed streamer are (1) to allow deghosting for an arbitrary source distribution without needing to know or to determine the source, and (2) to increase stability in the vicinity of notches. Using measurements at two depths (or G_0^{DD}, as described below) introduces a depth-sensitive denominator.

2 Tutorial on Green's theorem-derived deghosting

2.1 Receiver deghosting

Green's theorem-derived-preprocessing is based on a perturbation approach in which the actual problem and medium are considered to be composed of a reference medium plus "sources." The latter arise as source terms in the differential equation that describes the wave propagation in the actual medium. A reference medium (and its associated Green's function) is chosen to facilitate solving the problem at hand, and the perturbations are represented as source terms necessary to write the actual propagation in terms of a reference-medium source-term picture. Within that general reference-medium and source-term framework, Green's theorem-derived preprocessing is remarkably wide ranging. For example, Figure 2 shows the configuration chosen for Green's theorem-derived deghosting. For deghosting, a reference medium that consists of a whole space of water requires three source terms: a source that corresponds to air and begins above the air-water boundary, the air guns in the water column, and a source that corresponds to earth and begins below the water-earth boundary. Choosing a hemispherical surface of integration bounded below by the measurement surface, and the prediction or observation point inside the surface of integration, gives receiver-deghosted data, P'_R (as explained in Appendix 11.1). A different choice of a reference medium (a half space of air and a half space of water, separated by an air/water boundary with two source terms), is useful for separating the reference wave P_0 ($P_0^d + P_0^{FS}$) and $P_s = P - P_0$. The prediction or observation point outside or inside the surface of integration gives wavefield separation in which the total wavefield P is separated into the reference wavefield P_0 (prediction or observation point outside) or the scattered wavefield P_s (prediction or observation point inside).

Green's theorem-derived deghosting (of both receiver and source) is based on Weglein et al. (2002), Zhang and Weglein (2005), Zhang and Weglein (2006), and Zhang (2007). Depending on the marine experiment, we have the following options for receiver deghosting. (1) If we have P measurements only, we can use a derived variation of Green's theorem (equation 3), a "double Dirichlet" Green's function (equation 7 or 8), and an estimate of the source wavelet to predict P and $\partial P/\partial z$ above the towed streamer(s). Then we can use the derived variation of Green's theorem, a "whole space" Green's function (equation 1), and the predicted P and $\partial P/\partial z$ to predict receiver-deghosted P'_R above the input P and $\partial P/\partial z$. (2) If we have a dual-sensor towed streamer or over/under towed streamers, we can use the derived variation of Green's theorem and a whole-space Green's function to directly predict receiver-deghosted P'_R above the towed streamer(s). The theory of case (2) assumes measurement of the pressure wavefield P and its normal derivative $\partial P/\partial n \equiv \nabla P(\mathbf{r}, \mathbf{r}_s, \omega) \cdot \hat{\mathbf{n}}$ where $\mathbf{r}$ is the receiver location, $\mathbf{r}_s$ is the source location, and $\hat{\mathbf{n}}$ is the unit normal to the measurement surface (pointing away from the enclosed volume V).

The reference medium is chosen to be a whole space of water (where a causal solution exists for the acoustic wave equation in 3D). In the $(\mathbf{r}, \omega)$ domain the causal whole-space Green's function is

$$G_0(\mathbf{r}, \mathbf{r}'_g, \omega) = G_0^d = \begin{cases} -(1/4\pi)\exp(ikR_+)/R_+ & \text{in 3D} \\ -(i/4)H_0^{(1)}(kR_+) & \text{in 2D,} \end{cases} \tag{1}$$

where $\mathbf{r}'_g$ is the observation or prediction location, $k = \omega/c_0$, c_0 is the wave speed in the reference medium, $R_+ = |\mathbf{r} - \mathbf{r}'_g|$, and $H_0^{(1)}$ is the zeroth-order Hankel function of the first kind (Morse

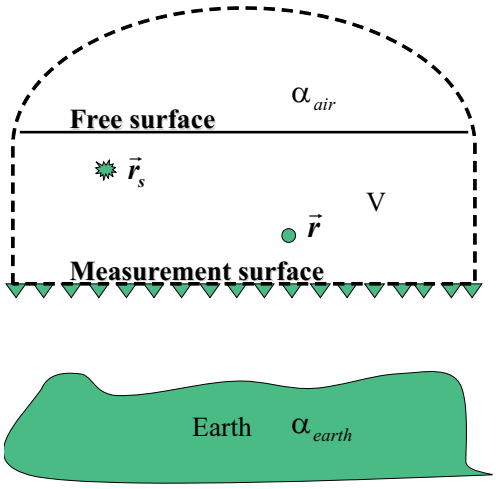

Figure 2: *Configuration for Green's theorem-derived deghosting (Zhang, 2007, Figure 2.10).* α_{air} *and* α_{earth} *are perturbations, the differences between the actual medium (half space of air, water, half space of earth) and the reference medium (whole space of water). The closed surface S of integration is the measurement surface plus the dashed line.* $\mathbf{r}$ *in the figure corresponds to* $\mathbf{r}'_g$ *in equation 2.*

and Feshbach, 1953, § 7.2). The observation or prediction point is chosen between the air/water boundary and the measurement surface, i.e., inside the volume V bounded by the closed surface of integration consisting of the measurement surface and the dashed line in Figure 2. For a discussion of why the causal whole-space Green's function exhibits the forms in equation 1, please see chapter 7 in Morse and Feshbach (1953).

The configuration in Figure 2, the derived variation of Green's theorem, and the acoustic wave equations for P and G_0^d combine to give the key equation,

$$P'_R(\mathbf{r}'_g, \mathbf{r}_s, \omega) = \oint_S dS\, \hat{\mathbf{n}} \cdot [P(\mathbf{r}, \mathbf{r}_s, \omega) \nabla G_0^d(\mathbf{r}, \mathbf{r}'_g, \omega) - G_0^d(\mathbf{r}, \mathbf{r}'_g, \omega) \nabla P(\mathbf{r}, \mathbf{r}_s, \omega)], \tag{2}$$

where S is the closed surface consisting of the measurement surface and the dashed line in Figure 2, and $\hat{\mathbf{n}}$ is the unit normal to S (pointing away from the enclosed volume V). The source location, $\mathbf{r}_s$, and observation or prediction point, $\mathbf{r}'_g$, are inside the volume V. Extending the radius of the hemisphere to infinity, invoking the Sommerfeld radiation condition, and assuming a horizontal measurement surface, the integral over the closed surface becomes an integral over the measurement surface (Weglein et al., 2002, equation 5),

$$P'_R(\mathbf{r}'_g, \mathbf{r}_s, \omega) = \int_{m.s.} dS [P(\mathbf{r}, \mathbf{r}_s, \omega) \frac{\partial}{\partial z} G_0^d(\mathbf{r}, \mathbf{r}'_g, \omega) - G_0^d(\mathbf{r}, \mathbf{r}'_g, \omega) \frac{\partial}{\partial z} P(\mathbf{r}, \mathbf{r}_s, \omega)]. \tag{3}$$

The algorithm in equation 3 lends itself to application in a marine single-shot experiment. If the predicted cable is above the towed cable and below the shots, equation 3 identifies and attenuates downgoing waves at the predicted cable (as shown in Appendix 11.1). Receiver ghosts,

source/receiver ghosts, the direct wave, and the direct wave's reflection at the air/water boundary are removed.

Green's theorem-derived receiver deghosting can be compared with a conventional $P + V_z$ sum method of deghosting (Amundsen, 1993b; Robertsson and Kragh, 2002; Kragh et al., 2004). Given a horizontal acquisition and adequate sampling to allow a Fourier transform from space to wavenumber, the two algorithms are equivalent. However, these givens can be an issue. In addition, the application of the $P+V_z$ sum, under certain circumstances, brings other assumptions. For example, a 1D layered earth is assumed and dense sampling is needed to support its inverse Hankel transform (Amundsen, 1993b, page 1336). The latter (a $P+V_z$ sum with a 1D layered earth) is often considered the current industry standard deghosting method. In contrast, the Green's theorem deghosting algorithm (1) can accommodate a 1D, 2D, or 3D earth and (2) stays in coordinate space. By imposing suitable restrictions, $P + V_z$ can be derived from Green's theorem, as shown in Section 6.1. The derivation follows in the tradition of Corrigan et al. (1991), Amundsen (1993b), and Weglein and Amundsen (2003). This derivation, which to our knowledge has not been published before, shows that deghosting in the wavenumber-frequency domain is a special case of the more general deghosting in the space-frequency domain derived from Green's theorem.

2.2 Source deghosting

We have shown how Green's theorem can be applied to select the portion of the seismic wavefield that is upgoing at a field position above the cable. The algorithm uses data from a single shot gather and the receiver coordinate as the integration variable. This section shows how the theory can be similarly applied for source deghosting, where the portion of the wavefield that is downgoing at the source is sought. Depending on the marine experiment, we have the following options for source deghosting. (1) If we have a collection of single source experiments, we can use the derived variation of Green's theorem (equation 3), a double Dirichlet Green's function (equation 7 or 8), and receiver-deghosted data P'_R to predict new P'_R and $\partial P'_R/\partial z$ above the receiver-deghosted data. Then we can use the derived variation of Green's theorem, a whole-space Green's function (equation 1), and the predicted P'_R and $\partial P'_R/\partial z$ to predict source- and receiver-deghosted P'_{SR} above the input P'_R and $\partial P'_R/\partial z$. (2) If we have over/under shots, we can use the derived variation of Green's theorem (equation 4), a whole-space Green's function, and receiver-deghosted data P'_R to directly predict source- and receiver-deghosted P'_{SR} above the receiver-deghosted data. An application of reciprocity to the entire set of shot records allows the original receiver-ghost removal to become a source-ghost removal. Then a second application of the derived variation of Green's theorem over receivers results in source- and receiver-deghosted data. An experiment with both over/under receivers and over/under sources can be receiver deghosted and source deghosted by a double application of the derived variation of Green's theorem (part of Weglein et al. (2002)).

The first step in Green's theorem-derived source deghosting uses source-receiver reciprocity. We interpolate shots so that the distance between shots is the same as the inline distance between receivers, assign "station numbers" to shots and receivers relative to a grid fixed in space, use the station numbers to re-sort the sail line from common-shot gathers (CSGs) to common-receiver gathers (CRGs), and exchange the locations of the shots and receivers. Source ghosts upgoing at the shots are now receiver ghosts downgoing at the "receivers," and a second application of equation 3 will remove them. This can be seen in Figure 3. Panel (a) shows the recorded data (for

(a) *Input*

(b) *R deghosted*

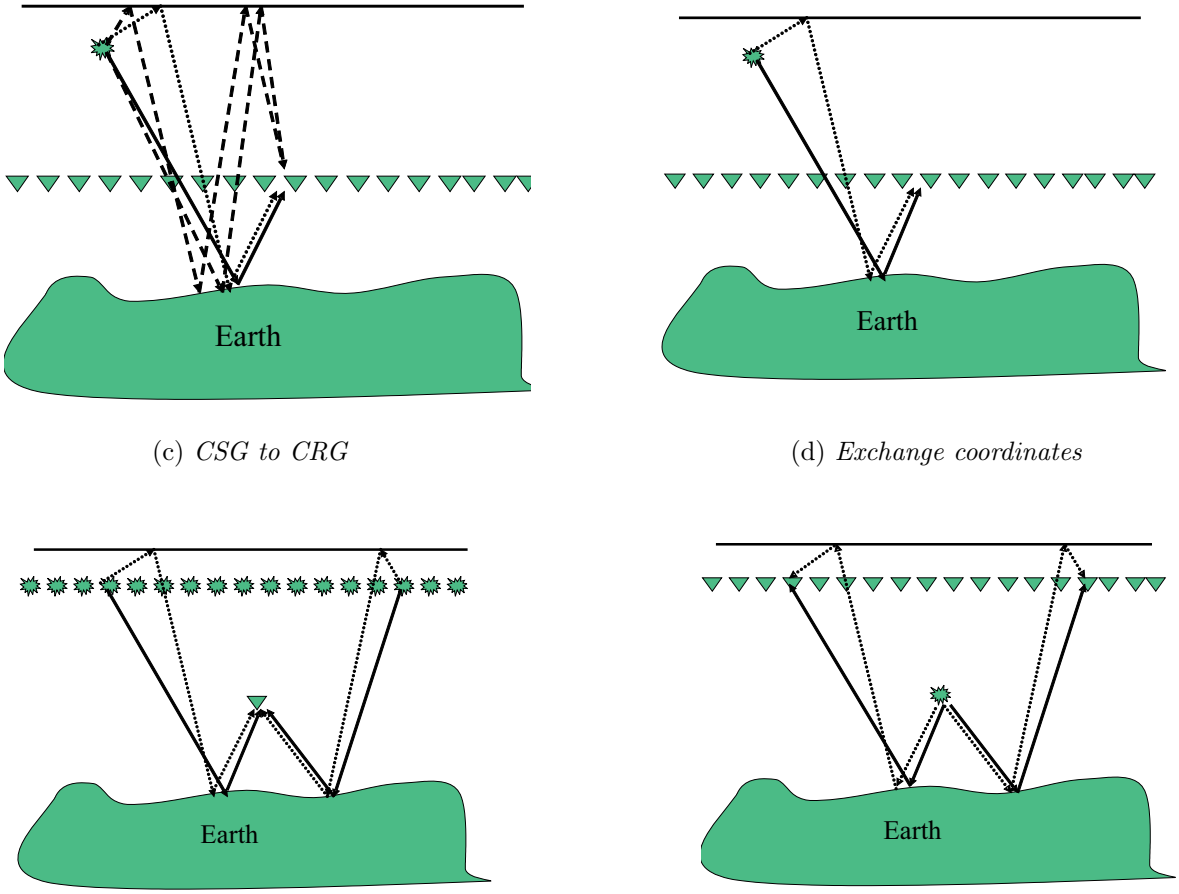

(c) *CSG to CRG*

(d) *Exchange coordinates*

Figure 3: *Figures are Zhang 2007, Figs. 2.14–2.16.*

simplicity only primaries and their ghosts are shown), and panel (b) shows receiver-deghosted data (the receiver ghosts and source/receiver ghosts have been attenuated, leaving primaries and their source ghosts). In panel (c) CSGs have been sorted to produce CRGs, and in panel (d) shot and receiver locations have been exchanged. The configuration in panel (d) looks like that in panel (a), so a second application of equation 3 will remove the source ghosts.

If the experiment has over/under shots, the integral analogous to equation 3 is

$$P'_{SR}(\mathbf{r}'_g, \mathbf{r}'_s, \omega) = \int_{\text{sources}} dS\, \hat{\mathbf{n}} \cdot [P'_R(\mathbf{r}'_g, \mathbf{r}, \omega) \nabla G_0^+(\mathbf{r}, \mathbf{r}'_s, \omega) - G_0^+(\mathbf{r}, \mathbf{r}'_s, \omega) \nabla P'_R(\mathbf{r}'_g, \mathbf{r}, \omega)]. \quad (4)$$

Otherwise, the second step in Green's theorem-derived source deghosting predicts a dual-sensor cable. Equation 3 uses a whole-space Green's function G_0^d to receiver deghost. We now take advantage of the flexibility of Green's theorem and construct and use a double Dirichlet Green's function G_0^{DD} to predict a dual-sensor cable above the receiver-deghosted cable. G_0^{DD} is constructed

(using the method of images) to vanish on both the air/water boundary and the measurement surface (Morse and Feshbach 1953, pages 812ff.; Osen et al. 1998; Tan 1999; Zhang 2007, pages 20ff.). In the $(\mathbf{r},\omega)$ domain, Green's theorem now takes the form

$$P'_R(\mathbf{r}''_g,\mathbf{r}_s,\omega) = \int_{\text{m.s.}} dS'_g\, P'_R(\mathbf{r}'_g,\mathbf{r}_s,\omega)\frac{\partial G_0^{DD}}{\partial z'_g}(\mathbf{r}'_g,\mathbf{r}''_g,\omega)\Big|_{z'_g=m.s.} \tag{5}$$

$$\frac{\partial P'_R}{\partial z''_g}(\mathbf{r}''_g,\mathbf{r}_s,\omega) = \int_{\text{m.s.}} dS'_g\, P'_R(\mathbf{r}'_g,\mathbf{r}_s,\omega)\frac{\partial^2 G_0^{DD}}{\partial z'_g \partial z''_g}(\mathbf{r}'_g,\mathbf{r}''_g,\omega)\Big|_{z'_g=m.s.}, \tag{6}$$

where $\mathbf{r}''_g$ is the observation or prediction point, $\mathbf{r}_s$ is the shot location, $\mathbf{r}'_g$ is the receiver location on the receiver-deghosted cable, and differentiating equation 5 with respect to the observation or prediction coordinate z''_g derives equation 6. P'_R is the result of receiver deghosting and source-receiver reciprocity. Green's theorem takes this form for the following reason. The surface integral vanishes at the air/water boundary because (a) P vanishes and (b) by construction, G_0^{DD} vanishes. By construction, G_0^{DD} also vanishes on the measurement surface (i.e., the receiver-deghosted cable), leaving the above form of Green's theorem.

In 2D the analytic form of the double Dirichlet Green's function G_0^{DD} in the $(\mathbf{r},\omega)$ domain is

$$G_0^{DD}(\mathbf{r}'_g,\mathbf{r}''_g,\omega) = -\frac{1}{b}\sum_{n=1}^{\infty}\frac{1}{\sqrt{\beta}}\exp\left(-\sqrt{\beta}\,|x'_g - x''_g|\right)\sin\left(\frac{n\pi}{b}z'_g\right)\sin\left(\frac{n\pi}{b}z''_g\right), \tag{7}$$

where (x''_g, z''_g) are the observation or prediction coordinates, (x'_g, z'_g) are the receiver coordinates on the receiver-deghosted cable, the air/water boundary is at $z'_g = 0$, the input (receiver-deghosted) cable is at $z'_g = b$, and we assume $\beta \equiv (n\pi/b)^2 - k^2 > 0$ (Osen et al., 1998; Tan, 1999). In 3D

$$G_0^{DD}(\mathbf{r}''_g,\mathbf{r}'_g,\omega) = \frac{2\pi i}{b}\sum_{n=1}^{\infty}H_0^{(1)}(\gamma\rho)\sin\left(\frac{n\pi}{b}z'_g\right)\sin\left(\frac{n\pi}{b}z''_g\right), \tag{8}$$

where $\gamma = i\sqrt{\beta}$ and $\rho = \sqrt{(x''_g - x'_g)^2 + (y''_g - y'_g)^2}$ (Osen et al., 1998). For a discussion as to why G_0^{DD} has these forms, please see page 820 in Morse and Feshbach (1953). For purposes of numeric evaluation, the Hankel function with imaginary argument is replaced by a hyperbolic Bessel function with real argument,

$$G_0^{DD}(\mathbf{r}'_g,\mathbf{r},\omega) = \frac{4}{b}\sum_{n=1}^{\infty}K_0(\sqrt{\beta}\rho)\sin\left(\frac{n\pi}{b}z'_g\right)\sin\left(\frac{n\pi}{b}z\right),$$

where K_0 is a modified Bessel function of the second kind (Morse and Feshbach, 1953, page 1323). Like the 2D double Dirichlet Green's function G_0^{DD}, K_0 exponentially decays (Figure 4), and its numerical evaluation rapidly converges.

The third step in Green's theorem-derived source deghosting is a repetition of receiver deghosting, except we are in the CRG domain and the input is the dual-sensor cable predicted in the second step. The predicted source-deghosted cable is above the input (the predicted dual-sensor cable).

The following two derivations (in 1D for simplicity) show that using two measurements at one depth can be more stable than two measurements at two different depths. Using P measured at two depths

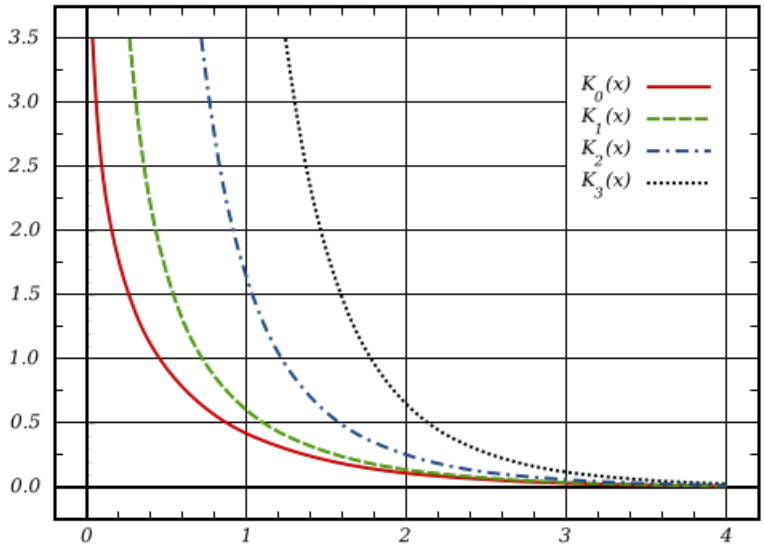

Figure 4: *Modified Bessel functions exponentially decay (Wikipedia, 2012).*

introduces a depth-sensitive denominator. Under perfect conditions the two methods are equivalent, but under practical conditions they are not. For example,

$$\begin{aligned} P &= A\exp(ikz) + B\exp(-ikz) \\ P(0) &= A + B \\ \frac{dP}{dz}(0) &= ik(A - B) \\ A &= \frac{dP/dz(0) + ikP(0)}{2ik} \\ B &= \frac{dP/dz(0) - ikP(0)}{-2ik} \end{aligned}$$

is stable. However, measurements at two depths or at G_0^{DD} (the latter comes from $G_0 = 0$ at two depths) gives

$$\begin{aligned} P(0) &= A + B \\ P(a) &= A\exp(ika) + B\exp(-ika) \\ A &= \frac{P(0)\exp(-ika) - P(a)}{-2i\sin(ka)} \\ B &= \frac{P(0)\exp(ika) - P(a)}{2i\sin(ka)}, \end{aligned}$$

which is sensitive in the vicinity of ghost notches (where $ka = n\pi$). If our interest is away from ghost notches, one-source experiments will be fine for source and receiver deghosting, whereas if our interest includes the ghost notches, two-source experiments can provide more stability for source-side deghosting. The choice depends on bandwidth and depth of sources and receivers. If our

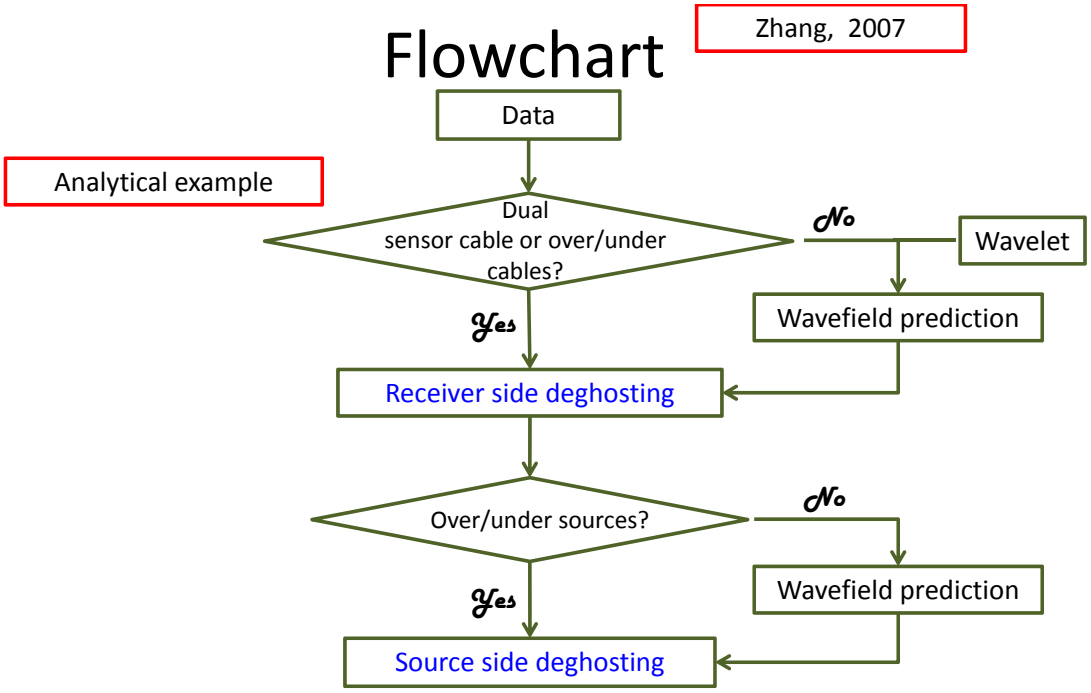

Figure 5: *Green's theorem-derived deghosting can accommodate various configurations of sources and receivers (Wang, 2012, slide 10).*

sources and receivers are at the ocean bottom, ghost notches come up early and double sources would be indicated. This also impacts receiver deghosting that uses measurements at two depths because of the sensitivity to ghost notches. The alternative method of receiver deghosting using the source wavelet $A(\omega)$, P along the cable, and the double Dirichlet Green's function G_0^{DD}, allows receiver deghosting without the need for measurements at two depths, but G_0^{DD} uses information at two different depths and hence may have stability issues compared with two measurements at one depth.

Figure 5 summarizes how Green's theorem-derived deghosting can accommodate various configurations of sources and receivers.

2.3 Code

The implementation of the above theory is done in a straightforward manner. The Green's theorem-derived algorithm computes the surface integral in equation 3. The method requires as input two wavefields, the pressure measurements P and their normal derivatives $\partial P/\partial z$. Measuring the latter requires a dual-sensor cable or over/under cables. The programs use data in the Seismic Unix (SU) format and integrate with all native SU programs.

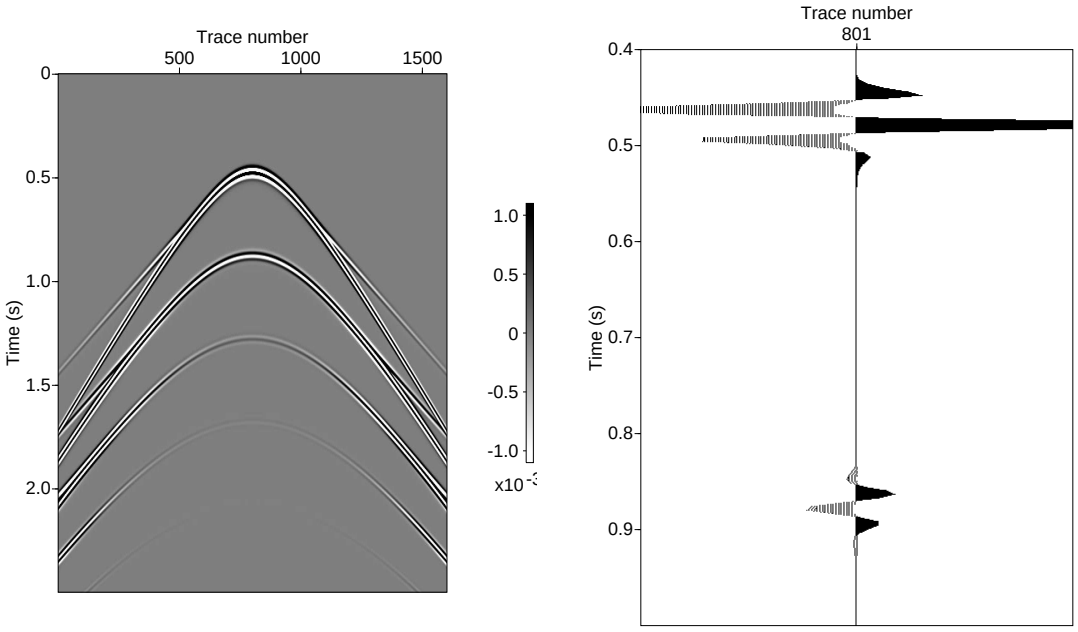

Figure 6: *Cagniard-de Hoop data: P_s at 11m. The first event is the water-bottom primary and its ghosts, and the second event is the first free-surface multiple and its ghosts. The right panel shows the zero-offset trace (801 of 1601). More detail is given in Appendix 11.2.1.*

2.4 Numerical example

We illustrate Green's theorem-derived deghosting using Cagniard-de Hoop data (more detail on the data is given in Appendix 11.2). The input data are shown in Figure 6. The first event is the water-bottom primary and its three ghosts (source ghost, receiver ghost, and source/receiver ghost), and the second event is the first free-surface multiple and its three ghosts. We begin by receiver deghosting (in the common-shot-gather (CSG) domain) using equation 3, and the output is a receiver-deghosted pseudocable above the towed cable and below the source, shown in Figure 7. The first event is the water-bottom primary and its source ghost (the receiver ghost and source/receiver ghost have been attenuated), and the second event is the first free-surface multiple and its source ghost (the receiver ghost and source/receiver ghost also attenuated).

Next we use source-receiver reciprocity to prepare for source deghosting. Resort the sail line from CSGs to common receiver gathers (CRGs) and exchange locations of shots and receivers. The source ghosts upgoing at the shots are now receiver ghosts downgoing at the receivers, and a second application of equation 3 will remove them. See Figure 3.

Next we use a double Dirichlet Green's function G_0^{DD} to predict new $P'_R, \partial P'_R/\partial z$ (a pseudo dual-sensor cable), i.e., equations 5 and 6 with $A(\omega) = 0$.

Finally, we source deghost by inputting the CRG data $(P'_R, \partial P'_R/\partial z)$ into equation 3. The predicted pseudocable is above the inputs and is shown in Figure 9. The first event is the water-bottom primary (its source ghost has been attenuated), and the second event is the first free-surface multiple (its source ghost has been attenuated). Source and receiver deghosting can also be seen by comparing

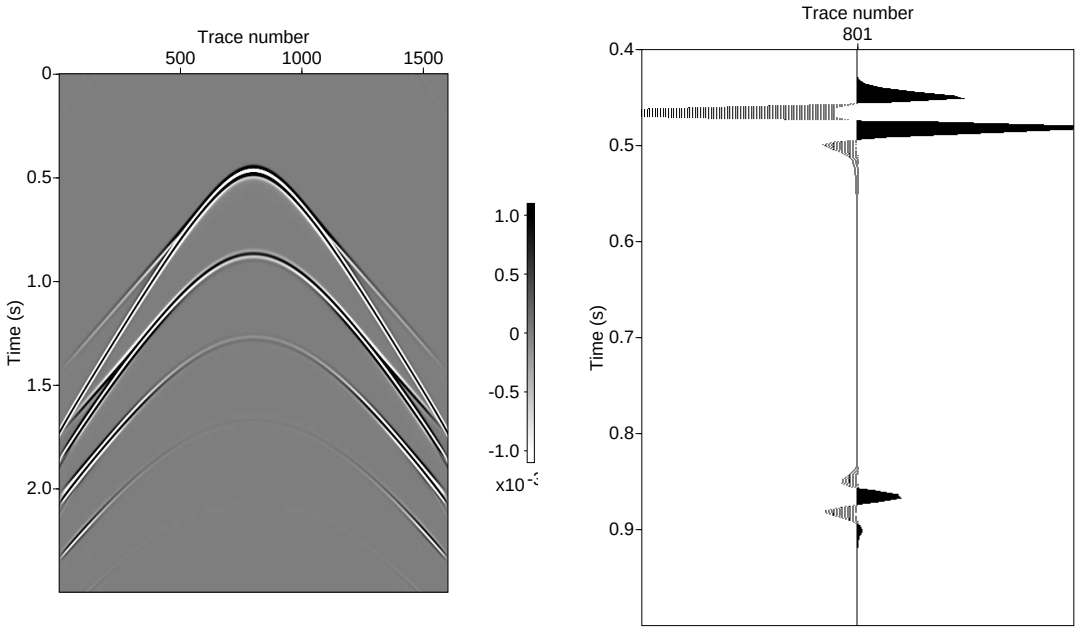

Figure 7: *Cagniard-de Hoop data: Receiver-deghosted P_s at 8m. Note that the receiver and source-receiver ghosts have been attenuated. The right panel shows the zero-offset trace (801 of 1601).*

Figures 8 and 9. Plotting the frequency spectra (Figure 10) shows that deghosting boosts low frequencies.

3 What does deghosting look like?

The purpose of this section is to show what receiver deghosting looks like for separate vs. overlapping events in the input data. Details on the input data are given in Appendix 11.2.

3.1 Separated events

Compare Figures 11 and 12 to see receiver-ghost attenuation. In Figure 11, the third event is the water-bottom primary's receiver ghost and source/receiver ghost, and the fifth event is the first free-surface multiple's receiver ghost and source/receiver ghost.

3.2 Partially interfering events

Compare Figures 13 and 14 to see receiver-ghost attenuation. In Figure 13, the bottom of the second event is the water-bottom primary's receiver ghost and source/receiver ghost, and the bottom of the third event is the first free-surface multiple's receiver ghost and source/receiver ghost.

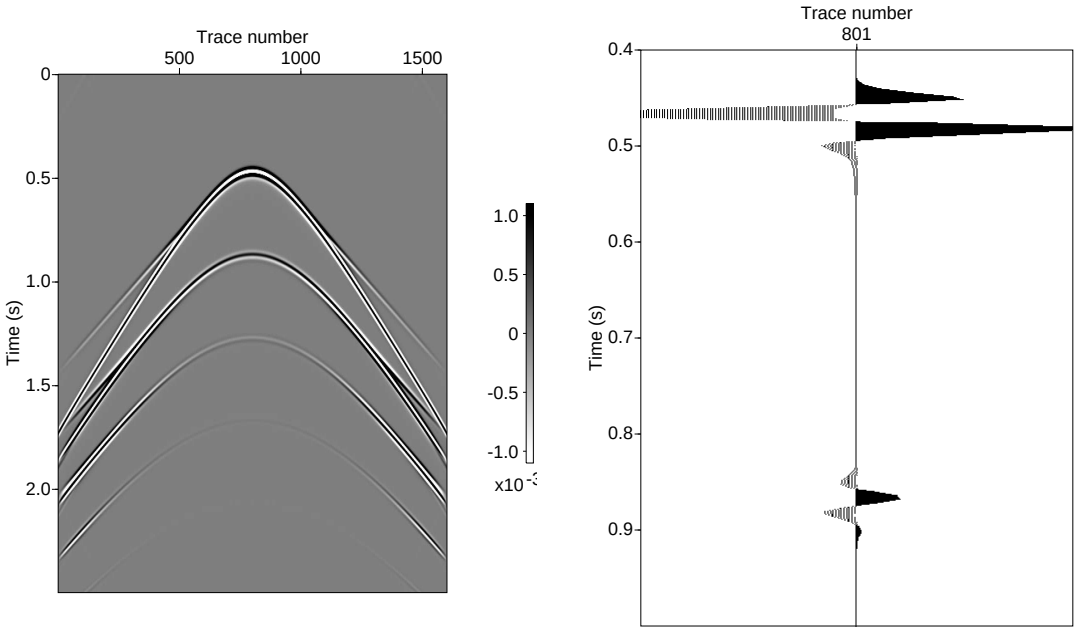

Figure 8: *Cagniard-de Hoop data: receiver deghosted at 8m (same as Figure 7).*

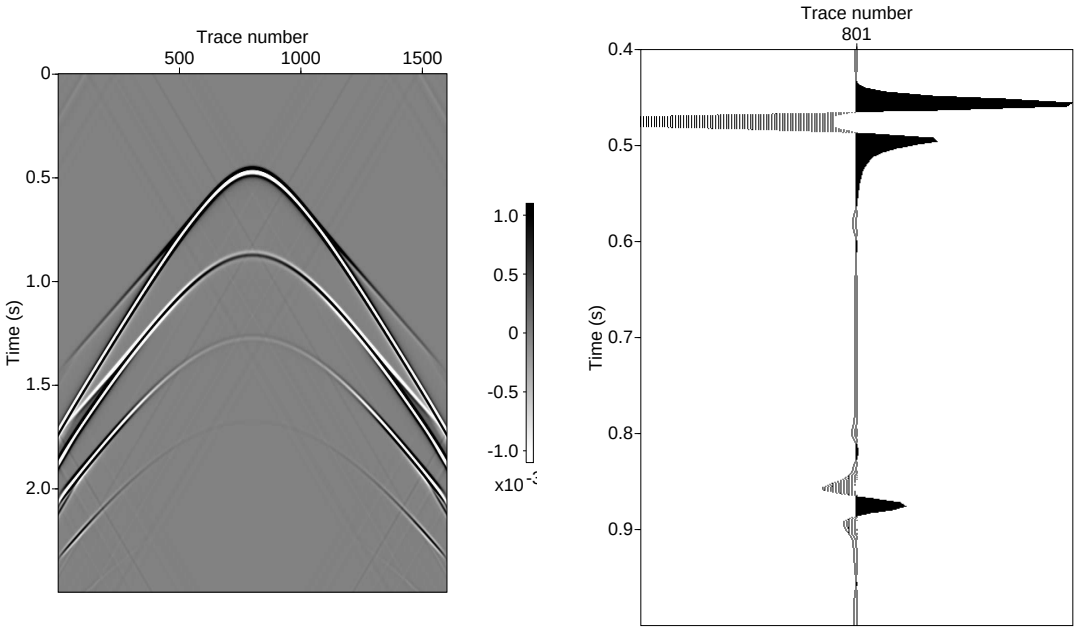

Figure 9: *Cagniard-de Hoop data: Source and receiver deghosted P_s at 1m. Note that the source ghosts have been attenuated. The right panel shows the zero-offset trace (801 of 1601).*

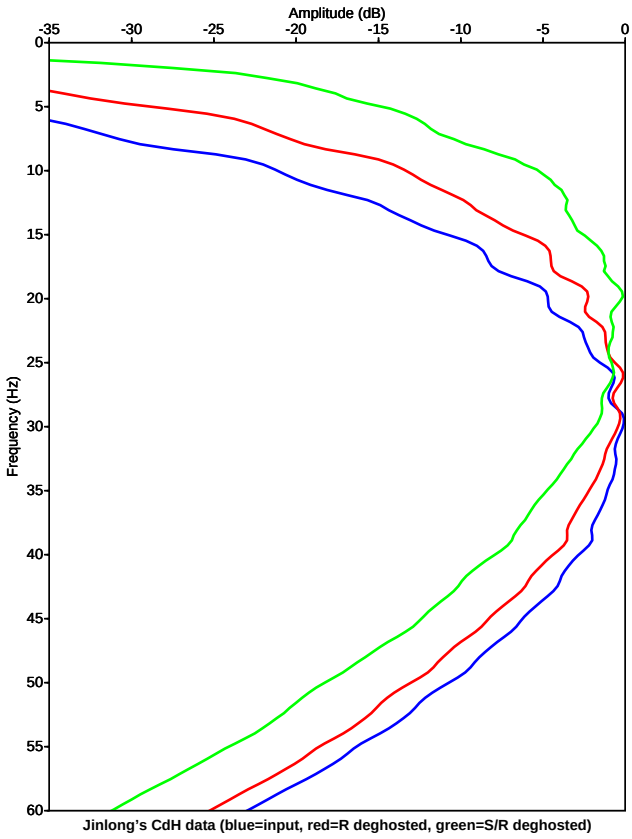

Figure 10: *Cagniard-de Hoop data: frequency spectra (blue=input, red=receiver deghosted, green=source and receiver deghosted). Note that deghosting boosts low frequencies. Source and receiver deghosting (green) has a larger effect than does receiver deghosting (red). Receiver deghosting results from one application of the algorithm to measured data, whereas source and receiver deghosting results from three applications: receiver deghosting, wavefield prediction (of the receiver deghosted data at a point above the cable), and source deghosting.*

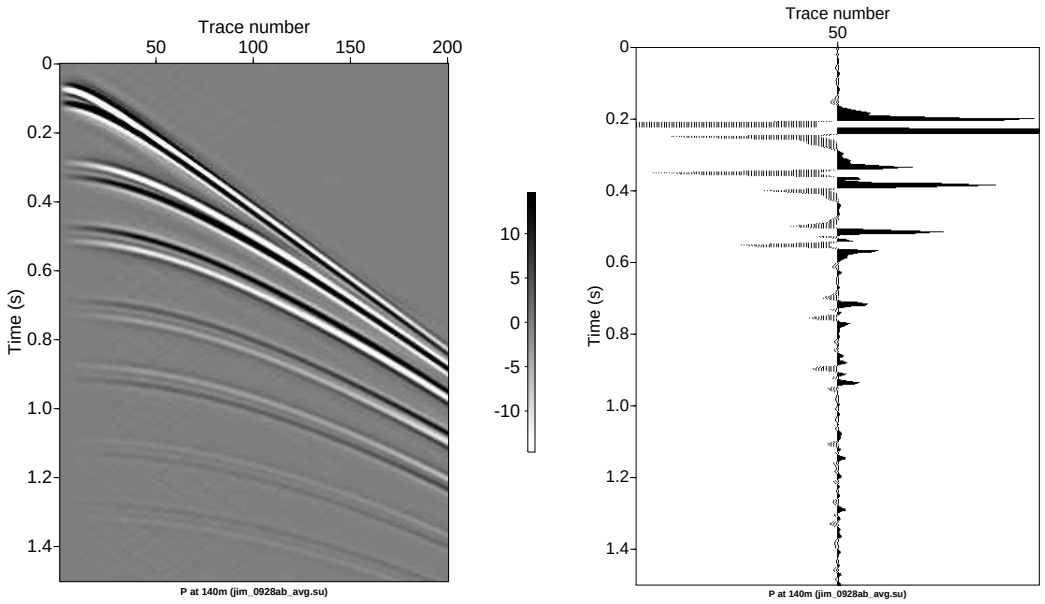

Figure 11: *Reflectivity data, separated events: source at 30m, receivers at 139m and 141m.*

3.3 Overlapping events

Compare Figures 15 and 16 to see receiver-ghost attenuation. In Figure 15, the bottom of the second event is the water-bottom primary's receiver ghost and source/receiver ghost, and the bottom of the third event is the first free-surface multiple's receiver ghost and source/receiver ghost.

3.4 SEAM data

Compare Figures 17 and 18 to see receiver-ghost attenuation. The bottom of the first event is the water-bottom primary's receiver ghost. Note the collapsed wavelets in Figure 18.

3.5 Field data

Compare Figures 19 and 20 to see receiver-ghost attenuation. The second event is the water-bottom primary's receiver ghost and source/receiver ghost, and the fourth and fifth events are likely receiver ghosts and source/receiver ghosts of sub-water-bottom primaries. Note the collapsed wavelets in Figure 20.

4 Deghosting user's guide

The purpose of this section is to list the advantages and disadvantages of various towed-cable configurations.

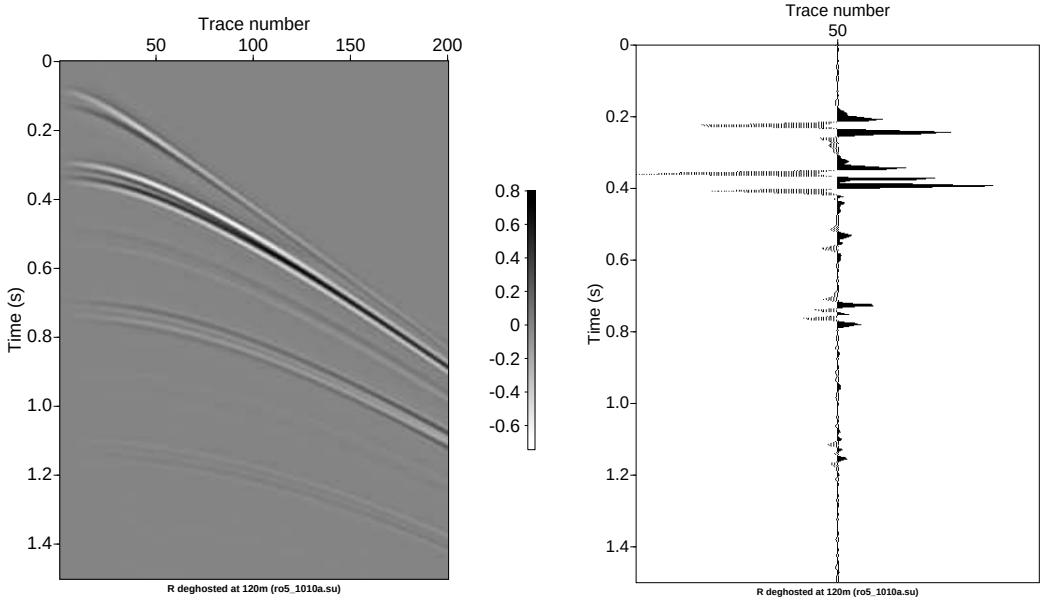

Figure 12: *Reflectivity data, separated events: receiver deghosted at 120m.*

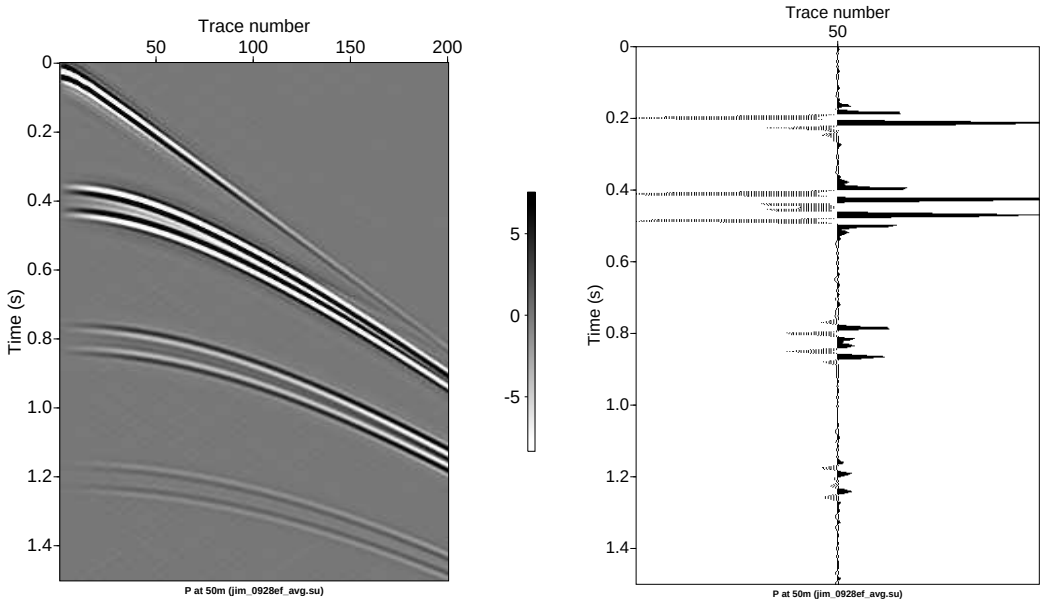

Figure 13: *Reflectivity data, partially interfering events: source at 9m, receivers at 49m and 51m.*

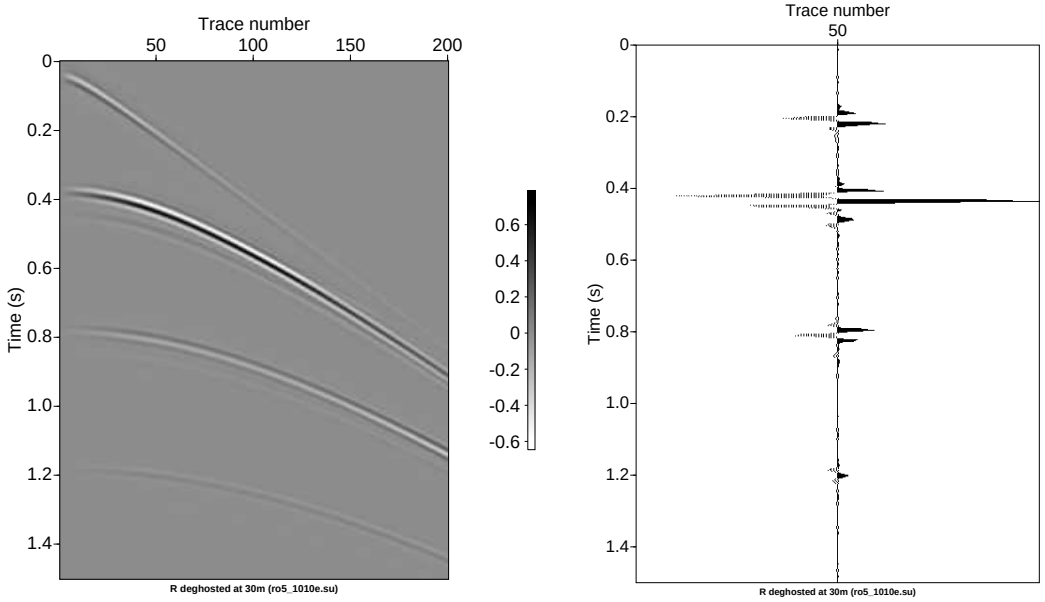

Figure 14: *Reflectivity data, partially interfering events: receiver deghosted at 30m.*

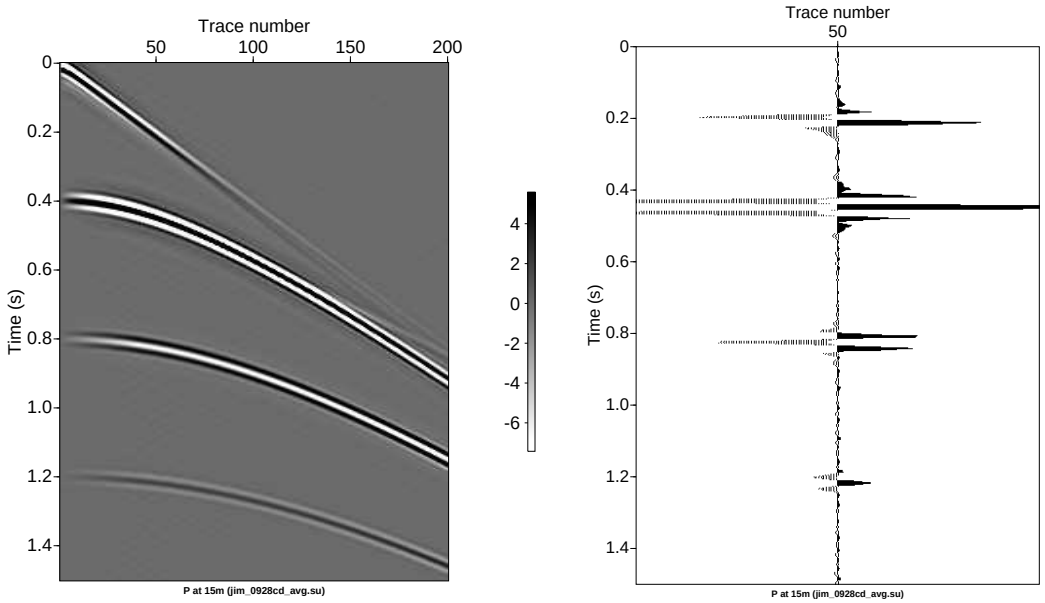

Figure 15: *Reflectivity data, overlapping events: source at 8m, receivers at 14m and 16m.*

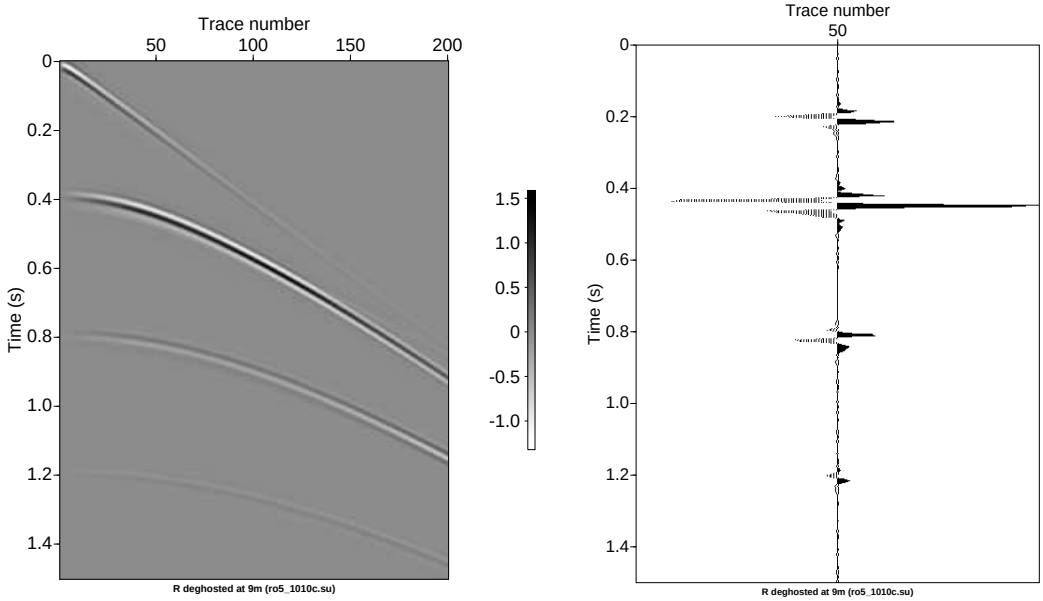

Figure 16: *Reflectivity data, overlapping events: receiver deghosted at 9m.*

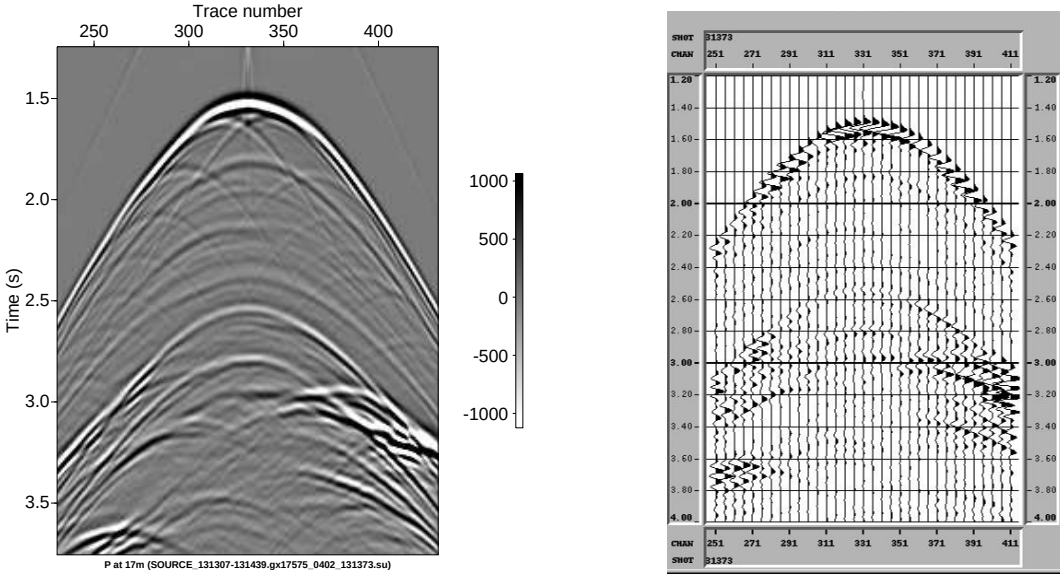

Figure 17: *SEAM Phase I data, shot 131373: source at 15m, receivers at 15m and 17m.*

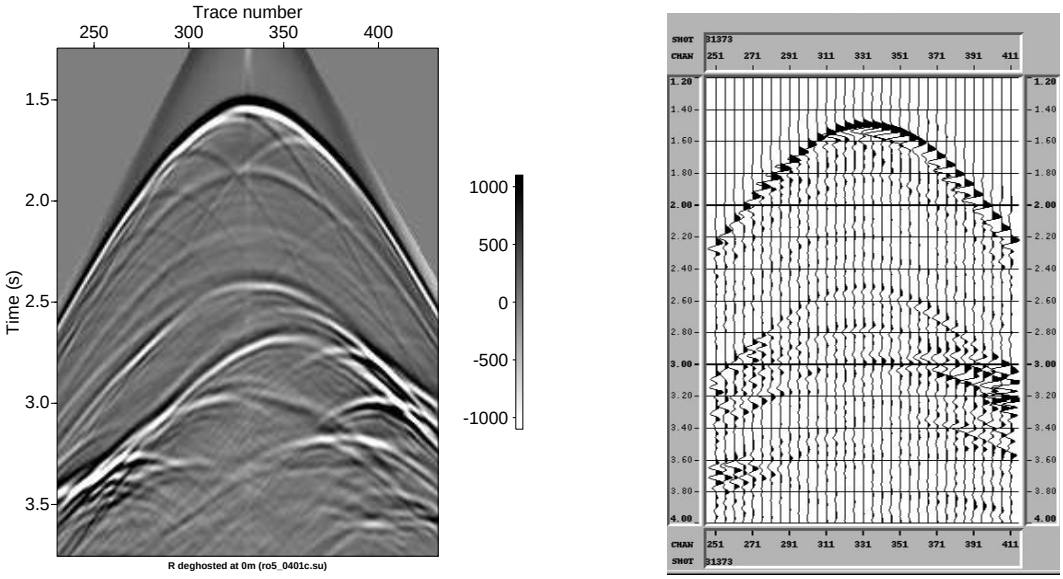

Figure 18: *SEAM Phase I data, shot 131373: receiver deghosted at 1m.*

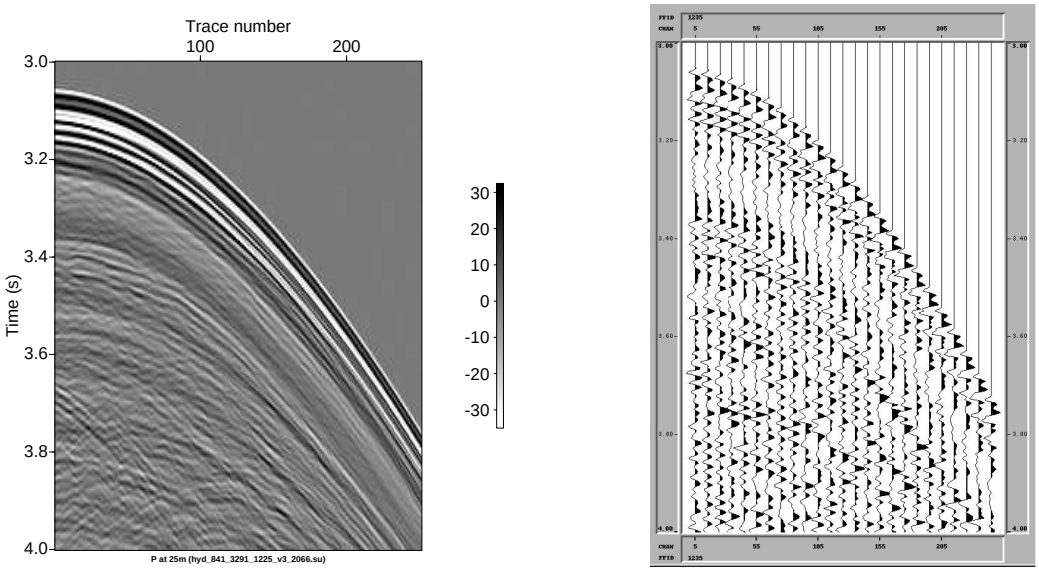

Figure 19: *Field data, deep-water Gulf of Mexico: source at 9m, receivers at 25m.*

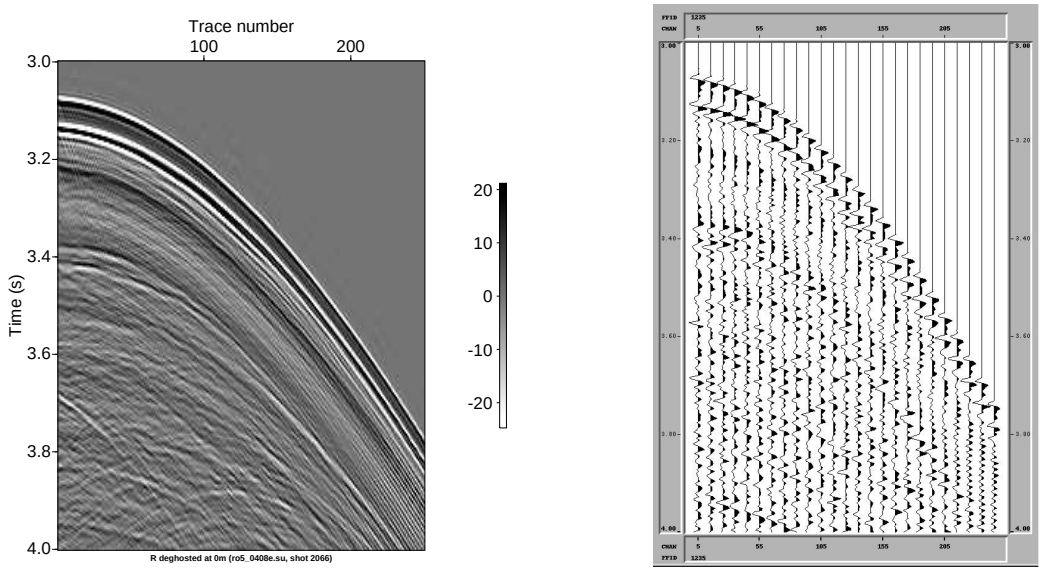

Figure 20: *Field data, deep-water Gulf of Mexico: receiver deghosted at 0m.*

4.1 Single cable

minus Receiver deghosting requires an estimate of source wavelet (Zhang 2007, page 32).

minus Receiver deghosting and source deghosting require wavefield prediction using a double Dirichlet Green's function G_0^{DD} (Osen et al., 1998; Tan, 1999), which uses information at two different depths and hence may have stability issues compared with two measurements at one depth.

4.2 Single cable with an extra hydrophone

minus This algorithm is "unstable" because it "is too sensitive" (Tan 1999, pages 1839, 1843).

4.3 Over/under cables

plus Zero-angle ghost notches for hydrophones at different depths are shifted relative each other (Figure 21).

minus Lin Tang has shown (Tang, 2012; 2013) that wavefield separation improves as cables get closer, and her best results are at $\Delta z = 1m$, but Kristin cables have $\Delta z = 7m$ and $9m$.

minus Absent over/under sources, source deghosting requires wavefield prediction using G_0^{DD}.

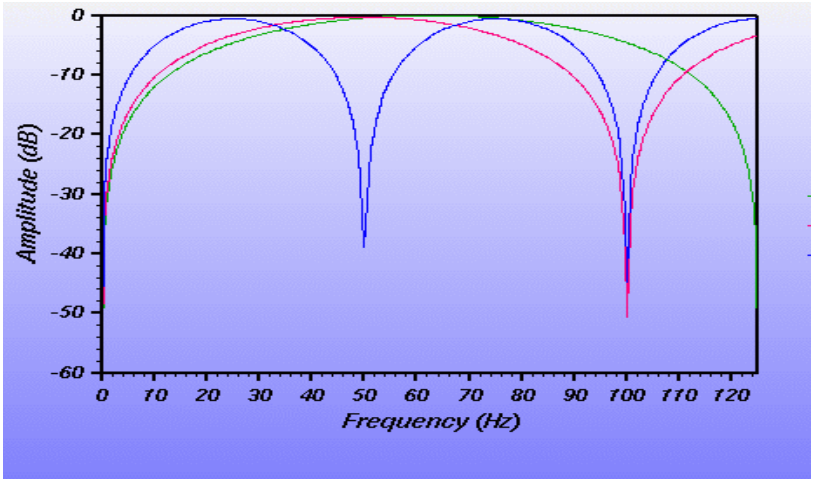

Figure 21: *Notches for hydrophones at depths 6m (green), 7.5m (red), and 15m (blue) using synthetic spike data with time delays of 8, 10, and 20 ms, respectively (Carlson et al. 2007, Figure 1).*

4.4 Dual-sensor cable

plus Zero-angle ghost notches for hydrophones and geophones have the same period ($c_0/2z_g$) but geophones are shifted by 1/2 period relative to hydrophones (Figure 22).

minus Geophone signal is swamped by ambient noise below 12-15Hz, reconstructed from hydrophone data, but reconstruction (of V_z) is only valid for downgoing data (Appendix 11.3).

minus Absent over/under sources, source deghosting requires wavefield prediction using G_0^{DD}.

4.5 Over/under cables or dual-sensor cable with over/under sources

plus Source deghosting doesn't require wavefield prediction using G_0^{DD}.

5 Test sensitivity of Green's theorem-derived deghosting

The purpose of this section is to test the sensitivity of Green's theorem-derived deghosting to errors in depth and to differences in configuration. The following model was used: a half space of air, water (300m deep), and a half space of acoustic earth ($c_1 = 2250m/s$, $\rho = 1.667g/cm^3$). A Cagniard-de Hoop program (written by Jingfeng Zhang), a 2D source, and a Ricker wavelet with maximum amplitude at 25Hz were used, and a 5% taper was applied to each end of the cables.

5.1 Sensitivity to depth

In this section, deghosting is compared for known and unknown cable depths. This is easily done with the program: if input data have cable depth z_g, when submitting tell the program that the

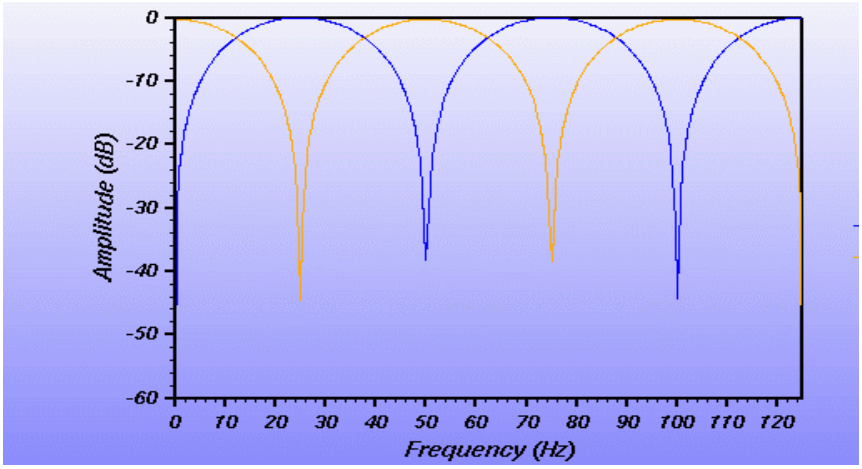

Figure 22: *Zero angle ghost notches for the hydrophone (blue) and geophone (orange) at a depth of 15m (Carlson et al. 2007, Figure 2).*

cable depth is $z_g + \Delta$.

The first test uses data containing separated events: source at 30m, over/under cables at 140m and 145m, and $\partial P/\partial z \simeq [P(145m) - P(140m)]/5m$. Toggle between Figures 23 and 24 to see receiver deghosting. The first event is the reference wavefield, the third event is the water-bottom primary's receiver ghost and source/receiver ghost, and the fifth event is the first free-surface multiple's receiver ghost and source/receiver ghost.

Now tell the program the cable is 1m shallower than it actually is. Figures 25 and 26 show the previous receiver-deghosted result (program given the correct depth) and the receiver-deghosted result with an incorrect depth. Now tell the program the cable is 10m shallower than it actually is. Figures 27 and 28 show the receiver-deghosted result with the correct depth and the receiver-deghosted result with an incorrect depth. Why is there no difference? Recall that $G_0^d, \partial G_0^d/\partial z$ are functions of $z_g' - z$, the difference between the prediction depth z_g' and the cable depth z. If I THINK the actual cable depth is z (when it's actually $z + \Delta$), I'm going to give the program the same difference.

5.2 Sensitivity to cable configuration

In this section, deghosting is compared for different cable configurations: one cable plus an estimate of the source wavelet, over/under cable, and dual-sensor cable.

How to approach one cable plus wavelet? Jingfeng Zhang's deghosting program was designed for two inputs of different sizes, P, A, where A is the isotropic source wavelet from a point source. For a shot, P has one trace for each hydrophone on the cable, and A has one trace. On the other hand, the current deghosting program was designed for two inputs of the same size: $P, \partial P/\partial z$ (or P, V_z). The current deghosting program was modified as follows.

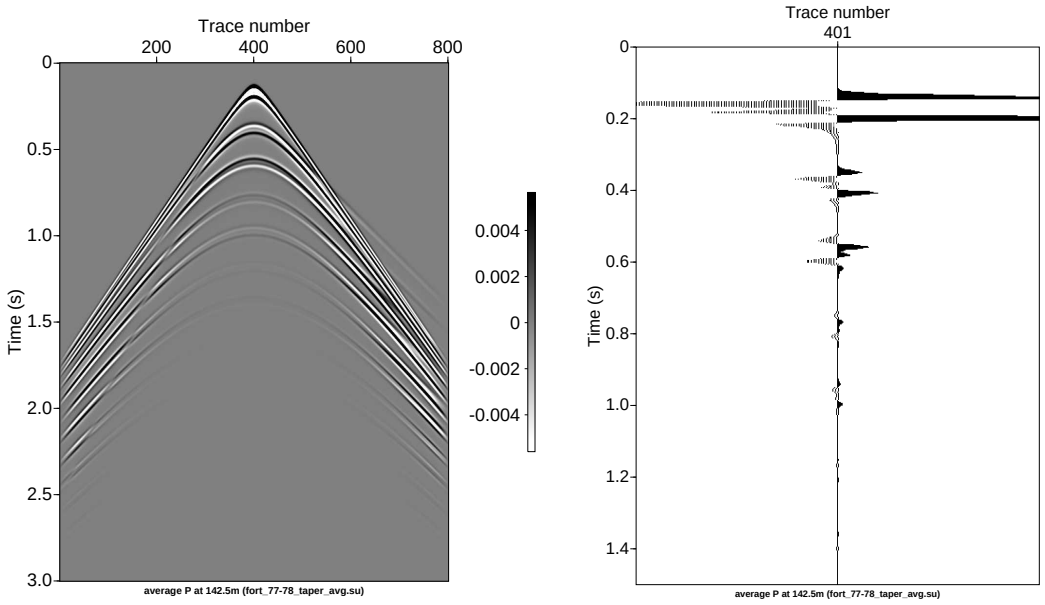

Figure 23: *Cagniard-de Hoop data, source at 30m, receivers at 140m and 145m.*

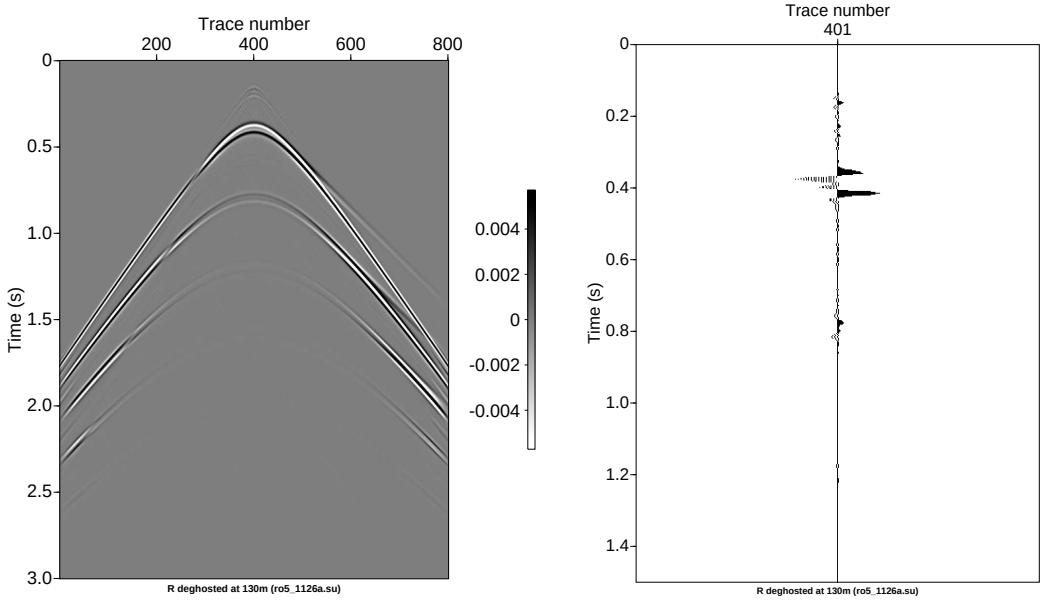

Figure 24: *Cagniard-de Hoop data, source at 30m, receivers at 140m and 145m: receiver deghosted at 130m.*

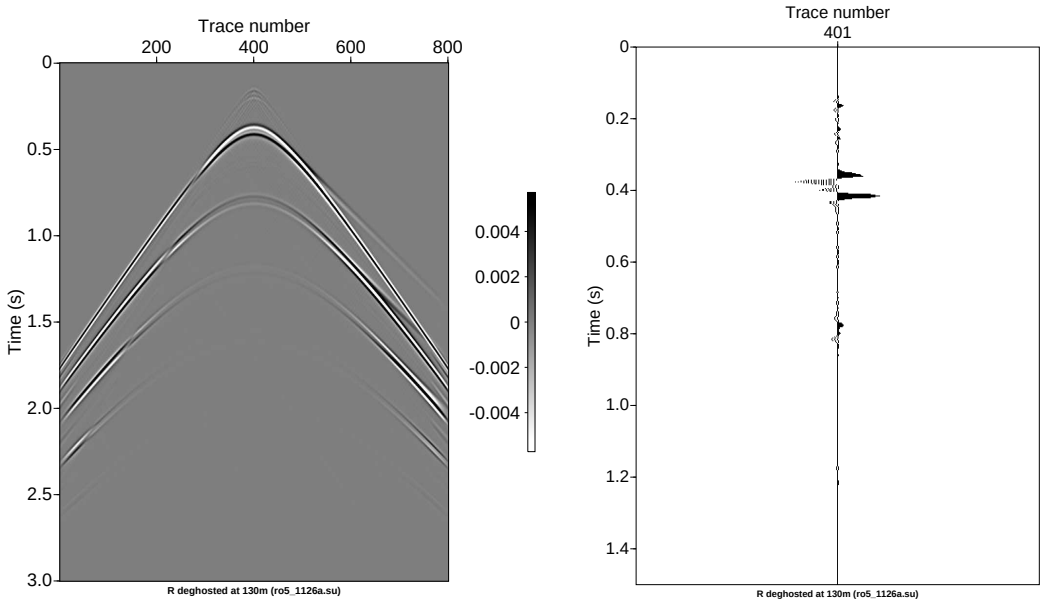

Figure 25: *Receiver-deghosted result in Figure 24, i.e., program given correct depth.*

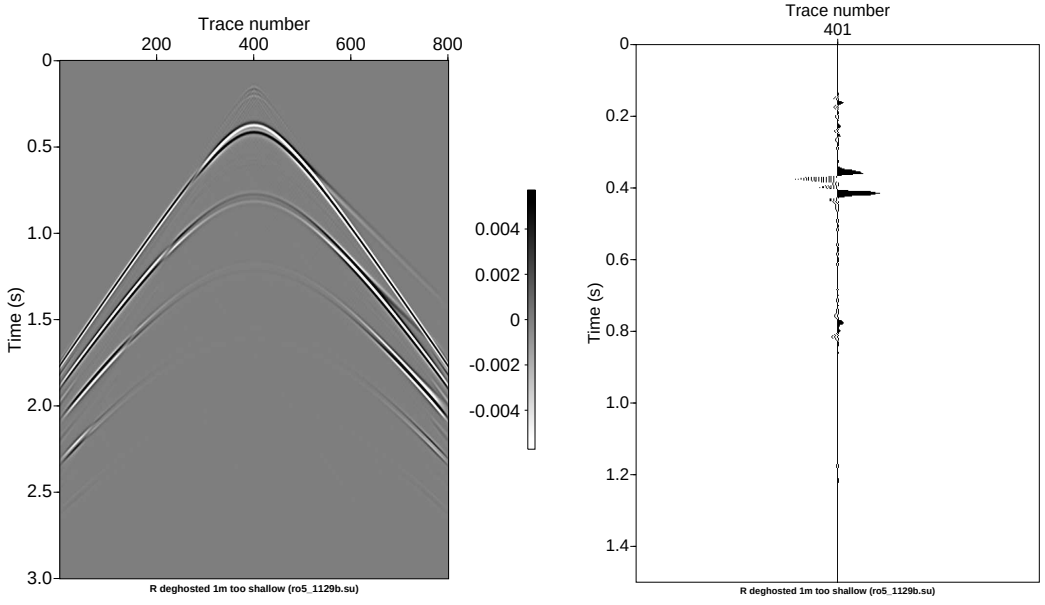

Figure 26: *Cagniard-de Hoop data, receiver-deghosted result when the program is told the cable is 1m shallower than it actually is.*

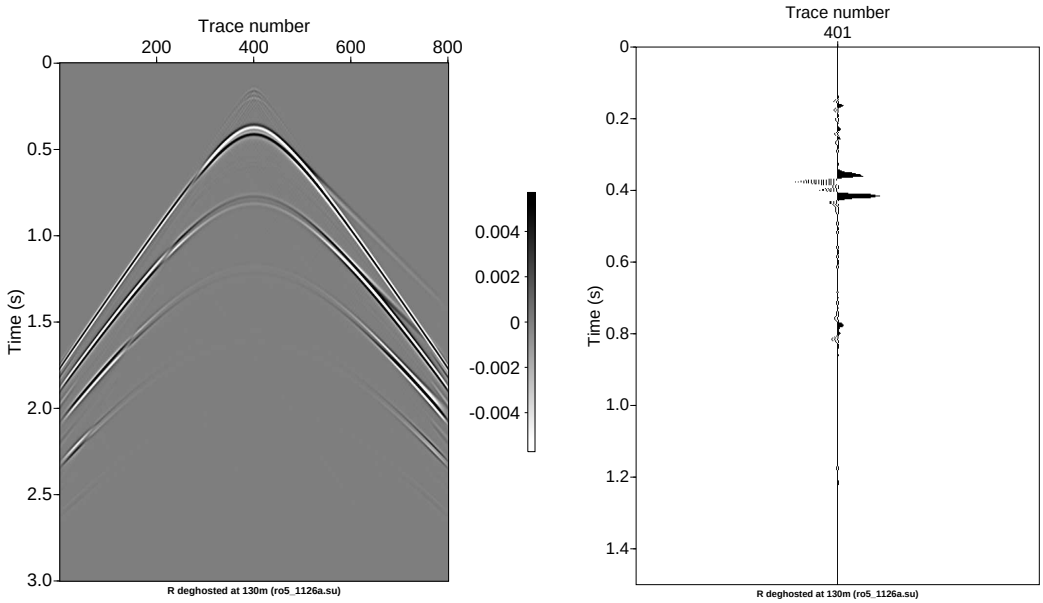

Figure 27: *Previous receiver-deghosted result (program given correct depth).*

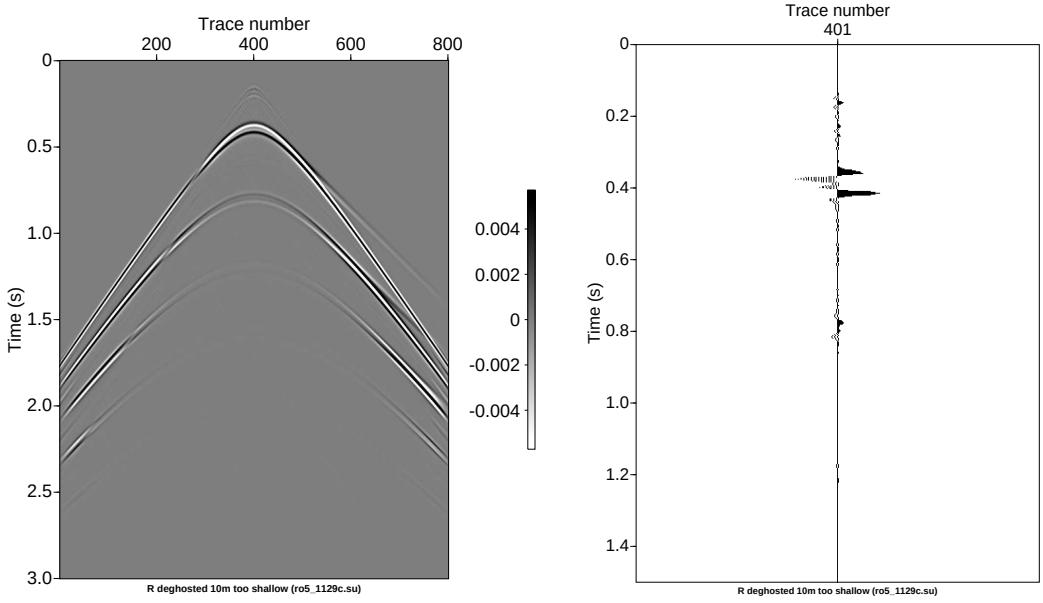

Figure 28: *Cagniard-de Hoop data, receiver-deghosted result when the program is told the cable is 10m shallower than it actually is.*

- The receiver-deghosting equivalents of equations 5 and 6 were added:

$$P'_R(\mathbf{r}'_g, \mathbf{r}_s, \omega) = A(\omega) G_0^{DD}(\mathbf{r}'_g, \mathbf{r}_s, \omega) + \int_{\text{m.s.}} dS\, \hat{\mathbf{n}} \cdot P(\mathbf{r}, \mathbf{r}_s, \omega) \nabla G_0^{DD}(\mathbf{r}'_g, \mathbf{r}, \omega)$$

$$\frac{\partial P'_R}{\partial z''_g}(\mathbf{r}''_g, \mathbf{r}_s, \omega) = A(\omega) \frac{\partial^2 G_0^{DD}}{\partial z'_g \partial z''_g}(\mathbf{r}''_g, \mathbf{r}_s, \omega) + \int_{\text{m.s.}} dS'_g\, P'_R(\mathbf{r}'_g, \mathbf{r}_s, \omega) \frac{\partial^2 G_0^{DD}}{\partial z'_g \partial z''_g}(\mathbf{r}'_g, \mathbf{r}''_g, \omega)\Big|_{z'_g = m.s.}$$

  (Zhang, 2007, equations 2.12 and 2.13).

- A (containing a single trace) is to be modified as follows. For synthetic data, pad and replicate the source wavelet so that its file is the same size as P. For field data, estimate $A(t)$ (e.g., modeled using air gun configuration), then pad and replicate.

Then P and A are input into equation 3.

For an over/under cable, test using the same program and model as above (Section 5.1). Reuse of the same data allows testing where the ghost notches are in the data: receiver notches are at multiples of $1500/(2 * 142.5) = 5.3Hz$, and source notches are at multiples of $1500/(2 * 30) = 25Hz$.

For a dual-sensor cable, we do not have a program to create geophone data, so will approximate a dual-sensor cable with over/under cables separated by 1m.

Figures 29 and 30 show the receiver deghosted result with over/under cables separated by 5m and over/under cables separated by 1m (the latter is to approximate a dual-sensor cable).

Now we use the receiver-deghosted result (created using over/under cables separated by 5m) and the double Dirichlet Green's function to predict new $P, \partial P/\partial z$. Figure 31 shows the result using data containing notches. Since G_0^{DD} has problems near notches, try again with data without notches: source at 2m (vs. 30m), over/under cables at 6m and 7m (vs. 140m and 145m), and $\partial P/\partial z \simeq [P(7m) - P(6m)]/1m$. In these data, receiver notches are at multiples of $1500/(2 * 6.5) = 115Hz$, and source notches are at multiples of $1500/(2 * 2) = 375Hz$. Figures 32 and 33 show the input data and receiver-deghosted result. The first event is the reference wavefield, the third event is the water-bottom primary's receiver ghost and source/receiver ghost, and the fifth event is the first free-surface multiple's receiver ghost and source/receiver ghost. Figures 34 shows the wavefield prediction using G_0^{DD} applied to these receiver-deghosted data.

5.3 Sensitivity of G_0^{DD} to depth

In this section, G_0^{DD} is tested at the wrong depth. We start with the Cagniard-de Hoop data in Figure 32, receiver deghost at 3.5m, and use G_0^{DD} to predict new $P, \partial P/\partial z$. Figures 35 through 40 show new $P, \partial P/\partial z$ values given the correct depth, 1m too deep, and 10m too deep. In section 5.1 (above), we showed that wavefield separation and deghosting are not sensitive to errors in cable depth because the difference between cable depth and prediction depth enters the equation. In contrast, wavefield prediction using G_0^{DD} is sensitive to depth because the depth of the free surface is fixed, so errors in the cable depth do affect the difference. An error of 1m in cable depth isn't noticeable (Figures 35, 36, 38, and 39), whereas an error of 10m in cable depth is noticeable (Figures 35, 37, 38, and 40).

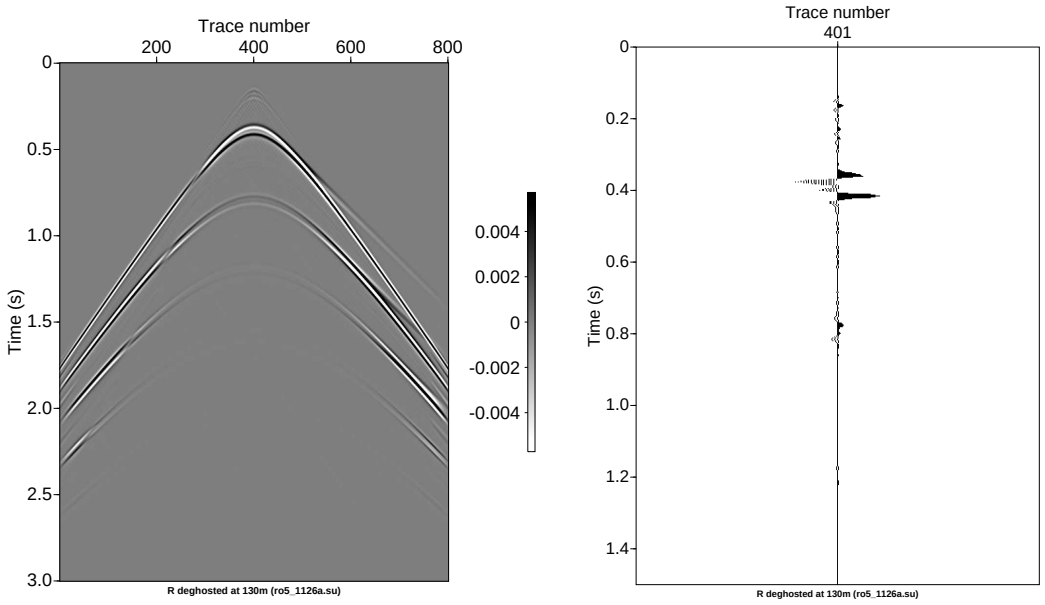

Figure 29: *Receiver-deghosted result in Figure 24, i.e., over/under cables separated by 5m.*

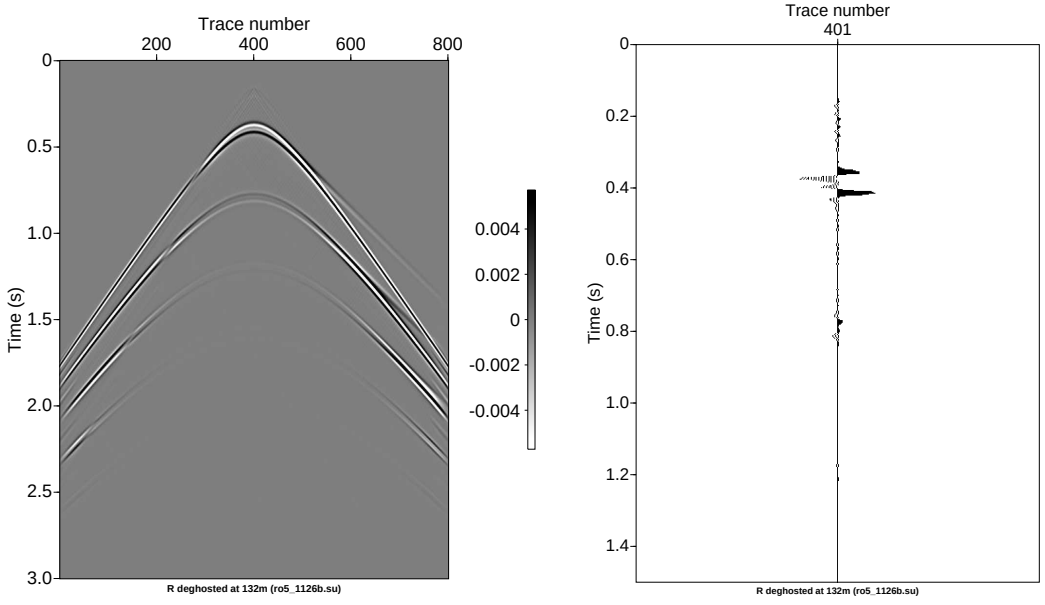

Figure 30: *Cagniard-de Hoop data, receiver-deghosted result where dual-sensor cable approximated with over/under cables separated by 1m.*

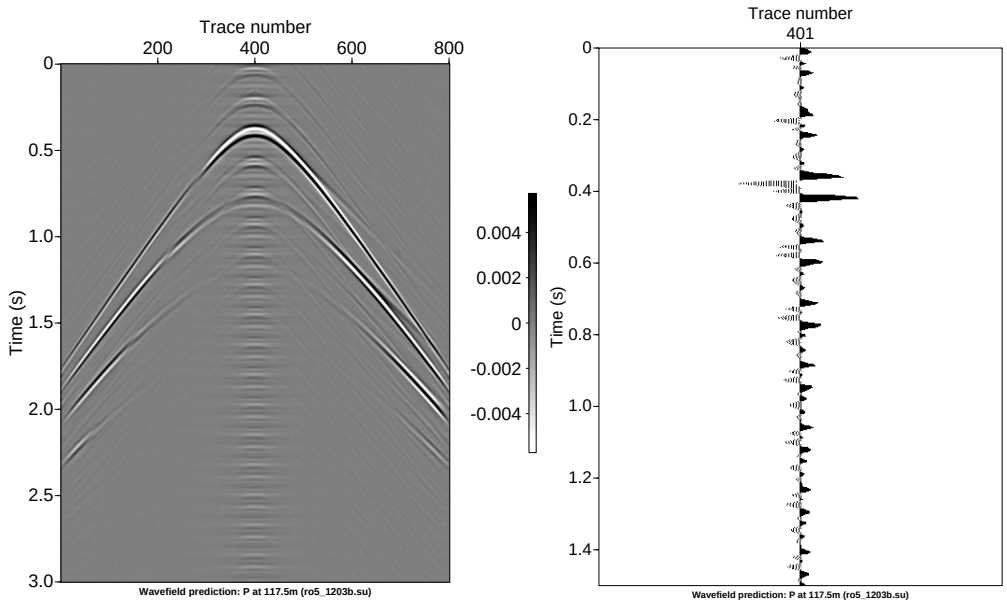

Figure 31: *Cagniard-de Hoop data, wavefield prediction of new $P, \partial P/\partial z$ using double Dirichlet Green's function G_0^{DD}. Ghost notches are in the input data (Figure 29).*

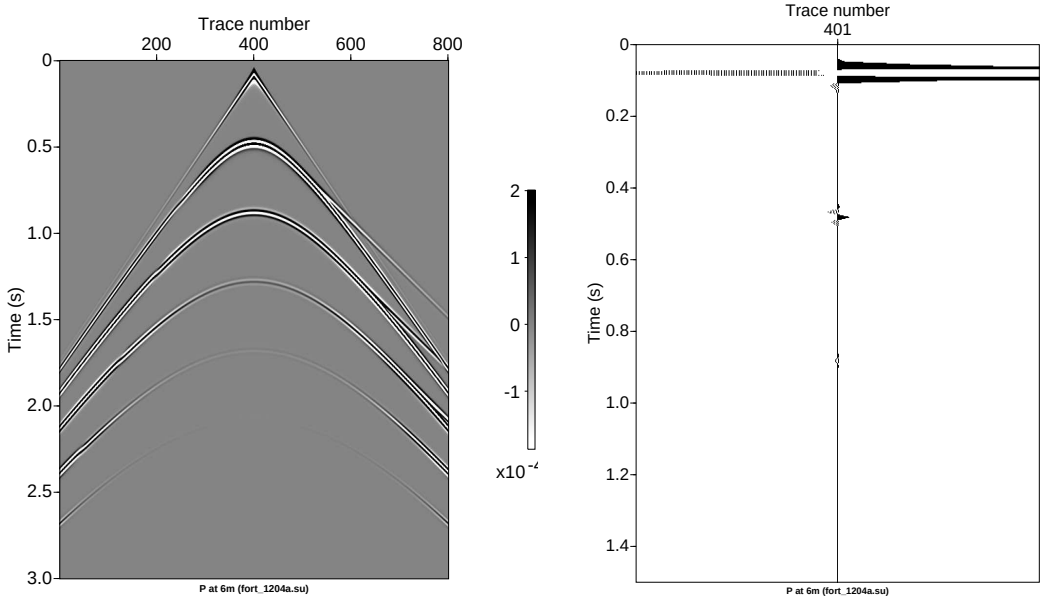

Figure 32: *Cagniard-de Hoop data, over/under cables separated by 1m, wavefield prediction of new $P, \partial P/\partial z$ using double Dirichlet Green's function G_0^{DD}. Ghost notches not in the input data.*

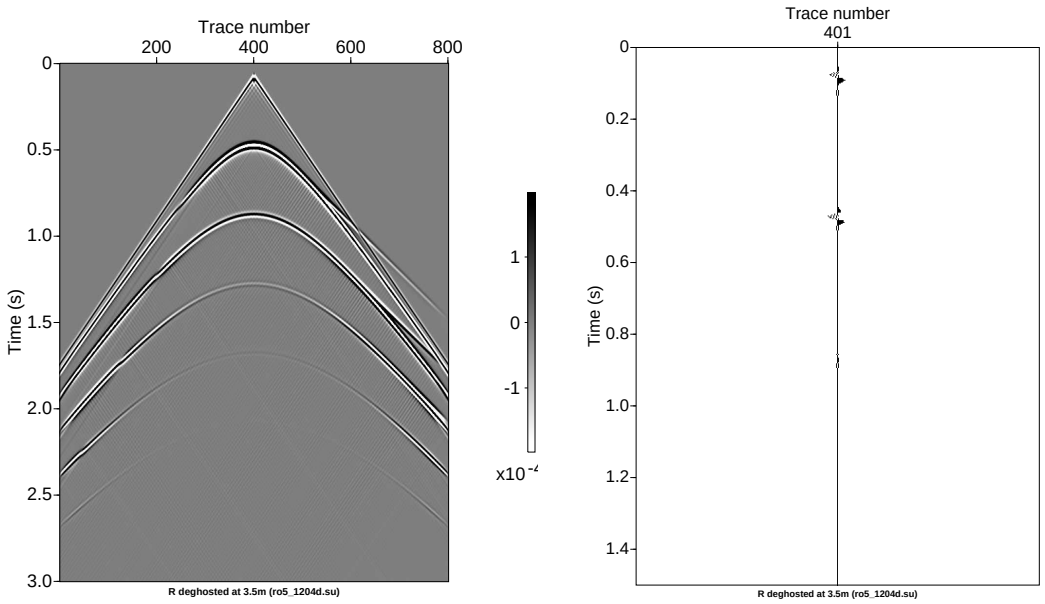

Figure 33: *Cagniard-de Hoop data: receiver-deghosted result using over/under cables separated by 1m.*

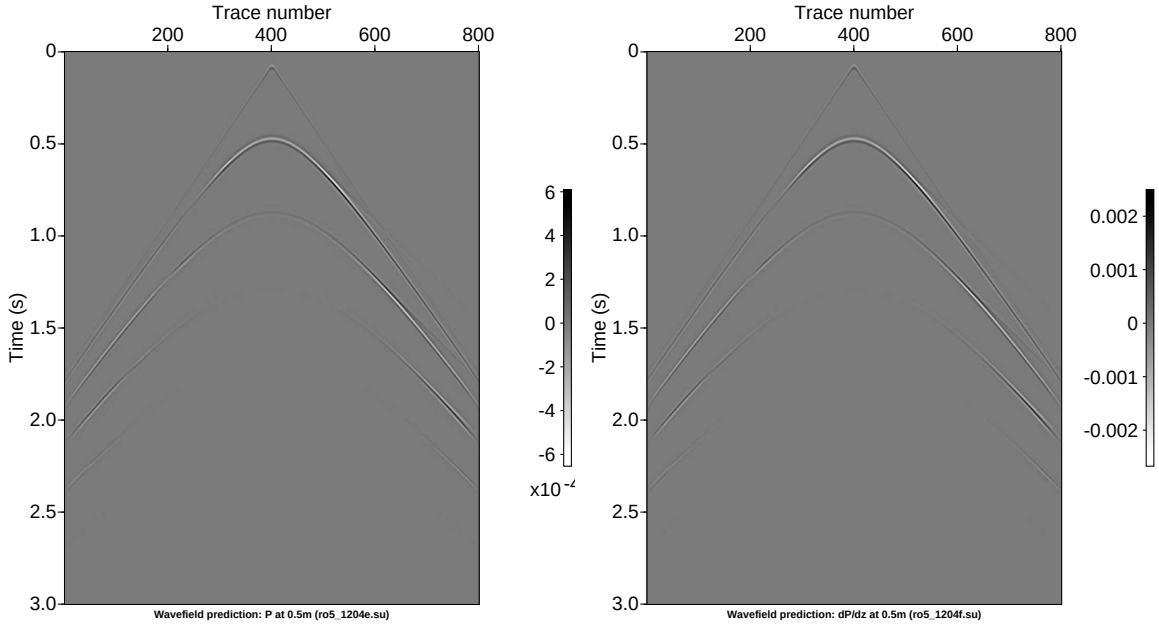

Figure 34: *Wavefield prediction P using receiver-deghosted result in Figure 33.*

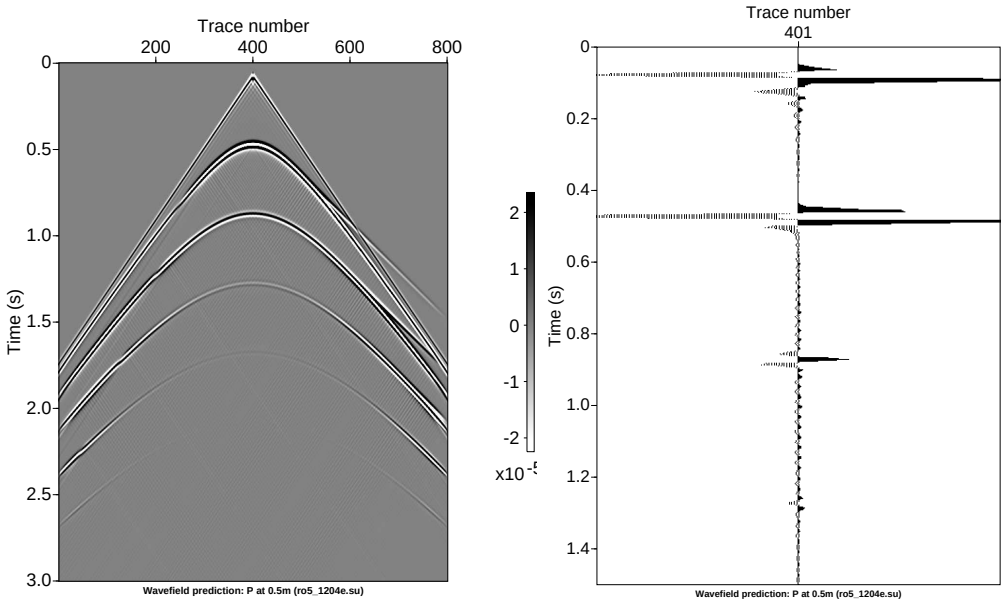

Figure 35: *Cagniard-de Hoop data: new P given correct depth.*

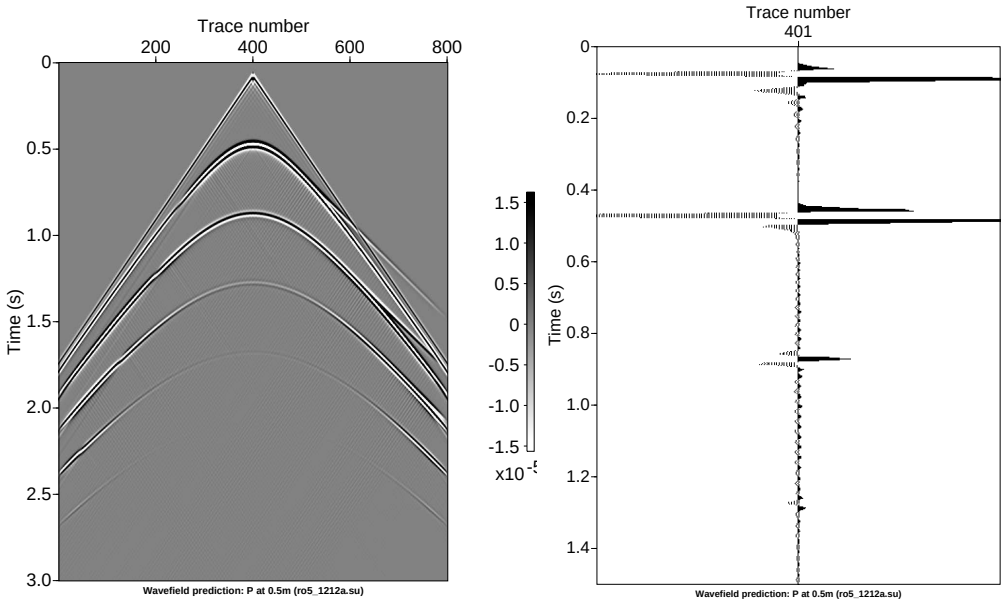

Figure 36: *Cagniard-de Hoop data: new P given incorrect depth (1m too deep).*

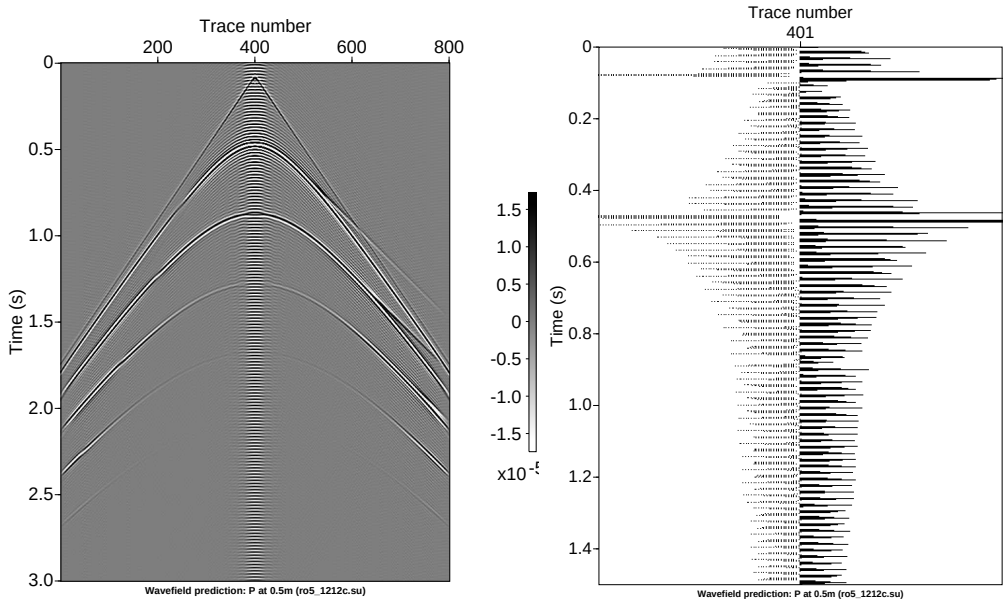

Figure 37: *Cagniard-de Hoop data: new P given incorrect depth (10m too deep).*

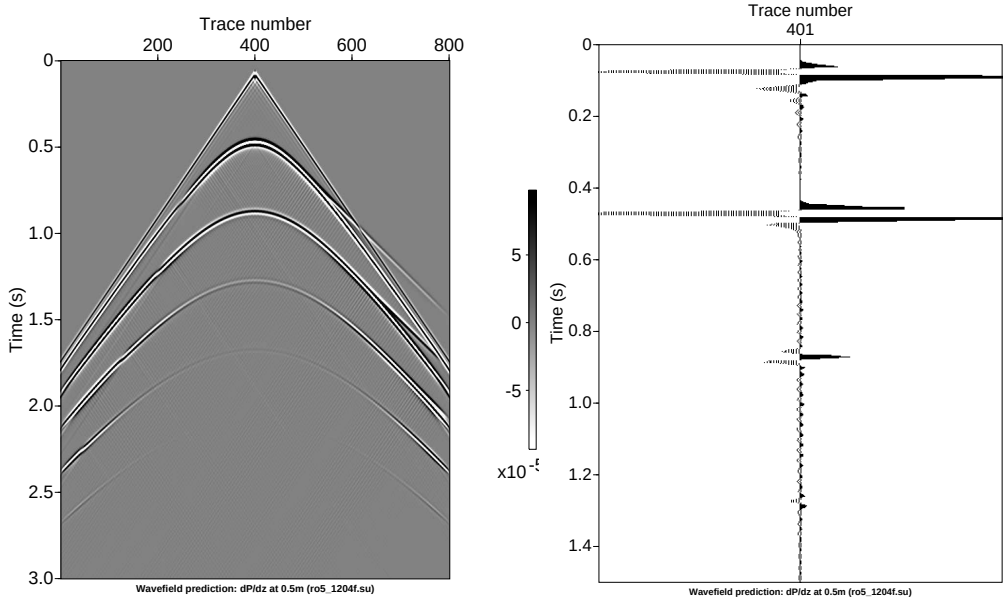

Figure 38: *Cagniard-de Hoop data: new $\partial P/\partial z$ given correct depth.*

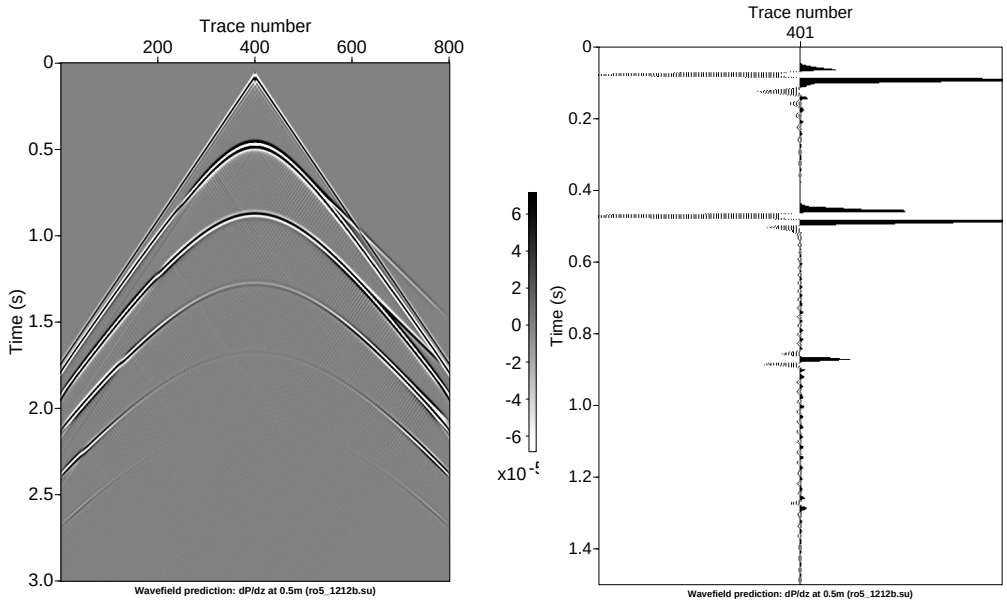

Figure 39: *Cagniard-de Hoop data: new $\partial P/\partial z$ given incorrect depth (1m too deep).*

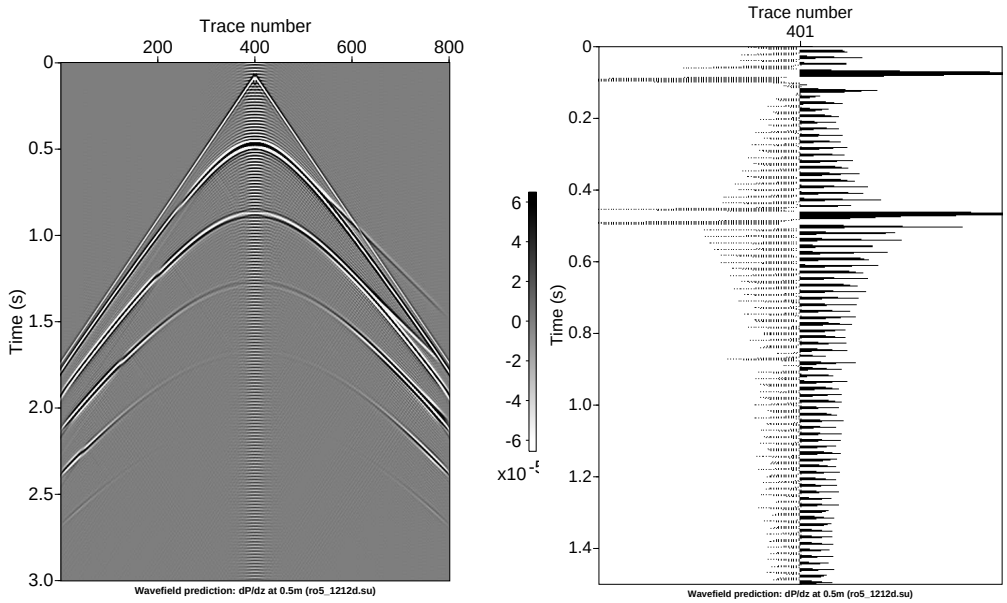

Figure 40: *Cagniard-de Hoop data: new $\partial P/\partial z$ given incorrect depth (10m too deep).*

6 Compare Green's theorem-derived deghosting and deghosting in the $\mathbf{k}, \omega$ domain

PGS receiver deghosting is described in four SEG Expanded Abstracts: Carlson et al. (2007), Tenghamn et al. (2007), Cambois et al. (2009), and Klüver et al. (2009). Their proprietary dual-sensor cable (GeoStreamer®) measures the total pressure wavefield p (using hydrophones) and the vertical component v_z of the total particle-velocity wavefield (using geophones). Variables p, v_z are decomposed into plane waves (in the $\mathbf{k}, \omega$ domain), where the transformed data are denoted by P, V_z. P is decomposed into upgoing P^{up} (receiver-deghosted) and downgoing P^{down} wavefields using

$$\left.\begin{matrix} P^{up} \\ P^{down} \end{matrix}\right\} = \frac{1}{2}\left(P \mp \frac{\rho\,\omega}{k_z} V_z\right), \qquad \text{Klüver (1)}$$

where $k_z = \sqrt{(\omega/c_0)^2 - k_x^2 - k_y^2}$, and Klüver 1 refers to Klüver et al. (2009) equation 1. There are key differences between this equation and Green's theorem-derived deghosting.

- Equation Klüver 1 is equation 17 in Amundsen (1993b), which is "valid for marine data acquired over a horizontally layered ... medium" (page 1336). Green's theorem-derived deghosting makes no assumptions about the subsurface.
- The transformation of p, v_z into P, V_z (and back) uses Hankel (and inverse Hankel) transforms. Numerical evaluation of the inverse Hankel transform "is a difficult task" because of rapid oscillations (page 1336). Green's theorem-derived deghosting stays in the $\mathbf{r}$ domain and requires no transformation to the $\mathbf{k}$ domain.

Amundsen's derivation of equation Klüver 1 is shown in Appendix 11.4.

6.1 An alternative to equation Klüver 1

What if we don't assume the earth is 1D? What would it look like if we transform in x, y? Note: In PGS notation, measured data are lowercase p, v_z, and measured data decomposed into plane waves via Hankel transform are uppercase P, V_z. In our notation, used in this derivation, measured data are uppercase P, V_z.

Substituting the (acoustic) partial differential equations for the pressure wavefield $P(\mathbf{r}', \omega)$ and Green's function $G_0(\mathbf{r}, \mathbf{r}', \omega)$ into Green's second identity gives

$$\int_V d\mathbf{r}' P(\mathbf{r}', \mathbf{r}_s, \omega)\delta(\mathbf{r}' - \mathbf{r}) = \int_V d\mathbf{r}' \rho(\mathbf{r}', \mathbf{r}_s, \omega) G_0(\mathbf{r}, \mathbf{r}', \omega)$$
$$+ \oint_S dS' \hat{n}' \cdot [P(\mathbf{r}', \mathbf{r}_s, \omega)\nabla' G_0(\mathbf{r}, \mathbf{r}', \omega) - G_0(\mathbf{r}, \mathbf{r}', \omega)\nabla' P(\mathbf{r}', \mathbf{r}_s, \omega)]. \qquad (9)$$

See (e.g.) Weglein et al. (2002) and Chapter 2 of Zhang (2007). For deghosting use the configuration shown in Figure 2, i.e., choose

- $\rho(\mathbf{r}', \mathbf{r}_s, \omega) = A(\omega)\delta(\mathbf{r}' - \mathbf{r}_s) + k^2\alpha_{air}(\mathbf{r}')P(\mathbf{r}', \mathbf{r}_s, \omega) + k^2\alpha_{earth}(\mathbf{r}')P(\mathbf{r}', \mathbf{r}_s, \omega)$, i.e., the actual medium is a reference medium (a whole space of water) plus three sources (air guns (first term), air (middle term), and earth(last term)),
- V is a hemisphere bounded below by the measurement surface,
- $\mathbf{r}$ is above the measurement surface and below the air/water boundary (i.e., $\in V$), and
- G_0 is a whole-space causal Green's function G_0^+.

Take the radius of the hemisphere to infinity and invoke the Sommerfeld radiation condition and equation 9 becomes

$$P'_R(\mathbf{r}, \mathbf{r}_s, \omega) = \int_{m.s.} dS' \hat{n}' \cdot [P(\mathbf{r}', \mathbf{r}_s, \omega)\nabla' G_0^+(\mathbf{r}, \mathbf{r}', \omega) - G_0^+(\mathbf{r}, \mathbf{r}', \omega)\nabla' P(\mathbf{r}', \mathbf{r}_s, \omega)]. \tag{10}$$

For simplicity, assume 2D, and equation 10 takes the form

$$\begin{aligned} P'_R(x, z, x_s, z_s, \omega) &= \int_{m.s.} dx' \\ &[P(x', z', x_s, z_s, \omega)\frac{\partial G_0^+}{\partial z'}(x, z, x', z', \omega) - G_0^+(x, z, x', z', \omega)\frac{\partial P}{\partial z'}(x', z', x_s, z_s, \omega)]. \end{aligned} \tag{11}$$

Fourier transform equation 11 with respect to x,

$$\begin{aligned} &\int dx \exp(ik_x x) P'_R(x, z, x_s, z_s, \omega) = \int dx \exp(ik_x x) \\ &\times \int_{m.s.} dx' [P(x', z', x_s, z_s, \omega)\frac{\partial G_0^+}{\partial z'}(x, z, x', z', \omega) - G_0^+(x, z, x', z', \omega)\frac{\partial P}{\partial z'}(x', z', x_s, z_s, \omega)]. \end{aligned} \tag{12}$$

The left-hand side (LHS) of equation 12 becomes $\widetilde{P'_R}(k_x, z, x_s, z_s, \omega)$. Substitute the bilinear form of Green's function in the right-hand side (RHS) of equation 12,

$$\begin{aligned} \text{RHS} &= \int dx \exp(ik_x x) \int_{m.s.} dx' [P(x', z', x_s, z_s, \omega) \\ &\times \frac{\partial}{\partial z'} \left[\frac{1}{2\pi} \int dk'_x \frac{\exp(-ik'_x(x - x')) \exp(ik'_z(z' - z))}{2ik'_z} \right] \\ &- \frac{1}{2\pi} \int dk'_x \frac{\exp(-ik'_x(x - x')) \exp(ik'_z(z' - z))}{2ik'_z} \frac{\partial P}{\partial z'}(x', z', x_s, z_s, \omega)], \end{aligned} \tag{13}$$

where $k'_z = \sqrt{(\omega/c_0)^2 - k'^2_x}$. Substitute $\mu = \mathbf{r} - \mathbf{r}'$ in equation 13,

$$\begin{aligned} \text{RHS} &= \int_{m.s.} dx' \int d\mu_x \exp(ik_x(\mu_x + x'))[P(x', z', x_s, z_s, \omega) \frac{1}{2\pi} \int dk'_x \frac{\exp(-ik'_x\mu_x) \exp(-ik'_z\mu_z)}{2ik'_z}(-ik'_z)(-1) \\ &- \frac{1}{2\pi} \int dk'_x \frac{\exp(-ik'_x\mu_x) \exp(-ik'_z\mu_z)}{2ik'_z} \frac{\partial P}{\partial z'}(x', z', x_s, z_s, \omega)] \\ &= \frac{1}{2\pi} \int_{m.s.} dx' \int d\mu_x \exp(ik_x(\mu_x + x'))[P(x', z', x_s, z_s, \omega) \int dk'_x \exp(-ik'_x\mu_x)(ik'_z) \end{aligned}$$

$$
\begin{aligned}
&- \int dk'_x \, \exp\left(-ik'_x \mu_x\right) \frac{\partial P}{\partial z'}(x', z', x_s, z_s, \omega)] \frac{\exp\left(-ik'_z \mu_z\right)}{2ik'_z} \\
&= \frac{1}{2\pi} \int dk'_x \, \frac{\exp\left(-ik'_z \mu_z\right)}{2ik'_z} \underbrace{\int d\mu_x \exp\left(-i(k'_x - k_x)\mu_x\right)}_{2\pi\delta(k'_x - k_x)} \\
&\times [ik'_z \underbrace{\int_{m.s.} dx' \exp\left(ik_x x'\right) P(x', z', x_s, z_s, \omega)}_{\widetilde{P}(k_x, z', x_s, z_s, \omega)} - \int dx' \, \exp\left(ik_x x'\right) \underbrace{\frac{\partial P}{\partial z'}(x', z', x_s, z_s, \omega)}_{i\omega\rho V_z(x', z', x_s, z_s, \omega)}]. \qquad (14)
\end{aligned}
$$

In equation 14, the integral over $d\mu_x$ gives a Dirac delta, $2\pi\delta(k'_x - k_x)$, the integral over dx' is a Fourier transform of the pressure wavefield and gives $\widetilde{P}(k_x, z', x_s, z_s, \omega)$, and the vertical derivative of the pressure wavefield is $i\omega\rho\, V_z(x', z', x_s, z_s, \omega)$. (The latter relationship is derived in Appendix 11.5.) The integral of dx' over the measurement surface allows a Fourier transform because, in the derivation of equation 10, the radius of the hemisphere was taken to infinity. We now have (for the right-hand side of equation 12)

$$
\begin{aligned}
\text{RHS} \; &= \frac{1}{2\pi} \int dk'_x \, \frac{\exp\left(-ik'_z \mu_z\right)}{2ik'_z} 2\pi\delta(k'_x - k_x) \\
&\times [ik'_z \widetilde{P}(k_x, z', x_s, z_s, \omega) - i\omega\rho \underbrace{\int dx' \, \exp\left(ik_x x'\right) V_z(x', z', x_s, z_s, \omega)}_{\widetilde{V_z}(k_x, z', x_s, z_s, \omega)}] \qquad (15)
\end{aligned}
$$

In equation 15, the integral over dx' is a Fourier transform of the vertical velocity field and gives $\widetilde{V_z}(k_x, z', x_s, z_s, \omega)$. Using $k'^2_z = \omega^2/c_0^2 - k'^2_x$ and $k_z^2 = \omega^2/c_0^2 - k_x^2$, equation 15 can be rewritten as

$$
\begin{aligned}
\text{RHS} \; &= \underbrace{\int dk'_x \, \delta(k'_x - k_x)}_{1} \frac{\exp\left(-ik'_z \mu_z\right)}{2ik'_z} [ik'_z \widetilde{P}(k_x, z', x_s, z_s, \omega) - i\omega\rho \widetilde{V_z}(k_x, z', x_s, z_s, \omega)] \\
&= \frac{\exp\left(-ik'_z \mu_z\right)}{2ik'_z} [ik'_z \widetilde{P}(k_x, z', x_s, z_s, \omega) - i\omega\rho \widetilde{V_z}(k_x, z', x_s, z_s, \omega)].
\end{aligned}
$$

Collecting terms gives

$$
\begin{aligned}
&\widetilde{P'_R}(k_x, z, x_s, z_s, \omega) \\
&= \frac{\exp\left(-ik'_z \mu_z\right)}{2ik'_z} (ik_z) [\widetilde{P}(k_x, z', x_s, z_s, \omega) - \frac{\omega\rho}{k_z} \widetilde{V_z}(k_x, z', x_s, z_s, \omega)] \\
&= \frac{1}{2} \exp\left(ik'_z(z' - z)\right) [\widetilde{P}(k_x, z', x_s, z_s, \omega) - \frac{\omega\rho}{k_z} \widetilde{V_z}(k_x, z', x_s, z_s, \omega)]. \qquad (16)
\end{aligned}
$$

In the last equation, the phase factor $\exp\left(ik'_z(z' - z)\right)$ takes the one-way wavefield $\widetilde{P'_R}$ from the cable depth z' to the predicted (deghosted) depth z. This demonstrates that the Green's theorem deghosting reduces to the Fourier form equation 16 under conditions that allow the steps in this demonstration. The standard-practice deghosting $P - V_z$ algorithm today is a version of 16 that accommodates a 3D point source, but assumes the earth is 1D. Equations 10 and 16 allow the lifting of the 1D assumption, and in addition equation 10 doesn't require a horizontal measurement surface.

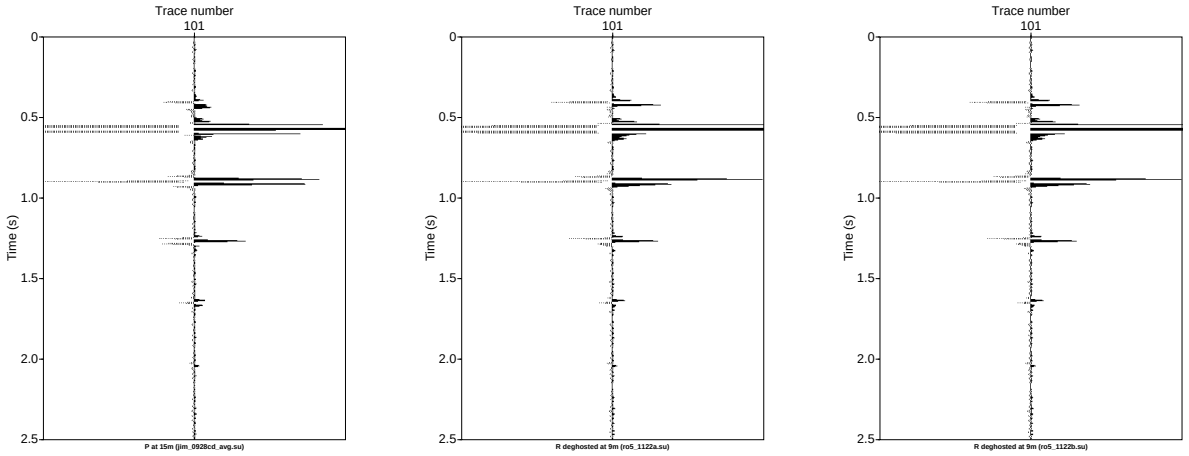

Figure 41: *Reflectivity data, overlapping events: source at 8m, receivers at 14m and 16m. Input (left), receiver deghosted using equation 10 (middle), receiver deghosted using equation 17 (right).*

7 Compare Green's theorem-derived deghosting and Fourier-Bessel integral

If we have a 3D source and 1D earth, it's better to use a Fourier-Bessel integral. Per Zhiqiang Wang (from Fang Liu), the integral can be restated from rectangular coordinates to polar coordinates as follows:

$$\int dy \int dx\, f(x,y,z) = \int \rho\, d\rho \int d\theta\, f(\rho,\theta,z)$$

$$\text{If } f(\rho,\theta,z) = f(\rho,z) \text{ (azimuthal symmetry), then}$$

$$\int \rho\, d\rho \int d\theta\, f(\rho,\theta,z) = 2\pi \int \rho\, d\rho\, f(\rho,z) = 2\pi \int x\, dx\, f(x,z) \text{ if 1 cable,} \tag{17}$$

Comparing the middle and right panels in Figure 41 shows no difference. I suspect this is because the program computes the Green's functions to a high degree of precision.

8 Remarks on the algorithm

1. An important relationship exists between Δz and Δx, where Δz is the depth between the input cable and output (predicted) cable in equation 3, and Δx is the interval between adjacent traces (receiver groups). For good results: $\Delta z \gtrsim 0.5\,\Delta x$. Where is this relationship coming from?

$$P'_R(\mathbf{r}'_g, \mathbf{r}_s, \omega) = \int_{\text{m.s.}} dx\, dy$$

$$[P(\mathbf{r}, \mathbf{r}_s, \omega) \underbrace{\frac{-1}{4\pi} \frac{\exp(ikR_+)}{R_+} \frac{z'_g - z}{R_+^2}(1 - ikR_+)}_{\partial G_0^{d+}/\partial z} - \underbrace{\frac{-1}{4\pi} \frac{\exp(ikR_+)}{R_+}}_{G_0^{d+}} \underbrace{i\omega\rho V_z(\mathbf{r}, \mathbf{r}_s, \omega)}_{\partial P/\partial z}],$$

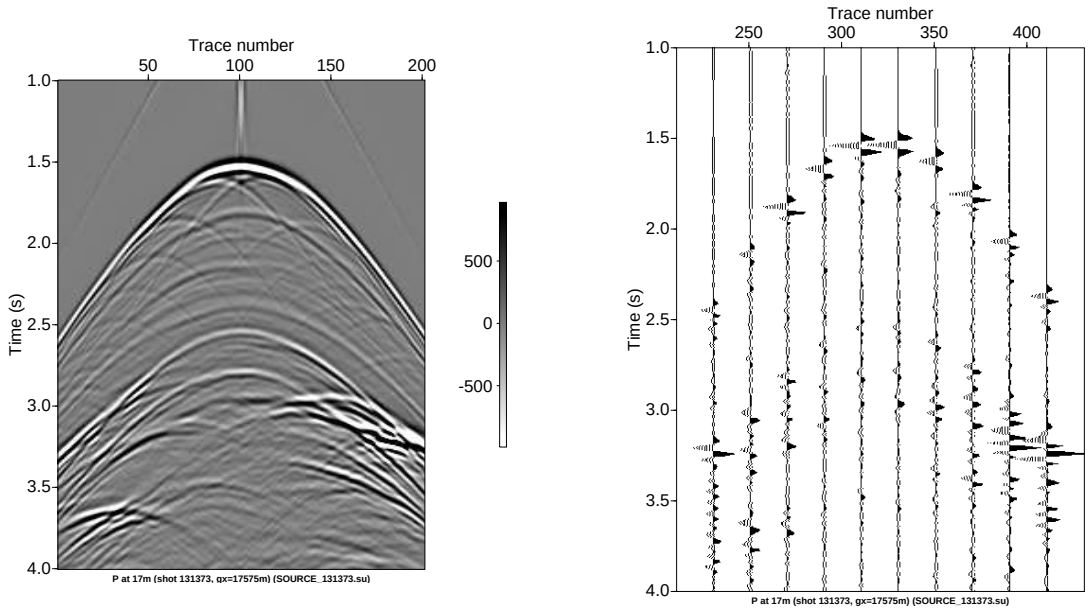

Figure 42: *SEAM Phase I data, shot 131373: P at 17m.*

where $R_+ = |\mathbf{r}'_g - \mathbf{r}_s|$. If $\Delta z = z'_g - z$ becomes too small, the first term in the integrand is suppressed and the quality of deghosting suffers. This is also discussed in Tang (2013).

2. The current deghosting program was tested on SEAM Phase I data. Creating a receiver-deghosted pseudo array requires that equation 10 be evaluated over the 661×661 receiver array for each of the 661×661 receivers. The job was submitted but would run for probably several weeks. Taking advantage of the local nature of the integrand, a new way of submitting the program was tried — restrict the integral to a radius of $100\Delta x$ or $10\Delta x$ around each predicted receiver. The latter job ran overnight, and the results look satisfactory. Comparing Figures 42 and 43 shows that the water-bottom primary's receiver ghost and source/receiver ghost are attenuated (the bottom of the first event). Comparing Figures 43 ($10\Delta x$) and 44 ($100\Delta x$) shows no difference.

3. The compute clusters I used at UH and PGS are shown in Appendices 11.6 and 11.7.

9 Conclusions

1. We have shown images before and after receiver deghosting for separated data (where the source and receivers are deep enough to separate events and their ghosts) through partially interfering events to overlapping events.

2. We have provided the pros and cons of each kind of cable configuration.

3. We have found that Green's theorem-derived deghosting is insensitive to the cable depth, gives better results as the vertical distance between over and under cables decreases, and (for wavefield prediction) is sensitive to the presence of ghost notches in the data.

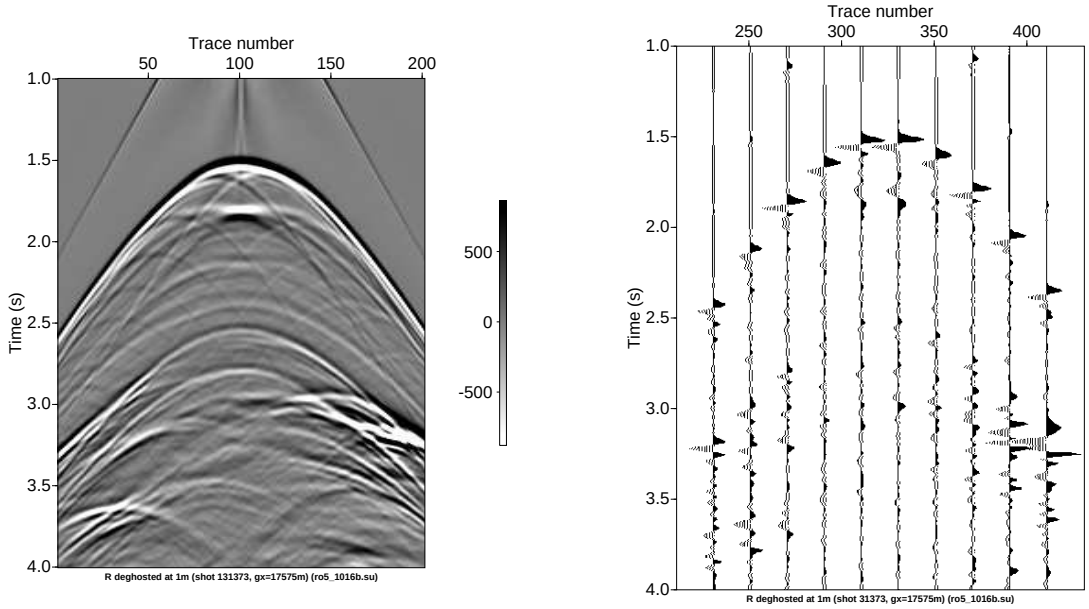

Figure 43: *SEAM Phase I data, shot 131373: receiver deghosted at 1m. The integral was restricted to a radius of* $10\Delta x$ *around each receiver on the measurement surface.*

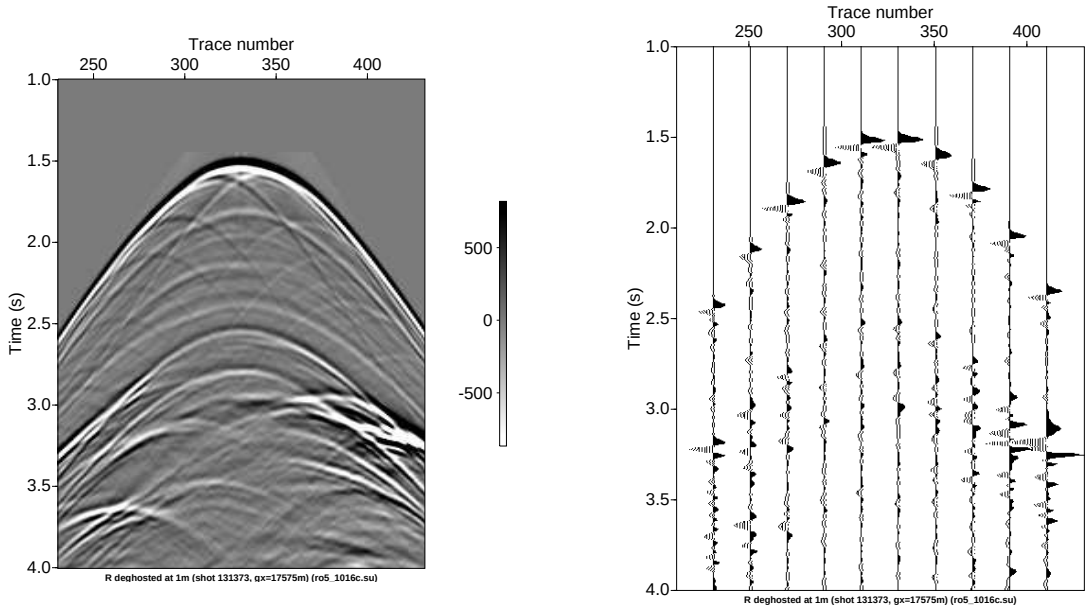

Figure 44: *SEAM Phase I data, shot 131373: receiver deghosted at 1m. The integral was restricted to a radius of* $100\Delta x$ *around each receiver on the measurement surface.*

4. We have shown that Green's theorem-derived deghosting has fewer requirements than does wavenumber-based deghosting.

10 Acknowledgements

We are grateful to the M-OSRP sponsors for their support of this research. The first author is also grateful to ExxonMobil and PGS for internships and to Nizar Chemingui (PGS), Paolo Terenghi (now at PGS), and the second author for mentoring.

11 Appendix

11.1 Receiver deghosting: Supplemental theory

Following Weglein et al. (2002) and Chapter 2 of Zhang (2007), to separate upward-moving and downward-moving waves, we define the following (see Figure 2):
(1) a reference medium consisting of a whole space of water with wavespeed c_0,
(2) a perturbation $\alpha_{\text{air}}(\mathbf{r})$ that is the difference between the reference medium (water) and the upper part (air) of the actual medium, defined by $1/c^2_{\text{air}} = 1/c^2_{\text{water}}(1-\alpha_{\text{air}})$,
(3) a perturbation $\alpha_{\text{earth}}(\mathbf{r})$ that is the difference between the reference medium (water) and the lower part (earth) of the actual medium, defined by $1/c^2_{\text{earth}} = 1/c^2_{\text{water}}(1-\alpha_{\text{earth}})$,
(4) an integration volume V consisting of a hemisphere bounded from below by the measurement surface,
(5) a surface (air-water interface) above the measurement surface (i.e., inside V),
(6) a source at $\mathbf{r}_s$ above the measurement surface (again inside V),
(7) a causal whole-space Green's function $G_0^+(\mathbf{r},\mathbf{r}'_g,\omega)$ in the reference medium,
(8) $k_0 = \omega/c_0$,
(9) the prediction/observation point $\mathbf{r}'_g \in V$ lying below the source $\mathbf{r}_s$ and above the measurement surface, and
(10) S as the hemisphere's surface.

For two wavefields P and G_0^+, Green's theorem becomes

$$\begin{aligned}&\oint_S dS\,\mathbf{n}\cdot[P(\mathbf{r},\mathbf{r}_s,\omega)\nabla G_0^+(\mathbf{r},\mathbf{r}'_g,\omega) - G_0^+(\mathbf{r},\mathbf{r}'_g,\omega)\nabla P(\mathbf{r},\mathbf{r}_s,\omega)]\\ =&\int_V d\mathbf{r}[P(\mathbf{r},\mathbf{r}_s,\omega)\nabla^2 G_0^+(\mathbf{r},\mathbf{r}'_g,\omega) - G_0^+(\mathbf{r},\mathbf{r}'_g,\omega)\nabla^2 P(\mathbf{r},\mathbf{r}_s,\omega)].\end{aligned} \tag{11.18}$$

Substituting the partial differential equations for the pressure wavefield P and causal whole-space Green's function G_0^+

$$(\nabla^2 + k_0^2)P(\mathbf{r},\mathbf{r}_s,\omega) = A(\omega)\delta(\mathbf{r}-\mathbf{r}_s) + k_0^2(\alpha_{air}+\alpha_{earth})P \tag{11.19}$$

$$(\nabla^2 + k_0^2)G_0^+(\mathbf{r},\mathbf{r}'_g,\omega) = \delta(\mathbf{r}-\mathbf{r}'_g) \tag{11.20}$$

into the right-hand side of equation 11.18 gives

$$\begin{aligned}
&\int_V d\mathbf{r}\{P(\mathbf{r},\mathbf{r}_s,\omega)[-k_0^2 G_0^+ + \delta(\mathbf{r}-\mathbf{r}'_g)] \\
&- G_0^+(\mathbf{r},\mathbf{r}'_g,\omega)[-k_0^2 P + A(\omega)\delta(\mathbf{r}-\mathbf{r}_s) + k_0^2(\alpha_{air}+\alpha_{earth})P]\} \\
=&\int_V d\mathbf{r}\{P(\mathbf{r},\mathbf{r}_s,\omega)\delta(\mathbf{r}-\mathbf{r}'_g) - P(\mathbf{r},\mathbf{r}_s,\omega)k_0^2 G_0^+(\mathbf{r},\mathbf{r}'_g,\omega) + G_0^+(\mathbf{r},\mathbf{r}'_g,\omega)k_0^2 P(\mathbf{r},\mathbf{r}_s,\omega) \\
&- k_0^2[\alpha_{air}(\mathbf{r})+\alpha_{earth}(\mathbf{r})]P(\mathbf{r},\mathbf{r}_s,\omega)G_0^+(\mathbf{r},\mathbf{r}'_g,\omega) - A(\omega)\delta(\mathbf{r}-\mathbf{r}_s)G_0^+(\mathbf{r},\mathbf{r}'_g,\omega)\}. \qquad (11.21)
\end{aligned}$$

The first term gives $P(\mathbf{r}'_g,\mathbf{r}_s,\omega)$ because the prediction/observation point $\mathbf{r}'_g$ is between the measurement surface and air-water surface, i.e., $\in V$. The cross terms $-P(\mathbf{r},\mathbf{r}_s,\omega)k_0^2 G_0^+(\mathbf{r},\mathbf{r}'_g,\omega) + G_0^+(\mathbf{r},\mathbf{r}'_g,\omega)k_0^2 P(\mathbf{r},\mathbf{r}_s,\omega)$ cancel. (This cancellation occurs in the frequency domain but not in the time domain.) $\alpha_{earth}(\mathbf{r}) = 0$ because the volume integral doesn't contain α_{earth}. The last term gives $A(\omega)G_0^+(\mathbf{r}_s,\mathbf{r}'_g,\omega)$ because the source (air guns) are between the measurement surface and air-water surface, i.e., are within the volume V. Substituting these four results into equation 11.21 gives for the left member of 11.21

$$P(\mathbf{r}'_g,\mathbf{r}_s,\omega) - \int_V d\mathbf{r}\, k_0^2\alpha_{air}(\mathbf{r})P(\mathbf{r},\mathbf{r}_s,\omega)G_0^+(\mathbf{r},\mathbf{r}'_g,\omega) - A(\omega)G_0^+(\mathbf{r}_s,\mathbf{r}'_g,\omega). \qquad (11.22)$$

Using the symmetry of the Green's function ($G_0^+(\mathbf{r}_s,\mathbf{r}'_g,\omega) = G_0^+(\mathbf{r}'_g,\mathbf{r}_s,\omega)$) and collecting terms gives

$$\begin{aligned}
&\oint_S \mathbf{n}\, dS \cdot [P(\mathbf{r},\mathbf{r}_s,\omega)\nabla G_0^+(\mathbf{r},\mathbf{r}'_g,\omega) - G_0^+(\mathbf{r},\mathbf{r}'_g,\omega)\nabla P(\mathbf{r},\mathbf{r}_s,\omega)] \\
=&P(\mathbf{r}'_g,\mathbf{r}_s,\omega) - \int_V d\mathbf{r}\, G_0^+(\mathbf{r},\mathbf{r}'_g,\omega)k_0^2\alpha_{air}(\mathbf{r})P(\mathbf{r},\mathbf{r}_s,\omega) - A(\omega)G_0^+(\mathbf{r}'_g,\mathbf{r}_s,\omega). \qquad (11.23)
\end{aligned}$$

The physical meaning of equation 11.23 is that the total wavefield at $\mathbf{r}'_g$ can be separated into three parts. There are three spatially distributed sources causing the wavefield P. From the extinction theorem/Green's theorem, the left-hand side of equation 11.23 is the contribution to the field at $\mathbf{r}'_g$ due to sources outside V. There is one source outside V, $\rho_{\text{earth}} = k^2\alpha_{\text{earth}}P$. The contribution it makes at $\mathbf{r}'_g$ is $\int G_0^+\rho_{\text{earth}}$ and upgoing. The two other sources ($\rho_{\text{air}} = k^2\alpha_{\text{air}}P$ and $\rho_{\text{air guns}}$) produce a down field at $\mathbf{r}'_g$.

Letting the radius of the hemisphere go to ∞, the Sommerfeld radiation condition gives

$$\int_{m.s.} dS\, \mathbf{n}\cdot[P(\mathbf{r},\mathbf{r}_s,\omega)\nabla G_0^+(\mathbf{r},\mathbf{r}'_g,\omega) - G_0^+(\mathbf{r},\mathbf{r}'_g,\omega)\nabla P(\mathbf{r},\mathbf{r}_s,\omega)] = P'_R(\mathbf{r}'_g,\mathbf{r}_s,\omega), \qquad (11.24)$$

where $P(\mathbf{r},\mathbf{r}_s,\omega)$ and $\nabla P(\mathbf{r},\mathbf{r}_s,\omega)\cdot\hat{\mathbf{n}}$ are respectively the hydrophone measurements and normal derivatives (in the frequency domain), and G_0^+ is the causal whole-space Green's function for a homogeneous acoustic medium with water speed.

An anonymous reviewer noted that "to transform the volume integral to a surface integral uses Gauss' theorem but also requires that the wavefield satisfies a Helmholtz equation, which can only be guaranteed for a homogeneous sub-volume." Green's theorem-based deghosting is computed above the measurement surface and below the air/water boundary, where the actual medium coincides with the homogeneous reference medium.

11.2 Input data

11.2.1 Cagniard-de Hoop data

Parameter	Value
Number of shots	1
Number of channels per shot	1601
Number of samples per trace	625
Time sampling	4 ms
Record length	2.5 s
Shot interval	n.a.
Group interval	3 m
Shortest offset	0 m
Gun depth	7 m
Streamer depth	9 m & 11 m

- Data created by Jinlong Yang using a Cagniard-de Hoop program written by Jingfeng Zhang (now at BP)
- Model: air/water boundary, water bottom at 300 m, 1D constant-density acoustic earth (c = 2250 m/s)
- 1 over/under towed streamer, $\partial P/\partial z \simeq (P(11\,m) - P(9\,m))/2\,m$

11.2.2 Reflectivity data: Separated events

Parameter	Value
Number of shots	1
Number of channels per shot	801
Number of samples per trace	1500
Time sampling	4ms
Record length	6s
Group interval	6.25m
Shortest offset	0m
Gun depth	30m
Streamer depth	139m & 141m

- Data created using reflectivity program
- Model: air/water boundary, water bottom at 300m, acoustic earth ($c_0 = 2250m/s$, $\rho = 1.667g/cm^3$)
- 3D source, frequency of source: 1-60Hz
- 5% taper applied to each end of cable
- $\partial P/\partial z \simeq [P(141m) - P(139m)]/2m$

11.2.3 Reflectivity data: Partially interfering events

Parameter	Value
Number of shots	1
Number of channels per shot	801
Number of samples per trace	1500
Time sampling	4ms
Record length	6s
Group interval	6.25m
Shortest offset	0m
Gun depth	9m
Streamer depth	49m & 51m

- Data created using reflectivity program
- Model: air/water boundary, water bottom at 300m, acoustic earth ($c_0 = 2250m/s$, $\rho = 1.667g/cm^3$) (same as Appendix 11.2.2)
- 3D source, frequency of source: 1-60Hz
- 5% taper applied to each end of cable
- $\partial P/\partial z \simeq [P(51m) - P(49m)]/2m$
- Gun depth same as Gulf of Mexico field data, streamer depth 2× Gulf of Mexico field data

11.2.4 Reflectivity data: Overlapping events

Parameter	Value
Number of shots	1
Number of channels per shot	801
Number of samples per trace	1500
Time sampling	4ms
Record length	6s
Group interval	6.25m
Shortest offset	0m
Gun depth	8m
Streamer depth	14m & 16m

- Data created using reflectivity program
- Model: air/water boundary, water bottom at 300m, acoustic earth ($c_0 = 2250m/s$, $\rho = 1.667g/cm^3$) (same as Appendix 11.2.2)
- 3D source, frequency of source: 1-60Hz
- 5% taper applied to each end of cable

- $\partial P/\partial z \simeq [P(16m) - P(14m)]/2m$
- Gun depth & streamer depth same as Total data

11.2.5 Synthetic data: SEAM Phase I deep-water Gulf of Mexico model

Parameter	Value
Number of shots	9×267
Number of channels per shot	661×661
Number of samples per trace	2001
Time sampling	8ms
Record length	16s
Shot interval	150m
Group interval	30m
Shortest offset	0m
Gun depth	15m
Streamer depth	15m & 17m

- 3D source, frequency of source: 1-30Hz
- Distance between towed streamers: 30m
- $\partial P/\partial z \simeq [P(17m) - P(15m)]/2m$

11.2.6 Field data: deep-water Gulf of Mexico*

Parameter	Value
Number of shots	2451
Number of channels per shot	960
Number of samples per trace	3585
Time sampling	4ms
Record length	14.34s
Shot interval	37.5m
Group interval	12.5m
Shortest offset	112m
Gun depth	9m
Streamer depth	25m

- 1 dual-sensor towed streamer
- $\partial P/\partial z = i\omega\rho V_z$ where ρ is density of reference medium (seawater)

*Courtesy of PGS.

11.3 Estimating source signature using a dual-sensor cable

Below some critical frequency, geophone readings are deleted and reconstructed using hydrophone readings and equation (B-6) in Amundsen et al. (1995),

$$\begin{aligned} V_z = & \frac{k_z}{\rho\omega}[\exp(-ik_z\Delta z) - \exp(ik_z\Delta z)]^{-1} \\ & \times \{2P(k_x, k_y, z_1, \omega) \\ & - [\exp(-ik_z\Delta z) + \exp(ik_z\Delta z)]P(x_r, y_r, z_2, \omega)\}, \end{aligned}$$

where the over and under cables are at depths z_1 and z_2 and $\Delta z \equiv z_2 - z_1$. The over cable is assumed to be the air/water boundary. In this case, $P(k_x, k_y, z_1, \omega) = 0$, $\Delta z \equiv z_2$, and equation (B-6) becomes

$$V_z = -i\frac{k_z}{\rho\omega}\frac{\cos(k_z z_2)}{\sin(k_z z_2)}P(x_r, y_r, z_2, \omega), \tag{11.25}$$

which has notches when $k_z z_2 = n\pi$ (n an integer). For $z_2 = 25m$ (deep-water Gulf of Mexico), this corresponds to

$$\begin{aligned} k_z &= \frac{n\pi}{z_2} = \frac{2\pi f}{c_0} \\ f &= \frac{n\pi c_0}{2\pi z_2} = \frac{nc_0}{2z_2} = \frac{1500n}{50} \\ &= \text{multiples of 30Hz.} \end{aligned} \tag{11.26}$$

Since the critical frequency is about half this, equation 11.25 is valid in the required range. However, equation (B-6) is valid only for the downgoing wavefield at the receivers (its derivation assumes that the observation or prediction depth ζ satisfies $\zeta > z_2 > z_1$). Hence, Green's theorem cannot be used to estimate the source wavelet given GeoStreamer® input data. Amundsen et al. (1995) makes the assumption that $\zeta > z_2 > z_1$ in order to lift the absolute values in the derivation of equation (B-4). Hence, equation (B-6) is valid only for observation or prediction points below the measurement surface.

11.4 Derivation of equation Klüver 1

The derivation can be broken down into the following steps:

1. Convert p, v_z into P, V_z via Hankel transform.
2. Decompose P into reference P_d and scattered P_r wavefields.
3. Find P, V_z for sources above the receivers.
4. Decompose P into upgoing U and downgoing D wavefields.
5. Show that equation 17 gives U and D.

In this derivation equation numbers are those in Amundsen (1993b).

11.4.1 Step 1.

Amundsen (1993b) assumes a Dirac delta source. This source is radially symmetric, so p, v_z depend only on the radial distance r and depth z. He uses cylindrical coordinates and decomposes data p, v_z into plane waves P, V_z using a Hankel transform,

$$\left\{ \begin{array}{c} P \\ V_z \end{array} \right\} (k_r, z_r, \omega) = \int_0^\infty dr\, r J_0(k_r r) \left\{ \begin{array}{c} p \\ v_z \end{array} \right\} (r, z_r, \omega), \qquad (1)$$

where r is horizontal distance, z_r is receiver depth, and k_r is horizontal wavenumber.

11.4.2 Step 2.

Amundsen (1993b), following Amundsen and Ursin (1991) and Ursin (1983), assumes the earth is a 1D stack of homogeneous layers bounded by homogeneous half spaces (Figure 45). Then

$$P_d(z_r) = \{\underbrace{\exp\left[ik_z|z_r - z_s|\right]}_{\text{direct wave}} - \underbrace{\exp\left[ik_z(z_r + z_s)\right]}_{\text{surface reflection}}\}\Gamma \qquad (4)$$

$$P_r(z_r) = \Re(z=0)\exp\left[-ik_z(z_r + z_s)\right]G_-(z_r)G_-(z_s)\Gamma, \qquad (5)$$

where

- Γ is the source contribution $-\omega^2 S(\omega)/(4\pi c^2 i k_z)$. This form of Γ is also used in Amundsen and Ursin 1991, equation 8. Γ can be restated in terms of our $A(\omega)$ using Amundsen 1993a, equation 33 and Amundsen 1993b, equations 3 and 6. The latter paper assumes a source of the form $\nabla^2\delta(\mathbf{x} - \mathbf{x}_s)S_s(\omega)$, and Fourier transforming gives $k^2 S_s(\omega) = (\omega^2/c^2)S_s(\omega) = -4\pi i k_z \Gamma = -2\pi A(\omega)$, or $\Gamma = A(\omega)/2ik_z$.
- $\Re(z = 0) = \mathcal{R}(k_r, z = 0, \omega)/(1 + \mathcal{R}(k_r, z = 0, \omega))$, and $\mathcal{R}(k_r, z = 0, \omega)$ is the reflection response of a stack of layers in the upper half space (Figures 45 and 46) at $z = 0$, modified by $1/(1 + \mathcal{R}(k_r, z = 0, \omega))$ due to the air/water boundary at $z = 0$ and adjusted to receiver depth by $\exp\left[-ik_z(z_r + z_s)\right]$. This is analogous to the derivation of the M-OSRP free-surface-multiple algorithm (Figure 47).
- $k_z = \sqrt{(\omega/c)^2 - k_r^2}$ is the vertical wavenumber in the first layer (water column), with velocity c.
- $G_-(z_r) = 1 - \exp\left(2ik_z z_r\right)$ is the receiver ghost, and $G_-(z_s) = 1 - \exp\left(2ik_z z_s\right)$ is the source ghost.

11.4.3 Step 3.

For $z_s < z_r$, the absolute value can be lifted,

$$P(z_r) = P_d(z_r) + P_r(z_r) \qquad (3)$$

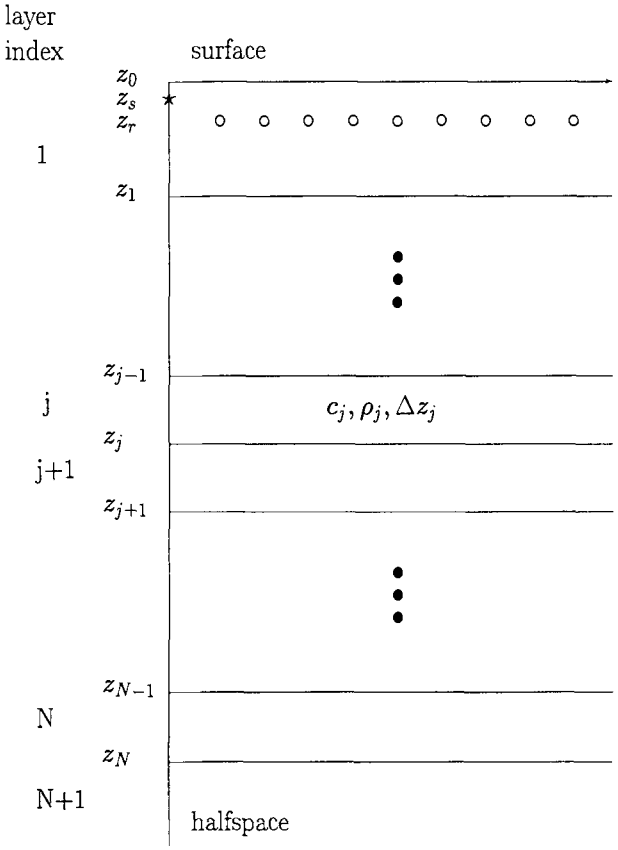

Figure 45: *The layered medium is sandwiched between a half space of air and a half space of earth. Layer j is characterized by thickness Δz_j, velocity c_j, and density ρ_j. The source and receivers are in the first layer at depths z_s and z_r, respectively (Amundsen and Ursin 1991, Fig. 1).*

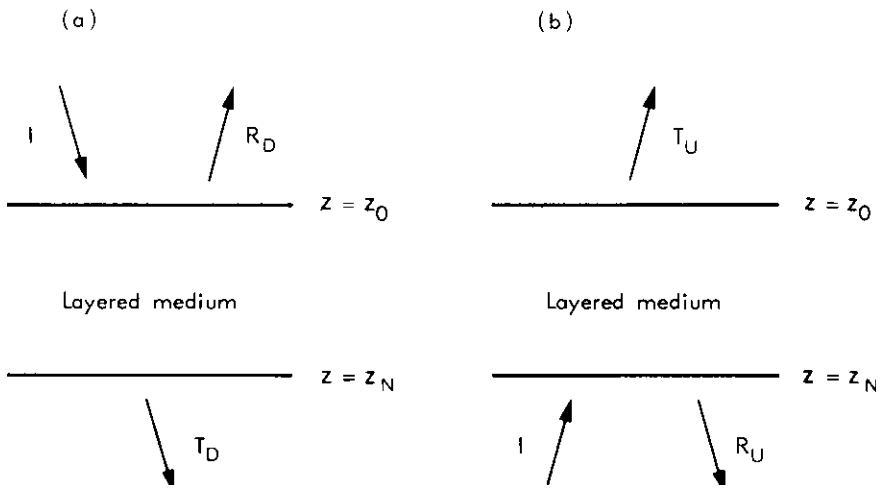

Figure 46: *Reflection and transmission matrices for a layered medium (Ursin 1983, Fig. 2).*

Free surface demultiple algorithm

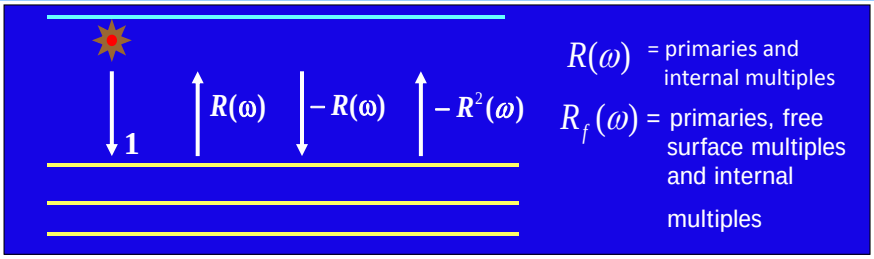

Total upfield $R_f(\omega) = \dfrac{R(\omega)}{1+R(\omega)}$

and, $R(\omega) = \dfrac{R_f(\omega)}{1-R_f(\omega)}$

$$R(\omega) = R_f(\omega) + R_f{}^2(\omega) + R_f{}^3(\omega)...$$

Figure 47:

$$= \{\underbrace{\exp[ik_z(z_r - z_s)] - \exp[ik_z(z_r + z_s)]}_{\exp[ik_z(z_r - z_s)](1 - \exp(2ik_z z_s))}\}\Gamma + \Re(z=0)\exp[-ik_z(z_r + z_s)]G_-(z_r)G_-(z_s)\Gamma$$

$$= \{\exp[ik_z(z_r - z_s)]\underbrace{(1 - \exp(2ik_z z_s))}_{G_-(z_s)}\}\Gamma + \Re(z=0)\exp[-ik_z(z_r + z_s)]G_-(z_r)G_-(z_s)\Gamma$$

$$= \{\exp[ik_z(z_r - z_s)] + \Re(z=0)\exp[-ik_z(z_r + z_s)]G_-(z_r)\}G_-(z_s)\Gamma. \qquad (9)$$

$\partial P/\partial z = i\omega\rho V_z$ (derived in Appendix 11.5) and equation 9 give

$$\begin{aligned}
V_z(z_r) &= -\frac{i}{\rho\omega}\frac{dP}{dz_r} \\
&= -\frac{i}{\rho\omega}\{\exp[ik_z(z_r - z_s)](ik_z) + \Re(z=0)\{\exp[-ik_z(z_r + z_s)](-ik_z)G_-(z_r) \\
&\quad + \exp[-ik_z(z_r + z_s)](-1)\exp(2ik_z z_r)(2ik_z)\}\}G_-(z_s)\Gamma \\
&= -\frac{i}{\rho\omega}(-ik_z)\{-\exp[ik_z(z_r - z_s)] + \Re(z=0)\{\exp[-ik_z(z_r + z_s)]G_-(z_r) \\
&\quad + 2\exp[-ik_z(z_r + z_s)]\exp(2ik_z z_r)\}\}G_-(z_s)\Gamma \\
&= -\frac{k_z}{\rho\omega}\{-\exp[ik_z(z_r - z_s)] + \Re(z=0)\{\exp[-ik_z(z_r + z_s)](1 - \exp(2ik_z z_r)) \\
&\quad + 2\exp[-ik_z(z_r + z_s)]\exp(2ik_z z_r)\}\}G_-(z_s)\Gamma \\
&= -\frac{k_z}{\rho\omega}\{-\exp[ik_z(z_r - z_s)] + \Re(z=0)\exp[-ik_z(z_r + z_s)]\underbrace{(1 + \exp(2ik_z z_r))}_{G_+(z_r)}\}G_-(z_s)\Gamma \\
&= -\frac{k_z}{\rho\omega}\{-\exp[ik_z(z_r - z_s)] + \Re(z=0)\exp[-ik_z(z_r + z_s)]G_+(z_r)\}G_-(z_s)\Gamma. \qquad (12)
\end{aligned}$$

11.4.4 Step 4.

For $z_s < z_r$, equation 5 gives the upgoing wave

$$U(z_r) = \Re(z=0)\exp[-ik_z(z_r + z_s)]G_-(z_s)\Gamma. \qquad (18)$$

For $z_s < z_r$, the downgoing wave is

$$\begin{aligned}
D(z_r) &= P(z_r) - U(z_r) \\
&= \{\exp[ik_z(z_r - z_s)] + \Re(z=0)\exp[-ik_z(z_r + z_s)]G_-(z_r)\}G_-(z_s)\Gamma - U(z_r) \\
&= \{\exp[ik_z(z_r - z_s)] + \Re(z=0)\exp[-ik_z(z_r + z_s)](1 - \exp(2ik_z z_r))\}G_-(z_s)\Gamma \\
&\quad - \Re(z=0)\exp[-ik_z(z_r + z_s)]G_-(z_s)\Gamma \\
&= \{\exp[ik_z(z_r - z_s)] - \Re(z=0)\exp[-ik_z(z_r + z_s)]\exp(2ik_z z_r)\}G_-(z_s)\Gamma \\
&= \exp[ik_z(z_r - z_s)]G_-(z_s)\Gamma - \exp(2ik_z z_r)\underbrace{\Re(z=0)\exp[-ik_z(z_r + z_s)]G_-(z_s)\Gamma}_{U(z_r)} \\
&= \underbrace{\exp[ik_z(z_r - z_s)](1 - \exp(2ik_z z_s))\Gamma}_{P_d(z_r)} - \exp(2ik_z z_r)U(z_r) \\
&= P_d(z_r) - \exp(2ik_z z_r)U(z_r). \qquad (19)
\end{aligned}$$

11.4.5 Step 5.

$$
\begin{aligned}
&\frac{1}{2}[P(z_r) \mp \frac{\rho\omega}{k_z} V_z(z_r)] \\
=&\frac{1}{2}[\{\exp[ik_z(z_r - z_s)] + \Re(z=0)\exp[-ik_z(z_r + z_s)] \underbrace{G_-(z_r)}_{1-\exp(2ik_z z_r)}\}G_-(z_s)\Gamma \underbrace{\mp\frac{\rho\omega}{k_z}(-1)\frac{k_z}{\rho\omega}}_{\pm} \\
&\times\{-\exp[ik_z(z_r - z_s)] + \Re(z=0)\exp[-ik_z(z_r + z_s)] \underbrace{G_+(z_r)}_{1+\exp(2ik_z z_r)}\}G_-(z_s)\Gamma] \\
=&\frac{1}{2}[\exp[ik_z(z_r - z_s)]\underbrace{(1 \pm (-1))}_{0,2} + \Re(z=0) \\
&\times \exp[-ik_z(z_r + z_s)]\underbrace{[(1 - \exp(2ik_z z_r)) \pm (1 + \exp(2ik_z z_r))]}_{2,-2\exp(2ik_z z_r)}]G_-(z_s)\Gamma.
\end{aligned}
$$

If + (in $\mp$)

$$
\begin{aligned}
\frac{1}{2}[P(z_r) + \frac{\rho\omega}{k_z} V_z(z_r)] &= \frac{1}{2}\Re(z=0)\exp[-ik_z(z_r + z_s)]2G_-(z_s)\Gamma \\
&= U(z_r).
\end{aligned}
$$

If - (in $\mp$)

$$
\begin{aligned}
\frac{1}{2}[P(z_r) - \frac{\rho\omega}{k_z} V_z(z_r)] &= \frac{1}{2}\exp[ik_z(z_r - z_s)]2 \underbrace{G_-(z_s)}_{1-\exp(2ik_z z_s)} \Gamma \\
&\quad + \underbrace{\frac{1}{2}\Re(z=0)\exp[-ik_z(z_r + z_s)](-2\exp(2ik_z z_r))G_-(z_s)\Gamma}_{-\exp(2ik_z z_r)U(z_r)} \\
&= \underbrace{\frac{1}{2}\exp[ik_z(z_r - z_s)]2(1 - \exp(2ik_z z_s))\Gamma}_{P_d(z_r)} - \exp(2ik_z z_r)U(z_r) \\
&= D(z_r).
\end{aligned}
$$

11.5 Derivation of $\partial P/\partial z = i\omega\rho V_z$

1. Apply Newton's second law of motion: $\mathbf{F} = m\, d\mathbf{V}/dt$.
2. Consider a unit volume in a fluid: $\mathbf{F} = \rho\, d\mathbf{V}/dt$.
3. Perform a Fourier transform: $\mathbf{F} = \rho(-i\omega\mathbf{V})$.
4. Force in a fluid is the pressure gradient: $\mathbf{F} = -\nabla P = \rho(-i\omega\mathbf{V})$.
5. Rewrite: $\nabla P = i\omega\rho\,\mathbf{V}$.
6. The z-component is the desired result.

11.6 Isis compute cluster at UH

- 14 AMD Opteron nodes (compute-0-10 to compute-0-23) each with 2 dual-core processors and 4GB of shared memory
- 10 Intel Xeon nodes (compute-0-0 to compute-0-9) each with 2.5GB of shared memory
  – compute-0-4 and compute-0-5 only have 1 dual-core processor (the other died in each and there were no replacements)
  – Remaining 8 nodes have 2 dual-core processors each
- 14TB of disk space (expanded from 2TB)

11.7 hdipb compute cluster at PGS

- hdipb000-010
- hdipb001-009 each have 16 Intel Xeon CPUs @ 2.13GHz and 132GB of RAM
- hdipb000 has 4 Intel Xeon CPUs @ 2.27GHz and 12GB of RAM
- hdipb002 has a failed hard drive
- hdipb009 runs noticeably slower than hdipb001,003-008 (Bryan Helvey suspects heat transfer efficiency is declining)
- hdipb010 used for spare parts

11.8 Follow Corrigan et al. (1991)

As preparation for the derivation in Section 6.1, the logic in Corrigan et al. (1991) was followed. In this derivation equation numbers are those in Corrigan et al. (1991). Start with Weglein and Secrest, 1990, equation 6,

$$A(\omega)G(\mathbf{r}_s,\mathbf{r}_g,\omega)=\int_S[P(\mathbf{r}',\mathbf{r}_s,\omega)\nabla' G(\mathbf{r}',\mathbf{r}_g,\omega)-G(\mathbf{r}',\mathbf{r}_g,\omega)\nabla' P(\mathbf{r}',\mathbf{r}_s,\omega)]\cdot\mathbf{n}' ds'. \qquad [1]$$

For simplicity, assume 2D,

$$A(\omega)G(0,-h;x_g,z_g;\omega)=\int dx'$$
$$\times\{P(x',0;0,-h;\omega)\frac{\partial G}{\partial z'}(x',0;x_g,z_g;\omega)-G(x',0;x_g,z_g;\omega)\frac{\partial P}{\partial z'}(x',0;0,-h;\omega)\}. \qquad [2]$$

Rearrange to get

$$\int dx' G(x',0;x_g,z_g;\omega)\frac{\partial P}{\partial z'}(x',0;0,-h;\omega)$$
$$=-A(\omega)G(0,-h;x_g,z_g;\omega)+\int dx'\{P(x',0;0,-h;\omega)\frac{\partial G}{\partial z'}(x',0;x_g,z_g;\omega)$$

$$\equiv F(x_g, z_g; 0, -h; \omega). \qquad [3]$$

Fourier transform equation [3] with respect to x_g (using equation [5]), and substitute the bilinear form of Green's function (equation [4]),

$$\int dx_g \exp(ikx_g) F(x_g, z'; 0, -h; \omega) = \int dx_g \exp(ikx_g) \int dx' G(x', 0; x_g, z'; \omega) \frac{\partial P}{\partial z'}(x', 0; 0, -h; \omega)$$

$$F(k, z'; 0, -h; \omega) = \int dx_g \exp(ikx_g) \int dx' \frac{\pi}{2} \int dk' \frac{\exp(-ik'(x_g - x')) \exp(ik'_z z')}{2ik'_z} \frac{\partial P}{\partial z'}(x', 0; 0, -h; \omega).$$

Multiply both sides by $2ik_z \exp(-ik_z z')$,

$$2ik_z \exp(-ik_z z') F(k, z'; 0, -h; \omega) = 2ik_z \exp(-ik_z z') \int dx_g \exp(ikx_g) \int dx'$$
$$\times \frac{\pi}{2} \int dk' \frac{\exp(-ik'(x_g - x')) \exp(ik'_z z')}{2ik'_z} \frac{\partial P}{\partial z'}(x', 0; 0, -h; \omega).$$

Inverse Fourier transform with respect to k,

$$\int dk \exp(-ikx) 2ik_z \exp(-ik_z z') F(k, z'; 0, -h; \omega)$$
$$= \int dk \exp(-ikx) 2ik_z \exp(-ik_z z') \int dx_g \exp(ikx_g)$$
$$\times \int dx' \frac{\pi}{2} \int dk' \frac{\exp(-ik'(x_g - x')) \exp(ik'_z z')}{2ik'_z} \frac{\partial P}{\partial z'}(x', 0; 0, -h; \omega)$$
$$\text{LHS} = \int dk \, 2ik_z \exp(-ikx - ik_z z') F(k, z'; 0, -h; \omega)$$
$$= \text{ RHS of equation [6].}$$

$$\text{RHS} = \frac{\pi}{2} \int dk \int dx_g \int dx' \int dk' \frac{2ik_z}{2ik'_z}$$
$$\times \exp(-ikx) \exp(-ik_z z') \exp(ikx_g) \exp(-ik' x_g) \exp(ik' x') \exp(ik'_z z') \frac{\partial P}{\partial z'}(x', 0; 0, -h; \omega)$$
$$= \frac{\pi}{2} \int dk \int dx' \int dk' \frac{k_z}{k'_z} \exp(-ikx) \exp(-ik_z z') \underbrace{\int dx_g \exp(-i(k' - k)x_g)}_{2\pi\delta(k'-k)}$$
$$\times \exp(ik' x') \exp(ik'_z z') \frac{\partial P}{\partial z'}(x', 0; 0, -h; \omega)$$
$$= \frac{\pi}{2} \int dk \int dx' \int dk' \frac{k_z}{k'_z}$$
$$\times \exp(-ikx) \exp(-ik_z z') 2\pi\delta(k' - k) \exp(ik' x') \exp(ik'_z z') \frac{\partial P}{\partial z'}(x', 0; 0, -h; \omega)$$
$$= \pi^2 \int dx' \int dk' \frac{1}{k'_z} \underbrace{\int dk \, k_z \exp(-ikx) \exp(-ik_z z') \delta(k' - k)}_{k'_z \exp(-ik'x) \exp(-ik'_z z')}$$

$$
\begin{aligned}
&\times \exp(ik'x') \exp(ik'_z z') \frac{\partial P}{\partial z'}(x', 0; 0, -h; \omega) \\
&= \pi^2 \int dx' \int dk' \, \frac{1}{k'_z} k'_z \exp(-ik'x) \exp(-ik'_z z') \exp(ik'x') \exp(ik'_z z') \frac{\partial P}{\partial z'}(x', 0; 0, -h; \omega) \\
&= \pi^2 \int dx' \underbrace{\int dk' \exp(-ik'(x - x'))}_{2\pi\delta(x-x')} \underbrace{\frac{1}{k'_z} k'_z \exp(ik'_z z') \exp(-ik'_z z')}_{1} \frac{\partial P}{\partial z'}(x', 0; 0, -h; \omega) \\
&= 2\pi^3 \underbrace{\int dx' \delta(x - x') \frac{\partial P}{\partial z'}(x', 0; 0, -h; \omega)}_{\partial P/\partial z'(x,0;0,-h;\omega)} \\
&= 2\pi^3 \frac{\partial P}{\partial z'}(x, 0; 0, -h; \omega) \\
&= \text{ constant times LHS of equation [6].}
\end{aligned}
$$

11.9 Source arrays

Yang and Weglein (2013) have tested the effect of source arrays vs. point sources.

References

Amundsen, L. and B. Ursin. "Frequency-wavenumber inversion of acoustic data." Geophysics 56 (1991): 1027–1039.

Amundsen, Lasse. "Short note: estimation of source-array signatures." Geophysics 58 (1993): 1865–1869.

Amundsen, Lasse. "Wavenumber-based filtering of marine point-source data." Geophysics 58 (1993): 1335–1348.

Amundsen, Lasse, Bruce G. Secrest, and Børge Arntsen. "Extraction of the normal component of the particle velocity from marine pressure data." Geophysics 60 (1995): 212–222.

Cambois, Guillaume, David Carlson, Craig Jones, Marina Lesnes, Walter Söllner, and Hocine Tabti. "Dual-sensor streamer data: calibration, acquisition QC and attenuation of seismic interferences and other noises." 79th Annual International Meeting, SEG, Expanded Abstracts. Society of Exploration Geophysicists, 2009, 142–146.

Carlson, David, Walter Söllner, Hocine Tabti, Eli Brox, and Martin Widmaier. "Increased resolution of seismic data from a dual sensor streamer cable." 77th Annual International Meeting, SEG, Expanded Abstracts. Society of Exploration Geophysicists, 2007, 994–998.

Clayton, R. W. and R. H. Stolt. "A Born-WKBJ inversion method for acoustic reflection data." Geophysics 46 (1981): 1559–1567.

Corrigan, D., A. B. Weglein, and D. D. Thompson. 1991 "Method and apparatus for seismic survey including using vertical gradient estimation to separate downgoing seismic wavefields.". US Patent number 5051961.

Klüver, Tilman, Peter Aaron, David Carlson, Anthony Day, and Roald van Borselen. "A robust strategy for processing 3D dual-sensor towed streamer data." 79th Annual International Meeting, SEG, Expanded Abstracts. Society of Exploration Geophysicists, 2009, 3088–3092.

Kragh, E., J. O. A. Robertsson, R. Laws, L. Amundsen, T. Rϕsten, T. Davies, K. Zerouk, and A. Strudley. "Rough sea deghosting using wave heights derived from low frequency pressure recordings - a case study." EAGE 66th Conference & Exhibition. 2004.

Mayhan, James D., Paolo Terenghi, Arthur B. Weglein, and Nizar Chemingui. "Green's theorem derived methods for preprocessing seismic data when the pressure P and its normal derivative are measured." 81st Annual International Meeting, SEG, Expanded Abstracts. Society of Exploration Geophysicists, 2011, 2722–2726.

Mayhan, James D., Arthur B. Weglein, and Paolo Terenghi. "First application of Green's theorem derived source and receiver deghosting on deep water Gulf of Mexico synthetic (SEAM) and field data." 82nd Annual International Meeting, SEG, Expanded Abstracts. Society of Exploration Geophysicists, 2012, 1–5.

Morse, P. M. and H. Feshbach. Methods of theoretical physics. New York: McGraw-Hill Book Co., 1953.

Osen, Are, Bruce G. Secrest, Lasse Amundsen, and Arne Reitan. "Wavelet estimation from marine pressure measurements." Geophysics 63 (November-December 1998): 2108–2119.

Robertsson, Johan O. A. and Ed Kragh. "Rough-sea deghosting using a single streamer and a pressure gradient approximation." Geophysics 67 (November-December 2002): 2005–2011.

Robinson, Enders A. and Sven Treitel. Digital Imaging and Deconvolution: The ABCs of Seismic Exploration and Processing. Tulsa, OK: Society of Exploration Geophysicists, 2008.

Schneider, W. A. "Integral formulation for migration in two and three dimensions." Geophysics 43 (1978): 49–76.

Stolt, Robert H. and Arthur B. Weglein. Seismic Imaging and Inversion: Application of Linear Inverse Theory. Information on this title: www.cambridge.org/9781107014909. Cambridge University Press, 2012.

Tan, T. H. "Wavelet spectrum estimation." Geophysics 64 (November-December 1999): 1836–1846.

Tang, L. "Study on factors that affect wave separation tests using Green's theorem with over/under cable configuration." M-OSRP 2012 Annual Meeting. 2013, 74–87.

Tang, Lin. Wave separation study. Presentation to M-OSRP, September 2012.

Tenghamn, Rune, Svein Vaage, and Claes Borresen. "A Dual-Sensor, Towed Marine Streamer; Its Viable Implementation and Initial Results." 77th Annual International Meeting, SEG, Expanded Abstracts. Society of Exploration Geophysicists, 2007, 989–993.

Ursin, Bjørn. "Review of elastic and electromagnetic wave propagation in horizontally layered media." Geophysics 48 (1983): 1063–1081.

Wang, Zhiqiang. Green's theorem for source and receiver deghosting Part I: methods, analytic and numeric examples, and impact on ISS multiple removal methods. Presentation given at 2011 M-OSRP Annual Meeting, 2012.

Weglein, A. B., F. V. Araújo, P. M. Carvalho, R. H. Stolt, K. H. Matson, R. T. Coates, D. Corrigan, D. J. Foster, S. A. Shaw, and H. Zhang. "Inverse Scattering Series and Seismic Exploration." Inverse Problems 19 (2003): R27–R83.

Weglein, A. B., R. H. Stolt, and J. D. Mayhan. "Reverse-time migration and Green's theorem: Part I — The evolution of concepts, and setting the stage for the new RTM method." Journal of Seismic Exploration 20 (February 2011): 73–90.

Weglein, A. B., R. H. Stolt, and J. D. Mayhan. "Reverse time migration and Green's theorem: Part II — A new and consistent theory that progresses and corrects current RTM concepts and methods." Journal of Seismic Exploration 20 (May 2011): 135–159.

Weglein, Arthur B. and Lasse Amundsen. "Short note: G_0^{D0} and G_0^D integral equations relationships; The triangle relation is intact." M-OSRP 2002 Annual Report. 2003, 32–35.

Weglein, Arthur B. and Bruce G. Secrest. "Wavelet estimation for a multidimensional acoustic earth model." Geophysics 55 (July 1990): 902–913.

Weglein, Arthur B., S. A. Shaw, K. H. Matson, J. L. Sheiman, R. H. Stolt, T. H. Tan, A. Osen, G. P. Correa, K. A. Innanen, Z. Guo, and J. Zhang. "New approaches to deghosting towed-streamer and ocean-bottom pressure measurements." 72nd Annual International Meeting, SEG, Expanded Abstracts. Society of Exploration Geophysicists, 2002, 2114–2117.

Wikipedia. 2012 "Bessel function.". Available online at http://en.wikipedia.org/wiki/Bessel_function.

Yang, J. and A. B. Weglein. "Free-surface multiple removal for source array data with interfering primaries and multiples." M-OSRP 2012 Annual Meeting. 2013, 94–108.

Zhang, Jingfeng. Wave theory based data preparation for inverse scattering multiple removal, depth imaging and parameter estimation: analysis and numerical tests of Green's theorem deghosting theory. PhD thesis, University of Houston, 2007.

Zhang, Jingfeng and Arthur B. Weglein. "Extinction theorem deghosting method using towed streamer pressure data: analysis of the receiver array effect on deghosting and subsequent free surface multiple removal." 75th Annual International Meeting, SEG, Expanded Abstracts. Society of Exploration Geophysicists, 2005, 2095–2098.

Zhang, Jingfeng and Arthur B. Weglein. "Application of extinction theorem deghosting method on ocean bottom data." 76th Annual International Meeting, SEG, Expanded Abstracts. Society of Exploration Geophysicists, 2006, 2674–2678.

Green's theorem preprocessing and multiple attenuation: Acquisition configuration impact and determining the reference velocity for on shore application

L. Tang and A. B. Weglein

April 29, 2013

Abstract

In this report, we examine the impact of acquisition design on Green's theorem-based wave separation. Green's theorem can separate the reference wave P_0 and the scattered wave P_s from the seismic data, depending on the choice of the observation point. It requires the wavefield and its normal derivatives on the measurement surface as the input, which can be provided using an over/under cable. The tests show that when the difference between the depths of the two cables gets smaller, the wave separation results are clearer and more accurate. In addition, the choice of the location of the predicted reference or scattered wave should be distant from the cable by at least half of the length of the receiver interval in order to avoid residuals. The effect of the interval between receivers is also considered.

1 Introduction

Preprocessing of the seismic data, including removal of reference waves, wavelet estimation, and removal of ghosts, is very important in seismic data processing. The direct arrival does not experience reflection from the earth, which is our ultimate goal, so it should be removed before the subsequent analysis. The seismic data are affected by both the source signature and the properties of the earth. Thus, we need to identify and remove the wavelet's contribution from the seismic data by using the information of the source signature (Weglein and Secrest (1990)). Deghosting will remove the down-going wave from the scattered wave and will enhance the low-frequency contents of the data (Zhang (2007), Mayhan and Weglein (2013)). These are the prerequisites of the following steps of multiple removal and depth imaging in the Inverse Scattering Series (ISS) algorithm (Weglein et al. (2003)). The consequences of and necessity for removing the reference wave and performing deghosting in preparation for ISS multiple removal are discussed in Yang and Weglein (2013).

All three of these processing steps can be achieved by using Green's theorem. It is an effective method that is used in different aspects of seismic processing. In Weglein and Secrest (1990), wave separation and wavelet estimation by using Green's theorem are discussed. By performing an integral along the measurement surface, we can predict the reference wave or the scattered wave, depending on the choice of observation point. Green's theorem can work in multiple dimensions and

is especially powerful and effective in the case of interfering events, compared with other methods such as simply muting the direct wave from the data, which leads to the loss of scattered wave information.

In marine seismic exploration, dual-sensor cables that can measure both the pressure wave P and the vertical velocities V_z are widely used. However, the two instruments of acquisition – geophone and hydrophone – will perform differently under some bandwidths. Another acquisition tool being employed recently is an over/under cable, which consists of two cables, each located at a different depth. In out tests, we generated synthetic data using the reflectivity method at two depths to model the over/under cable configuration.

This theory is implemented by Jim Mayhan in M-OSRP and has been tested in source and receiver deghosting, wave prediction, and wavelet estimation for synthetic data and field data, both for isolated events and for interfering events (Mayhan and Weglein (2013)). In this report we will mainly focus the discussion on wave separation tasks. During tests using an over/under cable configuration, we found that several factors can affect the accuracy and performance of the theory. Here we studied the impacts of the depth difference between the over cable and the under cable, the choice of the location of the predicted depth, and the interval of the receivers.

2 Theory

In scattering theory, we treat the actual medium as a combination of an unperturbed medium, called the reference medium, and a perturbation. Correspondingly, the total measured wavefield P is the summation of the reference wave P_0 and the scattered wave P_s. P_0 does not experience the earth, which is our interest, thus we need to remove it before further processing and analysis. In the marine environment, for the purpose of separating P_0 and P_s, we choose as the reference medium a half-space of water with speed c_0 plus a half space of air. The reference wave then consists of two parts: P_0^d, which travels from the source to the receiver directly, plus the wave P_0^{FS}, which goes upward from the source to the air-water interface (the free surface) and then is reflected down to the receiver. We consider an acoustic medium and assume that a point source and multiple receivers are located at $\vec{r_s} = (x_s, y_s, z_s)$ and $\vec{r} = (x, y, z)$, where z_s and z are the depths of the source and receivers, respectively. The total wave P satisfies the acoustic wave equation

$$\left(\nabla^2 + \frac{\omega^2}{c^2(\vec{r})}\right) P(\vec{r}, \vec{r_s}, \omega) = A(\omega)\delta(\vec{r} - \vec{r_s}), \tag{2.1}$$

where $A(\omega)$ is the source wavelet. Now, we introduce the perturbation $\alpha(\vec{r})$, which is defined as

$$\frac{1}{c^2(\vec{r})} = \frac{1}{c_0^2}(1 - \alpha(\vec{r})). \tag{2.2}$$

Then Equation 2.1 becomes

$$\left(\nabla^2 + \frac{\omega^2}{c_0^2}\right) P(\vec{r}, \vec{r_s}, \omega) = \frac{\omega^2}{c_0^2}\alpha(\vec{r})P(\vec{r}, \vec{r_s}, \omega) + A(\omega)\delta(\vec{r} - \vec{r_s}). \tag{2.3}$$

In the above equation, the perturbation α has two parts, α_{earth} and α_{air}. On the other hand, in the reference world with the free surface, the Green's function satisfies equation

$$\left(\nabla'^2 + \frac{\omega^2}{c_0^2}\right) G_0(\vec{r'}, \vec{r}, \omega) = \delta(\vec{r'} - \vec{r}) - \delta(\vec{r'} - \vec{r_I}). \tag{2.4}$$

Here, $\vec{r_I}$ is the image source mirrored by the free surface. We can see that G_0 vanishes at the free surface when $z' = 0$. Green's theorem gives the relationship of two arbitrary functions ψ and ϕ in a volume V surrounded by surface S as,

$$\begin{aligned} &\int_V \left(\psi(\vec{r})\nabla^2\phi(\vec{r}) - \phi(\vec{r})\nabla^2\psi(\vec{r})\right) d\vec{r} \\ &= \oint_S \left[\psi(\vec{r})\nabla\phi(\vec{r}) - \phi(\vec{r})\nabla\psi(\vec{r})\right] \cdot d\vec{S}. \end{aligned} \tag{2.5}$$

Now, substituting $\psi(\vec{r})$ as $P(\vec{r'}, \vec{r_s}, \omega)$ and $\phi(\vec{r})$ as $G_0(\vec{r'}, \vec{r}, \omega)$, and having $\frac{\omega^2}{c_0^2} = k^2$ from Equation 2.3 and 2.4, we have

$$\begin{aligned} &\int_V P(\vec{r'}, \vec{r_s}, \omega) \left(\delta(\vec{r'} - \vec{r}) - \delta(\vec{r'} - \vec{r_I}) - k^2 G_0(\vec{r'}, \vec{r}, \omega)\right) d\vec{r'} \\ - &\int_V G_0(\vec{r'}, \vec{r}, \omega) \left(A(\omega)\delta(\vec{r'} - \vec{r_s}) + k^2\alpha(\vec{r'})P(\vec{r'}, \vec{r_s}, \omega) - k^2 P(\vec{r'}, \vec{r_s}, \omega)\right) d\vec{r'} \\ = &\oint_S \left[P(\vec{r'}, \vec{r_s}, \omega)\nabla' G_0(\vec{r'}, \vec{r}, \omega) - G_0(\vec{r'}, \vec{r}, \omega)\nabla' P(\vec{r'}, \vec{r_s}, \omega)\right] \cdot d\vec{S'}. \end{aligned} \tag{2.6}$$

Next, by choosing the volume as the space between the free surface and the measurement surface, and setting the observation point $\vec{r}$ below the cable, only the term of the actual source $\delta(\vec{r'} - \vec{r_s})$ on the left-hand side of the equation will survive (only $\vec{r_s}$ is inside the volume). Thus Equation 2.6 could be simplified as

$$\begin{aligned} A(\omega)G_0(\vec{r}, \vec{r_s}, \omega) &= -\oint_S \left[P(\vec{r'}, \vec{r_s}, \omega)\nabla' G_0(\vec{r'}, \vec{r}, \omega) - G_0(\vec{r'}, \vec{r}, \omega)\nabla' P(\vec{r'}, \vec{r_s}, \omega)\right] \cdot d\vec{S'} \\ &= \int_{m.s.} \left[P(\vec{r'}, \vec{r_s}, \omega)\nabla' G_0(\vec{r'}, \vec{r}, \omega) - G_0(\vec{r'}, \vec{r}, \omega)\nabla' P(\vec{r'}, \vec{r_s}, \omega)\right] \cdot \vec{n} dr'. \end{aligned} \tag{2.7}$$

The left-hand side of Equation 2.7 is the reference wave P_0, if we choose the causal Green's function G_0. Therefore this equation will calculate the reference wave P_0 below the cable by performing a surface integral, which requires P and the normal derivatives of P on the surface. To convert the surface integral to the integral along the measurement surface, we consider the properties of P and G_0 at the free surface, and the direction of $d\vec{S'}$ is defined as pointing out of the surface.

Likewise, if we choose the volume as the space below the measurement surface to infinity and set the observation point $\vec{r}$ above the cable, then only the term with perturbation α_{earth} will contribute to the volume integral, and thus the Equation 2.6 becomes

$$\int_V G_0(\vec{r'}, \vec{r}, \omega) k^2 \alpha(\vec{r'}) P(\vec{r'}, \vec{r_s}, \omega) d\vec{r'}$$

$$= -\oint_S \left[P(\vec{r}', \vec{r_s}, \omega)\nabla' G_0(\vec{r}', \vec{r}, \omega) - G_0(\vec{r}', \vec{r}, \omega)\nabla' P(\vec{r}', \vec{r_s}, \omega)\right] \cdot d\vec{S}'$$

$$= \int_{m.s.} \left[P(\vec{r}', \vec{r_s}, \omega)\nabla' G_0(\vec{r}', \vec{r}, \omega) - G_0(\vec{r}', \vec{r}, \omega)\nabla' P(\vec{r}', \vec{r_s}, \omega)\right] \cdot \vec{n} dr'. \quad (2.8)$$

The volume integral represents the scattered wave that results from the "sources" inside the volume (the earth), since when the perturbation α is zero, this quantity will vanish. In addition, because the G_0 here is the Green's function in the reference world with the free surface, the scattered wave also has the component of reflection from the free surface. We treat P and G_0 at infinity as zero (in accord with the Sommerfeld radiation condition) and choose the normal direction to simplify the surface integral to the integral along the cable.

From Equations 2.7 and 2.8, we can see that given the wavefield P and the normal derivatives of wavefield P_n on the measurement surface, we can easily calculate the reference wave P_0 and the scattered wave P_s, depending on the observation point we choose. In other words, the reference wave and the scattered wave are separated by using Green's theorem.

3 Factors that affect the wave-separation result

3.1 The depth difference between the upper cable and the lower cable

The above Green's theorem-based theory for separation of the reference wave P_0 and the scattered wave P_s requires as input the wavefield P as well as its normal derivatives dP/dz at the measurement surface. The wavefield P comes from the recorded data, whereas the normal derivatives need to be calculated in the case of a geophone in the marine environment. When using an over/under cable, an easy way to calculate the normal derivatives is to subtract the data of the upper cable from those of the lower cable and then divide by their depth difference, i.e.,

$$\frac{dP(\frac{z_1+z_2}{2})}{dz} = \frac{P(z_2) - P(z_1)}{z_2 - z_1}. \quad (3.1)$$

As the above equation shows, the normal derivative of P here is at the depth of $(z_1 + z_2)/2$, rather than at z_1 or z_2, where wavefield P is measured. This mismatch may affect the wave separation results.

In our synthetic tests using the reflectivity method, we first used a 1D acoustic model with the source at 5m and two cables, one at a depth of 45m and one at 50m. Thus the two cables are separated by 5m here. An example of the total wavefield at depth 50m is shown in Figure 1. Using Green's theorem, the scattered wave P_s is predicted at 20m and P_0 is predicted at 80m, as shown in Figure 2. Next, we reduced the depth difference between the two cables to 1m (one cable at 49m, the other at 50m), and in that case performing the integral gives the predicted P_s at 20m and P_0 at 80m as shown in Figure 3. From these two results, we can clearly see that when the depth difference is 5m, as in Figure 2, there are several residuals in both cases of P_0 and P_s, while in Figure 3, the predicted results are very clean. This indicates that reducing the difference in cable depths can significantly increase the accuracy of wave separation results, since the depth of P_n now matches better with the depth of P in the Green's theorem integral.

3.2 The choice of predicted cable depth

Other factors may affect the estimated results, too. The actual experiment shows that the choice of the predicted cable depth can change the quality of the result. Figure 4 shows the choice of different depths when predicting the scattered wave P_s using the same over/under cable located at 49m and 50m. Here we define the depth difference between the predicted cable and the measurement surface as $\triangle z$. We also define the interval between receivers as $\triangle x$. As we can see, the predicted result has many residuals when $\triangle z$ is very small compared with $\triangle x$. Only when $\triangle z$ is at least half of $\triangle x$ are the predicted results acceptable. Likewise, Figure 5 shows the predicted results of P_0 at different depths. We again got the similar conclusion that only when the depth difference between the predicted cable and the actual cable is larger than at least 1/2 of the interval of receivers, does the predicted direct wave have few residuals.

This requirement so far is empirically identified. One possible reason behind it lies in the form of Green's function that is used and in its derivatives in the frequency domain. For example, in the 2D case, the Green's function and its derivatives are

$$G_0(\vec{r},\vec{r}',\omega) = -\frac{i}{4}(H_0^{(1)}(kR_+) - H_0^{(1)}(kR_-)), \tag{3.2}$$

$$\frac{\partial G_0}{\partial z'}(\vec{r},\vec{r}',\omega) = -\frac{ik}{4}\left(H_1^{(1)}(kR_+)\frac{z-z'}{R_+} + H_1^{(1)}(kR_-)\frac{z+z'}{R_-}\right), \tag{3.3}$$

where $R_\pm = \sqrt{(x-x')^2 + (y-y')^2 + (z \mp z')^2}$. From the above expressions, we can see that the term of $\frac{z-z'}{R_+}$ in $\frac{\partial G_0}{\partial z'}$ contains $z - z'$, which is the $\triangle z$ we defined above. When $\triangle z$ is very small, there might be some numerical issue occurs at the term of $\frac{z-z'}{R_+}$ in $\frac{\partial G_0}{\partial z'}$.

3.3 Interval between receivers

The Green's theorem performs an integral along the measurement surface in theory, which in reality becomes a summation over the receivers. Then it is natural to think that reducing the interval between receivers could make the summation be more closer to an integral. Figure 6 and Figure 7 shows the results of P_0 and P_s using cables with different receiver intervals $\triangle$x of 1m, 5m, and 12.5m, respectively. The results show barely any difference between them; the estimated results are not improved when the receiver interval gets smaller, nor do the results get worse when the interval is larger. One probable explanation is that a 12.5m interval is good enough to imitate the integral as Green's theorem describes. If the spacial sampling is larger than 12.5m, it will be larger than Nyquist rate and producing alias effect, since we are using a Ricker wavelet with maximum frequency of 60 Hz.

4 Conclusions

In this paper we examined the wave separation results obtained by using Green's theorem under different conditions. The effects of (1) the difference in the depth between the over cable and the under cable, (2) the choice of the location of the predicted reference wave or scattered wave, and

(3) the receiver intervals, are studied and tested. The tests show that to get good wave separation results, the depth difference between the two cables should be quite small, and we choose to predict the wave far enough away from the cable (at least $1/2 \triangle x$). In addition, the receiver interval $\triangle x$ can be as large as 12.5m and still give good prediction results.

5 Acknowledgements

We are grateful to all M-OSRP sponsors for long-term encouragement and support in this research. Jim Mayhan and Jinlong Yang are appreciated for their helpful feedback on this report and discussions. The first author extends her deepest gratitude to Dr. Arthur Weglein for his guidance, encouragement and support.

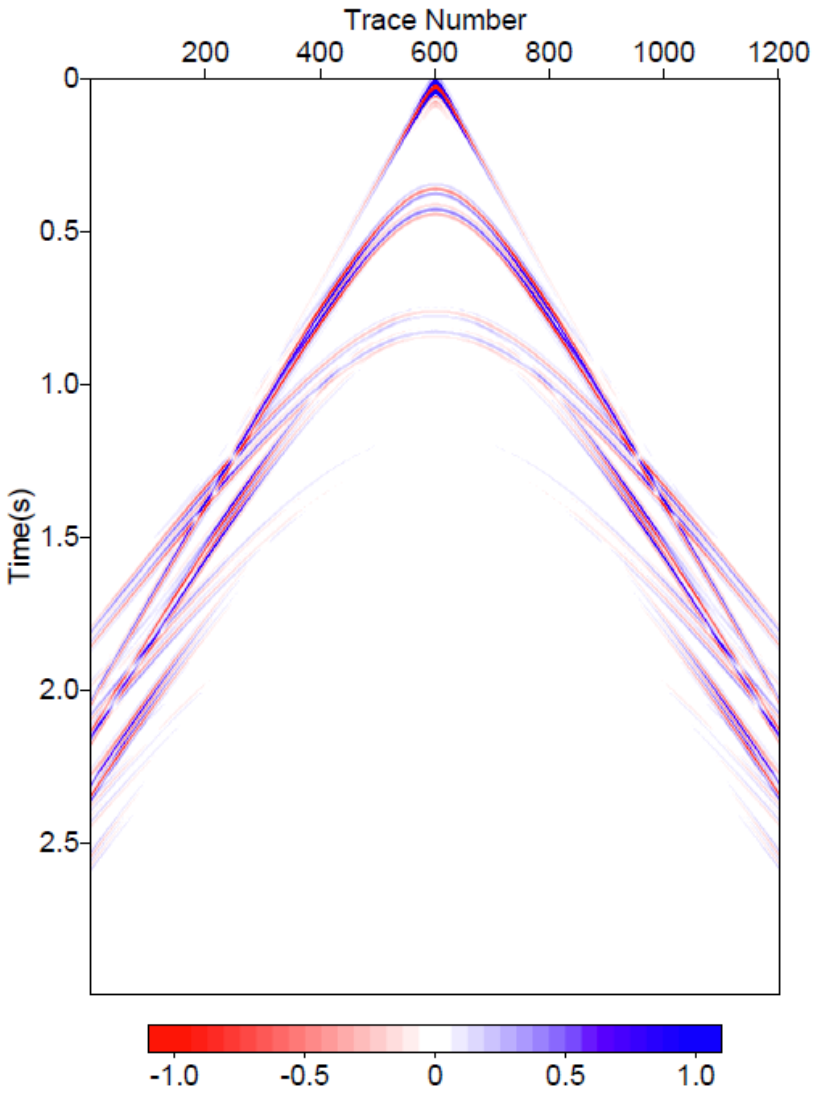

Figure 1: Total wavefield P at 50m.

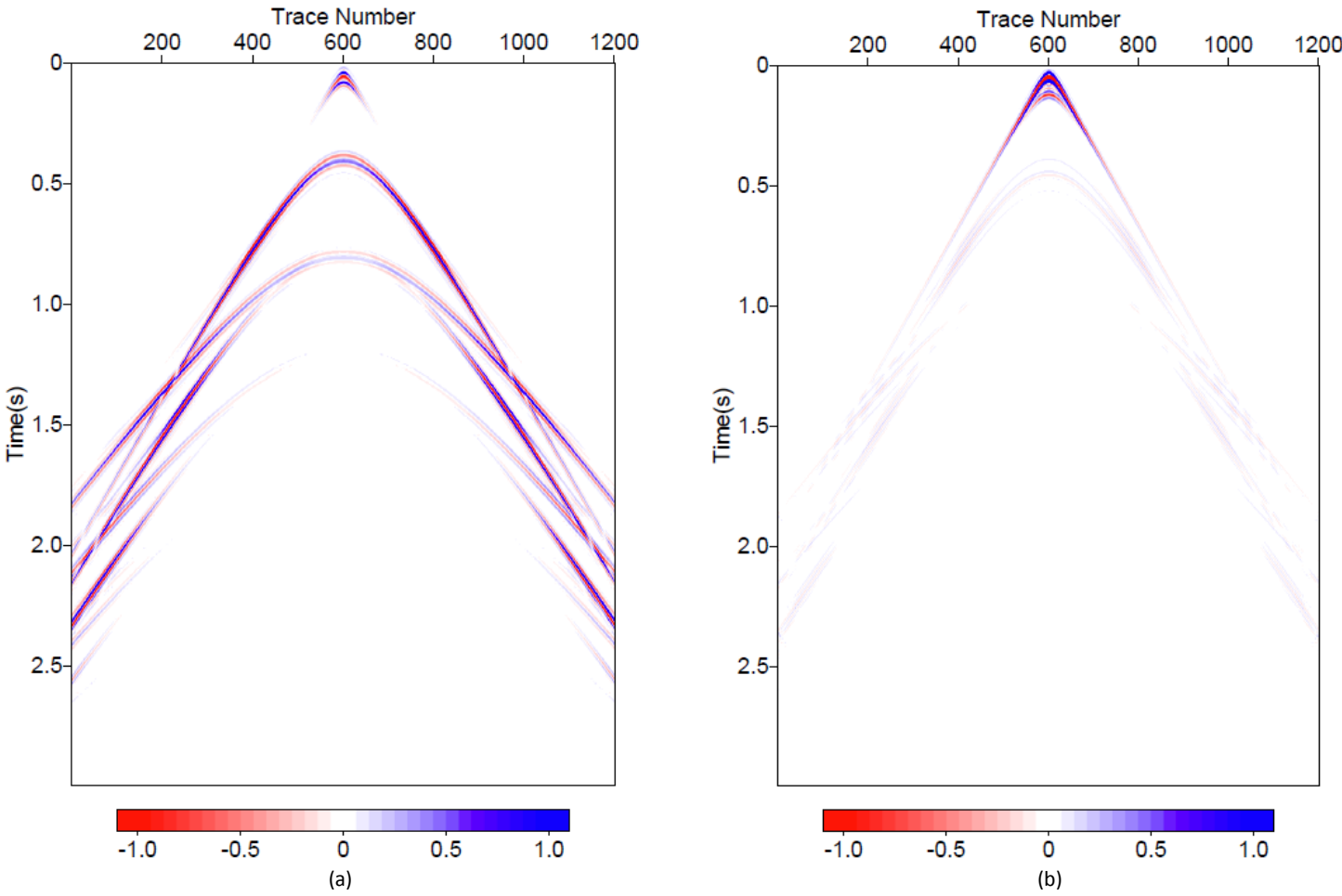

Figure 2: Using an over/under cable with a 5m depth difference. (a) P_s predicted at 20m, (b) P_0 predicted at 80m.

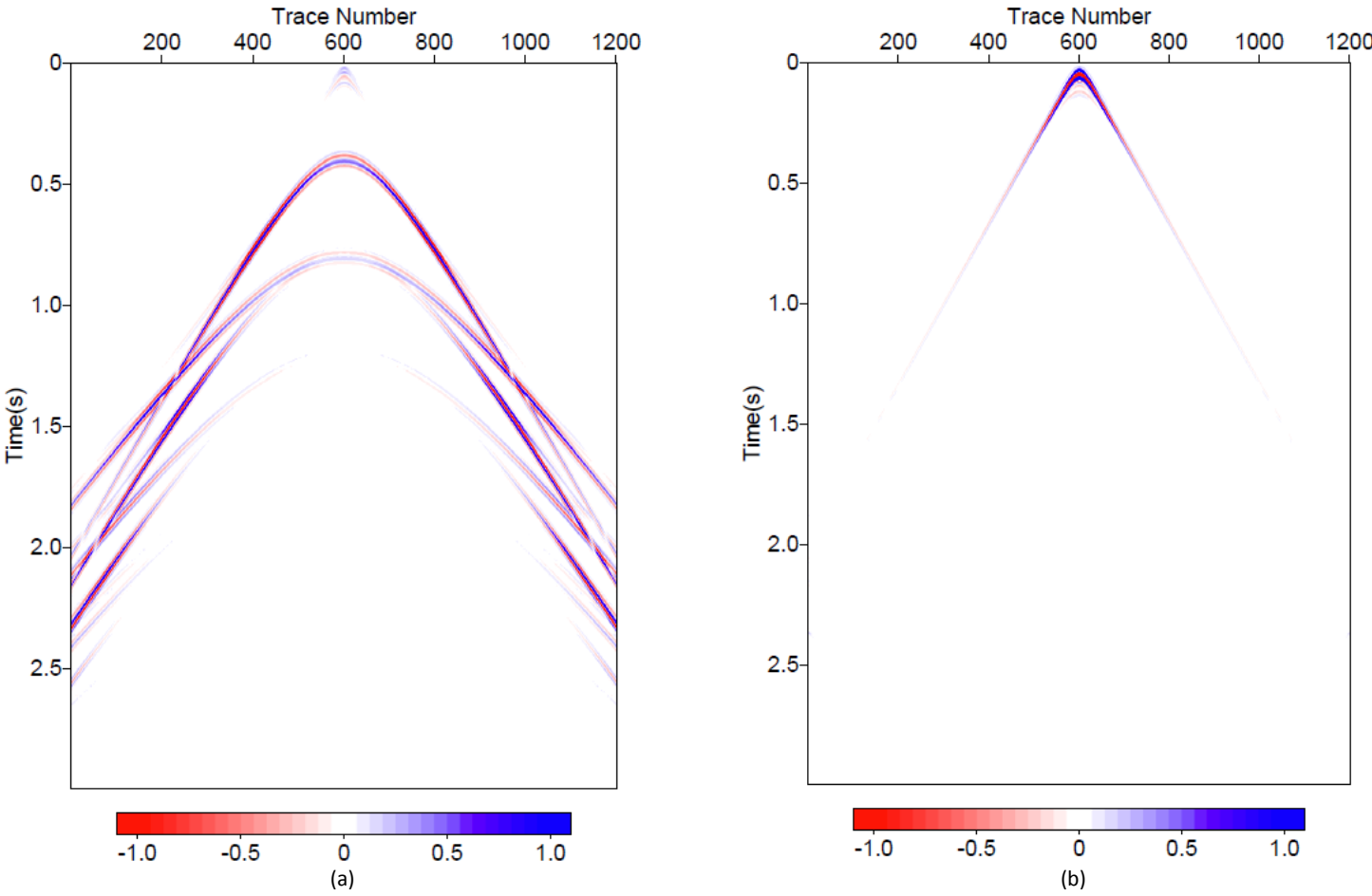

Figure 3: Using an over/under cable with a 1m depth difference. (a) P_s predicted at 20m, (b) P_0 predicted at 80m.

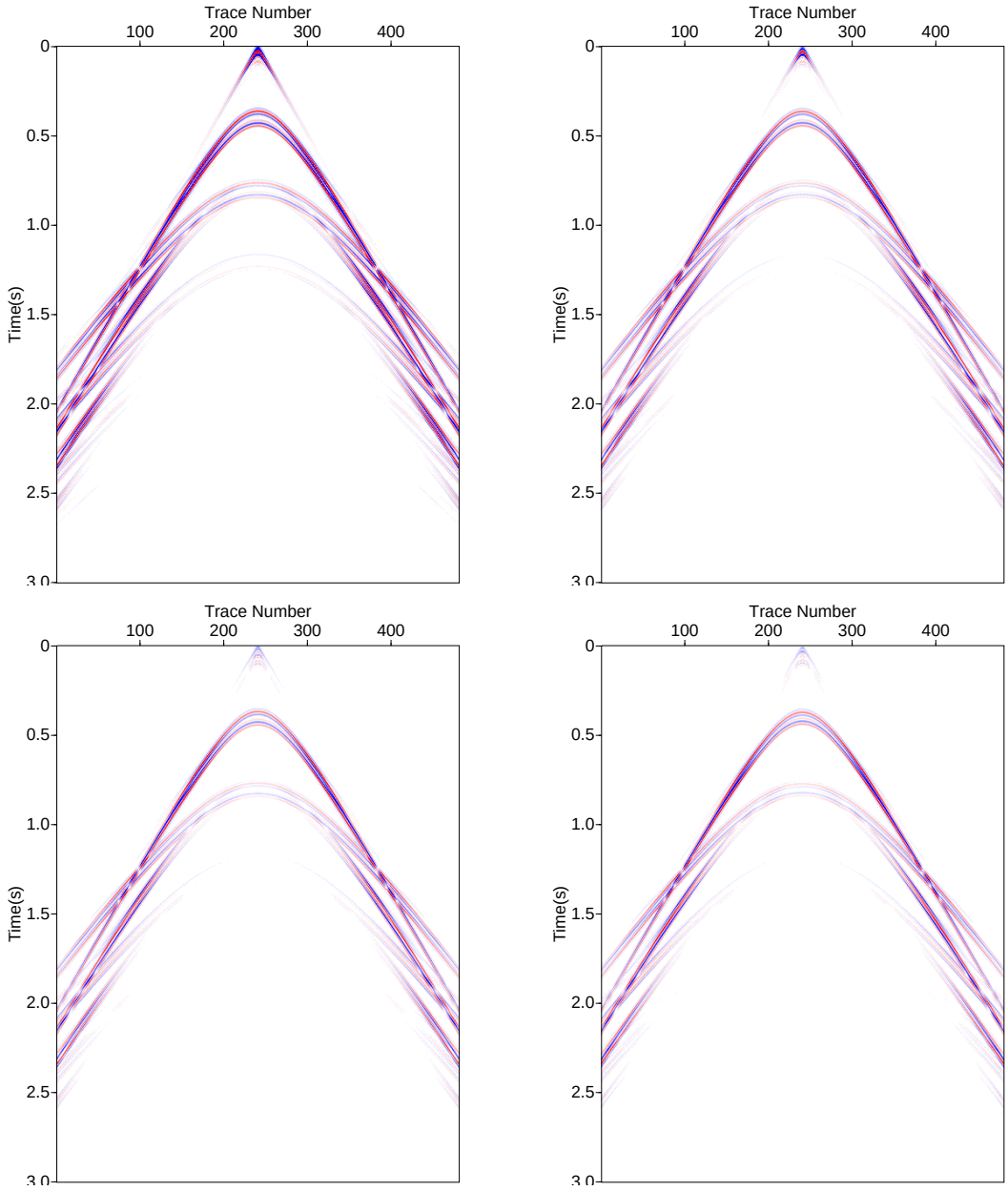

Figure 4: Predicted P_s at: (a) 48.43m ($\triangle z$ =1/8 $\triangle x$), (b) 46.88m ($\triangle z$ =1/4 $\triangle x$), (c) 43.75m ($\triangle z$ =1/2 $\triangle x$), and (d) 37.5m ($\triangle z = \triangle x$).

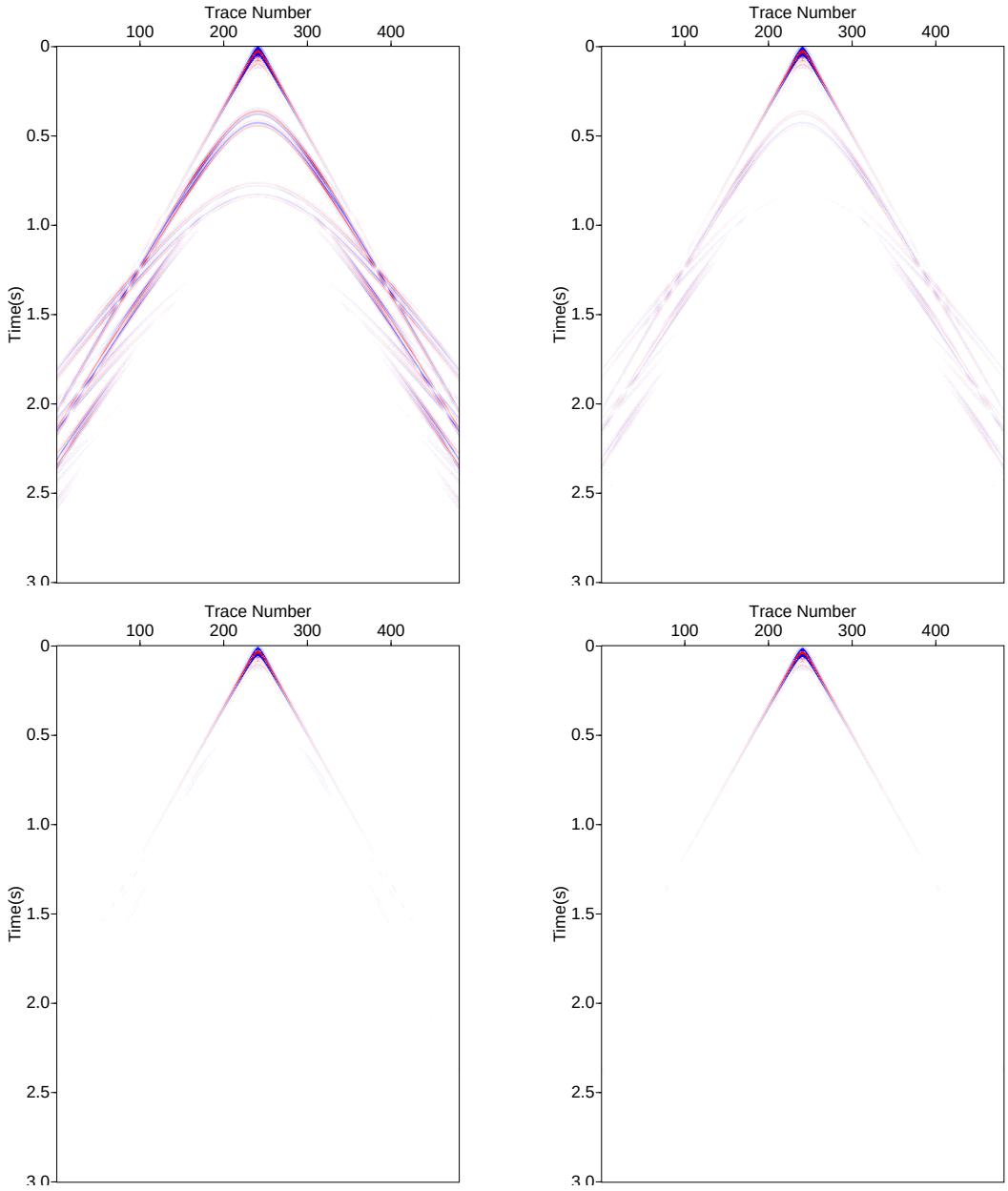

Figure 5: Predicted P_0 at: (a) 51.56m ($\triangle z$ =1/8 $\triangle x$), (b) 53.13m ($\triangle z$ =1/4 $\triangle x$), (c) 56.25m ($\triangle z$ =1/2 $\triangle x$), and (d) 62.5m ($\triangle z = \triangle x$).

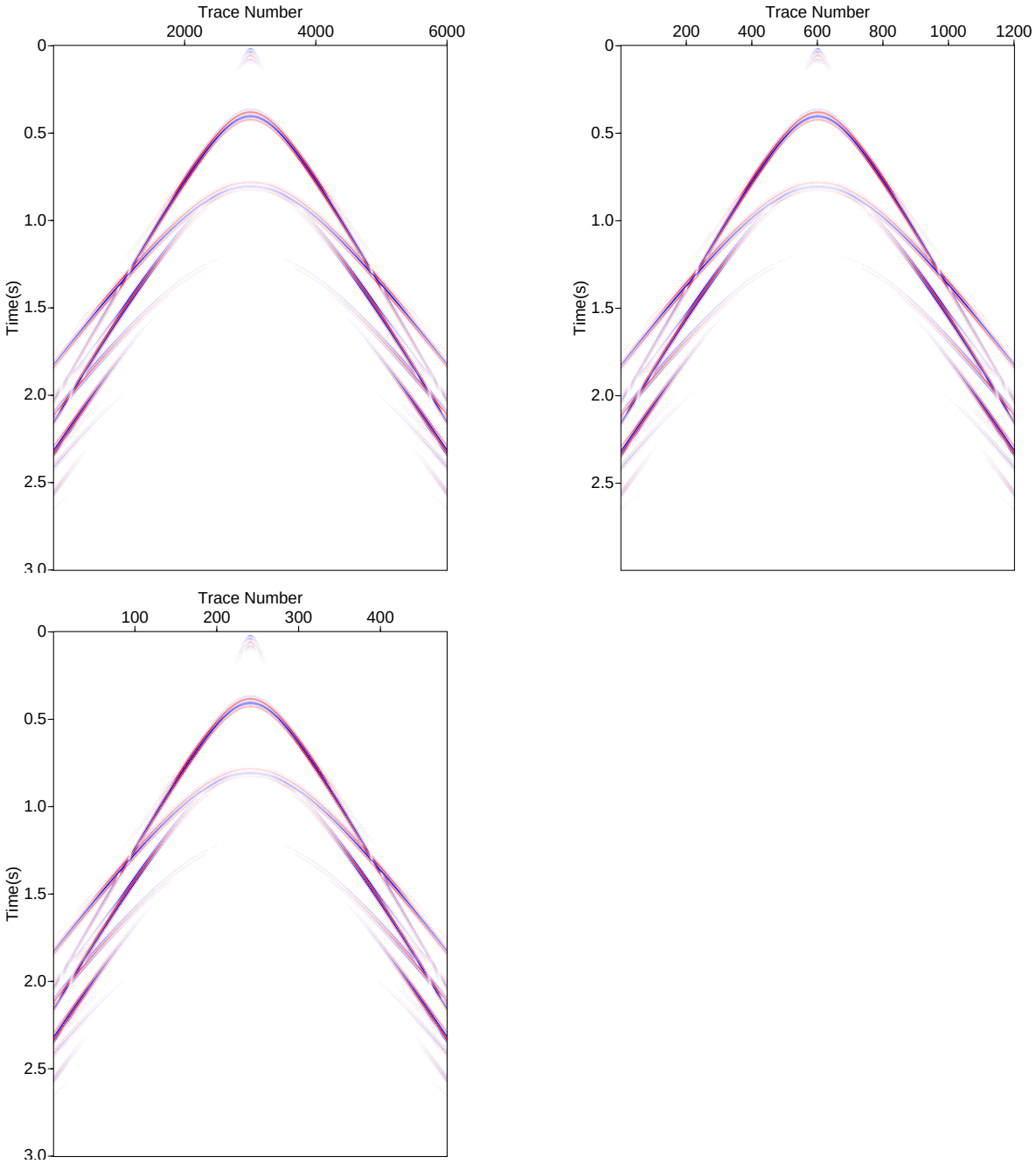

Figure 6: Predicted P_s using the receiver interval: (a) $\triangle x$=1m, (b) $\triangle x$=5m, and (c) $\triangle x$=12.5m

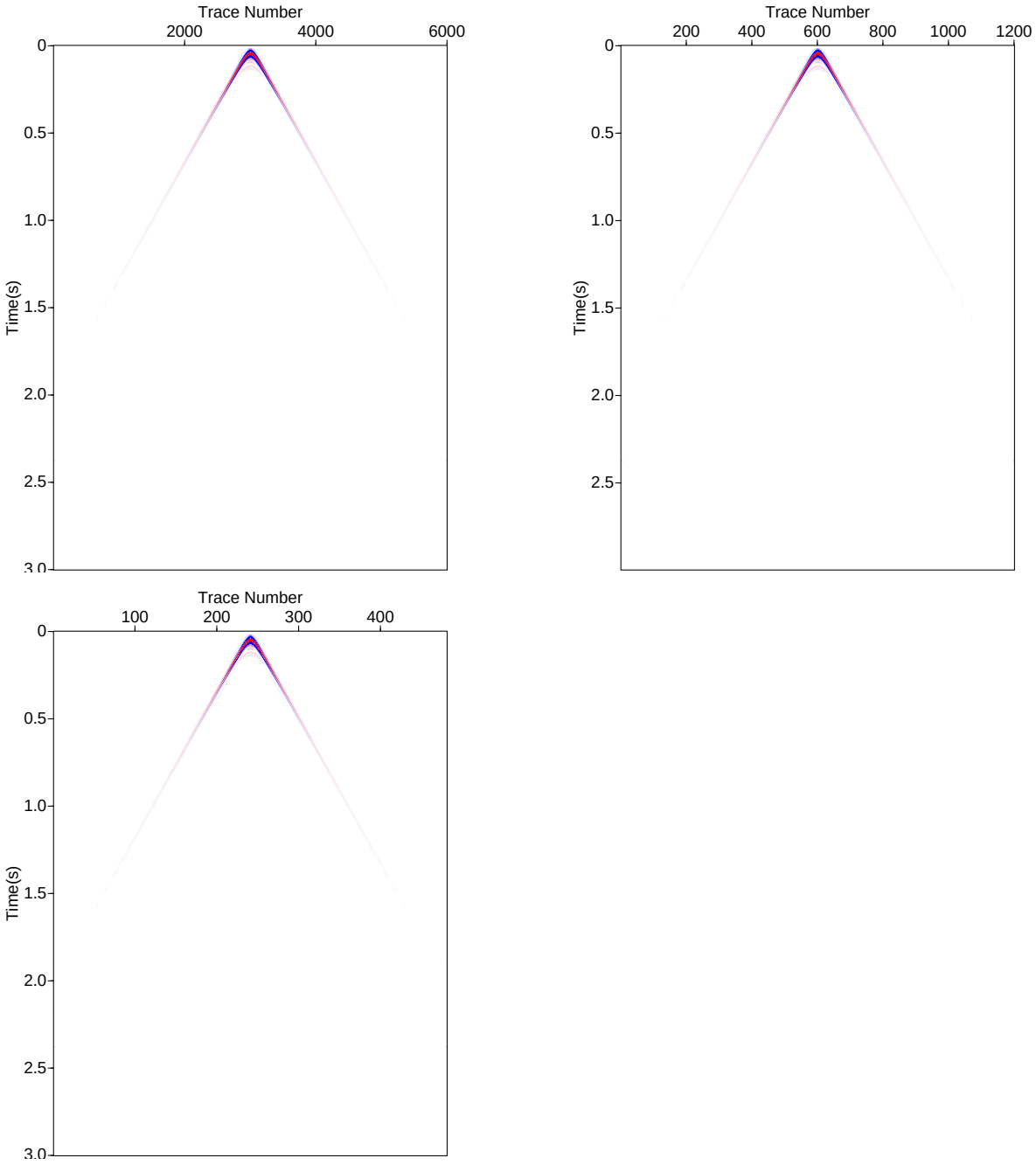

Figure 7: Predicted P_0 using the receiver interval: (a) $\triangle x$=1m, (b) $\triangle x$=5m, and (c) $\triangle x$=12.5m.

References

Mayhan, J.D. and A. B. Weglein. "Green's theorem-derived deghosting of marine seismic data." Mission-Oriented Seismic Research Program Annual Report (2013).

Weglein, A. B., F. V. Araújo, P. M. Carvalho, R. H. Stolt, K. H. Matson, R. T. Coates, D. Corrigan, D. J. Foster, S. A. Shaw, and H. Zhang. "Inverse Scattering Series and Seismic Exploration." Inverse Problems (2003): R27–R83.

Weglein, Arthur B. and Bruce G. Secrest. "Wavelet estimation for a multidimensional acoustic earth model." Geophysics 55 (July 1990): 902–913.

Yang, J. and A. B. Weglein. "ISS free-surface multiple removal for source array data with interfering primaries and multiples." Mission-Oriented Seismic Research Program Annual Report (2013).

Zhang, J. Wave theory based data preparation for inverse scattering multiple removal, depth imaging and parameter estimation: analysis and numerical tests of Green's theorem deghosting theory. PhD thesis, University of Houston, 2007.

Comparison and analysis of space and temporal frequency, and, spatial wave-number and temporal frequency (e.g., P-Vz) Green's theorem de-ghosting methods, with different receiver spacing and aperture: Implications for 3 D de-ghosting

Jing Wu, Arthur B.Weglein and James D. Mayhan

April 29, 2013

Abstract

As one important segment of preprocessing, the result of deghosting influences the following processing steps.To thoroughly understand Green's theorem-derived deghosting, which is achieved by an integral in the frequency-space domain, the analysis and comparison are made with P+Vz deghosting method, which is achieved in the frequency-wavenumber domain. Under some specific assumptions, these two methods are equivalent. However, some influential factorsâĂŞâĂŞthe spatial sampling interval, spatial aperture, and vertical component of the wavenumberâĂŞâĂŞ cause these two methods have different numerical results.

1 Introduction

Deghosting is not only important for the following processing steps, but it also acts as a challenge for seismic exploration and its applications in the oil industry. Amundseen (1993) proposed a deghosting method (P+Vz for short),which achieves receiver deghosting in the frequency-wavenumber domain. The method requires the acquisition geometry to be horizontal in order to obtain the accurate vertical component of velocity., Additionally, the algorithm suitable for a1Dmedium or for one that is approximately horizontal in order to make a 0th Hankel Transform.

With the development of Green's theorem (Weglein et al. (2002);Zhang and Weglein (2005);Zhang and Weglein (2006)), another method for deghosting has become available. On the basis of its advantageous flexibility in choosing an appropriate reference medium, Zhang (2007) and Mayhan et al. (2012) developed a Green's theorem-derived deghosting method, which is achieved in frequency-space domain.There are no assumptions acting on the Green's theorem deghosting. It has a wider application range than does P+Vz, especially for a complicated subsurface and in difficult acquisition conditions.

In this paper, the theoretical equivalence between these two methods will be demonstrated by setting some specific assumptions. As P+Vz is achieved in the frequency-wavenumber domain, the spatial sampling interval and spatial aperture are two important factors affecting the final result. In addition, since the vertical component of wavenumber is a denominator in P+Vz formula, the singularity may cause instability and artifact. Thus, those factors will be analyzed and compared individually between these two deghosting methods in different domains.

2 Theoretical equivalence between two deghosting methods

Under the assumption of the horizontal acquisition geometry and a1D medium, the P+Vz formula for receiver deghosting is

$$U(k_r, z', r_s, z_s, \omega) = \frac{1}{2}[P(k_r, z', r_s, z_s, \omega) - \frac{\rho\omega}{k_z} V_z(k_r, z', r_s, z_s, \omega)]. \tag{2.1}$$

where U is upgoing wave; P is pressure field data ; V_z is the vertical component of partial velocity; k_r is horizontal wavenumber; k_z is vertical wavenumber; x_s, z_s is source location; z' is measurement depth; rho is density of water; $omega$ is circular frequency.

For Green's theorem deghosting, the homogeneous whole space of water is chosen as reference medium. The air, air gun, and earth are treated as three sources. After choosing the volume V as the half space above the measurement surface, we can arrive at the formula for receiver deghosting. The result corresponds to the upgoing waves, which is caused by the contribution from the earth. The formula is

$$P'_R(r, r_s, \omega) = \int_{m.s.} dS[P(r', r_s, \omega)\frac{\partial}{\partial n'} G_0^d(r, r', \omega) - G_0^d(r, r', \omega)\frac{\partial}{\partial n'} P(r', r_s, \omega)]. \tag{2.2}$$

where P'_R is receiver deghosting wave at position r; P and $\frac{\partial}{\partial n'} P$ are pressure field data and gradient of pressure on the measurement surfacer' respectively.

G_0^d is the Green's function for a point source in a whole-space water medium, and it has the following format:

$$G_0^d(r, r', \omega) = -1/4\pi exp(ikR_+)/R_+. \tag{2.3}$$

where $R_+ = |r - r'|$.

So now if after applying spatial Fourier transform on Green's theorem deghosting formula, the new form is same as the one given by P+Vz, we can say these two methods are theoretically equivalent.

2.1 Derivation of P+Vz from Green's theorem (take point source as an example)

For a point source, with a horizontal receiver cable (the first assumption), the Green's theorem deghosting formula can be written as

$$\begin{aligned} P'_R(x, y, z, x_s, y_s, z_s, \omega) &= \iint dx'dy[P(x', y, z', x_s, y_s, z_s, \omega)\frac{\partial}{\partial z'} G_0^d(x, y, z, x', y, z', \omega) \\ &\quad - G_0^d(x, y, z, x', y, z', \omega)\frac{\partial}{\partial z'} P(x', y, z', x_s, y_s, z_s, \omega)]. \end{aligned} \tag{2.4}$$

With constant velocity, G_0^d is invariant under lateral translation, so

$$G_0^d(x, y, z, x', y, z', \omega) = G_0^d(x - x', y - y, z, , z', \omega). \tag{2.5}$$

Then equation(4) can be written as

$$\begin{aligned} P'_R(x,y,z,x_s,y_s,z_s,\omega) &= \iint dx'dy[P(x',z',x_s,z_s,\omega)\frac{\partial}{\partial z'}G_0^d(x-x',y-y,z,,z',\omega) \\ &\quad -G_0^d(x-x',y-y,z,,z',\omega)\frac{\partial}{\partial z'}P(x',z',x_s,z_s,\omega)] \end{aligned} \tag{2.6}$$

Equation 6 is clearly a two-dimension convolution format, so when we are transforming to wavenumber domain(k_x, k_y) from the space domain(x, y), the result shows as a product. If the medium is 1D (the second assumption), then 2D Fourier Transform can be replaced by Hankel transform to improve calculation speed.Then

$$\begin{aligned} P'_R(k_r,z,r_s,z_s,\omega) = P(k_r,z',r_s,z_s,\omega)\frac{\partial}{\partial z'}G_0^d(k_r,z,z',\omega) \\ -G_0^d(k_r,z,z',\omega)\frac{\partial}{\partial z'}P(k_r,z',r_s,z_s,\omega). \end{aligned} \tag{2.7}$$

$G_0^d(k_r,z,z',\omega)$ can be written as:

$$G_0^d(k_x,z,z',\omega) = \frac{e^{ik_z(z'-z)}}{2ik_z}. \tag{2.8}$$

where $k_z = \sqrt{\frac{w^2}{c^2} - k_r^2}$.

$$\frac{\partial}{\partial z'}G_0^d(k_r,z,z',\omega) = \frac{e^{ik_z(z'-z)}}{2}. \tag{2.9}$$

Substituting formulas(8) and (9) into formula (7),

$$\begin{aligned} P'_R(k_r,z,r_s,z_s,\omega) &= P(k_r,z',x_s,z_s,\omega)\frac{e^{ik_z(z'-z)}}{2} - \frac{e^{ik_z(z'-z)}}{2ik_z}\frac{\partial}{\partial z'}P(k_r,z',x_s,z_s,\omega). \\ &= e^{ik_r(z'-z)} * \frac{1}{2}[P(k_r,z',r_s,z_s,\omega) - \frac{1}{ik_z}\frac{\partial}{\partial z'}P(k_r,z',r_s,z_s,\omega)]. \end{aligned} \tag{2.10}$$

$e^{ik_z(z'-z)}$ represents upward continuation from z' to z. When $z = z'$,we get

$$P'_R(k_r,z',r_s,z_s,\omega) = \frac{1}{2}[P(k_r,z',r_s,z_s,\omega) - \frac{1}{ik_z}\frac{\partial}{\partial z'}P(k_r,z',r_s,z_s,\omega)]. \tag{2.11}$$

Substituting equation (12) into equation(11),

$$\frac{\partial}{\partial z}P = i\rho\omega V_z. \tag{2.12}$$

We arrive at

$$P'_R(k_r,z',r_s,z_s,\omega) = \frac{1}{2}[P(k_r,z',r_s,z_s,\omega) - \frac{\rho\omega}{k_z}V_z(k_r,z',r_s,z_s,\omega)]. \tag{2.13}$$

This resulting equation is the same as the P+Vz formula (equation (1), above). Thus, to some extent, we can say that these two methods are theoretically equivalent and just are calculated in different domains. Without those constraints, the Green's theorem deghosting has a broader application.

2.2 Derivation of P+Vzfrom Green's theorem (take Line source as an example)

For a line source, the derivation is similar to that for a point source, except we only require a 1D spatial transform from x to k_x. Again, we get the same conclusion that these two methods are theoretically equivalent under some assumptions. Only horizontal acquisition geometry is needed here but without 1D medium, since no Hankel Transform.

3 Analysis of numerical influencing factors

With regard to wavenumber, we cannot ignore the effect from spatial sampling interval and spatial aperture. Those effects may contaminate the result or make it lose its resolution and in so doing sometimes may make the profile even worse. In this section, we will discuss the influences of these two factors separately. After that, another influential factor, vertical wavenumber k_z, will be analyzed.

3.1 Influence factor - spatial sample interval

In order to prevent alias, the sampling interval should satisfies the Nyquist Condition:

$$\Delta x \leq \frac{\pi}{k_{max}}. \tag{3.1}$$

$$\Delta t \leq \frac{\pi}{\omega_{max}}. \tag{3.2}$$

By using the dispersion relation,

$$k_{max} \leq \frac{\omega_{max}}{c}. \tag{3.3}$$

Finally, the spatial sample interval should satisfy:

$$\Delta x \leq \frac{\pi c}{\omega_{max}}. \tag{3.4}$$

So the spatial sampling interval should be very small to prevent alias. Both the calculations in space and wavenumber-domain will be effected by this factor. So low-pass filter is an inevitable step before calculation.

3.2 Influence factor - spatial aperture

We can treat the limited-aperture data as a result of truncation acting on the unlimited-aperture data. The calculations with limited-aperture data, no matter the integral in space domain or product in wavenumber domain, will produce edge effect and weighted sum. To reduce the influence of edge effect, we need add a smoothing window on the truncated data. But for weighted sum, the only way to get an accurate result is increase aperture.

On the basis of the formula of equation (3), $G_0^d$with point source reduces when going away from the âĂIJsourceâĂİ point r', meanwhile$\frac{\partial}{\partial z'}G_0^d$ reduces even faster. So the integral will get an stable result even with small aperture, although it's less accurate under such condition.

Amundsen (1993) gave some analysis of the influence of limited spatial aperture on P+Vz. The relation between finite-aperture $[r_1, r_2]$ data $\hat{P}(k_r, z', \omega)$and infinite-aperture data $P(k_r, z', \omega)$ is

$$\begin{aligned}\hat{P}(k_r, z', \omega) &= \int_{r_1}^{r_2} dr r J_0(k_r r) \int_0^{\infty} dk_r' k_r' J_0(k_r' r) P(k_r', z, \omega) \\ &= \int_0^{\infty} dk_r' \mathcal{K}(r_1, r_2, k_r', k_r) P(k_r, z, \omega) \end{aligned} \tag{3.5}$$

with a resolution kernel

$$\mathcal{K}(r_1, r_2, k_r', k_r) = K(r_2, k_r', k_r) - K(r_1, k_r', k_r) \tag{3.6}$$

$$\begin{aligned}K(r, k_r', k_r) &= k_r' \int_0^r dr r J_0(k_r' r) J_0(k_r r) \\ &= k_r' \frac{r k_r J_1(r k_r) J_0(r k_r') - r k_r' J_1(r k_r') j_0(r k_r)}{k_r^2 - k_r'^2}. \end{aligned} \tag{3.7}$$

Obviously, the result of P+Vz depends on the aperture, both on the near and far offset.

3.3 Influence of k_z

In the P+Vz formula, the vertical wavenumber component k_z works as a denominator. The result will be unstable when the value of k_z, which is a factor of denominator, is very small.

As we know, $k_z = \sqrt{\frac{w^2}{c^2} - k_r^2}$. The biggest value of both $\frac{w}{c}$ and k_r are usually less than 1, so it's not difficult to understand that k_z is a small value, especially when the former two values are close to each other. The result will not be exact whether we add a small value after such k_z or pass through these points. As around these points, the calculation becomes very sensitive, a small change of k_z may exert a huge influence. Additionally, ignoring these points is at the cost of reducing the method's deghosting effectiveness. Especially when the ghost events have a dip angle at the far offset, k_z is very small. Ignoring these points cannot remove the ghost in these areas. So the reference wave often has residual after calculation.

4 Conclusion and Discussion

Both of the two methods examined here are achieved by rigorous theoretical derivation and have validity. In addition, they are in principle equivalent if we invoke some specific assumptions on Green's theorem-deghosting formula, which demonstrates the greater applicability of Green's theorem deghosting method and the limitations of P+Vz deghosting method.

There are some conclusions we can draw after analyzing the different factors.(1) If the spatial sampling interval is small enough and the spatial aperture is big, both of these methods can give

a satisfactory result and Green's theorem-deghosting method may give a even better result. (2) If the events have a big dip angle in the far offset, then the P+Vz method becomes unstable; however, the Green's theorem-deghosting method is still useful. (3) If the deghosting result is requested to be at the depth of the cable, P+Vz exactly satisfies the requirement; Green's theorem deghosting will lose effectiveness if the target depth is too close to the cable depth. (4) When the subsurface is more complicated, Green's theorem deghosting can give a more satisfactory result.

5 Acknowledgements

We are grateful to all M-OSRP sponsors for long-term encouragement and support in this research. All members in M-OSRP are thanked for the help of finishing this paper and valuable discussions in this research program.

References

Amundseen, L. "Wavenumber-based filtering of marine point-source data." Geophysics 58 (September 1993): 1335–1348.

Mayhan, J. D., Paolo Terenghi, Arther B. Weglein, and Chemingui Nizar. "Green's theorem derived methods for preprocessing seismic data when the pressure P and its normal derivative are measured." 81st Annual International Meeting,SEG, Expanded Abstracts. . Soc. Expl. Geophys., 2012. 2722–2726.

Weglein, Arthur B., S. .A. Shaw, K. H. Matson, J. L. Sheiman, R. H. Solt, T. H. Tan, A. Osen, G. P. Correa, K. A. Innanen, Z. Guo, and J. Zhang. "New approaches to deghosting towed-streamer and ocean-bottum pressure measurements." 72nd Annual International Meeting, SEG, Expanded Abstracts (2002): 1016–1019.

Zhang, Jingfeng. Wave theory based data preparation for inverse scattering multiple removal, depth imaging and parameter estimation: analysis and numerical tests of Green's theorem deghosting theory. PhD thesis, University of Houston, 2007.

Zhang, Jingfeng and Arthur B. Weglein. "Extinction theorem deghosting method using towed streamer pressure data: Analysis of the receiver array effect on deghosting and subsequent free surface multiple removal." 75st Annual International Meeting,SEG, Expanded Abstracts. Soc. Expl. Geophys., 2005, 2095–2100.

Zhang, Jingfeng and Arthur B. Weglein. "Application of extinction theorem deghosting method on ocean bottom data." 75st Annual International Meeting,SEG, Expanded Abstracts. Soc. Expl. Geophys., 2006, 2674–2678.

(1) Incorporating the source array in the ISS free surface multiple elimination algorithm: the impact on removing a multiple that interferes with a primary; and (2)the first test of wavelet deconvolution on the internal multiple algorithm

J. Yang and A. B. Weglein

April 29, 2013

Abstract

This report discusses free-surface multiple removal from source-array data that have interfering or proximal primaries and multiples, by using the inverse scattering series (ISS) method (Carvalho, 1992; Weglein et al., 1997; 2003). If all the prerequisites are provided, the ISS free-surface multiple elimination (FSME) algorithm can accurately predict the free-surface multiples for the interfering data. Therefore, through a simple subtraction, the ISS method can remove the free-surface multiples without any subsurface information. After removing the free-surface multiples, the ISS internal multiple attenuation algorithm (Araújo et al., 1994; Weglein et al., 1997) with and without deconvolution of source wavelet is also tested. The test results show that with deconvolving the source wavelet, the internal multiple attenuation algorithm provides more accurate amplitude and shape of the predicted internal multiple.

1 Introduction

In marine seismic exploration, multiple removal is a classic long-standing problem. Various methods (e.g., Carvalho, 1992; Verschuur et al., 1992; Araújo et al., 1994; Weglein et al., 1997; Berkhout and Verschuur, 1999; Dragoset et al., 2008) have been developed to either attenuate or eliminate free-surface and internal multiples, and each method has different assumptions, advantages, and limitations.

Among these methods, the ISS FSME method (Carvalho, 1992; Weglein et al., 1997) does not need any subsurface information, which is a big advantage, especially under conditions of complex geology. The ISS method predicts the free-surface multiples accurately while the feedback-loop method (Verschuur et al., 1992) only provides approximate predictions. Therefore, the ISS method can remove the free-surface multiples through a simple subtraction, while the feedback-loop method has to remove the multiples adaptively using certain criteria (energy minimization, for example). The energy minimization criterion works well when there are no overlapping primaries and multiples in the input data. If primaries and multiples are overlapping and interfering destructively, the energy minimization criterion can fail and the adaptive subtraction will not work very well. The ISS method can in principle predict the multiples accurately if all of the requirements are provided.

The prerequisites include (1) removing the reference wavefield, (2) an estimation of the source wavelet and radiation pattern, (3) an obliquity factor, and (4) source and receiver deghosting. Green's theorem wave separation methods (Weglein and Secrest, 1990; Weglein et al., 2002) that are consistent with the ISS method have been applied to provide these criteria, since they are both multidimensional wave theoretic methods and do not need any subsurface information.

The current ISS FSME method (e.g., Carvalho, 1992; Araújo, 1994; Weglein et al., 1997) assumes an isotropic point source, i.e., the source has no variation of amplitude or phase with take-off angle. In actual marine seismic exploration, a source array is widely employed to increase the power of the source, broaden the bandwidth, and cancel the random noise. The source array is usually designed to make its signature short and sharp in the vertical-downward direction and to render its spectrum smooth and broad over the frequency band of interest (Giles and Johnston, 1973; Nooteboom, 1978; Brandsaeter et al., 1979). A large marine air-gun array will exhibit directivity and produce significant variations of the source signature (Loveridge et al., 1984). That directivity has significant effects on AVO analysis and removing or attenuating multiples. In seismic processing, it is essential that we characterize the source (and receiver) array's effect on any seismic processing methods. Therefore, to improve the accuracy of the predicted multiples, the ISS FSME algorithm is extended by accommodating a source array. That accommodation can enhance the fidelity of amplitude and phase prediction of free surface multiples at all offsets.

Furthermore, the current ISS internal attenuation algorithm (Araújo et al., 1994; Weglein et al., 1997) predicts the correct travel-times and only approximate amplitudes of all the internal multiples, because the input data is band limited and the ISS subseries for internal multiple is attenuation but not elimination. In addition, in the internal multiple attenuation algorithm we assume that the input data are a spike data. However, the data usually convolve with a source wavelet. The source wavelet has significant effects on the shape and amplitude of the predicted internal multiples. To improve the shape and amplitude of internal multiple prediction, the internal multiple attenuation algorithm is modified and tested by incorporating the source wavelet.

If multiples are removed completely, the residual multiples presented in the final migration images can affect Amplitude-Versus-Offset (AVO) analysis and then make the subsequent seismic interpretation work harder, and in some cases they may lead to incorrect interpretation. For example, in the Gulf of Mexico, these residual multiples can be mistakenly interpreted as subsalt primary reflections and can also lead to inaccurate salt-body definitions. Hence, effective demultiple algorithms are required in marine seismic data processing.

The report is organized as follows: First, the modified ISS FSME algorithm (Yang and Weglein, 2012) is briefly reviewed and analyzed. Second, the synthetic data with interfering events are tested by using both the current and the modified ISS FSME algorithms. Third, the internal multiple attenuation algorithm with and without deconvolution of source wavelet is tested. Finally, we discuss our findings and conclusions.

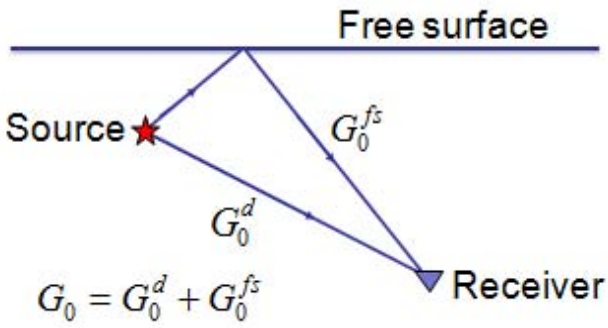

Figure 1: The reference Green's function G_0 consists of two parts: $G_0 = G_0^d + G_0^{fs}$. G_0^d is the direct Green's function, and G_0^{fs} is the additional part of the Green's function caused by the presence of the free surface.

2 The ISS FSME algorithm with source array

Starting from two basic differential equations (Weglein et al., 2003), which govern wave propagation in an actual medium and a reference medium, respectively,

$$LP = \rho \tag{2.1}$$

$$L_0 G_0 = \delta, \tag{2.2}$$

the forward and inverse scattering series can be derived. Here L and L_0 are respectively the differential operators in the actual media and the reference media. The perturbation V can be defined as $L_0 - L$. G_0 is the Green's function in the reference medium, and P is the total wavefield in the actual medium; that wavefield is generated by an arbitrary source distribution ρ.

As we know, if a given term in the forward scattering series creates a certain type of data, that term in the inverse scattering series removes that type of data; e.g., if there is no free surface, there are no ghosts and free-surface multiples in the data. Hence, the reference Green's function G_0 must consist of two contributions: the direct arrival G_0^d and its ghost G_0^{FS}, shown in figure 1, where G_0^{FS} acts to create (in the forward series) and remove (in the inverse series) ghosts and free-surface multiples.

The inverse scattering series algorithm for free-surface multiple removal is derived as follows:

(1) The data D are calculated by removing the reference wavefield P_0 from the total wavefield P on the measurement surface. In Tang's report (Tang and Weglein, 2013), the authors discuss how to obtain an accurate P_0 by adjusting the measurement parameters.

(2) Using Green's theorem (Zhang, 2007; Mayhan and Weglein, 2013) deghosting algorithm, both source and receiver side deghosted data D_1' are obtained as

$$D_1' = G_0^d V_1 P_0^d, \tag{2.3}$$

where the deghosted data D_1' are also the first term in the series for data without free-surface effects and P_0^d is the direct reference wavefield, which can be solved by deghosting P_0.

(3) V_1 can be expressed in terms of the deghosted data from equation 2.3 (the first-order equation in the data) by inverting G_0^d and P_0^d.

(4) Substituting V_1 into the second-order free-surface subseries and replacing the inner Green's function G_0 with G_0^{FS}, the second-order term is obtained as

$$D_2' = G_0^d V_2' P_0^d = -G_0^d V_1 G_0^{FS} V_1 P_0^d \tag{2.4}$$

by choosing the portion of V_2 in terms of the presence of the free surface.

(5) The final expression is a series for deghosted and free-surface demultipled data D' in terms of deghosted data D_1' and the projection of the source signature $\rho(k,q,\omega)$, as follows:

$$D_n'(k_g,k_s,\omega) = \frac{1}{i\pi}\int \frac{dk}{\rho(k,q,\omega)} D_1'(k_g,k,\omega) q e^{iq(\epsilon_g+\epsilon_s)} D_{n-1}'(k,k_s,\omega), \tag{2.5}$$

and

$$D'(k_g,k_s,\omega) = \sum_{n=1}^{\infty} D_n'(k_g,k_s,\omega), \tag{2.6}$$

where k_g, k_s and ω represent the Fourier conjugates of receiver, source, and time, respectively. ϵ_g and ϵ_s are the receivers' and sources' depth below the free surface, respectively. The obliquity factor q is given by $q = sgn(\omega)\sqrt{\omega^2/c_0^2 - k^2}$, and c_0 is the reference velocity. $\rho(k,q,\omega)$ is the projection of source signature in the f-k domain and $k^2 + q^2 = \omega^2/c_0^2$. The projection of source signature $\rho(k,q,\omega)$ can be directly achieved from the reference wavefield that is separated from the measured data by using Green's theorem method (Weglein and Secrest, 1990) by choosing air-water as its reference medium.

To obtain the projection of the source signature $\rho(k,q,\omega)$ from the reference wavefield, we assume that the source array is invariant from one shot to the next. In other words, the geometry or the distribution of the source array remains for each shot. The direct reference wavefield P_0^d for a 2D case can be expressed as an integral of the direct reference Green's function G_0^d over all air-guns in an array,

$$P_0^d(x,z,x_s,z_s,\omega) = \int dx'dz' \rho(x',z',\omega) G_0^d(x,z,x'+x_s,z'+z_s,\omega), \tag{2.7}$$

where (x,z) and (x_s,z_s) are the prediction point and source point, respectively. (x',z') is the distribution of the source with respect to the source locator (x_s,z_s). Using the bilinear form of Green's function and Fourier transforming over x, we obtain the relationship between ρ and P_0^d as

$$P_0^d(k,z,x_s,z_s,\omega) = \rho(k,q,\omega)\frac{e^{iq|z-z_s|}}{2iq} e^{ikx}. \tag{2.8}$$

Since $k^2+q^2 = \omega^2/c_0^2$, q is not a free variable, hence, we can not obtain $\rho(x,z,\omega)$ in space-frequency domain by taking an inverse Fourier transform on $\rho(k,q,\omega)$. However, the projection of the source signature $\rho(k,q,\omega)$ can always be achieved directly from the direct reference wavefield P_0^d in the f-k domain, where the variable k or q represent the amplitude variations of the source signature with angles. Ikelle et al. (1997) also proposed a similar quantity $A(k,\omega)$, the inverse source wavelet, and solved it indirectly using the energy minimization criterion.

The modified algorithm accommodates a source (and receiver) array and can provide added value compared to previous methods that assumed a single point source (air-gun) for the fidelity of amplitude and phase prediction of free surface multiples at all offsets. The modified FSME algorithm is fully multidimensional and does not require any subsurface information. Therefore, it is consistent with Green's theorem methods that provide all the data requirements. The details of the derivation for equations 2.5 and 2.8 can be found in last annual report (Yang and Weglein, 2012). In addition, the modified FSME algorithm is also consistent with the current FSME algorithm (Carvalho, 1992; Weglein et al., 1997; 2003) when the source array reduces to a point source. When the source array reduces to an isotropic point source $A(\omega)$, the source distribution $\rho(\vec{r}'-\vec{r}_s,\omega)$ becomes $A(\omega)\delta(\vec{r}'-\vec{r}_s)$ and the direct reference wavefield P_0^d becomes $A(\omega)G_0^d$. Thus, the recursive expression equation 2.5 reduces to

$$D'_n(k_g,k_s,\omega)=\frac{1}{i\pi A(\omega)}\int dk D'_1(k_g,k,\omega)qe^{iq(\epsilon_g+\epsilon_s)}D'_{n-1}(k,k_s,\omega), \tag{2.9}$$

which is exactly the current FSME algorithm.

3 Free-surface multiple removal for synthetic data with interfering primaries and multiples

In this section, I will show numerical tests of the free-surface multiple removal for both the point-source data and the source-array data with interfering primaries and multiples. The numerical tests are based on a simple 1D acoustic model with varying velocity and constant density, as shown in Figure 2a. The model has one shallow reflector at 90m, so the primary is interfering and overlapping with the free-surface multiples. The depths of the source and receiver are 7m and 9m, respectively. Using the Cagniard-de Hoop method, we generate the synthetic data for this model by applying two kinds of source separately: one is a point source and the other is a source array, as shown in Figure 2b. Here, we assume that the source array only varies laterally with identical source signatures, but this assumption is not necessary in the ISS FSME theory. The advantage of the Cagniard-de Hoop method is that we can accurately calculate any specific event we are interested in, so that we can compare it with the results predicted by our ISS FSME algorithm.

The ISS free-surface multiple elimination method has the ability to predict accurately the phase and amplitude of multiples if its pre-requisites (acquisition signature and deghosted data) are satisfied. If the input data are not deghosted, ISS free-surface multiple removal method can predict the exact phase but only approximate amplitude of multiples. For example, Figure 3a is the input data with ghosts. Inputting it into ISS free-surface multiple elimination algorithm, Figures 3b is its corresponding free-surface multiple prediction. Figure 3c shows the result after free-surface multiple removal through a simple subtraction. We can see that the multiples are not removed and even worse the primary is altered. Therefore, to remove the multiples effectively, the input data should be deghosted before inputting into the ISS FSME algorithm.

3.1 Free-surface multiple removal for the point-source data

The data are generated by an isotropic point source by using the Cagniard-de Hoop method. For simplicity, only the primary and the first-order free-surface multiple are generated, as shown in

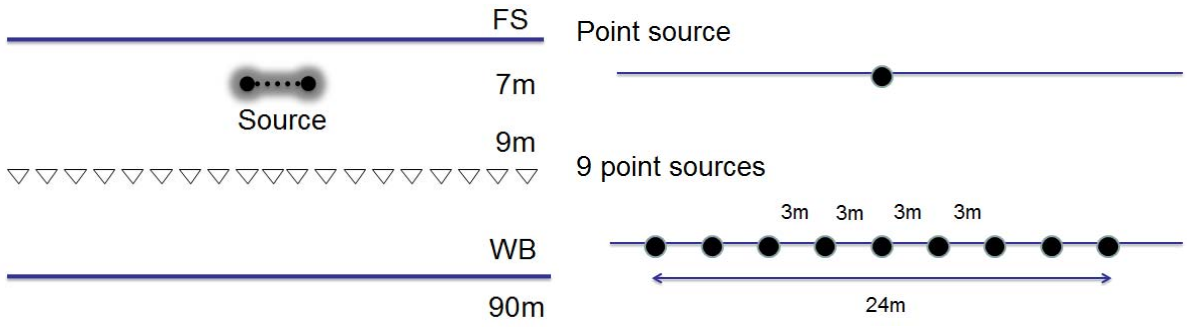

(a) (b)

Figure 2: (a) One-dimensional acoustic constant-density medium. The depths of source, receiver, and water bottom are 7m, 9m, and 90m, respectively. The trace interval is 3m. (b) Two sources are applied in the model, one with a point source and another with nine point sources. The range of the source array is 24m.

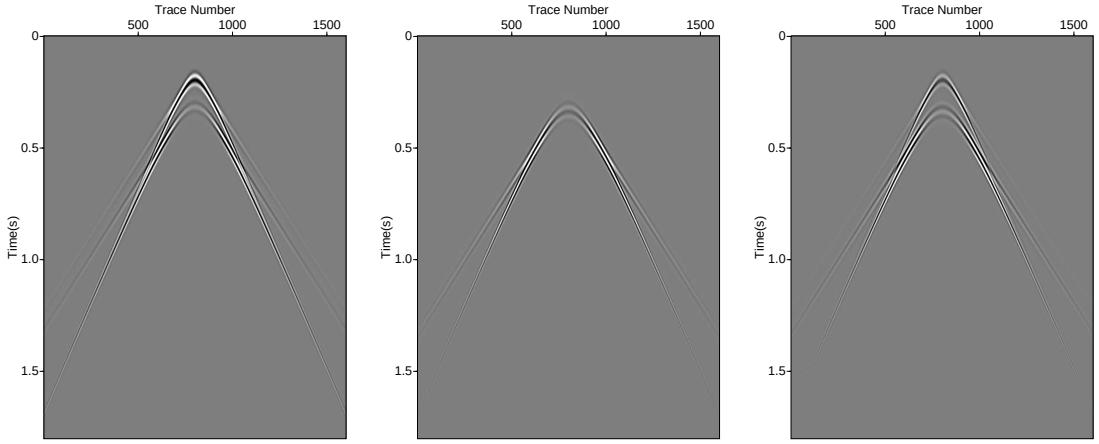

(a) (b) (c)

Figure 3: (a) Input data with ghosts; (b) The free-surface multiple prediction; (c) After free-surface multiple removal through a simple subtraction.

Figure 4a. Here, we assume the ghosts are not generated or have been removed. Figure 4a indicates that the primary and free-surface multiple are overlapping when the offset exceeds approximately 1000m. Furthermore, in Figure 4c it can be seen that they are destructively overlapping. Therefore, the adaptive subtraction method cannot deal with this kind of situation, because the method is based on the energy-minimization criterion, which assumes that the energy of the data will be minimized after the multiples are removed. However, in this case, the energy increases after removal of the multiples.

Since the data are a point-source data, we can apply the current FSME algorithm (Carvalho, 1992; Weglein et al., 1997; 2003) to predict free-surface multiples. The current FSME algorithm

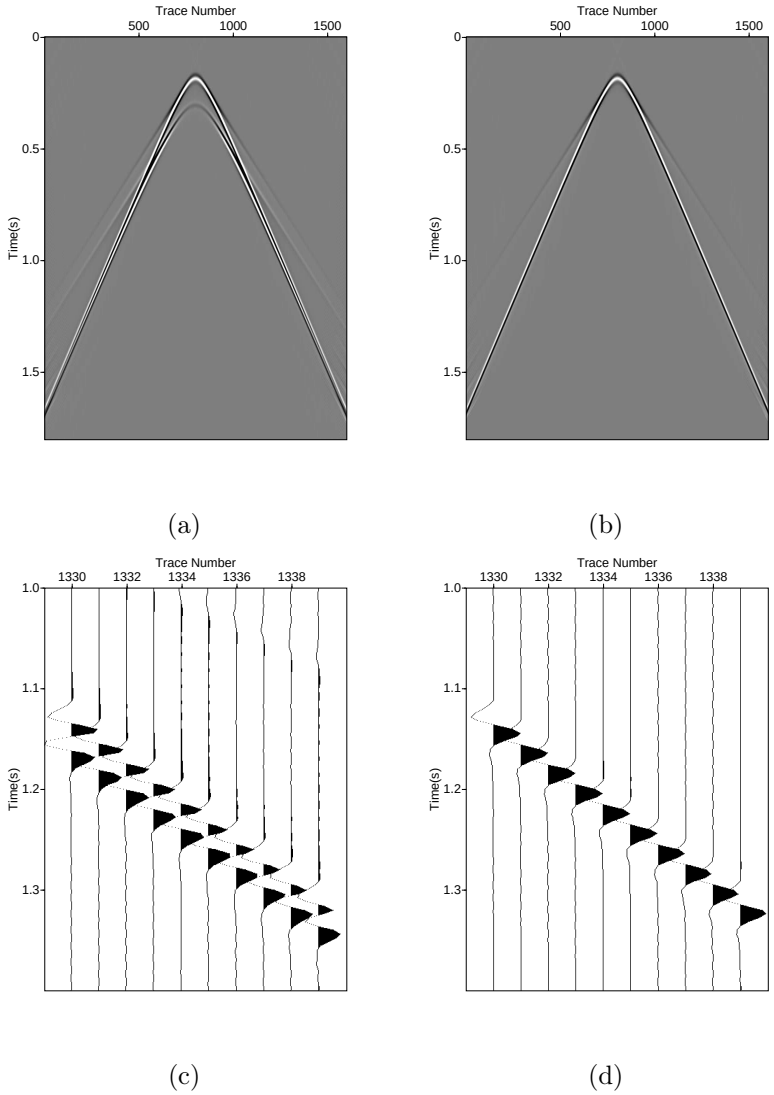

Figure 4: (a) The point-source data set; (b) After removing the free-surface multiple from the point-source data; (c) and (d) are their corresponding wiggle plots for the traces from 1330 to 1420 (offset from 1590m to 1860m).

is sufficient to predict both the accurate amplitude and phase of the free-surface multiples. Then, through a simple subtraction, the free-surface multiples can be removed completely, as shown in Figure 4b. For details, picking one trace (offset = $1800m$) from each of the two Figures 4a and 4b and comparing them, we can see that the amplitude of the primary increases after the free-surface multiples are removed, as shown in Figure 5. That is the reason why the energy-minimization criterion can fail in this case.

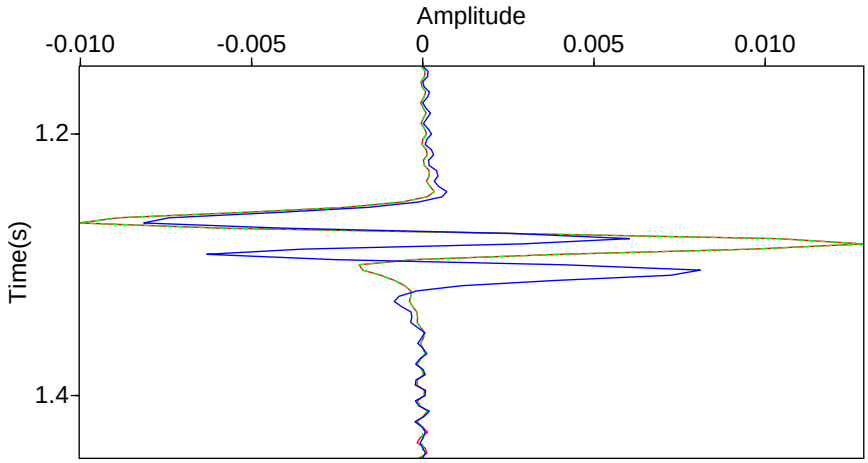

Figure 5: The wiggle plot for one trace at offset = $1800m$: Blue: the input data (primary and the first-order free-surface multiple); Green dash: after removing free-surface multiple; Red: the original primary. After free-surface multiple removal, the primary is boosted.

3.2 Free-surface multiple removal for the source-array data

The source-array data are generated by nine point sources. Here, we assume the nine point sources are identical and aligning in one line; in other words, the source array only varies laterally. Similarly, using the Cagniard-de Hoop method, only the primary and the first-order free-surface multiple are produced, as shown in Figure 6a. The primary and multiple are overlapping and interfering destructively, hence, only the ISS method may be able to remove the free-surface multiples.

For the source-array data, we first apply the current FSME algorithm to predict the free-surface multiples. It predicts phase accurately but only an approximate amplitude. After removing the free-surface multiple, Figure 6b shows that most multiples are removed, but there are still some residual multiples. Whether this result is valuable or not depends on the objective. If the amplitude is not critical, then this method is sufficient. For cases like AVO analysis and inversion, in which the amplitude is important, such residual multiples could produce serious errors in the prediction.

Next, we apply the modified FSME algorithm (Yang and Weglein, 2012) to predict the free-surface multiples. It can predict both amplitude and phase very accurately for the source-array data. After a simple subtraction, all the multiples are eliminated completely, as shown in Figure 6c. Therefore, the modified FSME algorithm works very well for the source-array data that have interfering events. Comparing Figures 6f and 6e, we can see that the primary is still affected by the residual multiple in Figure 6e, while in Figure 6f, the primary remains untouched as the original primary. For detail, we pick one trace (offset = $1800m$) from each of these two figures and compare them. The results are plotted in figure 7. The primary in Figure 6e is weaker than that in Figure 6f, and this amplitude error can seriously affect AVO analysis.

The numerical tests in (Yang et al., 2013) also show more details about how to obtain the direct

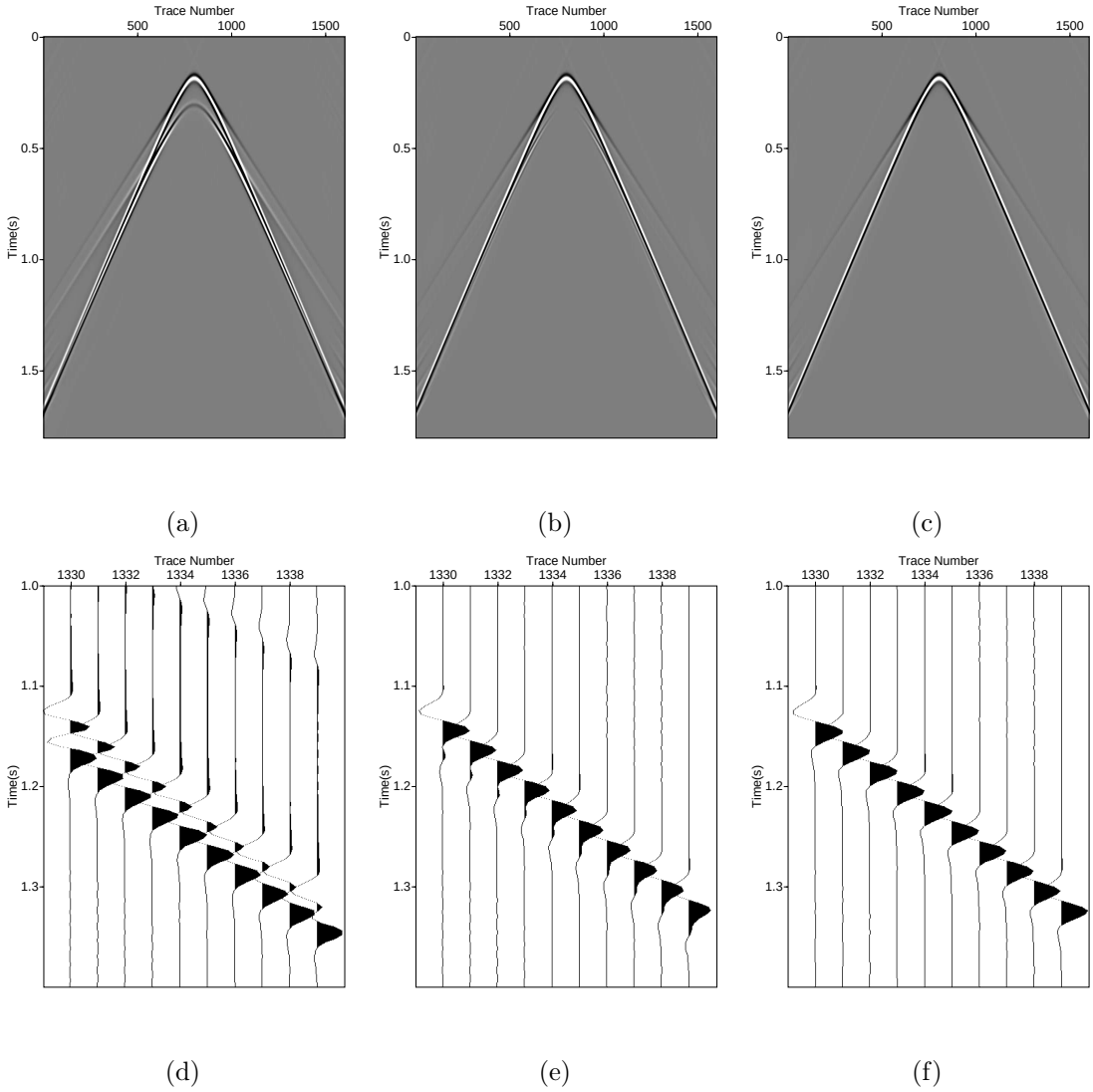

Figure 6: (a) The source array data set; After the free-surface multiple removal (b) using the current FSME algorithm and (c) using the modified FSME algorithm. (d), (e), and (f) are their corresponding wiggle plots for the traces from 1330 to 1420 (offset from 1590m to 1860m).

reference wavefield and source and receiver deghosted data. These numerical tests for the synthetic data with interfering events have demonstrated the effectiveness and advantages of the ISS FSME method. For point-source data the current FSME algorithm is sufficient to remove free-surface multiples, while for source-array data the modified FSME algorithm leads to very accurate results.

4 Internal multiple attenuation with and without deconvolution of source wavelet

The output of the free-surface multiple elimination algorithm will input the ISS internal multiple attenuation algorithm. In this section, the internal multiple attenuation algorithm with and without

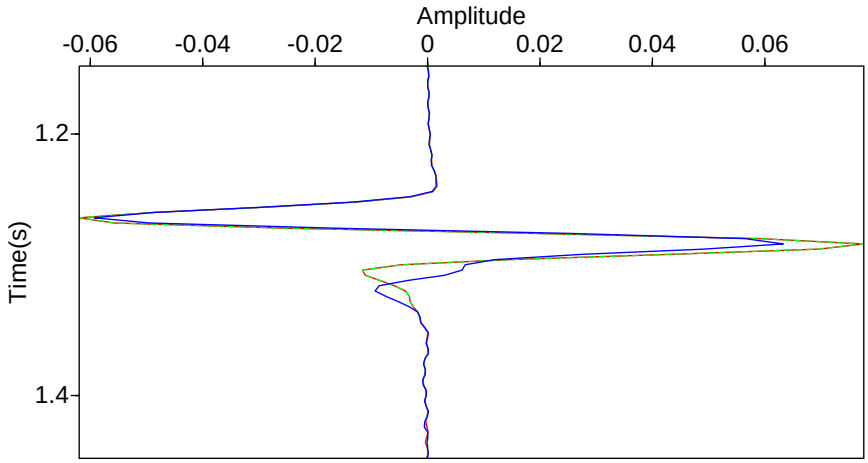

Figure 7: The wiggle plot for one trace (offset = $1800m$) after removing the free-surface multiple: Blue: using the current FSME algorithm; Green dash: using the modified FSME algorithm; Red: the original primary. The red line and green dash line are overlapping.

deconvolution of source wavelet will be applied to predict the internal multiples.

4.1 The ISS internal multiple attenuation algorithm

The ISS internal multiple attenuation algorithm for the first-order internal multiple prediction is proposed by Araújo (1994) and Weglein et al. (1997). Figure 8 illustrates how the algorithm constructs a first-order internal multiple. The first-order internal multiple is created by combining three events using convolutions and cross-correlations. The travel time of the internal multiple is predicted by adding the travel-times of the two deeper events and subtracting the travel time of a shallower one. Since, not all combinations of subevents will generate an internal multiple, the depth integrals are constrained to impose a lower-higher-lower relationship between the three subevents as represented in Figure 8. Therefore, the third subevent has a pseudodepth above the two other events such that $z_2 < z_3$ and $z_2 < z_1$.

The internal multiple attenuation algorithm assumes that the input data are a spike data. Actually, the input data generally convolves with a source wavelet. Therefore, the internal multiple attenuation algorithm can only predict an approximate amplitude and shape of the internal multiple. To improve the amplitude and shape, the internal multiple attenuation algorithm will be modified by accommodating the source wavelet. First, the input data are deconvolved by the source wavelet and the output of the algorithm convolves the source wavelet back. In Liang's report (Liang and Weglein, 2013), the authors also discussed the source wavelet effects on the internal multiple prediction for a more layer model.

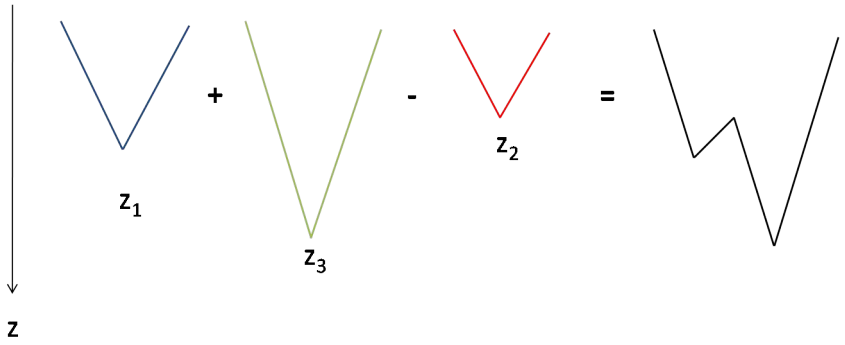

Figure 8: Subevents of an internal multiple. The internal multiple (black) is constructed by three arrivals (blue, green and red) that satisfy a lower-higher-lower relationship in pseudodepths, z_i.

4.2 Internal multiple prediction for the synthetic data

The internal multiple attenuation algorithm with and without deconvolution of source wavelet will be tested using a simple earth model, as shown in Figure 9a. Figure 9b is the source wavelet that we applied. Figure 10 shows the synthetic data that are generated by finite difference method and their predicted internal multiples. In the input data, the first two strongest events are the primaries, and the other events are internal multiples. Figures 10b and 10c show the predicted internal multiples using the ISS internal multiple attenuation algorithm with and without deconvolution of the source wavelet. From Figures 10b and 10c, we can see that both algorithms predict the correct travel time of the internal multiple and different amplitude and shape of the internal multiple.

To see the details of the predicted internal multiples, we pick the middle trace at the time window $0.85s$ to $1.15s$ from each figure in Figure 10. Comparing Figures 10e with 10d, we can see that the shape of the internal multiple predicted by the internal multiple attenuator without deconvolution of source wavelet is totally different with the original one and their amplitudes are not comparable. However, comparing Figures 10f with 10d, it shows that the amplitude and shape the internal multiple predicted by the internal multiple attenuation algorithm with deconvolution of source wavelet are similar with the original one, as shown in Figure 11. It demonstrates that the internal multiple attenuation algorithm with deconvolution of source wavelet gives more accurate internal multiple prediction, in which the predicted phase is accurate, the predicted shape looks similar, and the predicted amplitude is almost the same. The predicted amplitude is not exact because the internal multiple attenuation algorithm is an attenuator but not eliminator and the input data is band limited.

The synthetic data test shows that incorporating the source wavelet into the internal multiple attenuation algorithm produces more accurate and encouraging results. The predicted internal multiple has the correct travel time and almost identical amplitude and shape. This is the first test accommodating the source wavelet into the internal multiple attenuation algorithm. There are more tests underway. In addition, there are some more test results given by Liang and Weglein (2013). The authors discussed the source wavelet effects on the internal multiple prediction for the 1D normal incident model and 1.5D more layers model.

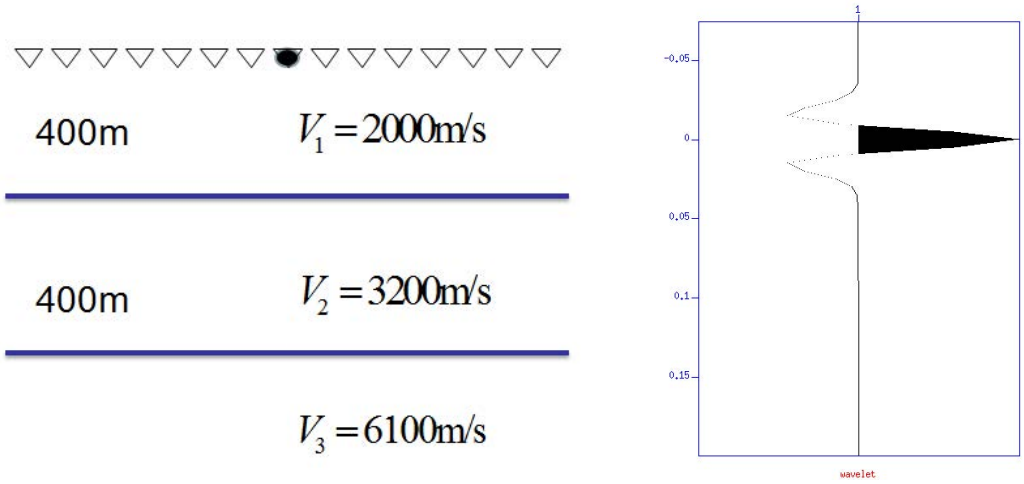

(a) (b)

Figure 9: (a) The earth model we used to generate the synthetic data. It is an one-dimensional acoustic constant-density medium. (b) Ricker wavelet.

5 Discussion and Conclusions

The inverse scattering series free-surface multiple removal method is tested on synthetic data that have interfering primaries and multiples. If all the prerequisites are provided, the ISS method has the ability to accurately predict the free-surface multiples without any subsurface information. For point-source data, the current ISS FSME algorithm is sufficient to accurately predict free-surface multiples, while for source-array data, the current algorithm can only predict phase accurately but amplitude approximately. This amplitude error can seriously affect the prediction results, in processes such as AVO analysis and inversion. However, the modified ISS FSME algorithm works very well for the source-array data. The numerical tests for the source-array data show that the modified FSME algorithm predicts more accurate results than does the current FSME algorithm. Therefore, for data with interfering events, the ISS FSME method can remove the free-surface multiples completely through a simple subtraction. Moreover, the internal multiple attenuation algorithm has been modified by accommodating the source wavelet and tested. The test results show that the internal multiple attenuation algorithm with deconvolution of the source wavelet predicts more accurate amplitude and shape of the internal multiples.

6 Acknowledgments

The first author is grateful to all M-OSRP sponsors for their support of this research and to Hong Liang and Lin Tang for their helpful and valuable reviews regarding this research. My special appreciation goes to my advisor, Dr. Arthur Weglein, for his teaching, guidance and patience.

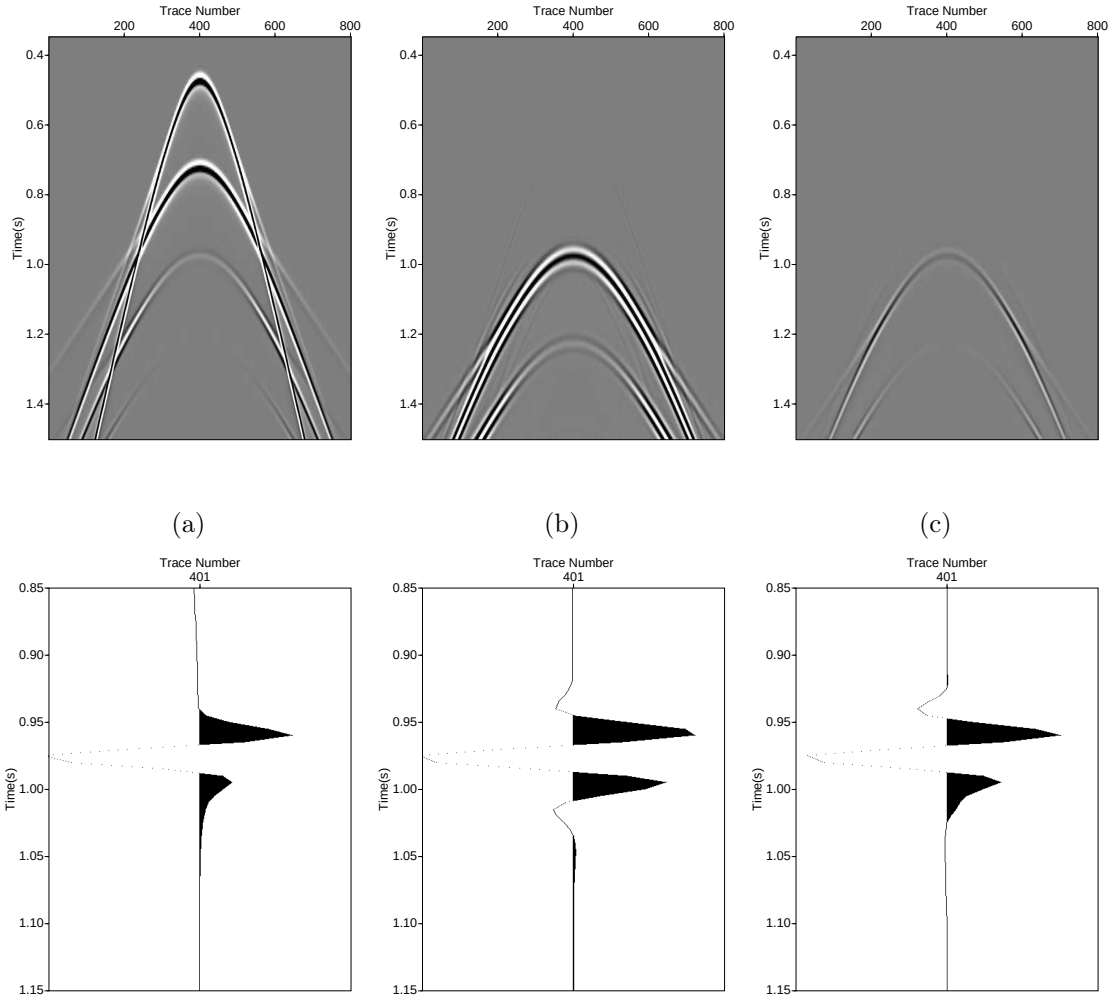

Figure 10: (a) The input data; (b) and (c) The internal multiples predicted by the ISS internal multiple attenuation algorithm without and with deconvolution of source wavelet, respectively. (d, e, f) are their corresponding wiggle plots at the time window $0.85s$ to $1.15s$.

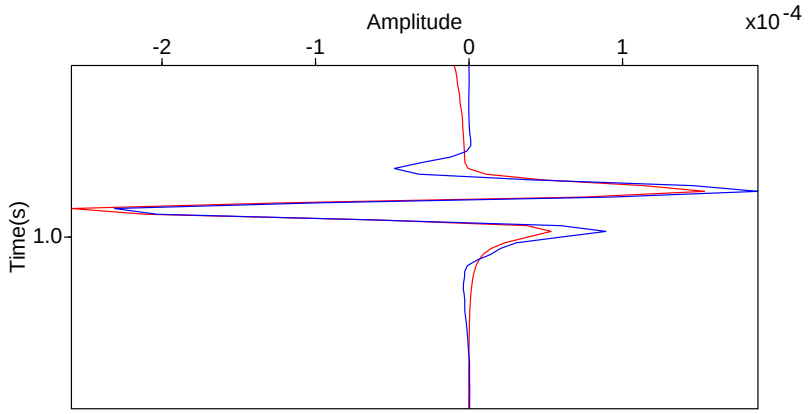

Figure 11: The comparison between the original internal multiple in the input data and internal multiple predicted by the internal multiple attenuation algorithm with deconvolution of source wavelet at zero offset.

References

Araújo, F. V. Linear and non-linear methods derived from scattering theory: backscattered tomography and internal multiple attenuation. PhD thesis, Universidade Federal da Bahia, 1994.

Araújo, F. V., A. B. Weglein, P. M. Carvalho, and R. H. Stolt. "Inverse scattering series for multiple attenuation: An example with surface and internal multiples." 64th Annual International Meeting, SEG, Expanded Abstracts (1994): 1039–1042.

Berkhout, A. J. and D. J. Verschuur. "Removal of internal multiples." 69th SEG Annual International Meeting (1999): 1334–1337.

Brandsaeter, H., A. Farestveit, and B. Ursin. "A new high-resolution or deep penetration air gun array." Geophysics 44 (1979): 865–879.

Carvalho, P. M. Free-surface multiple reflection elimination method based on nonlinear inversion of seismic data. PhD thesis, Universidade Federal da Bahia, 1992.

Dragoset, B., I. Moore, M. Yu, and W. Zhao. "Removal of internal multiples." 78th SEG Annual International Meeting (2008): 2426–2430.

Giles, B. F. and R. C. Johnston. "System approach to air gun array design." Geophys. Prosp. 21 (1973): 77–101.

Ikelle, Luc T., Graham Roberts, and Arthur B. Weglein. "Source signature estimation based on the removal of the first-order multiples." Geophysics 62 (1997): 1904–1920.

Liang, H. and A. B. Weglein. "Source wavelet effects on the ISS internal multiple leading order attenuation algorithm and its higher order modification." MOSRP Annual Report (2013).

Loveridge, M. M., G. E. Parkes, L. Hatton, and M. H. Worthington. "Effects of marine source array directivity on seismic data and source signature deconvolution." First Break 2 (1984): 16–22.

Mayhan, J. and A. B. Weglein. "Green's theorem-derived deghosting of marine seismic data." MOSRP Annual Report 1 (2013).

Nooteboom, J. J. "Signature and amplitude of linear air gun arrays." Geophys. Prosp. 26 (1978): 194–201.

Tang, L. and A. B. Weglein. "Study on factors that affect wave separation tests using Green's theorem with an over/under cable configuration." MOSRP Annual Report 1 (2013).

Verschuur, D. J., A. J. Berkhout, and C. P. A. Wapenaar. "Adaptive surface-related multiple elimination." Geophysics 57 (1992): 1166–1177.

Weglein, A. B., F. V. Araújo, P. M. Carvalho, R. H. Stolt, K. H. Matson, R. T. Coates, D. Corrigan, D. J. Foster, S. A. Shaw, and H. Zhang. "Inverse Scattering Series and Seismic Exploration." Inverse Problems (2003): R27–R83.

Weglein, A. B., F. A. Gasparotto, P. M. Carvalho, and R. H. Stolt. "An Inverse-Scattering Series Method for Attenuating Multiples in Seismic Reflection Data." Geophysics 62 (November-December 1997): 1975–1989.

Weglein, Arthur B. and Bruce G. Secrest. "Wavelet estimation for a multidimensional acoustic earth model." Geophysics 55 (July 1990): 902–913.

Weglein, Arthur B., S. .A. Shaw, K. H. Matson, J. L. Sheiman, R. H. Solt, T. H. Tan, A. Osen, G. P. Correa, K. A. Innanen, Z. Guo, and J. Zhang. "New approaches to deghosting towed-streamer and ocean-bottem pressure measurements." 72nd Annual International Meeting, SEG, Expanded Abstracts (2002): 1016–1019.

Yang, J. and A. B. Weglein. "Incorporating source and receiver arrays in the Inverse Scattering Series free-surface multiple elimination algorithm: theory and examples that demonstrate impact." MOSRP Annual Report 1 (2012): 114–132.

Yang, Jinlong, James D. Mayhan, Lin Tang, and Arthur B. Weglein. "Accommodating the source (and receiver) array in free-surface multiple elimination algorithm: impact on interfering or proximal primaries and multiples." Submitted to 83rd SEG international meeting (2013).

Zhang, Jingfeng. Wave theory based data preparation for inverse scattering multiple removal, depth imaging and parameter estimation: analysis and numerical tests of Green's theorem deghosting theory. PhD thesis, University of Houston, 2007.

Accuracy of the internal multiple prediction when a time-saving method based on two angular quantities (angle constraints) is applied to the ISS internal multiple attenuation algorithm

Hichem Ayadi and Arthur B. Weglein

April 29, 2013

Abstract

The inverse scattering series (ISS) is a direct inversion method for a multidimensional acoustic, elastic and anelastic earth. It communicates that all inversion processing goals can be achieved directly and without any subsurface information. This task is reached through a task-specific subseries of the ISS. Using primaries in the data as subevents of the first-order internal multiples, the leading-order attenuator can predict the time of all the first-order internal multiples and is able to attenuate them.

However, the ISS internal multiple attenuation algorithm can be a computationally demanding method, especially in a complex earth. By using an approach that is based on two angular quantities and that was proposed in Terenghi et al. (2012), the cost of the algorithm can be controlled. The idea is to use the two angles as key-control parameters, by limiting their variation, to disregard some calculated contributions of the algorithm that are negligible. Moreover, the range of integration can be chosen as a compromise of the required degree of accuracy and the computational time saving.

This time-saving approach is presented in this report and applied to the ISS internal multiple attenuation algorithm. Through a numerical analysis, the relationship between accuracy and performance is examined and discussed.

1 Introduction

In exploration seismology, a source of energy generated on or near the surface of the earth or of water produces waves that propagate into the subsurface. The wave travels through the earth until it hits a rock layer or a material with a different impedance. A part of the energy is reflected back towards the surface and is recorded at the measurement surface by geophones or hydrophones. An arrival of seismic energy is called an event. An event that experiences just one upward reflection is a primary. A ghost is an event that starts its path by propagating up from the source and reflecting down from the free surface (a source ghost), or ends its path by propagating down to the receiver (a receiver ghost). An event that experiences more that one downward reflection is a multiple. We consider two kinds of multiples. A free-surface multiple is a multiple that experiences more than one upward reflection and at least one downward reflection at the air-water or air-land surface. An internal multiple is an event that experiences more than one upward reflection and all downward

reflections from below the free surface. Ghosts and multiples are considered to be noise. A primary has only one upward reflection, which makes it relatively easy to extract information from about the subsurface.
In this report we will focus only on the study of primaries and internal multiples.

Araújo et al. (1994) and Weglein et al. (1997) have proposed the ISS internal-multiple-attenuation algorithm. It is a leading-order contribution towards the elimination of first-order internal multiples. The algorithm is based on the construction of an internal-multiple attenuator coming from a subseries of the ISS. It has received positive attention for stand-alone capability for attenuating first-order internal multiples in marine and offshore plays.

Terenghi et al. (2012) introduced two angular quantities that can be used as a key-control parameter on the computational cost of the ISS leading-order internal-multiple-attenuation algorithm. The two angles, α (the dip of the reflection in the subsurface) and γ (the incidence angle between the propagation vector of a wave and the normal to the reflector), are related to the wavefield variables in the f-k domain. Therefore, control of this angle can be key to our ability to control the time loop of the algorithm. That has been discussed by Terenghi et al. (2012). In this report, we will discuss how the computational cost can relate to the accuracy of internal-multiple prediction. In other words, is it possible to reduce the computational time of the ISS internal-multiple attenuation algorithm without affecting its efficiency?

In the first part of this report, a description of the internal-multiple-attenuation algorithm will be provided. It discusses how the first-order internal-multiple attenuator can be constructed from a subseries of the ISS. Then, the computational cost savings proposed by Terenghi et al. (2012) will be developed and applied to the ISS internal-multiple-attenuation algorithm. Finally, a numerical analysis will be presented, in order to discuss the accuracy and efficiency of the algorithm with this key control.

2 The ISS internal multiple attenuation algorithm

In seismic processing, many processing methods make assumptions and require subsurface information. However, sometimes these assumptions are difficult or impossible to satisfy in a complex world. Furthermore, when the assumptions are not satisfied, the method is not functional. The inverse scattering series states that all processing objectives can be achieved directly and without any subsurface information.
The inverse scattering series is based on scattering theory, which is a form of perturbation analysis. It describes how a scattered wavefield (the difference between the actual wavefield and the reference wavefield) relates to the perturbation (the difference between the actual medium and the reference medium).

The forward scattering series construction starts with the differential equations governing wave propagation in the media:

$$LG = \delta(r - r_s), \tag{2.1}$$

$$L_0 G_0 = \delta(r - r_s). \tag{2.2}$$

Where L and L_0 are the actual and the reference differential operators, respectively, and G and G_0 are the actual and reference GreenâĂŹs functions, respectively.

Define the scattered field as $\psi_s = G - G_0$ and the perturbation as $V = L_0 - L$.
The Lippmann-Schwinger equation relates G, G_0, and V:

$$G = G_0 + G_0 V G \tag{2.3}$$

Substituting iteratively the Lippmann-Schwinger equation into itself gives the forward scattering series:

$$\begin{aligned} \psi_s &= G_0 V G_0 + G_0 V G_0 V G_0 + G_0 V G_0 V G_0 V G_0 + ... \\ &= (\psi_1) + (\psi_2) + (\psi_3) + ..., \end{aligned} \tag{2.4}$$

where, (ψ_n) is the portion of the scattered wavefield that is the nth order in V. The measured values of ψ_s are the data D.

The perturbation V can also be expanded as a series,

$$V = V_1 + V_2 + V_3 + ... \tag{2.5}$$

Substituting V into the forward scattering series and evaluating the scattered field on the measurement surface results in the inverse scattering series:

$$(\psi_s)_m = (G_0 V_1 G_0)_m \tag{2.6}$$

$$0 = (G_0 V_2 G_0)_m + (G_0 V_1 G_0 V_1 G_0)_m \tag{2.7}$$

$$0 = (G_0 V_3 G_0)_m + (G_0 V_2 G_0 V_1 G_0)_m + (G_0 V_1 G_0 V_2 G_0)_m + (G_0 V_1 G_0 V_1 G_0 V_1 G_0)_m \tag{2.8}$$

$$...$$

the inverse scattering series internal-multiple-attenuation concept is based on the analogy between the forward series and the inverse series. The forward series could generate primaries and internal multiples through the action of G_0 on the perturbation V, while, the inverse series can achieve a full inversion of V by using G_0 and the measured data. The way that G_0 acts on the perturbation to construct the internal multiples suggests the way to remove them.
In the forward series, the first-order internal multiples have their leading-order contribution from the third term: $G_0 V G_0 V G_0 V G_0$. This suggests that the leading-order attenuator of internal multiples can be found in the third term in the inverse series equation (2.8). In Weglein et al. (1997) a subseries that attenuates internal multiples was identified and separated from the entire inverse scattering series.

The ISS internal-multiple-attenuation algorithm is a subseries of the inverse scattering series. The algorithm begins with the input data $D(k_g, k_s, \omega)$, which are the data in the ω temporal frequency deghosted and with free-surface multiple removed. Here k_s, k_g are the source and receiver horizontal wavenumber, respectively. Then, let us define $b_1(k_g, k_s, \omega)$ which corresponds to an uncollapsed f-k migration of effective incident plane-wave data as

$$b_1(k_g, k_s, \omega) = (-2iq_s) D(k_g, k_s, \omega) \tag{2.9}$$

where $q_s = sgn(\omega)\sqrt{(\frac{\omega}{c_0})^2 - k_s}$ is the sourceâĂŹs vertical wavenumber and c_0 the reference velocity. The second term in the algorithm is the leading-order attenuator b_3, which attenuates all the first-order internal multiples. The leading-order attenuator for a 2D earth is given by,

$$\begin{aligned} b_3(k_s, k_g, \omega) &= \frac{1}{(2\pi)^2} \int_{-\infty}^{+\infty} dk_1 \int_{-\infty}^{+\infty} dk_2 e^{-iq_1(z_g - z_s)} e^{-iq_2(z_g - z_s)} \\ &\int_{-\infty}^{+\infty} dz_1 b_1(k_g, k_1, z_1) e^{i(q_g + q_1)z_1} \\ &\int_{-\infty}^{z_1 - \epsilon} dz_2 b_1(k_1, k_2, z_2) e^{-i(q_1 + q_2)z_2} \\ &\int_{z_2 + \epsilon}^{+\infty} dz_3 b_1(k_2, k_s, z_3) e^{i(q_2 + q_s)z_3} \end{aligned} \tag{2.10}$$

where z_1, z_2, and z_3 are the pseudo-depths. ϵ is a small positive parameter chosen in order to make sure that $z_1 > z_2$ and $z_3 > z_2$ are satisfied.

Finally, using the input data and the leading-order attenuator of the first-order internal multiples, the data with the first-order internal multiples attenuated is given by

$$D(k_g, k_s, \omega) + D_3(k_g, k_s, \omega) \tag{2.11}$$

with $D_3(k_g, k_s, \omega) = (-2iq_s)^{-1} b_3(k_g, k_s, \omega)$.

3 Computational cost saving using two angle constraints.

Terenghi et al. (2012) discuss two angular quantities that can be used in order to reduce the computational cost of the ISS internal-multiple-attenuator algorithm. The idea is to construct key-control parameters that allow to disregard some part of the calculus that is insignificant during the computation. In other words, use this key-parameters to optimize some intervals of calculus in the algorithm. The approach used is based on certain angular quantities in order to control the cost of the algorithm.

Stolt and Weglein (2012) define the image-function wavenumber as a difference between the receiver and source-side wavenumbers

$$\vec{k_m} = \vec{k_g} - \vec{k_s} = (\vec{\kappa_g} - \vec{\kappa_g}, q_g - q_s) \tag{3.1}$$

Here $\vec{\kappa_s}$ and $\vec{\kappa_g}$ are the horizontal components of the source and receiver wavenumbers, respectively.

This definitions allows the construction of two angles, α and γ (cf. Figure 1). The dip angle α corresponds to the angle between the surface and the horizontal component. The incident angle γ is

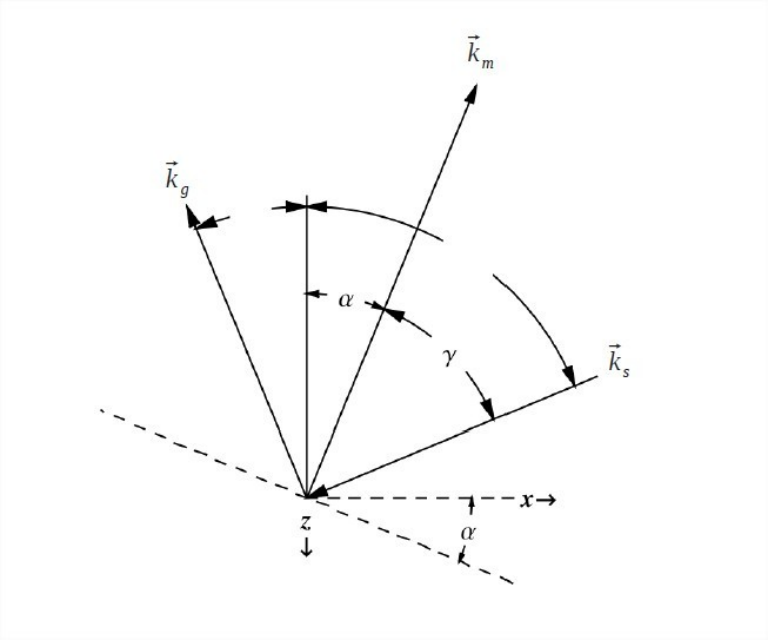

Figure 1: Plane waves at an interface in the subsurface. α is the angle between $\vec{\kappa_m}$ and the vertical. γ is the angle between $\vec{\kappa_m}$ and $\vec{\kappa_r}$ or $\vec{\kappa_s}$. Figure from Terenghi et al. (2012).

the angle between the image-function wavenumber and the source- (or receiver-)side wavenumber. Using simple trigonometry, α and γ can be related to the field quantities in the $f-k$ domain:

$$\alpha = tan^{-1}\left(\frac{\sqrt{\vec{\kappa_m}.\vec{\kappa_m}}}{\mid q_g - q_s \mid}\right) \tag{3.2}$$

$$\gamma = \frac{1}{2}\left(-\frac{c_0^2}{\omega^2}(\vec{\kappa_g}.\vec{\kappa_s} + q_g q_s)\right) \tag{3.3}$$

The dependence of α and γ on the temporal frequency is carried by the occurrences of the vertical wavenumber q. Further, the relationship between α, γ and ω is monotonic. This means that at fixed values of $\vec{\kappa_s}$ and $\vec{\kappa_g}$ any given value of ω unequivocally identifies angles α and γ. Then, increasing the temporal frequencies in the data map to decreasing values of the reflection dip and the frequencies in the data maps to decreasing values of the reflection dip and the aperture angle. At set values of $\vec{\kappa_s}$ and $\vec{\kappa_g}$ it is possible to conclude that any desired finite angle-domain interval maps to a similar finite frequency domain interval. This may be used in order to decrease the number of loops. Indeed, looking at the eq (2.10), has b_3 - in 2D - two integrations over the wavenumber component. Therefore, it is possible to constrain the algorithm within a range of angular quantities,

$$\alpha_{min} \leq \alpha \leq \alpha_{max} \tag{3.4}$$

$$\gamma_{min} \leq \gamma \leq \gamma_{max} \tag{3.5}$$

By using the α/γ and ω relationship, the total frequency interval can also be constrained as

$$max(\omega_{\gamma}^{min}, \omega_{\alpha}^{min}) \leq \omega \leq min(\omega_{\gamma}^{max}, \omega_{\alpha}^{max}) \tag{3.6}$$

Then, the reduction of the total frequency interval allows us to reduce the interval of integration of b_3 and which means reducing the number of loops.

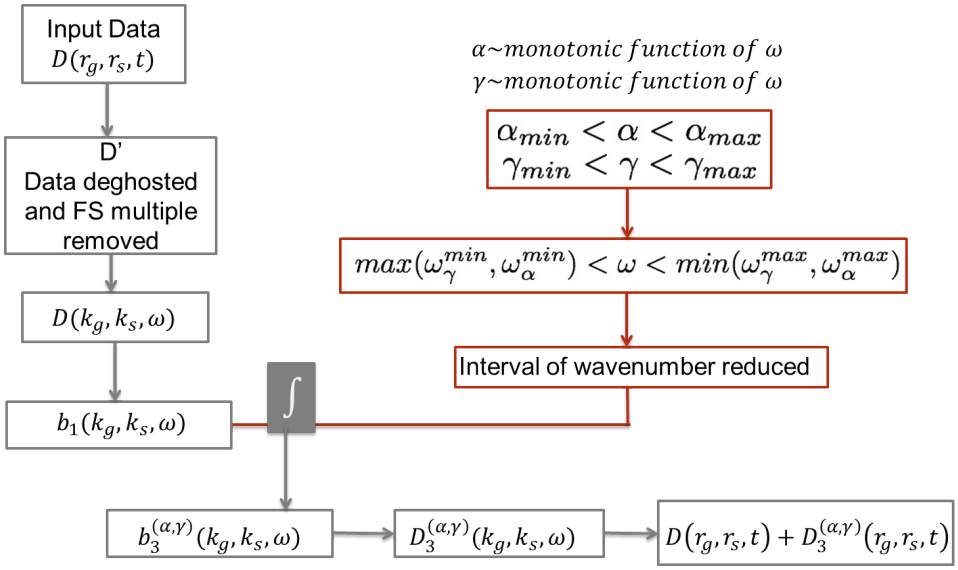

Figure 2: Process of the ISS internal multiple attenuation with angle constraints.

The Figure 2 recapitulates in a graph all of the process described previously. In the next section, a numerical analysis continues and illustrates the discussion from sections 2 and 3, in which the efficiency and accuracy of the angle-constraints method are presented.

4 Numerical analysis

In this section numerical examples are shown in order to illustrate the concepts previously presented. The model considered in this numerical analysis is a three layer earth at depths : $z = 1000$m, 1300m and 1700m. The source shot ($z = 910$ and $x = 6086$) is recorded by 928 receivers. The maximum offset is at 2320m. Figure 3 shows the shot gather with the different events: primaries (green array) and internal multiples.

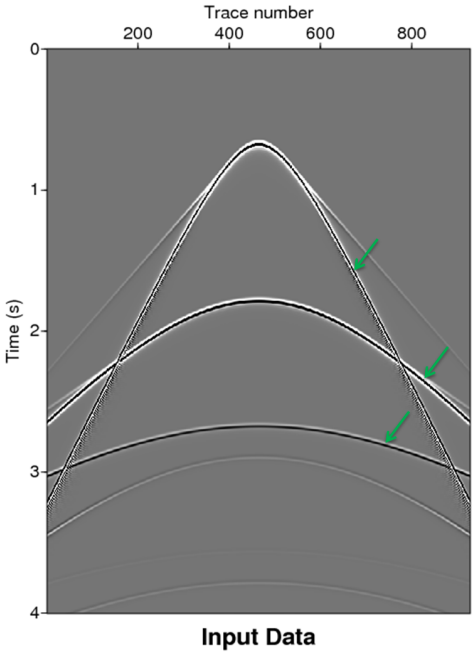

Figure 3: Shot gather recorded. The three primaries resulting from the three layers are shown in green.

Figure 4, illustrates the internal-multiple prediction using the ISS internal multiple attenuation algorithm. All first-order the internal multiple are predicted.

Figure 6 illustrates the internal-multiple prediction following the process uses angle constraints, as shown in the Figure 2. The model is in 1D; consequently, just one angle (the incident angle γ) can be constraint. The analysis made in 1D for γ can be extended to α by analogy.

A first interpretation would be that we do not need to compute for a full open angle in order to have an accurate prediction of the internal multiples. Notice that a prediction with a full open angle corresponds to an internal multiple prediction without any angle constraints. Even so, with reduction to a certain angle (γ_{limite}) the prediction of the internal multiples is degraded.

Figure 7 shows the amplitude for different γ_{max} angles at zero offset and comparing with the amplitude for a full open γ-angle. It is clear that the amplitude, at zero offset, is not affected. The first-order internal multiple are predicted at the right time and the right amplitude.

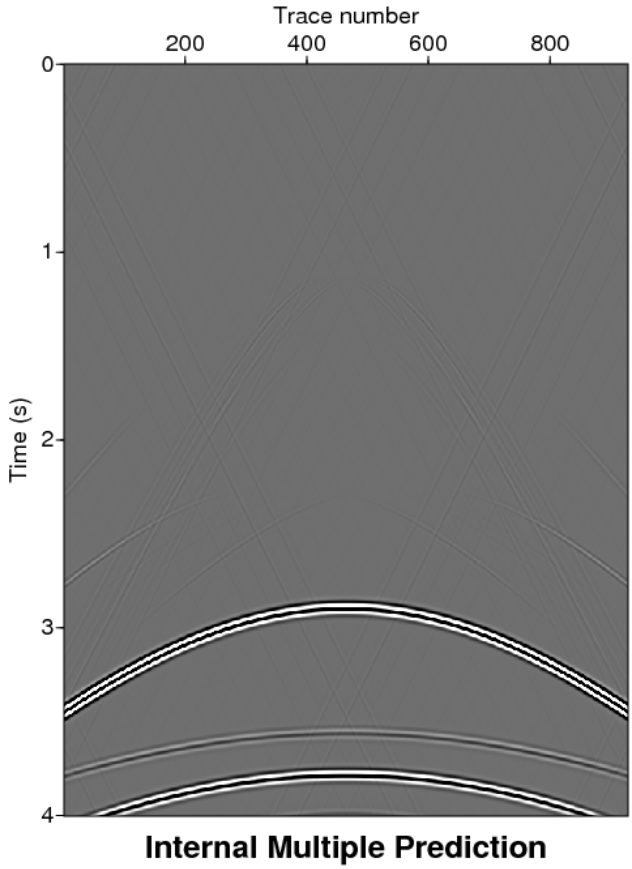

Figure 4: Prediction of all the first-order internal multiples.

Figure 8 plots the amplitude for different values of γ_{max} at offset 1405m and comparing with the amplitude for a full open γ-angle. In Figure 6, the prediction of the internal multiples for $\gamma_{max} = 20°$ seems to be the same as that for $\gamma_{max} = 25°$ and Figure 4. If we look more precisely at the amplitude, we can see that it has been affected. The amplitude for $\gamma_{max} = 20°$ does not correspond exactly to the amplitude for $\gamma_{max} = 90$, for the same trace number. However, for $\gamma_{max} = 25°$, the amplitude is exactly the same as that for the full open Îş angle. Notice that even if the amplitude is affected, the internal multiple are still predicted at the right time.

If we look at the shape (cf. Figure 9), the same interpretation can be made. For $\gamma_{max} = 25°$ the shape matches with an usual internal multiple prediction (full open γ-angle). Bellow this incident angle, the shape do not match which means that the prediction can not be considered accurate.

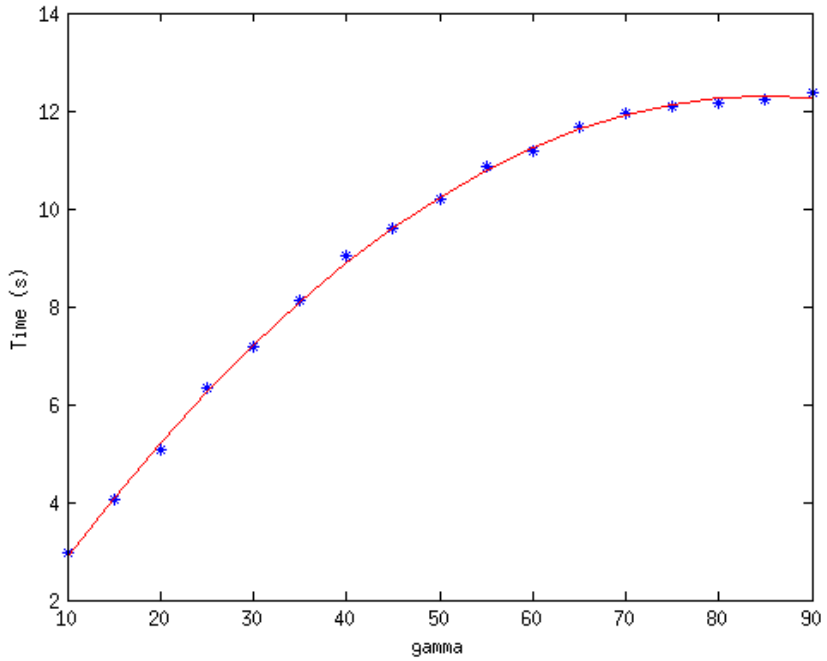

Figure 5: Computational time in function of the incident angle chosen.

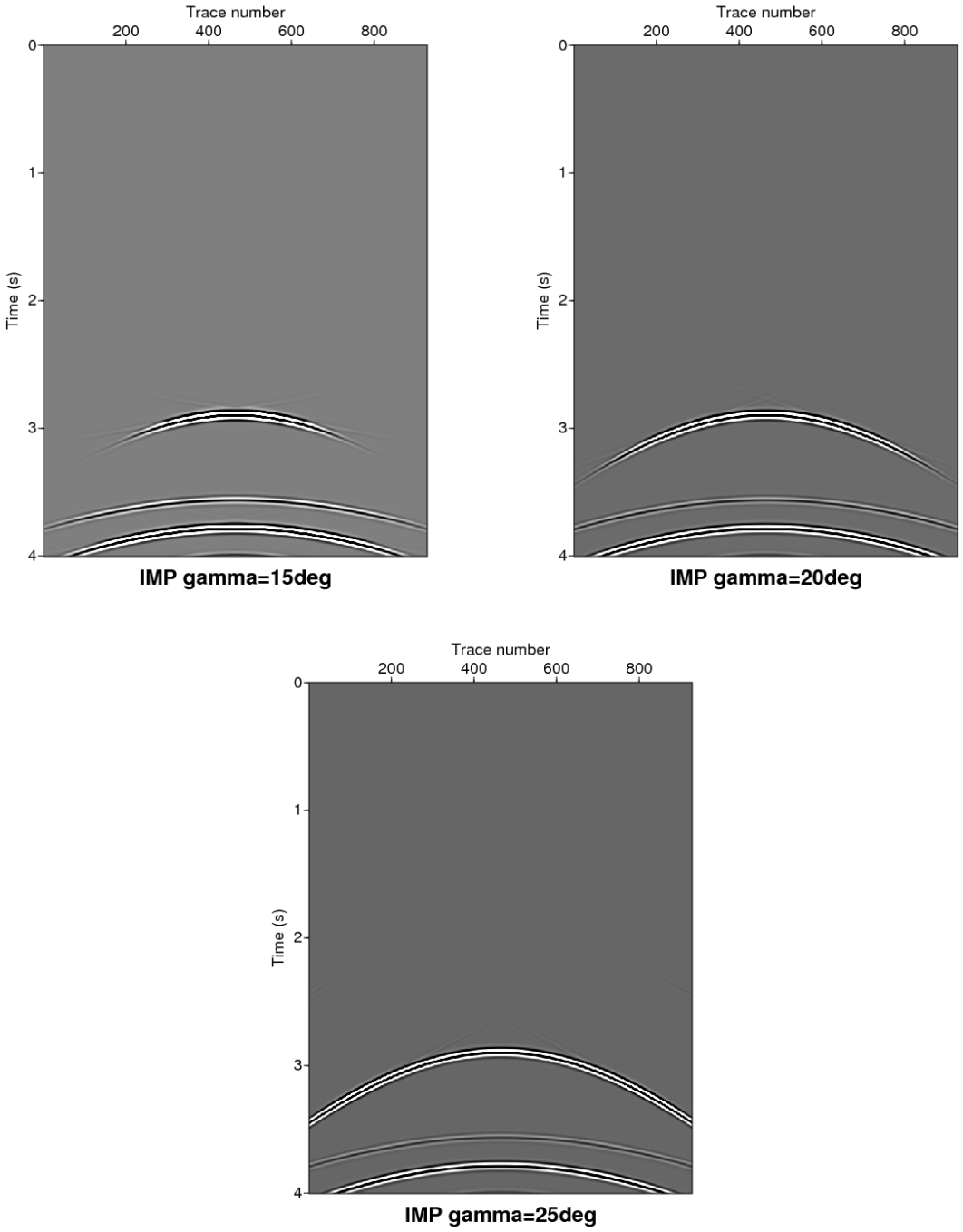

Figure 6: Internal-multiple prediction for different angles of γ: $\gamma_{max} = 15°$, $\gamma_{max} = 20°$ and $\gamma_{max} = 25°$.

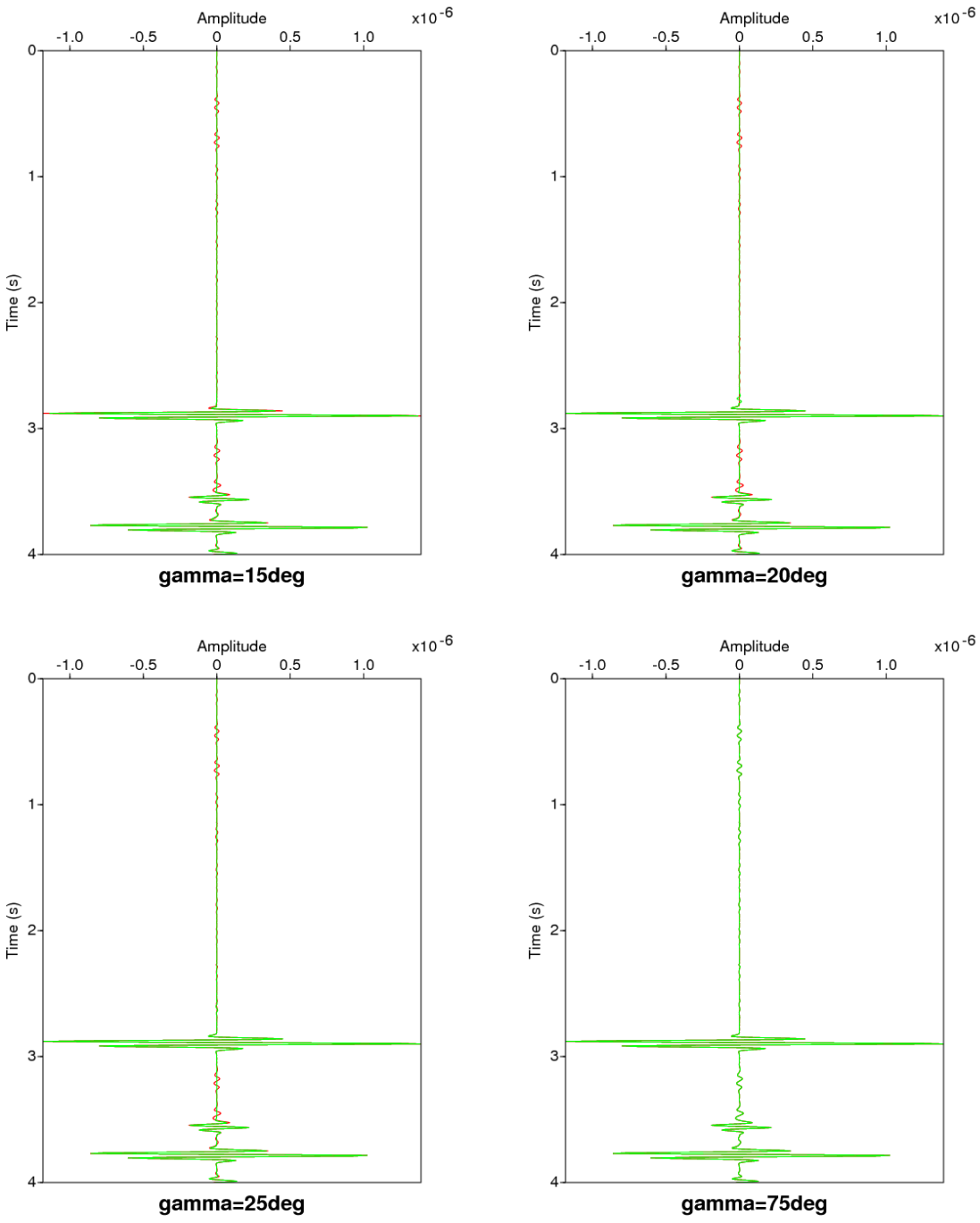

Figure 7: Amplitude for different γ_{max} angles at zero offset.

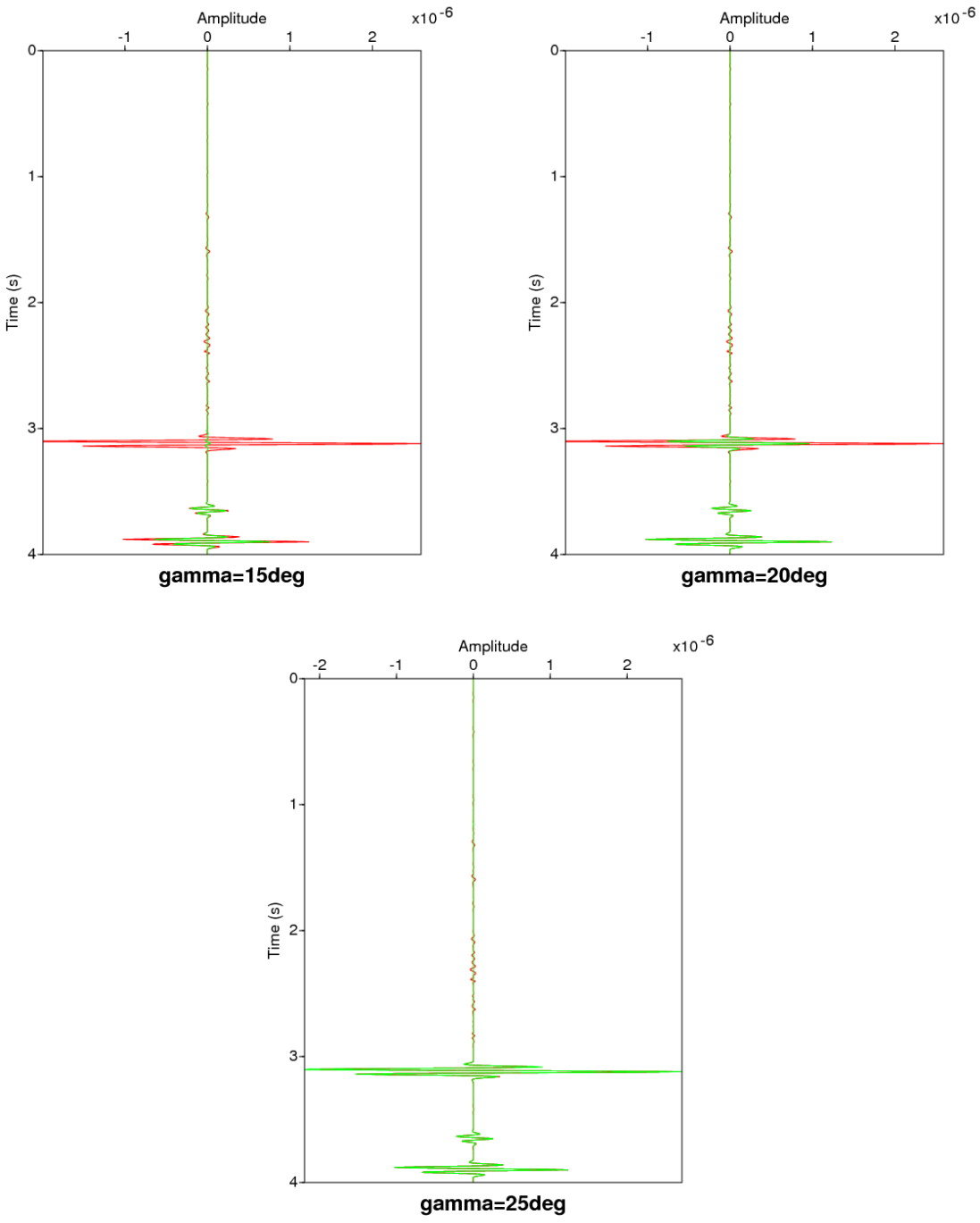

Figure 8: Amplitude for different γ_{max} angles at offset 1405m.

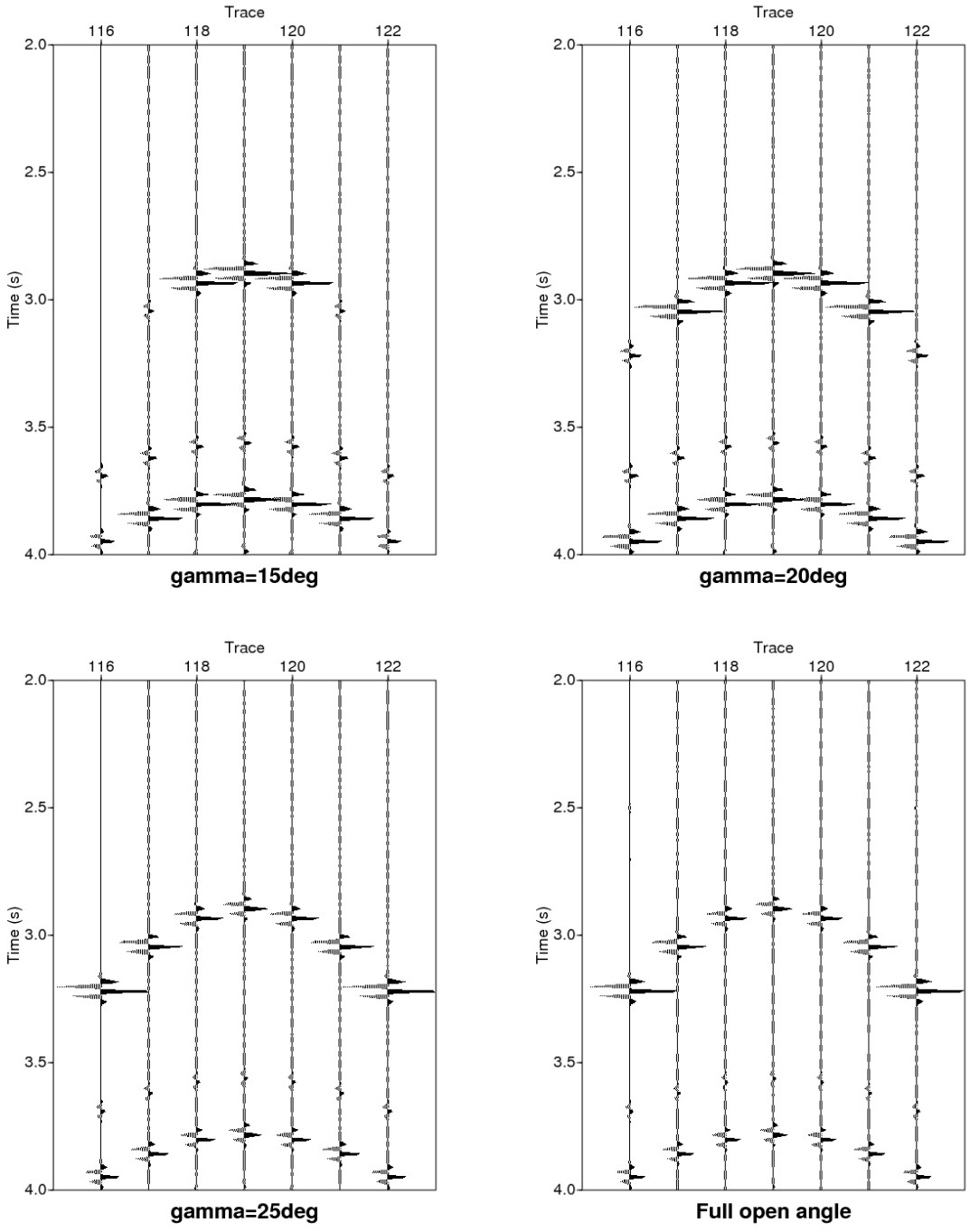

Figure 9: Wiggle plot for $\gamma_{max} = 15°$, $\gamma_{max} = 20°$, $\gamma_{max} = 25°$ and full open γ-angle. Source at trace number 119.

5 Discussion and conclusions

Terenghi et al. (2012) have introduced a time saving method: the angle constraints. Looking at the procedure (cf. Figure 2) and the performance analysis (cf. Figure 5), it is undeniable that applied to an algorithm defined in source and receiver transformed domain like the ISS internal multiple attenuation, this approach can reduce considerably the computational cost of the algorithm. Studying the impact of this key-control method in the algorithm, it appears that a compromise between the time saved and the accuracy of the internal multiple prediction has to be made. Indeed, above a certain "angle limit" the internal multiple prediction stays accurate and precise. Below, the internal multiples are still predicted at the right time but with an approximate amplitude. This "angle limit" depends on the depth of the reflector which generate the multiples and the maximum offset. Thus, the angle constraints is a trade-off tool between accuracy and cost of the algorithm. In other words, the ISS internal multiple algorithm will have its computational time reduced according to the degree of accuracy required by the user. The next step will be to identify this two angles using the input data in order to be able to define the constraint limits.

6 Acknowledgements

First, we would like to express our appreciation to Total E&P USA for establishing the research scholar position for the first author in M-OSRP. Also, we would like to thank all the sponsors for their support. We thank all the member of the M-OSRP group and specially Hong Liang, Chao Ma and Wilberth Herrera for the different rewarding discussions. A special acknowledgement to Paolo Terenghi for his avant-gardism and his contribution that inspired this work.

References

Weglein, A. B., F. V. Araújo, P. M. Carvalho, R. H. Stolt, K. H. Matson, R. T. Coates, D. Corrigan, D. J. Foster, S. A. Shaw, and H. Zhang. "Inverse Scattering Series and Seismic Exploration." Inverse Problems (2003): R27–R83.

Araújo, F. V., A.B. Weglein, P.M. Carvalho and R.M. Stolt."Inverse scattering series for multiple attenuation: An example with surface and internal multiples" SEG Technical Program Expanded Abstract (1994): 1039-1041.

Stolt, Robert H. and Arthur B. Weglein."Seismic Imaging and Inversion : Volume 1: Application of Linear Inverse Theory." Cambridge, United Kingdom: Cambridge University Press (2012).

Weglein, A.B.,F.A. Gasparotto, P.M. Carvalho and R.M. Stolt. " An inverse-scattering series method for attenuating multiples in seismic reflection data." Geophysics (1997): 1975-1989.

Weglein, A.B., S. Hsu, P. Terenghi, X. Li and R.M. Stolt. "Multiple attenuation : Recent advances and the road ahead 2011." The Leading Edge (2011): 864-875.

Terenghi P. and A.B. Weglein "ISS internal multiple attenuation with angle constraints" Annual report (2012): R242–R266.

One dimensional analysis of the effects of including multiples as part of input into the ISS multiple removal algorithm: comparison between free-surface and internal

C. Ma and A. B. Weglein, M-OSRP, University of Houston

April 29, 2013

Abstract

Internal-multiple removal becomes more important and challenging as seismic exploration moves towards more complex areas. To meet this challenge, a multi-dimensional method that does not assume the earth properties is developed; the method is based on the inverse scattering series (ISS)(Araújo, 1994; Weglein et al., 1997). Tests of the current ISS leading-order internal-multiple attenuation algorithm have shown a stand-alone capability of this algorithm and indicate promising future applications (Fu et al., 2010; Luo et al., 2011; Terenghi et al., 2011; Hsu et al., 2011). However, there are still subjects to be studied (Weglein et al., 2011). The current leading-order algorithm uses primaries in the input data as subevents to predict the first-order internal multiples. Focusing on the effects of internal multiples acting as subevents, we compare the different outputs of the current algorithm using different input data (*i.e.*, data with and without internal-multiples). We analyze the output in both two-reflector and three-reflector examples to show different effects. Also, we compare those effects with the effects of including free-surface multiples in the ISS free-surface multiple removal algorithm and analyze the similarities and differences between these two cases. Their similarities and differences demonstrate the characteristic of requiring specific contributions from terms in the inverse series in order to collectively accomplish certain seismic processing tasks (*e.g.*, free-surface multiple removal and internal-multiple elimination). This characteristic further demonstrate to us the necessity of including higher-order terms in the inverse series to address the limitations of the current leading-order algorithm.

1 Introduction

Traditionally, seismic exploration assumes the seismic data contain only primaries (events that experience only one upward reflection in history). Hence, that assumption requires the removal of multiples (events that experience multiple reflections). Depending on the location of downward reflection, multiples are divided into free-surface multiples and internal multiples. Free-surface multiples are events that experience at least one downward reflection at the air-water or air-land surface (i.e., at the free surface), whereas internal multiples are events that experience *all* of their downward reflections below the free surface.

Many methods that are based on assumptions regarding the data characteristics or the nature of earth have been developed to remove multiples (Weglein and Dragoset, 2005). Such methods are effective when those assumptions are satisfied or mildly violated. However, as seismic exploration moves towards more complex areas, these methods have limitations due to their assumptions and the requirements for subsurface information. This motivates development of new methods that avoid those assumptions or requirements.

The application of inverse scattering series methods in exploration seismic reflection data was introduced by Weglein et al. (1981) and Stolt and Jacobs (1980). It provides a comprehensive framework for achieving seismic data processing goals. Within that overall seismic processing series, different sub-series can be isolated to achieve free-surface-multiple removal, internal-multiple elimination, depth imaging and inversion of primaries.

The current ISS leading-order internal-multiple-attenuation algorithm was first proposed by Araújo (1994) and Weglein et al. (1997). It is entirely data driven and requires no subsurface information, and it predicts all internal multiples at all depths at once with the correct time and well-approximated amplitude of true internal multiples (Weglein et al., 2003). Matson (1997) extends the theory to land and ocean-bottom survey application. Higher-order terms are captured to extend the leading-order algorithm from attenuation to elimination (Ramírez and Weglein, 2005; Ramirez, 2007). The first towed streamer data are test by Maston et al. (1999) and first land data are shown in Fu et al. (2010). More recent tests (Luo et al., 2011; Terenghi et al., 2011; Hsu et al., 2011) show encouraging results and stand-alone capability of the ISS leading-order internal-multiple-attenuation algorithm.

However, there are still subjects remaining to be studied (Weglein et al., 2011). Previous work on current leading-order internal-multiple-attenuation algorithm mainly focused on predicting multiples by using primaries in the seismic data. Zhang and Shaw (2010) use a two-reflector analytic example to show a more complicated prediction (*i.e.*, higher-order internal multiples are predicted) when the input data contain internal multiples. Ma et al. (2011) and Liang et al. (2011) show that in the cases where there are three or more than three reflectors, not only higher-order internal multiples but also spurious events are generated by the leading-order algorithm, and they propose higher-order terms to address that spurious prediction. In this report, we show similarities and differences of including the corresponding multiples in the input data of the free-surface-multiple-elimination algorithm and internal-multiple-elimination algorithm.

2 1D analytic example – Free-surface-multiple prediction

For the purpose of comparison, we first examine the role of free-surface multiples in a free-surface-multiple removal case. The ISS free-surface-multiple elimination subseries was developed by Carvalho (1992) and Weglein et al. (1997). The subseries for deghosted and free-surface demultipled data D' is given by deghosted data D'_1 as follows (Weglein et al., 2003):

$$D'_n(k_g, k_s, \omega) = \frac{1}{i\pi\rho_0 B(\omega)} \int_{-\infty}^{\infty} dk q e^{iq(\epsilon_g+\epsilon_s)} D'_1(k_g, k, \omega) D'_{n-1}(k, k_s, \omega)$$

$$n = 2, 3, 4, \cdots, \tag{2.1}$$

and

$$D'(k_g, k_s, \omega) = \sum_{n=1}^{\infty} D'_n(k_g, k_s, \omega), \tag{2.2}$$

where $B(\omega)$ and ρ_0 are source signature and reference density, respectively.

In the free-surface-multiple elimination equation 2.2, the first term, D'_1, is the deghosted input data, including both primaries and multiples; the nth term ($n \geq 2$) can be considered to be the prediction of the $(n-1)$th-order free-surface multiples. Equation 2.1 and equation 2.2 show that the ISS free-surface-multiple-removal algorithm works one temporal frequency at a time and works order by order.

In a 1D earth with a normal incident plane wave and a source wavelet with a unit amplitude, i.e., $A(\omega) = 1$, the algorithm can be written as (Weglein et al., 2003):

$$\begin{aligned} R =& \frac{R_{FS}}{1 - R_{FS}} \\ =& R_{FS} + R_{FS}^2 + R_{FS}^3 + \cdots, \end{aligned} \tag{2.3}$$

where R_{FS} and R are data with and without free-surface multiples, respectively. Notice that the free-surface is characterized by a reflection coefficient of -1 for a pressure wavefield. Similarly, we can consider the second term in equation 2.3 as the prediction of the first-order free-surface multiples and the third term as the prediction of the second-order free-surface multiples, etc.

We use a 1D analytic example to illustrate the prediction of the free-surface multiples. The model (Figure 1) has two reflectors, and the deghosted data, $D(t)$, with two primaries, three first-order (blue terms) and four second-order (red terms) free-surface multiples, can be written as:

$$\begin{aligned} R_{FS}(t) = R_1\delta(t - t_1) + R'_2\delta(t - t_2) &- R_1^2\delta(t - 2t_2) - R_2'^2\delta(t - 2t_2) - 2R_1R'_2\delta(t - t_1 - t_2) \\ &+ R_1^3\delta(t - 3t_1) + R_2'^3\delta(t - 3t_2) + 3R_1R_2'^2\delta(t - t_1 - 2t_2) + 3R_1^2R'_2\delta(t - 2t_1 - t_2) + \cdots, \end{aligned} \tag{2.4}$$

where R_1 and R'_2 are amplitudes of the first and second primaries, respectively. We have assumed the downward reflection coefficient at the free-surface to be -1.

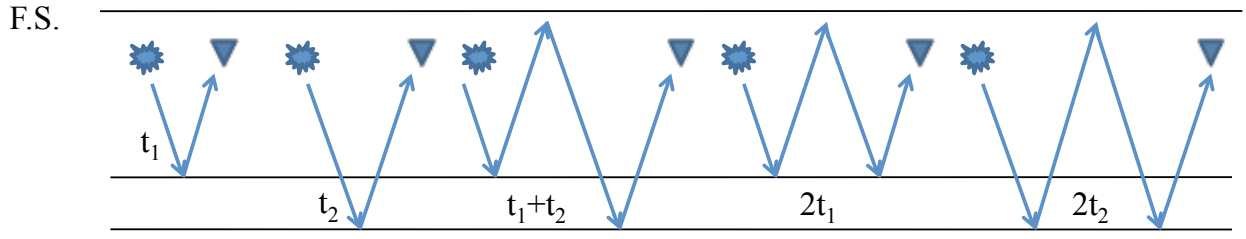

Figure 1: A two-reflector model with a free surface.

In the temporal frequency domain, the data are

$$R_{FS}(\omega) = R_1 e^{i\omega t_1} + R_2' e^{i\omega t_2} - R_1^2 e^{i\omega 2t_1} - R_2'^2 e^{i\omega 2t_2} - 2R_1 R_2' e^{i\omega(t_1+t_2)} + R_1^3 e^{i\omega 3t_1} + R_2'^3 e^{i\omega 3t_2} + 3R_1^2 R_2' e^{i\omega(2t_1+t_2)} + 3R_1 R_2'^2 e^{i\omega(t_1+2t_2)} + \cdots . \quad (2.5)$$

The first- and second-order free-surface-multiple predictions in equation 2.3 are

$$R_{FS}^2(\omega) = R_1^2 e^{i\omega 2t_1} + R_2'^2 e^{i\omega 2t_2} + 2R_1 R_2' e^{i\omega(t_1+t_2)} - 6R_1 R_2'^2 e^{i\omega(t_1+2t_2)} - 6R_1^2 R_2' e^{i\omega(2t_1+t_2)} - 2R_1^3 e^{i\omega 3t_1} - 2R_2'^3 e^{i\omega 3t_2} + \cdots , \quad (2.6)$$

and

$$R_{FS}^3(\omega) = R_1^3 e^{i\omega 3t_1} + R_2'^3 e^{i\omega 3t_2} + 3R_1 R_2'^2 e^{i\omega(t_1+2t_2)} + 3R_1^2 R_2' e^{i\omega(2t_1+t_2)} + \cdots , \quad (2.7)$$

respectively.

From equation 2.6, we can conclude that (Weglein et al., 2003) when $R_{FS}^2(\omega)$ is added to $R_{FS}(\omega)$, two things happen: (1) The first-order free-surface multiples are eliminated (blue terms in equations 2.5 and 2.6 cancel each other) and (2) Higher-order free-surface multiples are altered. Together with $R_{FS}^3(\omega)$, second-order free-surface multiples are eliminated (red terms in equations 2.5, 2.6 and 2.7 cancel each other) as shown in equation 2.8.

$$\begin{aligned} R_{FS}(\omega): &\quad 1 \times [R_1^3 e^{i\omega 3t_1} + R_2'^3 e^{i\omega 3t_2} + 3R_1^2 R_2' e^{i\omega(2t_1+t_2)} + 3R_1 R_2'^2 e^{i\omega(t_1+2t_2)}] \\ R_{FS}^2(\omega): &\quad -2 \times [R_1^3 e^{i\omega 3t_1} + R_2'^3 e^{i\omega 3t_2} + 3R_1^2 R_2' e^{i\omega(2t_1+t_2)} + 3R_1 R_2'^2 e^{i\omega(t_1+2t_2)}] \\ R_{FS}^3(\omega): &\quad 1 \times [R_1^3 e^{i\omega 3t_1} + R_2'^3 e^{i\omega 3t_2} + 3R_1 R_2'^2 e^{i\omega(t_1+2t_2)} + 3R_1^2 R_2' e^{i\omega(2t_1+t_2)}] \end{aligned} \quad (2.8)$$

The alteration in $R_{FS}^2(\omega)$ prepares for the elimination of second-order free-surface multiples using $R_{FS}^3(\omega)$. Hence, strictly speaking, $R_{FS}^2(\omega)$ is not just a first-order free-surface-multiple predictor. Also we can infer that $R_{FS}^3(\omega)$ is not just a second-order free-surface-multiple predictor.

To explicitly show the roles of lower-order free-surface multiples as input for removing higher-order free-surface multiples, we further categorize the results as follows. Consider the input data containing primary and free-surface multiples, i.e.,

$$R_{FS}(\omega) = P + F,$$

where P and F stand for primaries and free-surface multiples, respectively.

Therefore, $R_{FS}^2(\omega)$ can be expressed as

$$R_{FS}^2(\omega) = (P+F)^2 = PP + PF + FP + FF.$$

Under this categorization, the blue and red terms in equation 2.6 come from combinations of PP and PF (or FP) terms, respectively.

Together with the 1D analytic example, we conclude that the PP combination in $R_{FS}^2(\omega)$ is used to eliminate first-order free-surface multiples, whereas the PF (or FP) combination in $R_{FS}^2(\omega)$ is used

to alter second-order free-surface multiples. In other words, the inclusion of lower-order free-surface multiples into the input data is *necessary* for the prediction and removal of higher-order free-surface multiples.

In this section, we use a 1D analytic example to exemplify the necessity of including lower-order free-surface multiples in the input data for removing higher-order free-surface multiples. Within the analytic example, the ISS free-surface subseries demonstrates the collaborative nature among the different terms in collectively fulfilling a task. It is interesting that the ISS free-surface-multiple removal anticipates that there are both primaries and free-surface multiples as input and uses both of them to achieve that task. In the next section, we will use a two-reflector example to discuss an analogous feature in an internal-multiple-attenuation case, and we will analyze the difference between these two cases.

3 1D analytic example – Internal-multiple prediction in a two-reflector example

The current leading-order internal-multiple-attenuation algorithm starts with the input data, $D(k_g, k_s, \omega)$, in 2D, which is the Fourier transform of the deghosted prestack data with the wavelet deconvolved and the free-surface multiples removed. In a 2D earth, the leading-order prediction of the first-order internal multiples is

$$\begin{aligned} b_3(k_g, k_s, \omega) = \frac{1}{(2\pi)^2} \int_{-\infty}^{\infty} dk_1 \int_{-\infty}^{\infty} dk_2 e^{-iq_1(z_g - z_s)} e^{iq_2(z_g - z_s)} \\ \times \int_{-\infty}^{\infty} dz_1 b_1(k_g, k_1, z_1) e^{i(q_g + q_1)z_1} \\ \times \int_{-\infty}^{z_1 - \epsilon} dz_2 b_1(k_1, k_2, z_2) e^{-i(q_1 + q_2)z_2} \\ \times \int_{z_2 + \epsilon}^{\infty} dz_3 b_1(k_2, k_s, z_3) e^{i(q_2 + q_s)z_3}, \end{aligned} \tag{3.1}$$

where ω is temporal frequency; k_s and k_g are the horizontal wavenumbers for the source and receiver coordinates, respectively; q_g and q_s are the vertical source and receiver wavenumbers defined by $q_i = sgn(\omega)\sqrt{\frac{\omega^2}{c_0^2} - k_i^2}$ for $i \in \{g, s\}$; z_s and z_g are source and receiver depths; and z_j ($i \in \{1, 2, 3\}$) represents pseudo-depth using a reference velocity migration. The quantity $b_1(k_g, k_s, z)$ corresponds to an uncollapsed migration (Weglein et al., 1997) of effective plane-wave incident data, and $b_1(k_g, k_s, q_g + q_s) = -2iq_s D(k_g, k_s, \omega)$.

For a 1D earth and a normal incident plane wave, equation 3.1 reduces to

$$b_3(k) = \int_{-\infty}^{\infty} dz_1 e^{ikz_1} b_1(z_1) \int_{-\infty}^{z_1 - \epsilon} dz_2 e^{-ikz_2} b_1(z_2) \int_{z_2 + \epsilon}^{\infty} dz_3 e^{ikz_3} b_1(z_3). \tag{3.2}$$

First, we examine a two-reflector example (Figure 2). The reflection data due to an impulsive incident wave are

$$D(t) = R_1\delta(t-t_1) + R_2'\delta(t-t_2) + R_4'\delta(t-(2t_2-t_1)) + \cdots, \tag{3.3}$$

where $R_2' = T_{01}R_2T_{10}$, and $R_4' = T_{01}R_2(-R_1)R_2T_{10}$. Note that in order to show the analogous feature, we include a first-order internal-multiple in the data.

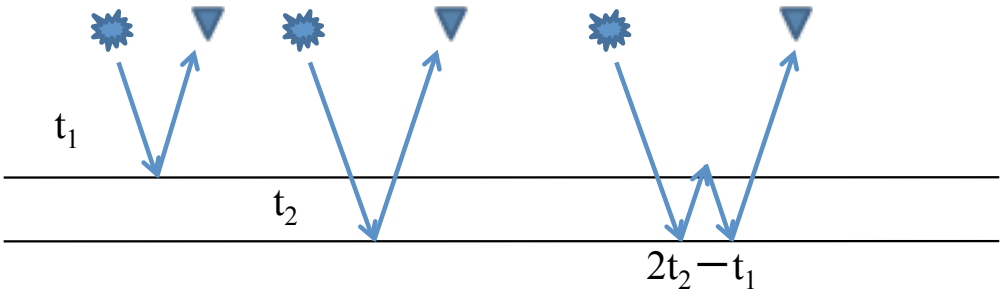

Figure 2: A two-reflector example with data containing two primaries and one first-order internal multiple.

A temporal Fourier transform of $D(t)$ gives the data in the frequency domain,

$$D(\omega) = R_1e^{i\omega t_1} + R_2'e^{i\omega t_2} + R_4'e^{i\omega(2t_2-t_1)} + \cdots. \tag{3.4}$$

For a 1D medium and a normal incident wave, $D(\omega) = b_1(k_z)$ and the vertical wave number is $k_z = \frac{2\omega}{c_0}$. Then, the reflection data can be expressed in terms of k_z,

$$b(k_z) = R_1exp[i(\frac{2\omega}{c_0})(\frac{c_0t_1}{2})] + R_2'exp[i(\frac{2\omega}{c_0})(\frac{c_0t_2}{2})] + R_4'exp[i(\frac{2\omega}{c_0})(\frac{c_0(2t_2-t_1)}{2})] + \cdots. \tag{3.5}$$

Define the pseudo-depths z_1 and z_2 in the reference medium as $z_1 \equiv \frac{c_0t_1}{2}$ and $z_2 \equiv \frac{c_0t_2}{2}$, respectively. Rewrite the data as,

$$b(k) = R_1e^{ik_zz_1} + R_2'e^{ik_zz_2} + R_4'e^{ik_z(2z_2-z_1)} + \cdots. \tag{3.6}$$

After performing the Inverse Fourier transform from k_z to z, $b(z) = \int_{-\infty}^{\infty} e^{-ik_zz}b(k_z)dz$, substituting the data into the algorithm 3.2, and Fourier transforming back to the time domain, we have

$$\begin{aligned} D_3(t) =& R_1R_2'^2\delta(t-(2t_2-t_1)) + 2R_1R_2'R_4'\delta(t-(3t_2-2t_1)) \\ &+ R_2'R_4'^2\delta(t-(3t_3-2t_2)) + R_1R_4'^2\delta(t-(4t_2-3t_1)). \end{aligned} \tag{3.7}$$

Equation 3.7 shows that the leading-order prediction of the first-order internal multiples includes (1) the first-order internal multiples (blue term) and (2) higher-order internal multiples (red terms). This is analogous to the free-surface case; see equation 2.6.

Also, to categorize the result, consider the input data containing primary and internal multiples, i.e.,

$$b_1 = P + I,$$

where P and I stand for primaries and internal multiples, respectively. The leading-order prediction of first-order internal multiples is

$$\begin{aligned} b_3 =& b_1 * b_1 * b_1 \\ =& (P+I)(P+I)(P+I) \\ =& PPP + PPI + PIP + IPP + PII + IPI + IIP + III \end{aligned} \tag{3.8}$$

Further analysis shows that the prediction of first-order internal multiples (blue term in equation 3.7) results from PPP combinations and prediction of all other higher-order internal multiples (red terms in equation 3.7) results from PPI (or IPP or IPI) combinations.

To summarize analogous points in the free-surface multiple and internal multiple cases: (1) both first-order and higher-order multiples are predicted in $R^2_{FS}(\omega)$ (or b_3); and (2) higher-order multiples are predicted because of the lower-order multiples in the input data acting as subevents.

3.1 Higher-order internal-multiples predicted in b_3

In section 2, it was shown that the second-order free-surface multiples predicted by $R^2_{FS}(\omega)$ are used to eliminate the second-order free-surface multiple, together with $R^3_{FS}(\omega)$. A question is whether the higher-order internal-multiples predicted in b_3 will play the same (or at lease an analogous) role in removing higher-order internal multiples

In order to answer that question, we first examine the prediction of a second-order internal-multiple attenuator (Araújo, 1994), i.e.,

$$\begin{aligned} b_5(k) = & \int_{-\infty}^{\infty} dz_1 e^{ikz_1} b_1(z_1) \int_{-\infty}^{z_1-\epsilon} dz_2 e^{-ikz_2} b_1(z_2) \int_{z_2+\epsilon}^{\infty} dz_3 e^{ikz_3} b_1(z_3) \\ & \times \int_{-\infty}^{z_3-\epsilon} dz_4 e^{ikz_4} b_1(z_4) \int_{z_4+\epsilon}^{\infty} dz_5 e^{-ikz_5} b_1(z_5). \end{aligned} \tag{3.9}$$

Given equation 3.9, the second-order internal-multiple prediction using the same input data (equation 3.3) is

$$D_5(t) = R'^3_2 R^2_1 \delta(t - (3t_2 - t_1)) + \cdots = T^3_{01} T^3_{10} R^3_2 R^1_1 \delta(t - (3t_2 - 2t_1)) + \cdots . \tag{3.10}$$

This is the prediction of the second-order internal-multiple. The corresponding real second-order internal multiple is $T_{01}T_{10}R^3_2 R^1_1 \delta(t - (3t_2 - 2t_1))$. Hence, the real second-order internal multiple in the data $D(t)$, the second-order internal-multiple prediction in $D_3(t)$, and $D_5(t)$ are

$$D(t): \qquad 1 \times [T_{01}T_{10}R^3_2 R^2_1 \delta(t - (3t_2 - 2t_1))]$$

$$
\begin{aligned}
D_3(t): &\quad (-2T_{01}T_{10} + (T_{01}T_{10}R_1)^2) \times [T_{01}T_{10}R_2^3R_1^2\delta(t-(3t_2-2t_1))] \\
D_5(t): &\quad (T_{01}T_{10})^2 \times [T_{01}T_{10}R_2^3R_1^2\delta(t-(3t_2-2t_1))] \qquad (3.11)
\end{aligned}
$$

Comparing equations 2.8 and 3.11, we find analogous roles of the higher-order internal-multiple prediction in $D_3(t)$. Taking $D_3(t)$ into consideration, it is easy to explain why the second-order internal-multiple attenuator $D_5(t)$ actually *increases*, rather than *attenuates*, the amplitude of the second-order internal-multiple. Recall that the second-order internal multiple in $D_3(t)$ is predicted because of lower-order internal multiples in the input data.

Therefore, besides the two points mentioned above, another related point is that (3) the ISS internal-multiple-attenuation algorithm also anticipates that there are both primaries and internal multiples as input, and it uses both to attenuate the higher-order internal-multiples.

3.2 b_3 – the first-order internal-multiple *attenuator*

However, unlike $R_{FS}^2(\omega)$ in free-surface case, b_3 predicts *approximated* amplitude of the first-order internal multiples. The leading-order algorithm means that b_3 *begins* the removal of the first-order internal multiples.

The reason that b_3 is only an attenuator is that there is no a priori information in the internal-multiple-attenuation algorithm, whereas there is a priori information in the free-surface-elimination algorithm.

Without a strictly mathematical proof, we can explain that difference as follows. First, both the ISS free-surface-multiple and internal-multiple predictions uses subevents to predict multiples; see Figure 3. Next, imagine that we move the internal-multiple generator (a) up until it coincides with the free-surface. Then the middle subevent is characterized by -1 and there will be no extra two-transmission coefficients, such as $T_{01}T_{10}$; the internal-multiple prediction reduces to free-surface-multiple prediction.

It is the fact that the internal-multiple-attenuation algorithm does not assume the location of the downward reflection that allows the algorithm to predict *all possible* first-order internal multiples at *all depths* at *once*.

In Ramírez and Weglein (2005) and Ramirez (2007), a sub-series is developed to completely eliminate first-order internal-multiples generated at the shallowest reflector. wilberth and zou.

4 1D analytic example – Internal-multiple prediction in a three-reflector example

In the last section, we uses a two-reflector example to analytically analyze the prediction of the leading-order internal-multiple-attenuation algorithm when the input data contain two primaries and one internal-multiple, and to find analogies and differences compared with the free-surface case.

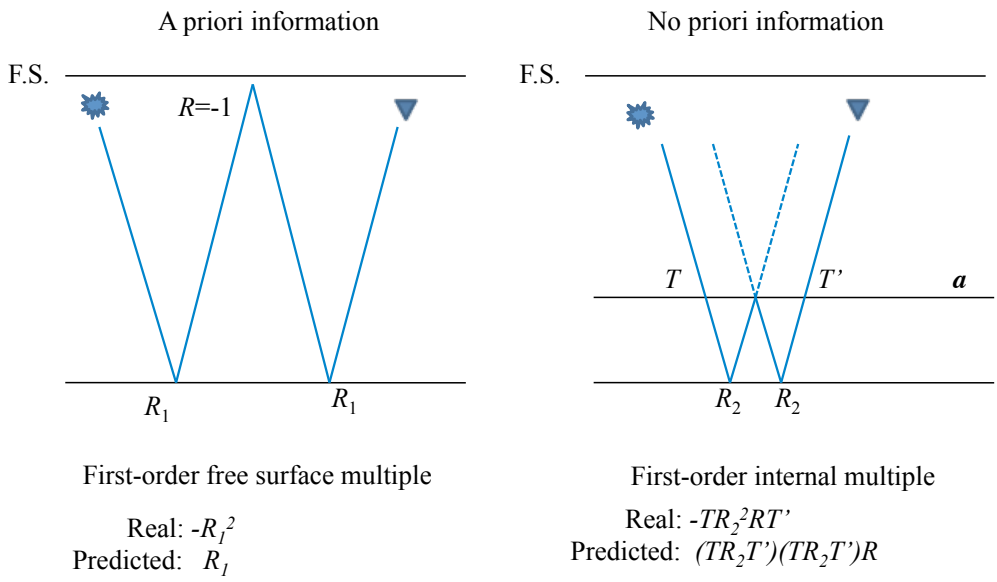

Figure 3: Comparison between free-surface-multiple prediction and internal-multiple prediction

In this section, we proceed to examination of a more complicated three-reflector example. In this example, we include one more primary from the third reflector in the input data and assume that the travel time of the third primary is larger than that of the first-order internal-multiple generated by the first two reflectors, i.e., $(2t_2 - t_1 < t_3)$; see Figure 4.

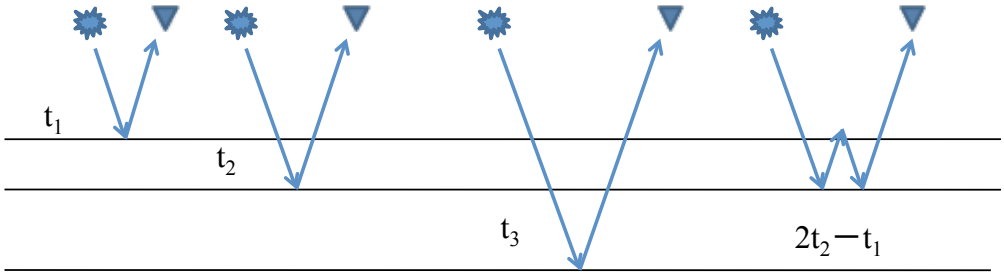

Figure 4: A three-reflector model with three primaries and one internal multiple.

The input data due to an impulsive incident wave are

$$D(t) = R_1\delta(t - t_1) + R_2'\delta(t - t_2) + R_4'\delta(t - (2t_2 - t_1)) + R_3'\delta(t - t_3) + \cdots, \tag{4.1}$$

where R_2' and R_4' are the same as in equation 3.3, and $R_3' = T_{01}R_2(-R_1)R_2T_{10}$ is the amplitude of the third primary.

Given these data, following the same procedure from equation 3.3 to equation 3.7, the leading-order

prediction (equation 3.2) is:

$$\begin{aligned} D_3(t) =& R_1(R_2')^2\delta(t-(2t_2-t_1)) + 2R_1R_2'R_3'\delta(t-(t_2+t_3-t_1)) \\ &+R_1(R_3')^2\delta(t-(2t_3-t_1)) + R_2(R_3')^2\delta(t-(2t_3-t_2)) \\ &+2R_1R_2'R_4'\delta(t-(3t_3-2t_1)) + R_2'(R_4')^2\delta(t-(3t_3-2t_2)) \\ &+2R_1R_3'R_4'\delta(t-(t_3+2t_2-2t_1)) + R_1(R_4')^2\delta(t-(4t_2-3t_1)) \\ &+2R_2'R_3'R_4'\delta(t-(t_3+t_2-t_1)) + (R_3')^2R_4'\delta(t-(2t_3-(2t_2-t_1))). \end{aligned} \tag{4.2}$$

Similarly to equation 3.7, equation 4.2 predicts first-order internal multiples (blue terms) and alters the amplitude of higher-order internal multiples (red terms). However, the last term is not either a primary nor an internal multiple. We name this event a spurious event. Further examination shows that this spurious event results from the PIP combination (Ma et al., 2011).

Besides a spurious prediction from PIP in a three-reflector model, Liang et al. (2011) shows that when there are more than three reflectors, PPI can generate a spurious prediction.

Hence, the effects of internal multiples being part of input (*i.e.*, combinations besides PPP in equation 3.8) include (1) helping to remove higher-order internal multiples, and (2) generating a spurious prediction when certain conditions are satisfied.

In the same way that there must be a reason for the prediction of higher-order internal multiples in b_3(*i.e.*, that it can be used to remove higher-order internal multiples, as shown in the last section), there must be a reason for the prediction of spurious events. The fact that there are no real events to correspond with these spurious events makes us believe there must be new terms in this series that can be located to cancel such spurious events.

In Ma et al. (2011) and Liang et al. (2011), new higher-order terms from the ISS are found to address the issue of the spurious events,

$$b_5^{PIP} = \int_{-\infty}^{\infty} dz_1 e^{ikz_1} b_1(z_1) \int_{-\infty}^{z_1-\epsilon} dz_2 e^{-ikz_2} b_3(z_2) \int_{z_2+\epsilon}^{\infty} dz_3 e^{ikz_3} b_1(z_3), \tag{4.3}$$

$$b_5^{PPI} = \int_{-\infty}^{\infty} dz_1 e^{ikz_1} b_1(z_1) \int_{-\infty}^{z_1-\epsilon} dz_2 e^{-ikz_2} b_1(z_2) \int_{z_2+\epsilon}^{\infty} dz_3 e^{ikz_3} b_3(z_3). \tag{4.4}$$

where $b_1(z)$ is an uncollapsed migration and $b_3(z)$ is the first-order attenuator. In appendix B, we give an argument for choosing $(G_0^d V_1' G_0^d V_3' G_0^d V_1' G_0^d)_m$ to derive b_5^{PIP}.

Compared with the internal-multiple-removal case, the reason there are no spurious predictions in the free-surface multiple-removal case is that the downward reflection of free-surface multiples happens at the free-surface and it only involves phase addition to prediction free-surface multiples.

5 Tests for the modification of leading-order internal-multiple attenuation algorithm

In the previous section, we showed that in the cases where there are three or more reflectors, the current leading-order internal-multiple-attenuation algorithm can produce spurious predictions. Specifically, the spurious prediction can be produced by a "Primary–Internal-multiple–Primary(PIP)"or a "Primary–Primary–Internal-multiple(PPI)"combination. Therefore, it is straightforward to conclude that when the amplitude of an internal-multiple is comparable to the amplitude of a primary, the spurious predictions are significant and need to be removed. This is the cases where the reservoirs are deep with more complex overburdens. Also, in the Middle East and eastern Canada, there are many strong near-surface internal-multiple generators, and it is necessary to include the higher-order terms to deal with spurious predictions. In this section, we use a three-reflector model

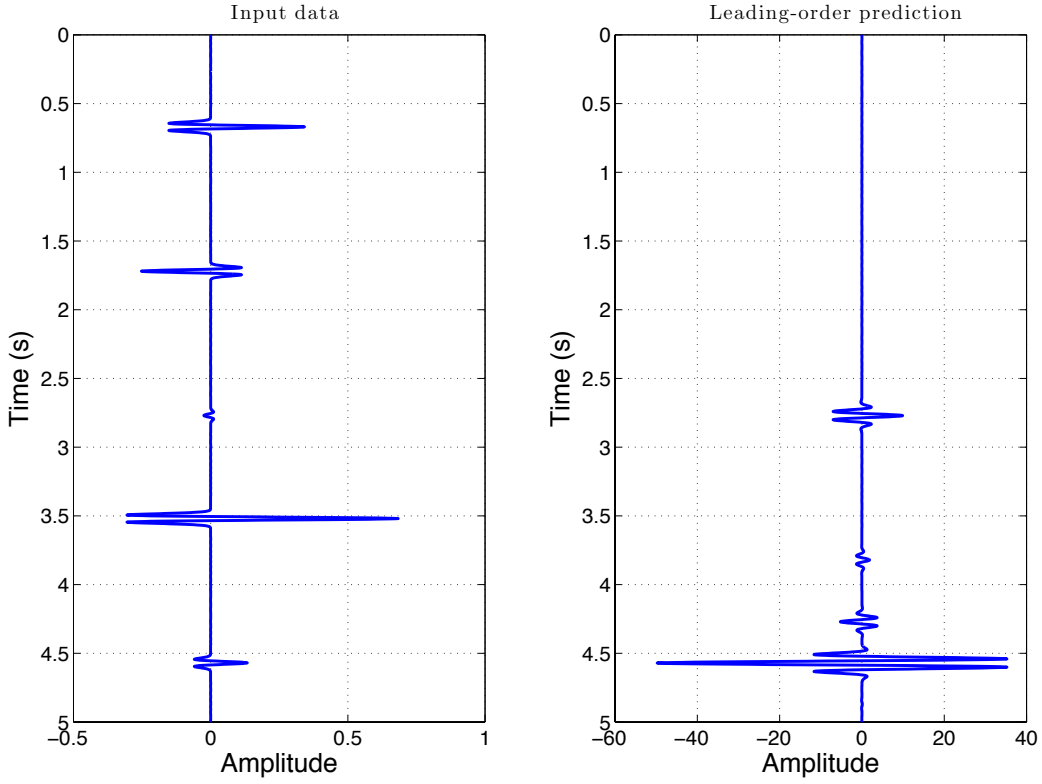

Figure 5: Input data (left) and leading-order prediction—b_3 (right).

with a strong internal multiple to test the higher-order term (equation 4.3). The parameters of this model are

$$V_1 = 1500m/s, \rho_1 = 1.0g/cm^3, d_1 = 500m;$$
$$V_2 = 1700m/s, \rho_2 = 1.8g/cm^3, d_2 = 900m;$$
$$V_3 = 1700m/s, \rho_3 = 1.1g/cm^3, d_3 = 1530m;$$
$$V_4 = 5000m/s, \rho_4 = 4.0g/cm^3.$$

The data are generated by convolving the reflectivity with a Ricker wavelet (peak frequency at 15 Hz); see Figure 5. The five events from top to bottom shown in data are P_1, P_2, I_{212}, P_3, and I_{312}, respectively. The subscripts indicate the reflection location of the primary or internal multiples.

Using these input data, the output of equation 3.2 is shown on the right half of Figure 5. The four events from top to bottom are I_{212}, I_{21212}, spurious event, and I_{312}, respectively. Notice the second-order internal multiple I_{21212} is not shown in the original input data.

The right half of Figure 6 shows the prediction of the introduced higher-order term; an event is predicted in order to address the spurious prediction. Notice that the polarity of this event is opposite of the polarity of the spurious event in b_3. However, the amplitude of the event shown in the right half of Figure 6 is much bigger than the spurious event shown in the left half of Figure 6, due to the wavelet issue. As the ISS internal-multiple attenuation algorithm required, the input data should first be deconvolved. More details are in hong,jinglong.

6 Conclusions

We analyze the one-dimensional prediction of the ISS leading-order internal-multiple-attenuation algorithm in both two reflector and three-reflector models. We found and analyzed the similarities and differences between the effects of including free-surface multiples as part of input data in a free-surface multiple removal algorithm and the effects of including internal multiples as part of input data in a leading-order internal-multiple-attenuation algorithm. These similarities and differences demonstrate that the limitation of current leading-order algorithm is fully anticipated and those limitations are resolvable by inverse series. We also provide detailed derivation of locating specific higher-order term to address that spurious prediction.

7 Acknowledgements

We are grateful to all M-OSRP sponsors for their long-term encouragement and support in this research. Special thanks to Hong Liang and Yanglei Zou for reviewing this report.

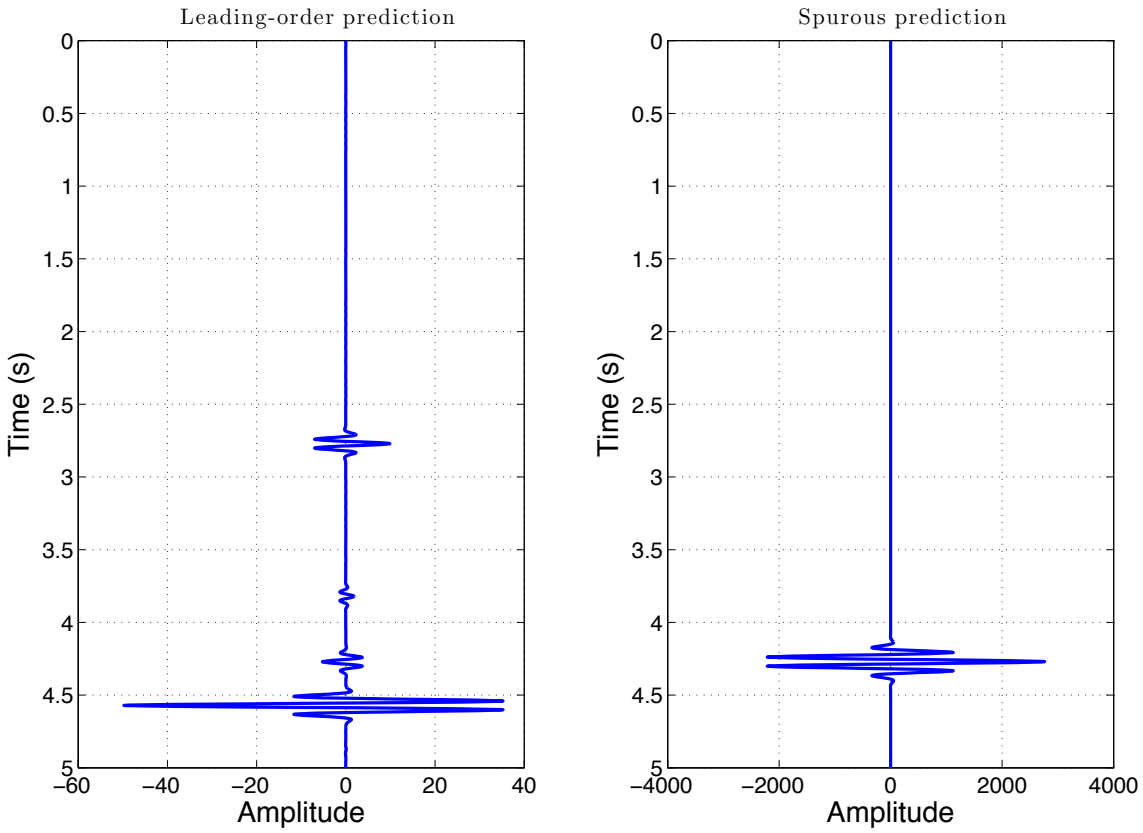

Figure 6: Leading-order prediction—b_3 (left) and higher-order modification—b_5^{PIP} (right)

Appendix A

In Ma et al. (2011), we stated that the higher-order terms addressing spurious prediction can be derived from a portion of a fifth-order term in the inverse series; see equation .1. In this appendix, we give an argument on why other portions of the fifth-order term cannot be employed for that purpose.

$$\begin{aligned}(G_0^d V_5' G_0^d)_m = &- (G_0^d V_1' G_0^d V_1' G_0^d V_1' G_0^d V_1' G_0^d V_1' G_0^d)_m - (G_0^d V_2' G_0^d V_1' G_0^d V_1' G_0^d V_1' G_0^d)_m \\ &- (G_0^d V_1' G_0^d V_2' G_0^d V_1' G_0^d V_1' G_0^d)_m - (G_0^d V_1' G_0^d V_1' G_0^d V_2' G_0^d V_1' G_0^d)_m \\ &- (G_0^d V_1' G_0^d V_1' G_0^d V_1' G_0^d V_2' G_0^d)_m - (G_0^d V_1' G_0^d V_3' G_0^d V_1' G_0^d)_m - (G_0^d V_1' G_0^d V_1' G_0^d V_3' G_0^d)_m \\ &- (G_0^d V_4' G_0^d V_1' G_0^d)_m - (G_0^d V_1' G_0^d V_4' G_0^d)_m.\end{aligned} \tag{.1}$$

First, we show that there are differences between different terms in equation .1; i.e., there exists no reduction in type III terms. To prove that, we first review the reduction case in type I terms.

- Type I

- Begin with equation (11′) in Weglein et al. (2003):

$$D_1' = (G_0^d V_1 G_0^d)_m, \tag{.2}$$

which is

$$\begin{aligned}D(x_g, z_g, x_s, z_s, \omega) = &\int_{-\infty}^{\infty} dx' \int_{-\infty}^{\infty} dz' \int_{-\infty}^{\infty} dx'' \int_{-\infty}^{\infty} dz'' \\ &\times G_0^d(x_g, z_g, x', z', \omega) V_1(x', z', x'', z'', \omega) G_0^d(x'', z'', x_s, z_s, \omega).\end{aligned} \tag{.3}$$

For the marine case, by first substituting the bilinear form of reference G_0^d (DeSanto, 1992)

$$G_0^d(x_g, z_g, x', z', \omega) = \int_{-\infty}^{\infty} dk_x' \int_{-\infty}^{\infty} dk_z' \frac{e^{ik_x'(x_g - x')} e^{ik_z'(z_g - z')}}{-k_x'^2 - k_z'^2 + k^2} \tag{.4}$$

and

$$G_0^d(x'', z'', x_s, z_s, \omega) = \int_{-\infty}^{\infty} dk_x'' \int_{-\infty}^{\infty} dk_z'' \frac{e^{ik_x''(x'' - x_s)} e^{ik_z''(z'' - z_s)}}{-k_x''^2 - k_z''^2 + k^2} \tag{.5}$$

into equation .3, and then Fourier transforming on both sides of the resulting equation on x_g and x_s, the RHS becomes

$$\begin{aligned}RHS = &\int_{-\infty}^{\infty} dx' \int_{-\infty}^{\infty} dz' \int_{-\infty}^{\infty} dx'' \int_{-\infty}^{\infty} dz'' \int_{-\infty}^{\infty} dx_g e^{-ik_g x_g} \int_{-\infty}^{\infty} dx_s e^{ik_s x_s} \\ &\times \int_{-\infty}^{\infty} dk_x' \int_{-\infty}^{\infty} dk_z' \frac{e^{ik_x'(x_g - x')} e^{ik_z'(z_g - z')}}{-k_x'^2 - k_z'^2 + k^2} V_1(x', z', x'', z'', \omega)\end{aligned} \tag{.6}$$

$$\times \int_{-\infty}^{\infty} dk_x'' \int_{-\infty}^{\infty} dk_z'' \frac{e^{ik_x''(x''-x_s)} e^{ik_z''(z''-z_s)}}{-k_x''^2 - k_z''^2 + k^2}.$$

Notice we use the convention mentioned on page R54 in Weglein et al. (2003), i.e.,

$$V_1(\mathbf{k}_1, -\mathbf{k}_2, \omega) = \int e^{-i\mathbf{k}_1 \cdot \mathbf{r}_1} V_1(\mathbf{r}_1, \mathbf{r}_2; \omega) e^{i\mathbf{k}_2 \cdot \mathbf{r}_2} d\mathbf{r}_1 d\mathbf{r}_2 \tag{.7}$$

where $\mathbf{k}_1 \equiv (k_g, -q_g)$ and $\mathbf{k}_2 \equiv (k_s, q_s)$.

Combining the terms x_g and x_s in equation .6, we have

$$\begin{aligned}
RHS = & \int_{-\infty}^{\infty} dx' \int_{-\infty}^{\infty} dz' \int_{-\infty}^{\infty} dx'' \int_{-\infty}^{\infty} dz'' \int_{-\infty}^{\infty} dx_g e^{-i(k_g - k_x')x_g} \int_{-\infty}^{\infty} dx_s e^{-i(k_x'' - k_s)x_s} \\
& \times \int_{-\infty}^{\infty} dk_x' \int_{-\infty}^{\infty} dk_z' \frac{e^{-ik_x'x'} e^{ik_z'(z_g - z')}}{-k_x'^2 - k_z'^2 + k^2} V_1(x', z', x'', z'', \omega) \int_{-\infty}^{\infty} dk_x'' \int_{-\infty}^{\infty} dk_z'' \frac{e^{ik_x''x''} e^{ik_z''(z''-z_s)}}{-k_x''^2 - k_z''^2 + k^2} \\
= & \int_{-\infty}^{\infty} dx' \int_{-\infty}^{\infty} dz' \int_{-\infty}^{\infty} dx'' \int_{-\infty}^{\infty} dz'' \delta(k_x' - k_g) \delta(k_x'' - k_s) \\
& \times \int_{-\infty}^{\infty} dk_x' \int_{-\infty}^{\infty} dk_z' \frac{e^{-ik_x'x'} e^{ik_z'(z_g - z')}}{-k_x'^2 - k_z'^2 + k^2} V_1(x', z', x'', z'', \omega) \int_{-\infty}^{\infty} dk_x'' \int_{-\infty}^{\infty} dk_z'' \frac{e^{ik_x''x''} e^{ik_z''(z''-z_s)}}{-k_x''^2 - k_z''^2 + k^2} \\
= & \int_{-\infty}^{\infty} dx' \int_{-\infty}^{\infty} dz' \int_{-\infty}^{\infty} dx'' \int_{-\infty}^{\infty} dz'' \\
& \times \int_{-\infty}^{\infty} dk_z' \frac{e^{-ik_g x'} e^{ik_z'(z_g - z')}}{-k_g^2 - k_z'^2 + k^2} V_1(x', z', x'', z'', \omega) \int_{-\infty}^{\infty} dk_z'' \frac{e^{ik_s x''} e^{ik_z''(z''-z_s)}}{-k_s^2 - k_z''^2 + k^2}
\end{aligned} \tag{.8}$$

Introducing the definition: $-k_g^2 + k^2 \equiv q_g^2$ and $-k_s^2 + k^2 \equiv q_s^2$, the RHS becomes,

$$\begin{aligned}
RHS = & \int_{-\infty}^{\infty} dx' \int_{-\infty}^{\infty} dz' \int_{-\infty}^{\infty} dx'' \int_{-\infty}^{\infty} dz'' e^{-ik_g x'} e^{ik_s x''} \\
& \times \int_{-\infty}^{\infty} dk_z' \frac{e^{ik_z'(z_g - z')}}{-k_g^2 - k_z'^2 + k^2} V_1(x', z', x'', z'', \omega) \int_{-\infty}^{\infty} dk_z'' \frac{e^{ik_z''(z''-z_s)}}{-k_s^2 - k_z''^2 + k^2} \\
= & \int_{-\infty}^{\infty} dx' \int_{-\infty}^{\infty} dz' \int_{-\infty}^{\infty} dx'' \int_{-\infty}^{\infty} dz'' e^{-ik_g x'} e^{ik_s x''} \frac{e^{iq_g|z_g - z'|}}{2iq_g} V_1(x', z', x'', z'', \omega) \frac{e^{iq_s|z''-z_s|}}{2iq_s},
\end{aligned} \tag{.9}$$

where, in the last step, we use (see e.g., DeSanto (1992))

$$\int_{-\infty}^{\infty} dk_z' \frac{e^{ik_z'(z_g - z')}}{-k_g^2 - k_z'^2 + k^2} = \frac{e^{iq_g|z_g - z'|}}{2iq_g}, \tag{.10}$$

and similarly

$$\int_{-\infty}^{\infty} dk_z'' \frac{e^{ik_z''(z''-z_s)}}{-k_s^2 - k_z''^2 + k^2} = \frac{e^{iq_s|z''-z_s|}}{2iq_s}. \tag{.11}$$

Because the perturbation is below the measurement surface (*i.e.*, $z' > z_g$ and $z'' > z_s$), we can remove the absolute value as follows

$$RHS = \int_{-\infty}^{\infty} dx' \int_{-\infty}^{\infty} dz' \int_{-\infty}^{\infty} dx'' \int_{-\infty}^{\infty} dz'' e^{-ik_g x'} e^{ik_s x''} \frac{e^{iq_g(z'-z_g)}}{ig_g} V_1(x', z', x'', z'', \omega) \frac{e^{ig_s(z''-z_s)}}{iq_s} \tag{.12}$$

$$= \frac{e^{-ig_g z_g}}{iq_g} \frac{e^{-iq_s z_s}}{iq_s} V_1(k_g, -q_g, k_s, q_s, \omega).$$

Then, for the first-order term in type I, we have,

$$D(k_g, z_g, k_s, z_s, \omega) = \frac{e^{-ig_g z_g}}{2iq_g} \frac{e^{-iq_s z_s}}{2iq_s} V_1(k_g, -q_g, k_s, q_s, \omega). \tag{.13}$$

• Equation (12′) in Weglein et al. (2003) is

$$D_2' = (G_0^d V_2 G_0^d)_m = -(G_0^d V_1 G_0^{fs} V_1 G_0^d)_m. \tag{.14}$$

The RHS is

$$\begin{aligned} RHS = -\int_{-\infty}^{\infty} dx' \int_{-\infty}^{\infty} dz' \int_{-\infty}^{\infty} dx'' \int_{-\infty}^{\infty} dz'' \int_{-\infty}^{\infty} dx''' \int_{-\infty}^{\infty} dz''' \int_{-\infty}^{\infty} dx'''' \int_{-\infty}^{\infty} dz'''' \\ \times G_0^d(x_g, z_g, x', z', \omega) V_1(x', z', x'', z'', \omega) G_0^{fs}(x'', z'', x''', z''', \omega) \\ \times V_1(x''', z''', x'''', z'''', \omega) G_0^d(x'''', z'''', x_s, z_s, \omega). \end{aligned} \tag{.15}$$

Inserting the bilinear forms of G_0^d and G_0^{fs},

$$G_0^d(x_g, z_g, x', z', \omega) = \int_{-\infty}^{\infty} dk_x' \int_{-\infty}^{\infty} dk_z' \frac{e^{ik_x'(x_g - x')} e^{ik_z'(z_g - z')}}{-k_x'^2 - k_z'^2 + k^2}; \tag{.16}$$

$$G_0^{fs}(x'', z'', x''', z''', \omega) = \int_{-\infty}^{\infty} dk_x'' \int_{-\infty}^{\infty} dk_z'' \frac{e^{ik_x''(x'' - x''')} e^{ik_z''(z'' + z''')}}{-k_x''^2 - k_z''^2 + k^2}; \tag{.17}$$

$$G_0^d(x'''', z'''', x_s, z_s, \omega) = \int_{-\infty}^{\infty} dk_x'''' \int_{-\infty}^{\infty} dk_z'''' \frac{e^{ik_x''''(x'''' - x_s)} e^{ik_z''''(z'''' - z_s)}}{-k_x''''^2 - k_z''''^2 + k^2}, \tag{.18}$$

into the above equation and Fourier transform on x_g and x_s, gives

$$\begin{aligned} RHS = -\int_{-\infty}^{\infty} dx' \int_{-\infty}^{\infty} dz' \int_{-\infty}^{\infty} dx'' \int_{-\infty}^{\infty} dz'' \int_{-\infty}^{\infty} dx''' \int_{-\infty}^{\infty} dz''' \int_{-\infty}^{\infty} dx'''' \int_{-\infty}^{\infty} dz'''' \\ \times \int_{-\infty}^{\infty} dk_x' \int_{-\infty}^{\infty} dk_z' \frac{e^{ik_x'(x_g - x')} e^{ik_z'(z_g - z')}}{-k_x'^2 - k_z'^2 + k^2} V_1(x', z', x'', z'', \omega) \int_{-\infty}^{\infty} dk_x'' \int_{-\infty}^{\infty} dk_z'' \frac{e^{ik_x''(x'' - x''')} e^{ik_z''(z'' + z''')}}{-k_x''^2 - k_z''^2 + k^2} \\ \times V_1(x''', z''', x'''', z'''', \omega) \int_{-\infty}^{\infty} dk_x'''' \int_{-\infty}^{\infty} dk_z'''' \frac{e^{ik_x''''(x'''' - x_s)} e^{ik_z''''(z'''' - z_s)}}{-k_x''''^2 - k_z''''^2 + k^2} \int_{-\infty}^{\infty} dx_g e^{-ik_g x_g} \int_{-\infty}^{\infty} dx_s e^{ik_s x_s} \end{aligned} \tag{.19}$$

$$
\begin{aligned}
&= -\int_{-\infty}^{\infty} dx' \int_{-\infty}^{\infty} dz' \int_{-\infty}^{\infty} dx'' \int_{-\infty}^{\infty} dz'' \int_{-\infty}^{\infty} dx''' \int_{-\infty}^{\infty} dz''' \int_{-\infty}^{\infty} dx'''' \int_{-\infty}^{\infty} dz'''' \\
&\times \int_{-\infty}^{\infty} dk_z' \frac{e^{-ik_g x'} e^{ik_z'(z_g - z')}}{-k_g^2 - k_z'^2 + k^2} V_1(x', z', x'', z'', \omega) \int_{-\infty}^{\infty} dk_x'' \int_{-\infty}^{\infty} dk_z'' \frac{e^{ik_x''(x''-x''')} e^{ik_z''(z''+z''')}}{-k_x''^2 - k_z''^2 + k^2} \\
&\times V_1(x''', z''', x'''', z'''', \omega) \int_{-\infty}^{\infty} dk_z'''' \frac{e^{ik_s x''''} e^{ik_z''''(z''''-z_s)}}{-k_s^2 - k_z''''^2 + k^2} \\
&= -\int_{-\infty}^{\infty} dx' \int_{-\infty}^{\infty} dz' \int_{-\infty}^{\infty} dx'' \int_{-\infty}^{\infty} dz'' \int_{-\infty}^{\infty} dx''' \int_{-\infty}^{\infty} dz''' \int_{-\infty}^{\infty} dx'''' \int_{-\infty}^{\infty} dz'''' \\
&\times e^{-ik_g x'} \int_{-\infty}^{\infty} dk_z' \frac{e^{ik_z'(z_g - z')}}{-k_g^2 - k_z'^2 + k^2} V_1(x', z', x'', z'', \omega) \int_{-\infty}^{\infty} dk_x'' \int_{-\infty}^{\infty} dk_z'' \frac{e^{ik_x''(x''-x''')} e^{ik_z''(z''+z''')}}{-k_x''^2 - k_z''^2 + k^2} \\
&\times V_1(x''', z''', x'''', z'''', \omega) e^{ik_s x''''} \int_{-\infty}^{\infty} dk_z'''' \frac{e^{ik_z''''(z''''-z_s)}}{-k_s^2 - k_z''''^2 + k^2}
\end{aligned}
$$

Recalling the definitions of $-k_g^2 + k^2 = q_g^2$ and $-k_s^2 + k^2 = q_s^2$, we have

$$
\begin{aligned}
RHS = &-\int_{-\infty}^{\infty} dx' \int_{-\infty}^{\infty} dz' \int_{-\infty}^{\infty} dx'' \int_{-\infty}^{\infty} dz'' \int_{-\infty}^{\infty} dx''' \int_{-\infty}^{\infty} dz''' \int_{-\infty}^{\infty} dx'''' \int_{-\infty}^{\infty} dz'''' \\
&\times e^{-ik_g x'} \frac{e^{iq_g |z_g - z'|}}{2ig_g} V_1(x', z', x'', z'', \omega) \int_{-\infty}^{\infty} dk_x'' \int_{-\infty}^{\infty} dk_z'' \frac{e^{ik_x''(x''-x''')} e^{ik_z''(z''+z''')}}{-k_x''^2 - k_z''^2 + k^2} \\
&\times V_1(x''', z''', x'''', z'''', \omega) e^{ik_s x''''} \frac{e^{iq_s |z'''' - z_s|}}{2ig_s} \\
= &-\int_{-\infty}^{\infty} dx' \int_{-\infty}^{\infty} dz' \int_{-\infty}^{\infty} dx'' \int_{-\infty}^{\infty} dz'' \int_{-\infty}^{\infty} dx''' \int_{-\infty}^{\infty} dz''' \int_{-\infty}^{\infty} dx'''' \int_{-\infty}^{\infty} dz'''' \\
&\times e^{-ik_g x'} \frac{e^{iq_g (z' - z_g)}}{2ig_g} V_1(x', z', x'', z'', \omega) \int_{-\infty}^{\infty} dk_x'' \int_{-\infty}^{\infty} dk_z'' \frac{e^{ik_x''(x''-x''')} e^{ik_z''(z''+z''')}}{-k_x''^2 - k_z''^2 + k^2} \\
&\times V_1(x''', z''', x'''', z'''', \omega) e^{ik_s x''''} \frac{e^{iq_s (z'''' - z_s)}}{2ig_s}
\end{aligned} \tag{.20}
$$

Considering the integral on x', z', x'''', z'''' and x'', x''' as a Fourier transform based on the convention (equation .7), we have

$$
\begin{aligned}
RHS = &-\int_{-\infty}^{\infty} dx'' \int_{-\infty}^{\infty} dz'' \int_{-\infty}^{\infty} dx''' \int_{-\infty}^{\infty} dz''' \frac{e^{-iq_g z_g}}{2ig_g} V_1(k_g, -q_g, x'', z'', \omega) \\
&\times \int_{-\infty}^{\infty} dk_x'' \int_{-\infty}^{\infty} dk_z'' \frac{e^{ik_x''(x''-x''')} e^{ik_z''(z''+z''')}}{-k_x''^2 - k_z''^2 + k^2} V_1(x''', z''', k_s, q_s, \omega) \frac{e^{-iq_s z_s}}{2ig_s} \\
= &-\int_{-\infty}^{\infty} dz'' \int_{-\infty}^{\infty} dz''' \frac{e^{-iq_g z_g}}{2ig_g} V_1(k_g, -q_g, k_x'', z'', \omega) \\
&\times \int_{-\infty}^{\infty} dk_x'' \int_{-\infty}^{\infty} dk_z'' \frac{e^{ik_z''(z''+z''')}}{-k_x''^2 - k_z''^2 + k^2} V_1(k_x'', z''', k_s, q_s, \omega) \frac{e^{-iq_s z_s}}{2ig_s}
\end{aligned} \tag{.21}
$$

Similarly, defining $-k_x''^2 + k^2 \equiv q_x''^2$, we have

$$\begin{aligned} RHS = &- \int_{-\infty}^{\infty} dz'' \int_{-\infty}^{\infty} dz''' \frac{e^{-iq_g z_g}}{2ig_g} V_1(k_g, -q_g, k_x'', z'', \omega) \\ &\times \int_{-\infty}^{\infty} dk_x'' \frac{e^{iq_x''|z''+z'''|}}{-2ig_x''} V_1(k_x'', z''', k_s, q_s, \omega) \frac{e^{-iq_s z_s}}{2ig_s} \\ = &- \int_{-\infty}^{\infty} dz'' \int_{-\infty}^{\infty} dz''' \frac{e^{-iq_g z_g}}{2ig_g} V_1(k_g, -q_g, k_x'', z'', \omega) \\ &\times \int_{-\infty}^{\infty} dk_x'' \frac{e^{iq_x''(z''+z''')}}{2ig_x''} V_1(k_x'', z''', k_s, q_s, \omega) \frac{e^{-iq_s z_s}}{2ig_s} \\ = &- \frac{e^{-iq_g z_g}}{2ig_g} V_1(k_g, -q_g, k_x'', q_x'', \omega) \int_{-\infty}^{\infty} dk_x'' \frac{1}{2ig_x''} V_1(k_x'', -q_x'', k_s, q_s, \omega) \frac{e^{-iq_s z_s}}{2ig_s} \\ = &- \frac{e^{-iq_g z_g}}{2ig_g} \frac{e^{-iq_s z_s}}{2ig_s} \int_{-\infty}^{\infty} dk V_1(k_g, -q_g, k, q, \omega) \frac{1}{2ig} V_1(k, -q, k_s, q_s, \omega) \end{aligned} \tag{.22}$$

Notice that the + sign in $\frac{e^{iq_x''|z''+z'''|}}{-2ig_x''}$ enables us to remove the absolute value.

The LHS of equation .14 is

$$LHS = \frac{e^{-ig_g z_g}}{2iq_g} \frac{e^{-iq_s z_s}}{2iq_s} V_2(k_g, -q_g, k_s, q_s, \omega) \tag{.23}$$

Comparing equation .23 and equation .22, we have

$$V_2(k_g, -q_g, k_s, q_s, \omega) = - \int_{-\infty}^{\infty} dk V_1(k_g, -q_g, k, q, \omega) \frac{1}{2ig} V_1(k, -q, k_s, q_s, \omega) \tag{.24}$$

- Equation (13′) in Weglein et al. (2003)

$$\begin{aligned} D_3' = &- (G_0^d V_1 G_0^{fs} V_1 G_0^{fs} V_1 G_0^d)_m \\ &- (G_0^d V_1 G_0^{fs} V_2 G_0^d)_m \\ &- (G_0^d V_2 G_0^{fs} V_1 G_0^d)_m \\ = &+ (G_0^d V_1 G_0^{fs} V_1 G_0^{fs} V_1 G_0^d)_m \end{aligned} \tag{.25}$$

Following the procedures from equation .14 through equation .22, the first term in .25 becomes

$$- \int_{-\infty}^{\infty} dk V_1(k_g, -q_g, k, q, \omega) \frac{1}{2ig} \int_{-\infty}^{\infty} dk' V_1(k, -q, k', q', \omega) \frac{1}{2ig'} V_1(k', -q', k_s, q_s, \omega) \tag{.26}$$

and the second term becomes

$$- \int_{-\infty}^{\infty} dk V_1(k_g, -q_g, k, q, \omega) \frac{1}{2ig} V_2(k, -q, k_s, q_s, \omega) \tag{.27}$$

Substituting $V_2(k_g, -q_g, k, q, \omega)$ (equation .24) into equation .27, we have

$$\int_{-\infty}^{\infty} dk V_1(k_g, -q_g, k, q, \omega) \frac{1}{2ig} \int_{-\infty}^{\infty} dk' V_1(k, -q, k', q', \omega) \frac{1}{2ig'} V_1(k', -q', k_s, q_s, \omega) \qquad (.28)$$

Therefore, equation .28 cancels out equation .26, and a reduction occurs.

- Type II terms

- Equation (11″) in Weglein et al. (2003) is

$$D' = (G_0^d V_1' G_0^d)_m, \qquad (.29)$$

which is

$$D'(k_g, z_g, k_s, z_s, \omega) = \frac{e^{-ig_g z_g}}{2iq_g} \frac{e^{-iq_s z_s}}{2iq_s} V_1'(k_g, -q_g, k_s, q_s, \omega). \qquad (.30)$$

Notice the LHS of equation .30 and .13 are different: D_1' is data with the free-surface multiples and D' is data without free-surface multiples.

- Equation (12″) in Weglein et al. (2003) is

$$(G_0^d V_2' G_0^d)_m = -(G_0^d V_1' G_0^d V_1' G_0^d)_m. \qquad (.31)$$

We derive the RHS of equation .31 following the same produce as we derive the RHS of equation .14. The difference resides the middle reference Green's function. With the middle reference Green's function being G_0^d, instead of G_0^{fs}, we cannot lift the absolute value in equation .22 without specifying the relationship between z' and z''. In other words, without specifying the relationship between z' and z'', the RHS of equation .31 is not computable from our data on the measurement surface. Hence, each type III term is different and not reducible. The same argument explains the differences in higher-order terms in type III.

Appendix B

In appendix A, we show that each part in a type III term is different, therefore we need to choose which part of the fifth-order term can be used to address spurious predictions. In appendix B, we show what specific differences/characters between the different terms allow us to make that choice.

First, we examine the difference between the third-order terms, which is

$$(G_0^d V_3' G_0^d)_m = -(G_0^d V_1' G_0^d V_1' G_0^d V_1' G_0^d)_m - (G_0^d V_1' G_0^d V_2' G_0^d)_m - (G_0^d V_2' G_0^d V_1' G_0^d)_m. \qquad (.32)$$

The third-order terms can be written as (Araújo, 1994)

$$V'_{33} = -\frac{1}{(2\pi)^2}\int_{-\infty}^{\infty}\int_{-\infty}^{\infty} dk_1 dz_1 e^{iq_g z_1} V_1(k_g,-k_1,z_1)\int_{-\infty}^{\infty}\int_{-\infty}^{\infty} dk_2 dz_3 \frac{e^{iq_1|z_1-z_3|}}{-2iq_1} V_1(k_1,-k_2,z_3) \quad (.33)$$
$$\times \int_{-\infty}^{\infty} dz_5 \frac{e^{iq_2|z_3-z_5|}}{-2iq_2} V_1(k_2,-k_s,z_5) e^{iq_s z_5}$$

$$\begin{aligned}
V'_{33} =& \frac{1}{(2\pi)^2}\int_{-\infty}^{\infty}\int_{-\infty}^{\infty} \frac{dk_1 dk_2}{4q_1 q_2}\int_{-\infty}^{\infty} dz_1 e^{1(q_g-q_1)z_1} V_1(k_g,-k_1,z_1)\int_{z_1}^{\infty} dz_3 e^{i(q_1-q_2)z_3} V_1(k_1,-k_2,z_3)\\
&\times \int_{z_3}^{\infty} dz_5 e^{i(q_2+q_s)z_5} V_1(k_2,-k_s,z_5)\\
&+\frac{1}{(2\pi)^2}\int_{-\infty}^{\infty}\int_{-\infty}^{\infty} \frac{dk_1 dk_2}{4q_1 q_2}\int_{-\infty}^{\infty} dz_1 e^{1(q_g-q_1)z_1} V_1(k_g,-k_1,z_1)\int_{z_1}^{\infty} dz_3 e^{i(q_1+q_2)z_3} V_1(k_1,-k_2,z_3)\\
&\times \int_{-\infty}^{z_3} dz_5 e^{i(-q_2+q_s)z_5} V_1(k_2,-k_s,z_5)\\
&+\frac{1}{(2\pi)^2}\int_{-\infty}^{\infty}\int_{-\infty}^{\infty} \frac{dk_1 dk_2}{4q_1 q_2}\int_{-\infty}^{\infty} dz_1 e^{i(q_g+q_1)z_1} V_1(k_g,-k_1,z_1)\int_{-\infty}^{z_1} dz_3 e^{i(-q_1-q_2)z_3} V_1(k_1,-k_2,z_3)\\
&\times \int_{z_3}^{\infty} dz_5 e^{i(q_2+q_s)z_5} V_1(k_2,-k_s,z_5)\\
&+\frac{1}{(2\pi)^2}\int_{-\infty}^{\infty}\int_{-\infty}^{\infty} \frac{dk_1 dk_2}{4q_1 q_2}\int_{-\infty}^{\infty} dz_1 e^{1(q_g+q_1)z_1} V_1(k_g,-k_1,z_1)\int_{-\infty}^{z_1} dz_3 e^{i(-q_1+q_2)z_3} V_1(k_1,-k_2,z_3)\\
&\times \int_{-\infty}^{z_3} dz_5 e^{i(-q_2+q_s)z_5} V_1(k_2,-k_s,z_5)
\end{aligned}$$

The third part in the above separation is chosen for the attenuation of first-order internal multiples because the relation between z', z'' and z''' ($z' > z''; z'' < z'''$) resembles the "lower-higher-lower "configuration of the first-order internal-multiples. With the model-type independent argument, the on-shell projection of $\mathbf{V}'_1(\mathbf{k}_g, \mathbf{k}_s, \omega)$, which is directly computable from measured data, can be used for internal-multiple attenuation. The internal-multiple-attenuation algorithm is developed using the on-shell projection of $\mathbf{V}'_1(\mathbf{k}_g, \mathbf{k}_s, \omega)$,

$$\int_{-\infty}^{\infty}\int_{-\infty}^{\infty} dk_1 dk_2 V'_1(k_g,-k_1,q_g+q_1)\frac{1}{2q_1}V'_1(k_1,-k_2,-q_1-q_2)\frac{1}{2q_2}V'_1(k_2,-k_s,q_2+q_s) + \sum residues. \quad (.34)$$

For comparison, other separations of the third-order term have no such capability.

For the $(G_0^d V'_1 G_0^d V'_1 G_0^d V'_1 G_0^d V'_1 G_0^d V'_1 G_0^d)_m$, following the same procedure, we can have

$$\begin{aligned}
&\frac{1}{(2\pi)^4}\int_{-\infty}^{\infty}\int_{-\infty}^{\infty} dk_1 dz_1 e^{iq_g z_1} V'_1(k_g,k_1,z_1)\int_{-\infty}^{\infty} dk_2 dz_3 \frac{e^{iq_1|z_1-z_3|}}{-2iq_1} V'_1(k_1,-k_2,z_3)\\
&\quad\times \int_{-\infty}^{\infty} dz_3 dz_5 \frac{e^{iq_2|z_3-z_5|}}{-2iq_2} V'_1(k_2,-k_3,z_5)\int_{-\infty}^{\infty} dz_4 dz_7 \frac{e^{iq_3|z_5-z_7|}}{-2iq_3} V'_1(k_3,-k_4,z_7)
\end{aligned}$$

$$\times \int_{-\infty}^{\infty} dz_9 \frac{e^{iq_4|z_7-z_9|}}{-2iq_4} V_1'(k_4, -k_s, z_9)$$

Only the separation $z_1 > z_3$, $z_3 < z_5$, $z_5 > z_7$ and $z_7 < z_9$ gives

$$\int_{-\infty}^{\infty}\int_{-\infty}^{\infty}\int_{-\infty}^{\infty}\int_{-\infty}^{\infty} dk_1 dk_2 dk_3 dk_4 V_1'(k_g, -k_1, q_g+q_1)\frac{1}{2iq_1}V_1'(k_1, -k_2, -q_1-q_2) \tag{.35}$$
$$\times \frac{1}{2iq_2}V_1'(k_2, -k_3, q_2+q_3)\frac{1}{-2iq_3}V_1'(k_3, -k_4, -q_3-q_4)\frac{1}{2iq_4}V_1'(k_4, -k_s, q_4+q_s) + \sum residues.$$

Using that separation (*i.e.*, $z_1 > z_3$, $z_3 < z_5$, $z_5 > z_7$, and $z_7 < z_9$, which resemble the configuration of a second-order internal multiple) will predict second-order internal multiples, rather than the prediction of the negative spurious events.

For $(G_0^d V_1' G_0^d V_3' G_0^d V_1' G_0^d)_m$, we have,

$$-\frac{1}{(2\pi)^2}\int_{-\infty}^{\infty}\int_{-\infty}^{\infty} dk_1 dz_1 e^{iq_g z_1} V_1'(k_g, -k_1, z_1)\int_{-\infty}^{\infty}\int_{-\infty}^{\infty} dk_2 dz_3 \frac{e^{iq_1|z_1-z_3|}}{-2iq_1} \tag{.36}$$
$$\times V_3'(k_1, -k_2, z_3)\int_{-\infty}^{\infty} dz_5 \frac{e^{iq_2|z_3-z_5|}}{-2iq_2} V_1'(k_2, -k_s, z_5) e^{iq_s z_5}$$

Choosing $z_1 > z_3$ and $z_3 < z_5$, we have

$$\int_{-\infty}^{\infty}\int_{-\infty}^{\infty} dk_1 dk_2 V_1'(k_g, -k_1, q_g+q_1)\frac{1}{2q_1}V_3'(k_1, -k_2, -q_1-q_2)\frac{1}{2q_2}V_1'(k_2, -k_s, q_2+q_s) + \sum residues. \tag{.37}$$

where the outer two V_1 terms can be computed by the data, and the middle V_3 term can also be computed indirectly by computing predicted first-order internal multiples by using equation .34.

In equation .36, z_3 is the effective pseudo-depth of the predicted internal multiple (*i.e.*, $z_3 = z_1' - z_3' + z_5'$).

References

Araújo, F. V. Linear and non-linear methods derived from scattering theory: backscattered tomography and internal multiple attenuation. PhD thesis, Universidade Federal da Bahia, 1994.

Carvalho, P. M. Free-surface multiple reflection elimination method based on nonlinear inversion of seismic data. PhD thesis, Universidade Federal da Bahia, 1992.

DeSanto, J. A. Scalar Wave Theory: Green's Functions and Applications. Springer-Verlag, 1992.

Fu, Qiang., Yi Luo, Panos G. Kelamix, ShouDong Huo, Ghada Sindi, Shih-Ying Hsu, and Arthur B. Weglein. "The inverse scattering series approach towards the elimination of land internal multiples." SEG Expanded Abstracts (2010): 3456–3461.

Hsu, S., Paolo Terenghi, Panos G.Kelamis, Qiang Fu, ShouDong Huo, Ghada Sindi, and Arthur B. Weglein. "The properties of the inverse scattering series internal multiple attenuation algorithm: Analysis and evaluation on synthetic data with lateral variations, choosing reference velocity and examining its sensitivity to near surface properties." M-OSRP Annual Report (2011): 16–28.

Liang, H., C. Ma, and A.B. Weglein. "A further general modification of the leading order ISS attenuator of first order internal multiples to accommodate primaries and internal multiples when an arbitrary number of reflectors generate the data: theory, development, and examples." M-OSRP 2011 Annual Report (2011): 148–166.

Luo, Y., Panos G.Kelamis, Qiang Fu, ShouDong Huo, Ghada Sindi, Shih-Ying Hsu, and Arthur Weglein. "Elimination of land internal multiples based on the inverse scattering series." The Leading Edge (2011): 884–889.

Ma, C., H. Liang, and A.B. Weglein. "Modifying the leading order ISS attenuator of first-order internal multiples to accommodate primaries and internal multiples: fundamental concept and theory, development, and examples exemplified when three reflectors generate the data." M-OSRP 2011 Annual Report (2011): 133–147.

Maston, K., D.Corrigan, A.Weglein, C.Y.Young, and P.Carvalho. "Inverse Scattering Internal Multiple Attenuation: Results From Complex Synthetic And Field Data Examples." SEG Expanded Abstract (1999): 1060–1063.

Matson, K. H. An inverse-scattering series method for attenuating elastic multiples from multicomponent land and ocean bottom seismic data. PhD thesis, University of British Columbia, 1997.

Ramírez, A. C. and A.B. Weglein. "An inverse scattering internal multiple elimination method: Beyond attenuation, a new algorithm and initial tests." SEG Expanded Abstracts. (2005): 2115–2118.

Ramirez, A.R. I-Inverse scattering subseries for removol of internal multiples and depth imaging primaries;II-Green's theorem as the foundation of interferometry and guiding new practical methods and applications. PhD thesis, University of Houston, 2007.

Stolt, R. H. and B. Jacobs. "Inversion of seismic data in a laterally heterogeneous medium." Stanford Exploration Project 24 (1980).

Terenghi, Paolo, Shih-Ying Hsu, Arthur B.Weglein, and Xu Li. "Exemplifying the specific properties of the inverse scattering series internal-multiple attenuation method that reside behind its capability for complex onshore and marine multiples." The Leading Edge (2011): 876–882.

Weglein, A., Shih-Ying Hsu, Paolo Terenghi, Xu Li, and Robert H. Stolt. "Multiple attenuation: Recent advances and the road ahead (2011)." The Leading Edge (2011): 864–875.

Weglein, A. B., F. V. Araújo, P. M. Carvalho, R. H. Stolt, K. H. Matson, R. T. Coates, D. Corrigan, D. J. Foster, S. A. Shaw, and H. Zhang. "Inverse Scattering Series and Seismic Exploration." Inverse Problems (2003): R27–R83.

Weglein, A. B., W. E. Boyce, and J. E. Anderson. "Obtaining three-dimensional velocity information directly from reflection seismic data: An inverse scattering formalism." Geophysics 46 (1981): 1116–1120.

Weglein, A. B., F. A. Gasparotto, P. M. Carvalho, and R. H. Stolt. "An Inverse-Scattering Series Method for Attenuating Multiples in Seismic Reflection Data." Geophysics 62 (November-December 1997): 1975–1989.

Weglein, A.B. and W.H. Dragoset. Multiple Attenuation. Geophysics reprint series. Soc. Expl. Geophys., 2005.

Zhang, H. and S. Shaw. "1-D analytic analysis of higher order internal multiples predicted via the inverse scattering series based algorithem." SEG Expanded Abstracts 29 (2010): 3493–3498.

Source wavelet effects on the inverse scattering series internal-multiple leading-order-attenuation algorithm and its higher-order modification that accommodate issues that arise when treating internal multiples as subevents

H. Liang and A. Weglein, M-OSRP, University of Houston

April 29, 2013

Abstract

The inverse scattering series (ISS) internal-multiple-attenuation method predicts internal multiples directly and without any subsurface information. The ISS leading-order attenuator of first-order internal multiples is the leading-order term in the subseries that contributes to the removal of first-order internal multiples. The basic idea behind the leading-order attenuator is that all the events in the data are treated as subevents and combined nonlinearly (three data sets are involved), and among all the combinations first-order internal multiples can be predicted by the combination that has all subevents correspond to primaries. While the ISS leading-order attenuator has demonstrated its capability for internal-multiple prediction/attenuation, it has strengths and limitations as implied by "leading-order" and "attenuator". On one hand, the ISS internal-multiple leading-order attenuator predicts exact time and approximate amplitude, but it has specific prerequisites such as knowledge of the source wavelet, as well as source and receiver deghosting, and free-surface-multiple removal. The information omitted from any prerequisite is left for the adaptive subtraction technique to clean up. On the other hand, the entire data set, consisting of primaries and internal multiples, is input into the algorithm. When internal multiples in the data themselves act as subevents, the leading-order attenuator produces not only first-order internal multiples, but also higher-order internal multiples and, at times, spurious events, which have been observed in the tests of Fu et al. (2010) and Luo et al. (2011). Weglein et al. (2011) have also noted this and suggested that the resolution of the problem would reside in other terms of the ISS. Ma et al. (2012) and Liang et al. (2012) identified higher-order terms from the ISS that retain the benefits of the leading-order attenuator while addressing the issues due to spurious events. The higher-order terms require the leading-order term as an ingredient. This report specifically examines the effects of source wavelet on the ISS internal-multiple leading-order attenuator and its higher-order modification. By comparing the internal-multiple and spurious-event prediction results with and without source wavelet deconvolution, we show how the source wavelet affects the shape and amplitude fidelity of the prediction of internal multiples and spurious events.

1 The leading-order ISS internal-multiple-attenuation algorithm

The ISS internal-multiple-attenuation algorithm is a subseries of the inverse scattering series. The algorithm starts with the deghosted input data from which the reference wavefield and free-surface multiples have been removed and source wavelet has been deconvolved, $D(k_g, k_s, \omega)$, where k_g and k_s are the horizontal wavenumbers corresponding to receiver and source coordinates x_g and x_s, respectively, and ω is the temporal frequency.

$$D(k_g, k_s, \omega) = (-2iq_s)^{-1} b_1(k_g, k_s, \omega), \tag{1.1}$$

where $b_1(k_g, k_s, \omega)$ corresponds to an uncollapsed FK migration of effective normal incident spike plane-wave data (Weglein et al., 2003; Hsu et al., 2011). The second term in the algorithm is the leading-order attenuator of first-order internal multiples, which predicts the negative of first-order internal multiples and alters all higher-order internal multiples (the order of an internal multiple is defined by the total number of downward reflections). The leading-order attenuator in a 2D earth is given by Araújo et al. (1994) and Weglein et al. (1997)

$$\begin{aligned} b_3(k_g, k_s, q_g + q_s) = \frac{1}{(2\pi)^2} \int_{-\infty}^{\infty} \int_{-\infty}^{\infty} dk_1 e^{iq_1(z_s - z_g)} dk_2 e^{iq_2(z_g - z_s)} \\ \times \int_{-\infty}^{\infty} dz_1 e^{i(q_g + q_1)z_1} b_1(k_g, -k_1, z_1) \\ \times \int_{-\infty}^{z_1 - \epsilon} dz_2 e^{i(-q_1 - q_2)z_2} b_1(k_1, -k_2, z_2) \\ \times \int_{z_2 + \epsilon}^{\infty} dz_3 e^{i(q_2 + q_s)z_3} b_1(k_2, -k_s, z_3), \end{aligned} \tag{1.2}$$

where c_0 is the reference velocity, $q_g = sgn(\omega)\sqrt{(\frac{\omega}{c_0})^2 - k_g^2}$ and $q_s = sgn(\omega)\sqrt{(\frac{\omega}{c_0})^2 - k_s^2}$ are the vertical wavenumbers, ϵ is a small positive parameter chosen to ensure that the relations between pseudo-depths $z_1 > z_2$ and $z_3 > z_2$ are satisfied, and z_g and z_s are source and receiver depths, respectively.

For a 1D earth and a normal incidence, wave equation 1.2 reduces to

$$b_3(k) = b_3^{PPP} = \int_{-\infty}^{\infty} dz_1 e^{ikz_1} b_1(z_1) \int_{-\infty}^{z_1 - \epsilon} dz_2 e^{-ikz_2} b_1(z_2) \int_{z_2 + \epsilon}^{\infty} dz_3 e^{ikz_3} b_1(z_3), \tag{1.3}$$

where the deghosted data, $D(t)$, for an incident spike wave, satisfy $D(\omega) = b_1(2\omega/c_0)$, and where $b_1(z) = \int_{-\infty}^{\infty} e^{-ikz} b_1(k) dk$, and $k = 2\omega/c_0$ is the vertical wavenumber. Here, we introduce a new notation, b_3^{PPP}, in which the superscript ("P" represents primary, and "I" represents internal multiple) indicates specific events in the data that are input into each of the three integrals. The events indicated in this notation are the ones that the algorithm can accommodate in its goal of removing first-order internal multiples. The data with first-order internal multiples attenuated are

$$D(t) + D_3(t), \tag{1.4}$$

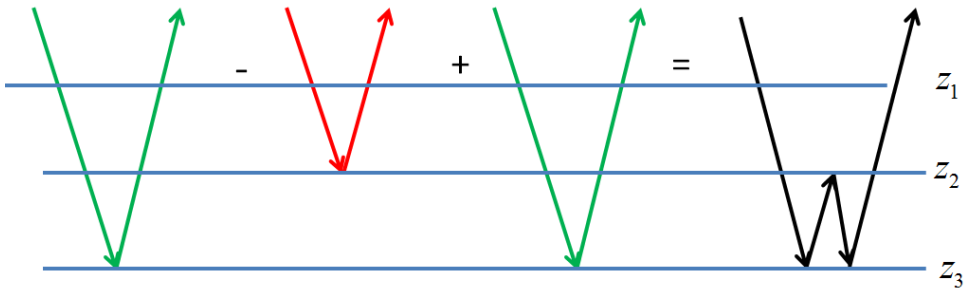

Figure 1: A first-order internal multiple constructed by three primary subevents that satisfy the "lower-higher-lower" pattern in pseudo-depth domain.

where $D_3(t)$ is the inverse Fourier transform of $D_3(\omega)$, and where $D_3(\omega) = b_3(k)$ for an incident spike wave. Weglein and Matson (1998) showed that this algorithm can be interpreted as the subevents construction of internal multiples. Figure 1 illustrates the construction of a first-order internal multiple using three primary subevents. The predicted time of the internal multiple is exact, and the predicted amplitude approximates the true amplitude (Weglein et al., 2003).

2 The higher-order modification of the ISS internal-multiple leading-order-attenuation algorithm

Early analysis of the ISS leading-order attenuator focused on the performance of internal multiples prediction by using subevents that correspond to primaries. However, the input data contain both primaries and internal multiples and all events in the data will be treated as subevents. Under some circumstances treating internal multiples as subevents in the first-order internal-multiple algorithm can lead to spurious events. Ma et al. (2012) and Liang et al. (2012) define the conditions when that can occur and explain how terms further in the ISS address and remove those spurious events. For instance, a spurious event may be generated by the leading-order attenuator when an internal multiple itself is treated as a subevent in the second integral of equation 1.3, as shown in Figure 2. It is worthing noting that in figure 2, the "lower-higher-lower" relationship between the psudeo-depths is required by b_3, and if it not satisfied this kind of subevent combination will not occur in b_3, and such type of a spurious event would not be produced.

Ma et al. (2012) identify a higher-order term from the inverse scattering series that can generate the negative of the spurious event.

$$b_5^{PIP}(k) = \int_{-\infty}^{\infty} dz_1 e^{ikz_1} b_1(z_1) \int_{-\infty}^{z_1-\epsilon} dz_2 e^{-ikz_2} b_3(z_2) \int_{z_2+\epsilon}^{\infty} dz_3 e^{ikz_3} b_1(z_3). \tag{2.1}$$

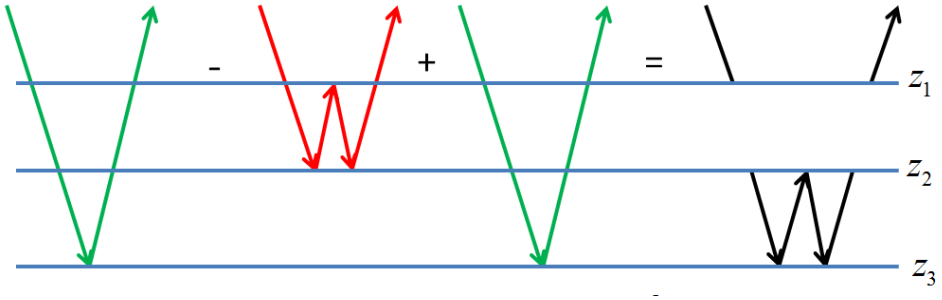

Figure 2: Subevent construction of a spurious event when an internal multiple itself is treated as a subevent in the second integral of the leading-order attenuator (number of reflectors $N >= 3$, and $2z_2 - z_1 < z_3$).

The output of the new ISS internal-multiple algorithm for this three-reflector case is

$$D(t) + D_3(t) + D_5^{PIP}(t), \tag{2.2}$$

where $D_5^{PIP}(t)$ is the inverse Fourier transform of $D_5^{PIP}(\omega)$ and where $D_5^{PIP}(\omega) = b_5^{PIP}(k)$ for spike data. The original algorithm (see equation 1.4) attenuates the first-order internal multiples and preserves primaries but can also output spurious events. The new algorithm in equation 2.2 provides the benefit of the original algorithm while addressing issues that are due to spurious events.

When there are more than three reflectors in the earth, other types of spurious events could also be generated by the leading-order attenuator (Liang et al. (2012)). In this report, we will focus only on the three-reflector case. Therefore, only the leading-order attenuator (equation 1.3) and the higher-order term (equation 2.1) will be examined in this report.

3 The source wavelet effects on ISS internal-multiple prediction exemplified using two examples

In the previous section, the input data are assumed to be source wavelet deconvolved, deghosted, and with free-surface multiples removed. If the data are generated by using a source wavelet instead of an incident spike wave in a 1D case, $b_1(k)$ is obtained by the following equation:

$$D(\omega) = A(\omega)b_1(2\omega/c_0). \tag{3.1}$$

Then, the internal multiples predicted by the leading-order attenuator (equation 1.3), which has opposite polarity as the true internal multiples, are obtained by

$$D_3(\omega) = A(\omega)b_3(\omega/c_0). \tag{3.2}$$

When adding equation 3.2 to equation 3.1, all the first-order internal multiples are attenuated, and higher-order internal multiples are altered. More details on incorporating source wavelet deconvolution into the ISS internal multiple attenuation algorithm can be referred to Yang and Weglein (2013). Including source wavelet deconvolution in the higher-order term for removing spurious event require this initial step in the leading-order attenuator. The predicted spurious events (with opposite polarity as the actual spurious event generated by the leading-order attenuator) are obtained by

$$D_5^{PIP}(\omega) = A(\omega)b_5^{PIP}(\omega/c_0). \tag{3.3}$$

Equations 3.1, 3.2, and 3.3 can be easily extended to multi-dimensional cases. In this section, we will examine the effects of a source wavelet on the prediction of internal multiples and spurious events. we apply the ISS internal-multiple leading-order attenuator and its higher-order modification with and without inclusion of source wavelet deconvolution for both 1D normal incidence and 1.5D shot gather examples, and then compare the results. In this report, we use the spectral division method to deconvolve the source wavelet from the input data. Other methods (e.g., Wiener filter) could also be used and more details about source wavelet deconvolution can be referred to Tang et al. (2012).

3.1 1D normal incidence example

Here we will examine the source wavelet effect on the leading-order attenuator and its higher-order modification (using the exact source wavelet that are used to generate synthetic data). Figure 3 shows a trace generated by the 1D normal-incidence reflectivity method (Ricker source wavelet with peak frequency 30Hz, and sampling interval in time dt=4ms). The reflectivity method can be used to generate primaries and internal multiples separately. In this figure three primaries are shown in red, and all the internal multiples are shown in blue.

Figure 4 shows the actual internal multiples in the data (top) and the internal multiples predicted by using the ISS leading-order attenuator ($-D_3$) without source wavelet deconvolution (bottom). These two results then are normalized by their respective maximum sample value, and plotted together in Figure 5. From Figures 4 and 5 we can see that the predicted time is exact, but the amplitude and shape of the predicted internal multiples are not matched with those of actual internal multiples. From Figure 5 we can also see the spurious event, at time $1.33s$ (in green circle), that is generated by the ISS leading-order attenuator. This event does not exist in the original input data and that's why it is called a spurious event. Figure 6 shows the comparison of the spurious event generated by the leading-order attenuator and the spurious event predicted by the higher-order term (equation 2.1). Both results are obtained without source wavelet deconvolution, and we can see that again the predicted amplitude and shape do not matched with the real ones.

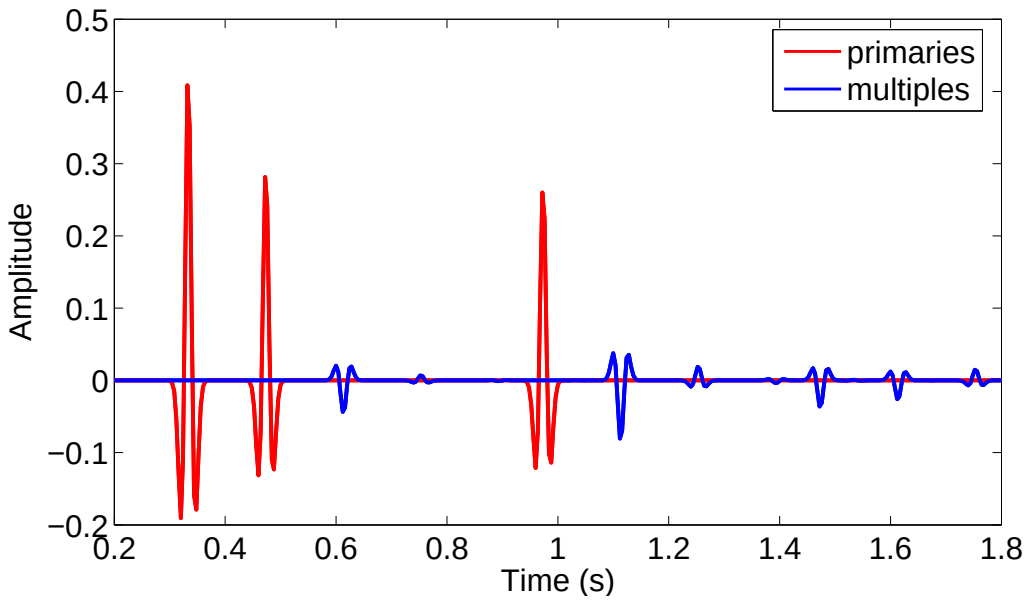

Figure 3: An input trace, including three primaries (red) and all internal multiples (blue).

Next we apply the procedures described in equations 3.1, 3.2, and 3.3 to incorporate the source wavelet deconvolution into internal multiple and spurious event predictions. Figure 7 shows the true internal multiples in the data (red) and internal multiples predicted by the ISS leading-order attenuator ($-D_3$) with source wavelet deconvolution (blue). It is shown that with the source wavelet deconvolution the shape of the internal multiple prediction matches the actual internal multiples very well. Also, the predicted time is exact and the predicted amplitude is approximate.

Figure 8 shows the comparison of the spurious events in D_3 and the spurious event predicted by the higher-order modification($-D_5^{PIP}$), and both results are obtained with source wavelet deconvolution. From the figure we can see that the predicted spurious event matches the one generated by the leading-order attenuator very well. By adding D_5^{PIP} to D_3 the spurious event is greatly attenuated and the internal multiple prediction is almost unchanged (compared to Figure 7), as shown in Figure 9. From Figure 9 we can conclude that the modified internal-multiple-prediction algorithm in equation 2.2 provides the benefit of original algorithm (equation 1.4) while addressing the limitation due to spurious events.

3.2 1.5D shot-gather example

In this section, we examine the source wavelet effects on the ISS internal-multiple leading-order attenuator and its higher-order modification for a 1.5D shot-gather example. The data are generated by using finite-difference code within the M-OSRP group (code courtesy of Fang Liu and Di Chang, and the source wavelet is a Ricker wavelet with 25Hz peak frequency). Figure 10 shows the three-

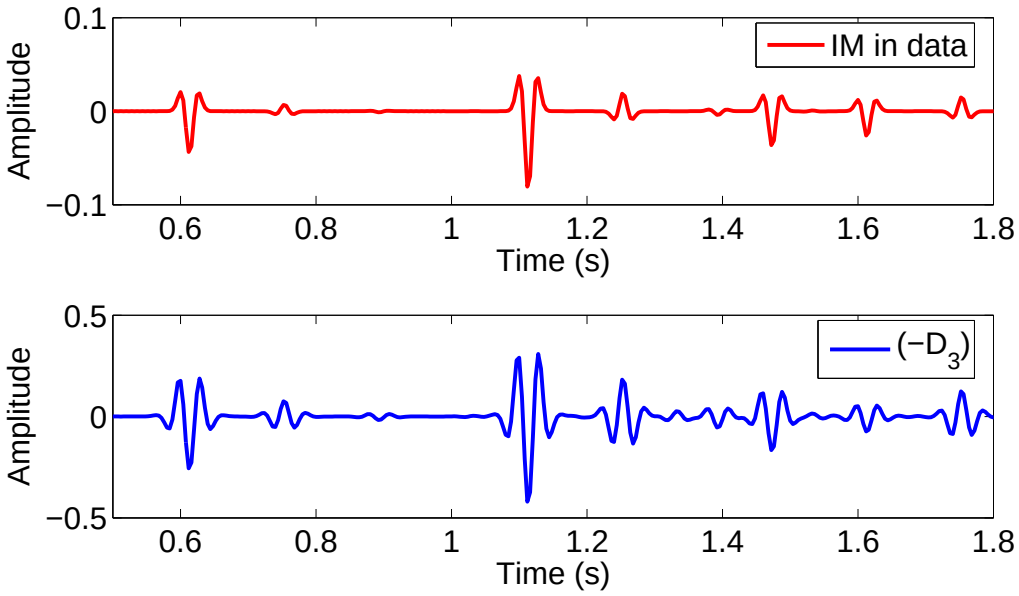

Figure 4: Top: actual internal multiples in the data; bottom: predicted multiples ($-D_3$) without source wavelet deconvolution.

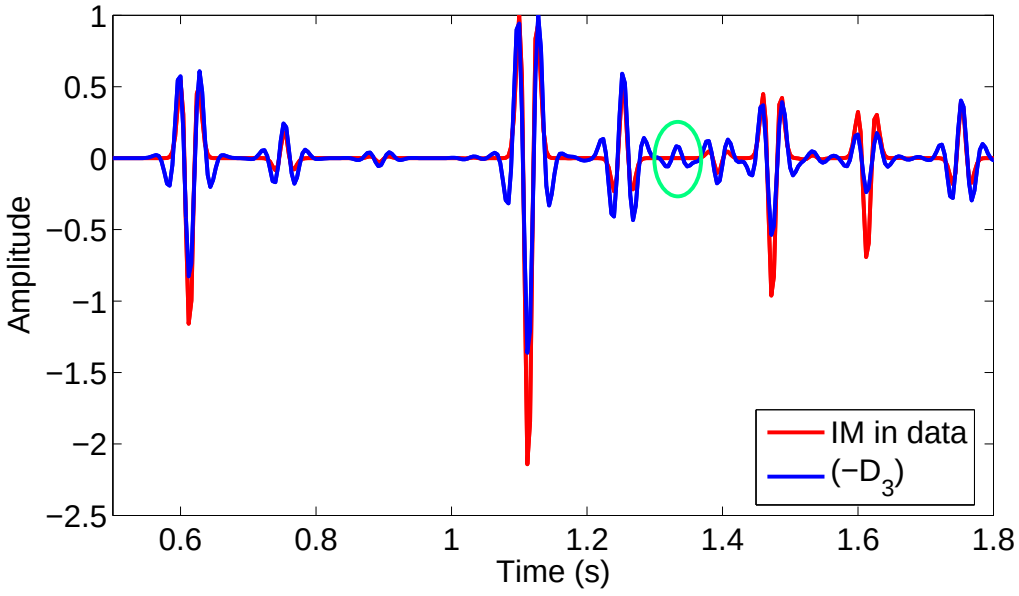

Figure 5: Internal multiples in the data (red) and predicted multiples ($-D_3$) without source wavelet deconvolution (blue). Both results are normalized by their maximum sample value, respectively. The green circle shows the spurious event.

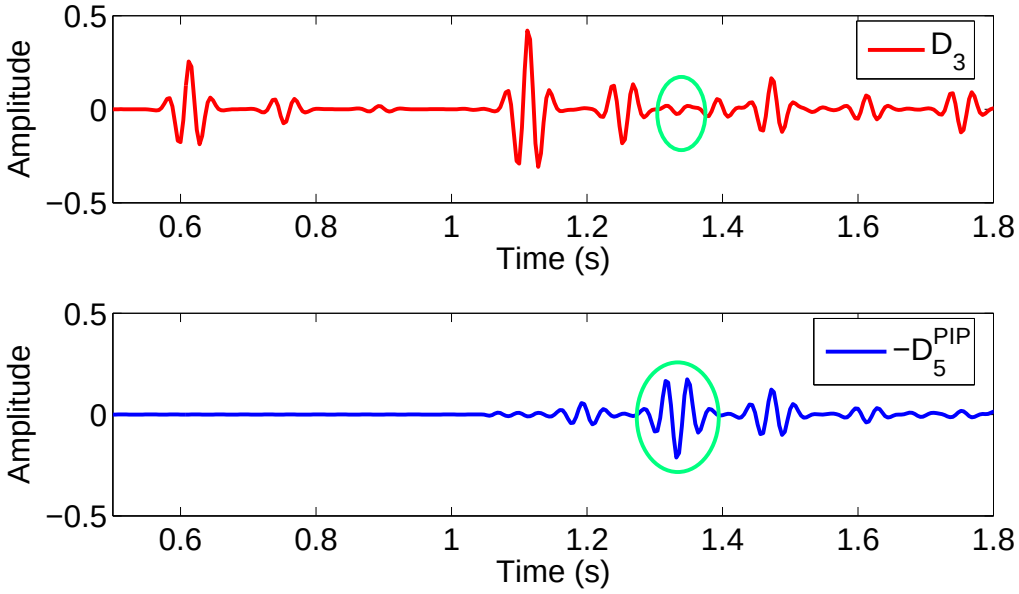

Figure 6: Top is the result of D_3 (spurious event at time 1.33s) and bottom is the result of $-D_5^{PIP}$ (predicted spurious event at time 1.33s). Both results are obtained without source wavelet deconvolution. Green circles show the spurious events.

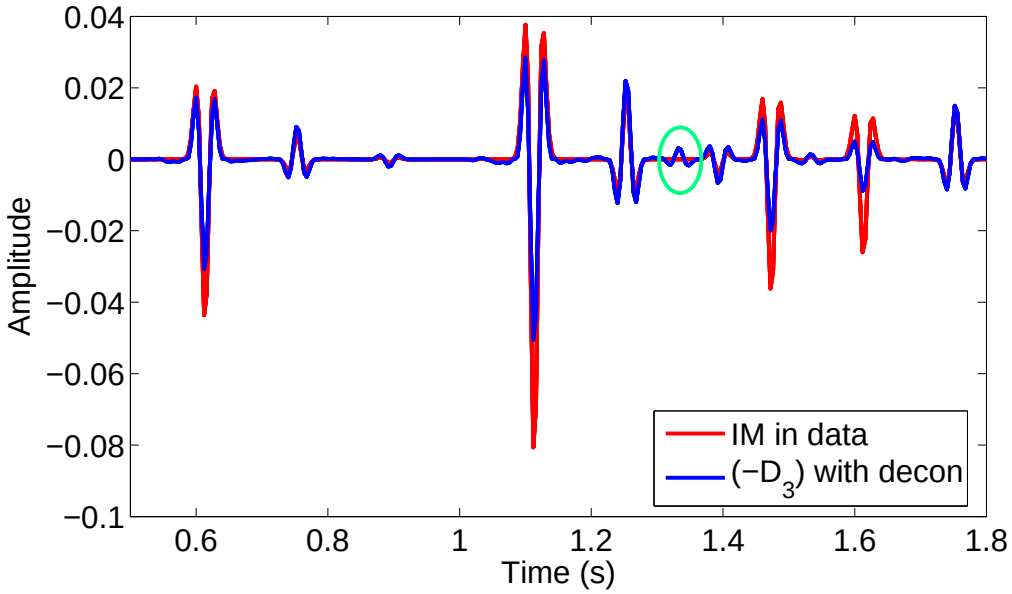

Figure 7: Actual internal multiples in the data (red) and internal multiples predicted by the ISS leading-order attenuator with source wavelet deconvolution (blue).

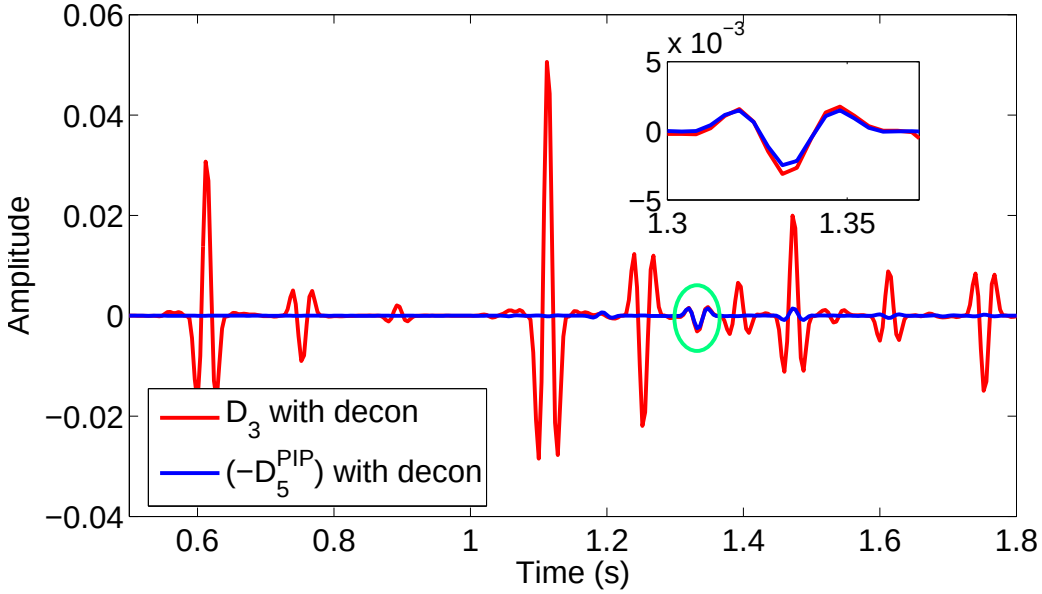

Figure 8: Comparison of spurious events (in green circle) in D_3 and spurious event prediction represented by $-D_5^{PIP}$, and the upper right box shows the zoomed part in the circle; both results are obtained with source wavelet deconvolution.

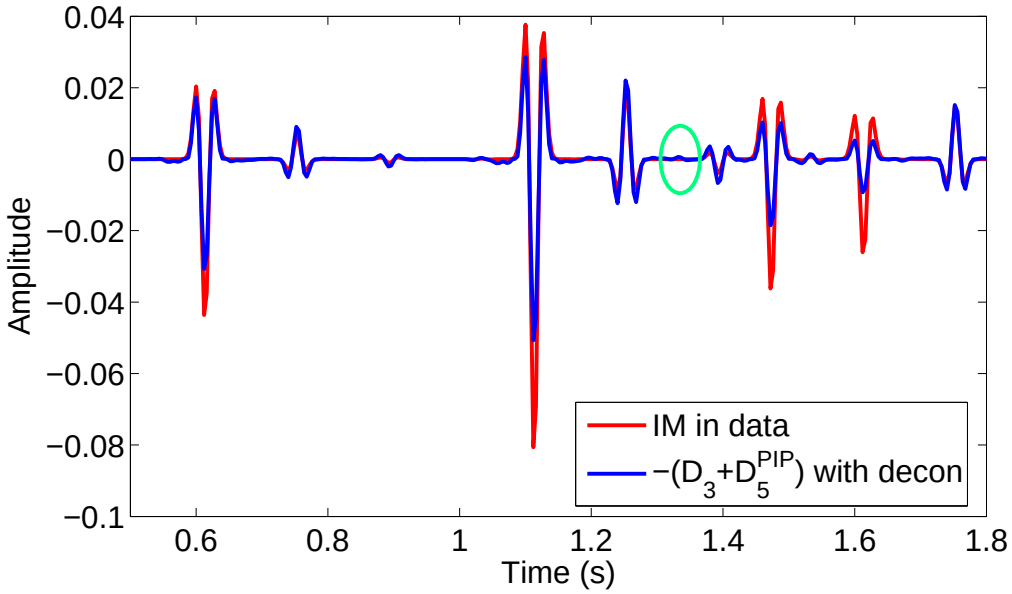

Figure 9: Comparison of actual internal multiples in data (red) and modified prediction represented by $-(D_3 + D_5^{PIP})$ (with source wavelet deconvolution). Green circles correspond to the spurious events.

reflector 1D model for data generation. Figures 11a and 11b show the shot gather without and with source wavelet deconvolution, respectively. The first five events in Figure 11a are: the first primary, the second primary, the first-order and second-order internal multiples generated between the first and second reflectors, and the third primary.

We first examine the source wavelet effects on the leading-order attenuator (b_3 term). Figures 12a and 12b show the predicted multiple ($-D_3$) with (right) and without (left) source wavelet deconvolution. We can see that without source wavelet deconvolution the predicted multiples spread out, and also the amplitudes of the predicted multiples in the two results are very different. Figure 13 shows for comparison wiggle plots of the multiple prediction without deconvolution (13a), the input shot gather (13b), and the multiple prediction with deconvolution (13c). We choose the time window so that all the events shown in the wiggle plots are internal multiples. The results show that with the source wavelet deconvolution, the shapes of the predicted internal multiples are more similar to those of actual internal multiples in the data. Then we compare the amplitudes of the actual internal multiples with those of the multiples predicted using two different schemes, respectively. Figure 14a shows the amplitude comparison of the zero-offset traces from the input shot gather (red) and the multiple predicted without source wavelet deconvolution (blue), and Figure 14b shows the amplitude comparison of zero-offset traces from the input shot gather (red) and the multiple predicted with source wavelet deconvolution (blue). In each of these two figures, the red event at about $1.25s$ is the third primary and the rest of the events are internal multiples. From these two figures we can see that by including the source wavelet deconvolution, the amplitudes of the predicted internal multiples approximate those of the actual internal multiples.

Next we will examine the source wavelet effects on the higher-order term addressing issues due to spurious events, i.e., the b_5^{PIP} term. Figures 15a and 15b show the results of $-D_3$ and D_5^{PIP} without source wavelet deconvolution, and Figures 16a and 16b show the corresponding results with source wavelet deconvolution. We extract the zero traces from each set of two figures and then compare them in the same plot. Figure 17a shows the comparison of zero-offset traces from $-D_3$ and D_5^{PIP}, both of which are obtained without source wavelet deconvolution. Figure 17b shows the comparison of zero-offset traces from $-D_3$ and D_5^{PIP} obtained with source wavelet deconvolution. From the results in these two figures, we can see that with the source wavelet deconvolution, both the amplitude and shape of the predicted spurious event match well those of actual spurious event generated by the leading-order attenuator.

3.3 Internal multiple prediction using estimated wavelet

In this section we estimated the source wavelet using the Green's theorem-derived method (Weglein and Secrest (1990)) and then use this estimated source wavelet to repeat the process in the Section 3.2. Further details about the source wavelet estimation based on Green's theorem and its application can be referred to Mayhan et al. (2012). It is worth noting that in this report the actual medium is an inhomogeneous acoustic medium with water on the top and the reference medium is a whole-water medium. Therefore, the total wavefield in the actual medium contains direct wave,

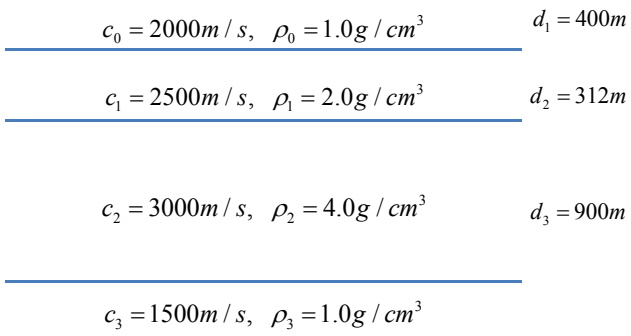

Figure 10: 1D model with both velocity and density variations.

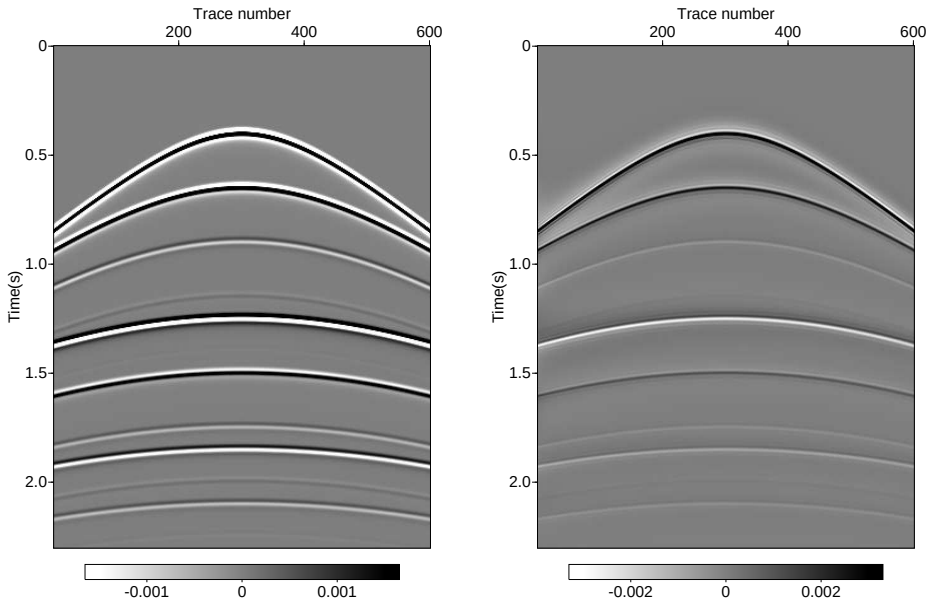

(a) (b)

Figure 11: (a) Shot gather without source wavelet deconvolution; (b) shot gather with source wavelet deconvolution.

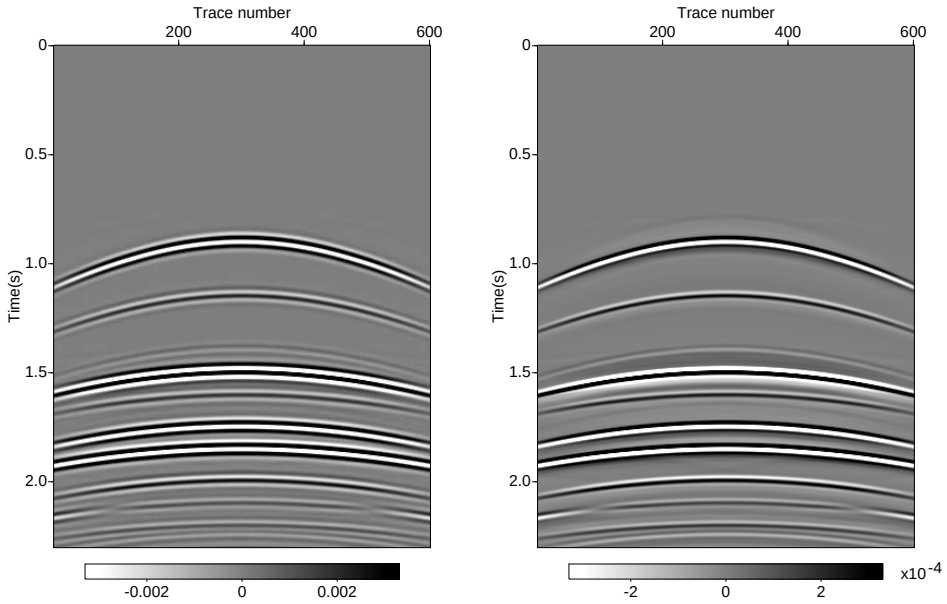

(a) (b)

Figure 12: Internal-multiple prediction ($-D_3$) without (a) and with (b) source wavelet deconvolution.

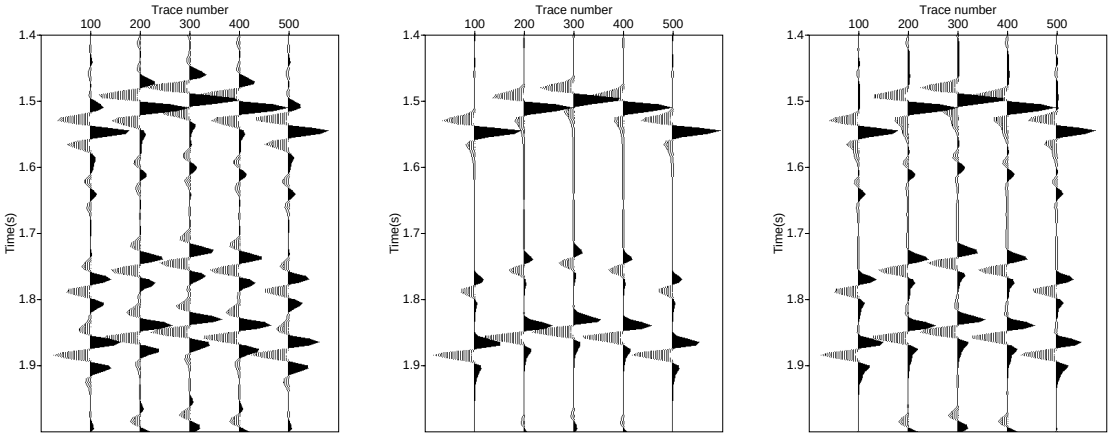

(a) (b) (c)

Figure 13: Wiggle plots of selected traces: (a) a multiple prediction without source wavelet deconvolution, (b) an input shot gather, (c) and a multiple prediction with deconvolution.

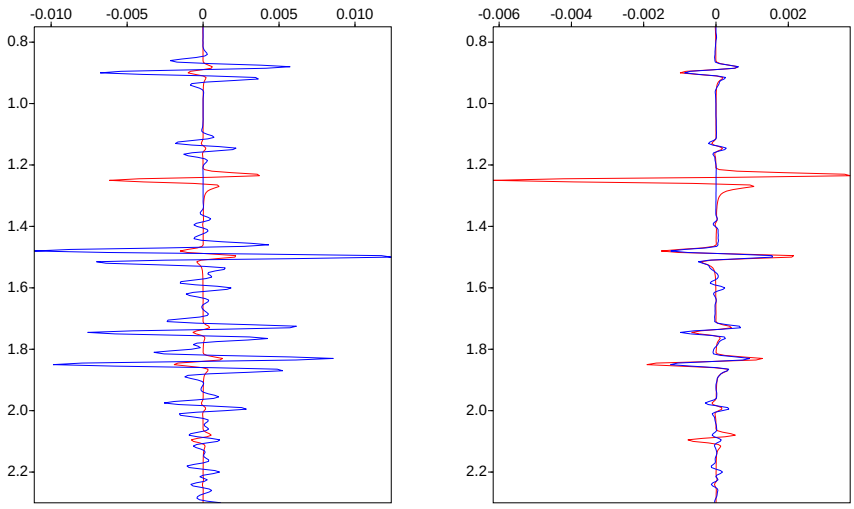

(a) (b)

Figure 14: (a) Comparison of the zero-offset traces extracted from Figures 11a (red) and 12a (blue); (b) Comparison of the zero-offset traces extracted from Figures 11a (red) and 12b (blue).

primaries and internal multiples while the reference wavefield in the reference medium contains direct wave only. The key equation of the source wavelet estimation is as follows,

$$\tilde{A}(\omega)G_0(\mathbf{r},\mathbf{r}_s,\omega) = \oint_S [\tilde{P}(\mathbf{r}',\mathbf{r}_s,\omega)\nabla' G_0(\mathbf{r}',\mathbf{r},\omega) - G_0(\mathbf{r}',\mathbf{r},\omega)\nabla'\tilde{P}(\mathbf{r}',\mathbf{r_s},\omega)]\cdot\mathbf{n}dS, \tag{3.4}$$

where $\mathbf{r_s}$, $\mathbf{r}'$, $\mathbf{r}$ represent the locations of source, receiver and prediction points, respectively; $\tilde{P}(\mathbf{r}',\mathbf{r}_s,\omega)$ is the Fourier transform of the pressure field, $G_0(\mathbf{r_i},\mathbf{r_j},\omega)$ is the Fourier transform of the Green's function in the reference medium. The source wavelet $A(\omega)$ can be obtained by averaging the reference wavefield divided by a Green's function:

$$A(\omega) = \frac{1}{N}\sum_{i=1}^{N}\frac{\tilde{P}_0(\mathbf{r}_i,\mathbf{r}_s,\omega)}{G_0(\mathbf{r}_i,\mathbf{r}_s,\omega)}. \tag{3.5}$$

From the equation 3.4 we can see that both the total wavefield and its derivative are needed to estimate the source wavefield. We calculate the derivative of the wavefield using the measured wavefield at two different depths:

$$\frac{dP}{dz} = \frac{P(205m) - P(200m)}{5m}. \tag{3.6}$$

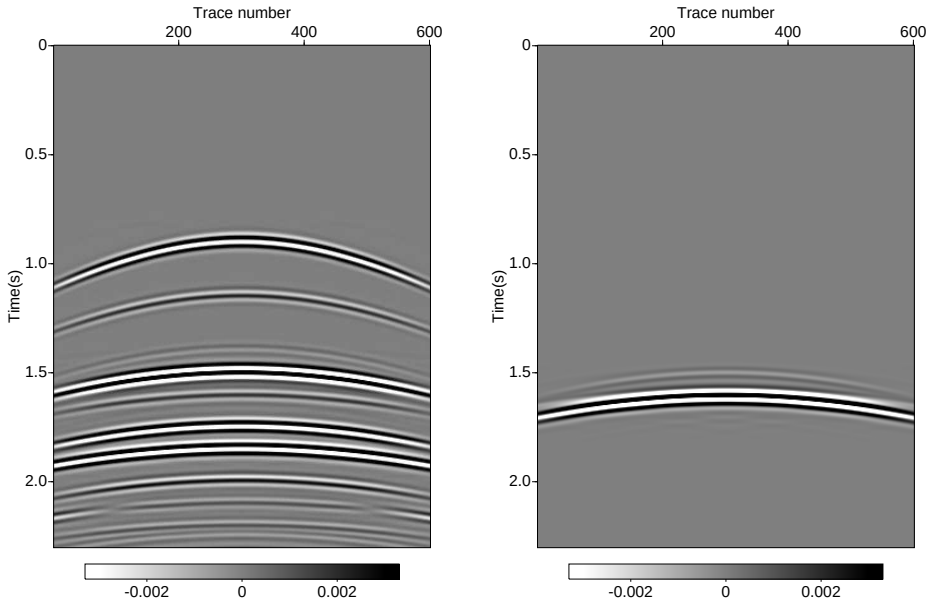

(a) (b)

Figure 15: Results without source wavelet deconvolution: (a) multiple prediction ($-D_3$) and (b) spurious-event prediction (D_5^{PIP}).

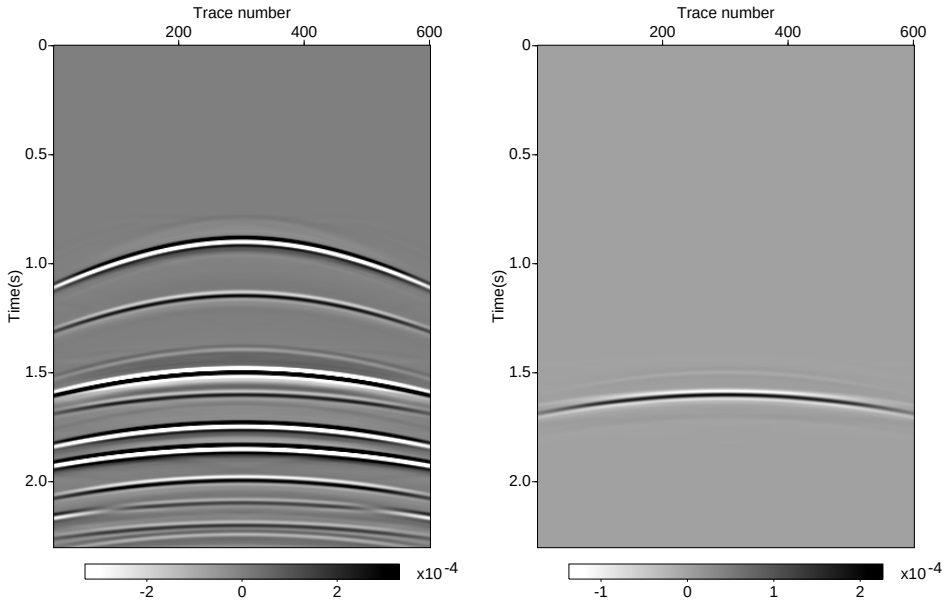

(a) (b)

Figure 16: Results with source wavelet deconvolution: (a) multiple prediction (- D_3) and (b) spurious event prediction (D_5^{PIP}).

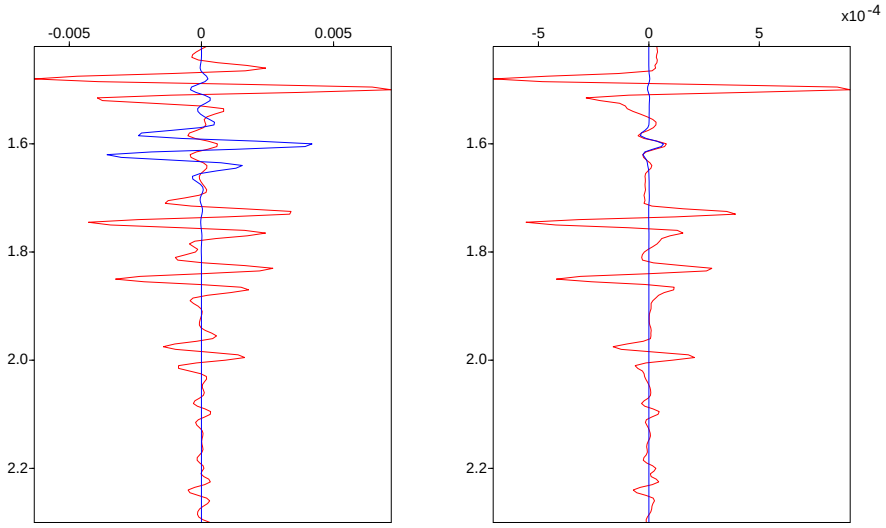

(a) (b)

Figure 17: (a) Comparison of the zero-offset traces extracted from Figures 15a (red) and 15b (blue); (b) Comparison of the zero-offset traces extracted from Figures 16a (red) and 16b (blue).

Figure 18a shows that the estimated source wavelet (blue) matches well the actual source wavelet (red). Figure 18b shows zero-offset traces of predicted internal multiples using actual (red) and estimated source wavelet (blue), and Figure 18c shows zero-offset traces of predicted spurious event using actual (red) and estimated source wavelet (blue). We can see that the results by using the estimated waevlets matches the resutls by using the actual wavelet.

4 Summary and discussion

We examine the source wavelet effects on both the ISS internal-multiple leading-order attenuator and higher-order term for removing spurious event by comparing the internal-multiple-prediction results with and without source wavelet deconvolution. From the comparison we can see that by including the source wavelet deconvolution in the ISS internal-multiple prediction, both the shape and amplitude of the predicted internal multiples can be improved (made closer to the true internal multiples). The accuracy of the source wavelet is important for the test results, and we have shown that the source wavelet can be estimated using Green's theorem.

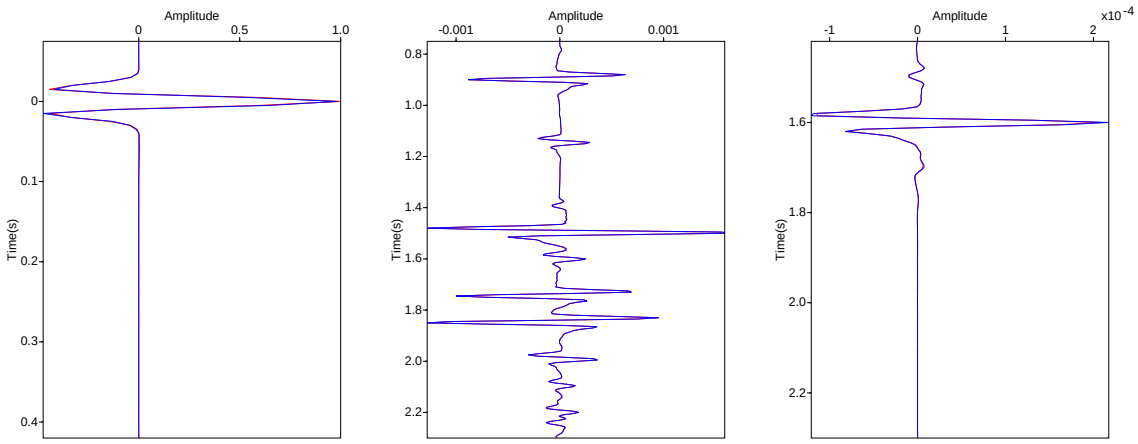

(a) (b) (c)

Figure 18: (a) Comparison of actual (red) and estimated (blue) source wavelets; (b) zero-offset traces of predicted internal multiples using actual (red) and estimated source wavelet (blue) (c) zero-offset traces of predicted spurious events using actual (red) and estimated source wavelet (blue).

5 Acknowledgements

The first author would like to thank Schlumberger/Westerngeco for the internship during Fall 2012 and for the permission to present the work. We are also grateful to all M-OSRP sponsors for their support of this research. Special thanks to Wilberth Herrera and Chao Ma for reviewing this report, and Jim Mayhan and Lin Tang for their help.

References

Araújo, F. V., A. B. Weglein, P. M. Carvalho, and R. H. Stolt. "Inverse scattering series for multiple attenuation: An example with surface and internal multiples." SEG Technical Program Expanded Abstracts (1994): 1039–1041.

Fu, Q., Y. Luo, G. K. Panos, S. Huo, G. Sindi, S. Hsu, and A. B. Weglein. "The inverse scattering series approach towards the elimination of land internal multiples." SEG Technical Program Expanded Abstracts (2010): 3456–3461.

Hsu, S., P. Terenghi, and A. B. Weglein. "The properties of the inverse scattering series internal multiple attenuation algorithm: Analysis and evaluation on synthetic data with lateral variations, choosing reference velocity and examining its sensitivity to near surface properties." Mission-Oriented Seismic Research Program (M-OSRP), Annual Report (2011): 16–28.

Liang, H., C. Ma, and A. B. Weglein. "A further general modification of the leading order ISS attenuator of first order internal multiples to accommodate primaries and internal multiples when an arbitrary number of reflectors generate the data: theory, development, and examples." M-OSRP 2011 Annual meeting (2012).

Luo, Y., P. G. Kelamis, Q. Fu, S. Huo, G. Sindi, S. Hsu, and A. B. Weglein. "Elimination of land internal multiples based on the inverse scattering series." The Leading Edge (2011): 884–889.

Ma, C., H. Liang, and A. B. Weglein. "Modifying the leading order ISS attenuator of first-order internal multiples to accommodate primaries and internal multiples: fundamental concept and theory, development, and examples exemplified when three reflectors generate the data." M-OSRP 2011 Annual meeting (2012).

Mayhan, J., A. B. Weglein, and P. Terenghi. "Green's theorem-derived preprocessing of marine seismic data." Mission-Oriented Seismic Research Program (M-OSRP), Annual Report (2012): 9–113.

Tang, L., P. Terenghi, and A. B. Weglein. "Application of the Wiener filter in wavelet estimation using Kristin data." Mission-Oriented Seismic Research Program (M-OSRP), Annual Report (2012): 267–276.

Weglein, A. B., F. V. Araújo, P. M. Carvalho, R. H. Stolt, K. H. Matson, R. T. Coates, D. Corrigan, D. J. Foster, S. A. Shaw, and H. Zhang. "Inverse Scattering Series and Seismic Exploration." Inverse Problems (2003): R27–R83.

Weglein, A. B., F. A. Gasparotto, P. M. Carvalho, and R. H. Stolt. "An inverse-scattering series method for attenuating multiples in seismic reflection data." Geophysics (1997): 1975–1989.

Weglein, A. B., S. Hsu, P. Terenghi, X. Li, and R. Stolt. "Multiple attenuation: Recent advances and the road ahead 2011." The Leading Edge (2011): 864–875.

Weglein, A. B. and K. H. Matson. "Inverse scattering internal multiple attenuation: an analytic example and subevent interpretation." Mathematical Methods in Geophysical Imaging V (1998): 108–117.

Weglein, A. B. and B. G. Secrest. "Wavelet estimation for a multidimensional acoustic or elastic earth." Geophysics (1990): 902–913.

Yang, J. and A. B. Weglein. "ISS internal multiple attenuation algorithm with source wavelet." Mission-Oriented Seismic Research Program (M-OSRP), Annual Report (2013).

Isolation of an elimination subseries for the surgical removal of first-order internal multiples with downward reflection at the shallowest reflector

Wilberth Herrera, Chao Ma, Hong Liang
and Arthur B. Weglein
M-OSRP, University of Houston,
617 Science Research Bldg. 1, Houston, TX 77004.

Abstract

In this work a subseries of the ISS is isolated, with the specific task of removing internal multiples of first-order, with downward reflection at the shallowest reflector. The algorithm predicts both the phase and exact amplitude of the internal multiples and does not modify any primary; therefore the internal multiples are removed surgically. This algorithm may be relevant and provide added value when one of the internal multiples under discussion is interfering destructively with (or is proximal to) a primary, and the attenuation of the internal multiple provided by previous algorithms is not adequate for the clean removal of the multiple and not touching the primary. To show how the elimination subseries proposed in this work deals with this challenging situation, an analytic example with three interfaces is included, with one of the relevant first-order internal multiples interfering destructively with the primary generated at the third reflector. We show in particular how the interfering internal multiple is eliminated with no damage to the amplitude or the phase of the primary, as is expected from a method for surgical removal of internal multiples.

1 Introduction

Today, there are a number of methodologies in the oil industry that are designed to predict internal multiples. These methods are followed by energy-minimization adaptive subtraction to try to accommodate all shortcomings in the prediction, as it addresses contributions left outside of the system by the prediction method. In other words, the energy-minimization adaptive subtraction deals with issues not included in the physical framework behind the prediction method.

In particular, by using the ISS and the concept of specific-task subseries, a multidimensional algorithm was derived in Araújo (1994), Araújo et al. (1994) and Weglein et al. (1997) to predict and attenuate internal multiples present in the data. However, there are situations in which the energy-minimization adaptive-subtraction technique is not suitable anymore, and the attenuation

of internal multiples is not enough for a correct interpretation of the seismic data. An example of this challenging situation for the oil industry can arise when an internal multiple is interfering destructively with (or is proximal to) a primary associated to a target e.g. subsalt targets. This situation is often present in onshore exploration, but it can also happen offshore. While the energy-minimization adaptive-subtraction technique is of value for isolated multiples, in this case it might also affect the primary that is experiencing interference from the internal multiple.

Therefore, it is important to develop new algorithms with enhanced capabilities. In response to this need, Ramírez and Weglein (2005) and Ramírez (2007) discuss early ideas for moving attenuation of internal multiples towards elimination through higher order terms in the ISS. Those ideas and concepts are here progressed and developed leading to a subseries which surgically removes at the same time all internal multiples of first-order having their single downward reflection generated at the shallowest reflector. We refer to this subseries as the leading-order internal multiple elimination subseries (LOIMES). We also illustrate how to use this subseries in a three-interface analytic model, to surgically remove the first-order internal multiple with its downward reflection at the shallowest interface and upward reflections at the second reflector. To highlight the importance of this work, the parameters of the model are chosen to mimic the situation described in the paragraphs above; i.e., to allow the internal multiple to interfere destructively with a primary. In particular, the primary that is experiencing interference corresponds to the third reflector.

The report's organization is as follows: Section 2 provides a review of the leading-order attenuation of internal multiples of first order, which is the initial step toward their complete elimination. In Section 3 we explain how to isolate the LOIMES, with emphasis on the first contribution beyond the leading-order attenuator; i.e., with full details of the derivation of the second term of the subseries provided. Section 4 is devoted to application of the LOIMES to the analytic model mentioned in the paragraph above. Finally, in Section 5 we present final comments and conclusions. There are two appendices, in which we show the details of the calculations needed to follow the main body of this paper.

2 Review of the internal multiple attenuation subseries

2.1 The inverse scattering series and seismic physics

The inverse scattering series (ISS) is a direct inversion method which can in principle determine, in seismic applications, subsurface properties of the earth using only the measured data D in a seismic experiment, and a Green's function for a chosen reference medium. The information about

the earth is contained in the perturbation operator V, which is the difference between the actual medium (the earth) and the reference medium. Also, the data are the value of the scattered field[1] at the measurement surface. The ISS starts with the expansion of the perturbation operator (at the measurement surface) as

$$V = V_1 + V_2 + V_3 + ... \tag{1}$$

where V_i is the portion of V that is ith order in the measured data. Then, at the measurement surface the ISS takes the form (Weglein et al. 2003)

$$\begin{aligned} G_0V_1G_0 &= D \\ G_0V_2G_0 &= -G_0V_1G_0V_1G_0 \\ G_0V_3G_0 &= -G_0V_1G_0V_1G_0V_1G_0 - G_0V_1G_0V_2G_0 - G_0V_2G_0V_1G_0 \\ &\vdots \end{aligned} \tag{2}$$

As D is provided by the seismic experiment, we can solve for V_1 in the first equation of (2). Then, we can substitute V_1 into the second equation and solve for V_2. Now we can substitute V_1 and V_2 into the third equation and solve for V_3. Following this procedure we can determine all the components in the right hand side of (1). However, empirical tests performed in Carvalho (1992) suggest that with no *a priori* information, convergence is restricted to small contrasts and short duration of the perturbation.

A solution for the issue of convergence explained in Weglein et al. (2003) is to split the inversion into specific tasks:

1. Removal of free-surface multiples.
2. Removal of internal multiples.
3. Location and imaging of reflectors in space.
4. Inversion for earth material properties.

A free-surface multiple is by definition a seismic event with at least one downward reflection at the air-water interface; the number of downward reflections at the air-water interface is the order of

[1]The scattered field is defined as $\psi_s \equiv G - G_0$, where G and G_0 are Green's functions for the actual and reference medium respectively.

the free-surface multiple. On the other hand, an internal multiple is by definition a seismic event with at least one downward reflection, and with all of its downward reflections created at the earth (Figure 1). The order an the internal multiple is defined as the number of downward reflections it experiences anywhere during its travel time.

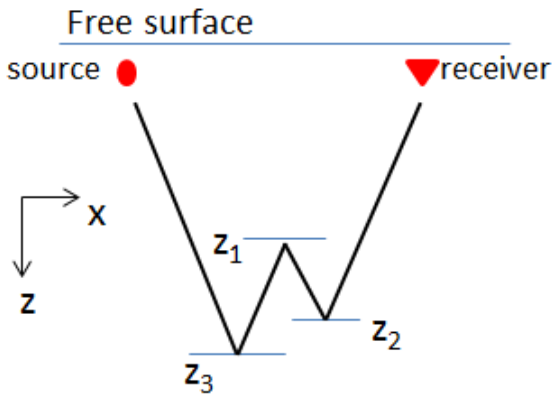

Figure 1: First-order internal multiple.

In Figure 1 the direction of increasing Z is downwards, hence $Z_2 > Z_1$ and $Z_3 > Z_1$. We also say that, on the basis of the locations where reflections occur, the interfaces generate an internal multiple of first order are in a "lower-higher-lower" configuration.

The recipe is to isolate distinct subseries from the ISS, with each subseries having as its goal only one of the specific tasks just listed. It turns out that those specific-task subseries have better convergence properties than the entire ISS. A fundamental part of this approach, mentioned in Weglein et al. (2003), is that the four tasks listed above are accomplished sequentially in the order in which they are mentioned. Each time a task is achieved, the problem is restarted, as if the task(s) accomplished had not existed before.

With regard to internal multiples, a subseries was isolated in Araújo (1994) and Weglein et al. (1997). Its task is attenuation of internal multiples of all orders. In particular, first-order internal multiples are attenuated by the leading-order contribution[2] of this subseries, conveniently named the *leading-order attenuator*.

[2]The leading-order contribution in a specific-task subseries refers here to the first term of that subseries that provides the initial contribution towards the achievement of the specific task.

2.2 The leading-order attenuator

As we will see in later sections, the LOIMES isolated in this work shares the same leading-order contribution that the internal multiple attenuation subseries (IMAS) has. Hence, it is important to first understand how the leading-order attenuator works, and then to move to higher-order contributions to the LOIMES. In this subsection we will provide a review of the leading-order attenuator.

A detailed study of the isolation of the IMAS, and in particular of the leading-order attenuator, is beyond the scope of this work. The interested reader can consult Araújo (1994), Ramírez (2007), and Weglein et al. (2003) for more details. For this work it is enough to say that the leading-order attenuator is contained in the third equation of the ISS. This is because first-order internal multiples experience three reflections and therefore they are of third order in data. The leading-order attenuator is isolated from $V_1G_0V_1G_0V_1$ in the references just mentioned.

For the 1D and normal-incidence case, the analytic expression for the leading-order attenuator is

$$b_3(k) = \int_{-\infty}^{\infty} dz e^{ikz} b_1(z) \int_{-\infty}^{z-\epsilon} dz' e^{-ikz'} b_1(z') \int_{z'+\epsilon}^{\infty} dz'' e^{ikz''} b_1(z''), \tag{3}$$

where ϵ is a small and positive parameter introduced to ensure the characteristic "lower-higher-lower" configuration for first-order internal multiples, which was mentioned in Section 2.1, and to avoid the configurations that include the contributions of the self-interactions $z'' = z'$ and $z' = z$. In the general case, ϵ is chosen to match the width of the source wavelet, and the consequence is that thin-bed multiples will not be attenuated (Weglein et al. 2003). However, we will consider 1D models and spike waves with normal incidence and therefore there is no wavelet to worry about, that is, there is no restriction on the value of ϵ other that it must be small and positive[3]. Also, $k = \frac{2\omega}{c_0}$ is the vertical wavenumber, and $b_1(z)$ is the result of performing Stolt's migration on the data of the model using the water speed, denoted c_0.

We will consider the 1D model shown in Figure 2, where Z_i denotes the depth of the ith reflector for $i = 1, 2, 3$.

[3]In practice, the computational implementation requires a discretization of time. In this case $\epsilon = \frac{c_0 \Delta t}{2}$, where Δt is a time sample interval and usually it has assigned the value of $1ms$. Also, c_0 is the water speed.

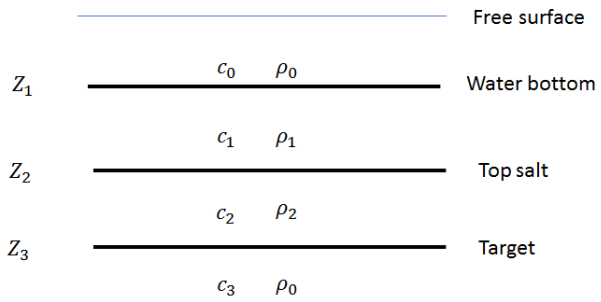

Figure 2: A 1D earth model, with three interfaces. The first interface, with depth Z_1, is the water bottom. The second interface, with depth Z_2, can be identified as the top salt, and the third interface, with depth Z_3, can be identified as the target.

We also consider data composed of primaries and internal multiples, generated by spike waves at normal incidence:

$$D(t) = R_1\delta(t-t_1) + R_2'\delta(t-t_2) + R_3'\delta(t-t_3) + IM, \tag{4}$$

where $R_2' = T_{01}R_2T_{10}$, $R_3' = T_{01}T_{12}R_2T_{21}T_{10}$, and t_i is the travel time of the primary associated with the interface at depth Z_i. Also, R_i is the reflection coefficient experienced by a wave that is reflected upward at the interface at depth Z_i. T_{ij} represents the transmission coefficient experienced by a wave traveling from the acoustic medium that has parameters (c_i, ρ_i) to the acoustic medium that has parameters (c_j, ρ_j).

In this case, the input of the leading-order attenuator, eq. (3), becomes (Appendix A.1):

$$b_1(z) = R_1\delta(z-z_1) + R_2'\delta(z-z_2) + R_3'\delta(z-z_3) + \cdots, \tag{5}$$

where $z_i = \frac{c_0 t_i}{2}$ represents the position of the reflector at depth Z_i, after Stolt's migration. The z_i are usually referred to as *pseudodepths*, and we say that eq. (5) is in the *pseudodepth* domain. Although the input data of the leading-order attenuator, eq. (5), includes primaries and internal multiples, we only consider the effect of the primaries. Initial steps towards the inclusion of internal multiples are addressed in Ma and Weglein (2012) and Liang and Weglein (2012).

According to Appendix A.2, in the time domain the result for the evaluation of eq. (3), using eq. (5), is

$$b_3(t) = -T_{01}T_{10} * (IM)_{j=1} - (T_{01}T_{10})^2 * T_{12}T_{21} * (IM)_{j=2} + \cdots , \tag{6}$$

where $(IM)_{j=1}$ is the sum of all first-order internal multiples with their downward reflection at the first (shallowest) reflector of the model, and $(IM)_{j=2}$ is the first-order internal multiple with its downward reflection at the second interface of the model. The analytic expressions are

$$(IM)_{j=1} = -T_{01}R_2R_1R_2T_{10}\delta(t-(2t_2-t_1))$$

$$-2T_{01}R_2R_1T_{21}R_3T_{12}T_{10}\delta(t-(t_2+t_3-t_1)) - T_{01}T_{12}^2R_3R_1R_3T_{21}^2\delta(t-(2t_3-t_1)). \tag{7}$$

$$(IM)_{j=2} = -T_{01}T_{12}R_3R_2R_3T_{10}T_{21}\delta(t-(2t_3-t_2)). \tag{8}$$

In order to see why $b_3(t)$ is an attenuator of internal multiples, let's add it to the data of the model:

$$b_1(t) + b_3(t) = primaries + [1 - T_{01}T_{10}](IM)_{j=1} + [1 - (T_{01}T_{10})^2 * T_{12}T_{21}] * (IM)_{j=2} + \cdots . \tag{9}$$

As $0 < T_{01}T_{10} < 1$, it becomes evident from (9) that the amplitude contribution of $(IM)_{j=1}$ i.e., the amplitude contribution of the internal multiples generated at the shallowest reflector is reduced by an amount $T_{01}T_{10}$ with respect to the contribution of those multiples prior to the addition of $b_3(z)$. $T_{01}T_{10}$ is referred to as *attenuation factor*.

An analogous situation is present for the internal multiple with its downward reflection at the second reflector. In this case, the amplitude contribution is reduced by an amount of $(T_{01}T_{10})^2 * T_{12}T_{21}$.

Finally, it is convenient to summarize some features of the leading-order attenuator:

- It is completely data-driven, and no subsurface information is required.
- It predicts the exact time and well understood amplitude of all first-order internal multiples.
- It also predicts the exact time and approximate amplitude for internal multiples with converted waves.

3 The leading-order internal multiple eliminator subseries (LOIMES)

In Section 2 we illustrated, using the specific model of Figure 2, how the leading-order attenuator decreases the amplitude contribution for first-order internal multiples with their downward reflection at the shallowest interface, by an amount of $T_{01}T_{10}$. This means that to promote this attenuation to an elimination, the contribution of higher-order terms from the elimination subseries need to move this attenuator factor to the unity: when those higher-order contributions are added to the initial attenuation provided by $b_3(t)$, the predicted amplitude will exactly match $(IM)_{j=1}$. Hence, the collective contribution of the terms in the elimination subseries will remove $(IM)_{j=1}$ from the data.

As the input of the ISS is water-speed migrated data, in order to isolate the terms within the ISS giving the right contributions, we need to express 1 in terms of reflection coefficients, and in particular in terms of R_1. This can be done by the following geometric series expansion:

$$1 = T_{01}T_{10} * \left(\frac{1}{T_{01}T_{10}}\right) = T_{01}T_{10} * \frac{1}{(1-R_1^2)} = T_{01}T_{10} * (1 + R_1^2 + R_1^4 + R_1^6 + R_1^8 + \ldots). \qquad (10)$$

Notice that, upon distribution of the product, the first term on the right-hand side of eq. (10) is the initial attenuation provided by the leading-order attenuator. Therefore, the remaining terms are the required amplitude contributions from the higher-order terms, in any subseries claiming to promote the attenuation to elimination. For simplicity, we will focus on isolation of the term within the ISS that provides the next contribution following the leading-order attenuation; i.e., on the isolation of the term whose contribution is $T_{01}T_{10} * R_1^2$ on the right-hand side of eq. (10).

The first step towards the isolation of the second term of the LOIMES from the ISS is to notice that $T_{01}T_{10} * R_1^2$ is the attenuation provided by the leading-order attenuator, $T_{01}T_{10}$, times the square power of R_1. As the prediction for first-order multiples of the leading-order attenuator, eq. (6), is already of third order in the data, the square power of R_1 means that to predict $T_{01}T_{10} * R_1^2 * (IM)_{j=1}$, the second term of the LOIMES should come from a term that is of fifth order in the data. That is, it must be somewhere within the fifth term in the ISS:

$$V_5 = -(V_1G_0V_1G_0V_1G_0V_1G_0V_1 + V_2G_0V_1G_0V_1G_0V_1 + V_1G_0V_2G_0V_1G_0V_1$$

$$+V_1G_0V_1G_0V_2G_0V_1 + V_1G_0V_1G_0V_1G_0V_2 + V_3G_0V_1G_0V_1 + V_1G_0V_3G_0V_1$$

$$+V_1G_0V_1G_0V_3 + V_4G_0V_1 + V_1G_0V_4). \tag{11}$$

The second step towards isolation of the portion of V_5 that contains $T_{01}T_{10} * R_1^2 * (IM)_{j=1}$, is to notice that the selected part should match the exact travel time of the true internal multiple. Using this argument, and upon some inspection of the terms in V_5 provided in Ramírez (2007), it is recognized that the correct term within V_5 should reside in the lower-higher-lower contribution of $V_1G_0V_3G_0V_1$, and in particular the contribution to V_3 coming from $V_1G_0V_1G_0V_1$ needs to be further selected. In other words we are looking for an expression like

$$b_5^{IM}(k) \equiv \int_{-\infty}^{\infty} dz e^{ikz} b_1(z) \int_{-\infty}^{z-\epsilon} dz' e^{-ikz'} F[b_1(z')] \int_{z'+\epsilon}^{\infty} dz'' e^{ikz''} b_1(z''), \tag{12}$$

where, as is common for subseries of the ISS, the integrals have been expressed in terms of water-speed migrated data; i.e., in terms of $b_1(z)$. $F[b_1(z')]$ is the portion of $V_1G_0V_1G_0V_1$, expressed in terms of $b_1(z)$, that provides the two extra contributions R_1 we are looking for. As R_1 arises in the data as a result of interactions of the wave with the shallowest interface, to obtain $F[b_1(z')]$ we must split $V_1G_0V_1G_0V_1$ in a way that these interactions become explicit.

On the other hand, after isolating the model-type independent contribution of the term $V_1G_0V_1G_0V_1$, and expressing the result in terms of the water-speed migrated data, we arrive at the following expression:

$$\int_{-\infty}^{\infty} dz e^{ikz} b_1(z) \int_{-\infty}^{\infty} dz' e^{-ikz'} b_1(z') \int_{-\infty}^{\infty} dz'' e^{ikz''} b_1(z''), \tag{13}$$

which is the same term from which the leading-order attenuator is extracted, when we are working with V_3. The next step is to introduce, in order to extract the desired interactions from eq. (13), the same parameter ϵ included in the leading-order attenuator, eq. (3), and then to break the two right integrals in eq. (13) as

$$\int_{-\infty}^{\infty} dz' = \int_{-\infty}^{z-\epsilon} dz' + \int_{z-\epsilon}^{z+\epsilon} dz' + \int_{z+\epsilon}^{\infty} dz'$$

$$\int_{-\infty}^{\infty} dz'' = \int_{-\infty}^{z'-\epsilon} dz'' + \int_{z'-\epsilon}^{z'+\epsilon} dz'' + \int_{z'+\epsilon}^{\infty} dz''. \tag{14}$$

By using eq. (14), we arrive at the following expansion of eq. (13):

$$\int_{-\infty}^{\infty} dz e^{ikz} b_1(z) \int_{-\infty}^{\infty} dz' e^{-ikz'} b_1(z') \int_{-\infty}^{\infty} dz'' e^{ikz''} b_1(z'') =$$

$$\int_{-\infty}^{\infty} dz e^{ikz} b_1(z) \int_{-\infty}^{z-\epsilon} dz' e^{-ikz'} b_1(z') \int_{z'+\epsilon}^{\infty} dz'' e^{ikz''} b_1(z'')$$

$$+ \int_{-\infty}^{\infty} dz e^{ikz} b_1(z) \int_{z+\epsilon}^{\infty} dz' e^{-ikz'} b_1(z') \int_{-\infty}^{z'-\epsilon} dz'' e^{ikz''} b_1(z'')$$

$$+ \int_{-\infty}^{\infty} dz e^{ikz} b_1(z) \int_{z+\epsilon}^{\infty} dz' e^{-ikz'} b_1(z') \int_{z'+\epsilon}^{\infty} dz'' e^{ikz''} b_1(z'')$$

$$+ \int_{-\infty}^{\infty} dz e^{ikz} b_1(z) \int_{-\infty}^{z-\epsilon} dz' e^{-ikz'} b_1(z') \int_{-\infty}^{z'-\epsilon} dz'' e^{ikz''} b_1(z'')$$

$$+ \int_{-\infty}^{\infty} dz e^{ikz} b_1(z) \int_{z-\epsilon}^{z+\epsilon} dz' e^{-ikz'} b_1(z') \int_{z'-\epsilon}^{z'+\epsilon} dz'' e^{ikz''} b_1(z'')$$

$$+ \int_{-\infty}^{\infty} dz e^{ikz} b_1(z) \int_{z-\epsilon}^{z+\epsilon} dz' e^{-ikz'} b_1(z') \int_{z'+\epsilon}^{\infty} dz'' e^{ikz''} b_1(z'')$$

$$+ \int_{-\infty}^{\infty} dz e^{ikz} b_1(z) \int_{z-\epsilon}^{z+\epsilon} dz' e^{-ikz'} b_1(z') \int_{-\infty}^{z'-\epsilon} dz'' e^{ikz''} b_1(z'')$$

$$+ \int_{-\infty}^{\infty} dz e^{ikz} b_1(z) \int_{z+\epsilon}^{\infty} dz' e^{-ikz'} b_1(z') \int_{z'-\epsilon}^{z'+\epsilon} dz'' e^{ikz''} b_1(z'')$$

$$+ \int_{-\infty}^{\infty} dz e^{ikz} b_1(z) \int_{-\infty}^{z-\epsilon} dz' e^{-ikz'} b_1(z') \int_{z'-\epsilon}^{z'+\epsilon} dz'' e^{ikz''} b_1(z'') =$$

$$B_{31}(k) + B_{32}(k) + B_{33}(k) + B_{34}(k)$$

$$+ B_{35}(k) + B_{36}(k) + B_{37}(k) + B_{38}(k) + B_{39}(k). \tag{15}$$

From (15), we further select the fifth term $B_{35}(k)$, as this is the term containing the interactions with the first reflector: $z'' = z'$ and $z' = z$. In this way we have isolated the interactions and

their neighborhood. As this neighborhood is small, we expect we have done enough to reach our goal of elimination of internal multiples of first order with their downward reflection at the shallowest interface. It is interesting that the parameter ϵ is applied in this context to include the self-interactions, rather than to avoid them, as is the case for the leading-order attenuator.

The last step is to define $F[b_1(z)]$ as the inverse Fourier transform of $B_{35}(k)$:

$$F[b_1(z)] = \mathcal{F}^{-1}\left[\int_{-\infty}^{\infty} dz e^{ikz} b_1(z) \int_{z-\epsilon}^{z+\epsilon} dz' e^{-ikz'} b_1(z') \int_{z'-\epsilon}^{z'+\epsilon} dz'' e^{ikz''} b_1(z'')\right]. \tag{16}$$

In this way, we arrive at the second contribution towards elimination of internal multiples of first order with their downward reflection at the shallowest interface:

$$b_5^{IM}(k) = \int_{-\infty}^{\infty} dz e^{ikz} b_1(z) \int_{-\infty}^{z-\epsilon} dz' e^{-ikz'} F[b_1(z')] \int_{z'+\epsilon}^{\infty} dz'' e^{ikz''} b_1(z''). \tag{17}$$

In Appendix $A.2$ we show in detail how to perform the integrals in eq. (17), for the same model as the one in Figure 2 in Section 2.2. In the time domain the result is

$$b_5^{IM}(t) = R_1^3 (R_2')^2 \delta(t - (2t_2 - t_1)) + 2R_2' R_1^3 R_3' \delta(t - (t_2 + t_3 - t_1)) +$$

$$R_3' R_1^3 R_3' \delta(t - (2t_3 - t_1)) + (R_2')^3 (R_3')^2 \delta(t - (2t_3 - t_2)), \tag{18}$$

which can be expressed in terms of eqs. (7) and (8) as

$$b_5^{IM}(t) = -T_{01}T_{10} * R_1^2 * (IM)_{j=1} - (T_{01}T_{10})^2 * T_{12}T_{21} * (R_2')^2 (IM)_{j=2}. \tag{19}$$

If we now add eq. (19) to the effect of the leading order attenuator; i.e., to eq. (9), we get

$$b_1(t) + b_3(t) + b_5^{IM}(t) = primaries + [1 - T_{01}T_{10}(1 + R_1^2)](IM)_{j=1} +$$

$$[1 - (T_{01}T_{10})^2 * T_{12}T_{21} * (1 + (R_2')^2)](IM)_{j=2} + ... \tag{20}$$

Let's restrict our attention to the amplitude of the internal multiples generated at the shallowest reflector, i.e., to the coefficient of $(IM)_{j=1}$ in eq. (20). In this case the attenuation factor $T_{01}T_{10}$

is changed to $T_{01}T_{10}(1+R_1^2)$. This new contribution contains the first and second terms of the geometric series on the right-hand side of eq. (10). Hence, the integral proposed for b_5^{IM}, eq. (17), correctly reproduces the expected amplitude contribution to take the attenuation of first-order internal multiples with their downward reflection at the shallowest reflector closer to elimination.

To isolate higher-order contributions of the LOIMES, a process analogous to the isolation of $b_5^{IM}(k)$, eq. (12), is necessary. For example, the term following $b_5^{IM}(k)$, denoted as $b_7^{IM}(k)$, will be contained in the seventh term of the ISS. Specifically it will be in $V_1G_0V_5G_0V_1$, from which the part of V_5 corresponding to $V_1G_0V_1G_0V_1G_0V_1G_0V_1$ is further selected, followed by an expansion analogous to eq. (15). The difference is that in this case, there will be four integrals whose intervals of integration need to split. After computing a few higher-order terms, we can write, upon some formal definitions, a compact form for b_{LO}^{IM}:

$$b_{LO}^{IM}(k) = \int_{-\infty}^{\infty} dz e^{ikz} b_1(z) \int_{-\infty}^{z-\epsilon} dz' e^{-ikz'} \times$$

$$\mathcal{F}^{-1}\left(\int_{-\infty}^{\infty} dz' e^{ikz'} b_1(z') \frac{1}{1-\int\int b_1(z')}\right) \int_{z'+\epsilon}^{\infty} dz'' e^{ikz''} b_1(z''), \tag{21}$$

where $\mathcal{F}^{-1}$ means the inverse Fourier transform and

$$\frac{1}{1-\int\int b_1(z')} \equiv 1 + \int\int b_1(z') + \left(\int\int b_1(z')\right)^2 + \left(\int\int b_1(z')\right)^3 + \ldots, \tag{22}$$

with

$$\left(\int\int b_1(z')\right)^n \equiv \int_{z'-\epsilon}^{z'+\epsilon} dz_1 e^{-ikz_1} b_1(z_1) \int_{z_1-\epsilon}^{z_1+\epsilon} dz_2 e^{ikz_2} b_1(z_2) \times$$

$$\int_{z_2-\epsilon}^{z_2+\epsilon} dz_3 e^{-ikz_3} b_1(z_3) \int_{z_3-\epsilon}^{z_3+\epsilon} dz_4 e^{ikz_4} b_1(z_4) \cdots \times$$

$$\int_{z_{(2n-2)}-\epsilon}^{z_{(2n-2)}+\epsilon} dz_{(2n-1)} e^{-ikz_{(2n-1)}} b_1(z_{(2n-1)}) \int_{z_{(2n-1)}-\epsilon}^{z_{(2n-1)}+\epsilon} dz_{2n} e^{ikz_{2n}} b_1(z_{2n}), \qquad n > 0. \tag{23}$$

$$\left(\int\int b_1(z')\right)^n \equiv 1, \qquad n = 0. \tag{24}$$

Finally, it can also be seen from eq. (20) that $b_5^{IM}(t)$ further attenuates the internal multiple of first order generated at the second reflector. However, the LOIMES by itself will not match the amplitude of this event. For that to occur, another subseries needs to be isolated such that, in cooperation with the LOIMES, the elimination takes place. Earlier work on this direction was also reported in Ramírez (2007).

4 Application of the LOIMES to an analytic model

As was mentioned in the introduction, one motivation for the surgical elimination of internal multiples is that in some situations current techniques such as the energy-minimization adaptive subtraction are no longer suitable and attenuation of internal multiples is not enough. An example of such a situation is present when an internal multiple is interfering destructively with a primary. On the other hand, as the LOIMES exactly predicts both the travel time and amplitude of the original internal multiple, it can be considered to be an example of a method for surgical removal of internal multiples, because it does not modify any other event. In this section we will use an analytic model in which an internal multiple of first order is interfering destructively with a primary, and the attenuation provided by the leading-order attenuator is not enough for correct interpretation of the primary. We will use this example to show the usefulness of the LOIMES by surgically removing the internal multiple.

The analytic model is the three-interface model of Figure 2, with the specific values for the parameters shown in Figure 3. We will use the notation P_i for the primary generated at the reflector Z_i. First-order internal multiples are denoted as IM_{ijk}, for $i, j, k = 1, 2, 3$, with j indicating the reflector in which the downward reflection is generated; i and k indicate the reflectors in which the upward reflections are generated.

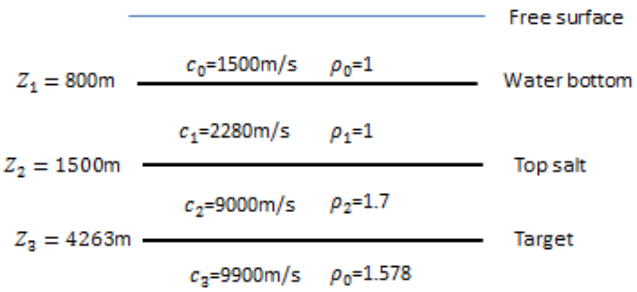

Figure 3: Specific analytic model. This model has the same configuration as that presented in Section 2, with the specified values for the depths, velocities, and densities.

The interfering events are the primary P_3 and the internal multiple IM_{212}, whose common travel time is 2.2947s. The amplitudes for P_3 and IM_{212} are 0.0045 and -0.1084, respectively. A trace is shown in Figure 4, from which the amplitude of the combined event $P_3 + IM_{212}$ can be read as -0.1039: the polarity is opposite that of the primary.

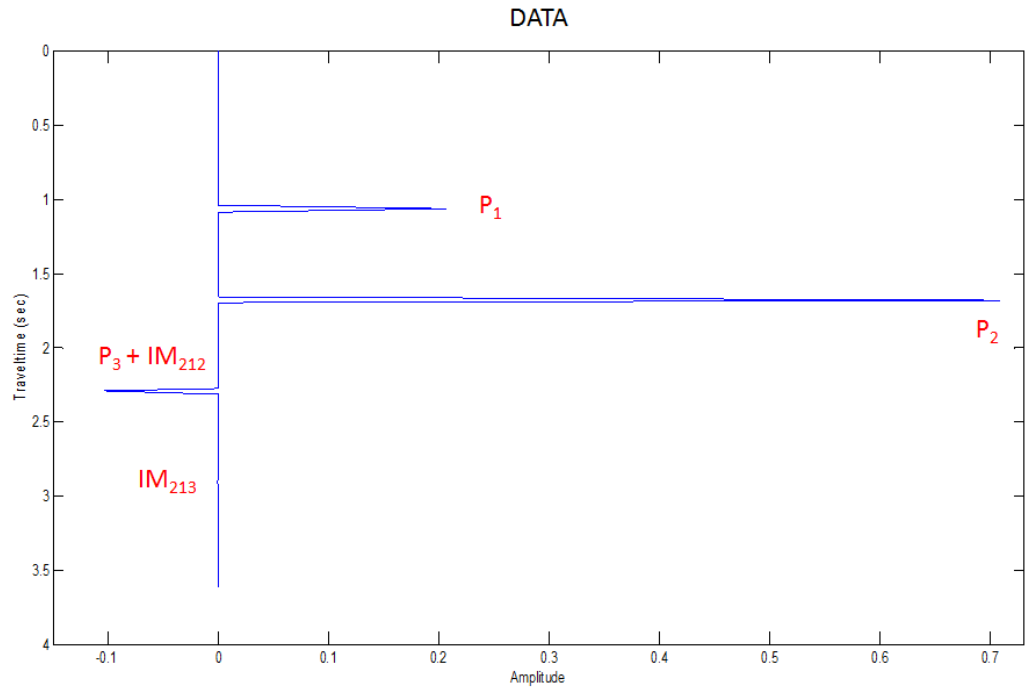

Figure 4: Data of the model. These data include primaries and the relevant internal multiples of first order.

The next step would be the application of $b_3(t)$ to attenuate internal multiples of first order. The result is shown in Figure 5, in which a small time window containing the travel time of the interfering event is shown with an increased scale, in order to make visible the attenuated amplitude. It can also be seen from the right side of Figure 5 that the primaries P_1 and P_2 are not affected at all. From the left side, we can see that the amplitude attenuation is not enough to change the polarity of the interfering event. This might lead to assignment of the incorrect polarity to the primary.

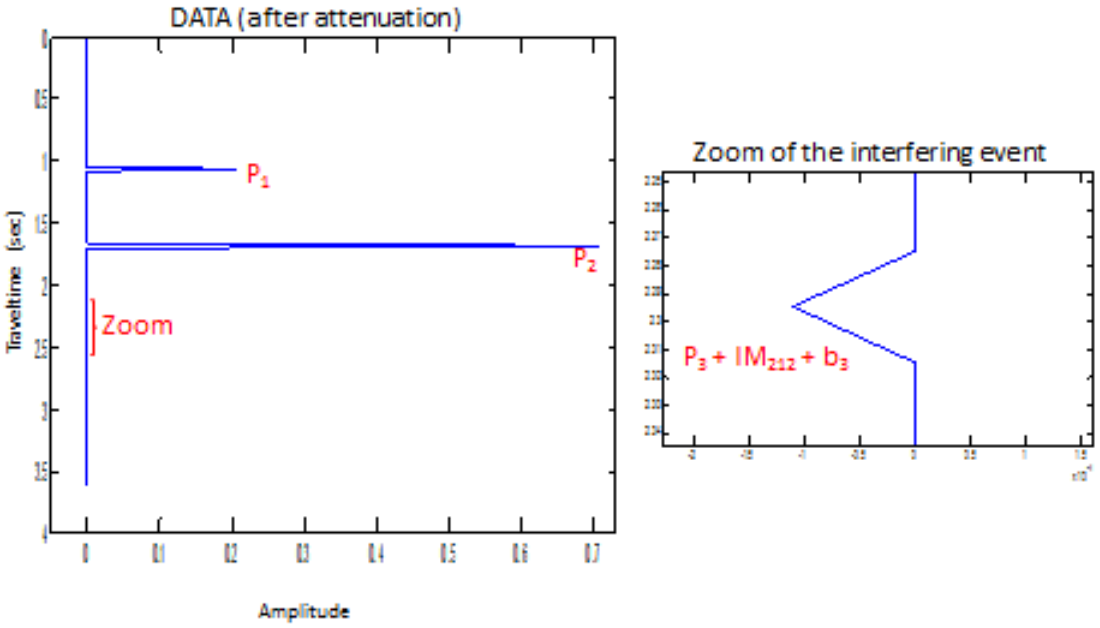

Figure 5: Data after the action of the leading-order attenuator, $b_3(t)$

From the above paragraph it is evident that an improvement in the predicted amplitude for IM_{212} is needed. As was explained in Section 3, this can be done if we include further terms from the LOIMES. This is shown in Figure 6, in which the effect of the second term, $b_5^{IM}(t)$, has been added to that of $b_3(t)$.

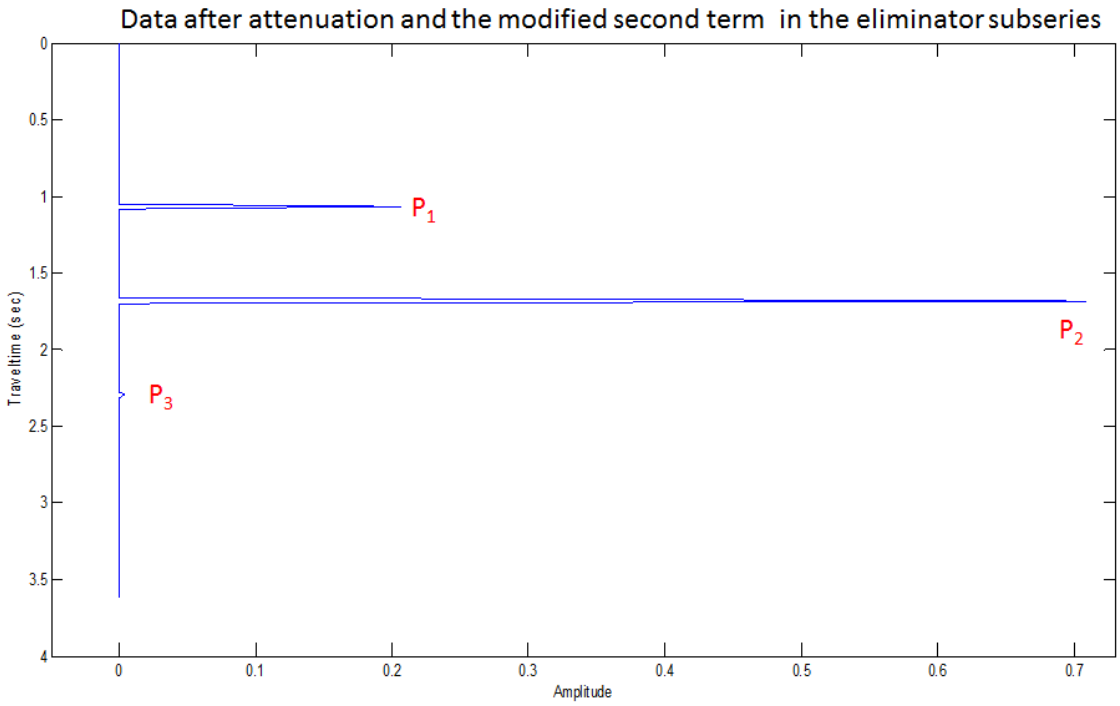

Figure 6: Data after the action of both the leading-order attenuator and $b_5^{IM}(t)$.

In this case, it can be seen that the primary P_3 appears with its original amplitude and polarity, 0.0045, which means that the interfering internal multiple has been removed. This illustrates, at least for the present model, the high rate of convergence of the LOIMES. However, for more complex models the convergence can be slower, and more terms might be needed. Also, from Figure 6, it can be noticed that neither the travel times nor the amplitudes of the primaries P_1 and P_2 are influenced or changed, as expected from a method for surgical removal of internal multiples.

5 Discussion and conclusions

In this work we have isolated a subseries whose task is to eliminate first-order internal multiples with their downward reflections at the shallowest interface. A generic term of this subseries is given by eqs. (21)-(24). This subseries is called the leading-order internal multiple elimination subseries (LOIMES). This elimination subseries predicts the phase and the exact amplitude of the internal multiples and does not modify any primary. Therefore, the surgical removal of such internal multiples is achieved.

We have also applied the LOIMES to an analytic example with three interfaces. The configuration is set up to produce an internal multiple (with downward reflection at the shallowest reflector) interfering destructively with the primary generated at the third reflector, in a way that the leading-order attenuator is not enough to let the primary show up in the data with its correct polarity. We show how the action of the third-order and fifth-order contributions of the algorithm remove the interfering internal multiple, making the primary to appear in the trace with its original amplitude and polarity. In practice however, it is not possible to know a priori the number of terms that are necessary to eliminate the interfering internal multiple. The recipe is to apply to the data one term at a time until no change is noticed in the primary. Although higher-order terms will imply an increased computational cost (more integrals need to be calculated), if the interfering primary is suspected to be the target, then the investment might be worthwhile, as a situation involving a drilling or no drilling decision might be involved and processing costs pale compared to drilling dry holes.

Interfering events are common in onshore exploration, but they may also occur offshore. Therefore, the algorithm in this work may provide added value in those challenging geologic configurations in which techniques such as the energy-minimization adaptive subtraction fails.

So far, we have assumed that the earth is acoustic. It would be interesting to study the properties of the LOIMES, with the assumption of the more realistic situation of an elastic earth, in which the internal multiple can include S-waves.

Further research in this topic includes extending the method beyond the normal incidence assumption of the present work, and to derive the corresponding multidimensional version of the subseries presented here. Additionally, current challenges in exploration seismology might also require the removal of other internal multiples of first-order, generated beneath the shallowest reflector. Hence, a more general research goal is to isolate a subseries, with the specific task of the elimination of first-order internal multiples generated at all reflectors.

So far, we have assumed that the earth is acoustic. It would be interesting to study the properties of the LOIMES, with the assumption of the more realistic situation of an elastic earth, in which the internal multiple can include S-waves.

A Calculation of the leading-order attenuator, $b_3(t)$

Now we will show the key steps involved in calculation of eq. (3). We will use the 1D model with three interfaces shown in Figure 2, with data generated by a spike wave with normal incidence, i.e.,

when the input is given by eq. (5). We will follow the procedure described in Weglein et al. (2003), in which a 1D model with two interfaces is presented.

A.1 Preparing the input for the Leading-order attenuator

The first task is to obtain $b_1(z)$ from the data of the model, eq. (4), which for convenience is repeated here:

$$D(t) = R_1\delta(t-t_1) + R_2'\delta(t-t_2) + R_3'\delta(t-t_3) + IM,$$

where R_2', R_3' and t_i are as in Section 3.

As it was mentioned in the main body of this work, formally $b_1(z)$ is obtained by Stolt's migration of eq. (4) using the water speed. However the procedure is captured, in this case, by a simple set of rules:

1. Perform a temporal Fourier transform

$$D(\omega) = R_1 e^{i\omega t_1} + R_2' e^{i\omega t_2} + R_3' e^{i\omega t_3} + ...$$

2. Define the vertical wavenumber and pseudodepths

$$k = 2\frac{\omega}{c_0} \qquad\qquad z_i = \frac{c_0 t_i}{2}.$$

   Now D can be written as

$$D(k) = R_1 e^{ikz_1} + R_2' e^{ikz_2} + R_3' e^{ikz_3} + ...$$

3. Perform a Fourier transform on k and denote the result as $b_1(z)$:

$$b_1(z) \equiv D(z) = R_1\delta(z-z_1) + R_2'\delta(z-z_2) + R_3'\delta(z-z_3) + ...$$

   In the general case, $b_1(z)$ is $D(z)$ times an obliquity factor. In our case, this factor is not needed as we are considering normal incidence of a plane wave; i.e., $b_1(z) \equiv D(z)$. The role of the obliquity factor in more general situations is to produce a plane wave in the Fourier domain (see Weglein et al. 2003).

The equation in item 3 is the input for the leading-order attenuator, eq. (3), and it matches exactly eq. (5) in Section 2.2.

A.2 Explicit calculation of the analytic expression for $b_3(t)$

We will now insert eq. (5) into eq. (3), which for convenience is repeated here:

$$\int_{-\infty}^{\infty} dz e^{ikz} b_1(z) \int_{-\infty}^{z-\epsilon} dz' e^{-ikz'} b_1(z') \int_{z'+\epsilon}^{\infty} dz'' e^{ikz''} b_1(z'').$$

We start the evaluation of the above expression with the integral on the right (we only take into account the primaries):

$$\int_{z'+\epsilon}^{\infty} dz'' e^{ikz''} b_1(z) = \int_{z'+\epsilon}^{\infty} dz'' e^{ikz''} [R_1 \delta(z''-z_1) + R_2' \delta(z''-z_2) + R_3' \delta(z''-z_2)] =$$

$$\int_{-\infty}^{\infty} dz'' e^{ikz''} [R_1 \delta(z''-z_1) H(z''-(z'+\epsilon)) + R_2' \delta(z''-z_2) H(z''-(z'+\epsilon)) +$$

$$R_3' \delta(z''-z_2) H(z''-(z'+\epsilon))] =$$

$$R_1 e^{ikz_1} H(z_1-(z'+\epsilon)) + R_2' e^{ikz_2} H(z_2-(z'+\epsilon)) + R_3' e^{ikz_3} H(z_3-(z'+\epsilon)). \tag{25}$$

As it will be used repeatedly throughout the present and the next appendices, it is worthwhile to say some words about the procedure to go from the second term to the third one in eq. (25). The interval of integration is extended from $z'-\epsilon$ to ∞, but Heaviside functions are introduced at each term of the integrand, with each Heaviside function having the appropriate argument to avoid the modification the original integral.

Substituting eq. (25) into the second integral of eq. (3) , we get

$$\int_{-\infty}^{z-\epsilon} dz' e^{-ikz'} [R_1 \delta(z'-z_1) + R_2' \delta(z'-z_2) + R_3' \delta(z'-z_3)] \times$$

$$[R_1 e^{ikz_1} H(z_1-(z'+\epsilon)) + R_2' e^{ikz_2} H(z_2-(z'+\epsilon)) + R_3' e^{ikz_3} H(z_3-(z'+\epsilon))]$$

$$= \int_{-\infty}^{z-\epsilon} dz' e^{-ikz'} R_1 \delta(z'-z_1) R_1 e^{ikz_1} H(z_1-(z'+\epsilon)) +$$

$$\int_{-\infty}^{z-\epsilon} dz' e^{-ikz'} R_1 \delta(z'-z_1) R_2' e^{ikz_2} H(z_2-(z'+\epsilon)) +$$

$$\int_{-\infty}^{z-\epsilon} dz' e^{-ikz'} R_1 \delta(z'-z_1) R_3' e^{ikz_3} H(z_3-(z'+\epsilon)) +$$

$$\int_{-\infty}^{z-\epsilon} dz' e^{-ikz'} R_2' \delta(z'-z_2) R_1 e^{ikz_1} H(z_1-(z'+\epsilon)) +$$

$$\int_{-\infty}^{z-\epsilon} dz' e^{-ikz'} R_2' \delta(z'-z_2) R_2' e^{ikz_2} H(z_2-(z'+\epsilon)) +$$

$$\int_{-\infty}^{z-\epsilon} dz' e^{-ikz'} R_2' \delta(z'-z_2) R_3' e^{ikz_3} H(z_3-(z'+\epsilon)) +$$

$$\int_{-\infty}^{z-\epsilon} dz' e^{-ikz'} R_3' \delta(z'-z_3) R_1 e^{ikz_1} H(z_1-(z'+\epsilon)) +$$

$$\int_{-\infty}^{z-\epsilon} dz' e^{-ikz'} R_3' \delta(z'-z_3) R_2' e^{ikz_2} H(z_2-(z'+\epsilon)) +$$

$$\int_{-\infty}^{z-\epsilon} dz' e^{-ikz'} R_3' \delta(z'-z_3) R_3' e^{ikz_3} H(z_3-(z'+\epsilon)) =$$

$$I_1 + I_2 + I_3 + I_4 + I_5 + I_6 + I_7 + I_8 + I_9. \tag{26}$$

Evaluating each of the integrals in eq. (26) we get

$$I_1 = \int_{-\infty}^{z-\epsilon} dz' e^{-ikz'} R_1 \delta(z'-z_1) R_1 e^{ikz_1} H(z_1-(z'+\epsilon)) = R_1^4 \underbrace{H(z_1-(z_1+\epsilon))}_{=0} H((z-\epsilon)-z_1) = 0,$$

$$I_2 = \int_{-\infty}^{z-\epsilon} dz' e^{-ikz'} R_1 \delta(z'-z_1) R_2' e^{ikz_2} H(z_2-(z'+\epsilon)) =$$

$$R_1 R_2' e^{ik(z_2-z_1)} H(z_2-(z_1+\epsilon)) H((z-\epsilon)-z_1),$$

$$I_3 = \int_{-\infty}^{z-\epsilon} dz' e^{-ikz'} R_1 \delta(z'-z_1) R_3' e^{ikz_3} H(z_3-(z'+\epsilon)) =$$

$$R_1 R_3' e^{ik(z_3-z_1)} H(z_3-(z_1+\epsilon)) H((z-\epsilon)-z_1),$$

$$I_4 = \int_{-\infty}^{z-\epsilon} dz' e^{-ikz'} R_2' \delta(z'-z_2) R_1 e^{ikz_1} H(z_1-(z'+\epsilon)) =$$

$$R_1 R_2' e^{ik(z_1-z_2)} \underbrace{H(z_1-(z_2+\epsilon))}_{=0} H((z-\epsilon)-z_2) = 0,$$

$$I_5 = \int_{-\infty}^{z-\epsilon} dz' e^{-ikz'} R_2' \delta(z'-z_2) R_2' e^{ikz_2} H(z_2-(z'+\epsilon)) =$$

$$R_2' \underbrace{H(z_2-(z_2+\epsilon))}_{=0} H((z-\epsilon)-z_2) = 0,$$

$$I_6 = \int_{-\infty}^{z-\epsilon} dz' e^{-ikz'} R_2' \delta(z'-z_2) R_3' e^{ikz_3} H(z_3-(z'+\epsilon)) =$$

$$R_2' R_3' e^{ik(z_3-z_2)} H((z-\epsilon)-z_2),$$

$$I_7 = \int_{-\infty}^{z-\epsilon} dz' e^{-ikz'} R_3' \delta(z'-z_3) R_1 e^{ikz_1} H(z_1-(z'+\epsilon)) =$$

$$R_1 R_3' e^{ik(z_1-z_3)} \underbrace{H(z_1-(z_3+\epsilon))}_{=0},$$

$$I_8 = \int_{-\infty}^{z-\epsilon} dz' e^{-ikz'} R_3' \delta(z'-z_3) R_2' e^{ikz_2} H(z_2-(z'+\epsilon)) =$$

$$R_2' R_3' e^{ik(z_2-z_3)} \underbrace{H(z_2-(z_3+\epsilon))}_{=0},$$

$$I_9 = \int_{-\infty}^{z-\epsilon} dz' e^{-ikz'} R_3' \delta(z' - z_3) R_3' e^{ikz_3} H(z_3 - (z' + \epsilon)) =$$

$$R_3' \underbrace{H(z_3 - (z_3 + \epsilon))}_{=0}.$$

Hence, the result of the second integral in eq. (3) is

$$I_1 + I_2 + I_3 + I_4 + I_5 + I_6 + I_7 + I_8 + I_9$$

$$= R_1 R_2' e^{ik(z_2 - z_1)} H((z-\epsilon) - z_1) + R_1 R_3' e^{ik(z_3 - z_1)} H((z-\epsilon) - z_1) + R_2' R_3' e^{ik(z_3 - z_2)} H((z-\epsilon) - z_2). \quad (27)$$

Substituting eq. (27), into the last integral of eq. (3), we finally have

$$b_3(k) = \int_{-\infty}^{\infty} dz e^{ikz} [R_1 \delta(z - z_1) + R_2' \delta(z - z_2) + R_3' \delta(z - z_3)] \times$$

$$[R_1 R_2' e^{ik(z_2 - z_1)} H((z - \epsilon) - z_1) + R_1 R_3' e^{ik(z_3 - z_1)} H((z - \epsilon) - z_1) + (R_2') R_3' e^{ik(z_3 - z_2)} H((z - \epsilon) - z_2)]$$

$$= \int_{-\infty}^{\infty} dz e^{ikz} R_1 \delta(z - z_1) R_1 R_2' e^{ik(z_2 - z_1)} H((z - \epsilon) - z_1) +$$

$$\int_{-\infty}^{\infty} dz e^{ikz} R_1 \delta(z - z_1) R_1 R_3' e^{ik(z_3 - z_1)} H((z - \epsilon) - z_1) +$$

$$\int_{-\infty}^{\infty} dz e^{ikz} R_1 \delta(z - z_1) R_2' R_3' e^{ik(z_3 - z_2)} H((z - \epsilon) - z_2) +$$

$$\int_{-\infty}^{\infty} dz e^{ikz} R_2' \delta(z - z_2) R_1 R_2' e^{ik(z_2 - z_1)} H((z - \epsilon) - z_1) +$$

$$\int_{-\infty}^{\infty} dz e^{ikz} R_2' \delta(z - z_2) R_1 R_3' e^{ik(z_3 - z_1)} H((z - \epsilon) - z_1) +$$

$$\int_{-\infty}^{\infty} dz e^{ikz} R_2' \delta(z - z_2) R_2' R_3' e^{ik(z_3 - z_2)} H((z - \epsilon) - z_2) +$$

$$\int_{-\infty}^{\infty} dz e^{ikz} R_3' \delta(z - z_3) R_1 R_2' e^{ik(z_2 - z_1)} H((z - \epsilon) - z_1) +$$

$$\int_{-\infty}^{\infty} dz e^{ikz} R_3' \delta(z - z_3) R_1 R_3' e^{ik(z_3 - z_1)} H((z - \epsilon) - z_1) +$$

$$\int_{-\infty}^{\infty} dz e^{ikz} R_3' \delta(z - z_3) R_2' R_3' e^{ik(z_3 - z_2)} H((z - \epsilon) - z_2) =$$

$$I_1' + I_2' + I_3' + I_4' + I_5' + I_6' + I_7' + I_8' + I_9'. \tag{28}$$

Evaluating now the integrals in (28), we get

$$I_1' = \int_{-\infty}^{\infty} dz e^{ikz} R_1 \delta(z - z_1) R_1 R_2' e^{ik(z_2 - z_1)} H((z - \epsilon) - z_1) =$$

$$R_1^2 R_2' e^{ik(z_2 - 2z_1)} \underbrace{H((z_1 - \epsilon) - z_1)}_{=0},$$

$$I_2' = \int_{-\infty}^{\infty} dz e^{ikz} R_1 \delta(z - z_1) R_1 R_3' e^{ik(z_3 - z_1)} H((z - \epsilon) - z_1) =$$

$$R_1^2 R_3' e^{ik(z_3 - 2z_1)} \underbrace{H((z_1 - \epsilon) - z_1)}_{=0},$$

$$I_3' = \int_{-\infty}^{\infty} dz e^{ikz} R_1 \delta(z - z_1) R_2' R_3' e^{ik(z_3 - z_2)} H((z - \epsilon) - z_2) =$$

$$R_1 R_2' R_3' e^{ik(z_1 + z_3 - z_2)} \underbrace{H((z_1 - \epsilon) - z_2)}_{=0},$$

$$I_4' = \int_{-\infty}^{\infty} dz e^{ikz} R_2' \delta(z - z_2) R_1 R_2' e^{ik(z_2 - z_1)} H((z - \epsilon) - z_1)$$

$$R_1(R_2')^2 e^{ik(2z_2-z_1)},$$

$$I_5' = \int_{-\infty}^{\infty} dz e^{ikz} R_2' \delta(z-z_2) R_1 R_3' e^{ik(z_3-z_1)} H((z-\epsilon)-z_1) =$$

$$R_2' R_1 R_3' e^{ik(z_2+z_3-z_1)},$$

$$I_6' = \int_{-\infty}^{\infty} dz e^{ikz} R_2' \delta(z-z_2) R_2' R_3' e^{ik(z_3-z_2)} H((z-\epsilon)-z_2) =$$

$$R_2' R_3' e^{ik(z_3-2z_2)} \underbrace{H((z_2-\epsilon)-z_2)}_{=0},$$

$$I_7' = \int_{-\infty}^{\infty} dz e^{ikz} R_3' \delta(z-z_3) R_1 R_2' e^{ik(z_2-z_1)} H((z-\epsilon)-z_1) =$$

$$R_3' R_1 R_2' e^{ik(z_3+z_2-z_1)},$$

$$I_8' = \int_{-\infty}^{\infty} dz e^{ikz} R_3' \delta(z-z_3) R_1 R_3' e^{ik(z_3-z_1)} H((z-\epsilon)-z_1) =$$

$$R_3' R_1^3 R_3' e^{ik(2z_3-z_1)},$$

$$I_9' = \int_{-\infty}^{\infty} dz e^{ikz} R_3' \delta(z-z_3) R_2' R_3' e^{ik(z_3-z_2)} H((z-\epsilon)-z_2) =$$

$$R_2'(R_3')^2 e^{ik(2z_3-z_2)}.$$

With the results above, the sum of the integrals in eq. (28) gives

$$b_3(k) = R_1(R_2')^2 e^{ik(2z_2-z_1)} + 2R_2' R_1 R_3' e^{ik(z_2+z_3-z_1)} +$$

$$= R_1(R_2')^2 e^{ik(2z_2-z_1)} + 2R_2'R_1R_3' e^{ik(z_2+z_3-z_1)} + R_3'R_1R_3' e^{ik(2z_3-z_1)} + R_2'(R_3')^2 e^{ik(2z_3-z_2)},$$

which in the time domain is expressed as

$$b_3(t) = R_1(R_2')^2\delta(t-(2t_2-t_1)) + 2R_2'R_1R_3'\delta(t-(t_2+t_3-t_1)) + R_3'R_1R_3'\delta(t-(2t_3-t_1)) + R_2'(R_3')^2\delta(t-(2t_3-t_2))$$

$$b_3(t) = -T_{01}T_{10} * (IM)_{j=1} - (T_{01}T_{10})^2 * T_{12}T_{21} * (IM)_{j=2}.$$

The above expression is exactly eq. (6). $(IM)_{j=1}$ and $(IM)_{j=2}$ represent the contributions of the internal multiples (of first order) with their downward reflection originating at the first (shallowest) and second reflectors, respectively. Their analytic expressions are given by eqs. (7) and (8):

$$(IM)_{j=1} = -T_{01}R_2R_1R_2T_{10}\delta(t-(2t_2-t_1))$$

$$-2T_{01}R_2R_1T_{21}R_3T_{12}T_{10}\delta(t-(t_2+t_3-t_1)) - T_{01}T_{12}^2R_3R_1R_3T_{21}^2\delta(t-(2t_3-t_1)).$$

$$(IM)_{j=2} = -T_{01}T_{12}R_3R_2R_3T_{10}T_{21}\delta(t-(2t_3-t_1)).$$

B Explicit calculation of the expression for $b_5^{IM}(t)$

In this appendix we will provide the details of the calculation of $b_5^{IM}(k)$, using the second term of the LOIMES, which is presented here for convenience:

$$b_5^{IM}(k) = \int_{-\infty}^{\infty} dz e^{ikz} b_1(z) \int_{-\infty}^{z-\epsilon} dz' e^{-ikz'} F[b_1(z')] \int_{z'+\epsilon}^{\infty} dz'' e^{ikz''} b_1(z''),$$

where

$$F[b_1(z)] = \mathcal{F}^{-1}\left[\int_{-\infty}^{\infty} dz e^{ikz} b_1(z) \int_{z-\epsilon}^{z+\epsilon} dz' e^{-ikz'} b_1(z') \int_{z'-\epsilon}^{z'+\epsilon} dz'' e^{ikz''} b_1(z'')\right].$$

We start with the evaluation of $F[b_1(z)]$. First we insert eq. (5) into the right integral of $F[b_1(z)]$. Then, by extension of the interval of integration and insertion of the convenient Heaviside functions, as in Appendix A, we get

$$\int_{z'-\epsilon}^{z'+\epsilon} dz'' e^{ikz''} b_1(z'') = \int_{z'-\epsilon}^{z'+\epsilon} dz'' e^{ikz''} [R_1\delta(z''-z_1) + R_2'\delta(z''-z_2) + R_3'\delta(z''-z_3)] =$$

$$R_1 e^{ikz_1} H(z_1-(z'-\epsilon))H((z'+\epsilon)-z_1) + R_2' e^{ikz_2} H(z_2-(z'-\epsilon))H((z'+\epsilon)-z_2) +$$

$$R_3' e^{ikz_3} H(z_3-(z'-\epsilon))H((z'+\epsilon)-z_3). \tag{29}$$

Substituting eq. (29) into the second integral in $F[b_1(z')]$, we have

$$\int_{z-\epsilon}^{z+\epsilon} dz' e^{-ikz'} b_1(z') [R_1 e^{ikz_1} H(z_1-(z'-\epsilon))H((z'+\epsilon)-z_1) +$$

$$R_2' e^{ikz_2} H(z_2-(z'-\epsilon))H((z'+\epsilon)-z_2) + R_3' e^{ikz_3} H(z_3-(z'-\epsilon))H((z'+\epsilon)-z_3)]$$

$$= \int_{z-\epsilon}^{z+\epsilon} dz' e^{-ikz'} [R_1\delta(z'-z_1) + R_2'\delta(z'-z_2) + R_3'\delta(z'-z_3)] \times$$

$$[R_1 e^{ikz_1} H(z_1-(z'-\epsilon))H((z'+\epsilon)-z_1) + R_2' e^{ikz_2} H(z_2-(z'-\epsilon))H((z'+\epsilon)-z_2)$$

$$+ R_3' e^{ikz_3} H(z_3-(z'-\epsilon))H((z'+\epsilon)-z_3)] =$$

$$\int_{z-\epsilon}^{z+\epsilon} dz' e^{-ikz'} R_1\delta(z'-z_1) R_1 e^{ikz_1} H(z_1-(z'-\epsilon))H((z'+\epsilon)-z_1) +$$

$$\int_{z-\epsilon}^{z+\epsilon} dz' e^{-ikz'} R_1\delta(z'-z_1) R_2' e^{ikz_2} H(z_2-(z'-\epsilon))H((z'+\epsilon)-z_2)) +$$

$$\int_{z-\epsilon}^{z+\epsilon} dz' e^{-ikz'} R_1\delta(z'-z_1) R_3' e^{ikz_3} H(z_3-(z'-\epsilon))H((z'+\epsilon)-z_3)) +$$

$$\int_{z-\epsilon}^{z+\epsilon} dz' e^{-ikz'} R_2' \delta(z'-z_2) R_1 e^{ikz_1} H(z_1-(z'-\epsilon)) H((z'+\epsilon)-z_1)+$$

$$\int_{z-\epsilon}^{z+\epsilon} dz' e^{-ikz'} R_2' \delta(z'-z_2) R_2' e^{ikz_2} H(z_2-(z'-\epsilon)) H((z'+\epsilon)-z_2)+$$

$$\int_{z-\epsilon}^{z+\epsilon} dz' e^{-ikz'} R_2' \delta(z'-z_2) R_3' e^{ikz_3} H(z_3-(z'-\epsilon)) H((z'+\epsilon)-z_3)+$$

$$\int_{z-\epsilon}^{z+\epsilon} dz' e^{-ikz'} R_3' \delta(z'-z_3) R_1 e^{ikz_1} H(z_1-(z'-\epsilon)) H((z'+\epsilon)-z_1)+$$

$$\int_{z-\epsilon}^{z+\epsilon} dz' e^{-ikz'} R_3' \delta(z'-z_3) R_2' e^{ikz_2} H(z_2-(z'-\epsilon)) H((z'+\epsilon)-z_2)+$$

$$\int_{z-\epsilon}^{z+\epsilon} dz' e^{-ikz'} R_3' \delta(z'-z_3) R_3' e^{ikz_3} H(z_3-(z'-\epsilon)) H((z'+\epsilon)-z_3)$$

$$I_1 + I_2 + I_3 + I_4 + I_5 + I_6 + I_7 + I_8 + I_9. \tag{30}$$

The integrals in (30) are evaluated as follows:

$$I_1 = \int_{z-\epsilon}^{z+\epsilon} dz' e^{-ikz'} R_1 \delta(z'-z_1) R_1 e^{ikz_1} H(z_1-(z'-\epsilon)) H((z'+\epsilon)-z_1) =$$

$$R_1^2 e^{-ikz_1} e^{ikz_1} H(z_1-(z-\epsilon)) H((z+\epsilon)-z_1) \underbrace{H(z_1-(z_1-\epsilon))}_{=1} \underbrace{H((z_1+\epsilon)-z_1)}_{=1} =$$

$$R_1^2 H(z_1-(z-\epsilon)) H((z+\epsilon)-z_1),$$

$$I_2 = \int_{z-\epsilon}^{z+\epsilon} dz' e^{-ikz'} R_1 \delta(z'-z_1) R_2' e^{ikz_2} H(z_2-(z'-\epsilon)) H((z'+\epsilon)-z_2) =$$

$$R_1 R_2' e^{-ikz_1} e^{ikz_2} H(z_1-(z-\epsilon)) H((z+\epsilon)-z_1) H(z_2-(z_1-\epsilon)) \underbrace{H((z_1+\epsilon)-z_2)}_{=0} = 0,$$

$$I_3 = \int_{z-\epsilon}^{z+\epsilon} dz' e^{-ikz'} R_1 \delta(z' - z_1) R_3' e^{ikz_3} H(z_3 - (z' - \epsilon)) H((z' + \epsilon) - z_3) =$$

$$R_1 R_3' e^{-ikz_1} e^{ikz_3} H(z_1 - (z - \epsilon)) H((z + \epsilon) - z_1) H(z_3 - (z_1 - \epsilon)) \underbrace{H((z_1 + \epsilon) - z_3)}_{=0} = 0,$$

$$I_4 = \int_{z-\epsilon}^{z+\epsilon} dz e^{-ikz'} R_2' \delta(z' - z_2) R_1 e^{ikz_1} H(z_1 - (z' - \epsilon)) H((z' + \epsilon) - z_1) =$$

$$R_1 R_2' e^{-ikz_2} e^{ikz_1} H(z_2 - (z - \epsilon)) H((z + \epsilon) - z_2) \underbrace{H(z_1 - (z_2 - \epsilon))}_{=0} H((z_2 + \epsilon) - z_1) = 0,$$

$$I_5 = \int_{z-\epsilon}^{z+\epsilon} dz e^{-ikz'} R_2' \delta(z' - z_2) R_2' e^{ikz_2} H(z_2 - (z' - \epsilon)) H((z' + \epsilon) - z_2) =$$

$$(R_2')^2 e^{-ikz_2} e^{ikz_2} H(z_2 - (z - \epsilon)) H((z + \epsilon) - z_2) H(z_2 - (z_2 - \epsilon)) H((z_2 + \epsilon) - z_2) =$$

$$(R_2')^2 H(z_2 - (z - \epsilon)) H((z + \epsilon) - z_2),$$

$$I_6 = \int_{z-\epsilon}^{z+\epsilon} dz e^{-ikz'} R_2' \delta(z' - z_2) R_3' e^{ikz_3} H(z_3 - (z' - \epsilon)) H((z' + \epsilon) - z_3) =$$

$$R_3' R_2' e^{-ikz_2} e^{ikz_3} H(z_2 - (z - \epsilon)) H((z + \epsilon) - z_2) \underbrace{H(z_3 - (z_2 - \epsilon))}_{=0} H((z_2 + \epsilon) - z_3) = 0,$$

$$I_7 = \int_{z-\epsilon}^{z+\epsilon} dz e^{-ikz'} R_3' \delta(z' - z_3) R_1 e^{ikz_1} H(z_1 - (z' - \epsilon)) H((z' + \epsilon) - z_1) =$$

$$R_1 R_3' e^{-ikz_3} e^{ikz_1} H(z_3 - (z - \epsilon)) H((z + \epsilon) - z_3) \underbrace{H(z_1 - (z_3 - \epsilon))}_{=0} H((z_3 + \epsilon) - z_1) = 0,$$

$$I_8 = \int_{z-\epsilon}^{z+\epsilon} dz e^{-ikz'} R_3' \delta(z' - z_3) R_2' e^{ikz_2} H(z_2 - (z' - \epsilon)) H((z' + \epsilon) - z_2) =$$

$$R_3' R_2' e^{-ikz_3} e^{ikz_2} H(z_3 - (z-\epsilon)) H((z+\epsilon) - z_3) \underbrace{H(z_2 - (z_3 - \epsilon))}_{=0} H((z_3+\epsilon) - z_2) = 0,$$

$$I_9 = \int_{z-\epsilon}^{z+\epsilon} dz e^{-ikz'} R_3' \delta(z' - z_3) R_3' e^{ikz_3} H(z_3 - (z' - \epsilon)) H((z'+\epsilon) - z_3) =$$

$$(R_3')^2 e^{-ikz_3} e^{ikz_3} H(z_3 - (z-\epsilon)) H((z+\epsilon) - z_3) H(z_3 - (z_3 - \epsilon)) H((z_3+\epsilon) - z_3) =$$

$$(R_3')^2 H(z_3 - (z-\epsilon)) H((z+\epsilon) - z_3). \tag{31}$$

Upon substitution of the integrals just calculated, we get

$$I_1 + I_2 + I_3 + I_4 + I_5 + I_6 + I_7 + I_8 + I_9 =$$

$$R_1^2 H(z_1 - (z-\epsilon)) H((z+\epsilon) - z_1) + (R_2')^2 H(z_2 - (z-\epsilon)) H((z+\epsilon) - z_2) +$$

$$(R_3')^2 H(z_3 - (z-\epsilon)) H((z+\epsilon) - z_3). \tag{32}$$

Finally, substituting eq. (32) into the third integral in $F[b_1(z')]$, and using the notation of eq. (15), we end up with

$$\int_{-\infty}^{\infty} dz e^{ikz} [R_1 \delta(z - z_1) + R_2' \delta(z - z_2) + R_3' \delta(z - z_3)] \times$$

$$[R_1^2 H(z_1 - (z-\epsilon)) H((z+\epsilon) - z_1) + (R_2')^2 H(z_2 - (z-\epsilon)) H((z+\epsilon) - z_2) +$$

$$(R_3')^2 H(z_3 - (z-\epsilon)) H((z+\epsilon) - z_3)] =$$

$$\int_{-\infty}^{\infty} dz e^{ikz} R_1 \delta(z - z_1) R_1^2 H(z_1 - (z-\epsilon)) H((z+\epsilon) - z_1) +$$

$$\int_{-\infty}^{\infty} dz e^{ikz} R_1 \delta(z - z_1)(R_2')^2 H(z_2 - (z - \epsilon))H((z + \epsilon) - z_2) +$$

$$\int_{-\infty}^{\infty} dz e^{ikz} R_1 \delta(z - z_1)(R_3')^2 H(z_3 - (z - \epsilon))H((z + \epsilon) - z_3) +$$

$$\int_{-\infty}^{\infty} dz e^{ikz} R_2' \delta(z - z_2) R_1^2 H(z_1 - (z - \epsilon))H((z + \epsilon) - z_1) +$$

$$\int_{-\infty}^{\infty} dz e^{ikz} R_2' \delta(z - z_2)(R_2')^2 H(z_2 - (z - \epsilon))H((z + \epsilon) - z_2) +$$

$$\int_{-\infty}^{\infty} dz e^{ikz} R_2' \delta(z - z_2)(R_3')^2 H(z_3 - (z - \epsilon))H((z + \epsilon) - z_3) +$$

$$\int_{-\infty}^{\infty} dz e^{ikz} R_3' \delta(z - z_3) R_1^2 H(z_1 - (z - \epsilon))H((z + \epsilon) - z_1) +$$

$$\int_{-\infty}^{\infty} dz e^{ikz} R_3' \delta(z - z_3)(R_2')^2 H(z_2 - (z - \epsilon))H((z + \epsilon) - z_2) +$$

$$\int_{-\infty}^{\infty} dz e^{ikz} R_3' \delta(z - z_3)(R_3')^2 H(z_3 - (z - \epsilon))H((z + \epsilon) - z_3) =$$

$$I_1' + I_2' + I_3' + I_4' + I_5' + I_6' + I_7' + I_8' + I_9'. \tag{33}$$

Evaluating the integrals above, we have

$$I_1' = \int_{-\infty}^{\infty} dz e^{ikz} R_1 \delta(z - z_1) R_1^2 H(z_1 - (z - \epsilon))H((z + \epsilon) - z_1) =$$

$$R_1^3 e^{ikz_1} H(z_1 - (z_1 - \epsilon))H((z_1 + \epsilon) - z_1) = R_1^3 e^{ikz_1},$$

$$I_2' = \int_{-\infty}^{\infty} dz e^{ikz} R_1 \delta(z - z_1)(R_2')^2 H(z_2 - (z - \epsilon))H((z + \epsilon) - z_2) =$$

$$R_1(R_2')^2 e^{ikz_1} H(z_2-(z_1-\epsilon)) \underbrace{H((z_1+\epsilon)-z_2)}_{=0} = 0,$$

$$I_3' = \int_{-\infty}^{\infty} dz e^{ikz} R_1 \delta(z-z_1)(R_3')^2 H(z_3-(z-\epsilon))H((z+\epsilon)-z_3) =$$

$$R_1(R_3')^2 e^{ikz_1} H(z_3-(z_1-\epsilon)) \underbrace{H((z_1+\epsilon)-z_3)}_{=0} = 0,$$

$$I_4' = \int_{-\infty}^{\infty} dz e^{ikz} R_2' \delta(z-z_2) R_1^2 H(z_1-(z-\epsilon))H((z+\epsilon)-z_1) =$$

$$R_1^2 R_2' e^{ikz_2} \underbrace{H(z_1-(z_2-\epsilon))}_{=0} H((z_2+\epsilon)-z_1) = 0,$$

$$I_5' = \int_{-\infty}^{\infty} dz e^{ikz} R_2' \delta(z-z_2)(R_2')^2 H(z_2-(z-\epsilon))H((z+\epsilon)-z_2) =$$

$$(R_2')^3 e^{ikz_2} H(z_2-(z_2-\epsilon))H((z_2+\epsilon)-z_2) = (R_2')^3 e^{ikz_2}, \tag{34}$$

$$I_6' = \int_{-\infty}^{\infty} dz e^{ikz} R_2' \delta(z-z_2)(R_3')^2 H(z_3-(z-\epsilon))H((z+\epsilon)-z_3) =$$

$$R_2'(R_3')^2 e^{ikz_2} H(z_3-(z_2-\epsilon)) \underbrace{H((z_2+\epsilon)-z_3)}_{=0} = 0,$$

$$I_7' = \int_{-\infty}^{\infty} dz e^{ikz} R_3' \delta(z-z_3) R_1^2 H(z_1-(z-\epsilon))H((z+\epsilon)-z_1) =$$

$$R_1^2 R_3' e^{ikz_3} \underbrace{H(z_1-(z_3-\epsilon))}_{=0} H((z_3+\epsilon)-z_1) = 0,$$

$$I_8' = \int_{-\infty}^{\infty} dz e^{ikz} R_3' \delta(z-z_3)(R_2')^2 H(z_2-(z-\epsilon))H((z+\epsilon)-z_2) =$$

$$(R_2')^2 R_3' e^{ikz_3} \underbrace{H(z_2 - (z_3 - \epsilon))}_{=0} H((z_2 + \epsilon) - z_1) = 0,$$

$$I_9' = \int_{-\infty}^{\infty} dz e^{ikz} R_3' \delta(z - z_2)(R_3')^2 H(z_3 - (z - \epsilon)) H((z + \epsilon) - z_3) =$$

$$(R_3')^3 e^{ikz_3} H(z_3 - (z_3 - \epsilon)) H((z_3 + \epsilon) - z_3) = (R_3')^3 e^{ikz_3}. \tag{35}$$

Adding the integrals above, we finally have

$$B_{35}(k) = R_1^3 e^{ikz_1} + (R_2')^3 e^{ikz_2} + (R_3')^3 e^{ikz_2}, \tag{36}$$

where notation from eq. (15) has been used. When transformed to the pseudodepth domain, eq. (36) becomes

$$F[b_1(z)] = R_1^3 \delta(z - z_1) + (R_2')^3 \delta(z - z_2) + (R_3')^3 \delta(z - z_3). \tag{37}$$

Now we will evaluate $b_5^{IM}(k)$,the second term in b_{LO}^{IM}, using eq. (37):

$$b_5^{IM}(k) = \int_{-\infty}^{\infty} dz e^{ikz} b_1(z) \int_{-\infty}^{z-\epsilon} dz' e^{-ikz'} F[b_1(z')] \int_{z'+\epsilon}^{\infty} dz'' e^{ikz''} b_1(z). \tag{38}$$

The 1st integral in the above expression is

$$\int_{z'+\epsilon}^{\infty} dz'' e^{ikz''} b_1(z) = \int_{z'+\epsilon}^{\infty} dz'' e^{ikz''} [R_1 \delta(z'' - z_1) + (R_2')\delta(z'' - z_2) +$$

$$(R_3')\delta(z'' - z_3)] =$$

$$R_1 e^{ikz_1} H(z_1 - (z' + \epsilon)) + R_2' e^{ikz_2} H(z_2 - (z' + \epsilon)) + R_3' e^{ikz_3} H(z_3 - (z' + \epsilon)). \tag{39}$$

Substituting eq. (39) in the second integral of eq. (38), we get

$$\int_{-\infty}^{z-\epsilon} dz' e^{-ikz'} [R_1^3 \delta(z' - z_1) + (R_2')^3 \delta(z' - z_2) + (R_3')^3 \delta(z' - z_3)] \times$$

$$[R_1 e^{ikz_1} H(z_1 - (z' + \epsilon)) + R_2' e^{ikz_2} H(z_2 - (z' + \epsilon)) + R_3' e^{ikz_3} H(z_3 - (z' + \epsilon))]$$

$$= \int_{-\infty}^{z-\epsilon} dz' e^{-ikz'} R_1^3 \delta(z' - z_1) R_1 e^{ikz_1} H(z_1 - (z' + \epsilon)) +$$

$$\int_{-\infty}^{z-\epsilon} dz' e^{-ikz'} R_1^3 \delta(z' - z_1) R_2' e^{ikz_2} H(z_2 - (z' + \epsilon)) +$$

$$\int_{-\infty}^{z-\epsilon} dz' e^{-ikz'} R_1^3 \delta(z' - z_1) R_3' e^{ikz_3} H(z_3 - (z' + \epsilon)) +$$

$$\int_{-\infty}^{z-\epsilon} dz' e^{-ikz'} (R_2')^3 \delta(z' - z_2) R_1 e^{ikz_1} H(z_1 - (z' + \epsilon)) +$$

$$\int_{-\infty}^{z-\epsilon} dz' e^{-ikz'} (R_2')^3 \delta(z' - z_2) R_2' e^{ikz_2} H(z_2 - (z' + \epsilon)) +$$

$$\int_{-\infty}^{z-\epsilon} dz' e^{-ikz'} (R_2')^3 \delta(z' - z_2) R_3' e^{ikz_3} H(z_3 - (z' + \epsilon)) +$$

$$\int_{-\infty}^{z-\epsilon} dz' e^{-ikz'} (R_3')^3 \delta(z' - z_3) R_1 e^{ikz_1} H(z_1 - (z' + \epsilon)) +$$

$$\int_{-\infty}^{z-\epsilon} dz' e^{-ikz'} (R_3')^3 \delta(z' - z_3) R_2' e^{ikz_2} H(z_2 - (z' + \epsilon)) +$$

$$\int_{-\infty}^{z-\epsilon} dz' e^{-ikz'} (R_3')^3 \delta(z' - z_3) R_3' e^{ikz_3} H(z_3 - (z' + \epsilon)) =$$

$$I_1'' + I_2'' + I_3'' + I_4'' + I_5'' + I_6'' + I_7'' + I_8'' + I_9''. \tag{40}$$

Evaluating each of the integrals in eq. (40), we have

$$I_1'' = \int_{-\infty}^{z-\epsilon} dz' e^{-ikz'} R_1^3 \delta(z' - z_1) R_1 e^{ikz_1} H(z_1 - (z' + \epsilon)) = R_1^4 \underbrace{H(z_1 - (z_1 + \epsilon))}_{=0} H((z - \epsilon) - z_1) = 0,$$

$$I_2'' = \int_{-\infty}^{z-\epsilon} dz' e^{-ikz'} R_1^3 \delta(z'-z_1) R_2' e^{ikz_2} H(z_2-(z'+\epsilon)) =$$

$$R_1^3 R_2' e^{ik(z_2-z_1)} H(z_2-(z_1+\epsilon)) H((z-\epsilon)-z_1),$$

$$I_3'' = \int_{-\infty}^{z-\epsilon} dz' e^{-ikz'} R_1^3 \delta(z'-z_1) R_3' e^{ikz_3} H(z_3-(z'+\epsilon)) =$$

$$R_1^3 R_3' e^{ik(z_3-z_1)} H(z_3-(z_1+\epsilon)) H((z-\epsilon)-z_1),$$

$$I_4'' = \int_{-\infty}^{z-\epsilon} dz' e^{-ikz'} (R_2')^3 \delta(z'-z_2) R_1 e^{ikz_1} H(z_1-(z'+\epsilon)) =$$

$$R_1 (R_2')^3 e^{ik(z_1-z_2)} \underbrace{H(z_1-(z_2+\epsilon))}_{=0} H((z-\epsilon)-z_2) = 0,$$

$$I_5'' = \int_{-\infty}^{z-\epsilon} dz' e^{-ikz'} (R_2')^3 \delta(z'-z_2) R_2' e^{ikz_2} H(z_2-(z'+\epsilon)) =$$

$$(R_2')^4 \underbrace{H(z_2-(z_2+\epsilon))}_{=0} H((z-\epsilon)-z_2) = 0,$$

$$I_6'' = \int_{-\infty}^{z-\epsilon} dz' e^{-ikz'} (R_2')^3 \delta(z'-z_2) R_3' e^{ikz_3} H(z_3-(z'+\epsilon)) =$$

$$(R_2')^3 R_3' e^{ik(z_3-z_2)} H((z-\epsilon)-z_2),$$

$$I_7'' = \int_{-\infty}^{z-\epsilon} dz' e^{-ikz'} (R_3')^3 \delta(z'-z_3) R_1 e^{ikz_1} H(z_1-(z'+\epsilon)) =$$

$$R_1 (R_3')^3 e^{ik(z_1-z_3)} \underbrace{H(z_1-(z_3+\epsilon))}_{=0},$$

$$I_8'' = \int_{-\infty}^{z-\epsilon} dz' e^{-ikz'} (R_3')^3 \delta(z'-z_3) R_2' e^{ikz_2} H(z_2-(z'+\epsilon)) =$$

$$R_2'(R_3')^3 e^{ik(z_2-z_3)} \underbrace{H(z_2-(z_3+\epsilon))}_{=0},$$

$$I_9'' = \int_{-\infty}^{z-\epsilon} dz' e^{-ikz'}(R_3')^3 \delta(z'-z_3) R_3' e^{ikz_3} H(z_3-(z'+\epsilon)) =$$

$$(R_3')^4 \underbrace{H(z_3-(z_3+\epsilon))}_{=0}.$$

Hence, the value of eq. (40) is

$$I_1'' + I_2'' + I_3'' + I_4'' + I_5'' + I_6'' + I_7'' + I_8'' + I_9''$$

$$= R_1^3 R_2' e^{ik(z_2-z_1)} H((z-\epsilon)-z_1) + R_1^3 R_3' e^{ik(z_3-z_1)} H((z-\epsilon)-z_1) + (R_2')^3 R_3' e^{ik(z_3-z_2)} H((z-\epsilon)-z_2). \tag{41}$$

Substituting eq. (41) in the last integral of eq. (37), we finally have

$$b_5^{IM}(k) = \int_{-\infty}^{\infty} dz e^{ikz} [R_1\delta(z-z_1) + R_2'\delta(z-z_2) + R_3'\delta(z-z_3)] \times$$

$$[R_1^3 R_2' e^{ik(z_2-z_1)} H((z-\epsilon)-z_1) + R_1^3 R_3' e^{ik(z_3-z_1)} H((z-\epsilon)-z_1) + (R_2')^3 R_3' e^{ik(z_3-z_2)} H((z-\epsilon)-z_2)] =$$

$$\int_{-\infty}^{\infty} dz e^{ikz} R_1\delta(z-z_1) R_1^3 R_2' e^{ik(z_2-z_1)} H((z-\epsilon)-z_1) +$$

$$\int_{-\infty}^{\infty} dz e^{ikz} R_1\delta(z-z_1) R_1^3 R_3' e^{ik(z_3-z_1)} H((z-\epsilon)-z_1) +$$

$$\int_{-\infty}^{\infty} dz e^{ikz} R_1\delta(z-z_1) (R_2')^3 R_3' e^{ik(z_3-z_2)} H((z-\epsilon)-z_2) +$$

$$\int_{-\infty}^{\infty} dz e^{ikz} R_2'\delta(z-z_2) R_1^3 R_2' e^{ik(z_2-z_1)} H((z-\epsilon)-z_1) +$$

$$\int_{-\infty}^{\infty} dz e^{ikz} R_2' \delta(z - z_2) R_1^3 R_3' e^{ik(z_3 - z_1)} H((z - \epsilon) - z_1) +$$

$$\int_{-\infty}^{\infty} dz e^{ikz} R_2' \delta(z - z_2) (R_2')^3 R_3' e^{ik(z_3 - z_2)} H((z - \epsilon) - z_2) +$$

$$\int_{-\infty}^{\infty} dz e^{ikz} R_3' \delta(z - z_3) R_1^3 R_2' e^{ik(z_2 - z_1)} H((z - \epsilon) - z_1) +$$

$$\int_{-\infty}^{\infty} dz e^{ikz} R_3' \delta(z - z_3) R_1^3 R_3' e^{ik(z_3 - z_1)} H((z - \epsilon) - z_1) +$$

$$\int_{-\infty}^{\infty} dz e^{ikz} R_3' \delta(z - z_3) (R_2')^3 R_3' e^{ik(z_3 - z_2)} H((z - \epsilon) - z_2) =$$

$$I_1''' + I_2''' + I_3''' + I_4''' + I_5''' + I_6''' + I_7''' + I_8''' + I_9''' \tag{42}$$

The integrals in eq. (42) are calculated as usual:

$$I_1''' = \int_{-\infty}^{\infty} dz e^{ikz} R_1 \delta(z - z_1) R_1^3 R_2' e^{ik(z_2 - z_1)} H((z - \epsilon) - z_1) =$$

$$R_1^4 R_2' e^{ik(z_2 - 2z_1)} \underbrace{H((z_1 - \epsilon) - z_1)}_{=0}.$$

$$I_2''' = \int_{-\infty}^{\infty} dz e^{ikz} R_1 \delta(z - z_1) R_1^3 R_3' e^{ik(z_3 - z_1)} H((z - \epsilon) - z_1) =$$

$$R_1^4 R_3' e^{ik(z_3 - 2z_1)} \underbrace{H((z_1 - \epsilon) - z_1)}_{=0}.$$

$$I_3''' = \int_{-\infty}^{\infty} dz e^{ikz} R_1 \delta(z - z_1) (R_2')^3 R_3' e^{ik(z_3 - z_2)} H((z - \epsilon) - z_2) =$$

$$R_1 (R_2')^3 R_3' e^{ik(z_1 + z_3 - z_2)} \underbrace{H((z_1 - \epsilon) - z_2)}_{=0}.$$

$$I_4''' = \int_{-\infty}^{\infty} dz e^{ikz} R_2' \delta(z - z_2) R_1^3 R_2' e^{ik(z_2 - z_1)} H((z - \epsilon) - z_1)$$

$$R_1^3 (R_2')^2 e^{ik(2z_2 - z_1)}.$$

$$I_5''' = \int_{-\infty}^{\infty} dz e^{ikz} R_2' \delta(z - z_2) R_1^3 R_3' e^{ik(z_3 - z_1)} H((z - \epsilon) - z_1) =$$

$$R_2' R_1^3 R_3' e^{ik(z_2 + z_3 - z_1)}.$$

$$I_6''' = \int_{-\infty}^{\infty} dz e^{ikz} R_2' \delta(z - z_2) (R_2')^3 R_3' e^{ik(z_3 - z_2)} H((z - \epsilon) - z_2) =$$

$$(R_2')^3 R_3' e^{ik(z_3 - 2z_2)} \underbrace{H((z_2 - \epsilon) - z_2)} = 0,$$

$$I_7''' = \int_{-\infty}^{\infty} dz e^{ikz} R_3' \delta(z - z_3) R_1^3 R_2' e^{ik(z_2 - z_1)} H((z - \epsilon) - z_1) =$$

$$R_3' R_1^3 R_2' e^{ik(z_3 + z_2 - z_1)},$$

$$I_8''' = \int_{-\infty}^{\infty} dz e^{ikz} R_3' \delta(z - z_3) R_1^3 R_3' e^{ik(z_3 - z_1)} H((z - \epsilon) - z_1) =$$

$$R_3' R_1^3 R_3' e^{ik(2z_3 - z_1)},$$

$$I_9''' = \int_{-\infty}^{\infty} dz e^{ikz} R_3' \delta(z - z_3) (R_2')^3 R_3' e^{ik(z_3 - z_2)} H((z - \epsilon) - z_2) =$$

$$(R_2')^3 (R_3')^2 e^{ik(2z_3 - z_2)}.$$

The sum of the integrals above gives

$$b_5^{IM} = R_1^3(R_2')^2 e^{ik(2z_2-z_1)} + 2R_2'R_1^3R_3' e^{ik(z_2+z_3-z_1)} +$$

$$R_3'R_1^3R_3' e^{ik(2z_3-z_1)} + (R_2')^3(R_3')^2 e^{ik(2z_3-z_2)}. \tag{43}$$

Upon Fourier transformation, eq. (43) becomes:

$$b_5^{IM}(t) = R_1^3(R_2')^2\delta(t-(2t_2-t_1)) + 2R_2'R_1^3R_3'\delta(t-(t_2+t_3-t_1)) +$$

$$R_3'R_1^3R_3'\delta(t-(2t_3-t_1)) + (R_2')^3(R_3')^2\delta(t-(2t_3-t_2)),$$

which is exactly eq. (18) in Section 3.

References

Araújo, F. V. *Linear and non-linear methods derived from scattering theory: backscattering tomography and internal-multiple attenuation.* PhD thesis, Universidade Federal da Bahía, Brazil, 1994. In Portuguese.

Araújo, F. V., Weglein A. B., Carvalho P. M., and Stolt R. H. "Inverse scattering series for multiple attenuation: an example with surface and internal multiples." *64th Ann. Int. SEG Mtg, Expanded Abstracts*. . Soc. Expl. Geophys., 1994. 1039–41.

Carvalho, P. M. *Free-surface multiple reflection elimination method based on nonlinear inversion of seismic data*. PhD thesis, Universidade Federal da Bahia, 1992. In Portuguese.

Liang, Hong and A. B. Weglein. "A further general modification of the leading order ISS attenuator of first order internal multiples to accommodate primaries and internal multiples when an arbitrary number of reflectors generate the data: theory, development, and examples." *M-OSRP 2012 Annual Meeting*. 2012, 148–166.

Ma, Chao and A. B. Weglein. "Modifying the leading-order ISS attenuator of first-order internal multiples to accomodate primaries and internal multiples: fundamental concept and theory, development, and examples exemplified when three reflectors generate the data." *M-OSRP 2012 Annual Meeting*. 2012, 133–147.

Ramírez, A. C. *I. - Inverse scattering subseries for removal of internal multiples and depth imaging primaries; II. - Green's theorem as the foundation of interferometry and guiding new practical methods and applications.* PhD thesis, University of Houston, 2007.

Ramírez, A. C. and Arthur B. Weglein. "An inverse scattering internal multiple elimination method: Beyond attenuation, a new algorithm and initial tests." *75st Annual International Meeting, SEG, Expanded Abstracts.* . Soc. Expl. Geophys., 2005.

Weglein, A. B., F. V. Araújo, P. M. Carvalho, R. H. Stolt, K. H. Matson, R. T. Coates, D. Corrigan, D. J. Foster, S. A. Shaw, and H. Zhang. "Inverse Scattering Series and Seismic Exploration." *Inverse Problems* 19 (2003): R27–R83.

Weglein, Arthur B., Fernanda Araújo Gasparotto, Paulo M. Carvalho, and Robert H. Stolt. "An Inverse-Scattering Series Method for Attenuating Multiples in Seismic Reflection Data." *Geophysics* 62 (November-December 1997): 1975–1989.

A method for the elimination of all first order internal multiples from all reflectors in a one D medium: theory and examples

Yanglei Zou, Arthur B. Weglein

April 29, 2013

Abstract

In this paper,an amplitude correction equation is derived by using reverse engineering method. This equation is more advanced than the internal-multiple attenuation equation for an eliminator. Although the amplitude correction equation is derived under 1D normal incidence, the idea behind this equation is not only valid under 1D normal incidence. The amplitude correction equation also provides hints for deriving a subseries from an inverse scattering series that can eliminate all internal multiples.

1 Introduction

In principle, the inverse scattering series(ISS) allows specific seismic processing objectives, such as free-surface-multiple removal and internal-multiple removal, to be achieved directly in terms of measured data (effective data), without any subsurface estimation of the earthą́s properties.

For internal-multiple removal, the Inverse Scattering Series Internal-Multiple Attenuator(ISS-IMA) can predict correct time and well-understood amplitude for all internal multiples without any subsurface information. Given that the ISS-IMA predicts the approximate amplitude and correct time of internal multiples, the ISS-IMA can remove internal multiples more effectively by using energy minimization adaptive subtraction(EMAS). However, events may interfere with each other in both on-shore and off-shore seismic data. In these cases, the EMAS criteria may fail. For example, when a primary destructively interferes with an internal multiple and the real energy of the primary is greater than the interfering event, the EMAS will not remove the internal multiples. The EMAS criteria is obtaining the minimum data energy; however, in this example, the criteria fails as the real primary has greater energy.

Predicting the correct amplitude of the internal multiples is an effective way of avoiding the limitations of EMAS. Wilberth Herrera and Weglein (2012) has derived a subseries directly from the ISS. The subseries can eliminate all first order internal multiples generated at the shallowest reflector and can further attenuate deeper internal multiples. The present work is a step further from the ISS-IMA

to an eliminator achieved directly in terms of data without any subsurface information. Two different types of equation approximation are also presented:(1) The first type of equation approximation can predict the correct amplitude of all first order internal multiples generated at the shallowest reflector. (2)The second type of equation approximation can predict the correct amplitude of all first order internal multiples generated at the shallowest and next shallowest reflectors.

In the Mission-Oriented Seismic Research Program (M-OSRP), tasks are first isolated and each task assumes the tasks before it are completed. As shown in Figure 1,the tasks before Internal Multiple Removal are prerequisites including reference wave removal,deghosting, free surface multiple removal and evaluation of the wavelet. Internal multiple removal is also a prerequisite for later tasks.

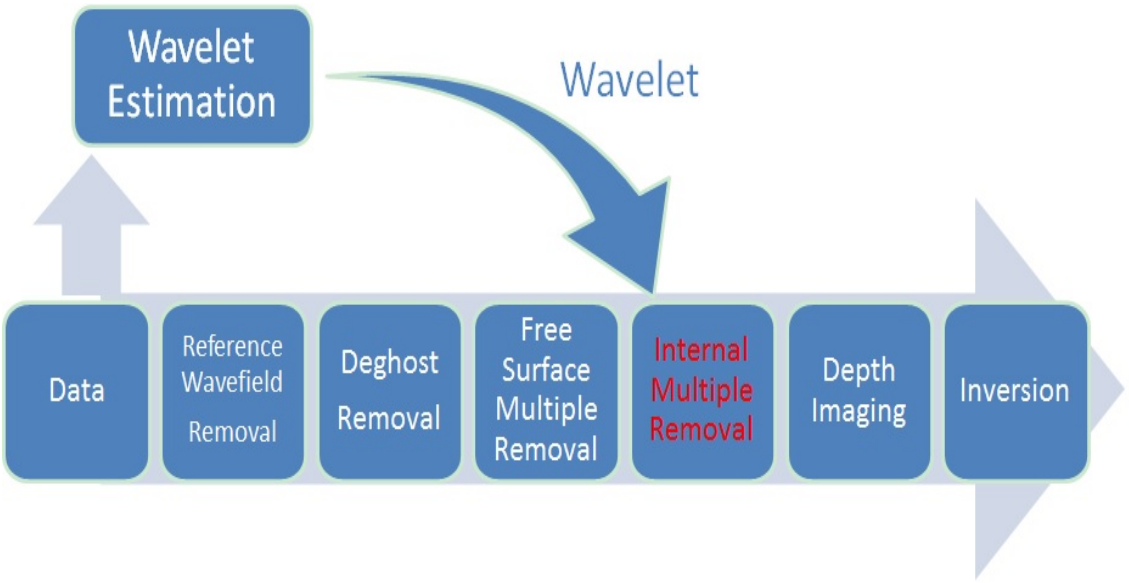

Figure 1: Task Isolation

2 Internal Multiple Attenuator(IMA) and Attenuation Factor(AF)

The ISS-IMA is first given by Araújo (1994) Weglein et al. (1997). The 1D normal incidence version of the ISS-IMA is presented as follows:

$$b_3^{IM}(k) = \int_{-\infty}^{\infty} dz e^{ikz} b_1(z) \int_{-\infty}^{z-\varepsilon_2} dz' e^{-ikz'} b_1(z') \int_{z'+\varepsilon_1}^{\infty} dz'' e^{ikz''} b_1(z''). \tag{2.1}$$

This equation can predict the correct time and well-understood amplitude of all internal multiples.

To demonstrate explicitly the mechanism of the internal multiple attenuation algorithm and to examine its properties, Weglein et al. (2003) considered the simplest two-layer model that can

produce an internal multiple. For this model, the reflection data caused by an impulsive incident wave $\delta(t - \frac{z}{c})$ is:

$$D'(t) = R_1\delta(t - t_1) + T_{01}R_2T_{10}\delta(t - t_2) + \cdots$$

where t_1, t_2 and R_1, R_2 are the two way times and reflection coefficients from the two reflectors,respectively; and T_{01} and T_{10} are the coefficients of transmission between model layers 0 and 1 and 1 and 0, respectively.

$$D'(\omega) = R_1e^{i\omega t_1} + T_{01}R_2T_{10}e^{i\omega t_2} + \cdots .$$

where$D'(\omega)$ is the temporal Fourier transform of $D'(t)$.
Given a 1D medium and a normal incident wave, $k_z = \frac{2\omega}{c_0}$ and $b(k_z) = D(\omega)$ the following is obtained:

$$b(k_z) = R_1e^{i\frac{2\omega}{c_0}\frac{c_0t_1}{2}} + T_{01}R_2T_{10}e^{i\frac{2\omega}{c_0}\frac{c_0t_2}{2}} + \cdots$$

The pseudo-depths z_1 and z_2 in the reference medium are defined as follows:

$$z_1 = \frac{c_0t_1}{2} \quad z_2 = \frac{c_0t_2}{2}.$$

The input data can now be expressed in terms of $k = k_z$, z_1 and z_2:

$$b(k) = R_1e^{ikz_1} + T_{01}R_2T_{10}e^{ikz_2} + \cdots$$

The date is now ready for the internal multiple algorithm.
Substituting $b(k)$ into the algorithm, we derive the prediction:

$$b_3k = R_1R_2^2T_{01}^2T_{10}^2e^{2ikz_2}e^{-ikz_1}$$

which in the time domain is:

$$b_3t = R_1R_2^2T_{01}^2T_{10}^2\delta(t - (2t_2 - t_1))$$

From the example it is easy to compute the actual first order internal multiple precisely:

$$- R_1R_2^2T_{01}T_{10}\delta(t - (2t_2 - t_1))$$

Therefore, the time prediction is precise, and the amplitude of the prediction has an extra power of $T_{01}T_{10}$ which is called the Attenuation Factor(AF), thus defining exactly the difference between the attenuation represented by b_3 and elimination.

To derive a general formula for the amplitude prediction of the algorithm, Ramírez and Weglein (2005) analyzed a model with n layers and respective velocities C_n, n is an integer. By using the definitions $R_1 = R_1'$, $R_N' = R_N\prod_{i=1}^{N-1}(T_{i-1,i}T_{i,i-1})$ and Einsteinąŕs summation, the reflection data from a normal incident spike wave we obtain the following:

$$D(t) = R_n'\delta(t - t_n) + internal\ multiples \tag{2.2}$$

The generalized prediction of the attenuator is obtained by the following:

$$b_3^{IM}(k) = R_i' R_j' R_k' e^{ikz_i} e^{ikz_j} e^{ikz_k} \tag{2.3}$$

which in the time domain becomes

$$b_3^{IM}(k) = R_i' R_j' R_k' \delta(t - (t_i + t_k - t_j)) \tag{2.4}$$

By evaluating Equation (3) for different values of i, j and k the amplitude prediction of first order internal multiples is obtained and can be generalized for any amount of layers in a 1D model. The generalization of the internal multiple amplitude states that the overabundance of transmission coefficients depends on the position of the generating reflector (where the downward reflection took place).Compared with the real amplitude of internal multiples in the data, we can obtain the AF(Figure 2 shows an example of the Attenuation Factor of a first order internal multiple generated at the second reflector).

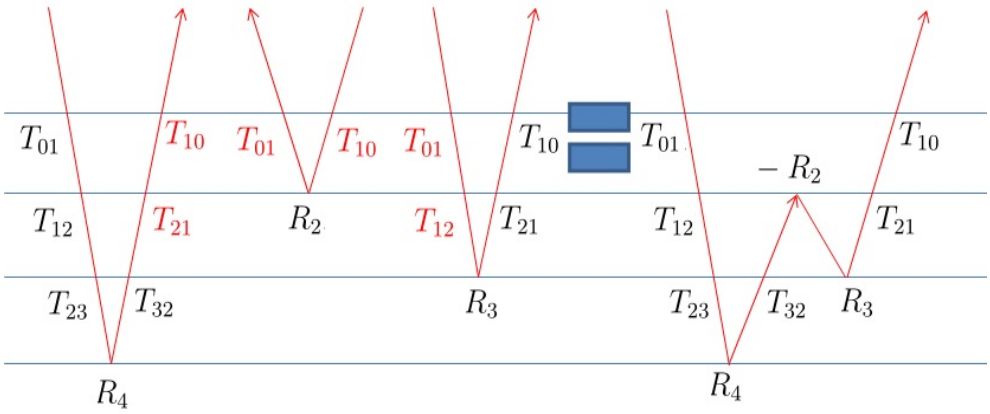

Figure 2: an example of the Attenuation Factor of a first order internal multiple generated at the second reflector

The attenuation factor, AF_j, in the prediction of internal multiples is given by the following:

$$AF_j = \begin{cases} T_{0,1}T_{1,0} \quad (for\ j = 1) \\ \prod_{i=1}^{N-1} (T_{i-1,i}^2 T_{i,i-1}^2) T_{j,j-1} T_{j-1,j} \quad (for\ 1 < j < J) \end{cases} \tag{2.5}$$

The attenuation factor AF_j can also be performed by using reflection coefficients:

$$AF_j = \begin{cases} 1 - R_1^2 \quad (for\ j = 1) \\ (1 - R_1^2)^2 (1 - R_2^2)^2 \cdots (1 - R_{j-1}^2)^2 (1 - R_j^2) \quad (for\ 1 < j < J) \end{cases} \tag{2.6}$$

The subscript j represents the generating reflector, and J is the total number of interfaces in the model.The interfaces are numbered starting with the shallowest location. The attenuator b_3^{IM} predicts the first order internal multiples by using three events within the data. The AF is directly related to the trajectory of the subevent, which forms the prediction of internal multiples.

3 Amplitude Correction Equation for Internal Multiple Attenuator(1D Normal Incidence)

The discussion above demonstrates that all first order internal multiples generated at the same reflector have the same AF. Therefore, a new function in the second integral must be developed to remove the AF and find the eliminator. That is from

$$b_3^{IM}(k) = \int_{-\infty}^{\infty} dz e^{ikz} b_1(z) \int_{-\infty}^{z-\varepsilon_2} dz' e^{-ikz'} b_1(z') \int_{z'+\varepsilon_1}^{\infty} dz'' e^{ikz''} b_1(z'') \tag{3.1}$$

to

$$b_E^{IM}(k) = \int_{-\infty}^{\infty} dz e^{ikz} b_1(z) \int_{-\infty}^{z-\varepsilon_2} dz' e^{-ikz'} F[b_1(z')] \int_{z'+\varepsilon_1}^{\infty} dz'' e^{ikz''} b_1(z'') \tag{3.2}$$

For the 1D normal incidence, $b_1(z)$ is expressed as follows:

$$b_1(z) = R_1\delta(z-z_1) + R_2'\delta(z-z_2) + R_3'\delta(z-z_3) + \cdots + R_n'\delta(z-z_n) + \cdots \tag{3.3}$$

The F function should be written as the following:

$$\begin{aligned} F[b_1(z')] =& \frac{R_1}{AF_{j=1}}\delta(z'-z_1) + \frac{R_2'}{AF_{j=2}}\delta(z'-z_2) + \cdots + \frac{R_n'}{AF_{j=n}}\delta(z'-z_n) + \cdots \\ =& \frac{R_1}{1-R_1^2}\delta(z'-z_1) + \frac{R_2'}{(1-R_1^2)^2(1-R_2^2)}\delta(z'-z_2) + \cdots \\ &+ \frac{R_n'}{(1-R_1^2)^2(1-R_2^2)^2\cdots(1-R_{n-1}^2)^2(1-R_n^2)}\delta(z'-z_n) + \cdots \end{aligned} \tag{3.4}$$

By using reverse engineering, the F function is discovered (See Appendix A for the equation derivation):

$$F[b_1(z)] = \lim_{\varepsilon'\to 0} c(z) \times \frac{\int_{z-\varepsilon}^{z+\varepsilon} c(z'')dz''}{\int_{z-\varepsilon}^{z+\varepsilon} b_1(z')dz'\{1 - [\int_{z-\varepsilon}^{z+\varepsilon} c(z'')dz'']^2\} + \varepsilon'} \tag{3.5}$$

$$c(z) = \frac{b_1(z)}{1 - \int_{-\infty}^{z-\varepsilon} dz' b_1(z') \int_{z'-\varepsilon}^{z'+\varepsilon} dz'' c(z'')} \tag{3.6}$$

To derive the F function from $b_1(z)$, c(z) must first be solved in Equation (12). Thereafter, c(z) is integrated into Equation (11).

3.1 First Type of Equation Approximation

Equation (12) is an integral equation:

$$c(z) = \frac{b_1(z)}{1 - \int_{-\infty}^{z-\varepsilon} dz' b_1(z') \int_{z'-\varepsilon}^{z'+\varepsilon} dz'' c(z'')}$$

Generally, this kind of equation does not have analytical solutions; hence, an approximation must be made for Equation (6). The simplest approximation is presented as follows:

$$\begin{aligned} c(z) =& \frac{b_1(z)}{1 - \int_{-\infty}^{z-\varepsilon} dz' b_1(z') \int_{z'-\varepsilon}^{z'+\varepsilon} dz'' c(z'')} \\ \approx& \frac{b_1(z)}{1-0} \\ \approx& b_1(z) \end{aligned} \tag{3.7}$$

It can be shown that the 1st kind approximation can predict correct amplitude for all 1st order internal multiples generated at the shallowest reflector and can further attenuate deeper internal multiples.

3.2 Second Type of Equation Approximation

A more accurate approximation is presented as follows::

$$\begin{aligned} c(z) =& \frac{b_1(z)}{1 - \int_{-\infty}^{z-\varepsilon} dz' b_1(z') \int_{z'-\varepsilon}^{z'+\varepsilon} dz'' c(z'')} \\ \approx& \frac{b_1(z)}{1 - \int_{-\infty}^{z-\varepsilon} dz' b_1(z') \int_{z'-\varepsilon}^{z'+\varepsilon} dz'' b_1(z'')} \end{aligned} \tag{3.8}$$

This type of approximation can predict the correct amplitude for all first order internal multiples generated at the shallowest and next shallowest reflectors and can further attenuate deeper internal multiples.

Only primaries are considered as the input in deriving all these equations. However, for these two types of approximations, the conclusion is still valid when we consider both primaries and internal multiples as input. By using these approximations to predict the amplitude of internal multiples generated at the shallowest and next shallowest reflectors, in the F function, only the part of the data preceding the second primary is used. Considering that the internal multiples do not arrive prior to the second primary, that part of the data remains the same when only primaries or both primaries and internal multiples are considered.

4 Numerical Examples

This section presents a numerical example that shows the result of the original ISS-IMA and the two types of equation approximation of the amplitude correction equation of ISS-IMA. Figure 3 and 4 show the model used in this study and the 1D normal incidence input data, respectively. In figure 4, the part in the red rectangular shows the part of data that we do following comparison.

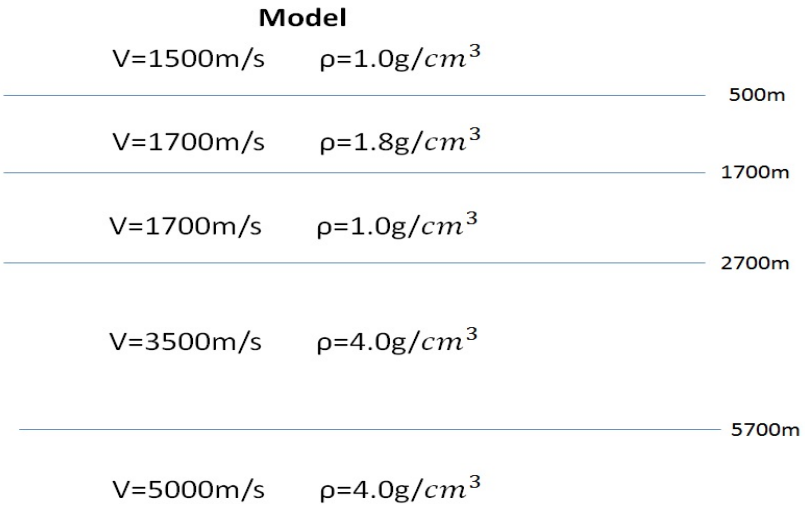

Figure 3: Model

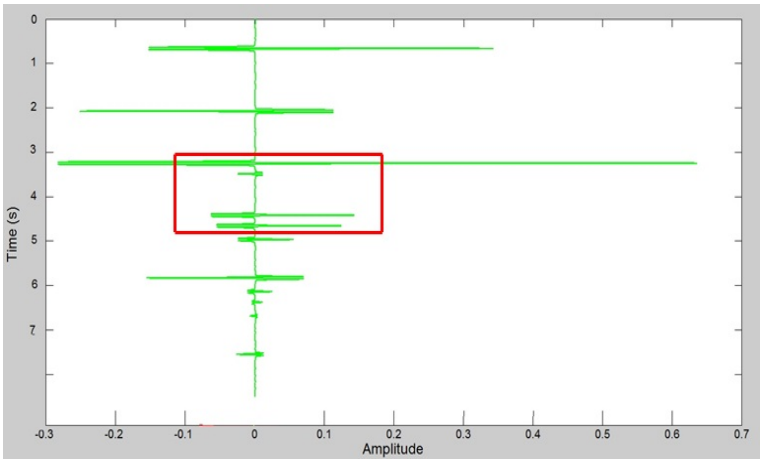

Figure 4: Input data(1D normal incidence)

The output of ISS-IMA in Figure 5 clearly shows that all multiples are predicted with the correct time and approximate amplitude. Figure 6, which displays the first type of equation approximation, shows that all internal multiples with a downward reflection at the shallowest reflector(IM_{212},IM_{312} and IM_{213})are removed. And in Figure 7,we can see all internal multiples generated at the shallowest and the next shallowest reflectors(IM_{212},IM_{312},IM_{213} and IM_{323}) are removed by the second type of equation approximation.

In the figure 5,6 and 7:
P_3 is the Third primary.
IM_{212},IM_{213},IM_{312} are internal multiples with a downward reflection at the shallowest reflector.The three numbers in the subscript refer to the historical number of reflectors in the internal multiples. For example, IM_{212} is a first order internal multiple with two upward reflection at the second reflector and a downward reflection at the first(shallowest) reflector.
IM_{323} is a internal multiples with a downward reflection at the next shallowest reflector.
The spurious event is an false event generated by IM_{212},P_3 and IM_{212}, which exist in every figure. (A method for removing the spurious events have been discovered by Chao Ma and B.Weglein (2012) H. Liang and Weglein (2012)).

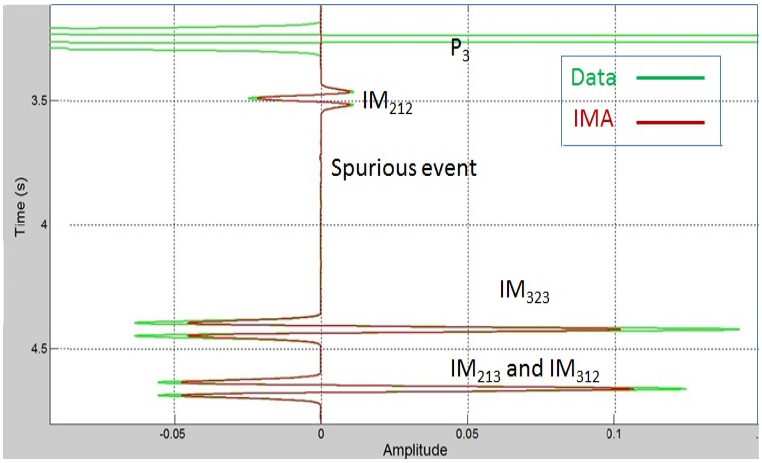

Figure 5: Output of the ISS-IMA

5 Conclusion

1.An amplitude correction equation for ISS-IMA(1D normal incidence) has been derived. The second type of approximation of the new equation can eliminate all first order internal multiples generated at the shallowest and next shallowest reflectors and further attenuate deeper internal multiples directly in terms of data and without any subsurface information.

2.This equation and its approximations:
(a)not generate any more events than IMA.

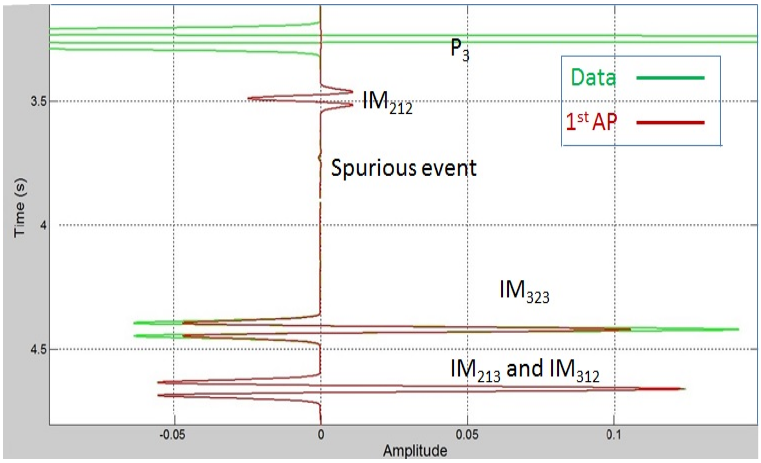

Figure 6: Output of the first type of equation approximation

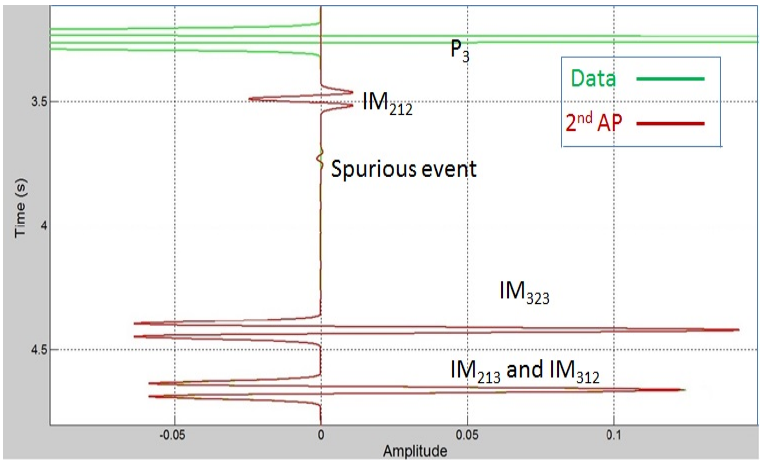

Figure 7: Output of the second type of equation approximation

(c)not touch primaries.

3.Although the equation is derived under 1D normal incidence, the idea that using data to remove the extra transmission coefficient in the second integral is not confined to 1D normal incidence. The equation probably can be expanded to 1D earth data with offset.

4.And this equation and its approximations provides hints for finding a subseries in the ISS that can remove internal multiples in multi-D earth.

6 Acknowledgements

We are grateful to all M-OSRP sponsors for long-term encouragement and support in this research. I would like to thank Dr.Weglein,Dr.Herrera,Hong Liang and Chao Ma for the help of finishing this paper and valuable discussions in this research program.
And special thanks to Chao Ma for reviewing this paper.

Appendix

A Derivation of Amplitude Correction Equation for Internal Multiple Attenuator(1D normal incidence)

The Amplitude Correction Equation for Internal Multiple Attenuator(1D normal incidence) is given by:

$$F[b_1(z)] = \lim_{\varepsilon'\to 0} c(z) \times \frac{\int_{z-\varepsilon}^{z+\varepsilon} c(z'')dz''}{\int_{z-\varepsilon}^{z+\varepsilon} b_1(z')dz'\{1-[\int_{z-\varepsilon}^{z+\varepsilon} c(z'')dz'']^2\}+\varepsilon'} \tag{A.1}$$

$$c(z) = \frac{b_1(z)}{1-\int_{-\infty}^{z-\varepsilon} dz' b_1(z') \int_{z'-\varepsilon}^{z'+\varepsilon} dz'' c(z'')} \tag{A.2}$$

with

$$b_1(z) = R_1\delta(z-z_1) + R_2'\delta(z-z_2) + R_3'\delta(z-z_3) + \cdots + R_n'\delta(z-z_n) + \cdots \tag{A.3}$$

$$c(z) = R_1\delta(z-z_1) + R_2\delta(z-z_2) + R_3\delta(z-z_3) + \cdots + R_n\delta(z-z_n) + \cdots \tag{A.4}$$

($\int_{z-\varepsilon}^{z+\varepsilon} dz'' c(z'')$ is a function of z)

First Let's calculate $\int_{z-\varepsilon}^{z+\varepsilon} dz'' c(z'')$ for the given c(z):

$$\begin{aligned}
\int_{z-\varepsilon}^{z+\varepsilon} dz'' c(z'') &= \int_{z-\varepsilon}^{z+\varepsilon} dz''[R_1\delta(z''-z_1) + R_2\delta(z''-z_2) + \cdots + R_n\delta(z''-z_n) + \cdots] \\
&= \int_{-\infty}^{\infty} dz''[R_1\delta(z''-z_1) + R_2\delta(z''-z_2) + \cdots + R_n\delta(z''-z_n) + \cdots] \\
&\quad \times H(z''-(z-\varepsilon))H((z+\varepsilon)-z'') \\
&= R_1 H(z_1-(z-\varepsilon))H((z+\varepsilon)-z_1) + R_2 H(z_2-(z-\varepsilon))H((z+\varepsilon)-z_2) \\
&\quad + \cdots + R_n H(z_n-(z-\varepsilon))H((z+\varepsilon)-z_n) + \cdots \\
&= R_1 H((z_1+\varepsilon)-z)H(z-(z_1-\varepsilon)) + R_2 H((z_2+\varepsilon)-z)H(z-(z_2-\varepsilon)) \\
&\quad + \cdots + R_n H((z_n+\varepsilon)-z)H(z-(z_n-\varepsilon)) + \cdots
\end{aligned}$$

Now we can prove the first part of the equation:

$$\begin{aligned}
&\lim_{\varepsilon'\to 0} c(z) \times \frac{\int_{z-\varepsilon}^{z+\varepsilon} c(z'')dz''}{\int_{z-\varepsilon}^{z+\varepsilon} b_1(z')dz'\{1-[\int_{z-\varepsilon}^{z+\varepsilon} c(z'')dz'']^2\}+\varepsilon'} \\
&= \lim_{\varepsilon'\to 0}[\frac{R_1^2}{R_1(1-R_1^2)+\varepsilon'}\delta(z-z_1) + \frac{R_2^2}{R_2'(1-R_2^2)+\varepsilon'}\delta(z-z_2) + \cdots
\end{aligned}$$

$$
\begin{aligned}
&+\frac{R_n^2}{R_n'(1-R_n^2)+\varepsilon'}\delta(z-z_n)+\cdots] \\
=&\frac{R_1^2}{R_1(1-R_1^2)}\delta(z-z_1)+\frac{R_2^2}{R_2'(1-R_2^2)}\delta(z-z_2)+\cdots \\
&+\frac{R_n^2}{R_n'(1-R_n^2)}\delta(z-z_n)+\cdots \\
=&\frac{R_1}{1-R_1^2}\delta(z-z_1)+\frac{R_2'}{(1-R_1^2)^2(1-R_2^2)}\delta(z-z_2)+\cdots \\
&+\frac{R_n'}{(1-R_1^2)^2(1-R_2^2)^2\cdots(1-R_{n-1}^2)^2(1-R_n^2)}\delta(z-z_n)+\cdots \\
=&\frac{R_1}{AF_{j=1}}\delta(z-z_1)+\frac{R_2'}{AF_{j=2}}\delta(z-z_2)+\cdots+\frac{R_n'}{AF_{j=n}}\delta(z-z_n)+\cdots \\
=&F[b_1(z)]
\end{aligned}
$$

For the second part of the equation:

$$
c(z)=\frac{b_1(z)}{1-\int_{-\infty}^{z-\varepsilon}dz' b_1(z')\int_{z'-\varepsilon}^{z'+\varepsilon}dz'' c(z'')} \tag{A.5}
$$

$$
\begin{aligned}
&b_1(z')\int_{z'-\varepsilon}^{z'+\varepsilon}dz'' c(z'') \\
=&R_1^2\delta(z'-z_1)+R_2R_2'\delta(z'-z_2)+R_3R_3'\delta(z'-z_3)+\cdots+R_nR_n'\delta(z'-z_n)+\cdots
\end{aligned}
$$

$$
\begin{aligned}
&\int_{-\infty}^{z-\varepsilon}dz' b_1(z')\int_{z'-\varepsilon}^{z'+\varepsilon}dz'' c(z'') \\
=&\int_{-\infty}^{z-\varepsilon}dz'[R_1^2\delta(z'-z_1)+R_2R_2'\delta(z'-z_2)+\cdots+R_nR_n'\delta(z'-z_n)+\cdots] \\
=&\int_{-\infty}^{\infty}dz' H((z-\varepsilon)-z')[R_1^2\delta(z'-z_1)+R_2R_2'\delta(z'-z_2)+\cdots+R_nR_n'\delta(z'-z_n)+\cdots] \\
=&R_1^2H((z-\varepsilon)-z_1)+R_2R_2'H((z-\varepsilon)-z_2)+\cdots+R_nR_n'H((z-\varepsilon)-z_n)+\cdots \\
=&R_1^2H(z-(z_1+\varepsilon))+R_2R_2'H(z-(z_2+\varepsilon))+\cdots+R_nR_n'H(z-(z_n+\varepsilon))+\cdots
\end{aligned}
$$

$$
\frac{b_1(z)}{1-\int_{-\infty}^{z-\varepsilon}dz' b_1(z')\int_{z'-\varepsilon}^{z'+\varepsilon}dz'' c(z'')}
$$

$$
\begin{aligned}
=&R_1\delta(z-z_1)+\frac{R_2'}{1-R_1R_1}\delta(z-z_2)+\frac{R_3'}{1-R_1R_1-R_2'R_2}\delta(z-z_3)+\cdots\\
&+\frac{R_n'}{1-R_1R_1-R_2'R_2-\cdots-R_{n-1}'R_{n-1}}\delta(z-z_n)\\
=&R_1\delta(z-z_1)+R_2\delta(z-z_2)+R_3\delta(z-z_3)+\cdots+R_n\delta(z-z_n)+\cdots\\
=&c(z)
\end{aligned}
$$

Thus the second equation is proved.

In the derivation we used:$R_i=\frac{R_i'}{1-R_1R_1-R_2'R_2-\cdots-R_{i-1}'R_{i-1}}$ It can be proved:

$$
\begin{aligned}
R_i=&\frac{R_i'}{(1-R_1^2)(1-R_2^2)\cdots(1-R_{i-2}^2)(1-R_{i-1}^2)}\\
=&\frac{R_i'}{(1-R_1^2)(1-R_2^2)\cdots(1-R_{i-2}^2)-(1-R_1^2)(1-R_2^2)\cdots(1-R_{i-2}^2)R_{i-1}^2}\\
=&\frac{R_i'}{(1-R_1^2)(1-R_2^2)\cdots(1-R_{i-2}^2)-(1-R_1^2)(1-R_2^2)\cdots(1-R_{i-2}^2)R_{i-1}R_{i-1}}\\
=&\frac{R_i'}{(1-R_1^2)(1-R_2^2)\cdots(1-R_{i-2}^2)-R_{i-1}'R_{i-1}}\\
=&\frac{R_i'}{1-R_1R_1-R_2'R_2-\cdots-R_{i-1}'R_{i-1}}
\end{aligned}
$$

B Test of first type of equation approximation using 1.5D acoustic synthetic data

The first type of equation approximation is presented as follows:

$$
\begin{aligned}
c(z)=&\frac{b_1(z)}{1-\int_{-\infty}^{z-\varepsilon}dz'b_1(z')\int_{z'-\varepsilon}^{z'+\varepsilon}dz''c(z'')}\\
\approx&\frac{b_1(z)}{1-0}\\
\approx&b_1(z)
\end{aligned}
\tag{B.1}
$$

Take it into function F:

$$
F[b_1(z)]_{1p}=\frac{b_1(z)}{1-[\int_{z-\varepsilon}^{z+\varepsilon}dz'b_1(z')]}
\tag{B.2}
$$

And then take fnction F in to the original function, we get first type of equation approximation as follows:

$$
b^{IM}(k)_{1p}=\int_{-\infty}^{\infty}dze^{ikz}b_1(z)\int_{-\infty}^{z-\varepsilon_2}dz'e^{-ikz'}\frac{b_1(z')}{1-[\int_{z'-\varepsilon}^{z'+\varepsilon}dz'''b_1(z''')]}\int_{z'+\varepsilon_1}^{\infty}dz''e^{ikz''}b_1(z'')
\tag{B.3}
$$

It has be shown that the 1st kind approximation can predict correct amplitude and time for all 1st order internal multiples generated at the shallowest reflector and can further attenuate deeper internal multiples in 1D normal incidence.

In this section, we will show the test of the first type of equation approximation using 1.5D synthetic data. The result is very encouraging—the predicted internal multiples have a shape similar to that of the multiples in the data, and the first type of equation approximation is trying to correct the amplitude. As the amplitude issue is very sensitive and complex, we still need further tests using a better data-modeling method, and we need to be able to remove errors that are generated from modeling and processing.

To test the performance of the first type of equation approximation, we used a 1.5D model with 2 reflectors and a single shot gather. The model is shown in Figure 8, on the left side, and the data are shown in Fig 2 on the right.*

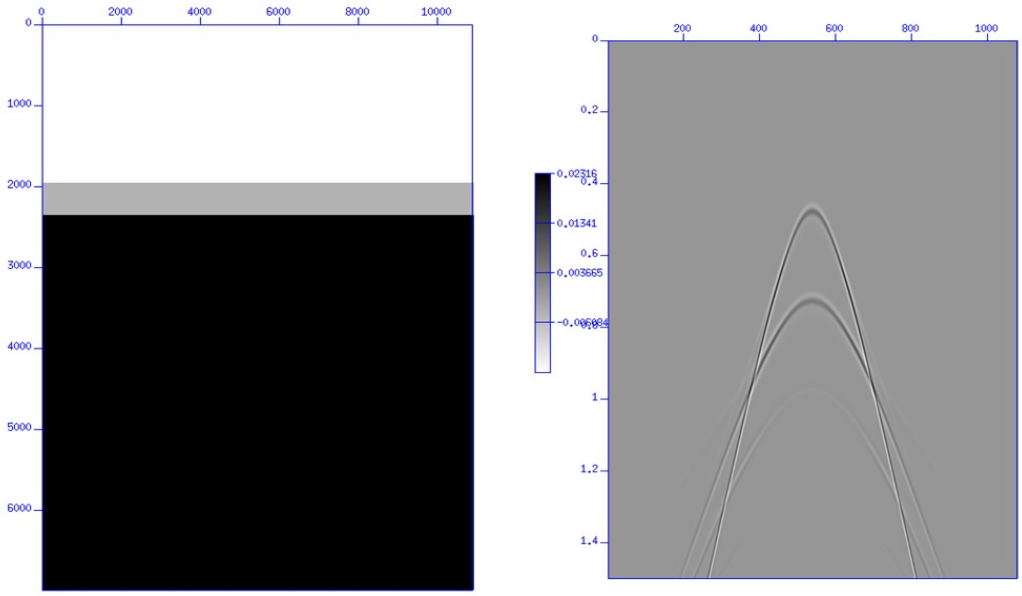

Figure 8: The model is shown on the left and the data is shown on the right.

The model has a constant density $\rho = 1g/cm^3$. The velocity in the first layer is 2000m/s, in the second layer it is 3200m/s, and in the third layer it is 6100m/s. Also, in the data we can see clearly the first and second primary and a 1^{st}-order internal multiple generated at the shallowest reflector. We used a Ricker wavelet to generate the data. First we deconvolved the data and then we calculated the first type of equation approximation using the deconvolved data. Next we convolved the first type of equation approximation with the wavelet. Finally we compared the convolved first

*The data is generated by the finite difference method which may create errors in the data.These errors are not exist in field data.To get synthetic data without errors in amplitude is an important part in our future plan.

type of equation approximation with the internal multiples in the original data.

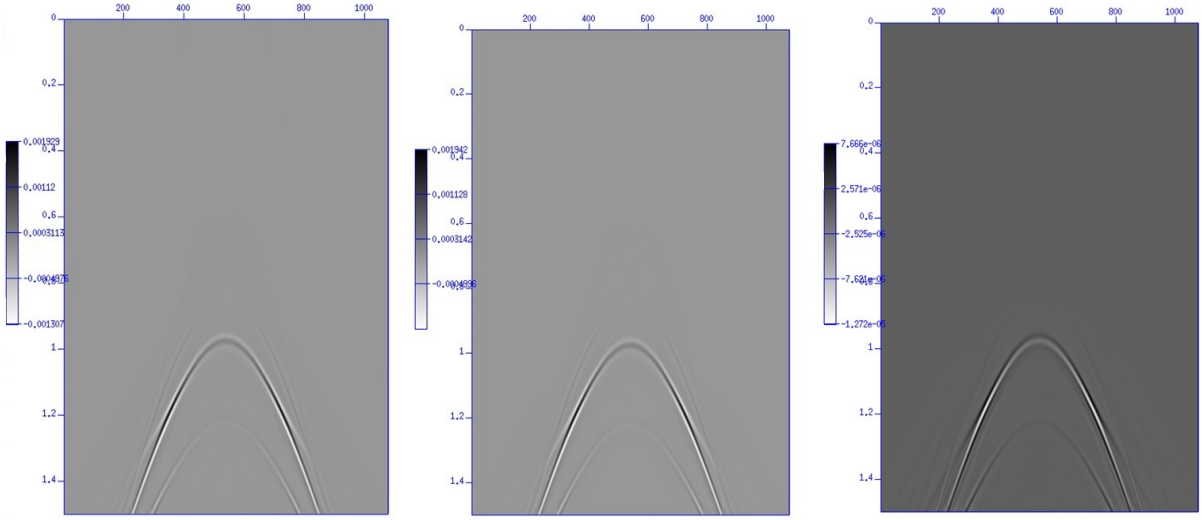

Figure 9: On the left is the predicted internal multiples by IMA, in the middle is the predicted multiples by first type of equation approximation, on the right is the difference between them.

In Figure 9, we compared the results of the IMA (internal multiple attenuator) and the first type of equation approximation. On the left are the internal multiples predicted by the IMA, in the middle are the multiples predicted by the first type of equation approximation, and on the right is the difference between them.

We can see from these figures that the first type of equation approximation is trying to fix the amplitude issue. In principle, the algorithm is able to predict the correct amplitude of all 1st order internal multiples generated at the shallowest reflector, but there are several steps here that may produce errors. First, the finite-difference method generates errors in the amplitude.† The deconvolution and convolution steps also generate some errors in the amplitude. Removing all those errors that arise from modeling and processing will be an important part of our future plan.

This test of the first type of equation approximation on 1.5D data is an important step toward the elimination of all internal multiples in multi-D. The result is very encouraging: the first type of equation approximation produces the same shape as does the IMA and is trying to correct the amplitude of predicted internal multiples. Because the amplitude issue is very sensitive and complex (errors from modeling and processing are introduced), we still need to do a lot more work to predict the correct amplitude.

Future plan:
1.Obtain data without errors (remove errors from modeling).
2.Remove the errors from processing (via deconvolution, convolution, and other steps.)

†these errors are from finite difference modeling and not exist in field data. Thus if we test field data, we will not need to consider these errors.

3.Test the first type of equation approximation for reflectors with a large reflection coefficient (the difference between the IMA results and those from the first type of equation approximation is greater in this situation.)
4.Test the second type of equation approximation in 1.5D.
5.Test these two kinds of equation approximation for multidimensional data.

I would like to thank Dr.Herrera, Hong Liang, Chao Ma, Lin Tang and Jinlong Yang for their help toward completion of this test and for valuable discussions in this research program.

References

Araújo, F. V. Linear and non-linear methods derived from scattering theory: backscattered tomography and internal multiple attenuation. PhD thesis, Universidade Federal da Bahia, 1994.

Chao Ma, Hong Liang and Arthur B.Weglein. "Modifying the leading order ISS attenuator of first-order internal multiples to accommodate primaries and internal multiples: fundamental concept andtheory, development, and examples exemplified when three reflectors generatethe data." Mission Oriented Seismic Research Program Annual Report (2012): 133–147.

H. Liang, C. Ma and A. B. Weglein. "A further general modification of the leading order ISS attenuator of first order internal multiples to accommodate primaries and internal multiples when an arbitrary number of reflectors generate the data: theory, development, and examples." Mission Oriented Seismic Research Program Annual Report (2012): 148–165.

Ramírez, A. C. and A.B. Weglein. "Progressing the analysis of the phase and amplitude prediction properties of the inverse scattering internal multiple attenuation algorithm.." J. of Seismic Expl. 13 (2005): 283–301.

Weglein, A. B., F. V. Araújo, P. M. Carvalho, R. H. Stolt, K. H. Matson, R. T. Coates, D. Corrigan, D. J. Foster, S. A. Shaw, and H. Zhang. "Inverse Scattering Series and Seismic Exploration." Inverse Problems (2003): R27–R83.

Weglein, A. B., F. A. Gasparotto, P. M. Carvalho, and R. H. Stolt. "An Inverse-Scattering Series Method for Attenuating Multiples in Seismic Reflection Data." Geophysics 62 (November-December 1997): 1975–1989.

Wilberth Herrera, Hong Liang Paolo Terenghi,Chao Ma and Arthur B. Weglein. "Progressing amplitude issues for testing 1D analytic data in leading order internal multiple algorithms." Mission Oriented Seismic Research Program Annual Report (2012): 167–188.

Short note: A first step towards a P wave field modeling plan

X. Lin and A. B. Weglein

April 29, 2013

Abstract

In 2D and 3D heterogeneous elastic media, the P- and S-wave equations are coupled. In this case, the equation result of ϕ_p will take all history and intermediate episodes of P- and S-wave propagation into account. Migration and inversion work, which require accurate P-P events, give us the motivation to model and predict only P-wave events from an elastic world. In this short note, we revisit a wave-theory method that is based on Weglein (2012) that can model both the phase and the amplitude of waves that spend all their history as P-waves. We also provide a basic implementation for obtaining operators that are related to the uncoupled P- and S- components.

1 Introduction

As we all know, wave-theory modeling is widely used because of its accuracy and its inclusion of propagation phenomena. However, the wave-theory method has a limitation in selecting a path or wave type of interest from all the events. Conventional finite-difference (wave-theory) modeling methods coded in Cartesian coordinates face the issue that P- and S-wave events come out simultaneously in the final record because all displacements are projected in the (x, y, z) domain. In the 2012 M-OSRP annual report(Weglein, 2012), the formalism of the uncoupled signal-channel P-wave equation was proposed . As that report pointed out, the wave-theory method that Weglein proposed can model and predict P-waves (and P-wave events in recorded data) without using the S-wave field. The P-wave modeling series allows for the selectivity of events that spend all their history as P-waves in a heterogeneous medium, so that we can select the path of interest on the basis of wave-type. In this note, we review the formalism of modeling and selecting P-wave events, and we introduce a basic method for transferring the displacement domain to the P-S domain for implementation.

2 Isotropic heterogeneous elastic media

2.1 2D media

We are familiar with the acoustic wave equation, as shown here,

$$\left[\nabla^2 + \frac{\omega^2}{c^2}\right]\phi = \rho$$

, where c is the wave velocity, ω is the angular frequency and ρ is a source term. In an elastic medium, the ρ part on the right will turn out to be very complicated. Here, with the help of the scattering theory, we choose to describe a medium as an isotropic homogeneous whole-space background plus a perturbation in the properties.The whole-space background and the perturbation combine to result in the properties in an actual medium. If we can express the perturbation operator as $(V_{pp}, V_{ps}, V_{sp}, V_{ss})$, then a coupled equation for a P- and S- wave pressure field (ϕ_p and ϕ_s) can be written as

$$\left[\nabla^2 + \frac{\omega^2}{\alpha_0^2}\right]\phi_p = V_{pp}\phi_p + V_{ps}\phi_s + f_p \tag{2.1}$$

$$\left[\nabla^2 + \frac{\omega^2}{\beta_0^2}\right]\phi_s = V_{ss}\phi_s + V_{sp}\phi_p + f_s \tag{2.2}$$

, where α_0 is the P-wave velocity and β_0 is the S-wave velocity. Let us introduce a Green's function as G_s, which satisfies

$$\left[\nabla^2 + \frac{\omega^2}{\beta_0^2} - V_{ss}\right]G_s = \delta. \tag{2.3}$$

Notice that the G_s^0 is different from G_s and is defined as

$$\left[\nabla^2 + \frac{\omega^2}{\beta_0^2}\right]G_s^0 = \delta. \tag{2.4}$$

Using the Lippmann-Schwinger equation, G_s can be expressed as a Born series with a shear-wave Green's function in the reference medium G_s^0, and a shear perturbation operator V_{ss}. In this case, $G_s = \sum_{k=0}^{\infty} G_s^0 \left(V_{ss} G_s^0\right)$.

Similarly, according to equations (2.2) and (2.3), the shear-wave field can be expressed with the compressional wave field ϕ_p, the source term f_s and the perturbation operator V_{sp}, by using the Lippmann-Schwinger equation, as

$$\phi_s = \int G_s(V_{sp}\phi_p + f_s) \tag{2.5}$$

where G_s is chosen as the causal solution. The final modeling formalism can be expressed as (Weglein, 2012),

$$\mathsf{V} = V_{pp} + V_{ps}\int G_s V_{sp} \tag{2.6}$$

$$\mathsf{f} = V_{ps} \int G_s f_s + f_p \tag{2.7}$$

$$\phi_p^0 = G_p^0 \mathsf{f} \tag{2.8}$$

$$\phi_p = \phi_p^0 + G_p^0 \mathsf{V} \phi_p^0 + G_p^0 \mathsf{V} G_p^0 \mathsf{V} \phi_p^0 + \cdots \tag{2.9}$$

where V and f are notations representing a complicated perturbation and a source term, respectively. In this equation, the source (f_p, f_s) is taken into account. If we assume that the source generates only P-waves, namely, that $f_s = 0$, then $\mathsf{f} = f_p$ in equation (2.7). In addition, and equation (2.9) is the modeling equation for P-waves in a 2D heterogeneous elastic medium.

2.2 3D media

In 3D isotropic heterogeneous media, the perturbation of three components (P, S_H, S_V) consists of a matrix. The index of S_H represents a shear-horizontal channel, and the index of S_V represents a shear-vertical channel. Similarly as in the 2D case, the source here only generates a P-wave, which is

$$\overrightarrow{f} = \begin{pmatrix} f_p \\ 0 \\ 0 \end{pmatrix}. \tag{2.10}$$

Three coupled equations for a three-component wave field are

$$\begin{aligned}
\left[\nabla^2 + \frac{\omega^2}{\alpha_0^2} - V_{pp}\right] \phi_p &= V_{PS_H} \phi_{S_H} + V_{PS_V} \phi_{S_V} + f_p \\
\left[\nabla^2 + \frac{\omega^2}{\beta_0^2} - V_{S_H S_H}\right] \phi_{S_H} &= V_{S_H P} \phi_P + V_{S_H S_V} \phi_{S_V} \\
\left[\nabla^2 + \frac{\omega^2}{\beta_0^2} - V_{S_V S_V}\right] \phi_{S_V} &= V_{S_V P} \phi_P + V_{S_V S_H} \phi_{S_H}.
\end{aligned} \tag{2.11}$$

After introducing three Green's functions, G_p^0, G_{S_H}, and G_{S_V}, which are causal solutions of

$$\begin{aligned}
\left[\nabla^2 + \frac{\omega^2}{\alpha_0^2}\right] G_p^0 &= \delta \\
\left[\nabla^2 + \frac{\omega^2}{\beta_0^2} - V_{S_H S_H}\right] G_{S_H} &= \delta \\
\left[\nabla^2 + \frac{\omega^2}{\beta_0^2} - V_{S_V S_V}\right] G_{S_V} &= \delta
\end{aligned} \tag{2.12}$$

, respectively, we can derive the P-wave field by using a scalar equation,

$$\phi_p = \phi_p^0 + G_p^0 \mathsf{V} \phi_p \tag{2.13}$$

$$\mathsf{V} = V_{pp} + V_{PS_H} \left(\sum_{k=0}^{\infty} (G_{S_H} V_{S_H S_V} G_{S_V} V_{S_V S_V})^k \right) G_{S_H} (V_{S_H P} + V_{S_H S_V} G_{S_V} V_{S_V P}) + V_{PS_V} G_{S_V}$$

$$\times \left(V_{S_V P} + V_{S_V S_H} \left(\sum_{k=0}^{\infty} (G_{S_H} V_{S_H S_V} G_{S_V} V_{S_V S_V})^k \right) G_{S_H} (V_{S_H P} + V_{S_H S_V} G_{S_V} V_{S_V P}) \right). \quad (2.14)$$

A Born series provides a modeling formalism for P-wave events(Weglein, 2012),

$$\phi_p = \phi_p^0 + G_p^0 \mathsf{V} \phi_p^0 + G_p^0 \mathsf{V} G_p^0 \mathsf{V} \phi_p^0 + \cdots. \quad (2.15)$$

Here, we make an assumption that the subsurface is isotropic and has horizontal reflectors without anisotropic fracturing or a special structure that could convert a P-wave into a S_H-wave. Given the fact that the polarizations of the two shear waves are both perpendicular to the polarization of the P-wave and that the S_H-wave vibration is normal to the incidence plane, the P-wave displacement cannot project onto the S_H vibration direction. Therefore, we only consider P- and S_V-wave conversions. In this situation, the perturbation part can be simplified as,

$$\mathsf{V} = V_{pp} + V_{PS_V} G_{S_V} V_{S_V P}, \quad (2.16)$$

where $G_{S_V} = \sum_{k=0}^{\infty} G_{S_V}^0 \left(V_{S_V S_V} G_{S_V}^0 \right)$. The case of the 3D isotropic heterogeneous medium P-event modeling degenerates to a 2D case when the assumption of only P- and S_V- conversion is made. On the other hand, if the complicated term V is replaced by V_{pp}, the P-events in predicting data will only have intermediate P-wave episodes in their history; i.e.

$$\phi_p = \phi_p^0 + G_p^0 V_{pp} \phi_p^0 + G_p^0 V_{pp} G_p^0 V_{pp} \phi_p^0 + \cdots \quad (2.17)$$

3 Basic multi-component elastic-medium method

The operators under the displacement domain are denoted by calligraphic type, such as $\mathcal{L}$, $\mathcal{V}$, that satisfy

$$\mathcal{L}\mathbf{u} = \mathbf{f}$$

$$\rho \omega^2 u_{im} (\overrightarrow{r_g}, \overrightarrow{r_s}, \omega) + \left(C_{ijkl} u_{km,l} (\overrightarrow{r_g}, \overrightarrow{r_s}, \omega) \right)_{,j} = -A(\omega) \delta_{im} \delta (\overrightarrow{r_g} - \overrightarrow{r_s}). \quad (3.1)$$

We have the perturbation under the displacement domain in an isotropic medium, which can be expressed as (Weglein and Stolt, 1992)

$$\mathcal{V} = -\rho_0 \begin{bmatrix} a_\rho \omega^2 + \alpha_0^2 a_\gamma \partial_x^2 + \beta_0^2 \partial_z a_\mu \partial_z & \left(\alpha_0^2 a_\gamma - 2\beta_0^2 a_\mu \right) \partial_z \partial_x + \beta_0^2 \partial_z a_\mu \partial_x \\ \partial_z \left(\alpha_0^2 a_\gamma - 2\beta_0^2 a_\mu \right) \partial_x + \beta_0^2 a_\mu \partial_z \partial_x & a_\rho \omega^2 + \alpha_0^2 \partial_z a_\gamma \partial_z + \beta_0^2 a_\mu \partial_x^2 \end{bmatrix} \quad (3.2)$$

where $a_\rho = \rho/\rho_0 - 1$, $a_\gamma = \gamma/\gamma_0 - 1$, $a_\mu = \mu/\mu_0 - 1$ and α_0, β_0 are P- and S-wave velocity in reference medium respectively. Here, for convenience in calculation, the perturbation operator can be transformed to the P-S domain by (Matson, 1997; Clayton and Brown, 1979)

$$V = \Pi \mathcal{V} \Pi^{-1} \Gamma^{-1} \quad (3.3)$$

where

$$\Pi = \begin{bmatrix} \partial_x & \partial_z \\ -\partial_z & \partial_x \end{bmatrix} \quad \Pi^{-1} = \begin{bmatrix} \partial_x & -\partial_z \\ \partial_z & \partial_x \end{bmatrix} \nabla^{-2} \quad \Gamma_0^{-1} = \begin{bmatrix} \frac{1}{\gamma_0} & 0 \\ 0 & \frac{1}{\mu_0} \end{bmatrix}$$

In these matrices, γ_0 is the P-wave modulus or longitudinal modulus ($\alpha_0 = \sqrt{\frac{\gamma_0}{\rho}}$), and μ_0 is the shear modulus ($\beta_0 = \sqrt{\frac{\mu_0}{\rho}}$) in reference medium. In a perturbation term under the P-S domain, there is an integral operator, ∇^{-2}, which will be discussed in the next section.
At the beginning, the role of $\mathcal{V}$ was to scatter the wave displacements as horizontal and vertical components. After this kind of transformation, the wave can be scattered as P- and S-wave pressure by the new perturbation operator V. So that the G_p^0 can be used to propagate the wave in reference medium as P-wave pressure and then wave can be scattered by V in consistence as shown in Figure 1.

4 Explanation of the ∇^{-2} operator acting on G_p^0

The value of the integral operator $\frac{1}{\nabla^2}$ can be determined by the term that it acts on (Zhang, 2006). For example, we can consider a simple term that is the first term of 2D P-wave-only modeling as

$$G_p^0 \frac{1}{\nabla^2} G_p^0 \tag{4.1}$$

, where G_p^0 satisfies

$$\left(\nabla'^2 + \frac{\omega^2}{\alpha_0^2}\right) G_p^0\left(x', z', x'', z'', \omega\right) = \delta\left(x' - x''\right)\delta\left(z' - z''\right). \tag{4.2}$$

Next, we Fourier transform over x' and z' to solve for G_p^0. After we transform back to the spatial domain, we can obtain the bilinear form of the Green's function,

$$G_p^0\left(x', z', x'', z'', \omega\right) = (\frac{1}{2\pi})^2 \int\int \frac{e^{ik_x^I(x'-x'')} e^{ik_z^I(z'-z'')}}{k^2 - k_x^{I2} - k_z^{I2}} dk_x^I dk_z^I. \tag{4.3}$$

The term can be written as

$$\begin{aligned} & G_p^0 \frac{1}{\nabla^2} G_p^0 \\ = \; & (\frac{1}{2\pi})^4 \int\int dx'' dz'' \int\int \frac{e^{ik_x'(x_g - x'')} e^{ik_z'(z_g - z'')}}{k^2 - k_x'^2 - k_z'^2} dk_x' dk_z' \\ & \times \frac{1}{\nabla''^2} \int\int \frac{e^{ik_x''(x''-x_s)} e^{ik_z''(z''-z_s)}}{k^2 - k_x''^2 - k_z''^2} dk_x'' dk_z''. \end{aligned} \tag{4.4}$$

The outside term of the Green's function with the integral operator can be expressed as,

$$\frac{1}{\nabla''^2}(-i\pi) e^{ik_s x''} \frac{e^{iq_s(z''-z_s)}}{q_s} = \frac{1}{-k_s^2 - q_s^2}(-i\pi) e^{ik_s x''} \frac{e^{iq_s(z''-z_s)}}{q_s} \tag{4.5}$$

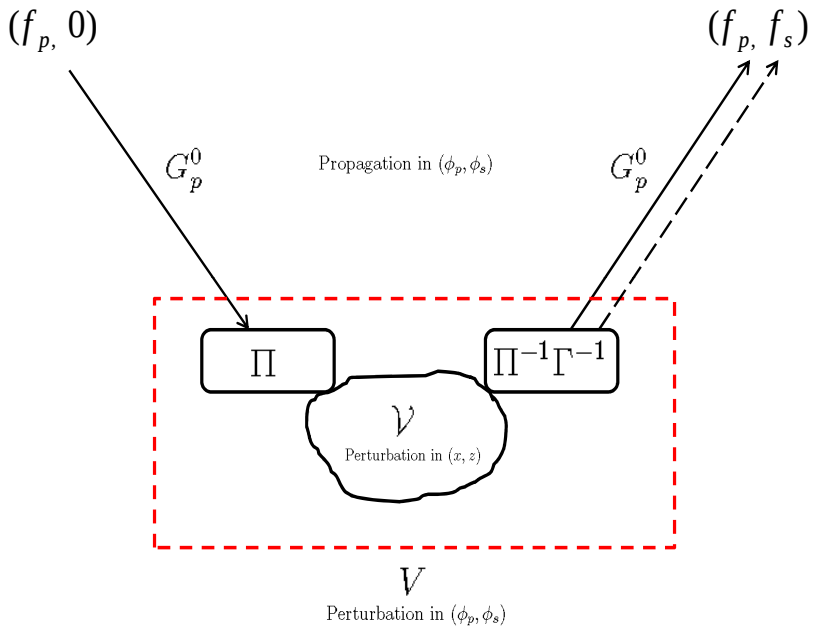

Figure 1: Scattering in P- and S-wave pressure domain.

where $q_s^2 = k^2 - k_s^2$. In this case, the assumption is that the source location must be shallower than the scattering point.

5 Conclusions and future plan

In this short note, we conclude that
(a) The formalism for modeling the phase and amplitude of a P-event has been established and is understood, and by using Born series modeling we can select the events that have only intermediate P-wave episodes in their histories. Equations (2.9) and (2.15) are forward series on which the

modeling of all possible P-event histories is based, as shown in Weglein (2012).
(b) The issue of perturbation under the P-S domain can be solved by the transform operator. However, the differential operators are very complicated even when we only look at V_{pp} in equation (2.17). For example, the perturbation term for a 1D earth (i.e., in which properties only vary in z) can be written as

$$V_{pp} = -\nabla^2 a_\gamma - \left[k_0^2(a_\rho\partial_x^2 + \partial_z a_\rho \partial_z) + 4\partial_z a_\mu \partial_z \partial_x^2 - 2\partial_z^2 a_\mu \partial_x^2 - 2a_\mu \partial_z^2 \partial_x^2\right] \frac{1}{\nabla^2}$$

, where $k_0 = \frac{\omega}{\alpha_0}$, $a_\mu = \frac{\beta_0^2}{\alpha_0^2}(\frac{\mu}{\mu_0} - 1)$. In forward modeling, the Born series form can be implemented because the Green's function in the reference medium, the perturbation and properties of the source are known. It is appropriate to examine a single-reflector 1.5D, where the source is a 2D line source (an oblique incident wave) and the properties vary in 1D at the beginning. The algorithm guarantee that the incidence will be pure P-wave. This test will allow us to understand how different types of waves, such as converted and unconverted waves, are constructed by a forward P-wave-only series.
(c) This formalism could be tested further by a modeling project (for example, SEAM) with a smoothed background associated with a small perturbation, in which the converted-wave always is treated as noise (Weglein, 2012).

6 Acknowledgements

We are grateful to all M-OSRP sponsors for their long-term encouragement and support. All members in the M-OSRP group are thanked for their help of valuable discussions and shared information. We especially thank Lin Tang for reading this note and giving suggestions.

References

Clayton, Robert W. and David Brown. The choice of variables for elastic wave extrapolation. Technical Report 06, SEP, 1979.

Matson, K. H. An inverse-scattering series method for attenuating elastic multiples from multicomponent land and ocean bottom seismic data. PhD thesis, University of British Columbia, 1997.

Weglein, Arthur B. "Short note: A formalism for (1) modeling the amplitude and phase of pressure waves from a heterogeneous elastic medium and (2) selecting and predicting P-wave events that have only experienced P-wave episodes in their history." Mission-Oriented Seismic Research Program Annual Report (2012): 364–370.

Weglein, Arthur B. and R.H. Stolt. "Approaches on linear and non-linear migration-inversion. Personal Communication." (1992).

Zhang, H. Direct non-linear acoustic and elastic inversion: Towards fundamentally new comprehensive and realistic target identification. PhD thesis, University of Houston, 2006.

Initial study and implementation of the convolutional Perfectly Matched Layer for modeling of the 2D acoustic wave equation

Wilberth Herrera* and Arthur Weglein*, M-OSRP/Physics Dept./UH*

April 29, 2013

Abstract

In this report, first steps and results of the implementation of the Convolutional Perfectly Matched Layer (CPML), for the modeling of the 2D acoustic heterogeneous wave equation are presented. We also compare the conditions to set to zero, for all angles of incidence, the reflection coefficient at the interface between two PML media, with the analogous conditions for the reflection coefficient at an interface between two acoustic media. A side product of the present work for the M-OSRP is a code to create synthetic data, using Finite-Difference (FD) methods with PML BCs.

We also provide a short description of the main stages involved in the original Reverse Time Migration (RTM) algorithm, with focus on the 2D acoustic heterogeneous wave equation. We include a derivation of the equations of the CPML for the backward propagation of the data, which is part of the RTM. As far as the authors knowledge, these equations and derivations have not been reported in the literature. The reason we include the RTM is because the present report can be considered part of a broader research project whose objective is to compare the RTM with PML BCs with the Green's theorem based RTM, developed within the M-OSRP.

1 Introduction

The M-OSRP is a research consortium, whose objective is to provide solutions to current challenges and problems present in exploration seismology, with the final goal of improving the location of hydrocarbons, and hence to increase the rate of successful drilling.

A particular challenge in which the M-OSRP is developing direct and impactful response, is in the inability to locate targets beneath complex media. For this, improved and more efficient modeling tools, that are capable to handle complex velocity and density profiles, are often necessary. In particular for the M-OSRP, this is a fundamental requirement as the methods developed in this consortium are amplitude sensitive.

Another reason for the need of improved modeling tools is provided by RTM, one of the most successful migration methods for complex media used by the oil industry nowadays. RTM allows

the imaging of two-way waves −e.g., waves that move down and up either from source to a reflector or from a reflector to the geophones (Weglein et al. 2011a, Weglein et al. 2011b). The computational implementation of this method starts with the modeling of the source wavefield, i.e., by extrapolation of the source wavefield forward in time, using the full two-way wave equation. The extrapolation of the source wavefield is followed by continuation of reflection data backwards in time, using also the full two-way wave equation. This is followed by an imaging condition (usually the zero-lag crosscorrelation between the two extrapolated fields) to find the reflectivity function (Whitmore 1983, Leveille et al. 2011, Stolt and Weglein 2011).

A modeling technique commonly used in exploration seismology is FD. In particular, the continuation (either of source wavefield or reflection data) stages of RTM are implemented using the time-domain Finite-Difference (TDFD) algorithm. The main advantage of FD methods is their ability to produce the full wavefield: reflections, refractions, turning waves, prismatic waves, etc. This capability is inherited by the RTM technique, as it is capable of imaging all the waves just mentioned, but the imaging condition prevents the algorithm from keeping the true amplitude information (Leveille et al. 2011). Some modifications to the imaging condition had been proposed in Zhang et al. (2005), Zhang et al. (2007) and Zhang and Sun (2008), in order to turn RTM into a true amplitude algorithm.

However, one drawback of the FD is the introduction of artifacts: the method intrinsically requires truncation of the computational domain in which the wave equation is being solved. Therefore, it is necessary to feed the computer with the values of the wavefield, at the boundary that results from truncation. It is also necessary to add some FD grid points beyond this boundary (Figure 1)*. The BCs imposed at the boundary of the computational domain are usually either Dirichlet or Neumann. Unfortunately, in the modeling of wave equations, the magnitude of their oscillatory solutions cannot be neglected at the location of this boundary. Therefore, truncation of the computational domain with either of the boundary conditions just mentioned will introduce artifacts in the form of reflections of waves striking its boundary. This is why both Dirichlet and Neumann boundary conditions are called hard-wall boundary conditions (Johnson 2007). These reflections are artifacts because they are not present in the original unbounded problem, and their presence in the computational simulation will clearly introduce noise that can potentially damage the final result of any process that involves modeling of wave propagation, and in particular the RTM algorithm. A common approach, to minimize the effects of these artifacts, consists of placing the boundaries of the computational domain far from the region of interest for the modeling. In this way, the time window of the simulation does not allow the reflections at the boundary to reach the region of interest, and no interference is produced. However, in practice a big computational domain significantly increases the cost of the simulation.

*The specific number of additional grid points is determined by the stencil that results from the FD scheme, that is chosen for modeling.

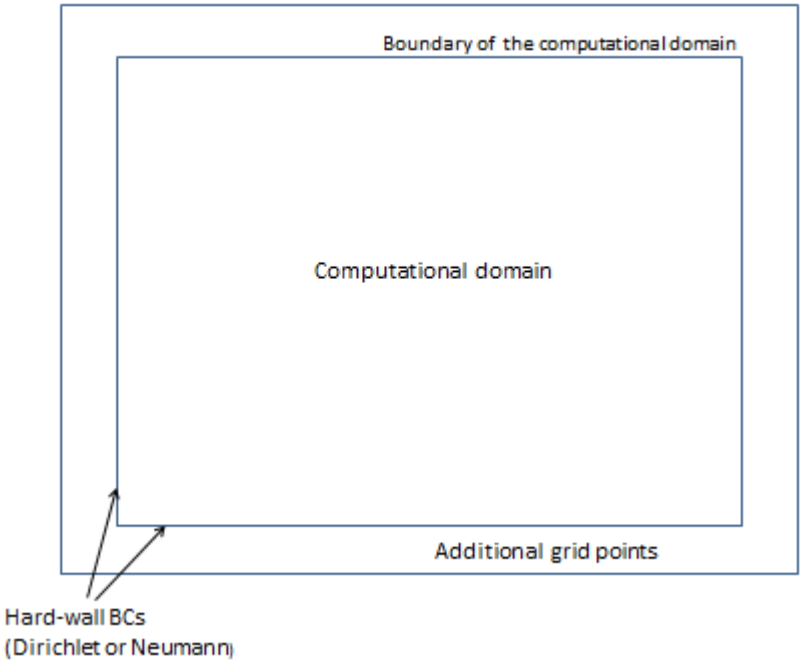

Figure 1: Array of a typical FD simulation in 2D: The computational domain is the region in which the relevant wave equation is solved, and the FD grid extends a few cells beyond this domain. At the boundary of the computational domain a Hard wall BC (Dirichlet or Neumann) it is usually imposed. The cells (or grid points), beyond the computational domain, are required by the stencil of the particular FD scheme involved in the modeling, and the value of the wavefield on these grid points are usually set to zero.

Several techniques have been developed in order to deal with the artifacts just mentioned (Merewether 1971, Bérenger 1977, Engquist and Majda 1977). A particular successful approach is that based on *absorbing boundary conditions* (ABCs), which means that waves propagating in the computational domain and striking the boundary are absorbed without reflection. Unfortunately, existing families of ABC's are restricted mostly to absorbing waves at normal incidence, which is not a bad assumption from a theoretical point of view: as the computational domain grows in size, most of the radiation hitting the boundary can be considered to have normal incidence (Bérenger 2007). However, as mentioned in the paragraph above, a big computational domain translates into high computational cost. Another disadvantage is that many ABC's are formulated only for homogeneous materials at regions close to the boundaries of the FD domain (Johnson 2007), while in practice many situations involve some kind of heterogeneities.

A major development towards the solution of this puzzle is presented in Bérenger (1994), concerning the reflection artifacts produced by truncation of the computational domain. The solution consisted of placing an *absorbing boundary layer* adjacent to the boundary of the computational domain.

The material filling this layer was designed to absorb incident waves without reflection (for all frequencies and any angle of incidence) at the interface between the propagation medium filling the computational domain and the domain itself. Such an absorbing boundary layer is called, because of its non reflective properties, a *perfectly matched layer,* or **PML**. This may sound unfamiliar, as a wave is usually reflected when it goes through an interface. However, Bérenger was able to show that a material with such non reflective properties can be constructed, at least theoretically. This method is so effective for the modeling of wave phenomena, that the computational domain does not need to be enlarged far beyond the region of interest for the simulation, and therefore the computational cost is not increased significantly with respect to the standard FD.

Although the PML method was originally developed for modeling the propagation of electromagnetic waves, it has been useful in exploration seismology in order to improve the results of the modeling of acoustic waves and of the image produced by RTM, and at the same time the PML has contributed to lower their computational cost. However, the implementation of the PML for RTM differs somewhat from that for the modeling, because RTM involves backpropagation of the acquisition data with time, while modeling only involves forward propagation of the source with time.

In a previous report (Herrera et al. 2012), a theoretical discussion of the PML technique for the modeling of the 2D acoustic wave equation was provided. In particular, both the original *split-field* formulation of Bérenger and the *complex stretching coordinate* approach were explained, and that was followed by an explanation of the existing relation among them.

In this report the work in Herrera et al. (2012) is further progressed. In particular, we provide a detailed analysis and comparison of the reflection coefficient between two PML media, with the reflection coefficient at an interface between two acoustic media. To the awareness of the authors, this comparison and analysis has not been reported elsewhere. We also present the Convolutional Perfectly Matched Layer (CPML) introduced in Roden and Gedney (2000) and Komatitsch and Martin (2007) and we show some examples resulting from the implementation of this technique in the modeling of the acoustic wavefield (i.e., for the forward propagation of the source wavefield in time).

In addition to the improvement of modeling tools within the M-OSRP and the results of RTM, our interest in the PML technique arises also from two recent papers Weglein et al. (2011a) and Weglein et al. (2011b). In these references a novel approach to RTM, using Green's theorem, is addressed. This new RTM might provide an alternative to the PML technique in RTM by placing the BCs on a Green's function rather than in the wavefield. This new RTM might also reduce the characteristically high computational cost of the standard RTM. This report can be considered as part of a broader research project, whose objective is to compare the effectiveness of this new Green's theorem approach with respect to the PML-based RTM. Hence, we include a short description of the original RTM algorithm as presented in Whitmore (1983), Baysal et al. (1983) and Stolt and Weglein (2011). We also provide a derivation for the equations of the CPML for the backward propagation of data. As far as the authors knowledge this derivation has not been reported previously in the literature.

The organization in the present report is as follows: starting with Section 2 we will provide, as

a motivation for the study and implementation of the PML, a brief discussion of the RTM using a velocity-stress formulation of the wave equation, i.e., the wave equation is written as a system of two coupled first-order partial differential equations. In Section 3 we will give a general and qualitative overview of the PML method as implemented for the modeling of wave propagation, appealing to a typical seismic experiment. We will also compare the reflection coefficient for an interface between two PML media with that of the interface between two acoustic media, in order to stress the differences between them and demonstrate why non reflective PML-PML interfaces are allowed. In Section 4 we briefly review the *complex coordinate stretching* approach for PML, and we follow that by a detailed discussion of the CPML for modeling i.e. forward propagation with time. Section 5 is devoted to a theoretical discussion and derivation of the equations for the implementation of the CPML for RTM i.e. for the backward propagation of the data with time. Two appendices are included: in the first one we describe the basics of FD methods on staggered grids, while in the second one we provide the relevant calculations of the CPML.

2 Reverse time migration

Reverse time migration was introduced in the early 1980s (Whitmore 1983 and Baysal et al. 1983) and consists, as does any other imaging algorithm, of three basic stages:

- Forward propagation of the source wavefield (modeling) in time.
- Backward propagation of the recorded data in time
- Application of an imaging condition to construct the image function.

As was mentioned in the introduction, RTM has the ability to image two-way wave equations, reflections, refractions, turning waves, prismatic waves, etc. In this section we will describe the RTM method. In the process we will also see why it can image all kinds of waves and hence why it is useful for complex geological environments. We will also point out the reason for the high computational cost of the algorithm. Further, in this work we will focus exclusively on 2D, but all the results can be trivially extended to 3D.

2.1 Forward propagation in time (or modeling)

In the modeling stage, the source wavefield is propagated from an initial time $t = 0$ corresponding to the ignition of the source, to the maximum recording time $t = T_{max}$ of the geophones. This propagation is typically performed by applying a suitable FD scheme, using an initial velocity and density model, to the full wave equation. In this way a wavefield ${}_sP(x, z, t)$ is created.

On the other hand, the acoustic (source-free) wave equation for a generic pressure wavefield $P(\mathbf{x}, t)$ is:

$$\nabla \cdot (a \nabla P) = \frac{1}{b} \frac{\partial^2 P}{\partial t^2}, \tag{2.1}$$

where $\mathbf{x} = (x, z)$ is a generic point in a 2D earth with z increasing in the downward direction and $c = \sqrt{ab}$ is the phase (or propagation) velocity of the wave, for parameters $a(\mathbf{x})$ and $b(\mathbf{x})$ of the medium. Notice that equation (2.1) does not require $a(\mathbf{x})$ and $b(\mathbf{x})$ to be constant, and hence it is valid for both homogeneous and heterogeneous media. For seismic applications, $a(\mathbf{x})$ is the inverse of the density:

$$a(\mathbf{x}) = \frac{1}{\rho(\mathbf{x})}. \tag{2.2}$$

As was explained in Johnson (2007) (and reviewed in Herrera et al. 2012) it is convenient for its PML implementation, to write equation (2.1) as an equivalent system of two coupled first-order differential equations:

$$\frac{\partial \mathbf{v}}{\partial t} = -a \nabla P \qquad\qquad \frac{\partial P}{\partial t} = -b \nabla \cdot \mathbf{v}, \tag{2.3}$$

where $\mathbf{v}(\mathbf{x}, t) \equiv {}_x v(\mathbf{x}, t)\hat{x} + {}_z v(\mathbf{x}, t)\hat{z}$ is a new auxiliary vector field that represents the velocity of the particles in the medium creating the field. For this reason $\mathbf{v}(\mathbf{x}, t)$ is called the velocity field.

It is easy to show the equivalence of equation (2.1) with equations (2.3): upon multiplication by b^{-1} and differentiation, with time, of the second of equations (2.3), we have

$$\frac{1}{b} \frac{\partial^2 P}{\partial t^2} = -\nabla \cdot \left(\frac{\partial \mathbf{v}}{\partial t} \right) = \nabla \cdot (a \nabla P). \tag{2.4}$$

For the modeling of a system like (2.3) it is convenient to implement an FD scheme using a staggered grid, as it has a high degree of accuracy (Graves 1996) and in general is more accurate than the usual nonstaggered grid (Gilles et al. 2000). Using a second-order approximation for time derivatives and a fourth-order approximation for space derivatives in a 2D model, the discretization of equations (2.3) in a staggered grid leads to (See Appendix A for an elementary introduction to finite difference on staggered grids, and for the derivation of the following expressions)

$$P_{i,j}^{n+1} = P_{i,j}^{n} - b_{i,j} \frac{\Delta t}{\Delta x} \left[\frac{9}{8} \left({}_x v_{i+\frac{1}{2},j}^{n+\frac{1}{2}} - {}_x v_{i-\frac{1}{2},j}^{n+\frac{1}{2}} \right) - \frac{1}{24} \left({}_x v_{i+\frac{3}{2},j}^{n+\frac{1}{2}} - {}_x v_{i-\frac{3}{2},j}^{n+\frac{1}{2}} \right) \right] -$$

$$b_{i,j} \frac{\Delta t}{\Delta z} \left[\frac{9}{8} \left({}_z v_{i,j+\frac{1}{2}}^{n+\frac{1}{2}} - {}_z v_{i,j-\frac{1}{2}}^{n+\frac{1}{2}} \right) - \frac{1}{24} \left({}_z v_{i,j+\frac{3}{2}}^{n+\frac{1}{2}} - {}_z v_{i,j-\frac{3}{2}}^{n+\frac{1}{2}} \right) \right] \tag{2.5}$$

$${}_x v_{i+\frac{1}{2},j}^{n+\frac{1}{2}} = {}_x v_{i+\frac{1}{2},j}^{n-\frac{1}{2}} - a_{i+\frac{1}{2},j} \frac{\Delta t}{\Delta x} \left[\frac{9}{8} \left(P_{i+1,j}^{n} - P_{i,j}^{n} \right) - \frac{1}{24} \left(P_{i+2,j}^{n} - P_{i+1,j}^{n} \right) \right] \tag{2.6}$$

$$ {}_zv_{i+\frac{1}{2},j}^{n+\frac{1}{2}} = {}_zv_{i+\frac{1}{2},j}^{n-\frac{1}{2}} - a_{i,j+\frac{1}{2}} \frac{\Delta t}{\Delta z} \left[\frac{9}{8} \left(P_{i,j+1}^{n} - P_{i,j}^{n} \right) - \frac{1}{24} \left(P_{i,j+2}^{n} - P_{i,j+1}^{n} \right) \right] \tag{2.7} $$

where $P_{i,j}^{n} \equiv P(i\Delta x, j\Delta z, n\Delta t)$, ${}_xv_{i+\frac{1}{2},j}^{n+\frac{1}{2}} \equiv {}_xv((i+1/2)\Delta x, j\Delta z, (n+1/2)\Delta t))$ and ${}_zv_{i,j+\frac{1}{2}}^{n+\frac{1}{2}} \equiv {}_zv(i\Delta x, (j+1/2)\Delta z, (n+1/2)\Delta t))$, $b_{i,j} \equiv b(i\Delta x, j\Delta z)$, $a_{i+1/2,j} \equiv a((i+1/2)\Delta x, j\Delta z)$ and $a_{i,j+1/2} \equiv a(i\Delta x, (j+1/2)\Delta z)$. Notice the evaluations at halfway points in the grid, characteristic of staggered FD schemes.

Usually Dirichlet BCs are imposed on the pressure field P and on both components of the velocity field. The initial condition of the pressure field is the field created by the source after a single propagation step Δt. With regard to the velocity field, the initial conditions are set to zero for both components.

The modeling process for RTM consists of applying equations (2.5)-(2.7) to the source wavefield ${}_sP(x,z,t)$: we start with equations (2.6) and (2.7) to update the components of the velocity field, using the initial values of the fields in their right-hand side. These updated values are then injected on the right hand side of equation (2.5) to update of the source field. Now, the updated value of the source field is reinjected into equations (2.6) and (2.7) for the second updating. This process continues until the time T_{max} is reached.

Figure 2 shows a snapshot of the modeling of a wavefield propagating in a homogeneous medium, using equations (2.5)-(2.7), with the initial and boundary conditions as described in the paragraph above. Note the strong reflections at the boundaries of the computational domain; they are a consequence of the imposed Dirichlet BCs on the fields. As was mentioned in the introduction, these reflections are not present in the real world and they are considered to be noise. Therefore they need to be at least minimized.

Figure 2: Snapshot of the propagation of an acoustic wave in an inhomogeneous medium, using a square FD grid with 1500 grid points at each direction, and Dirichlet BCs at all boundaries of the computational domain. The arrows show the reflections produced at the boundaries of the computational domain by the Dirichlet BCs.

In Figure 2 a square grid with 1500 grid points in each direction is assumed, with a spacing of $5m$ between each grid point at any direction; i.e., the simulation covers an area of $7500 \times 7500m^2$, and $\Delta x = \Delta z = 5m$ in equations (2.5)-(2.7). The time step is chosen as $\Delta t = 0.0005s$ and the propagation velocity is the speed of sound in water, $c = 1500m/s$. With these values it can be seen that the Courant-Friedrichs-Lewy (CFS) condition, equation (A.14), is satisfied. The wavelet of the source is the Gaussian's derivative, with a dominant frequency $f_0 = 0.8926Hz$.

2.2 Backward propagation in time

The second stage consists of backward propagation of the recorded data $D(x, z = 0, t)$ from $t = T_{max}$ to $t = 0$. This backward propagation is carried out using the same wave equation, the same FD scheme (but solving for the fields at a previous time in terms of the fields at later times), and the same velocity and density model as was used for the modeling. The data are imposed as a time-varying boundary condition for the upper boundary of the computational domain: we start with

the data $D(x, z = 0, t = T_{max})$ and we propagate these data back into the earth by a time length Δt. Next, the boundary condition is replaced by the data $D(x, z = 0, t = T_{max} - \Delta t)$ followed by a further propagation by a length Δt. This cycle is continued until the time $t = 0$ is reached. In this way a wavefield ${}_rP(x, z, t)$ is created.

On the other hand, following the discretization for the modeling described in Appendix A, but solving for fields at earlier times, we get the following equations:

$$P_{i,j}^{n-1} = P_{i,j}^{n} + b_{i,j}\frac{\Delta t}{\Delta x}\left[\frac{9}{8}\left({}_xv_{i+\frac{1}{2},j}^{n-\frac{1}{2}} - {}_xv_{i-\frac{1}{2},j}^{n-\frac{1}{2}}\right) - \frac{1}{24}\left({}_xv_{i+\frac{3}{2},j}^{n-\frac{1}{2}} - {}_xv_{i-\frac{3}{2},j}^{n-\frac{1}{2}}\right)\right] + b_{i,j}\frac{\Delta t}{\Delta z}\left[\frac{9}{8}\left({}_zv_{i,j+\frac{1}{2}}^{n-\frac{1}{2}} - {}_zv_{i,j-\frac{1}{2}}^{n-\frac{1}{2}}\right) - \frac{1}{24}\left({}_zv_{i,j+\frac{3}{2}}^{n-\frac{1}{2}} - {}_zv_{i,j-\frac{3}{2}}^{n-\frac{1}{2}}\right)\right] \tag{2.8}$$

$${}_xv_{i+\frac{1}{2},j}^{n-\frac{1}{2}} = {}_xv_{i+\frac{1}{2},j}^{n+\frac{1}{2}} + a_{i+\frac{1}{2},j}\frac{\Delta t}{\Delta x}\left[\frac{9}{8}\left(P_{i+1,j}^{n} - P_{i,j}^{n}\right) - \frac{1}{24}\left(P_{i+2,j}^{n} - P_{i-1,j}^{n}\right)\right] \tag{2.9}$$

$${}_zv_{i,j+\frac{1}{2}}^{n-\frac{1}{2}} = {}_zv_{i+\frac{1}{2},j}^{n+\frac{1}{2}} + a_{i,j+\frac{1}{2}}\frac{\Delta t}{\Delta z}\left[\frac{9}{8}\left(P_{i,j+1}^{n} - P_{i,j}^{n}\right) - \frac{1}{24}\left(P_{i,j+2}^{n} - P_{i,j-1}^{n}\right)\right] \tag{2.10}$$

Hence, the backward propagation in time consists of applying the discretized equations (2.8)-(2.10) to ${}_rP(x, z, t)$, with the data as a boundary condition at the top of the computational domain (i.e. at $z = 0$). It is important to highlight that in this case, unlike in the modeling, the boundary condition for ${}_rP(x, z, t)$ at the top of the computational domain is time-varying, while at other boundaries Dirichlet BCs are kept at all times. For the velocity field, as for modeling, Dirichlet BCs are imposed at all boundaries and at all times. With regard to initial conditions for the velocity field, as for the modeling, zero initial conditions are set up.

As for the modeling, Dirichlet BCs will produce reflections at the end of the computational domain. Although we cannot argue in this case that these boundary reflections are not in the real world (actually, the whole backward propagation concept is not in the real world, as time naturally flows forward), they still need to be removed in order to prevent noise which can potentially damage the effectiveness of the algorithm.

2.3 Imaging condition (zero-lag crosscorrelation)

In the final stage an imaging condition involving ${}_sP(x, z, t)$ and ${}_rP(x, z, t)$, the wavefields created at the two previous stages is applied. The most common imaging condition is the so-called zero-lag crosscorrelation:

$$R(x, z) = \Sigma_{shots}\int_0^{T_{max}} {}_sP(x, z, t)\ {}_rP(x, z, t)dt, \tag{2.11}$$

where $R(x,z)$ is the image (or reflectivity) function. This is when unwanted boundary reflections from previous stages can reduce the effectiveness of the algorithm, as they will be included in the image.

Notice that in equation (2.11) the two wavefields are needed at the same time. However, because both of them are propagated in opposite directions of time, it is not possible to write a code generating both of them at an specific cycle in time i.e., for a given time t_0 we can access ${}_sP(x,z,t_0)$ but we can only access $P_r(x,z,T_{max}-t_0)$. The solution is to store in memory either ${}_sP(x,z,t)$ or ${}_rP(x,z,t)$. Usually ${}_sP(x,z,t)$ is the one selected for storage. In this way, as ${}_rP(x,z,t)$ is backpropagated with time, the corresponding ${}_sP(x,z,t)$ needed for the imaging condition, equation (2.1), is extracted from memory.

The storage of ${}_sP(x,z,t)$ (or maybe ${}_rP(x,z,t)$) at all times is the reason for the high memory requirement (and hence for the expensive computational cost) of RTM, and much of the current research is devoted to lowering this memory requirement (Symes 2007, Clapp 2009, McGarry et al. 2010).

The usage of the full wave equation (rather than some sort of approximation) is what endows RTM with the capability to succeed in areas with complex geological structure. All wave types created in complex environments are solutions of the wave equation, and because RTM uses the wave equation it therefore can handle all waves from complex environments. In other words, when an approximation is imposed on the wave equation in order to simplify the imaging process, the set of solutions of the resulting wave equation is only a subset of the solutions of the full wave equation, and as a result the imaging process can only deal with this subset. A common restriction on the subset of solutions of an approximated wave equation is a maximum incident angle of the waves that can be included in the imaging process.

It is worthwhile to mention that the imaging condition in equation (2.11) is not only valid for RTM, and it can be useful in different migration schemes. Finally, different imaging conditions have been applied in order to improve the results of RTM (Liu et al. 2011, Leveille et al. 2011).

3 PML and finite difference

We will start this section with a qualitative description of the PML method. On the other hand, in Herrera et al. (2012) the original *split-field* formulation for the acoustic wave equation was discussed in detail. In particular the mathematical definition of a PML medium was provided and how to obtain a zero reflection coefficient at the interface between the propagation (acoustic) media and the PML media was explained. In that work the *complex stretching coordinate* approach to PML was also presented.

In the present section we will also progress the discussion in Herrera et al. (2012). In particular we will analyze with more detail the reflection coefficient between two PML media, by direct comparison with the reflection coefficient between two ordinary acoustic media. The reason for this is to stress

out the differences between a PML medium and an acoustic medium, which is a very special PML medium.

Strictly speaking, we will focus on the forward modeling step of RTM; i.e., on the extrapolation of the source wavefield. This assumption is implicit in the fact that we will be dealing with waves propagating forward in time. However, in Section 5 we will discuss briefly the modifications for the backward propagation of the recorded data in time , and we will provide the corresponding FD equations.

3.1 A general overview of PML

In this subsection we will explain in general what the PML technique is about. First of all, it is a computational technique developed for the simulation of unbounded wave phenomena, using the FD method in the time domain. We will assume a single line of geophones i.e.; we will rely on a $2D$ seismic experiment to explain the technique.

It is useful for the implementation of the PML technique to split the space of a seismic experiment into two different zones or regions: first we have the interest region, which is where the entire seismic experiment is performed, and of course it is also where we want to see the results of the RTM. In this region we have the sources, the geophones, the reflectors and a portion of the radiation pattern, which includes of course the waves scattered towards the geophones (i.e., the data). Second, we have the radiation region, consisting of all the space not included in the interest region. This region is the place where the waves produced in the seismic experiment propagate at late times. Because the space in a seismic experiment is unbounded, this region is infinite and therefore it is also called the infinite region (Figure 3).

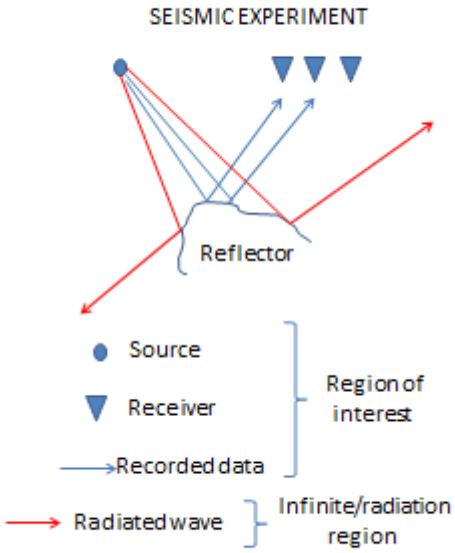

Figure 3: Array of a typical seismic experiment in $2D$: The blue-colored components (including the source, geophones, reflectors and recorded waves) constitute the region of interest for the computational implementation of the PML technique. The red-colored components (the scattered waves not recorded by the geophones) are part of the radiation pattern that eventually propagates to the radiation zone.

To ensure that all interesting phenomena in the seismic experiment are included in the computational implementation of RTM, we place the edges of the computational domain outside the region of interest. The objective is to at least attenuate the reflections created by both of the first two steps in the RTM technique (extrapolation of the source wavefield and continuation of the reflection data) due to the hard-wall B.C's imposed at the boundary of the FD domain. As was mentioned in the introduction, the PML technique is designed for this task, and the idea is to cover the edges of the computational domain with a layer made of a very special material called PML medium. This layer extends in the direction opposite to that of the FD boundary i.e. it is positioned in the interior of the computational domain.

The PML medium is engineered to absorb, without reflection, any radiating wave escaping from the region of interest of the seismic experiment, and incident at the interface between the computational domain and the PML layer [†]. Once in the PML medium, such an incident wave is attenuated until it strikes the boundary of the FD domain, where it is reflected due to the hard-wall boundary conditions. The reflected wave keeps being attenuated as long as it remains in the interior of the

[†]The definition of a PML medium only involves a set of equations governing the propagation of waves in its interior, and it is allowed to have an arbitrary shape. When the shape of the PML medium is a layer, then it is usually called, by abuse of language, just PML instead of PML layer.

PML medium, but this attenuation stops when the reflected wave returns to the region of the computational domain filled with the original propagation medium. However, at this stage, the amplitude of the wave is so attenuated by the PML medium that even if it travels inside the region of interest, its effects can be neglected (Figure 4).

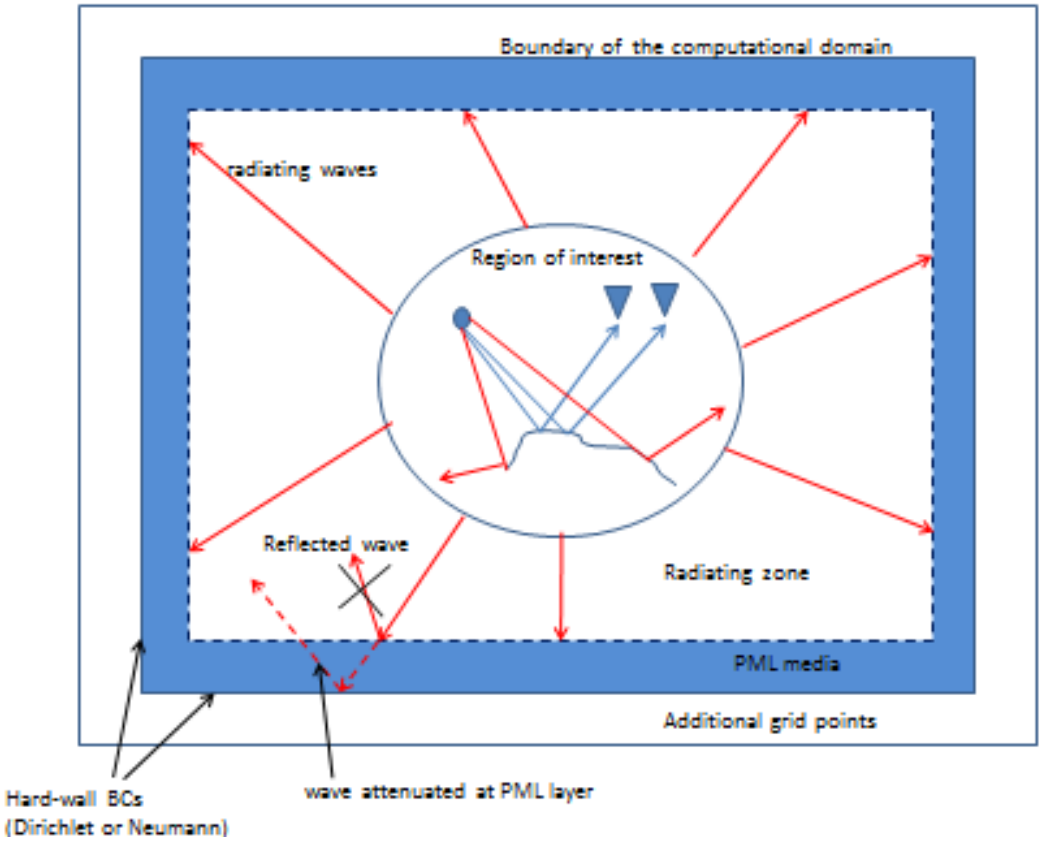

Figure 4: Finite-difference implementation of the PML technique in $2D$: The scattered waves escaping from the interest zone (red colored) eventually strike the radiation zone-PML interface and are transmitted without reflection. Once in the PML medium, the transmitted waves keep being attenuated before and after they are reflected at the boundary of the FD domain, as long as they remain in the interior of the PML zone. In this way, once the waves have exited the PML zone, they are so well attenuated that their effects in the region of interest can be neglected.

3.2 The reflection coefficient

For completeness, we start with the definition of a PML medium according to the *split-field* formulation as reviewed in Herrera et al. (2012). For simplicity we will focus on the same situation discussed in the reference just mentioned, namely on the $2D$ version of the acoustic wave equation,

written as in equations (2.3). Making the derivatives and the components of the vector field $\mathbf{v}$ explicit, equations (2.3) are equivalent to the following set of equations:

$$\frac{\partial\ _x v}{\partial t} = -a\frac{\partial P}{\partial x} \qquad\qquad \frac{\partial\ _z v}{\partial t} = -a\frac{\partial P}{\partial z}$$

$$\frac{\partial P}{\partial t} = -b\left(\frac{\partial\ _x v}{\partial x} + \frac{\partial\ _z v}{\partial z}\right). \tag{3.1}$$

Now we are ready to define a general heterogeneous acoustic-PML medium. Assuming an artificial splitting of the pressure field into two nonphysical subcomponents

$$P = P_x + P_z, \tag{3.2}$$

and the introduction of four positive and nonphysical constants (q_x, q_x^*, q_z, q_z^*), called PML parameters, the definition of the $2D$ acoustic PML media is given by the following set of equations:

$$\frac{\partial\ _x v}{\partial t} + q_x\ _x v = -a\frac{\partial}{\partial x}(P_x + P_z), \tag{3.3}$$

$$\frac{\partial\ _z v}{\partial t} + q_z\ _z v = -a\frac{\partial}{\partial y}(P_x + P_z), \tag{3.4}$$

$$\frac{\partial P_x}{\partial t} + q_x^* P_x = -b\frac{\partial\ _x v}{\partial x}, \tag{3.5}$$

$$\frac{\partial P_z}{\partial t} + q_z^* P_z = -b\frac{\partial\ _z v}{\partial z}. \tag{3.6}$$

Notice that if

$$q_x = q_x^* = q_z = q_z^* = 0, \tag{3.7}$$

the acoustic PML medium reduces to the original acoustic medium of equations (3.1). For this reason the medium defined by equations (3.1) is called the *acoustic host medium*.

Notice from equations (3.3)-(3.6) that this formalism is defined in the time domain. This is in contrast with the *complex stretching coordinate* approach to be reviewed later on this section, which is defined in the frequency domain.

In Herrera et al. (2012) the reflection coefficient at a vertical interface between two PML media (Figure 5) was calculated as

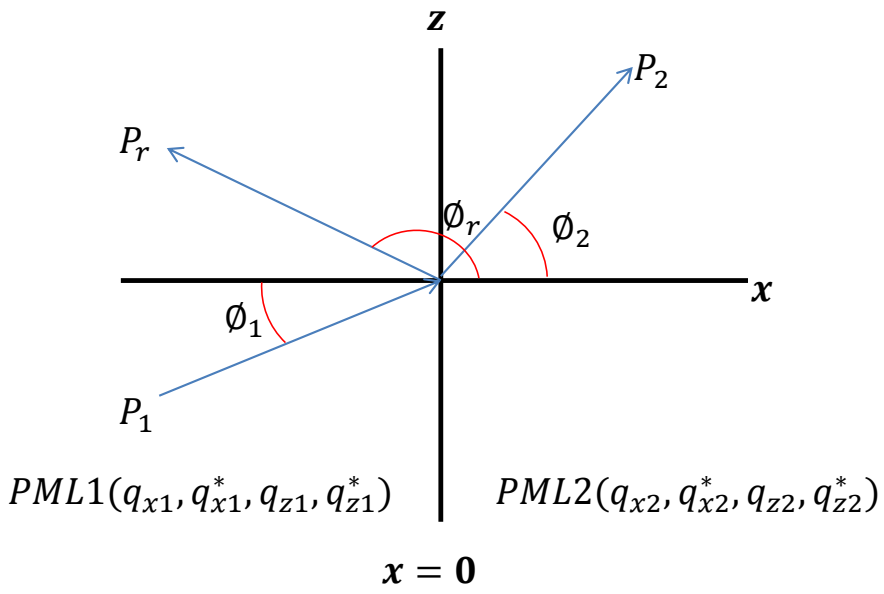

Figure 5: Two semi-infinite PML media defined by two sets of parameters $(q_{x1}, q_{x1}^*, q_{z1}, q_{z1}^*)$ and $(q_{x2}, q_{x2}^*, q_{z2}, q_{z2}^*)$ for $x < 0$ and $x > 0$, respectively, are placed adjacent to each other with the interface at $x = 0$. An incident wave P_1 is striking the interface at an angle ϕ_1, resulting in a transmitted wave P_2 with refraction angle ϕ_2 and a reflected wave P_r with reflection angle ϕ_r.

$$r_{PML} = \frac{\sqrt{\frac{s_{x1}^*}{s_{x1}}}\, cos\phi_1 - \sqrt{\frac{s_{x2}^*}{s_{x2}}}\, cos\phi_2}{\sqrt{\frac{s_{x1}^*}{s_{x1}}}\, cos\phi_1 + \sqrt{\frac{s_{x2}^*}{s_{x2}}}\, cos\phi_2}, \tag{3.8}$$

where ϕ_1 and ϕ_2 are the incidence and transmission angles, respectively, and

$$s_x = \left(1 + \frac{i}{\omega} q_x\right) \tag{3.9}$$

$$s_z = \left(1 + \frac{i}{\omega} q_z\right) \tag{3.10}$$

$$s_x^* = \left(1 + \frac{i}{\omega} q_x^*\right) \tag{3.11}$$

$$s_z^* = \left(1 + \frac{i}{\omega} q_z^*\right). \tag{3.12}$$

In the above equations s_x, s_z, s_x^*, s_z^* are called *stretching factors*.

On the other hand, for two acoustic media described by pairs (ρ_1, c_1) and (ρ_2, c_2), with a vertical (or any orientation) interface between them, the reflection coefficient is

$$r_{ac} = \frac{\rho_2 c_2 cos\phi_1 - \rho_1 c_1 cos\phi_2}{\rho_2 c_2 cos\phi_1 + \rho_1 c_1 cos\phi_2}, \tag{3.13}$$

where ϕ_1 and ϕ_2 are the incidence and transmission angles, respectively. Next we will derive simultaneously the conditions to set both r_{pml} and r_{ac} equal to zero *for all angles of incidence*. This is clarify the difference between the physics of PML and acoustic media, and to understand why PML interfaces allow for total transmission.

Let us start by imposing the impedance matching condition in the two acoustic media:

$$c_1 \rho_1 = \rho_2 c_2. \tag{3.14}$$

In this case r_{ac} becomes

$$r_{ac} = \frac{cos\phi_1 - cos\phi_2}{cos\phi_1 + cos\phi_2}. \tag{3.15}$$

Equation (3.15) is distinguished by the fact that it only depends on the incident and transmission angles. A similar expression for r_{PML} is obtained by imposing the *matching condition*[‡] on the pairs (s_{x1}, s_{x1}^*) and (s_{x2}, s_{x2}^*) :

$$s_{x1} = s_{x1}^*, \qquad s_{x2} = s_{x2}^*. \tag{3.16}$$

With (3.16) we end up with:

$$r_{PML} = \frac{cos\phi_1 - cos\phi_2}{cos\phi_1 + cos\phi_2}. \tag{3.17}$$

The next step is to impose a further condition on (3.15) and (3.17) to make them zero. For (3.15) Snell's Law for acoustic media is needed:

$$\frac{sin\phi_1}{c_1} = \frac{sin\phi_2}{c_2}. \tag{3.18}$$

[‡]Do not confuse This *matching condition* for PML media with the *impedance matching condition* for acoustic media, equation 3.14

From (3.18) it is evident that $c_1 = c_2$ implies $\phi_1 = \phi_2$, which upon insertion into (3.15) results in $r_{ac} = 0$ at any angle of incidence. For (3.17) Snell's Law for PML media is necessary (Herrera et al. 2012):

$$\sqrt{s_{z1}s_{z1}^*}\ sin\ \phi_1 = \sqrt{s_{z2}s_{z2}^*}\ sin\ \phi_2. \tag{3.19}$$

In this case the conditions

$$s_{z1} = s_{z2}, \qquad s_{z1}^* = s_{z2}^* \tag{3.20}$$

together with (3.19) imply $\phi_1 = \phi_2$ and therefore $r_{PML} = 0$ independently of the angle of incidence. Let us analyze all these conditions now for both r_{ac} and r_{PML}.

For the acoustic case, the two conditions to set $r_{ac} = 0$ (equation (3.14) together with $c_1 = c_2$) imply

$$\rho_1 = \rho_2. \tag{3.21}$$

The physical interpretation of (3.21) together with $c_1 = c_2$ is that the only way to have zero reflectivity (at all angles of incidence) at an interface between two acoustic media is if the two acoustic media are exactly the same material; i.e., if there is no interface. This is the reason we are so familiar with the fact that whenever an interface interferes with the trajectory of a wave, a reflected wave is created.

On the other hand, PML media behave dramatically differently at an interface. To see that notice that in this case the conditions to set $r_{PML} = 0$, equations (3.16) and (3.20), act on disjoint sets of the PML parameters. In particular equation (3.16) does not include -unlike the acoustic case- any expression containing PML parameters from both sides of the interface. Equation (3.16) can be thought of as being analogous to the impedance matching condition for PML media, because its effect on r_{PML} is identical to the effect of the impedance matching condition on r_{ac}. This gives the freedom to set $r_{PML} = 0$ but keeping different values of the PML parameters on both sides of the interface, which by definition implies two different PML media.

Upon imposition of the conditions to set $r_{PML} = 0$, the configuration in Figure 5 becomes

$$PML\ 1 : (q_{x1}, q_{x1}, q_z, q_z^*) \qquad\qquad PML\ 2 : (q_{x2}, q_{x2}, q_z, q_z^*), \tag{3.22}$$

and this is true for all frequencies and all angles of incidence. Also, the non-reflective property remains true for a wave going from medium $PML\ 2$ to medium $PML\ 1$. Therefore, when one of the two PML media is the acoustic host medium, equation (3.22) takes the form

$$PML\ 1 : (0, 0, 0, 0) \qquad\qquad PML\ 2 : (q_x, q_x, 0, 0), \tag{3.23}$$

or

$$PML\ 1 : (q_x, q_x, 0, 0) \qquad PML\ 2 : (0, 0, 0, 0). \tag{3.24}$$

The same discussion can be held if the interface between the two PML media is now parallel to the x direction. In this case the non-reflective property arises if the parameters satisfy

$$PML\ 1 : (q_x, q_x^*, q_{z1}, q_{z1}) \qquad PML\ 2 : (q_x, q_x^*, q_{z2}, q_{z2}), \tag{3.25}$$

for $z < 0$ and $z > 0$ respectively, independently of the direction of the incident wave. Moreover if $PML\ 1$ is the acoustic host medium (3.22) reduces to

$$PML\ 1 : (0, 0, 0, 0) \qquad PML\ 2 : (0, 0, q_z, q_z), \tag{3.26}$$

and if $PML\ 2$ is the acoustic host medium (3.22) reduces to

$$PML\ 1 : (0, 0, q_z, q_z) \qquad PML\ 2 : (0, 0, 0, 0). \tag{3.27}$$

Using the non-reflective configurations of equations (3.22)-(3.27), we arrive at the array of PML layers shown in Figure 6 for the modeling of wave propagation phenomena in FD, where L is the thickness of the PML layer.

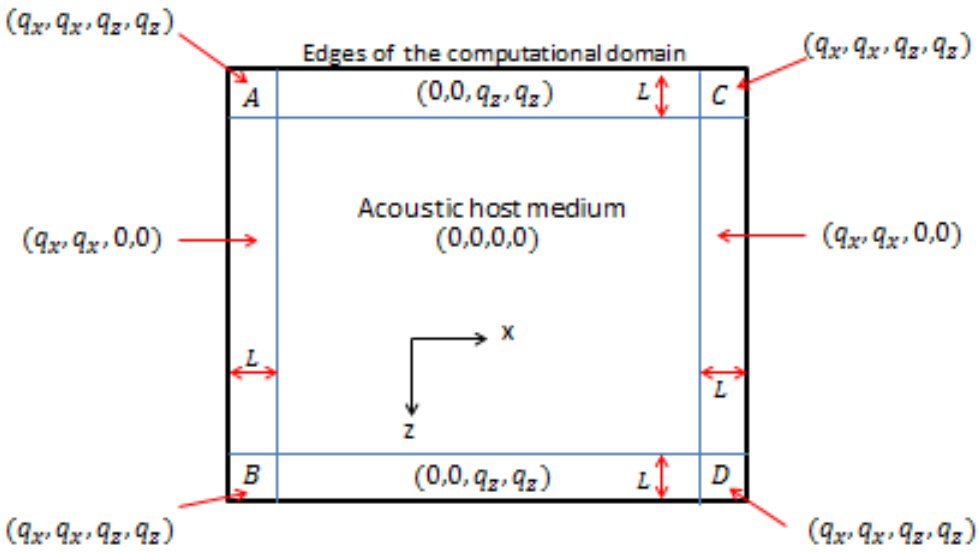

Figure 6: FD grid with PML layers. Appropriate values of the PML parameters are assigned to each PML region, in order to have non-reflective properties at any of the acoustic-PML or PML-PML interfaces.

4 Convolutional Perfectly Matched Layer

After the previous section's brief review and the analysis of the reflection coefficient between two PML media, we now will focus on the so-called Convolutional Perfectly Matched Layer (CPML) described in Roden and Gedney (2000) and Komatitsch and Martin (2007). This is a formulation of a PML in the time domain, which offers several improvements with respect to the original *split-field* formulation of Bérenguer.

As in the previous section, we will focus on forward propagation in time, leaving the discussion of the CPML, for backward propagation in time for the next section.

4.1 Complex Coordinate Stretching approach to PML

To begin, we will review the *complex coordinate stretching* approach, from which the CPML is naturally derived. Let us start by writing the acoustic wave equation, expression (2.3), in the frequency domain:

$$i\omega\mathbf{v} = -a\nabla P \qquad\qquad i\omega P = -b\nabla\cdot\mathbf{v}. \tag{4.1}$$

By definition, in the *complex coordinate stretching* approach the PML equations are obtained upon replacement of the equations in (4.1) by the following expressions:

$$i\omega\mathbf{v} = -a\nabla' P \qquad\qquad i\omega P = -b\nabla^*\cdot\mathbf{v}, \tag{4.2}$$

with

$$\nabla' = \frac{1}{s_x(x)}\frac{\partial}{\partial x}\hat{x} + \frac{1}{s_z(z)}\frac{\partial}{\partial z}\hat{z} \qquad\qquad \nabla^* = \frac{1}{s_x^*(x)}\frac{\partial}{\partial x}\hat{x} + \frac{1}{s_z^*(z)}\frac{\partial}{\partial z}\hat{z}, \tag{4.3}$$

where the *stretching functions* [§], $s_x(x)$, $s_z(z)$, $s_x^*(x)$ and $s_z^*(z)$ are complex-valued analytic functions of their corresponding argument. Note that if the *stretching functions* are set to 1, then we end with the original acoustic media defined by equation (2.3); i.e., in this formalism the acoustic host medium is a PML medium with stretching functions set to 1.

Now we introduce the *complex stretched coordinates*

$$dx' = s_x(x)dx \qquad dz' = s_z(z)dz \qquad dx^* = s_x^*(x)dx \qquad dz^* = s_z^*(z)dz, \tag{4.4}$$

From equation (4.3) we have the following results:

$$\frac{\partial}{\partial x'} = \frac{1}{s_x(x)}\frac{\partial}{\partial x} \qquad \frac{\partial}{\partial z'} = \frac{1}{s_z(z)}\frac{\partial}{\partial z} \qquad \frac{\partial}{\partial x^*} = \frac{1}{s_x^*(x)}\frac{\partial}{\partial x} \qquad \frac{\partial}{\partial z'} = \frac{1}{s_z^*(z)}\frac{\partial}{\partial z}. \tag{4.5}$$

The proofs of the above expressions are all similar and hence we show explicitly the steps leading only to the first relation in equation (4.5):

$$\frac{\partial g}{\partial x'} = \frac{\partial g}{\partial x}\frac{\partial x}{\partial x'} = \frac{1}{s_x(x)}\frac{\partial g}{\partial x}, \tag{4.6}$$

where the first expression in equation (4.4) has been used. Then, using equation (4.5), we can write equation (4.3) as

$$\nabla' = \frac{\partial}{\partial x'}\hat{x} + \frac{\partial}{\partial z'}\hat{z} \qquad\qquad \nabla^* = \frac{\partial}{\partial x^*}\hat{x} + \frac{\partial}{\partial z^*}\hat{z}, \tag{4.7}$$

[§]Usually $s_x(x)$, $s_z(z)$, $s_x^*(x)$ and $s_z^*(z)$ are called stretching factors. We choose to call them stretching functions to highlight their dependence on either x or z, and also to avoid confusion with the constant stretching factors defined in subsection 3.2 in the *split-field* formulation.

and hence we use the name *complex coordinate stretching*: equations (4.7) imply that equations (4.2) are defined in coordinate systems (x', z') and (x^*, z^*), which are the original coordinate system (x, z) *stretched* by the *complex* stretching functions.

In Herrera et al. (2012) it was explained that the expressions in equations (4.2) are equivalent to equations (3.3)-(3.6) (the defining equations of the *split-field* formulation of Bérenger) when written in the Fourier domain.

4.2 Mathematical Formulation of the Convolutional Perfectly Matched Layer

We are now ready to explain the CPML. We start by writing the expressions in (4.2) in the time domain. Upon an Inverse Fourier Transform we get the following equations:

$$\frac{\partial\ _x v}{\partial t} = \mathcal{F}^{-1}\left\{-\frac{a}{s_x}\frac{\partial P}{\partial x}\right\} \qquad \frac{\partial\ _z v}{\partial t} = \mathcal{F}^{-1}\left\{-\frac{a}{s_z}\frac{\partial P}{\partial z}\right\} \tag{4.8}$$

$$\frac{\partial P}{\partial t} = -b\left(\mathcal{F}^{-1}\left\{\frac{1}{s_x^*}\frac{\partial\ _x v}{\partial x}\right\} + \mathcal{F}^{-1}\left\{\frac{1}{s_z^*}\frac{\partial\ _z v}{\partial z}\right\}\right), \tag{4.9}$$

where equations (4.8) are the components of the vector equation in (4.2).

By using the convolution theorem in time,

$$\mathcal{F}[f_1(t) * f_2(t)] = F_1(\omega)F_2(\omega), \tag{4.10}$$

equations (4.9) and (4.10) can be expressed respectively as

$$\mathcal{F}^{-1}\left\{-\frac{a}{s_x}\frac{\partial P}{\partial x}\right\} = \mathcal{F}^{-1}\left\{-\frac{a}{s_x}\right\} * \frac{\partial P}{\partial x} \qquad \mathcal{F}^{-1}\left\{-\frac{a}{s_z}\frac{\partial P}{\partial z}\right\} = \mathcal{F}^{-1}\left\{-\frac{a}{s_z}\right\} * \frac{\partial P}{\partial z} \tag{4.11}$$

and

$$\frac{\partial P}{\partial t} = b\left(\mathcal{F}^{-1}\left\{-\frac{1}{s_x}\right\} * \frac{\partial\ _z v}{\partial x} + \left\{-\frac{1}{s_z}\right\} * \frac{\partial\ _z v}{\partial z}\right). \tag{4.12}$$

The presence of the convolution operation in equations (4.11) and (4.12) is why this approach to the Perfectly Matched Layer is called the Convolutional Perfectly Matched Layer or CPML. The next step is to provide expressions for the above convolutions, which are ready for Finite-Difference schemes in staggered grids. This is done in Appendix B, where the following results are shown:

$$\frac{\partial\ _x v}{\partial t} = -a\left\{\frac{\partial P(t)}{\partial x} + \xi_x(t) * \frac{\partial P}{\partial x}\right\} \qquad \xi_x(t) = -q_x u(t) e^{-q_x t} \tag{4.13}$$

$$\frac{\partial\ {}_zv}{\partial t} = -a\left\{\frac{\partial P(t)}{\partial z} + \xi_z(t) * \frac{\partial P}{\partial z}\right\} \qquad \xi_z(t) = -q_z u(t) e^{-q_z t} \tag{4.14}$$

$$\frac{\partial P}{\partial t} = -b\left\{\frac{\partial}{\partial x} + \xi_x^*(t) * \frac{\partial}{\partial x}\right\}\ {}_xv - b\left\{\frac{\partial}{\partial z} + \xi_z^*(t) * \frac{\partial}{\partial z}\right\}\ {}_zv, \tag{4.15}$$

where

$$\xi_x^*(t) = -q_x^* u(t) e^{-q_x^* t} \qquad \xi_z^*(t) = -q_z^* u(t) e^{-q_z^* t}, \tag{4.16}$$

and $u(t)$ is the Heaviside function. As we will restrict ourselves to configurations with $r_{PML} = 0$, it is enough, from Figure 6, to consider $q_k = q_k^*$ for $k = x, z$; i.e.,

$$\xi_x^*(t) = \xi_x(t) \qquad \xi_z^*(t) = \xi_z(t). \tag{4.17}$$

Equations (4.13)-(4.15), together with the following recursive relations, also proved in Appendix B,

$$(\ {}_{pk}\psi)^n = e^{-q_k \Delta t}(\ {}_{pk}\psi)^{n-1} + (e^{-q_k \Delta t} - 1)(\partial_k P)^n \qquad k = x, z, \tag{4.18}$$

$$(\ {}_{vk}\psi)^n = e^{-q_k \Delta t}(\ {}_{vk}\psi)^{n-1} + (e^{-q_k \Delta t} - 1)(\partial_k\ {}_kv)^n \qquad k = x, z, \tag{4.19}$$

constitute the basic sets of equations of the CPML, where

$${}_{pk}\psi(t) \equiv (\xi_k * \partial_k P)(t) = \int_{-\infty}^{\infty} \xi_k(\tau)\partial_k P(t-\tau)d\tau = \int_0^t \xi_k(\tau)\partial_k P(t-\tau)d\tau \qquad k = x, z, \tag{4.20}$$

$${}_{vk}\psi(t) \equiv (\xi_k * \partial_k\ {}_kv)(t) = \int_{-\infty}^{\infty} \xi_k(\tau)\partial_k\ {}_kv(t-\tau)d\tau = \int_0^t \xi_k(\tau)\partial_k\ {}_kv(t-\tau)d\tau \qquad k = x, z, \tag{4.21}$$

are the convolutions and

$$(\ {}_{pk}\psi)^n \equiv (\ {}_{pk}\psi)(n\Delta t) \tag{4.22}$$

$$(\ {}_{vk}\psi)^n \equiv (\ {}_{vk}\psi)(n\Delta t) \tag{4.23}$$

are the usual notations for evaluation at a discrete time. Using the notation defined in equations (4.20)-(4.21), equations (4.13)-(4.15) can be written as

$$\frac{\partial\ {}_x v}{\partial t} = -a\frac{\partial P}{\partial x} - a\ {}_{px}\psi(t) \tag{4.24}$$

$$\frac{\partial\ {}_z v}{\partial t} = -a\frac{\partial P}{\partial z} - a\ {}_{pz}\psi(t) \tag{4.25}$$

$$\frac{\partial P}{\partial t} = -b\left(\frac{\partial\ {}_x v}{\partial x} + \frac{\partial\ {}_z v}{\partial z}\right) - b(\ {}_{vx}\psi(t) + \ {}_{vz}\psi(t)), \tag{4.26}$$

The discretized expressions for equations (4.24)-(4.26) are

$$\frac{\partial\ {}_x v^n}{\partial t}_{i+\frac{1}{2},j} = \frac{{}_x v^{n+\frac{1}{2}}_{i+\frac{1}{2},j} - {}_x v^{n-\frac{1}{2}}_{i+\frac{1}{2},j}}{\Delta t} =$$

$$-a_{i+\frac{1}{2},j}\frac{1}{\Delta x}\left[\frac{9}{8}\left(P^n_{i+1,j} - \ P^n_{i,j}\right) - \frac{1}{24}\left(P^n_{i+2,j} - P^n_{i-1,j}\right)\right] - a_{i+\frac{1}{2},j}\ ({}_{px}\psi^n_{i+\frac{1}{2},j}) \tag{4.27}$$

$$\frac{\partial\ {}_z v^n}{\partial t}_{i,j+\frac{1}{2}} = \frac{{}_z v^{n+\frac{1}{2}}_{i,j+\frac{1}{2}} - {}_z v^{n-\frac{1}{2}}_{i,j+\frac{1}{2}}}{\Delta t} =$$

$$-a_{i,j+\frac{1}{2}}\frac{1}{\Delta z}\left[\frac{9}{8}\left(P^n_{i,j+1} - \ P^n_{i,j}\right) - \frac{1}{24}\left(P^n_{i,j+2} - P^n_{i,j-1}\right)\right] - a_{i,j+\frac{1}{2}}\ ({}_{pz}\psi^n_{i,j+\frac{1}{2}}) \tag{4.28}$$

$$\frac{\partial P}{\partial t}^{n+\frac{1}{2}}_{i,j} = \frac{P^{n+1}_{i,j} - P^n_{i,j}}{\Delta t} = -b_{i,j}\frac{1}{\Delta x}\left[\frac{9}{8}\left({}_x v^{n+\frac{1}{2}}_{i+\frac{1}{2},j} - \ {}_x v^{n+\frac{1}{2}}_{i-\frac{1}{2},j}\right) - \frac{1}{24}\left({}_x v^{n+\frac{1}{2}}_{i+\frac{3}{2},j} - \ {}_x v^{n+\frac{1}{2}}_{i-\frac{3}{2},j}\right)\right]$$

$$-b_{i,j}\frac{1}{\Delta z}\left[\frac{9}{8}\left({}_z v^{n+\frac{1}{2}}_{i,j+\frac{1}{2}} - \ {}_z v^{n+\frac{1}{2}}_{i,j-\frac{1}{2}}\right) - \frac{1}{24}\left({}_z v^{n+\frac{1}{2}}_{i,j+\frac{3}{2}} - \ {}_z v^{n+\frac{1}{2}}_{i,j-\frac{3}{2}}\right)\right] - b_{i,j}(\ {}_{vx}\psi^{n+\frac{1}{2}}_{i,j} + \ {}_{vz}\psi^{n+\frac{1}{2}}_{i,j}) \tag{4.29}$$

respectively. From equations (4.27)-(4.29) we get

$${}_x v^{n+\frac{1}{2}}_{i+\frac{1}{2},j} = \ {}_x v^{n-\frac{1}{2}}_{i+\frac{1}{2},j} - a_{i+\frac{1}{2},j}\frac{\Delta t}{\Delta x}\left[\frac{9}{8}\left(P^n_{i+1,j} - \ P^n_{i,j}\right) - \frac{1}{24}\left(P^n_{i+2,j} - P^n_{i-1,j}\right)\right] - a_{i+\frac{1}{2},j}\ \Delta t\ ({}_{px}\psi^n_{i+\frac{1}{2},j}) \tag{4.30}$$

$$ {}_zv_{i,j+\frac{1}{2}}^{n+\frac{1}{2}} = {}_zv_{i+\frac{1}{2},j}^{n-\frac{1}{2}} - a_{i,j+\frac{1}{2}} \frac{\Delta t}{\Delta z} \left[\frac{9}{8} \left(P_{i,j+1}^n - P_{i,j}^n \right) - \frac{1}{24} \left(P_{i,j+2}^n - P_{i,j-1}^n \right) \right] - a_{i,j+\frac{1}{2}} \, \Delta t \, \left({}_{pz}\psi_{i,j+\frac{1}{2}}^n \right) \tag{4.31} $$

$$ P_{i,j}^{n+1} = P_{i,j}^n - b_{i,j} \frac{\Delta t}{\Delta x} \left[\frac{9}{8} \left({}_xv_{i+\frac{1}{2},j}^{n+\frac{1}{2}} - {}_xv_{i-\frac{1}{2},j}^{n+\frac{1}{2}} \right) - \frac{1}{24} \left({}_xv_{i+\frac{3}{2},j}^{n+\frac{1}{2}} - {}_xv_{i-\frac{3}{2},j}^{n+\frac{1}{2}} \right) \right] $$

$$ - b_{i,j} \frac{\Delta t}{\Delta z} \left[\frac{9}{8} \left({}_zv_{i,j+\frac{1}{2}}^{n+\frac{1}{2}} - {}_zv_{i,j-\frac{1}{2}}^{n+\frac{1}{2}} \right) - \frac{1}{24} \left({}_zv_{i,j+\frac{3}{2}}^{n+\frac{1}{2}} - {}_zv_{i,j-\frac{3}{2}}^{n+\frac{1}{2}} \right) \right] - b_{i,j} \, \Delta t \, \left({}_{vx}\psi_{i,j}^{n+\frac{1}{2}} + {}_{vz}\psi_{i,j}^{n+\frac{1}{2}} \right), \tag{4.32} $$

where the discretizations for ${}_{vx}\psi_{i,j}^{n+\frac{1}{2}}$, ${}_{vz}\psi_{i,j}^{n+\frac{1}{2}}$, ${}_{px}\psi_{i+\frac{1}{2},j}^n$ and ${}_{pz}\psi_{i,j+\frac{1}{2}}^n$ are

$$ {}_{vx}\psi_{i,j}^{n+\frac{1}{2}} = {}_xa_i \; {}_{vx}\psi_{i,j}^{n-\frac{1}{2}} + {}_xb_i \frac{1}{\Delta x} \left[\frac{9}{8} \left({}_xv_{i+\frac{1}{2},j}^{n+\frac{1}{2}} - {}_xv_{i-\frac{1}{2},j}^{n+\frac{1}{2}} \right) - \frac{1}{24} \left({}_xv_{i+\frac{3}{2},j}^{n+\frac{1}{2}} - {}_xv_{i-\frac{3}{2},j}^{n+\frac{1}{2}} \right) \right], \tag{4.33} $$

$$ {}_{vz}\psi_{i,j}^{n+\frac{1}{2}} = {}_za_j \; {}_{vz}\psi_{i,j}^{n-\frac{1}{2}} + {}_zb_j \frac{1}{\Delta z} \left[\frac{9}{8} \left({}_zv_{i,j+\frac{1}{2}}^{n+\frac{1}{2}} - {}_zv_{i,j-\frac{1}{2}}^{n+\frac{1}{2}} \right) - \frac{1}{24} \left({}_zv_{i,j+\frac{3}{2}}^{n+\frac{1}{2}} - {}_zv_{i,j-\frac{3}{2}}^{n+\frac{1}{2}} \right) \right], \tag{4.34} $$

$$ {}_{px}\psi_{i+\frac{1}{2},j}^n = {}_xa_{i+\frac{1}{2}} \; {}_{px}\psi_{i+\frac{1}{2},j}^{n-1} + {}_xb_{i+\frac{1}{2}} \frac{1}{\Delta x} \left[\frac{9}{8} \left(P_{i+1,j}^n - P_{i,j}^n \right) - \frac{1}{24} \left(P_{i+2,j}^n - P_{i-1,j}^n \right) \right], \tag{4.35} $$

and

$$ {}_{pz}\psi_{i,j+\frac{1}{2}}^n = {}_za_{j+\frac{1}{2}} \; {}_{pz}\psi_{i,j+\frac{1}{2}}^{n-1} + {}_zb_{j+\frac{1}{2}} \frac{1}{\Delta z} \left[\frac{9}{8} \left(P_{i,j+1}^n - P_{i,j}^n \right) - \frac{1}{24} \left(P_{i,j+2}^n - P_{i,j-1}^n \right) \right], \tag{4.36} $$

where the recursion relations, equations (4.18) and (4.19), and the fourth-order approximation for spatial derivatives, equation (A.13), have been used and the following notation has been introduced:

$$ {}_kb = e^{q_k \Delta t} \qquad k = x, z, \tag{4.37} $$

$$ {}_ka = e^{q_k \Delta t} \qquad k = x, z, \tag{4.38} $$

in agreement with equations (4.18) and (4.19).

Notice that equations (4.27)-(4.29) are essentially (2.5)-(2.7) with additional convolutional terms. This is an advantage of the CMPL over the original *split-field* formulation: the computational code for a standard (velocity-stress) Finite-Difference scheme in a staggered grid can be used, and then updated with the convolutional terms, which are non zero only within the PML region.

On the other hand, several improvements have been incorporated into the PML and in particular into the CPML. We will now explain some of these improvements, which will be included in the examples shown below.

First of all, note that if we can modify the stretching factors without modifying equations (3.16) and (3.20), the reflection coefficient r_{PML} is still zero. Using this freedom, a modification of the stretching factors, equations (3.9)-(3.12), was proposed in Kuzuoglu and Mittra (2003) and included in Komatitsch and Martin (2007):

$$s_x = \left(1 + \frac{i}{\alpha_x + \omega} q_x\right) \tag{4.39}$$

$$s_z = \left(1 + \frac{i}{\alpha_z + \omega} q_z\right) \tag{4.40}$$

$$s_x^* = \left(1 + \frac{i}{\alpha_x + \omega} q_x^*\right) \tag{4.41}$$

$$s_z^* = \left(1 + \frac{i}{\alpha_z + \omega} q_z^*\right), \tag{4.42}$$

where $\alpha_x, \alpha_z \geq 0$. Applying the PML factors given by the configuration with $r_{PML} = 0$, equation (3.22), to the modified stretching factors, equations (4.39)-(4.42), it is easy to see that equations (3.16) and (3.20) remain unchanged and hence the condition $r_{PML} = 0$ remains unchanged[¶].

The purpose of α_x, α_z is to improve the absorbtion of already evanescent waves, whose attenuation rate is low enough so that their reflections at the boundary cannot be neglected. Also, experience and empirical tests have shown that an optimum value for these constants is πf_0, where f_0 is the dominant frequency of the source wavelet (Komatitsch and Martin 2007).

All derivations in Appendix B can be repeated with minor changes for the modified stretching factors just introduced through equations (4.39)-(4.42). The only changes to the basic equations of the CPML are as follows:

$$\xi_x(t) = -q_x u(t) e^{-(q_x + \alpha_x)t}, \tag{4.43}$$

[¶] There is at least another modification that is relevant for waves at grazing incidence, but it seems that this modification plays no role for the acoustic and elastic equation (Komatitsch and Martin 2007). Such a claim is supported by the results described below in this report.

$$\xi_z(t) = -q_z u(t) e^{-(q_z+\alpha_z)t}, \tag{4.44}$$

$$\xi_x^*(t) = -q_x^* u(t) e^{-(q_x^*+\alpha_z)t} \qquad \xi_z^*(t) = -q_z^* u(t) e^{-(q_z^*+\alpha_z)t}, \tag{4.45}$$

and

$$(\psi_k P)^n = {}_k b(\psi_k P)^{n-1} + {}_k a(\partial_k P)^{n-1} \qquad k = x, z, \tag{4.46}$$

where

$${}_k b = e^{-(q_k+\alpha_k))\Delta t} \qquad k = x, z, \tag{4.47}$$

$${}_k a = \frac{q_k}{q_k + \alpha_k}({}_k b - 1) \qquad k = x, z. \tag{4.48}$$

Other modifications to the CPML involve the stretching factors equations (4.39)-(4.42), and the process of discretization for FD. In particular we will explain how to minimize the discretization error in the reflection coefficient r_{PML} and the so-called late-time (low-frequency) reflections.

In Taflove and Hagness (2005) it is explained that after discretization, even if equations (3.16) and (3.20) are satisfied, the theoretical reflection coefficient r_{PML} is not zero anymore. This is because the discretization process intrinsically produces reflections. The modification to reduce these reflections consists of smoothly varying the value of the PML factors, from zero at the interface with the acoustic medium to a maximum value q_k^{max} at the end on the computational domain (the outer side of the PML). Usually the following polynomial variation is chosen

$$q_k(d) = q_k^{max} \left(\frac{d_k}{L_k}\right)^N \qquad k = x, z, \tag{4.49}$$

where L_k is the width of the PML layer, d_k is the distance to the corresponding acoustic-PML interface, and it has been shown that $N = 3$ *or* 4 for optimal performance (see Taflove and Hagness 2005 and references therein). The remaining question is how to choose q_k^{max} in (4.49). To answer this question we need first to remember that the attenuation factor for a wave, after its two-way propagation inside the PML layer, is (assuming the wave is far from the corners where more than a single reflection at the end of the computational domain can occur)

$$R(\phi_1) = e^{-2\frac{q_k}{c} cos\phi_1 L_k} \qquad k = x, z \tag{4.50}$$

where q_k are constant PML factors. A proof for equation (4.50) can be found in Herrera et al. (2012). When the PML factors are position-dependent, the generalization of (4.50) is straightforward (Komatitsch and Martin 2007, Taflove and Hagness 2005, Bérenger 2007):

$$R(\phi_1) = e^{-\frac{2}{c}\ cos\phi_1 \int_0^{L_k} q_k(k)dk} \qquad k = x, z, \tag{4.51}$$

where the integral forms of expressions in equation (4.4) are useful.

Upon insertion of the polynomial grading, equation (4.49), into equation (4.51), we get for space-varying PML parameters the following attenuation factor:

$$R(\phi_1) = e^{-\frac{2}{c}\ cos\phi_1 L_k/(N+1)} \qquad k = x, z, \tag{4.52}$$

where we are restricting our calculations to $L_k = L$ for $k = x, z$. Assuming that N, L_k, and the reflection error at normal incidence, $R(0)$, are set up, then from equation (4.52) we get

$$q_k^{max} = -\frac{(N+1)\ c\ ln[R(0)]}{2L_k} \qquad k = x, z. \tag{4.53}$$

For inhomogeneous media, the generalization of (4.53) is

$$q_k^{max} = -\frac{(N+1)\ c_{eff}\ ln[R(0)]}{2L_k} \qquad k = x, z, \tag{4.54}$$

where c_{eff} is a mean value of the velocities.

A further modification to the stretching factors involves the constants α_x and α_z just introduced in equations (4.45)-(4.48). As with the PML parameters, the discretization process spoils the optimum performance of these constants, and hence that of the PML. The solution is analogous to the solution with the PML parameters, allow the constants to vary spatially. Assuming that the acoustic PML boundary is at $k = 0$ for $k = x, z$, and also that the PML fills the space $0 < k < L_k$, the variation is as follows (Bérenger 2007, Taflove and Hagness 2005):

$$\alpha_k(k) = \alpha_k^{max} \left(\frac{L_k - k}{L_k} \right)^{m_a}, 0 \leq k \leq L \qquad for \quad k = x, z, \tag{4.55}$$

where m_a is a positive integer called the scaling order. The key property of equation (4.55) is that it has its maximum value α_k^{max} at the front interface $x = 0$ and it decays to zero within the PML. The value of α_k^{max} is the recommended optimum value mentioned above; i.e., πf_0. If the PML is placed at a position different from $k = 0$ for $k = x, z$, a translation of equation (4.55) is necessary in order to preserve the property just explained.

In Figure 7 we show the modeling example of Figure 2 for a homogeneous medium, but with CPML BCs included. We have chosen a thickness of ten grid points for the PML layer, for all boundaries: i.e., $L_k = 10\Delta k$ for $k = x, z$. The values $N = 3$ and $m_a = 1$ in equations (4.49) and (4.55) are selected. Also a theoretical reflection error at normal incidence $R(0) = e^{-16} \approx 1.125352 \times 10^{-7}$ is chosen for (4.53). There is no a priori reason for these values, but experience has shown they are usually good enough (Taflove and Hagness 2005).

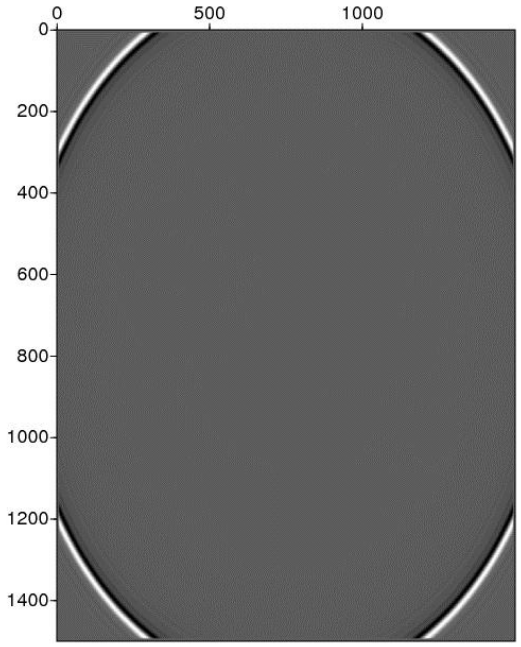

Figure 7: Attenuation of the CPML to the reflections at the boundaries of the computational domain, for the homogeneous medium of Figure 2.

By comparison with Figure 2, we can see in Figure 7 how the inclusion of CPML BCs attenuates the reflections created at the boundaries of the computational domain.

In Figure 8, we include an example of a heterogeneous medium with a single reflector at $4000m$. The speed on the upper medium is still $1500m/s$ but in the second layer we have now $3000m/s$. As in the homogeneous example, a theoretical reflection error at normal incidence $R(0) = e^{-16}$ is chosen for equation (4.54). On panel (a) we show the result of the standard FD, with Dirichlet BCs at the end of the computational domain. On panels (b) and (c) we show the same simulation at two different times, with CPML BCs. Notice in panel (b) that the reflections at the boundaries in the upper medium are very well attenuated. In panel (c) the attenuation of reflections at the boundaries in the lower medium can be seen.

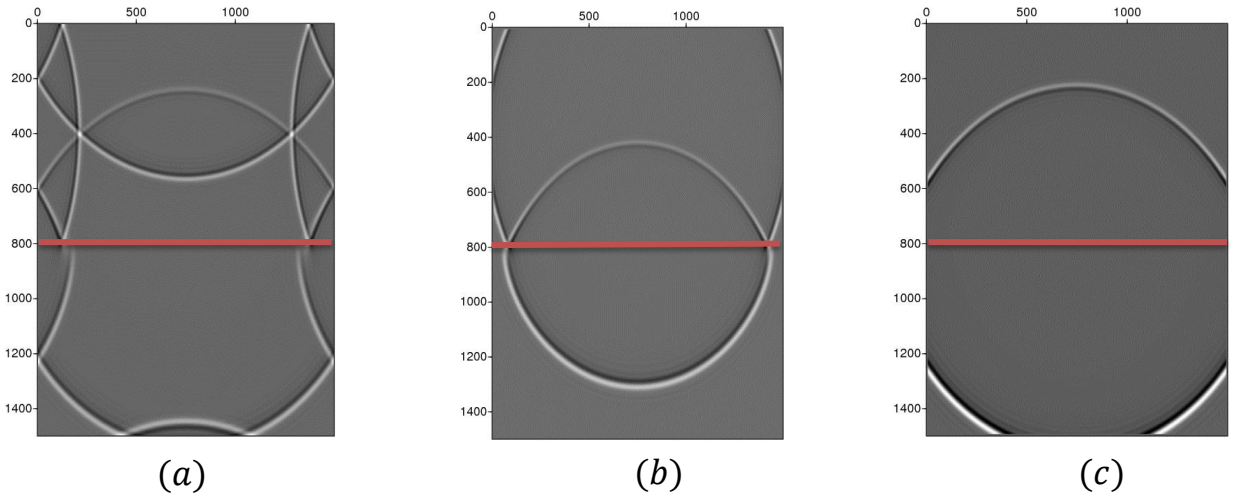

Figure 8: CPML implemented in a heterogeneous medium, with a single reflector at $4000m$, which corresponds to grid points in row 800 : (a) A snapshot of the standard FD with Dirichlet BCs, without CPML. (b) Reflections at the boundaries of the upper medium are very well attenuated by the CPML. (c) Reflections at the boundaries of the lower medium are very well attenuated by the CPML.

5 Discussion of using a CPML for backward propagation in time

In the present section we will discuss the theory behind using the CPML for backward propagation in time, as it is slightly different from the corresponding implementation for modeling. The computational implementation of the CPML for backward propagation is currently being studied within the M-OSRP. The key point is that according to the RTM, in backward propagation with time the data are a time-varying boundary condition at the upper surface of the computational domain. This forbids the inclusion of a PML wall at this surface, because a PML region would absorb and thereby modify the data to be propagated to the subsurface. Hence, PML boundaries can only be incorporated (for a 2D experiment) on the sides and the bottom of the computational domain (see Figure 9).

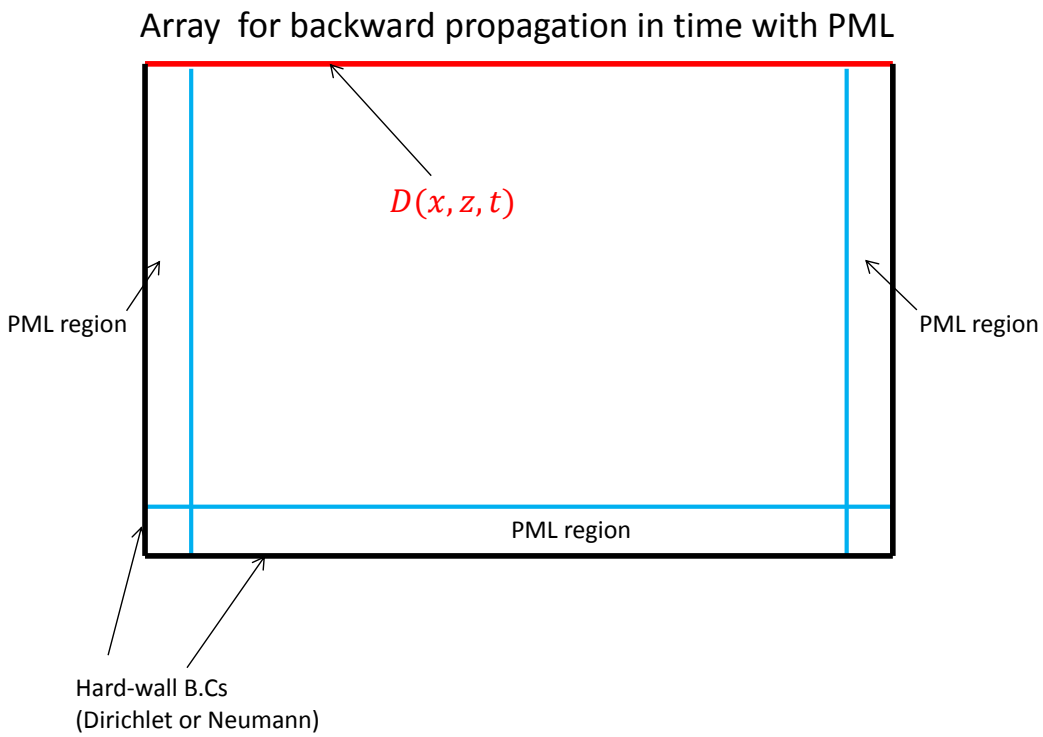

Figure 9: Array of the computational domain of FD, for backward propagation of the Data in time, and including PML layers. Note the absence of a PML layer at the top boundary in order prevent interference of a PML with the back-propagation of the data, since the data are the boundary condition.

To derive the equations for the backward propagation incorporating the CPML, we will follow the approach presented in Du Qi-Zhen et al. (2010) where the equations for the backward propagation for the *split-field* formulation of the PML were derived. For this, we need to construct fields $\tilde{P}(x,z,\tilde{t})$, ${}_x\tilde{v}(x,z,\tilde{t})$ and ${}_z\tilde{v}(x,z,\tilde{t})$ where

$$\tilde{t} = T_{max} - t, \tag{5.1}$$

with $0 \leq t \leq T_{max}$ being the time variable in the forward propagation and T_{max} the maximum recording time as in the forward propagation. Notice that as t goes backward from t_{max} to 0, $\tilde{t}$ goes forward from 0 to T_{max}. The next step is to define

$$P(x,z,t) \equiv \tilde{P}(x,z,T_{max}-t) = \tilde{P}(x,z,\tilde{t}), \tag{5.2}$$

$$ {}_xv(x,z,t) \equiv {}_x\tilde{v}(x,z,T_{max}-t) = {}_x\tilde{v}(x,z,\tilde{t}), \tag{5.3}$$

$$ {}_zv(x,z,t) \equiv {}_z\tilde{v}(x,z,T_{max}-t) = {}_z\tilde{v}(x,z,\tilde{t}), \tag{5.4}$$

where $P(x,z,t)$, ${}_xv(x,z,t)$, and ${}_zv(x,z,t)$ are the wavefield and the components of the velocity field defined in the forward propagation. In this way we have expressed the backward propagation in t of P, ${}_xv$, and ${}_zv$ in terms of a usual forward propagation in $\tilde{t}$ of $\tilde{P}$, ${}_x\tilde{v}$, and ${}_z\tilde{v}$.

The next step is to determine the differential equations that govern the propagation of the tilde fields in terms of $\tilde{t}$. Using the chain rule, we have for the wavefield

$$\frac{\partial P(x,z,t)}{\partial t} = \frac{\partial \tilde{P}(x,z,\tilde{t})}{\partial t} = \frac{\partial \tilde{P}(x,z,\tilde{t})}{\partial \tilde{t}}\frac{\partial \tilde{t}}{\partial t} = -\frac{\partial \tilde{P}(x,z,\tilde{t})}{\partial \tilde{t}}, \tag{5.5}$$

and analogous expressions for the components of the velocity field:

$$\frac{\partial\ {}_xv(x,z,t)}{\partial t} = -\frac{\partial\ {}_x\tilde{v}(x,z,\tilde{t})}{\partial \tilde{t}} \tag{5.6}$$

$$\frac{\partial\ {}_zv(x,z,t)}{\partial t} = -\frac{\partial\ {}_z\tilde{v}(x,z,\tilde{t})}{\partial \tilde{t}}. \tag{5.7}$$

In other words, we have

$$\frac{\partial}{\partial t} = -\frac{\partial}{\partial \tilde{t}}. \tag{5.8}$$

As there are no changes in the space variables, by substitution of equations (5.6)-(5.8) into equation (3.1) we end with the following set of equations:

$$\frac{\partial \tilde{P}}{\partial \tilde{t}} = b\left(\frac{\partial\ {}_x\tilde{v}}{\partial x} + \frac{\partial\ {}_z\tilde{v}}{\partial z}\right) \tag{5.9}$$

$$\frac{\partial\ {}_x\tilde{v}}{\partial \tilde{t}} = a\frac{\partial \tilde{P}}{\partial x} \tag{5.10}$$

$$\frac{\partial\ {}_z\tilde{v}}{\partial \tilde{t}} = a\frac{\partial \tilde{P}}{\partial z}. \tag{5.11}$$

Notice that equations (5.9)-(5.11) differ from the expressions in equation (3.1) only by the negative sign, which is irrelevant as far as the wave equation is concerned: i.e., equations (5.9)-(5.11) are also

equivalent to the acoustic wave equation. Hence, we have translated the backward propagation (with respect to t) of the acoustic wave equation, into a forward propagation in $\tilde{t}$ of the wave equation; i.e., we can apply the process described in section 4 and Appendix B for the implementation of the CPML. In this way, we arrive at equations that are analogous to equations (4.24)-(4.26):

$$\frac{\partial\ {}_x\tilde{v}}{\partial\tilde{t}} = a\frac{\partial\tilde{P}}{\partial x} + a\ {}_{\tilde{p}x}\psi(\tilde{t}) \tag{5.12}$$

$$\frac{\partial\ {}_z\tilde{v}}{\partial\tilde{t}} = a\frac{\partial P}{\partial z} + a\ {}_{\tilde{p}z}\tilde{\psi}(\tilde{t}) \tag{5.13}$$

$$\frac{\partial\tilde{P}}{\partial\tilde{t}} = b\left(\frac{\partial\ {}_x\tilde{v}}{\partial x} + \frac{\partial\ {}_z\tilde{v}}{\partial z}\right) + b(\ {}_{\tilde{v}x}\tilde{\psi}(\tilde{t}) + \ {}_{\tilde{v}y}\tilde{\psi}(\tilde{t})), \tag{5.14}$$

where ${}_*\tilde{\psi}$ is the convolution in $\tilde{t}$ satisfying

$${}_*\tilde{\psi}^{\tilde{n}} = \ {}_ka\ {}_*\tilde{\psi}^{\tilde{n}-1} + \ {}_kb\ \partial_*^{\tilde{n}-1} \qquad k = x, z. \tag{5.15}$$

for a generic subindex $*$ in equations (5.12)-(5.14). Also, $\tilde{n}$ is the number of iterations in $\tilde{t}$.

The next task is to write equations (5.12)-(5.15) in terms of t and the non-tilded fields, as those are the ones contained in the imaging condition. The resulting equations are

$$\frac{\partial\ {}_xv}{\partial t} = -a\left(\frac{\partial P}{\partial x} + \ {}_{px}\psi(t)\right) \tag{5.16}$$

$$\frac{\partial\ {}_zv}{\partial t} = -a\left(\frac{\partial P}{\partial z} + \ {}_{pz}\psi(t)\right) \tag{5.17}$$

$$\frac{\partial P}{\partial t} = -b\left(\frac{\partial\ {}_xv}{\partial x} + \frac{\partial\ {}_zv}{\partial z}\right) - b(\ {}_{vx}\psi(t) + \ {}_{vz}\psi(t)) \tag{5.18}$$

$${}_*\psi^n = \ {}_ka\ {}_*\psi^{n+1} + \ {}_kb\ \partial_*^n \qquad k = x, z. \tag{5.19}$$

Note that a generic convolution ${}_*\psi$ now satisfies a recursive relation in which earlier times are calculated in terms of later times, as needed for a backward propagation. This recursive relation can be proved by following the procedure described in Appendix B, and expressing $\tilde{t}$ in terms of t.

Upon discretization of equations (5.12)-(5.15) and isolation of fields at earlier times in terms of later times, we arrive at the equations to be implemented in the backward propagation in time for RTM:

$$P_{i,j}^{n-1} = P_{i,j}^{n} + b_{i,j}\frac{\Delta t}{\Delta x}\left[\frac{9}{8}\left({}_{x}v_{i+\frac{1}{2},j}^{n-\frac{1}{2}} - {}_{x}v_{i-\frac{1}{2},j}^{n-\frac{1}{2}}\right) - \frac{1}{24}\left({}_{x}v_{i+\frac{3}{2},j}^{n-\frac{1}{2}} - {}_{x}v_{i-\frac{3}{2},j}^{n-\frac{1}{2}}\right)\right] +$$

$$b_{i,j}\frac{\Delta t}{\Delta z}\left[\frac{9}{8}\left({}_{z}v_{i,j+\frac{1}{2}}^{n-\frac{1}{2}} - {}_{z}v_{i,j-\frac{1}{2}}^{n-\frac{1}{2}}\right) - \frac{1}{24}\left({}_{z}v_{i,j+\frac{3}{2}}^{n-\frac{1}{2}} - {}_{z}v_{i,j-\frac{3}{2}}^{n-\frac{1}{2}}\right)\right] + b_{i,j}\Delta t({}_{vx}\psi_{i,j}^{n-\frac{1}{2}} + {}_{vz}\psi_{i,j}^{n-\frac{1}{2}}) \quad (5.20)$$

$${}_{z}v_{i,j+\frac{1}{2}}^{n-\frac{1}{2}} = {}_{z}v_{i+\frac{1}{2},j}^{n+\frac{1}{2}} + a_{i,j+\frac{1}{2}}\frac{\Delta t}{\Delta z}\left[\frac{9}{8}\left(P_{i,j+1}^{n} - P_{i,j}^{n}\right) - \frac{1}{24}\left(P_{i,j+2}^{n} - P_{i,j-1}^{n}\right)\right] + a_{i,j+\frac{1}{2}}\Delta t\ ({}_{pz}\psi_{i,j+\frac{1}{2}}^{n}) \quad (5.21)$$

$${}_{x}v_{i+\frac{1}{2},j}^{n-\frac{1}{2}} = {}_{x}v_{i+\frac{1}{2},j}^{n+\frac{1}{2}} + a_{i+\frac{1}{2},j}\frac{\Delta t}{\Delta x}\left[\frac{9}{8}\left(P_{i+1,j}^{n} - P_{i,j}^{n}\right) - \frac{1}{24}\left(P_{i+2,j}^{n} - P_{i-1,j}^{n}\right)\right] + a_{i+\frac{1}{2},j}\Delta t\ ({}_{px}\psi_{i+\frac{1}{2},j}^{n}) \quad (5.22)$$

$${}_{vx}\psi_{i,j}^{n-\frac{1}{2}} = {}_{x}a_{i}\ {}_{vx}\psi_{i,j}^{n+\frac{1}{2}} + {}_{x}b_{i}\frac{1}{\Delta x}\left[\frac{9}{8}\left({}_{x}v_{i+\frac{1}{2},j}^{n-\frac{1}{2}} - {}_{x}v_{i-\frac{1}{2},j}^{n-\frac{1}{2}}\right) - \frac{1}{24}\left({}_{x}v_{i+\frac{3}{2},j}^{n-\frac{1}{2}} - {}_{x}v_{i-\frac{3}{2},j}^{n-\frac{1}{2}}\right)\right] \quad (5.23)$$

$${}_{vz}\psi_{i,j}^{n-\frac{1}{2}} = {}_{z}a_{j}\ {}_{vz}\psi_{i,j}^{n+\frac{1}{2}} + {}_{z}b_{j}\frac{1}{\Delta z}\left[\frac{9}{8}\left({}_{z}v_{i,j+\frac{1}{2}}^{n-\frac{1}{2}} - {}_{z}v_{i,j-\frac{1}{2}}^{n-\frac{1}{2}}\right) - \frac{1}{24}\left({}_{z}v_{i,j+\frac{3}{2}}^{n-\frac{1}{2}} - {}_{z}v_{i,j-\frac{3}{2}}^{n-\frac{1}{2}}\right)\right] \quad (5.24)$$

$${}_{px}\psi_{i+\frac{1}{2},j}^{n} = {}_{x}a_{i+\frac{1}{2}}\ {}_{px}\psi_{i+\frac{1}{2},j}^{n+1} + {}_{x}b_{i+\frac{1}{2}}\frac{1}{\Delta x}\left[\frac{9}{8}\left(P_{i+1,j}^{n} - P_{i,j}^{n}\right) - \frac{1}{24}\left(P_{i+2,j}^{n} - P_{i-1,j}^{n}\right)\right] \quad (5.25)$$

$${}_{pz}\psi_{i,j+\frac{1}{2}}^{n} = {}_{z}a_{j+\frac{1}{2}}\ {}_{pz}\psi_{i,j+\frac{1}{2}}^{n+1} + {}_{z}b_{j+\frac{1}{2}}\frac{1}{\Delta z}\left[\frac{9}{8}\left(P_{i,j+1}^{n} - P_{i,j}^{n}\right) - \frac{1}{24}\left(P_{i,j+2}^{n} - P_{i,j-1}^{n}\right)\right] \quad (5.26)$$

6 Discussion and Conclusions

In this report we have described the first steps, within the M-OSRP, toward implementation of the Convolutional Perfectly Matched Layer CPML, as presented in Komatitsch and Martin (2007) and Roden and Gedney (2000). We focus our attention on modeling the 2D acoustic wave equation. In particular we present an example of the implementation of the CPML for a homogeneous medium. We also include an example for a heterogeneous medium, with a single reflector, with velocity and density variations. In both cases it is evident the effectiveness of the CPML in the attenuation

of the reflections at the boundary of the computational domain, arising as a consequence of the imposed Dirichlet BCs

For the examples mentioned above, we have used the staggered-grid finite-difference scheme described in Appendix *A*. The reason for the staggered grid is that it is more convenient than the familiar non-staggered scheme, when the wave equation is formulated as a coupled system of first-order differential equations; i.e., when it is formulated as in equation (2.3). On the other hand, the requirement in this report of equation (2.3) comes from the PML technique, which is our main interest. The reason we focus on the CPML is that, as explained in section 4, it is easy to implement in the time domain, and it incorporates some improvements over the original *split-field* formulation.

In order to provide a better understanding of the CPML, we have also included a detailed comparison of the reflection coefficient at an interface between two PML media, with the reflection coefficient at an interface between two acoustic media. In particular we have analyzed and compared the conditions to set up both coefficients to zero for all angles of incidence. The result of this analysis is a better understanding of the reflection coefficient between two PML media and why, unlike the acoustic case, two PML media allow (for certain configurations) zero reflection coefficient for all angles of incidence: equation (3.16), the analogous of the impedance matching condition for PML media, does not include any expression containing PML parameters from both sides of the interface. This gives the freedom to set $r_{PML} = 0$ but keeping different values of the PML parameters on both sides of the interface, which by definition imply two different PML media.

As is mentioned in the introduction, this report can be considered as part of a broader research project whose objective is to compare the effectiveness of the new Green's theorem approach for RTM, as described in Weglein et al. (2011a) and Weglein et al. (2011b), with the PML-based RTM. For this reason, we have included a brief discussion of the original approach for RTM, as described in Whitmore (1983), Baysal et al. (1983) and Stolt and Weglein (2011), with focus on the 2D acoustic heterogeneous wave equation. We have also derived the equations (both the continuous and discrete versions) of the CPML for the backward propagation of data, as required by RTM. The result for the continuous equations is comprised in equations (5.16)-(5.18) and equation (5.19) for the convolutions. Comparing these equations with the CPML equations for the forward modeling, equations (4.24)-(4.26) and equations (4.18)-(4.19) for the convolutions, it can be seen that the only differences are in the convolutions, as for the backward propagation they satisfy a recursive relation in which earlier times are calculated in terms of later times. As far as the authors knowledge, these results have not been reported elsewhere.

Although the final goal is the implementation of RTM with PML layers, a side product of this research project is a code to create synthetic data with PML layers. This code allows for both velocity and density variation, for an acoustic, 2D earth. However, the code can be easily adapted to allow a 3D earth. The fact that the code incorporates the CPML technique implies that the computational domain does not need to be much bigger that the size of the experiment that is to be simulated: in this case, the noise produced by reflections at the boundary are significantly reduced by the PML layers. This implies a faster algorithm.

Topics for further research in this research project include the extension of RTM to include processing

of internal multiples, derivation and implementation of the equations of the RTM with CPML BCs for TTI anisotropy, and modification of the source-wavefield reconstruction method for RTM, presented in McGarry et al. (2010) and Bo-Feng et al. (2010), to include PML BCs.

7 Acknowledgements

We are grateful to the M-OSRP sponsors. The first author wants to acknowledge Dr. Fang Liu, and Di Chang and Hichem Ayadi for useful discussions and suggestions during the realization of this work. We also want to thank to Hong Liang and also Hichem Ayadi for reading a first draft of this report.

A A Staggered finite difference

A.1 Second-order and fourth-order approximations to the derivative

In here we will show how to obtain the basic equations for second and fourth order discretizations of the derivative, needed for the derivation and implementation of the Finite Difference equations governing the CPML. We will follow the approach described in Garcia (2009) Assume for simplicity that we have a finite-difference grid with a single dimension x. In a standard finite-difference scheme we assume that the values of a generic field $u(x)$ are known at the grid points; i.e., we know the values $u_i \equiv u(ih)$, where h is the distance between two adjacent grid points. However, it is useful for our purposes to assume that we can also access the values of u at half the distance between grid points; i.e., we can also access $u_{i+1/2} \equiv u((i+1/2)h)$.

What we want to calculate is the derivative of u at $x = ih$; i.e., we want du_i/dx (Figure 10).

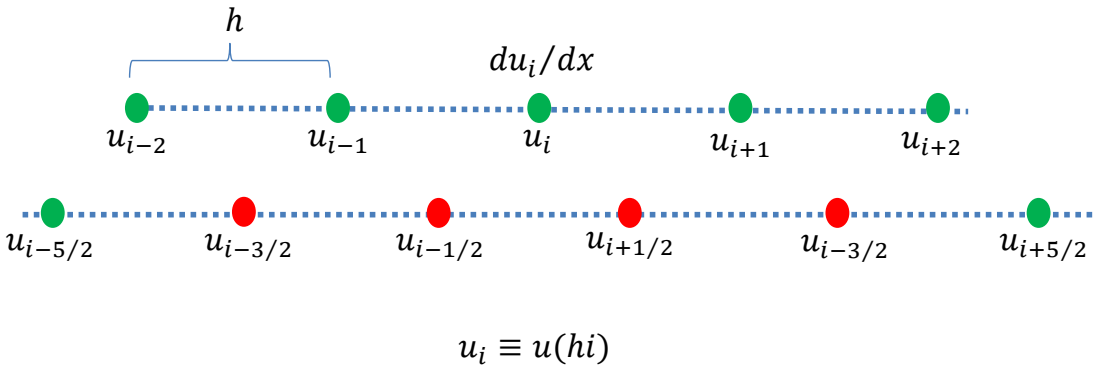

Figure 10: A 1D grid in which a generic function (or field) is known at the grid points u_i for integer $i > 0$, and also at points $u_{i+1/2}$ located half the distance between the grid points.

For this we need the formula for the Taylor expansion:

$$f(x+a) = f(x) + af'(x) + \frac{a^2}{2!}f''(x) + \frac{a^3}{3!}f'''(x) + \cdots \tag{A.1}$$

Applying equation (A.1) to Taylor expand $u(x)$, we get, for $a = h/2$ and $a = -h/2$, the following expressions:

$$u_{i+1/2} = u_i + \frac{h}{2}u_i' + \frac{h^2}{8}u_i'' + \frac{h^3}{48}u_i''' + \frac{h^4}{384}u_i'''' + \cdots \tag{A.2}$$

$$u_{i-1/2} = u_i - \frac{h}{2}u_i' + \frac{h^2}{8}u_i'' - \frac{h^3}{48}u_i''' + \frac{h^4}{384}u_i'''' + \cdots \tag{A.3}$$

Subtracting (A.3) from (A.2) and neglecting terms of second order in h and higher, we obtain the *second-order approximation* for $\frac{du_i}{dx}$:

$$u_i' = \frac{u_{i+1/2} - u_{i-1/2}}{h} + O(h_2) \tag{A.4}$$

The goal now is to get a *fourth-order approximation* for $\frac{du_i}{dx}$. For this we subtract again (A.3) from (A.2), but we keep terms up to order h^3 :

$$u_{i+1/2} - u_{i-1/2} = hu_i' + \frac{h^3}{24}u''' + O(h^5). \tag{A.5}$$

Next, we apply equation (A.1) to Taylor expand $u(x)$, for $a = 3h/2$ and $a = -3h/2$:

$$u_{i+3/2} = u_i + \frac{3h}{2}u_i' + \frac{9h^2}{8}u_i'' + \frac{27h^3}{48}u_i''' + \frac{81h^4}{384}u_i'''' + \cdots \tag{A.6}$$

$$u_{i-3/2} = u_i - \frac{3h}{2}u_i' + \frac{9h^2}{8}u_i'' - \frac{27h^3}{48}u_i''' + \frac{81h^4}{384}u_i'''' + \cdots \tag{A.7}$$

Subtracting now (A.7) from (A.6) and keeping terms up to order h^3, we obtain

$$u_{i+3/2} - u_{i-3/2} = 3hu_i' + \frac{9h^3}{8}u_i''' + O(h^5). \tag{A.8}$$

Suppose now that we want an expression for $\frac{du_i}{dx}$ of the form

$$u_i' = A(u_{i+1/2} - u_{i-1/2}) + B(u_{i+3/2} - u_{i-3/2}), \tag{A.9}$$

with A and B constants to be determined. Inserting the right-hand side of (A.5) and (A.8) into (A.9) we get

$$u'_i = A(hu'_i + \frac{h^3}{24}u''') + B(3hu'_i + \frac{9h^2}{8}u'''_i) = (Ah + 3hB)u'_i + (A\frac{h^3}{24} + B\frac{9h^3}{8})u'''_i, \tag{A.10}$$

which gives the following system of equations for A and B :

$$Ah + 3hB = 1 \qquad A\frac{h^3}{24} + B\frac{9h^3}{8} = 0. \tag{A.11}$$

Solving (A.11) we get

$$A = \frac{9}{8h} \qquad B = -\frac{1}{24h}, \tag{A.12}$$

Substitution of (A.12) into (A.9) we end up with the fourth-order approximation we were looking for:

$$u'_i \approx \frac{1}{h}\left(\frac{9}{8}(u_{i+1/2} - u_{i-1/2}) - \frac{1}{24}(u_{i+3/2} - u_{i-3/2})\right). \tag{A.13}$$

A.2 Staggered grid for finite Difference

Here we will explain the basics of a staggered grid, suitable for systems like equation (2.3), which we include here for further convenience.

The central feature of a staggered grid is that some quantities are assumed to be known at the grid points and other at the half-grid points (some quantities may have mixed components at grid points and half-grid points). To be specific, assume that the pressure field P is known at the grid points and denote its value at the grid point (i, j, n) as $P^n_{i,j}$; i.e., $P^n_{i,j} \equiv P(i\Delta x, j\Delta z, n\Delta t)$, where Δx, Δz, and Δt are the distances between two adjacent grid points at the x, z, and t directions, respectively. Assume also that the $\hat{x}$ and $\hat{z}$ components of the velocity field are known at half-grid points in the corresponding spatial direction and at the grid points in the corresponding remaining direction. Both components are known at half-grid points in the time direction: ${}_xv^{n+\frac{1}{2}}_{i+\frac{1}{2},j} \equiv {}_xv((i+1/2)\Delta x, j\Delta z, (n+1/2)\Delta t))$ and ${}_zv^{n+\frac{1}{2}}_{i,j+\frac{1}{2}} \equiv {}_zv(i\Delta x, (j+1/2)\Delta z, (n+1/2)\Delta t))$. See Figure 11, where for simplicity only the spatial x direction is shown, together with the time direction.

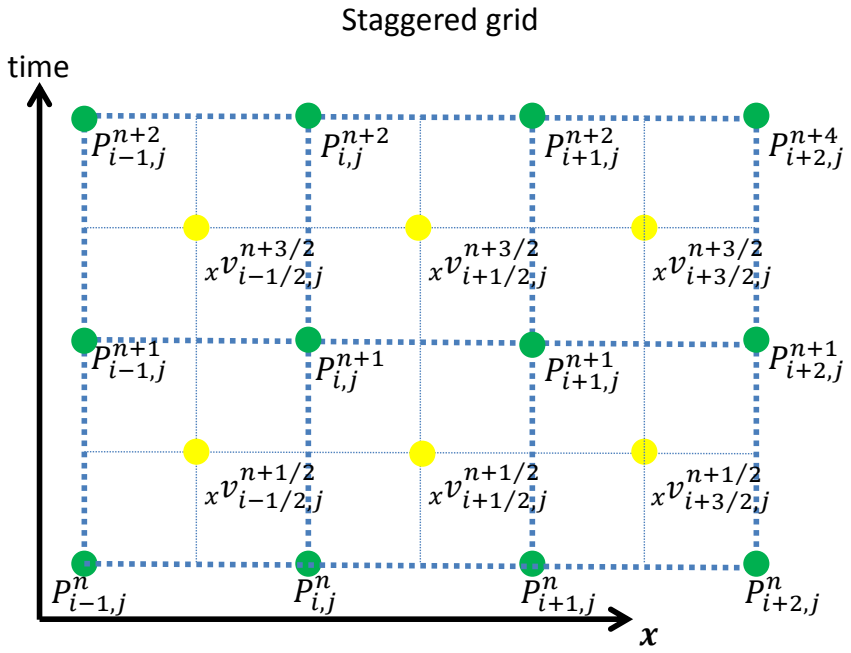

Figure 11: Projection on the $x-t$ plane of a staggered grid with two spatial directions, in which the pressure field P is known at the grid (green) points (i,j,n), while the x-component ${}_xv$ of the auxiliary velocity field is known at points located at half the distance between two adjacent grid points (yellow points).

For stability of the FD scheme, the time step must be constrained by the Courant-Friedrichs-Lewy (CFS) condition (Courant et al. 1928):

$$c\Delta t\sqrt{\frac{1}{\Delta x^2}+\frac{1}{\Delta z^2}}\leq 1. \tag{A.14}$$

In the following, we will use a second-order approach for time derivatives and a fourth-order approach for spatial derivatives. The tricky point is to realize the position in the grid, at which each derivative in (2.3) is to be evaluated in such a way that, upon the application of the corresponding approximation (second-order for time and fourth-order for space derivatives) we end up with the fields evaluated at the correct positions; i.e., at the positions where they are assumed to be known.

It turns out that the correct position for evaluation of the derivative of the pressure field P in (2.3) is $(i,j,n+1/2)$:

$$\begin{aligned}\frac{\partial P}{\partial t}{}^{n+\frac{1}{2}}_{i,j} = \frac{P^{n+1}_{i,j}-P^{n}_{i,j}}{\Delta t} = -b_{i,j}\frac{1}{\Delta x}\left[\frac{9}{8}\left({}_xv^{n+\frac{1}{2}}_{i+\frac{1}{2},j}-{}_xv^{n+\frac{1}{2}}_{i-\frac{1}{2},j}\right)-\frac{1}{24}\left({}_xv^{n+\frac{1}{2}}_{i+\frac{3}{2},j}-{}_xv^{n+\frac{1}{2}}_{i-\frac{3}{2},j}\right)\right]\\ -b_{i,j}\frac{1}{\Delta z}\left[\frac{9}{8}\left({}_zv^{n+\frac{1}{2}}_{i,j+\frac{1}{2}}-{}_zv^{n+\frac{1}{2}}_{i,j-\frac{1}{2}}\right)-\frac{1}{24}\left({}_zv^{n+\frac{1}{2}}_{i,j+\frac{3}{2}}-{}_zv^{n+\frac{1}{2}}_{i,j-\frac{3}{2}}\right)\right],\end{aligned} \tag{A.15}$$

where we have applied (A.4) and (A.13) for the time and spatial derivatives, respectively. By close examination, it can be seen that all fields in (A.15) are evaluated at the right positions.

With regard to the components of the velocity field ${}_xv$ and ${}_zv$, the correct positions for the evaluation of their time derivatives in (2.3) are $(i+1/2, j, n)$ and $(i, j+1/2, n)$, respectively:

$$\frac{\partial\ {}_xv^n}{\partial t}_{i+\frac{1}{2},j} = \frac{{}_xv^{n+\frac{1}{2}}_{i+\frac{1}{2},j} - {}_x\,v^{n-\frac{1}{2}}_{i+\frac{1}{2},j}}{\Delta t} = -a_{i+\frac{1}{2},j}\frac{1}{\Delta x}\left[\frac{9}{8}\left(P^n_{i+1,j} - \ P^n_{i,j}\right) - \frac{1}{24}\left(P^n_{i+2,j} - P^n_{i-1,j}\right)\right] \quad \text{(A.16)}$$

$$\frac{\partial\ {}_zv^n}{\partial t}_{i,j+\frac{1}{2}} = \frac{{}_zv^{n+\frac{1}{2}}_{i,j+\frac{1}{2}} - {}_z\,v^{n-\frac{1}{2}}_{i,j+\frac{1}{2}}}{\Delta t} = -a_{i,j+\frac{1}{2}}\frac{1}{\Delta z}\left[\frac{9}{8}\left(P^n_{i,j+1} - \ P^n_{i,j}\right) - \frac{1}{24}\left(P^n_{i,j+2} - P^n_{i,j-1}\right)\right]. \quad \text{(A.17)}$$

From equations (A.15)-(A.17) we obtain the final expressions for the forward propagation of (2.3) in time:

$$P^{n+1}_{i,j} = P^n_{i,j} - b_{i,j}\frac{\Delta t}{\Delta x}\left[\frac{9}{8}\left({}_xv^{n+\frac{1}{2}}_{i+\frac{1}{2},j} - \ {}_xv^{n+\frac{1}{2}}_{i-\frac{1}{2},j}\right) - \frac{1}{24}\left({}_xv^{n+\frac{1}{2}}_{i+\frac{3}{2},j} - \ {}_xv^{n+\frac{1}{2}}_{i-\frac{3}{2},j}\right)\right]$$

$$- b_{i,j}\frac{\Delta t}{\Delta z}\left[\frac{9}{8}\left({}_zv^{n+\frac{1}{2}}_{i,j+\frac{1}{2}} - \ {}_zv^{n+\frac{1}{2}}_{i,j-\frac{1}{2}}\right) - \frac{1}{24}\left({}_zv^{n+\frac{1}{2}}_{i,j+\frac{3}{2}} - \ {}_zv^{n+\frac{1}{2}}_{i,j-\frac{3}{2}}\right)\right]$$

$${}_xv^{n+\frac{1}{2}}_{i+\frac{1}{2},j} = \ {}_xv^{n-\frac{1}{2}}_{i+\frac{1}{2},j} - a_{i+\frac{1}{2},j}\frac{\Delta t}{\Delta x}\left[\frac{9}{8}\left(P^n_{i+1,j} - \ P^n_{i,j}\right) - \frac{1}{24}\left(P^n_{i+2,j} - P^n_{i-1,j}\right)\right]$$

$${}_zv^{n+\frac{1}{2}}_{i,j+\frac{1}{2}} = \ {}_zv^{n-\frac{1}{2}}_{i+\frac{1}{2},j} - a_{i,j+\frac{1}{2}}\frac{\Delta t}{\Delta z}\left[\frac{9}{8}\left(P^n_{i,j+1} - \ P^n_{i,j}\right) - \frac{1}{24}\left(P^n_{i,j+2} - P^n_{i,j-1}\right)\right], \quad \text{(A.18)}$$

which are equations (2.5), (2.6) and (2.7) of section 2.

B Derivation of the equations of a CPML

In this Appendix we will derive the equations governing the CPML; i.e., equations (4.13)-(4.18). For this goal let us focus first on the first expression in equation (4.8):

$$\frac{\partial\ {}_xv}{\partial t} = \mathcal{F}^{-1}\left\{-\frac{a}{s_x}\frac{\partial P}{\partial x}\right\} = \mathcal{F}^{-1}\left\{-\frac{a}{s_x}\right\} * \frac{\partial P}{\partial x}, \quad \text{(B.1)}$$

where the Inverse Fourier transform of the derivative of the pressure field is denoted by the same symbol as is used in the Fourier space. Let us now calculate the Inverse Fourier transform of the inverse of the stretching factor times a:

$$\mathcal{F}^{-1}\left\{-\frac{a}{s_x}\right\} = -a\mathcal{F}^{-1}\left\{\frac{1}{s_x}\right\} = -a\mathcal{F}^{-1}\left\{\frac{1}{1+\frac{q_x}{i\omega}}\right\} = -a\mathcal{F}^{-1}\left\{\frac{i\omega}{q_x+i\omega}\right\}, \tag{B.2}$$

On the other hand, applying to (B.2) the following results from Fourier analysis

$$\mathcal{F}(u(t)e^{-q_x t}) = \frac{1}{q_x+i\omega} \qquad \mathcal{F}(f'(t)) = i\omega\mathcal{F}(f(t)) = i\omega F(\omega), \tag{B.3}$$

where $u(t)$ is the Heaviside function, we get the expression

$$\mathcal{F}\left(\frac{\partial}{\partial t}(u(t)e^{-q_x t})\right) = i\omega\mathcal{F}(u(t)e^{-q_x t}) = \frac{i\omega}{a+i\omega}, \tag{B.4}$$

Taking the inverse Fourier transform, equation (B.4) can be written as

$$\mathcal{F}^{-1}\left\{\frac{i\omega}{q_x+i\omega}\right\} = \frac{\partial}{\partial t}(u(t)e^{-q_x t}) = -q_x u(t)e^{-q_x t} + e^{-q_x t}\delta(t) \tag{B.5}$$

which can be further simplified and written as

$$\mathcal{F}^{-1}\left\{\frac{i\omega}{q_x+i\omega}\right\} = -q_x u(t)e^{-q_x t} + \delta(t), \tag{B.6}$$

where we have evaluated the exponential in the second term on the right of (B.5) at $t = 0$. This is possible because the Delta function only makes sense within an integral, in which case any function multiplying the Delta function is evaluated (in this case) at zero. Upon insertion of equation (B.6) into equation (B.1), we have shown that

$$\frac{\partial\ {}_x v}{\partial t} = -a\left\{(\delta(t)+\xi_x(t)) * \frac{\partial P}{\partial x}\right\} \qquad \xi_x(t) \equiv -q_x u(t)e^{-q_x t}. \tag{B.7}$$

Using in (B.7) the distribution property of the convolution, and the result

$$\delta(t) * \frac{\partial P}{\partial x} = \int_{-\infty}^{\infty} \delta(t-t')\frac{\partial P(t')}{\partial x}dt' = \frac{\partial P(t)}{\partial x}, \tag{B.8}$$

we get exactly equations (4.13):

$$\frac{\partial\ {}_x v}{\partial t} = -a\left\{\frac{\partial P(t)}{\partial x} + \xi_x(t) * \frac{\partial P}{\partial x}\right\} \qquad \xi_x(t) = -q_x u(t) e^{-q_x t}.$$

Applying analogous calculations to the second expression in equation (4.8) allows us to obtain equation (4.14) and

$$\frac{\partial\ {}_z v}{\partial t} = -a\left\{\frac{\partial P(t)}{\partial z} + \xi_z(t) * \frac{\partial P}{\partial z}\right\} \qquad \xi_z(t) = -q_z u(t) e^{-q_z t}.$$

Finally, applying the same calculations to the convolutions in equation (4.9), we get equations (4.15) and (4.16):

$$\frac{\partial P}{\partial t} = -b\left\{\frac{\partial}{\partial x} + \xi_x^*(t) * \frac{\partial}{\partial x}\right\}\ {}_x v - b\left\{\frac{\partial}{\partial z} + \xi_z^*(t) * \frac{\partial}{\partial z}\right\}\ {}_z v,$$

where

$$\xi_x^*(t) = -q_x^* u(t) e^{-q_x^* t} \qquad \xi_z^*(t) = -q_z^* u(t) e^{-q_z^* t}.$$

We will now devote our efforts to calculation of the convolutions present in the equations of the CPML, equation (4.18). We start with the definition of the convolution for the pressure field P, equation (4.20):

$$(\ {}_{px}\psi)(t) = (\xi_x * \partial_x P)(t) = \int_{-\infty}^{\infty} \xi_x(\tau)\partial_x P(t-\tau)d\tau = \int_0^t \xi_x(\tau)\partial_x P(t-\tau)d\tau,$$

where $u(t)$ is the Heaviside function. As was mentioned in Section 2, the last expression is obtained because we are assuming the experiment starts at $t = 0$, so the pressure field and therefore its derivative are zero for negative arguments.

Evaluating the above expression for a discrete time; i.e., equation (4.22)

$$(\ {}_{px}\psi)^n \equiv (\psi_x P)(n\Delta t),$$

we obtain

$$(\ {}_{px}\psi)^n = (\xi_x * \partial_x P)^n = \int_0^{n\Delta t} \xi_x(\tau)(\partial_x P)^{n\Delta t-\tau} d\tau = \sum_{m=0}^{n-1} \int_{m\Delta t}^{(m+1)\Delta t} \xi_x(\tau)(\partial_x P)^{n\Delta t-\tau} d\tau =$$

$$\sum_{m=0}^{n-1} (\partial_x P)^{\Delta t(n-(m+1/2))} \int_{m\Delta t}^{(m+1)\Delta t} \xi_x(\tau) d\tau = \sum_{m=0}^{n-1} (\partial_x P)^{\Delta t(n-(m+1/2))} Z_x(m), \qquad \text{(B.9)}$$

where

$$Z_x(m) = \int_{m\Delta t}^{(m+1)\Delta t} \xi_x(\tau) d\tau. \tag{B.10}$$

The fifth expression in equation (B.9) is obtained by evaluating $\partial_x P$ at half the distance between grid points in the time direction; i.e., at $\tau = (m+1/2)\Delta t$. This can be done because we are working with a staggered grid.

Now we will calculate (B.10)

$$Z_x(m) = \int_{m\Delta t}^{(m+1)\Delta t} \xi_x(\tau) d\tau = -q_x \int_{m\Delta t}^{(m+1)\Delta t} e^{-q_x \tau} d\tau = e^{-q_x \tau}\Big|_{m\Delta t}^{(m+1)\Delta t} =$$

$$e^{-q_x (m+1)\Delta t} - e^{-q_x m\Delta t} = e^{-q_x m\Delta t}(e^{-q_x \Delta t} - 1), \tag{B.11}$$

which, upon substitution in (B.9), gives us

$$(\ {}_{px}\psi)^n = (e^{-q_x \Delta t} - 1) \sum_{m=0}^{n-1} (\partial_x P)^{\Delta t (n-(m+1/2))} e^{-q_x m\Delta t}. \tag{B.12}$$

Expressions analogous to (B.12) are also valid for the convolutions in equations (4.14) and (4.15), upon inclusion of the obvious changes.

We will now focus our efforts on proving equation (4.18), a recursive relation for equation (B.12). Notice that without a recursive relation the CPML will be too costly, as equation (B.12) requires, at a given computation time, the values of $\partial_x P$ at all earlier times. This "all earlier times" requirement increases the memory needed and reduces the efficiency of the algorithm.

For convenience we start with the recursive relation in Komatitsch and Martin (2007):

$$(\ {}_{px}\psi)^n = e^{-q_x \Delta t}(\ {}_{px}\psi)^{n-1} + (e^{-q_x \Delta t} - 1)(\partial_x P)^{n-1/2}. \tag{B.13}$$

The left-hand side of the above equation is written, upon substitution of (B.13) and with some manipulation, as

$$e^{-q_x \Delta t}(\ {}_{px}\psi)^{n-1} + (e^{-q_x \Delta t} - 1)(\ {}_{px}\psi)^{n-1/2} =$$

$$e^{-q_x \Delta t}\left[(e^{-q_x \Delta t} - 1) \sum_{m=0}^{n-2} (\partial_x P)^{\Delta t((n-1)-(m+1/2))} e^{-q_x m\Delta t}\right] + (e^{-q_x \Delta t} - 1)(\partial_x P)^{\Delta t(n-1/2)} =$$

$$(e^{-q_x\Delta t}-1)\left[\sum_{m=0}^{n-2}(\partial_x P)^{\Delta t(n-(m+1)-1/2)}e^{-q_x(m+1)\Delta t}+(\partial_x P)^{\Delta t(n-1/2)}\right]. \tag{B.14}$$

We now change the summation index using

$$l=m+1 \qquad m=0\rightarrow l=1 \qquad m=n-2\rightarrow l=n-1, \tag{B.15}$$

to write (B.15) as

$$(e^{-q_x\Delta t}-1)\left[\sum_{l=1}^{n-1}(\partial_x P)^{\Delta t(n-l-1/2)}e^{-q_x l\Delta t}+(\partial_x P)^{\Delta t(n-1/2)}\right]=$$

$$(e^{-q_x\Delta t}-1)\left[\sum_{l=0}^{n-1}(\partial_x P)^{\Delta t(n-(l+1/2))}e^{-q_x l\Delta t}\right]. \tag{B.16}$$

Comparing equations (B.12) and (B.16) and using equation (B.14), we finally obtain equation (B.13). Expressions analogous to (B.13) can also be obtained for ${}_{pz}\psi$, ${}_{vx}\psi$ and ${}_{vz}\psi$.

By evaluation of $\partial_x P$ at locations in the grid other that at half the grid, i.e., at the vertices, we obtain slight variations of equation (B.13). An example of such expressions, useful for our purposes, is exactly equation (4.18):

$$({}_{pk}\psi)^n = e^{-q_k\Delta t}({}_{pk}\psi)^{n-1}+(e^{-q_k\Delta t}-1)(\partial_k P)^n, \qquad k=x,z,$$

with analogous expressions for ${}_{vx}\psi$ and ${}_{vz}\psi$.

References

Baysal, Edip, Dan D. Kosloff, and John W. C. Sherwood. "Reverse time migration." Geophysics 48 (1983): 1514–1524.

Bérenger, J. P. Note Technique. DGA/ETCA/DET/390, 1977.

Bérenger, Jean-Pierre. "A Perfectly Matched Layer for the Absorption of Electromagnetic Waves." Journal of Computational Physics 114 (1994): 185–200.

Bérenger, Jean-Pierre. Perfectly Matched Layer (PML) for Computational Electromagnetics. Morgan and Claypool Publishers, 2007.

Bo-Feng, Huazhong Wang, Lixin Tian, and Donghong Zhou. "A strategy for source wavefield reconstruction in reverse time migration." 81st Annual International Meeting, SEG. . Soc. Expl. Geophys., 2010. 3164–3168.

Clapp, R. P. "Reverse Time Migration with random boundaries." 79th Annual International Meeting, SEG, Expanded Abstracts. . Volume 28 . Soc. Expl. Geophys., 2009. 2809–2813.

Courant, R., K. O. Friedrichs, and H. Lewy. "Über die partiellen Differenzengleichungen der mathematischen Physic." Mathematische Annalen 100 (1928): 32–74.

Du Qi-Zhen, Sun Rui-Yan, Qin Tong, Zhu Yi-Tong, and Bi Li-Fei. "A study of perfectly matched layers for joint multicomponent reverse-time migration." Applied Geophysics 7 (2010): 166–173.

Engquist, B. and A. Majda. "Absorbing boundary conditions for the numerical simulation of waves.." Math. Comput. 31 (1977): 629.

Garcia, Jade Rachele S. 3D finite-difference time-domain modeling of acoustic wave propagation based on domain decomposition. Technical report, CNRS-IRD-UNSA-OCA, 2009.

Gilles, L., S. G. Hagness, and L. Vazquez. "Comparison Between Staggered and Unstaggered Finite-Difference Time-Domain Grids for Few-Cycle Temporal Optical Soliton Propagation." Journal of Computational Physics 161 (2000): 379–400.

Graves, Robert W. "Simulating Seismic Wave Propagation in 3D Elastic Media Using Staggered-Grid Finite Differences." Bulletin of Seismological Society of America 86 (August 1996): 1901–1106.

Herrera, W., J. D. Mayhan, and A. B. Weglein. "A BACKGROUND REVIEW OF THE THEORY OF THE PERFECTLY MATCHED LAYER (PML) METHOD: THE ACOUSTIC WAVE EQUATION." M-OSRP 2012 Annual Meeting. 2012, 189–219.

Johnson, Steven G. Notes on Perfectly Matched Layers (PMLs). Technical report, MIT, 2007. http://math.mit.edu/~stevenj/18.369/pml.pdf.

Komatitsch, Dimitri and Roland Martin. "An unsplit convolutional perfectly matched layer improved at grazing incidence for the seismic wave equation." Geophysics 72 (2007): SM155–SM167.

Kuzuoglu, M. and R. Mittra. "Frequency dependence of the constitutive parameters of causal perfectly matched absorbers." IEEE Microw. Guid. Wave Letters 50 (2003): 348–350.

Leveille, Jacques P., Ian F. Jones, Zheng-Zheng Zhou, Bin Wang, and Faqi Liu. "Subsalt imaging for exploration, production, and development: A review." Geophysics 76 (2011): WB3–WB20.

Liu, F., Guanquan Zhang, Scott A. Morton, and Jacques P. Leveille. "An effective imaging condition for reverse-time migration using wavefield decomposition." Geophysics 76 (2011): S29–S39.

McGarry, R. G., J. A. Mahovsky, P. P. Moghaddam, D.S. Foltinek, and D. J. Eaton. "Reverse-Time depth Migration with reduced memory requirements:." U.S. Patent 0054082 A1 (2010).

Merewether, D. IEEE Trans. Electromagn. Comput. 13 (1971): 41.

Roden, J. A. and S. D. Gedney. "Convolutional PML (CPML): An Efficient FDTD Implementation of the CFS-PML for Arbitrary Media." Microwave and Optical Technology Letters 27 (2000): 334–339.

Stolt, Robert H. and Arthur B. Weglein. Seismic Imaging and Inversion, Volume 1. Cambridge University Press, 2011.

Symes, W. W. "Reverse-time migration with optimal checkpinting." Geophysics 72 (2007): SM213–SM221.

Taflove, Allen and Susan C. Hagness. computational electrodynamics, THE FINITE-DIFFERENCE TIME-DOMAIN METHOD. ARTECH HOUSE, 2005.

Weglein, A. B., R. H. Stolt, and J. D. Mayhan. "Reverse-time migration and Green's theorem: Part I — The evolution of concepts, and setting the stage for the new RTM method." Journal of Seismic Exploration 20 (February 2011): 73–90.

Weglein, A. B., R. H. Stolt, and J. D. Mayhan. "Reverse time migration and Green's theorem: Part II — A new and consistent theory that progresses and corrects current RTM concepts and methods." Journal of Seismic Exploration 20 (May 2011): 135–159.

Whitmore, D. N. "Iterative depth imaging by back time propagation." 53^{rd} Annual International Meeting, SEG, Expanded Abstracts. . Soc. Expl. Geophys., 1983. 382–385.

Zhang, Y., S. Xu, N. Bleistein, and G. Zhang. "True amplitude angle domain common image gathers from one-way wave equation migrations." Geophysics 72 (2007): S49–58.

Zhang, Y., G. Zhang, and N. Bleistein. "Theory of true amplitude one-way wave equations and true amplitude common-shot migrations." Geophysics 70 (2005): E1–10.

Zhang, Yu and James Sun. "Practical issues of reverse time migration: true-amplitude gathers, noise removal and harmonic-source encoding." 70th EAGE Conference and Exhibition. . 2008.

The first *wave theory* RTM, examples with a layered medium, predicting the source and receiver at depth and then imaging, providing the correct location and reflection amplitude at every depth location, and where the data includes primaries and all internal multiples.

Fang Liu and Arthur B. Weglein

April 29, 2013

Abstract

Reverse time migration (RTM) is the cutting-edge imaging method used in seismic exploration. In earlier RTM publications, density was often used to balance a medium with velocity variation, such that the acoustic impedance − the product of velocity and density − stays constant. Thus, reflections from sharp boundaries are avoided. In order to be more complete, consistent, realistic, and predictive, density variation is intentionally included in our study so that we can test its impact on the Green's theorem-based wave-theory RTM algorithms.

The major objectives of this article are to advance our understanding and to provide concepts, added imaging capabilities, and new algorithms for RTM. Although our objective of extracting useful subsurface information from recorded data is not different from that of well-known previous RTM publications, our approach is different: we use wave theory as much as possible to maximize the benefit from the Green's function and Green's theorem, rather than use the more popular methodology of running finite-difference modeling backwards in time.

A significant artifact in RTM is caused by the fact that numerous subsurface seismic events necessary for backward propagation never return to the measurement surface. This unwanted phenomenon also exists for the wave-field-prediction method formulated from Green's theorem: Green's formula (in its general form, i.e., equation (2.5)), which links the wave field on the entire outer surface with interior field values, also requires data from everywhere on the surface. Weglein et al. (2011a) and Weglein et al. (2011b) proposed a special Green's function with vanishing Dirichlet and Neumann boundary conditions at the deeper boundary to cope with that issue. This article provides a natural extension of the two aforementioned papers, into a medium with density variation and more complicated geological structures.

The major advantage of RTM over many other seismic imaging methods is its additional ability to handle two-way propagation without assuming that the events in the input data are only up-going and that all multiples have been removed. This article demonstrates with numerical examples that both up- and down-going waves can be precisely predicted from the data (including internal multiples) on the top surface only. In our example, the contribution of the transmission events that never return to the measurement surface is deliberately eliminated, and it is not necessary for those events to enter the calculation.

The Green's function with vanishing Dirichlet and Neumann boundary conditions at the deeper boundary demonstrates many remarkable properties. For example, it vanishes if the receiver is deeper than the source, it violates reciprocity, and its value is not affected by any heterogeneity outside the region between the source and receiver. The double vanishing boundary condition also leads us to a wave-theory solution for a model that has many reflectors and lacks internal multiples.

In this paper, two approaches have been used to derive the Green's function with vanishing Dirichlet and Neumann boundary conditions at the deeper boundary. The first is an analytical boundary-matching method in the frequency domain, and the second is the numerical finite-difference approach identical to many current finite-difference forward-modeling procedures in the industry. The second method can be extended to multiple dimensions with lateral variation in the medium properties. We find these two methods agree with each other with regard to the intrinsic accuracy issue of the finite-difference approximation to differential equations.

In this paper, we also have some very early and very positive news on the first wave theory RTM imaging tests, with a discontinuous reference medium and images that have the correct depth and amplitude (that is, producing the reflection coefficient at the correctly located target) with primaries and multiples in the data. That is an implementation of Weglein et al. (2011a;b) with creative implementation and testing and analysis.

1 Introduction

One of the major early objectives of Reverse Time Migration (RTM) is to obtain a better image of salt flanks through diving waves than is obtained by directly imaging through the complex overburden. The key new capability of the RTM method compared with one-way migration algorithms is to allow two-way wave propagation in the imaging procedure. This article follows closely the idea established in Weglein et al. (2011a;b): achieving a Green's function with vanishing Dirichlet and Neumann boundary conditions at the deeper boundary, to eliminate the need for measurement at depth.

To achieve the two-way imaging, we study the behavior of our Green's function in three examples: (1) a homogeneous model, (2) a single reflector model, and (3) a two-reflector model with internal multiples. In order to get two-way propagation without complexity and approximation, we study 1D examples with both up- and down-going wave propagation. We provide the details to demonstrate the underlying physics.

As stated in Whitmore (1983); Baysal et al. (1983); Luo and Schuster (2004); Fletcher et al. (2006); Liu et al. (2009) and Vigh et al. (2009), accurate medium properties above the target are required for the RTM procedure discussed in this article. The major difference is that in most RTM algorithms in the industry, a smoothed version of the velocity is used in the imaging procedure to avoid reflections from the velocity model itself, while the exact velocity models (often discontinuous) are used in all three examples in this article.

To apply the firm footing and math-physics foundation established in Weglein et al. (2011a;b) in an arbitrary medium, we first study in detail the properties of the Green's functions with vanishing boundary conditions at the deeper boundary $z' = \mathcal{B}$. The understanding of the aforementioned

properties provides us with a straightforward procedure for constructing a Green's function with the double vanishing boundary condition for a 1D medium with arbitrary complexity. We adopt the notations of the aforementioned articles as much as possible while introducing some minor modifications to allow smooth expansions into new territories.

One of the remarkable properties of the Green's function in this article is that, although both the causal Green's function G_0^+ and the anti-causal Green's function G_0^- vary with the medium below the source, the Green's function with both vanishing Dirichlet and Neumann boundary conditions does not. The implications are that if we want to predict the wave field at depth z, the medium's properties deeper than z are not required. Such a property is very difficult to visualize if G_0^+ or G_0^- is used to make the prediction, since both of them will change with the medium's properties deeper than z. It is worthwhile to note that this property of the Green's function with vanishing boundary conditions is also demonstrated by the WKBJ Green's function used in the derivation of FK and phase-shift migrations. While the WKBJ Green's function is an approximate solution for a medium with smooth variations, and the Green's function with double vanishing boundary conditions in this report is exact and for a discontinuous medium, nevertheless we find their similarity worth reporting.

The property that allows an easy iterative procedure for constructing a Green's function with double vanishing boundary conditions is the following: the field values of the Green's function vanishing at the deeper surface are not affected by heterogeneity beyond the region between the field point and the source. Consequently, we can start the calculation from a field location sufficiently close to the source that the medium in between is homogeneous. In this case, the initial field value (for all time and frequency values) can be calculated from a much simpler medium obtained by extending the homogeneity to the entire space*. This initial field value contains two parts: the first part† is the out-going G_0^+ and is produced by the actual source, and the second term is the downward propagation portion‡ that will cancel with the downward propagation energy of G_0^+. Consequently, it will give a solution that vanishes completely below the source, satisfying both Dirichlet and Neumann boundary conditions. For the solution of the wave field above the initial field, standard analytic boundary-matching methods or discrete finite-difference procedures can be used to iteratively extrapolate the function values to locations further and further away from the source location.

Another property of the Green's function with both Dirichlet and Neumann boundary conditions vanishing is that it contains no multiples or reflections from the energy produced by the source, even for models with an arbitrary number of reflectors. This property, derived from precise Green's theory, agrees with many methodologies in the current seismic imaging procedures (which are often derived with some approximation to the wave equation): a smooth model is preferred, in order to exclude reflections and multiples caused by the velocity model.

The major contributions of this article are:

*For example, equation (14) of Weglein et al. (2011b) or equation (3.1) in this paper.

†The second term of equation (14) of Weglein et al. (2011b).

‡The first term of equation (14) of Weglein et al. (2011b).

- It provides two methods to calculate the Green's function with vanishing Dirichlet and Neumann boundary conditions for arbitrary 1D medium.
- It incorporates the density variation for Green's theorem RTM.
- It provides the finite-difference scheme for calculating the Green's function that vanishes at the deeper boundary.
- It provides a two-way propagation and downward continuation of wave fields, by using Green's function with double vanishing boundary conditions.
- It demonstrates remarkable properties of the precise analytical Green's function that coincide with many existing seismic imaging ideas derived with different degrees of approximation.

The following notations are worth mentioning at the beginning: G_0^+ and G_0^- are used to denote causal and anti-causal Green's functions, respectively. G_0^{DN} is used to denote the Green's function with vanishing Dirichlet and Neumann boundary conditions at the deeper boundary. $k = \omega/c_0$ where c_0 is the constant velocity of the reference medium, and ω is the angular frequency.

Although Green's theorem and Green's functions are more often discussed in the frequency domain, in this paper the Green's functions and wave field prediction examples are always graphed in the time domain since this domain is more easily accessible (without expressing the values in complex numbers). A very straightforward Fourier transform is sufficient to make the domain change:

$$f(t) = \frac{1}{2\pi} \int_{-\infty}^{\infty} \widetilde{f}(\omega) e^{-i\omega t} d\omega. \tag{1.1}$$

The Green's function, resulting from an ideal impulsive source, contains frequency information of an arbitrary frequency. For display, we convolve it with a band-limited wavelet (the first derivative of a Gaussian function[§]) to avoid aliasing beyond the Nyquist frequency.

2 Green's theorem wave-field prediction with density variation

In many migration methods, density variation is often left out of the acoustic wave equation since it does not affect the travel time. In reverse time migration, however, density serves a very important role even in the early stage: in order to have a reflectionless medium with velocity variations, a counterbalancing density variation is introduced to make sure the acoustic impedance is constant. Therefore in our derivation of Green's theorem-based RTM, we explicitly incorporate the density variations in the acoustic medium. First, let us assume the wave propagation problem in a volume V bounded by a shallower depth $\mathcal{A}$ and deeper depth $\mathcal{B}$:

[§]The wavelet is $i\omega e^{-\omega^2/\beta}$ in the frequency domain or $\frac{1}{2}\sqrt{\frac{\beta}{\pi}} e^{-\beta t^2/4}$ in the time domain, where $\beta = (20\pi)^2$

$$\left\{\frac{\partial}{\partial z'}\frac{1}{\rho(z')}\frac{\partial}{\partial z'}+\frac{\omega^2}{\rho(z')c^2(z')}\right\}P(z',\omega)=0 \qquad , \qquad \mathcal{A}<z'<\mathcal{B}, \tag{2.1}$$

where z' is the depth, and $\rho(z')$ and $c(z')$ are the density and velocity fields, respectively. In exploration seismology, we let the shallower depth $\mathcal{A}$ be the measurement surface where the seismic acquisition can be accomplished economically. The volume V is the finite volume defined in the "finite volume model" for migration, the details of which can be found in Weglein et al. (2011a). We measure P at the measurement surface $z'=\mathcal{A}$, and the objective is to predict P anywhere between the shallower surface and another surface with greater depth, $z'=\mathcal{B}$. This can be achieved via the solution of the wave-propagation equation in the same medium by an idealized impulsive source or Green's function:

$$\left\{\frac{\partial}{\partial z'}\frac{1}{\rho(z')}\frac{\partial}{\partial z'}+\frac{\omega^2}{\rho(z')c^2(z')}\right\}G_0(z,z',\omega)=\delta(z-z') \qquad , \qquad \mathcal{A}<z'<\mathcal{B}, \tag{2.2}$$

where z is the location of the source, and z' and z increase in a downward direction. It can be achieved as follows:

- Multiply equation (2.2) by $P(z',\omega)$.
- Multiply equation (2.1) by $G_0(z,z',\omega)$.
- Integrate the difference of the two aforementioned products (both are functions of z') over the variable z' from $\mathcal{A}$ to $\mathcal{B}$.

The right-hand side of the operation above is:

$$\int_{\mathcal{A}}^{\mathcal{B}} P(z',\omega)\delta(z-z')dz'=P(z,\omega), \tag{2.3}$$

where in the derivation above we assume z is inside the volume V (i.e., $\mathcal{A}<z<\mathcal{B}$). Omitting the arguments of the following functions: $P(z',\omega)$, $G_0(z,z',\omega)$, $c(z')$ and $\rho(z')$, since their arguments will not be changed in the derivation process, the left-hand side of the operation above is:

$$
\begin{aligned}
&\int_{\mathcal{A}}^{\mathcal{B}} \left[P \frac{\partial}{\partial z'} \left\{ \frac{1}{\rho} \frac{\partial G_0}{\partial z'} \right\} + \frac{\omega^2 P G_0}{\rho c^2} - G_0 \frac{\partial}{\partial z'} \left\{ \frac{1}{\rho} \frac{\partial P}{\partial z'} \right\} - \frac{\omega^2 P G_0}{\rho c^2} \right] dz' \\
=&\int_{\mathcal{A}}^{\mathcal{B}} \left[P \frac{\partial}{\partial z'} \left\{ \frac{1}{\rho} \frac{\partial G_0}{\partial z'} \right\} - G_0 \frac{\partial}{\partial z'} \left\{ \frac{1}{\rho} \frac{\partial P}{\partial z'} \right\} \right] dz' \\
=&\int_{\mathcal{A}}^{\mathcal{B}} \left[P \frac{\partial}{\partial z'} \left\{ \frac{1}{\rho} \frac{\partial G_0}{\partial z'} \right\} + \frac{\partial P}{\partial z'} \frac{1}{\rho} \frac{\partial G_0}{\partial z'} - G_0 \frac{\partial}{\partial z'} \left\{ \frac{1}{\rho} \frac{\partial P}{\partial z'} \right\} - \frac{\partial G_0}{\partial z'} \frac{1}{\rho} \frac{\partial P}{\partial z'} \right] dz' \\
=&\int_{\mathcal{A}}^{\mathcal{B}} \left[\frac{\partial}{\partial z'} \left\{ \frac{P}{\rho} \frac{\partial G_0}{\partial z'} \right\} - \frac{\partial}{\partial z'} \left\{ \frac{G_0}{\rho} \frac{\partial P}{\partial z'} \right\} \right] dz' = \int_{\mathcal{A}}^{\mathcal{B}} \frac{\partial}{\partial z'} \left\{ \frac{P}{\rho} \frac{\partial G_0}{\partial z'} - \frac{G_0}{\rho} \frac{\partial P}{\partial z'} \right\} dz' \\
=&\int_{\mathcal{A}}^{\mathcal{B}} \frac{\partial}{\partial z'} \left\{ \frac{1}{\rho} \left[P \frac{\partial G_0}{\partial z'} - G_0 \frac{\partial P}{\partial z'} \right] \right\} dz' \\
=&\frac{1}{\rho} \left\{ P \frac{\partial G_0}{\partial z'} - G_0 \frac{\partial P}{\partial z'} \right\} \Bigg|_{z'=\mathcal{A}}^{z'=\mathcal{B}}.
\end{aligned}
\tag{2.4}
$$

Equating the results obtained by the left- and right-hand-side operations, and restoring the specific arguments of each function, we have:

$$
P(z,\omega) = \frac{1}{\rho(z')} \left\{ P(z',\omega) \frac{\partial G_0(z,z',\omega)}{\partial z'} - G_0(z,z',\omega) \frac{\partial P(z',\omega)}{\partial z'} \right\} \Bigg|_{z'=\mathcal{A}}^{z'=\mathcal{B}}, \tag{2.5}
$$

where $\mathcal{A}$ and $\mathcal{B}$ are the shallower and deeper boundaries, respectively, of the volume to which the Green's theorem is applied. It is identical to equation (43) of Weglein et al. (2011a), except for the additional density contribution to the Green's theorem. Similar density contributions can be found in many seismic imaging procedures, such as equation (21) of Clayton and Stolt (1981).

In the arguments of G_0, z is the location of the source, and z' is the location of the receiver. The Green's theorem given in equation (2.5) predicts the data $P(z,\omega)$ in an arbitrary location using the data $P(z',\omega)$ at the measurement surface. In this specific application, z is the depth at which the wave-field prediction is carried out.

Note that in equation (2.5), the field values at the surface of the volume V are necessary for predicting the field value inside V. The surface of V contains two parts: the shallower portion $z' = \mathcal{A}$ and the deeper portion $z' = \mathcal{B}$. In seismic exploration, the need for data at $z' = \mathcal{B}$ is often the issue. For example, one of the significant artifacts of the current RTM procedures is caused by

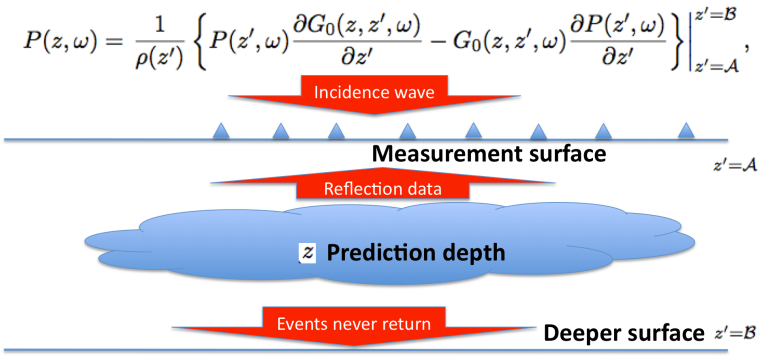

Figure 1: Green's theorem predicts the wave field at an arbitrary depth z between the shallower depth $\mathcal{A}$ and deeper depth $\mathcal{B}$.

this phenomenon: there are events necessary for accurate wave-field prediction that reach $z' = \mathcal{B}$ but never return to $z' = \mathcal{A}$, as is demonstrated in Figure 1. The solution, based on Green's theorem without any approximation, was first published in Weglein et al. (2011a) and Weglein et al. (2011b), the basic idea can be summarized as the following.

Since the wave equation is a second-order differential equation, its solution is not unique. In other words, for a wave equation with a specific medium property, there are an infinite number of solutions. This freedom in choosing the Green's function has been taken advantage of in many seismic-imaging procedures. For example, the most popular choice in wave-field prediction is the physical solution G_0^+. In downward continuing an up-going wave field to a subsurface, the anti-causal solution G_0^- is often used.

If both G_0 and $\partial G_0/\partial z'$ vanish at the deeper boundary $z' = \mathcal{B}$, where measurement is often much more expensive than acquiring data at the shallower boundary $z' = \mathcal{A}$, then only the data at the shallower surface (i.e., the actual measurement surface) is needed in the calculation. We use G_0^{DN} to denote the Green's function with vanishing Dirichlet and Neumann boundary conditions at the deeper boundary.

3 The vanishing property of G_0^{DN} and its independence of the medium's properties below the source

First, let us look at some properties of the Green's function detailed in equation (14) of Weglein et al. (2011b):

$$G_0^{DN}(z,z',\omega) = \frac{-1}{2ik}\left(e^{-ik(z-z')} - e^{ik|z-z'|}\right), \tag{3.1}$$

where $k = \omega/c_0$ and the quantity c_0 is the unchanged homogeneous velocity in the entire space, and z and z' are the locations of the source and receiver, respectively. This Green's function is

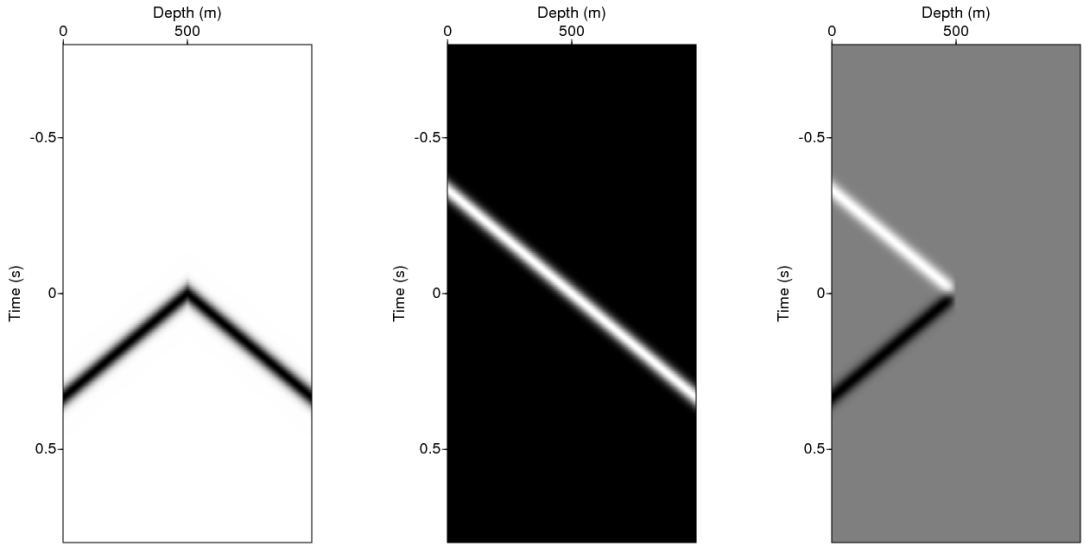

Figure 2: The construction of G_0^{DN} for a homogeneous medium with constant velocity $1500m/s$. The source depth is 500m. The left panel is the causal solution (if we denote $k = \omega/c_0$ and H is the Heaviside function, the causal Green's function is $G_0^+(z, z', \omega) = e^{ik|z-z'|}/(2ik)$ in the frequency domain or $G_0^+(z, z', t) = \frac{-c_0}{2} H(t - |z - z'|/c_0)$ in the time domain). The middle panel shows the homogeneous solution $(-e^{ik(z'-z)}/(2ik)$ in the frequency domain or $\frac{c_0}{2} H(t - (z' - z)/c_0)$ in the time domain) that cancels with the left panel below the source. The right panel results from summing the two panels on its left and is the desired Green's function with double vanishing boundary conditions.

for a whole-space homogeneous medium with c_0 as its velocity. It also satisfies the Dirichlet and Neumann boundary conditions at the deeper boundary $\mathcal{B}$:

$$G_0^{DN}(z,z',\omega)\big|_{z'=\mathcal{B}} = 0,$$
$$\frac{\partial G_0^{DN}(z,z',\omega)}{\partial z'}\bigg|_{z'=\mathcal{B}} = 0.$$

The construction of equation (3.1) (i.e., G_0^{DN} in a homogeneous medium) is detailed in Weglein et al. (2011b); we only provide its graphic version in this article in Figure 2.

In equation (3.1), the second term is the causal solution for the same homogeneous medium, and the first term is a specific solution to the homogeneous[¶] wave equation, introduced to perfectly cancel the causal solution at the deeper boundary. The major objective of this Green's function is to eliminate the need for measurement at the deeper surface: $z' = \mathcal{B}$.

According to equation (2.5), for arbitrary values of the wave field $P(z',\omega)$, this objective implies $G_0(z,z',\omega)|_{z'=\mathcal{B}} = \frac{\partial G_0(z,z',\omega)}{\partial z'}\Big|_{z'=\mathcal{B}} = 0$, since normally the data are available only at the measurement surface: $z' = \mathcal{A}$. The variable z is used to denote the depth to which we want to continue the wave field downward. It is obvious that $\mathcal{A} < z' < \mathcal{B}$. First, if $z < z'$, this Green's operator vanishes, since

$$\begin{aligned} G_0^{DN}(z,z',\omega) &= \frac{-1}{2ik}\left(e^{-ik(z-z')} - e^{ik|z-z'|}\right) \\ &\overset{z<z'}{=} \frac{-1}{2ik}\left(e^{ik(z'-z)} - e^{ik(z'-z)}\right) \\ &\equiv 0. \end{aligned} \tag{3.2}$$

According to equation (3.2), this Green's function vanishes not only for the isolated location at $\mathcal{B}$, but also in the extended entire half-space below the source, which include $z' = \mathcal{B}$.

Obviously this Green's function satisfies the wave equation of the whole-space homogeneous medium (i.e., equation (7) of Weglein et al. (2011b)):

$$\left(\frac{d^2}{dz'^2} + \frac{\omega^2}{c_0^2}\right) G_0^{DN}(z,z',\omega) = \delta(z-z'). \tag{3.3}$$

If we have an inhomogeneous medium $c(z')$ such that $c(z') = c_0$ when $z' < z$, the Helmholtz equation for this inhomogeneous medium is

[¶]In this article the adjective homogeneous has different meaning when it acts on medium or equation. In the first case it means medium with constant acoustic property in the entire space, while in the second case it means a wave equation without the source term.

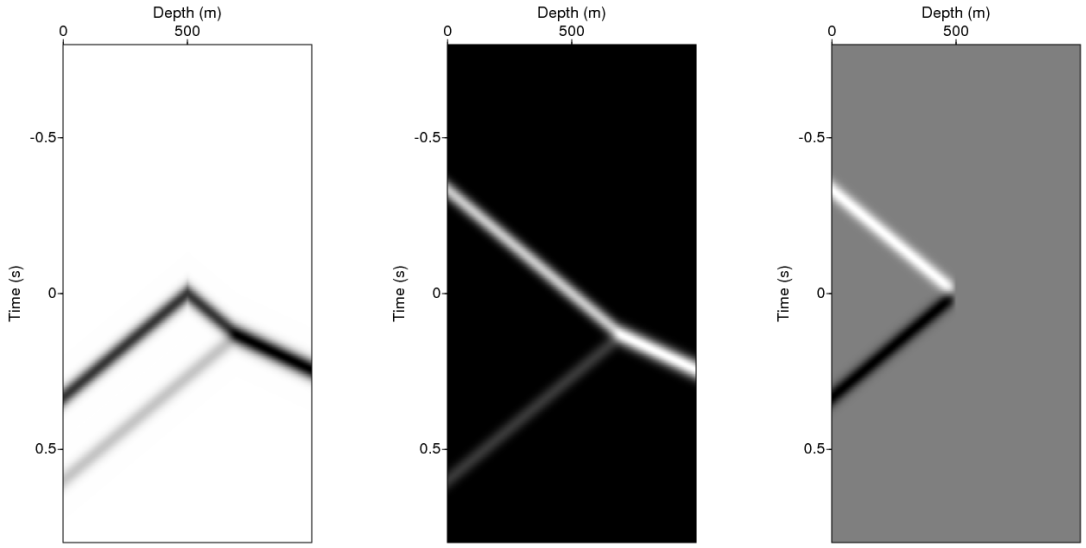

Figure 3: The construction of G_0^{DN} for a medium with one reflector (the velocities above and below the reflector are $1500m/s$ and $2700m/s$, respectively). The source depth is 500m and is above the single reflector at $700m$. The left panel is the causal solution G_0^+, and the middle panel shows the homogeneous solution that cancels with the left panel below the source. The right panel results from summing the two panels on its left and is the desired Green's function with double vanishing boundary conditions.

$$\left(\frac{d^2}{dz'^2} + \frac{\omega^2}{c^2(z')}\right) \mathcal{G}_0(z, z', \omega) = \delta(z - z'). \tag{3.4}$$

When $z' < z$, wave equation (3.4) is satisfied by Green's function (3.1) since it satisfies the homogeneous wave equation (3.3), which is identical to the inhomogeneous equation (3.4) when $z' < z$.

For the other possibility, that $z' > z$, wave equation (3.4) is also satisfied by Green's function (3.1) since it completely vanishes in this region. If we substitute G_0^{DN} for $\mathcal{G}_0$, left-hand side of equation (3.4) vanishes since the spatial partial derivative is zero, while the right-hand side vanishes due to the fact that the source z is located outside the region of interest. Consequently, equation (3.4) is satisfied by the Green's function in equation (3.3).

As an example, introducing a single reflector below the source for the Green's function in equation (16) of Weglein et al. (2011b) will not change the value of the Green's function. The construction of G_0^{DN} with its source located above the single reflector is detailed in Weglein et al. (2011b); here we provide its graphical version in Figure 3. The equivalence of the Green's function (3.1) to

equation (39) in Weglein et al. (2011b) can be demonstrated as follows. Since a is the depth of the reflector, and we consider the case in which the source is above the reflector, we have $z < a$ and $\mathtt{sgn}(a - z) = 1$. According to Appendix B of Weglein et al. (2011b), we have: $D_1 = 0$, $C_1 = -\frac{T}{2ik}e^{ik|a-z|}e^{-ik_1 a} = -\frac{T}{2ik}e^{ik(a-z)}e^{-ik_1 a}$. Thus, the wave field below the reflector (i.e., $z' > a$, the transmitted wave) can be simplified as:

$$\begin{aligned}
&\frac{T}{2ik}e^{ik|a-z|}e^{ik_1(z'-a)} + C_1 e^{ik_1 z'} + D_1 e^{-ik_1 z'} \\
=&\frac{T}{2ik}e^{ik|a-z|}e^{ik_1(z'-a)} - \frac{T}{2ik}e^{ik|a-z|e^{-ik_1 a}}e^{ik_1 z'} + 0 \times e^{-ik_1 z'} \\
=&\frac{T}{2ik}e^{ik|a-z|}e^{ik_1(z'-a)} - \frac{T}{2ik}e^{ik|a-z|}e^{ik_1(z'-a)} \equiv 0.
\end{aligned} \tag{3.5}$$

Obviously, this Green's function vanishes if $z' > a$ (is deeper than the reflector). The same vanishing property is also displayed for G_0^{DN} without the single reflector below the source; the details can be found in equation (3.2).

Since $A_1 = \frac{-1}{2ik}e^{-ikz}$, and $B_1 = \frac{-R}{2ik}e^{ik(2a-z)}$, and if $z' < a$ is above the reflector, the reflected wave in equation (39) of Weglein et al. (2011b) can be simplified as follows:

$$\begin{aligned}
&\frac{e^{ik|z'-z|}}{2ik} + R\frac{e^{-ik(z'-a)}}{2ik}e^{ik(a-z)} + A_1 e^{ikz'} + B_1 e^{-ikz'} \\
=&\frac{e^{ik|z'-z|}}{2ik} + R\frac{e^{ik(2a-z'-z)}}{2ik} + A_1 e^{ikz'} + B_1 e^{-ikz'} \\
=&\frac{e^{ik|z'-z|}}{2ik} + R\frac{e^{ik(2a-z'-z)}}{2ik} - \frac{e^{ik(z'-z)}}{2ik} - \frac{R}{2ik}e^{ik(2a-z)}e^{-ikz'} \\
=&\frac{e^{ik|z'-z|}}{2ik} + R\frac{e^{ik(2a-z'-z)}}{2ik} - \frac{e^{ik(z'-z)}}{2ik} - R\frac{e^{ik(2a-z'-z)}}{2ik} \\
=&\frac{e^{ik|z'-z|}}{2ik} - \frac{e^{ik(z'-z)}}{2ik} = \frac{-1}{2ik}\left(e^{ik(z'-z)} - e^{ik|z'-z|}\right).
\end{aligned} \tag{3.6}$$

Consequently, it is identical to the Green's function (3.1) for $z' < a$ (i.e., to equation (14) of Weglein et al. (2011b), the Green's function with the same vanishing Dirichlet and Neumann boundary conditions at the deeper boundary for a whole-space homogeneous medium). In other words, the reflector below the source will not change the values of the Green's function with vanishing Dirichlet and Neumann boundary conditions at the deeper boundary.

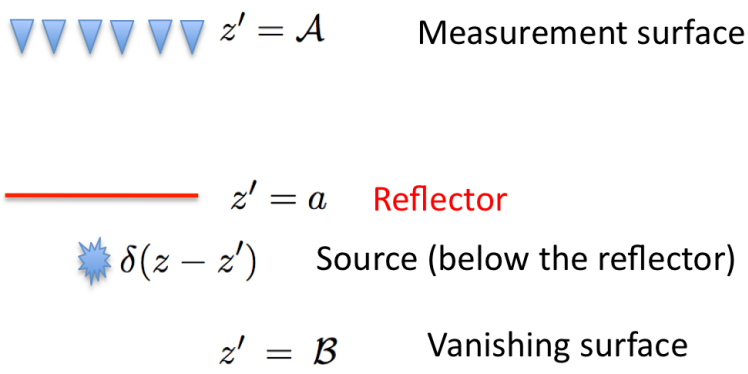

Figure 4: The configuration of the experiment with the source below a single reflector.

4 G_0^{DN} for a model with a single reflector

4.1 Case I: source above the reflector

This case had been derived and documented in detail in Weglein et al. (2011b). The only additional contribution we have in this article is the density term in the amplitude of the Green's function:

$$G_0^{DN}(z, z', \omega) = \frac{\rho_0}{2ik}\left(e^{ik|z-z'|} - e^{-ik(z-z')}\right). \tag{4.1}$$

In the equation above, the density at the source location is the extra contribution in extending the Green's function in equation (39) of Weglein et al. (2011b). A similar density term can be found in the Green's function of Clayton and Stolt (1981).

We can also Fourier transform equation (4.1) to the time domain to have:

$$G_0^{DN}(z, z', t) = \frac{\rho_0 c_0}{2}\left(H\left[t - \frac{z' - z}{c_0}\right] - H\left[t - \frac{|z' - z|}{c_0}\right]\right). \tag{4.2}$$

4.2 Case II: source below the reflector

From the previous section, if $z < a$, the solution is trivial since $G_0^{DN}(z, z', \omega) = G_0^{DN}(z, z', \omega)$. It is critical to derive G_0^{DN} for $z > a$. The physical experiment is the following (see Figure 4): The locations of the measurement surface and the deeper surface are $\mathcal{A}$ and $\mathcal{B}$, respectively. The depth of the single reflector and source are a and z, respectively. The causal Green's function with the source located at depth z and receiver at depth z' is denoted as $G_0^{+}(z, z', \omega)$.

If the impulsive source is below the reflector, it will produce an out-going wave $\frac{\rho_1 e^{ik_1|z'-z|}}{2ik_1}$ in the second medium; i.e., the Green's function with homogeneous properties (ρ_1, c_1). After the out-going

field is obtained, the reflection in the second medium and the transmission in the first medium can be solved as a classical reflection problem, as is presented in equations (12.5) and (12.8), and the final result is:

$$\frac{1}{\rho_1}G_0^+(z,z',\omega)=\begin{cases}\frac{1-R}{2ik_1}e^{ik_1(z-a)}e^{ik(a-z')} & \texttt{if } (z'<a)\\ \frac{1}{2ik_1}\left(e^{ik_1|z'-z|}-Re^{ik_1(z'+z-2a)}\right) & \texttt{if } (z'>a)\end{cases}, \tag{4.3}$$

where $R=\frac{\rho_1c_1-\rho_0c_0}{\rho_1c_1+\rho_0c_0}$ is the reflection coefficient of a plane wave incident from above. Since $\mathcal{B}$ is the depth of the deeper surface, for our wave-field prediction purpose we have $\mathcal{A}<z<\mathcal{B}$. Consequently, G_0^+ will produce two packets of down-going waves at the deeper surface $\mathcal{B}$: $\frac{\rho_1e^{ik_1(\mathcal{B}-z)}}{2ik_1}$ (the direct wave or the homogeneous propagation as if the entire space is filled with the second medium) and $-R\frac{\rho_1e^{ik_1(\mathcal{B}+z-2a)}}{2ik_1}$ (the reflection wave$^{\|}$).

For $z'>z$, G_0^+ can be expressed as:

$$\frac{e^{ik_1|z'-z|}-Re^{ik_1(z'+z-2a)}}{2ik_1/\rho_1}=\frac{e^{ik_1(z'-z)}-Re^{ik_1(z'+z-2a)}}{2ik_1/\rho_1}=\frac{e^{-ik_1z}-Re^{ik_1(z-2a)}}{2ik_1/\rho_1}e^{ik_1z'}.$$

In order to have a Green's function that vanishes at the deeper boundary $z'=\mathcal{B}$, we can introduce a homogeneous solution that cancels with the causal solution. As a result, the desired homogeneous solution, denoted as $\phi(z,z',\omega)$, must be

$$\phi(z,z',\omega)=\frac{Re^{ik_1(z-2a)}-e^{-ik_1z}}{2ik_1/\rho_1}e^{ik_1z'}\qquad\texttt{if } (z'>z). \tag{4.4}$$

We denote the amplitude factor of the down-going wave $e^{ik_1z'}$ as $F_1(z,\omega)=\frac{e^{-ik_1z}-Re^{ik_1(z-2a)}}{2ik_1/\rho_1}$. Our objective is to produce a homogeneous propagation that will produce $-F_1(z,\omega)e^{ik_1z'}$ for $z'>z$ that cancels G_0^+ at the deeper boundary $z'=\mathcal{B}$. Since the actual medium has a single invariant velocity c_1 for $z'>a$ and there is no velocity change at the source location, $z'=z$, this implies that it is also the solution for a broader region (i.e., $z'>a$):

$$\phi(z,z',\omega)=\frac{Re^{ik_1(z-2a)}-e^{-ik_1z}}{2ik_1/\rho_1}e^{ik_1z'}\qquad\texttt{if } (z'>a). \tag{4.5}$$

With the solution for $z'>a$, the wave propagation for $z'<a$ can be unambiguously solved via boundary conditions detailed in Appendix A. The medium's properties are listed in Table 1, and R is used to denote the reflection coefficient of this model when the incident wave is coming from above:

Depth Range	Velocity	Density
$(-\infty, a)$	c_0	ρ_0
(a, ∞)	c_1	ρ_1

Table 1: The properties of an acoustic medium with a single reflector at depth a.

$R = \frac{\rho_1 c_1 - \rho_0 c_0}{\rho_1 c_1 + \rho_0 c_0}$; other coefficients such as the reflection coefficient from below, and the transmission coefficients, can all be easily expressed as a simple function** of R.

According to the classical reflection problem listed in Appendix A, the incident wave (i.e., for $z' < a$) intended to produce the transmission packet in equation (4.5) for the purpose of canceling the boundary values of G_0^+ at the deeper boundary $z' = \mathcal{B}$ is:

$$\frac{-F_1}{1+R} e^{ik_1 a} e^{ik(z'-a)} = \frac{R e^{ik_1(z-a)} - e^{ik_1(a-z)}}{2ik_1(1+R)/\rho_1} e^{ik(z'-a)}. \tag{4.6}$$

However, the above incident wave will produce a corresponding reflection wave in the upper medium (i.e., $z' < a$) as a byproduct:

$$\frac{-F_1 R}{1+R} e^{ik_1 a} e^{ik(a-z')} = \frac{R^2 e^{ik_1(z-a)} - R e^{ik_1(a-z)}}{2ik_1(1+R)/\rho_1} e^{ik(a-z')}. \tag{4.7}$$

We can summarize the solution below the reflector in equation (4.5) and the solution above the reflector in equations (4.6) and (4.7) to have:

$$\phi(z, z', \omega) = \begin{cases} \frac{R e^{ik_1(z-a)} - e^{ik_1(a-z)}}{2ik_1(1+R)/\rho_1} e^{ik(z'-a)} + \frac{R^2 e^{ik_1(z-a)} - R e^{ik_1(a-z)}}{2ik_1(1+R)/\rho_1} e^{ik(a-z')} & \texttt{if } (z' < a) \\ \frac{R e^{ik_1(z-2a)} - e^{-ik_1 z}}{2ik_1/\rho_1} e^{ik_1 z'} & \texttt{if } (z' > a) \end{cases}. \tag{4.8}$$

Combining equations (4.3) and (4.8), the Green's function that satisfies the Dirichlet and Neumann boundary conditions at the deeper boundary $z' = \mathcal{B}$ is:

$$\begin{aligned} &\frac{1}{\rho_1} G_0^{DN}(z, z', \omega) = \frac{G_0^+(z, z', \omega) + \phi(z, z', \omega)}{\rho_1} = \\ &\begin{cases} \frac{1-R}{2ik_1} e^{ik_1(z-a)} e^{ik(a-z')} + \\ \frac{R e^{ik_1(z-a)} - e^{ik_1(a-z)}}{2ik_1(1+R)} e^{ik(z'-a)} + \frac{R^2 e^{ik_1(z-a)} - R e^{ik_1(a-z)}}{2ik_1(1+R)} e^{ik(a-z')} & \texttt{if } (z' < a) \\ \frac{e^{ik_1|z'-z|} - R e^{ik_1(z'+z-2a)}}{2ik_1} + \frac{R e^{ik_1(z-2a)} - e^{-ik_1 z}}{2ik_1} e^{ik_1 z'} & \texttt{if } (z' > a) \end{cases}. \end{aligned} \tag{4.9}$$

‖The amplitude factor is $-R$ instead of R since the incident wave comes from the second medium (below) rather than the first medium (above).

**For example, the reflection coefficient from below is $-R$, and the transmission coefficients from above and below are $1 + R$ and $1 - R$, respectively.

The above expression can be simplified as:

$$G_0^{DN}(z,z',\omega) = \begin{cases} \frac{Re^{ik_1(z-a)}-e^{ik_1(a-z)}}{2ik_1(1+R)/\rho_1}e^{ik(z'-a)} + \frac{e^{ik_1(z-a)}-Re^{ik_1(a-z)}}{2ik_1(1+R)/\rho_1}e^{ik(a-z')} & \texttt{if } (z' < a) \\ \frac{e^{ik_1|z'-z|}-e^{ik_1(z'-z)}}{2ik_1/\rho_1} & \texttt{if } (z' > a) \end{cases} . \quad (4.10)$$

The procedure above is shown in Figure 5 in the time domain.

Let us study the vanishing property of G_0^{DN} with the source location z below a reflector. If $z' > z$ (which automatically implies the solution in equation (4.10), since the source is located below the reflector: $z > a$), we have:

$$G_0^{DN}(z,z',\omega) = \frac{e^{ik_1|z'-z|} - e^{ik_1(z'-z)}}{2ik_1/\rho_1} = \frac{e^{ik_1(z'-z)} - e^{ik_1(z'-z)}}{2ik_1/\rho_1} \equiv 0 \quad (4.11)$$

According to equation (4.11), G_0^{DN} for $z > a$ also vanishes in the half-space below the source, which includes $z' = \mathcal{B}$, a behavior demonstrated by G_0^{DN} for $z < a$ as well.

Following the argument for G_0^{DN} for $z < a$, it is obvious that any variations of $c(z')$ below the source location z will not change the value of the Green's function with double vanishing boundary conditions. A very important consequence is that any heterogeneity below the prediction point (i.e., the source depth z) will not have any impact on G_0^{DN} and consequently will not affect the imaging result at z. It is worthwhile to remind the reader that this fact had already been in many publications − for example in "Finite Volume Model for Migration" from Weglein et al. (2011a).

In summary, combining equations (4.1) and (4.10), the frequency domain solution for G_0^{DN} with a single reflector located at depth a is:

$$G_0^{DN}(z,z',\omega) = \begin{cases} \frac{\rho_0}{2ik}\left(e^{ik|z-z'|} - e^{ik(z'-z)}\right) & \texttt{if } (z < a), \\ \frac{\rho_1}{2ik_1}\left(e^{ik_1|z'-z|} - e^{ik_1(z'-z)}\right) & \texttt{if } (a < z' \texttt{ and } a < z), \\ \frac{Re^{ik_1(z-a)}-e^{ik_1(a-z)}}{2ik_1(1+R)/\rho_1}e^{ik(z'-a)} + & \\ \frac{e^{ik_1(z-a)}-Re^{ik_1(a-z)}}{2ik_1(1+R)/\rho_1}e^{ik(a-z')} & \texttt{if } (z' < a \texttt{ and } a < z). \end{cases} \quad (4.12)$$

It can be transformed into the time domain via equation (1.1) to have:

$$G_0^{DN}(z,z',t) = \begin{cases} \frac{\rho_0 c_0}{2}\left(H\left[t+\frac{z-z'}{c_0}\right]-H\left[t-\frac{|z-z'|}{c_0}\right]\right) & \texttt{if } (z<a), \\ \frac{\rho_1 c_1}{2}\left(H\left[t+\frac{z-z'}{c_1}\right]-H\left[t-\frac{|z-z'|}{c_1}\right]\right) & \texttt{if } (a<z' \texttt{ and } a<z), \\ \frac{\rho_1 c_1}{2(1+R)}\left\{\begin{array}{r} H\left(t+\frac{z'-a}{c_0}+\frac{z-a}{c_1}\right) \\ -H\left(t-\frac{z'-a}{c_0}-\frac{z-a}{c_1}\right) \\ +RH\left(t+\frac{z'-a}{c_0}-\frac{z-a}{c_1}\right) \\ -RH\left(t-\frac{z'-a}{c_0}+\frac{z-a}{c_1}\right) \end{array}\right\} & \texttt{if } (z'<a \texttt{ and } a<z). \end{cases} \tag{4.13}$$

Another important property of G_0^{DN} for a model with a single reflector is that, from both equations (4.12) and (4.13), G_0^{DN} for $a<z$ and for $a<z'$ is the same even if the single reflector does not exist[††]. Note that in this case the additional heterogeneity (i.e., the single reflector) is outside the interval (z',z), and it is obvious that the geologic complexity beyond the (z',z) zone will not affect the value of G_0^{DN}.

The independence of G_0^{DN} from the heterogeneity outside the interval (z',z) agrees with the WKBJ Green's function. The WKBJ Green's function is derived as an approximate solution for a smoothed medium and is not a function of any heterogeneity outside (z',z).

In the procedure to construct G_0^{DN}, we start from the causal solution in equation (4.3). Here the last term is a reflection resulting from the up-going wave produced by the source. Note that this term is canceled after adding the homogeneous solution ϕ in equation (4.8). Consequently, their sum G_0^{DN} contains no reflection generated from the source.

It is well-known that reflections are omitted in both the WKBJ approximation and in many current seismic imaging procedures that prefer a smooth and reflectionless velocity model. In many current imaging algorithms, the velocity field is smoothed to minimize the reflections caused by the velocity, whereas in the logic for Green's function with double vanishing boundary conditions, the discontinuous model is kept intact. Nevertheless, both approaches yield the same reflectionless conclusion.

The procedure in this section to calculate G_0^{DN} for a simple single-reflector model is already very tedious. The major difficulty is to find a homogeneous solution ϕ that will cancel both the downward reflection originating from the source and the downward propagation of the source below the source location. For more complicated geological models, the procedure will be much more demanding.

Fortunately, a much simpler procedure, easily generalizable to more complicated models, can be derived from the fact that the values of G_0^{DN} are not affected by any heterogeneity outside the interval (z',z).

[††]This solution is the same as in equation (3.1) if (1) c_0 is replaced by c_1, and (2) the trivial density contribution at the source ρ_1 is added. And consequently this solution is equivalent with G_0^{DN} with a homogeneous velocity c_1 and constant density ρ_1 that contains no reflector.

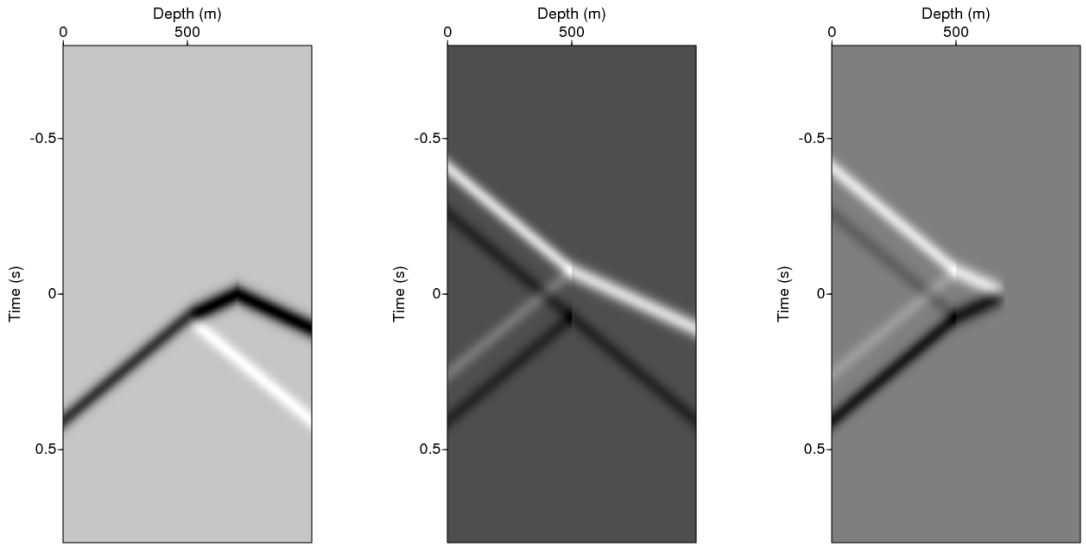

Figure 5: The construction of G_0^{DN} for a medium with one reflector (the velocities above and below the reflector are $1500m/s$ and $2700m/s$, respectively). The source depth is 700m and is below the single reflector at $500m$. The left panel is the causal solution G_0^+, and the middle panel shows the homogeneous solution that cancels with the left panel below the source. The right panel results from summing the two panels on its left and is the desired Green's function with double vanishing boundary conditions.

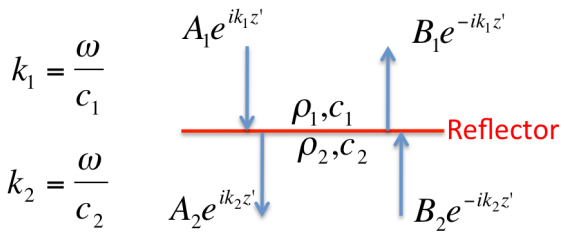

Figure 6: The diagram for upward continuation. A reflector is located at depth a, the medium properties above and below the reflector are (ρ_1, c_1) and (ρ_2, c_2), respectively. In this case we assume that the wave below the reflector $A_2 e^{ik_2 z'} + B_2 e^{-ik_2 z'}$ is known, the objective is to compute the wave above the reflector $A_1 e^{ik_1 z'} + B_1 e^{-ik_1 z'}$.

5 Upward continuation procedure: wave-theory approach

In the process of calculating G_0^{DN} with the source below many reflectors, we start from the wave field of the layer that contains the source. The wave field in this layer can be calculated through equation (4.1), and can be expressed as:

$$A_n e^{ik_n z'} + B_n e^{-ik_n z'},$$

where the source is assumed to be in the n^{th}-layer (with velocity c_n and density ρ_n, respectively), $k_n = \frac{\omega}{c_n}$, $A_n = -\frac{\rho_n}{2ik_n} e^{-iz}$, $B_n = \frac{\rho_n}{2ik_n} e^{iz}$. The objective is to find the wave field at the $(n-1)^{\text{th}}$ layer: $A_{n-1} e^{ik_{n-1} z'} + B_{n-1} e^{-ik_{n-1} z'}$, as shown in Figure 6. The theory is listed below. The continuity of the wave field and its derivatives requires:

$$\begin{aligned} A_1 e^{ik_1 a} + B_1 e^{-ik_1 a} &= A_2 e^{ik_2 a} + B_2 e^{-ik_2 a}, \\ \frac{ik_1}{\rho_1}\left(A_1 e^{ik_1 a} - B_1 e^{-ik_1 a}\right) &= \frac{ik_2}{\rho_2}\left(A_2 e^{ik_2 a} - B_2 e^{-ik_2 a}\right). \end{aligned} \tag{5.1}$$

If we define: $\gamma = \frac{\rho_1 k_2}{\rho_2 k_1} = \frac{\rho_1 c_1}{\rho_2 c_2}$, equation (5.1) can be written in matrix form:

$$\begin{pmatrix} e^{ik_1 a} & -e^{-ik_1 a} \\ e^{ik_1 a} & e^{-ik_1 a} \end{pmatrix} \begin{pmatrix} A_1 \\ B_1 \end{pmatrix} = \begin{pmatrix} \gamma & 0 \\ 0 & 1 \end{pmatrix} \begin{pmatrix} e^{ik_2 a} & -e^{-ik_2 a} \\ e^{ik_2 a} & e^{-ik_2 a} \end{pmatrix} \begin{pmatrix} A_2 \\ B_2 \end{pmatrix}, \tag{5.2}$$

with the solution:

$$\begin{aligned}\begin{pmatrix} A_1 \\ B_1 \end{pmatrix} &= \frac{1}{2}\begin{pmatrix} e^{-ik_1a} & e^{-ik_1a} \\ -e^{ik_1a} & e^{ik_1a} \end{pmatrix}\begin{pmatrix} \gamma & 0 \\ 0 & 1 \end{pmatrix}\begin{pmatrix} e^{ik_2a} & -e^{-ik_2a} \\ e^{ik_2a} & e^{-ik_2a} \end{pmatrix}\begin{pmatrix} A_2 \\ B_2 \end{pmatrix} \\ &= \frac{1}{2}\begin{pmatrix} \gamma e^{-ik_1a} & e^{-ik_1a} \\ -\gamma e^{ik_1a} & e^{ik_1a} \end{pmatrix}\begin{pmatrix} e^{ik_2a} & -e^{-ik_2a} \\ e^{ik_2a} & e^{-ik_2a} \end{pmatrix}\begin{pmatrix} A_2 \\ B_2 \end{pmatrix} \\ &= \frac{1}{2}\begin{pmatrix} (1+\gamma)e^{i(k_2-k_1)a} & (1-\gamma)e^{-i(k_1+k_2)a} \\ (1-\gamma)e^{i(k_1+k_2)a} & (1+\gamma)e^{i(k_1-k_2)a} \end{pmatrix}\begin{pmatrix} A_2 \\ B_2 \end{pmatrix}.\end{aligned} \tag{5.3}$$

Since $\frac{1+\gamma}{2} = \frac{1}{2} + \frac{\rho_1 c_1}{2\rho_2 c_2} = \frac{\rho_2 c_2 + \rho_1 c_1}{2\rho_2 c_2} = \frac{1}{1+R}$, and $\frac{1-\gamma}{2} = \frac{1}{2} - \frac{\rho_1 c_1}{2\rho_2 c_2} = \frac{\rho_2 c_2 - \rho_1 c_1}{2\rho_2 c_2} = \frac{R}{1+R}$, the above results can be rewritten as:

$$\begin{pmatrix} A_1 \\ B_1 \end{pmatrix} = \frac{1}{1+R}\begin{pmatrix} e^{i(k_2-k_1)a} & Re^{-i(k_1+k_2)a} \\ Re^{i(k_1+k_2)a} & e^{i(k_1-k_2)a} \end{pmatrix}\begin{pmatrix} A_2 \\ B_2 \end{pmatrix}. \tag{5.4}$$

For example, for G_0^{DN} with $z > a$, the wave field immediately below the single reflector is $\frac{\rho_1}{2ik_1}\left(-e^{ik_1(z'-z)} + e^{ik_1(z-z')}\right)$. If it is expressed in the form $A_2 e^{ik_1 z'} + B_2 e^{-ik_1 z'}$, we have $A_2 = -\frac{\rho_1 e^{-ik_1 z}}{2ik_1}$, $B_2 = \frac{\rho_1 e^{ik_1 z}}{2ik_1}$ and consequently we have:

$$\begin{aligned}\begin{pmatrix} A_1 \\ B_1 \end{pmatrix} &= \frac{1}{1+R}\begin{pmatrix} e^{i(k_1-k)a} & Re^{-i(k+k_1)a} \\ Re^{i(k+k_1)a} & e^{i(k-k_1)a} \end{pmatrix}\frac{\rho_1}{2ik_1}\begin{pmatrix} -e^{-ik_1 z} \\ e^{ik_1 z} \end{pmatrix} \\ &= \frac{\rho_1}{2ik_1}\frac{1}{1+R}\begin{pmatrix} \left\{Re^{ik_1(z-a)} - e^{ik_1(a-z)}\right\}e^{-ika} \\ \left\{e^{ik_1(z-a)} - Re^{ik_1(a-z)}\right\}e^{ika} \end{pmatrix}.\end{aligned} \tag{5.5}$$

From equation (5.5), we can easily produce the wave field above the reflector: $A_1 e^{ikz'} + B_1 e^{-ikz'} = \frac{\rho_1}{2ik_1}\frac{\left\{Re^{ik_1(z-a)} - e^{ik_1(a-z)}\right\}e^{ik(z'-a)} + \left\{e^{ik_1(z-a)} - Re^{ik_1(a-z)}\right\}e^{ik(a-z')}}{1+R}$.

Compared with the previous section, the example above is a much simpler derivation of G_0^{DN} with a single reflector above the source.

For example, for G_0^{DN} in a two-reflector model, the wave field immediately below the second reflector is $A_3 e^{ik_2 z'} + B_3 e^{-ik_2 z'} = \frac{\rho_2}{2ik_2}\left(-e^{ik_2(z'-z)} + e^{ik_2(z-z')}\right)$. It is obvious that in this case $A_3 = -\frac{\rho_2 e^{-ik_2 z}}{2ik_2}$, $B_2 = \frac{\rho_2 e^{ik_2 z}}{2ik_2}$ and consequently, we have:

$$\begin{pmatrix} A_2 \\ B_2 \end{pmatrix} = \frac{1}{1+R_2} \begin{pmatrix} e^{i(k_2-k_1)a_2} & R_2 e^{-i(k_1+k_2)a_2} \\ R_2 e^{i(k_1+k_2)a_2} & e^{i(k_1-k_2)a_2} \end{pmatrix} \frac{\rho_2}{2ik_2} \begin{pmatrix} -e^{-ik_2 z} \\ e^{ik_2 z} \end{pmatrix}$$
$$= \frac{\rho_2}{2ik_2} \frac{1}{1+R_2} \begin{pmatrix} \left\{R_2 e^{ik_2(z-a_2)} - e^{ik_2(a_2-z)}\right\} e^{-ik_1 a_2} \\ \left\{e^{ik_2(z-a_2)} - R_2 e^{ik_2(a_2-z)}\right\} e^{ik_1 a_2} \end{pmatrix}. \tag{5.6}$$

Renaming $R = R_1$, and $a = a_1$, the combination of equations (5.4) and (5.6) gives:

$$\begin{pmatrix} A_1 \\ B_1 \end{pmatrix} = \frac{1}{1+R_1} \begin{pmatrix} e^{i(k_1-k)a_1} & R_1 e^{-i(k+k_1)a_1} \\ R_1 e^{i(k+k_1)a_1} & e^{i(k-k_1)a_1} \end{pmatrix} \begin{pmatrix} A_2 \\ B_2 \end{pmatrix}$$
$$= \frac{\rho_2/(1+R_2)}{2ik_2(1+R_1)} \begin{pmatrix} e^{i(k_1-k)a_1} & R_1 e^{-i(k+k_1)a_1} \\ R_1 e^{i(k+k_1)a_1} & e^{i(k-k_1)a_1} \end{pmatrix} \begin{pmatrix} \left\{R_2 e^{ik_2(z-a_2)} - e^{ik_2(a_2-z)}\right\} e^{-ik_1 a_2} \\ \left\{e^{ik_2(z-a_2)} - R_2 e^{ik_2(a_2-z)}\right\} e^{ik_1 a_2} \end{pmatrix}$$
$$= \frac{\rho_2}{2ik_2(1+R_1)(1+R_2)} \times$$
$$\begin{pmatrix} \left[e^{ik_1(a_1-a_2)} \left\{R_2 e^{ik_2(z-a_2)} - e^{ik_2(a_2-z)}\right\} + e^{ik_1(a_2-a_1)} \left\{R_1 e^{ik_2(z-a_2)} - R_1 R_2 e^{ik_2(a_2-z)}\right\}\right] e^{-ika_1} \\ \left[e^{ik_1(a_1-a_2)} \left\{R_1 R_2 e^{ik_2(z-a_2)} - R_1 e^{ik_2(a_2-z)}\right\} + e^{ik_1(a_2-a_1)} \left\{e^{ik_2(z-a_2)} - R_2 e^{ik_2(a_2-z)}\right\}\right] e^{ika_1} \end{pmatrix}. \tag{5.7}$$

If we define: $\lambda \equiv e^{ik_2(z-a_2)}$, $\mu \equiv e^{ik(z'-a_1)}$ and $\nu \equiv e^{ik_1(a_2-a_1)}$, the Green's function can be expressed as:

$$\frac{\left[\nu^{-1}(R_2\lambda - \lambda^{-1}) + R_1\nu(\lambda - R_2\lambda^{-1})\right]\mu + \left[R_1\nu^{-1}(R_2\lambda - \lambda^{-1}) + \nu(\lambda - R_2\lambda^{-1})\right]\mu^{-1}}{2ik_2(1+R_1)(1+R_2)/\rho_2} \tag{5.8}$$

6 Upward continuation: finite-difference approach

In order to demonstrate the general philosophy of our method, we study wave propagation in an arbitrary acoustic medium $c(z)$ (with only velocity variation). It can be extended to a medium with density variation as well. First we have the equation for the causal Green's function with source located at depth z_s:

$$\left(\frac{\partial^2}{\partial z^2} - \frac{1}{c^2(z)}\frac{\partial^2}{\partial t^2}\right) G_0^+(z, z_s, t) = \delta(z - z_s)\delta(t). \tag{6.1}$$

We then consider a homogeneous equation (without the source) in the same velocity field $c(z)$:

$$\left(\frac{\partial^2}{\partial z^2} - \frac{1}{c^2(z)}\frac{\partial^2}{\partial t^2}\right)\phi(z,t) = 0. \tag{6.2}$$

Note that for a small positive number ε, and for $z > z_s + \varepsilon$, the source term of equation (6.1) vanishes: $\delta(z - z_s)\delta(t) = 0$. Consequently, equation (6.1) is a homogeneous wave equation for $z > z_s + \varepsilon$, i.e., identical to equation (6.2).

In the aforementioned source-free region, the difference scheme (with second-order accuracy in both space and time) is:

$$\frac{\phi_{m+1,n} + \phi_{m-1,n} - 2\phi_{m,n}}{(\Delta z)^2} - \frac{1}{c^2}\frac{\phi_{m,n+1} + \phi_{m,n-1} - 2\phi_{m,n}}{(\Delta t)^2} = 0, \tag{6.3}$$

where in the subscript, the variable m denotes the index for depth z, and the variable n denotes the index for time t: $\phi_{m,n} = \phi(m\Delta z, n\Delta t)$. If we define $p \overset{\Delta}{=} \frac{c\Delta t}{\Delta z}$, we have:

$$\phi_{m,n+1} = (2 - 2p^2)\phi_{m,n} - \phi_{m,n-1} + p^2(\phi_{m+1,n} + \phi_{m-1,n}), \tag{6.4}$$

for forward marching in time, and

$$\phi_{m-1,n} = (2 - 2p^{-2})\phi_{m,n} - \phi_{m+1,n} + p^{-2}(\phi_{m,n+1} + \phi_{m,n-1}), \tag{6.5}$$

for upward marching in depth. Since both difference schemes with second-order accuracy in equations (6.4) and (6.5) are of the same type, according to the analysis in Alford et al. (1974), equation (6.4) is stable for $\frac{c\Delta t}{\Delta z} \leq \sqrt{0.5}$, and equation (6.5) is stable for $\frac{c\Delta t}{\Delta z} \geq \sqrt{2}$.

Since the value of $G_0^{DN}(z, z')$ is completely determined by the medium in the interval (z', z), if the medium between z' and z is homogeneous, we can extend the local homogeneous medium to the entire space and we have a much simpler problem already solved in equation (14) of Weglein et al. (2011b). In equation (6.5), the initial values are listed on the right-hand side of the formula, with depth levels that have indices m and $m + 1$, respectively. The field values for the depth level with index $m - 1$ can be straightforwardly computed by using equation (6.5), and by using the values at depth indices $m - 1$ and m, the field at depth index $m - 2$ can be likewise calculated. That procedure is very similar to the scheme popularly implemented in finite-difference forward-modeling algorithms that march forward in time.

The two levels of initial field values are from equation (14) of Weglein et al. (2011b), which satisfies the double vanishing Green's function at the lower boundary. These initial field values will not be changed by the scheme in equation (6.5); all the complexity to match the boundary conditions at the current level is carried on to the next depth level with index $m - 1$. It guarantees that both Dirichlet and Neumann boundary conditions at $z' = \mathcal{B}$ are satisfied.

Note that in equation (6.5), the velocity field c is a function of depth and can be arbitrary, enabling the flexibility of the scheme for a medium with any spatially varying velocities.

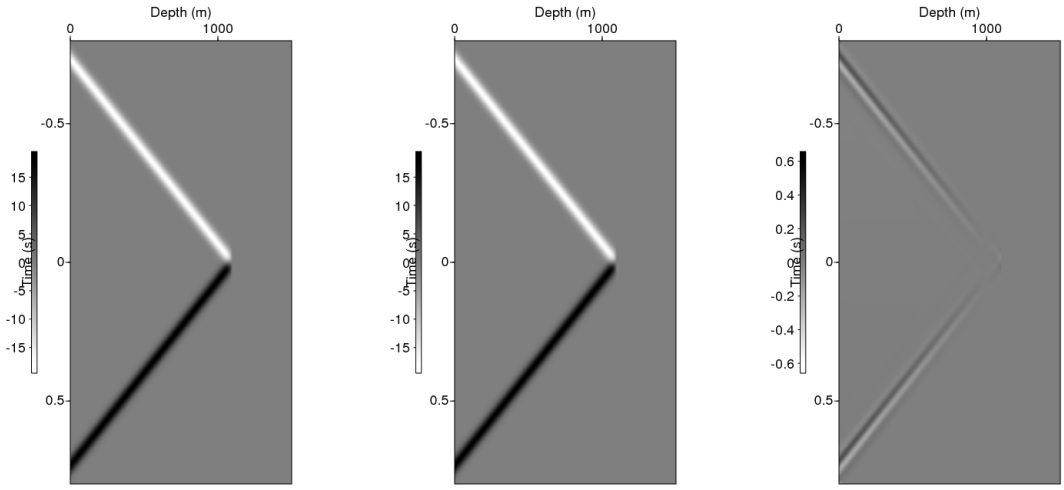

Figure 7: $G_0^{DN}(z = 1100m, z', t)$ for a homogeneous medium with velocity $1500m/s$. The left panel is generated through the finite-difference scheme from equation (6.5). The middle panel is computed from the analytic method and is presented in equation (4.1). The difference between the left and middle panels is shown in the right panel.

7 G_0^{DN} for a model with two reflectors

The G_0^{DN} in this case is for the medium listed in Table 2. The final result is:

$$G_0^{DN}(z,z',\omega) = \begin{cases} \frac{\rho_0}{2ik}\left(e^{ik|z-z'|} - e^{ik(z'-z)}\right) & \texttt{if } (z < a_1) \\ \frac{\rho_1}{2ik_1}\left(e^{ik_1|z'-z|} - e^{ik_1(z'-z)}\right) & \texttt{if } (z' > a_1 \texttt{ and } a_1 < z < a_2) \\ \frac{R_1 e^{ik_1(z-a_1)} - e^{ik_1(a_1-z)}}{2ik_1(1+R_1)/\rho_1} e^{ik_1(z'-a_1)} + & \\ \frac{e^{ik_1(z-a_1)} - R_1 e^{ik_1(a_1-z)}}{2ik_1(1+R_1)/\rho_1} e^{ik_1(a_1-z')} & \texttt{if } (z' < a_1 \texttt{ and } a_1 < z < a_2), \\ \frac{\rho_2}{2ik_2}\left(e^{ik_2|z-z'|} - e^{ik_2(z'-z)}\right) & \texttt{if } (a_2 < z' \texttt{ and } a_2 < z), \\ \frac{R_2 e^{ik_2(z-a_2)} - e^{ik_2(a_2-z)}}{2ik_1(1+R_2)/\rho_2} e^{ik_1(z'-a_2)} + & \\ \frac{e^{ik_2(z-a_2)} - R_2 e^{ik_2(a_2-z)}}{2ik_1(1+R_2)/\rho_2} e^{ik_1(a_2-z')} & \texttt{if } (a_1 < z' < a_2 \texttt{ and } a_2 < z), \\ \frac{\rho_2}{2i(1+R_1)(1+R_2)} \left\{ \begin{array}{r} \nu^{-1}(R_2\lambda - \lambda^{-1})\mu \\ +R_1\nu(\lambda - R_2\lambda^{-1})\mu \\ +R_1\nu^{-1}(R_2\lambda - \lambda^{-1})\mu^{-1} \\ +\nu(\lambda - R_2\lambda^{-1})\mu^{-1} \end{array} \right\} & \texttt{if } (a_2 < z \texttt{ and } z' < a_1). \end{cases} \tag{7.1}$$

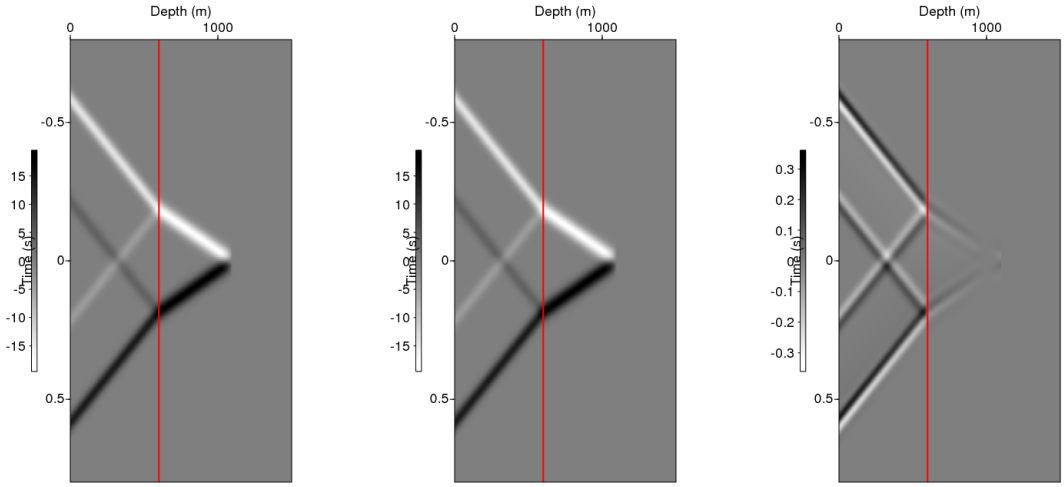

Figure 8: $G_0^{DN}(z = 1100m, z', t)$ for a medium with a reflector at a depth of $600m$. The velocities above and below the reflector are $1500m/s$ and $2700m/s$, respectively. The left panel is generated through the finite-difference scheme from equation (6.5). The middle panel is computed from the analytic method and is presented in equation (4.10). The difference between the left and middle panels is shown in the right panel.

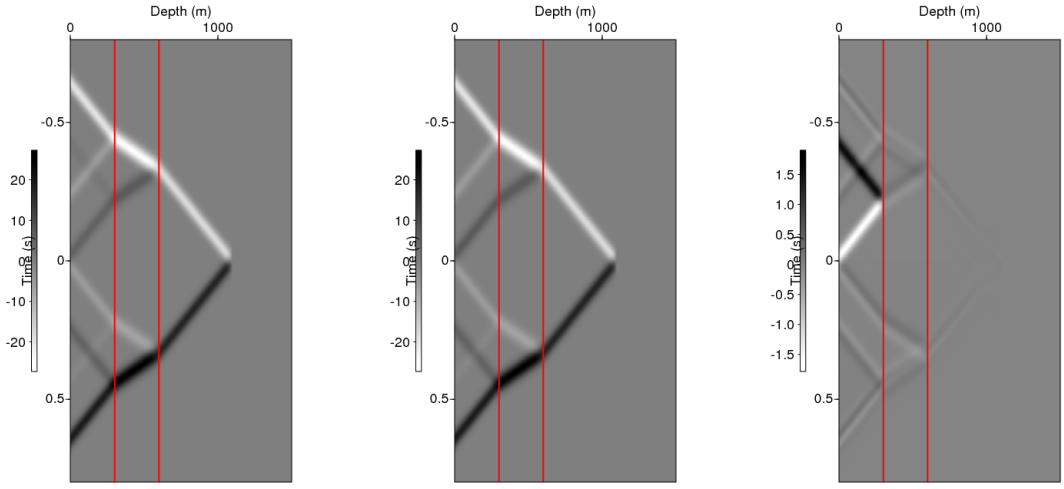

Figure 9: $G_0^{DN}(z = 1100m, z', t)$ for a medium with two reflectors, located at depths of $300m$ and $600m$, respectively. The medium velocities are (from top to bottom) $1500m/s$, $2700m/s$, and $1500m/s$. The left panel is generated through the finite-difference scheme from equation (6.5). The middle panel is computed from the analytic method and is presented in equation (7.1). The difference between the left and middle panels is shown in the right panel.

In the equation above: $\lambda \equiv e^{ik_2(z-a_2)}$, $\mu \equiv e^{ik(z'-a_1)}$, and $\nu \equiv e^{ik_1(a_2-a_1)}$. The details of the above result are listed below:

- Case 1, the source is above the first reflector (i.e., $z < a_1$): the solution in this case is essentially for a whole-space homogeneous medium with velocity c_0 and density ρ_0. The Green's function in this case is the simplest (identical to that for equation (4.1)) and has only two events.
- Case 2, the source is between the first and second reflectors and the receiver is below the first reflector (i.e., $a_1 < z < a_2$ and $a_1 < z'$): the solution in this case is exactly the same as that for a simpler medium that lacks the shallower reflector. It is obtained from equation (4.1), with (c_0, ρ_0) being replaced by (c_1, ρ_1), or the second case of equation (4.10). The G_0^{DN} in this case has two events.
- Case 3, the source is between the first and second reflectors and the receiver is above the first reflector (i.e., $a_1 < z < a_2$ and $z'a_1$. It is the first case of equation (4.10). The G_0^{DN} in this case has four events).
- Case 4, the source and receiver are both below the second reflector (i.e., $a_2 < z$ and $a_2 < z'$): the solution in this case is exactly the same as that for a simpler medium that lacks the shallower reflectors. It is obtained from equation (4.1), with (c_0, ρ_0) being replaced by (c_2, ρ_2).
- Case 5, the source is below the second reflector and the receiver is between the first and second reflectors (i.e., $a_2 < z$ and $a_1 < z' < a_2$). It is obtained from equation (4.10) with (c_1, ρ_1) being replaced by (c_2, ρ_2) and with (c_0, ρ_0) being replaced by (c_1, ρ_1). There are four events in this situation.
- Case 6, the source is below the second reflector and the receiver is above the first reflector (i.e., $a_2 < z$ and $z' < a_1$): this is the most complicated situation and contains eight events. It is calculated by using equation (5.7).

8 Wave-field prediction with the RTM Green's function

In this section, we demonstrate the behavior of the Green's function that satisfies both Dirichlet and Neumann boundary conditions at the deeper boundary. The study consists of three geological models with progressive complexity.

8.1 Example I: homogeneous case

This example had already been documented in Appendix A of Weglein et al. (2011b) for an acoustic medium without density variation; it is given here to make a smooth transition into more complicated examples and to demonstrate the impact of density in the algorithms. With $k = \omega/c_0$, the general solution of a wave propagating in the whole space homogeneous medium with velocity c_0 is:

$$P(z',\omega) = \alpha e^{ikz'} + \beta e^{-ikz'}, \tag{8.1}$$

where α and β can be any value. At the measurement surface $z' = \mathcal{A}$, we will detect the wave field and its partial derivative over z' as follows:

$$\begin{aligned} P(z')\big|_{z'=\mathcal{A}} &= \alpha e^{ik\mathcal{A}} + \beta e^{-ik\mathcal{A}}, \\ \left.\frac{\partial P(z',\omega)}{\partial z'}\right|_{z'=\mathcal{A}} &= ik\left(\alpha e^{ik\mathcal{A}} - \beta e^{-ik\mathcal{A}}\right). \end{aligned} \tag{8.2}$$

From equation (4.1), the values of the Green's function needed on the boundary $z' = \mathcal{A}$ are:

$$\begin{aligned} G_0^{DN}(z,z',\omega)\big|_{z'=\mathcal{A}} &= \frac{\rho(z)}{2ik}\left[e^{ik|z-z'|} - e^{ik(z'-z)}\right]_{z'=\mathcal{A}} = \frac{\rho_0}{2ik}\left[e^{ik|z-\mathcal{A}|} - e^{ik(\mathcal{A}-z)}\right], \\ \left.\frac{\partial}{\partial z'}G_0^{DN}(z,z',\omega)\right|_{z'=\mathcal{A}} &= \frac{\rho(z)}{2}\left[\mathtt{sgn}(z'-z)e^{ik|z-z'|} - e^{ik(z'-z)}\right]_{z'=\mathcal{A}} \\ &= \frac{\rho_0}{2}\left[\mathtt{sgn}(\mathcal{A}-z)e^{ik|z-\mathcal{A}|} - e^{ik(\mathcal{A}-z)}\right]. \end{aligned} \tag{8.3}$$

Using the boundary values of the wave field P and Green's operator G_0^{DN} at the boundary $z' = \mathcal{A}$ (in equations (8.2) and (8.3)), we can predict the wave field as follows,

$$\begin{aligned} P(z,\omega) =& \frac{1}{\rho(z')}\left[P(z',\omega)\frac{\partial G_0^{DN}(z,z',\omega)}{\partial z'} - G_0^{DN}(z,z',\omega)\frac{\partial P(z',\omega)}{\partial z'}\right]_{z'=\mathcal{A}}^{z'=\mathcal{B}} \\ =& -\frac{1}{\rho_0}\left[P(z',\omega)\frac{\partial G_0^{DN}(z,z',\omega)}{\partial z'} - G_0^{DN}(z,z',\omega)\frac{\partial P(z',\omega)}{\partial z'}\right]_{z'=\mathcal{A}} \\ =& -\frac{\alpha e^{ik\mathcal{A}} + \beta e^{-ik\mathcal{A}}}{2}\left[\mathtt{sgn}(\mathcal{A}-z)e^{ik|z-\mathcal{A}|} - e^{ik(\mathcal{A}-z)}\right] \\ &+\frac{\alpha e^{ik\mathcal{A}} - \beta e^{-ik\mathcal{A}}}{2}\left[e^{ik|z-\mathcal{A}|} - e^{ik(\mathcal{A}-z)}\right]. \end{aligned} \tag{8.4}$$

For the purpose of predicting the wave field below the measurement surface $z' = \mathcal{A}$, we obviously have the situation $z > \mathcal{A}$. Consequently, the equation above can be simplified as,

$$\begin{aligned} P(z,\omega) =& \frac{\alpha e^{ik\mathcal{A}} + \beta e^{-ik\mathcal{A}}}{2}\left[e^{ik(z-\mathcal{A})} + e^{ik(\mathcal{A}-z)}\right] + \frac{\alpha e^{ik\mathcal{A}} - \beta e^{-ik\mathcal{A}}}{2}\left[e^{ik(z-\mathcal{A})} - e^{ik(\mathcal{A}-z)}\right] \\ =& \alpha e^{ik\mathcal{A}}e^{ik(z-\mathcal{A})} + \beta e^{-ik\mathcal{A}}e^{ik(\mathcal{A}-z)} \\ =& \alpha e^{ikz} + \beta e^{-ikz}. \end{aligned} \tag{8.5}$$

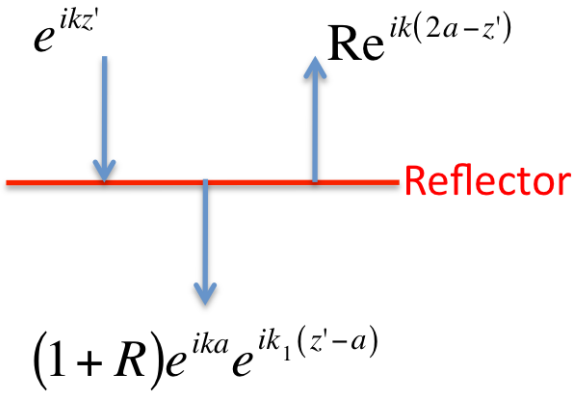

Figure 10: The incident, reflection, and transmission waves in example II. Here $k = \omega/c_0$, $k_1 = \omega/c_1$, and a is the depth of the single reflector. $R = (\rho_1 c_1 - \rho_0 c_0)/(\rho_1 c_1 + \rho_0 c_0)$ is the reflection coefficient for a down-going incident plane wave. $e^{ikz'}$ is the incident wave. $Re^{ik(2a-z')}$ is the reflection data. $(1+R)e^{ika}e^{ik_1(z'-a)}$ is the transmission wave.

The above expression is exactly the actual wave field that we assumed in equation (8.1). In other words, the original wave field, with both up-going and down-going waves, is perfectly reconstructed at an arbitrary depth.

It would sound irrational that we can also perfectly predict the wave field if there are reflectors below z. However, according to d'Alembert's formula for a 1D wave equation for any interval, the introduction of additional reflectors into the homogeneous reference medium below z will not alter the possible type of waves between a and z, which remains homogeneous: $\alpha e^{ikz} + \beta e^{-ikz}$, where α and β are arbitrary numbers. The examples of using this Green's function derived from homogeneous media for nonhomogeneous velocity models can be found in Examples II and III.

8.2 Example II: a single reflector

With the models listed in Table 1, an incident plane wave $e^{ikz'}$ will produce various waves, as shown in Figure 10. Obviously the wave at the measurement surface is:

$$\begin{aligned} P(z' = \mathcal{A}, \omega) &= e^{ik\mathcal{A}} + Re^{ik(2a-\mathcal{A})}, \\ \left.\frac{P(z' = \mathcal{A}, \omega)}{\partial z'}\right|_{z'=\mathcal{A}} &= ik\left(e^{ik\mathcal{A}} - Re^{ik(2a-\mathcal{A})}\right). \end{aligned} \tag{8.6}$$

First let us consider the simpler situation, predicting the wave field above the reflector: $P(z, \omega)$ where $z < a$. The Green's function can be found in equation (4.1). Note that in this case, we use a reflectionless Green's function to downward continue a reflection.

$$
\begin{aligned}
G_0^{DN}(z,z',\omega)\big|_{z'=\mathcal{A}} &= \frac{\rho(z)}{2ik}\left[e^{ik|z-z'|}-e^{ik(z'-z)}\right]_{z'=\mathcal{A}} = \frac{\rho_0}{2ik}\left[e^{ik(z-\mathcal{A})}-e^{ik(\mathcal{A}-z)}\right], \\
\frac{\partial}{\partial z'}G_0^{DN}(z,z',\omega)\Big|_{z'=\mathcal{A}} &= \frac{\rho_0}{2}\left[-e^{ik(z-\mathcal{A})}-e^{ik(\mathcal{A}-z)}\right].
\end{aligned}
\tag{8.7}
$$

In the equation above, we take advantage of the fact that $\mathtt{sgn}(\mathcal{A}-z)=-1$. With the boundary values from equations (8.6) and (8.7), we can predict the wave field at arbitrary location z using equation (2.5):

$$
\begin{aligned}
P(z,\omega) =& \frac{e^{ik\mathcal{A}}+Re^{ik(2a-\mathcal{A})}}{2}\left[e^{ik(z-\mathcal{A})}+e^{ik(\mathcal{A}-z)}\right]+\frac{e^{ik\mathcal{A}}-Re^{ik(2a-\mathcal{A})}}{2}\left[e^{ik(z-\mathcal{A})}-e^{ik(\mathcal{A}-z)}\right] \\
=& e^{ik\mathcal{A}}e^{ik(z-\mathcal{A})}+Re^{ik(2a-\mathcal{A})}e^{ik(\mathcal{A}-z)} \\
=& e^{ikz}+Re^{ik(2a-z)}.
\end{aligned}
\tag{8.8}
$$

Next let us predict the wave field below the reflector: $P(z,\omega)$, where $z>a$. The value of Green's function at the measurement surface, needed in equation (2.5), can be found in equation (4.10) and is given as:

$$
\begin{aligned}
G_0^{DN}(z,z',\omega)\big|_{z'=\mathcal{A}} &= \frac{\rho_1}{2ik_1}\left\{\frac{R\lambda-\lambda^{-1}}{1+R}\mu+\frac{\lambda-R\lambda^{-1}}{1+R}\mu^{-1}\right\}, \\
\frac{\partial}{\partial z'}G_0^{DN}(z,z',\omega)\Big|_{z'=\mathcal{A}} &= \frac{\rho_1 k}{2k_1}\left\{\frac{R\lambda-\lambda^{-1}}{1+R}\mu-\frac{\lambda-R\lambda^{-1}}{1+R}\mu^{-1}\right\},
\end{aligned}
\tag{8.9}
$$

where $\lambda\equiv e^{ik_1(z-a)}$ and $\mu\equiv e^{ik(\mathcal{A}-a)}$. With all the terms in equations (8.6) and (8.9), we can predict the wave field below the reflector using equation (2.5):

Depth Range	Velocity	Density
$(-\infty, a_1)$	c_0	ρ_0
(a_1, a_2)	c_1	ρ_1
(a_2, ∞)	c_1	ρ_1

Table 2: The properties of an acoustic medium with two reflectors, at depth a_1 and a_2.

$$
\begin{aligned}
P(z,\omega) &= \frac{1}{\rho(z')}\left\{P(z',\omega)\frac{\partial G_0^{DN}(z,z',\omega)}{\partial z'} - G_0^{DN}(z,z',\omega)\frac{\partial P(z',\omega)}{\partial z'}\right\}\Bigg|_{z'=\mathcal{A}}^{z'=\mathcal{B}} \\
&= \frac{1}{\rho(z')}\left[G_0^{DN}(z,z',\omega)\frac{\partial P(z',\omega)}{\partial z'} - P(z',\omega)\frac{\partial G_0^{DN}(z,z',\omega)}{\partial z'}\right]_{z'=\mathcal{A}} \\
&= \frac{\rho_1 k}{\rho_0 k_1}\left\{\frac{\lambda - R\lambda^{-1}}{1+R}\mu^{-1}e^{ik\mathcal{A}} - \frac{R\lambda - \lambda^{-1}}{1+R}\mu R e^{ik(2a-\mathcal{A})}\right\} \\
&= \frac{\rho_1 k}{\rho_0 k_1}e^{ika}\left\{\frac{\lambda - R\lambda^{-1}}{1+R} - \frac{R^2\lambda - R\lambda^{-1}}{1+R}\right\} \\
&= \frac{\rho_1 c_1}{\rho_0 c_0(1+R)}e^{ika}\left\{\left[1-R^2\right]\lambda + \left[R-R\right]\lambda^{-1}\right\} \\
&= \frac{\rho_1 c_1}{\rho_0 c_0}(1-R)\lambda e^{ika} = \frac{\rho_1 c_1}{\rho_0 c_0}\frac{2\rho_0 c_0}{\rho_1 c_1 + \rho_0 c_0}\lambda e^{ika} = \frac{2\rho_1 c_1}{\rho_1 c_1 + \rho_0 c_0}\lambda e^{ika} \\
&= (R+1)\lambda e^{ika} = (1+R)e^{ika}e^{ik_1(z-a)}.
\end{aligned}
\tag{8.10}
$$

In the derivation above, we take advantage of the fact that $\mu \cdot e^{ik(2a-\mathcal{A})} = \mu^{-1}e^{ik\mathcal{A}} = e^{ika}$. The final result above is exactly the transmission wave in the second medium illustrated in Figure 10. Note that the down-going incident wave and the up-going reflection data act together to produce the down-going transmission data in the second medium, with correct amplitude and phase.

In the G_0^{DN} expression in equation (8.9), the λ terms are for the down-going wave, and the λ^{-1} terms are for the up-going wave. In other words, both down-going and up-going energy is present in the formalism. However, the action of the data cancels the up-going terms (i.e., the terms containing λ^{-1}) in the second medium, as it should.

8.3 Example III: a model with two reflectors: reconstruction of internal multiples in the subsurface

As was chosen in Example II, the incident wave here is $e^{ikz'}$, and the reflection data contain two primaries, corresponding to each reflector, and an infinite number of internal multiples. The measurement at $z' = \mathcal{A}$ is:

$$
\begin{aligned}
P(z'=\mathcal{A},\omega) &= e^{ik\mathcal{A}} + R_1 e^{ik(2a_1-\mathcal{A})} \\
&\quad + \left(1-R_1^2\right) e^{ik(2a_1-\mathcal{A})} \sum_{n=0}^{\infty} (-1)^n R_1^n R_2^{n+1} e^{ik_1(2n+2)[a_2-a_1]}, \\
\frac{1}{ik}\left.\frac{P(z'=\mathcal{A},\omega)}{\partial z'}\right|_{z'=\mathcal{A}} &= e^{ik\mathcal{A}} - R_1 e^{ik(2a_1-\mathcal{A})} \\
&\quad - \left(1-R_1^2\right) e^{ik(2a_1-\mathcal{A})} \sum_{n=0}^{\infty} (-1)^n R_1^n R_2^{n+1} e^{ik_1(2n+2)[a_2-a_1]},
\end{aligned}
\tag{8.11}
$$

where $R_1 = \frac{\rho_1 c_1 - \rho_0 c_0}{\rho_1 c_1 + \rho_0 c_0}$ and $R_2 = \frac{\rho_2 c_2 - \rho_1 c_1}{\rho_2 c_2 + \rho_1 c_1}$ are the reflection coefficients for the first and second reflectors, respectively. Since $1+R_1$ and $1-R_1$ are the transmission coefficients for a down-going and an up-going wave through the first reflector, respectively, $1-R_1^2 = (1+R_1)(1-R_1)$ is the total transmission loss for seismic energy passing through the first reflector. To predict the wave field in the second medium (i.e., $a_1 < z' < a_2$), the Green's function can be found in equation (4.12) and is:

$$
\begin{aligned}
G_0^{DN}(z,z',\omega)\big|_{z'=\mathcal{A}} &= \frac{\rho_1}{2ik_1}\left\{\frac{R_1\lambda-\lambda^{-1}}{1+R_1}\mu + \frac{\lambda-R_1\lambda^{-1}}{1+R_1}\mu^{-1}\right\}, \\
\left.\frac{\partial}{\partial z'}G_0^{DN}(z,z',\omega)\right|_{z'=\mathcal{A}} &= \frac{\rho_1 k}{2k_1}\left\{\frac{R_1\lambda-\lambda^{-1}}{1+R_1}\mu - \frac{\lambda-R_1\lambda^{-1}}{1+R_1}\mu^{-1}\right\},
\end{aligned}
\tag{8.12}
$$

where in the equation above $\lambda \equiv e^{ik_1(z-a_1)}$ and $\mu \equiv e^{ik(\mathcal{A}-a_1)}$. With all the terms in equations (8.11) and (9.34), we can predict the wave field below the reflector using equation (2.5):

$$
\begin{aligned}
P(z,\omega) &= \frac{1}{\rho(z')}\left\{P(z',\omega)\frac{\partial G_0^{DN}(z,z',\omega)}{\partial z'} - G_0^{DN}(z,z',\omega)\frac{\partial P(z',\omega)}{\partial z'}\right\}\Bigg|_{z'=\mathcal{A}}^{z'=\mathcal{B}} \\
&= \frac{1}{\rho(z')}\left[G_0^{DN}(z,z',\omega)\frac{\partial P(z',\omega)}{\partial z'} - P(z',\omega)\frac{\partial G_0^{DN}(z,z',\omega)}{\partial z'}\right]_{z'=\mathcal{A}} \\
&= \frac{\rho_1 k}{\rho_0 k_1}\left\{\frac{\lambda - R_1\lambda^{-1}}{1+R_1}\mu^{-1}e^{ik\mathcal{A}} - \frac{R_1\lambda - \lambda^{-1}}{1+R_1}\mu R_1 e^{ik(2a_1-\mathcal{A})}\right\} \\
&- \frac{\rho_1 k}{\rho_0 k_1}\left\{\frac{R_1\lambda - \lambda^{-1}}{1+R_1}\mu\left(1-R_1^2\right)e^{ik(2a_1-\mathcal{A})}\sum_{n=0}^{\infty}(-1)^n R_1^n R_2^{n+1}e^{ik_1(2n+2)[a_2-a_1]}\right\} \\
&= \frac{\rho_1 k}{\rho_0 k_1}e^{ika_1}\left\{\frac{\lambda - R_1\lambda^{-1}}{1+R_1} - \frac{R_1^2\lambda - R_1\lambda^{-1}}{1+R_1}\right\} \\
&- e^{ika_1}\frac{\rho_1 k}{\rho_0 k_1}\left(1-R_1\right)\left\{R_1\lambda - \lambda^{-1}\right\}\sum_{n=0}^{\infty}(-1)^n R_1^n R_2^{n+1}e^{ik_1(2n+2)[a_2-a_1]} \\
&= \frac{\rho_1 c_1}{\rho_0 c_0(1+R_1)}e^{ika_1}\left\{\left[1-R_1^2\right]\lambda + \left[R_1 - R_1\right]\lambda^{-1}\right\} \\
&+ e^{ika_1}\frac{\rho_1 k}{\rho_0 k_1}\left(1-R_1\right)\left\{e^{ik_1(a_1-z)} - R_1 e^{ik_1(z-a_1)}\right\}\sum_{n=0}^{\infty}(-1)^n R_1^n R_2^{n+1}e^{ik_1(2n+2)[a_2-a_1]}. \\
&= \frac{\rho_1 c_1}{\rho_0 c_0}\left(1-R_1\right)\lambda e^{ika_1} \\
&+ e^{ika_1}\frac{\rho_1 k}{\rho_0 k_1}\left(1-R_1\right)\left\{e^{ik_1(a_1-z)} - R_1 e^{ik_1(z-a_1)}\right\}\sum_{n=0}^{\infty}(-1)^n R_1^n R_2^{n+1}e^{ik_1(2n+2)[a_2-a_1]}. \\
&= (1+R_1)e^{ika_1}e^{ik_1(z-a_1)} \\
&+ e^{ika_1}\frac{\rho_1 k}{\rho_0 k_1}\left(1-R_1\right)\left\{e^{ik_1(a_1-z)} - R_1 e^{ik_1(z-a_1)}\right\}\sum_{n=0}^{\infty}(-1)^n R_1^n R_2^{n+1}e^{ik_1(2n+2)[a_2-a_1]}.
\end{aligned}
\tag{8.13}
$$

In the derivation above we take advantage of the fact that $\mu e^{ik(2a_1-A)} = e^{ika_1}$. Also, many simplifications are detailed in the process of deriving equation (8.10). Since $\frac{\rho_1 k}{\rho_0 k_1}\left(1-R_1\right) = \frac{\rho_1 c_1}{\rho_0 c_0}\frac{2\rho_0 c_0}{\rho_1 c_1+\rho_0 c_0} = \frac{2\rho_1 c_1}{\rho_1 c_1+\rho_0 c_0} = 1+R_1$, the expression above can be simplified as:

$$
\begin{aligned}
P(z,\omega) &= (1+R_1)e^{ika_1}e^{ik_1(z-a_1)} \\
&+ e^{ika_1}(1+R_1)\sum_{n=0}^{\infty}(-1)^n R_1^n R_2^{n+1}e^{ik_1[(2n+2)a_2-(2n+1)a_1-z]} \\
&+ e^{ika_1}(1+R_1)\sum_{n=0}^{\infty}(-1)^{n+1} R_1^{n+1} R_2^{n+1}e^{ik_1[z+(2n+2)a_2-(2n+3)a_1]}.
\end{aligned}
\tag{8.14}
$$

It is very interesting to look each term of the expression above.

- $(1+R_1)e^{ika_1}e^{ik_1(z-a_1)}$ is the down-going wave straight from the source.
- For the simplest case, $n=0$, the results are:

$$e^{ika_1}(1+R_1)R_2e^{ik_1(2a_2-a_1-z)} - e^{ika_1}(1+R_1)R_1R_2e^{ik_1(z+2a_2-3a_1)},$$

  where the first term is the up-going primary reflected from the second reflector, and the second term is the down-going leg of the first-order internal multiple.

- For the case $n=1$, we have:

$$-e^{ika_1}(1+R_1)R_1R_2^2e^{ik_1(4a_2-3a_1-z)} + e^{ika_1}(1+R_1)R_1^2R_2^2e^{ik_1(z+4a_2-5a_1)},$$

  where the first term is the up-going leg of the first-order internal multiple, and the second term is the down-going leg of the second-order internal multiple.

The details to predict the wave field below the second reflector are as follows:

$$\begin{aligned}
G_0^{DN}(z,z',\omega)\big|_{z'=\mathcal{A}} &= \frac{\left[\nu^{-1}(R_2\lambda-\lambda^{-1})+R_1\nu(\lambda-R_2\lambda^{-1})\right]\mu+\left[R_1\nu^{-1}(R_2\lambda-\lambda^{-1})+\nu(\lambda-R_2\lambda^{-1})\right]\mu^{-1}}{2ik_2(1+R_1)(1+R_2)/\rho_2},\\
\frac{\partial}{\partial z'}G_0^{DN}(z,z',\omega)\bigg|_{z'=\mathcal{A}} &= \frac{\left[\nu^{-1}(R_2\lambda-\lambda^{-1})+R_1\nu(\lambda-R_2\lambda^{-1})\right]\mu-\left[R_1\nu^{-1}(R_2\lambda-\lambda^{-1})+\nu(\lambda-R_2\lambda^{-1})\right]\mu^{-1}}{2k_2(1+R_1)(1+R_2)/(k\rho_2)},
\end{aligned} \tag{8.15}$$

where $\lambda \equiv e^{ik_2(z-a_2)}$, $\mu \equiv e^{ik(\mathcal{A}-a_1)}$, and $\nu \equiv e^{ik_1(a_2-a_1)}$. The wave field from Example III (i.e., equation (8.11)) can be rewritten as:

$$\begin{aligned}
P(z'=\mathcal{A},\omega) &= e^{ik\mathcal{A}} + R_1e^{ik(2a_1-\mathcal{A})}\\
&\quad + \left(1-R_1^2\right)e^{ik(2a_1-\mathcal{A})}\sum_{n=0}^{\infty}(-1)^nR_1^nR_2^{n+1}\nu^{2n+2},\\
\frac{1}{ik}\,\frac{P(z'=\mathcal{A},\omega)}{\partial z'}\bigg|_{z'=\mathcal{A}} &= e^{ik\mathcal{A}} - R_1e^{ik(2a_1-\mathcal{A})}\\
&\quad - \left(1-R_1^2\right)e^{ik(2a_1-\mathcal{A})}\sum_{n=0}^{\infty}(-1)^nR_1^nR_2^{n+1}\nu^{2n+2}.
\end{aligned} \tag{8.16}$$

After obtaining the values of the Green's function and wave field at the shallower boundary, we can use the Green's theorem of equation (2.5), with input from equations (8.15) and (8.16), to predict the wave field below the second reflector:

$$
\begin{aligned}
P(z,\omega) &= \frac{1}{\rho(z')}\left\{P(z',\omega)\frac{\partial G_0^{DN}(z,z',\omega)}{\partial z'} - G_0^{DN}(z,z',\omega)\frac{\partial P(z',\omega)}{\partial z'}\right\}\Bigg|_{z'=\mathcal{A}}^{z'=\mathcal{B}} \\
&= \frac{1}{\rho(z')}\left[G_0^{DN}(z,z',\omega)\frac{\partial P(z',\omega)}{\partial z'} - P(z',\omega)\frac{\partial G_0^{DN}(z,z',\omega)}{\partial z'}\right]_{z'=\mathcal{A}} \\
&= \frac{\rho_2 k}{\rho_0 k_2}e^{ika_1}\frac{R_1\nu^{-1}(R_2\lambda-\lambda^{-1})+\nu(\lambda-R_2\lambda^{-1})}{(1+R_1)(1+R_2)} \\
&- \frac{\rho_2 k}{\rho_0 k_2}e^{ika_1}R_1\frac{\nu^{-1}(R_2\lambda-\lambda^{-1})+R_1\nu(\lambda-R_2\lambda^{-1})}{(1+R_1)(1+R_2)} \\
&- \frac{\rho_2 k}{\rho_0 k_2}e^{ika_1}(1-R_1^2)\sum_{n=0}^{\infty}(-1)^n R_1^n R_2^{n+1}\nu^{2n+2}\frac{\nu^{-1}(R_2\lambda-\lambda^{-1})+R_1\nu(\lambda-R_2\lambda^{-1})}{(1+R_1)(1+R_2)}.
\end{aligned}
\tag{8.17}
$$

Since $\frac{\rho_2 k}{\rho_0 k_2} = \frac{\rho_2 c_2}{\rho_0 c_0} = \frac{\rho_1 c_1}{\rho_0 c_0}\frac{\rho_2 c_2}{\rho_1 c_1} = \frac{1+R_1}{1-R_1}\frac{1+R_2}{1-R_2}$, the equation above can be simplified as:

$$
P(z,\omega) = \frac{e^{ika_1}}{(1-R_1)(1-R_2)}\begin{pmatrix}
\left[R_1R_2\nu^{-1}+\nu\right]\lambda & - & \left[R_1\nu^{-1}+R_2\nu\right]\lambda^{-1} \\
-\left[R_1R_2\nu^{-1}+R_1^2\nu\right]\lambda & + & \left[R_1\nu^{-1}+R_1^2R_2\nu\right]\lambda^{-1} \\
-(1-R_1^2)\lambda\displaystyle\sum_{n=0}^{\infty}(-1)^n\left[R_1^nR_2^{n+2}\nu^{2n+1}+R_1^{n+1}R_2^{n+1}\nu^{2n+3}\right] & & \\
+(1-R_1^2)\lambda^{-1}\displaystyle\sum_{n=0}^{\infty}(-1)^n\left[R_1^nR_2^{n+1}\nu^{2n+1}+R_1^{n+1}R_2^{n+2}\nu^{2n+3}\right]. & &
\end{pmatrix}
\tag{8.18}
$$

Since

$$
\sum_{n=0}^{\infty}(-1)^n\left[R_1^nR_2^{n+2}\nu^{2n+1}+R_1^{n+1}R_2^{n+1}\nu^{2n+3}\right] = R_2^2\nu+(1-R_2^2)\sum_{n=0}^{\infty}(-1)^nR_1^{n+1}R_2^{n+1}\nu^{2n+3}, \tag{8.19}
$$

and

$$
\sum_{n=0}^{\infty}(-1)^n\left[R_1^nR_2^{n+1}\nu^{2n+1}+R_1^{n+1}R_2^{n+2}\nu^{2n+3}\right] = R_2\nu, \tag{8.20}
$$

equation (9.31) can be simplified as follows:

$$
\begin{aligned}
P(z,\omega) &= \frac{e^{ika_1}(1-R_1^2)\nu}{(1-R_1)(1-R_2)}\left(\lambda - R_2\lambda^{-1} - R_2^2\lambda + R_2\lambda^{-1} - (1-R_2^2)\lambda\sum_{n=0}^{\infty}(-1)^n R_1^{n+1}R_2^{n+1}\nu^{2n+2}\right) \\
&= \frac{e^{ika_1}(1-R_1^2)(1-R_2^2)}{(1-R_1)(1-R_2)}\lambda\sum_{n=0}^{\infty}(-1)^n R_1^n R_2^n \nu^{2n+1} \\
&= (1+R_1)(1+R_2)e^{ika_1}e^{ik_2(z-a_2)}\sum_{n=0}^{\infty}(-1)^n R_1^n R_2^n e^{ik_1(2n+1)(a_2-a_1)}.
\end{aligned}
$$

In the derivation above, we rewrite the trivial quantity 1 as the special case of $(-1)^n R_1^n R_2^n \nu^{2n}$ with $n = 0$. The expression above is exactly the wave field in the deepest layer: only the down-going wave is present with correct amplitude; the up-going waves cancel each other, as actually happened in the subsurface.

9 Downward continuation of both source and receiver

The original Green's theorem in this report is derived to downward continue the wave field (i.e., receivers) to the subsurface over a source-free region. It can also be used to downward continue the sources down to the subsurface by taking advantage of reciprocity: the recording is the same after the source and receiver locations are exchanged.

Assuming we have data on the measurement surface: $D(z_g, z_s)$ (its ω dependency is ignored), we can use $G_0^{DN}(z, z_g)$ to downward continue it from z_g to the target depth z:

$$
D\left(z, z_s\right) = \frac{1}{\rho(z_g)}\left\{\frac{\partial D\left(z_g, z_s\right)}{\partial z_g} G_0^{DN}\left(z, z_g\right) - D\left(z_g, z_s\right)\frac{\partial G_0^{DN}\left(z, z_g\right)}{\partial z_g}\right\}. \tag{9.1}
$$

Taking the $\frac{\partial}{\partial z_s}$ operation on equation (9.1), we have a similar procedure to downward continue $\frac{D(z_g, z_s)}{\partial z_s}$ to the subsurface:

$$
\frac{\partial D\left(z, z_s\right)}{\partial z_s} = \frac{1}{\rho(z_g)}\left\{\frac{\partial^2 D\left(z_g, z_s\right)}{\partial z_g \partial z_s} G_0^{DN}\left(z, z_g\right) - \frac{\partial D\left(z_g, z_s\right)}{\partial z_s}\frac{\partial G_0^{DN}\left(z, z_g\right)}{\partial z_g}\right\}. \tag{9.2}
$$

With equations (9.1) and (9.2), we downward continue the data D and its partial derivative over z_s to the subsurface location z. According to reciprocity, $D\left(z, z_s\right) = E\left(z_s, z\right)$, where $E\left(z_s, z\right)$ is resulted from exchanging the source and receiver locations in the experiment to generate D at the subsurface. The imaginary data $E\left(z_s, z\right)$ can be considered as the recording of receiver at z_s for a source located at z.

For this imaginary experiment, the source is located at depth z, according to the Green's theorem which is derived for a source-free region, we can downward continue the recording at z_s to any depth $Z \leq z$.

In seismic migration, we downward continue $E(z_s, z)$ to the same subsurface depth z with $G_0^{DN}(z, z_s)$ to have an experiment with coincident source and receiver:

$$\begin{aligned} E(z,z) &= \frac{1}{\rho(z_s)} \left\{ \frac{\partial E(z_s,z)}{\partial z_s} G_0^{DN}(z,z_s) - E(z_s,z) \frac{\partial G_0^{DN}(z,z_s)}{\partial z_s} \right\}, \\ &= \frac{1}{\rho(z_s)} \left\{ \frac{\partial D(z,z_s)}{\partial z_s} G_0^{DN}(z,z_s) - D(z,z_s) \frac{\partial G_0^{DN}(z,z_s)}{\partial z_s} \right\}. \end{aligned} \tag{9.3}$$

With the value of $D(z, z_s)$ and $\frac{\partial D(z,z_s)}{\partial z_s}$ in equations (9.2) and (9.1), we can simplify equation (9.3) as follows:

$$\begin{aligned} \rho(z_g)\rho(z_s)E(z,z) = {} & D(z_g,z_s) \frac{\partial G_0^{DN}(z,z_g)}{\partial z_g} \frac{\partial G_0^{DN}(z,z_s)}{\partial z_s} - \frac{\partial D(z_g,z_s)}{\partial z_s} \frac{\partial G_0^{DN}(z,z_g)}{\partial z_g} G_0^{DN}(z,z_s) \\ & + \frac{\partial^2 D(z_g,z_s)}{\partial z_g \partial z_s} G_0^{DN}(z,z_g) G_0^{DN}(z,z_s) - \frac{\partial D(z_g,z_s)}{\partial z_g} \frac{\partial G_0^{DN}(z,z_s)}{\partial z_s} G_0^{DN}(z,z_g). \end{aligned} \tag{9.4}$$

If the $z_s < z_g$ and there is no heterogeneity above z_s, the $\frac{\partial}{\partial z_s}$ operation on $D(z_g, z_s)$ is equivalent to multiplying $-ik$, in this case, equation (9.5) can be simplified further:

$$E(z,z) = -\frac{\frac{\partial G_0^{DN}(z,z_s)}{\partial z_s} + ikG_0^{DN}(z,z_s)}{\rho(z_s)} D(z,z_s).$$

As an example, the data in a 2-reflector model (with an ideal impulsive source located at z_s, the depth of receiver is $z_g > z_s$, the depth of reflector are a_1 and a_2, respectively) can be expressed as:

$$\begin{aligned} D(z_g,z_s) = {} & \frac{\rho_0}{2ik} \left\{ e^{ik(z_g - z_s)} + R_1 e^{ik(2a_1 - z_g - z_s)} \right\} \\ & + \frac{\rho_0}{2ik} \left\{ \left(1 - R_1^2\right) e^{ik(2a_1 - z_g - z_s)} \sum_{n=0}^{\infty} (-1)^n R_1^n R_2^{n+1} e^{ik_1(2n+2)[a_2 - a_1]} \right\}. \end{aligned} \tag{9.5}$$

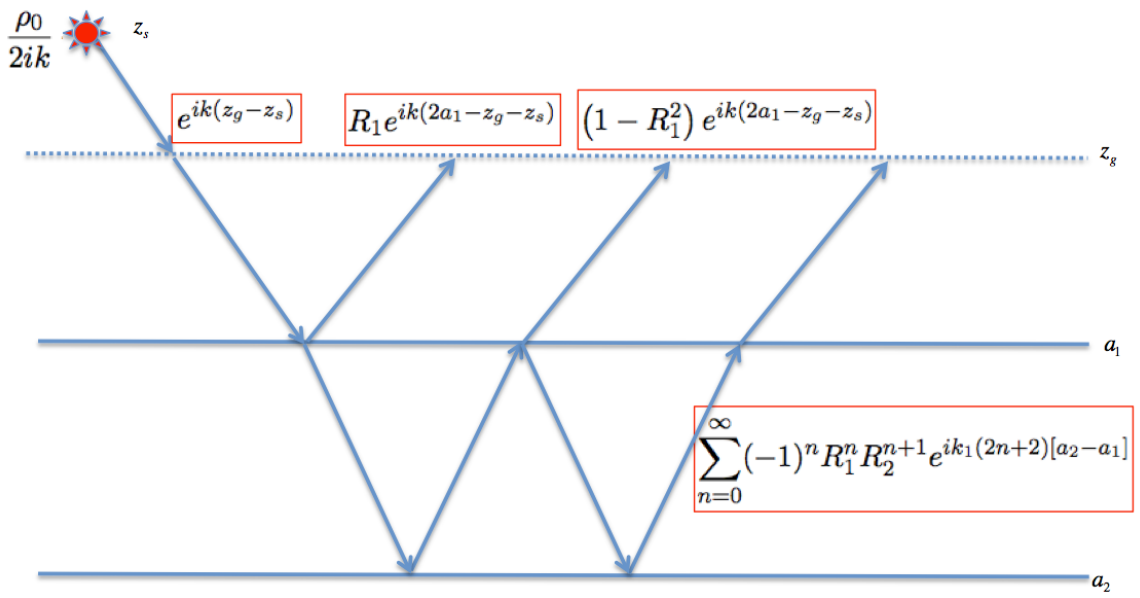

Figure 11: The history of various events in equation (9.5).

If we define $x = e^{ikz_s}$, $y = e^{ikz_g}$, $\sigma = e^{ikz}$, $\beta = \sum_{n=0}^{\infty}(-1)^n R_1^n R_2^{n+1} e^{ik_1(2n+2)[a_2-a_1]}$, and $\alpha = e^{ik(2a_1)}\left(R_1 + (1-R_1^2)\beta\right)$, the data can be expressed as:

$$\begin{aligned} D(z_g, z_s) &= \frac{\rho_0 x^{-1}}{2ik}\left\{y + \alpha y^{-1}\right\}, \\ \frac{\partial D(z_g, z_s)}{\partial z_g} &= \frac{\rho_0}{2} x^{-1}\left\{y - \alpha y^{-1}\right\}, \\ \frac{\partial D(z_g, z_s)}{\partial z_s} &= -\frac{\rho_0}{2} x^{-1}\left\{y + \alpha y^{-1}\right\}, \\ \frac{\partial^2 D(z_g, z_s)}{\partial z_g \partial z_s} &= \frac{\rho_0 k}{2i} x^{-1}\left\{y - \alpha y^{-1}\right\}. \end{aligned} \tag{9.6}$$

9.1 Above the first reflector

For $z < a_1$, the boundary values of the Green's function are:

$$\begin{array}{lll} G_0^{DN}(z,z_g) & = \rho_0 \frac{e^{ik(z-z_g)}-e^{ik(z_g-z)}}{2ik} & = \rho_0 \frac{\sigma y^{-1}-\sigma^{-1}y}{2ik}, \\ G_0^{DN}(z,z_s) & & = \rho_0 \frac{\sigma x^{-1}-\sigma^{-1}x}{2ik}, \\ \frac{\partial G_0^{DN}(z,z_s)}{\partial z_g} & & = \rho_0 \frac{\sigma y^{-1}+\sigma^{-1}y}{-2}, \\ \frac{\partial G_0^{DN}(z,z_s)}{\partial z_s} & & = \rho_0 \frac{\sigma x^{-1}+\sigma^{-1}x}{-2}. \end{array} \tag{9.7}$$

We have:

$$\begin{aligned} D(z,z_s) &= \frac{G_0^{DN}(z,z_g)\frac{\partial D(z_g,z_s)}{\partial z_g} - \frac{\partial G_0^{DN}(z,z_g)}{\partial z_g} D(z_g,z_s)}{\rho(z_g)} \\ &= \frac{\rho_0 x^{-1}}{4ik}\left(\sigma + \alpha\sigma^{-1} - \sigma^{-1}y^2 - \alpha\sigma y^{-2}\right) + \frac{\rho_0 x^{-1}}{4ik}\left(\sigma + \alpha\sigma^{-1} + \sigma^{-1}y^2 + \alpha\sigma y^{-2}\right) \\ &= \frac{\rho_0 x^{-1}}{2ik}\left(\sigma + \alpha\sigma^{-1}\right), \end{aligned} \tag{9.8}$$

and,

$$\frac{-1}{\rho(z_s)}\left(\frac{\partial G_0^{DN}(z,z_s)}{\partial z_s} + ikG_0^{DN}(z,z_s)\right) = \frac{\sigma x^{-1}+\sigma^{-1}x}{2} - \frac{\sigma x^{-1}+\sigma^{-1}x}{2} = \sigma^{-1}x. \tag{9.9}$$

And consequently, we have:

$$\begin{aligned} E(z,z) &= -\frac{1}{\rho(s)}\left(\frac{\partial G_0^{DN}(z,z_s)}{\partial z_s} + ikG_0^{DN}(z,z_s)\right) D(z,z_s) = \frac{1+\alpha\sigma^{-2}}{2ik/\rho_0} \\ &= \frac{\rho_0}{2ik}\left\{1 + e^{ik(2a_1-2z)}\left(R_1 + (1-R_1^2)\sum_{n=0}^{\infty}(-1)^n R_1^n R_2^{n+1} e^{ik_1(2n+2)[a_2-a_1]}\right)\right\}. \end{aligned} \tag{9.10}$$

The result above can be Fourier transformed into the time domain to have:

$$E(z,z,t) = -\frac{\rho_0 c_0}{2}\left\{\begin{array}{l} H(t) + R_1 H\left(t - \frac{2a_1-2z}{c_0}\right) \\ +(1-R_1^2)\sum\limits_{n=0}^{\infty}(-1)^n R_1^n R_2^{n+1} H\left(t - \frac{2a_1-2z}{c_0} - \frac{(2n+2)(a_2-a_1)}{c_1}\right) \end{array}\right\}. \tag{9.11}$$

The terms in the expression above can be interpreted as follows:

- The overall factor $-\frac{\rho_0 c_0}{2}$ is the amplitude of G_0^+ in the first medium.

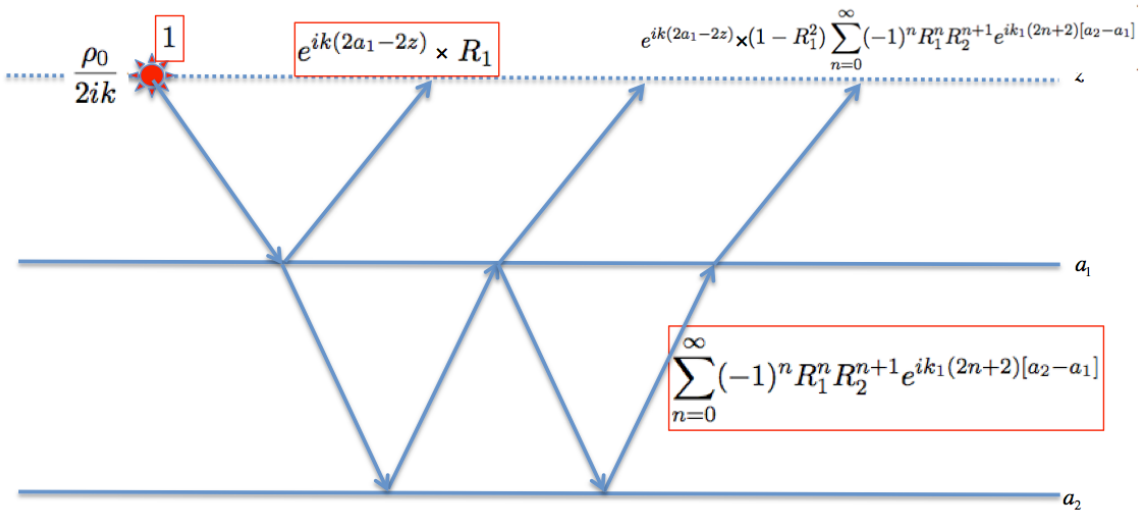

Figure 12: The history of various events in equation (9.10).

- The first term $H(t) = H\left(t - \frac{z-z}{c_0}\right)$ is propagation phase for the direct wave traveling from the source at z to a receiver coincide with the source at z. This term should be removed before applying the imaging condition.
- The second term $R_1 H\left(t - \frac{2a_1-2z}{c_0}\right)$ is the first primary.
- The third term $(1-R_1^2)\sum_{n=0}^{\infty}(-1)^n R_1^n R_2^{n+1} H\left(t - \frac{2a_1-2z}{c_0} - \frac{(2n+2)[a_2-a_1]}{c_1}\right)$ incorporate the second primary and all the internal multiples.

Balancing out the $-\frac{\rho_0 c_0}{2}$ factor, the data after removing the direct wave is denoted as $\mathcal{D}(z,t) \triangleq \frac{-2}{\rho_0 c_0} E(z,z,t) - H(t)$:

$$\mathcal{D}(z,t) = R_1 H\left(t - \frac{2a_1 - 2z}{c_0}\right) + (1-R_1^2)\sum_{n=0}^{\infty}(-1)^n R_1^n R_2^{n+1} H\left(t - \frac{2a_1 - 2z}{c_0} - \frac{(2n+2)(a_2-a_1)}{c_1}\right). \tag{9.12}$$

If we use the $t = 0$ imaging condition, we have:

$$\mathcal{D}(z,t) = \begin{cases} 0 & \texttt{if } (z < a_1) \\ R_1 & \texttt{if } (z = a_1) \end{cases} \tag{9.13}$$

In other words, we obtained the image of the first reflector at its actual depth a_1 with its correct reflection coefficient as amplitude.

9.2 Between the first and second reflectors

For $a_1 < z < a_2$, we have:

$$\begin{aligned} G_0^{DN}(z, z_g) &= \frac{\rho_1}{2ik_1}\frac{1}{1+R_1}\left((R_1\lambda - \lambda^{-1})\mu + (\lambda - R_1\lambda^{-1})\mu^{-1}\right), \\ \frac{\partial G_0^{DN}(z, z_g)}{\partial z_g} &= \frac{\rho_1 k}{2k_1}\frac{1}{1+R_1}\left((R_1\lambda - \lambda^{-1})\mu - (\lambda - R_1\lambda^{-1})\mu^{-1}\right), \end{aligned} \tag{9.14}$$

where $\lambda = e^{ik_1(z-a_1)}$, $\mu = e^{ik(z_g-a_1)}$. Using equations (9.14) and (9.6), we have:

$$\begin{aligned} D(z, z_s) &= \frac{1}{\rho(z_g)}\left(G_0^{DN}(z, z_g)\frac{\partial D(z_g, z_s)}{\partial z_g} - \frac{\partial G_0^{DN}(z, z_g)}{\partial z_g} D(z_g, z_s)\right) \\ &= \frac{\rho_0}{2ik}\frac{\rho_1 k x^{-1}}{\rho_0 k_1(1+R_1)}\left\{(\lambda - R_1\lambda^{-1})\mu^{-1}y - (R_1\lambda - \lambda^{-1})\mu\alpha y^{-1}\right\} \\ &= \frac{\rho_1 x^{-1}}{2ik_1(1+R_1)}\left\{(\lambda - R_1\lambda^{-1})e^{ika_1} - (R_1\lambda - \lambda^{-1})\alpha e^{-ika_1}\right\} \end{aligned} \tag{9.15}$$

If we define: $\beta = \sum_{n=0}^{\infty}(-1)^n R_1^n R_2^{n+1} e^{i(2n+2)[a_2-a_1]}$, we have: $\alpha = e^{2ika_1}\left(R_1 + (1-R_1^2)\beta\right)$, and the equation above can be simplified as:

$$\begin{aligned} D(z, z_s) &= \frac{\rho_1 x^{-1} e^{ika_1}}{2ik_1(1+R_1)}\left\{(\lambda - R_1\lambda^{-1}) - (R_1\lambda - \lambda^{-1})\left(R_1 + (1-R_1^2)\beta\right)\right\} \\ &= \frac{\rho_1 x^{-1} e^{ika_1}}{2ik_1}\frac{1-R_1^2}{1+R_1}\left\{\lambda - (R_1\lambda - \lambda^{-1})\beta\right\} \\ &= \frac{\rho_1 x^{-1} e^{ika_1}}{2ik_1}(1-R_1)\left\{\lambda + (\lambda^{-1} - R_1\lambda)\beta\right\} \\ &= \frac{\rho_0}{2ik}x^{-1}e^{ika_1}(1+R_1)\left\{\lambda + (\lambda^{-1} - R_1\lambda)\beta\right\} \end{aligned} \tag{9.16}$$

If we define: $\gamma = 1 - R_1\beta = \sum_{n=0}^{\infty}(-1)^n R_1^n R_2^n e^{ik_1(2n)(a_2-a_1)}$, the expression above can be rewritten as:

$$D(z, z_s) = \frac{\rho_0}{2ik}(1+R_1)e^{ik(a_1-z)}\left\{\lambda^{-1}\beta + \lambda\gamma\right\}. \tag{9.17}$$

The expression above can be verified as the following. The overall factor $\frac{\rho_0}{2ik}$ is the amplitude of the G_0^+ at the source. $e^{ik(a_1-z)}$ is the propagation from the source to the first reflector. $1+R_1$ is the transmission coefficient through the first reflector. The first term $\lambda^{-1}\beta$ can be expanded as:

$$\begin{aligned}\lambda^{-1}\beta &= e^{ik_1(a_1-z)}\sum_{n=0}^{\infty}(-1)^n R_1^n R_2^{n+1} e^{ik_1(2n+2)(a_2-a_1)} \\ &= R_2 e^{ik_1(2a_2-a_1-z)} - R_1 R_2^2 e^{ik_1(4a_2-3a_1-z)} + \cdots,\end{aligned} \tag{9.18}$$

and incorporate all the up-going events. The second term $\lambda\gamma$ can be expanded as:

$$\begin{aligned}\lambda\gamma &= e^{ik_1(z-a_1)}\sum_{n=0}^{\infty}(-1)^n R_1^n R_2^n e^{ik_1(2n)(a_2-a_1)} \\ &= e^{ik_1(z-a_1)} - R_1 R_2 e^{ik_1(z+2a_2-3a_1)} + R_1^2 R_2^2 e^{ik_1(z+4a_2-5a_1)} + \cdots,\end{aligned} \tag{9.19}$$

and incorporate all the down-going events. And,

$$\begin{aligned}G_0^{DN}(z,z_s) &= \frac{\rho_1}{2ik_1}\frac{1}{1+R_1}\left((R_1\lambda-\lambda^{-1})\xi + (\lambda - R_1\lambda^{-1})\xi^{-1}\right), \\ \frac{\partial G_0^{DN}(z,z_s)}{\partial z_s} &= \frac{\rho_1 k}{2k_1}\frac{1}{1+R_1}\left((R_1\lambda-\lambda^{-1})\xi - (\lambda - R_1\lambda^{-1})\xi^{-1}\right),\end{aligned} \tag{9.20}$$

where $\lambda = e^{ik_1(z-a_1)}$, $\xi = e^{ik(z_s-a_1)}$.

$$\begin{aligned}-\frac{1}{\rho(z_s)}\left(\frac{\partial G_0^{DN}(z,z_s)}{\partial z_s} + ikG_0^{DN}(z,z_s)\right) &= \frac{k\rho_1}{2k_1\rho_0}\frac{(\lambda^{-1}-R_1\lambda)\xi + (R_1\lambda^{-1}-\lambda)\xi^{-1}}{1+R_1} \\ &+ \frac{k\rho_1}{2k_1\rho_0}\frac{(\lambda^{-1}-R_1\lambda)\xi - (R_1\lambda^{-1}-\lambda)\xi^{-1}}{1+R_1} \\ &= \frac{k\rho_1}{k_1\rho_0}\frac{(\lambda^{-1}-R_1\lambda)\xi}{1+R_1}\end{aligned} \tag{9.21}$$

We have:

$$\begin{aligned}-\frac{1}{\rho(z_s)}\left(\frac{\partial G_0^{DN}(z,z_s)}{\partial z_s} + ikG_0^{DN}(z,z_s)\right)D(z,z_s) &= \frac{\rho_1}{2ik_1}\left\{\lambda^{-1}\beta+\lambda\gamma\right\}\left\{\lambda^{-1}-R_1\lambda\right\} \\ = \frac{\rho_1}{2ik_1}\left\{\beta\lambda^{-2} - R_1\gamma\lambda^2 + \gamma - \beta R_1\right\}\end{aligned} \tag{9.22}$$

Let's check the physical meaning of the terms above. The first term:

$$\begin{aligned}\beta\lambda^{-2} &= \left[\sum_{n=0}^{\infty}(-1)^n R_1^n R_2^{n+1} e^{ik_1(2n+2)(a_2-a1)}\right] e^{ik_1(2a_1-2z)} \\ &= R_2 e^{ik_1(2a_2-2z)} - R_1 R_2^2 e^{ik_1(4a_2-2a_1-2z)} + R_1^2 R_2^3 e^{ik_1(6a_2-4a_1-2z)} + \cdots\end{aligned} \tag{9.23}$$

incorporates the upward reflections (from the second reflector) towards depth z from below (labeled as event 2, 6, 10, $\cdots$ in Figure 13). And the second term :

$$\begin{aligned}-R_1\gamma\lambda^2 &= -R_1\left[\sum_{n=0}^{\infty}(-1)^n R_1^n R_2^n e^{ik_1(2n)(a_2-a_1)}\right] e^{ik_1(2z-2a_1)} \\ &= -R_1 e^{ik_1(2z-2a_1)} + R_1^2 R_2 e^{ik_1(2z+2a_2-4a_1)} - R_1^3 R_2^2 e^{ik_1(2z+4a_2-6z_1)} + \cdots\end{aligned} \tag{9.24}$$

incorporate the downward reflections (from the first reflector) towards depth z from above (labeled as event 1, 5, 9, $\cdots$ in Figure 13). The rest of events can be interpreted as follows:

$$\begin{aligned}\gamma - \beta R_1 = 1 - 2\beta R1 &= 1 - 2R_1\sum_{n=0}^{\infty}(-1)^n R_1^n R_2^{n+1} e^{ik(2n+2)(a_2-a_1)} \\ &= 1 + 2\left[-R_1 R_2 e^{ik_1(2a_2-2a_1)}\right]^1 + 2\left[-R_1 R_2 e^{ik_1(2a_2-2a_1)}\right]^2 + 2\left[-R_1 R_2 e^{ik_1(2a_2-2a_1)}\right]^3 + \cdots\end{aligned} \tag{9.25}$$

where in the final expression above, the first term 1 is the propagation phase for the direct arrival from the source (this term is a unit since the source and receiver coincide). The second term $2\left[-R_1 R_2 e^{ik(2a_2-2a_1)}\right]^1$ represents two separate propagations labeled as event 3 and 4 in Figure 13, both events with distinct propagation history share the same propagation time. The third term $2\left[-R_1 R_2 e^{ik(2a_2-2a_1)}\right]^2$ represents two separate propagations labeled as event 7 and 8 in Figure 13, and again both events with distinct propagation history share the same propagation time.

The final result can be Fourier transformed into the time domain as:

$$E(z,z,t) = -\frac{\rho_1 c_1}{2}\left\{\begin{array}{l} H(t) + 2\sum\limits_{n=1}^{\infty}(-1)^n R_1^n R_2^n H\left(t - \frac{2n(a_2-a_1)}{c_1}\right) \\ + \sum\limits_{n=0}^{\infty}(-1)^{n+1} R_1^{n+1} R_2^n H\left(t - \frac{2z+2na_2-2(n+1)a_1}{c_1}\right) \\ + \sum\limits_{n=0}^{\infty}(-1)^n R_1^n R_2^{n+1} H\left(t - \frac{2(n+1)a_2-2na_1-2z}{c_1}\right) \end{array}\right\} \tag{9.26}$$

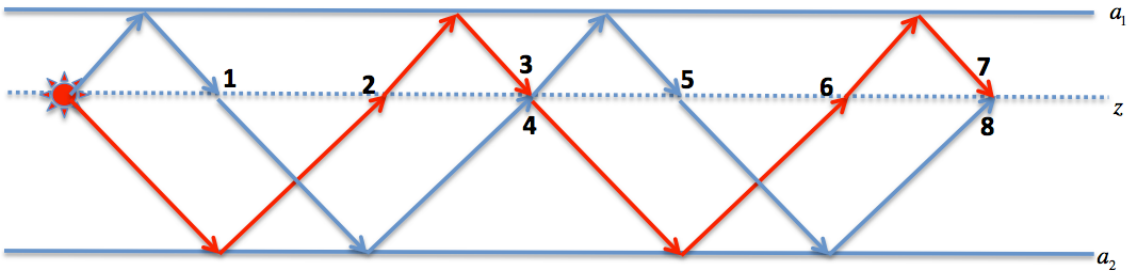

Figure 13: The diagram of events for an experiment with both source and receiver coincide at depth z which located between the first reflector at depth a_1 and the second reflector at depth a_2.

Balancing out the $-\frac{\rho_1 c_1}{2}$ factor, the data after removing the direct wave is denoted as $\mathcal{D}(z,t) \stackrel{\Delta}{=} \frac{-2}{\rho_1 c_1} E(z,z,t) - H(t)$:

$$\mathcal{D}(z,t) = \left\{ \begin{array}{l} 2\sum\limits_{n=1}^{\infty} (-1)^n R_1^n R_2^n H\left(t - \frac{2n(a_2-a_1)}{c_1}\right) \\ +\sum\limits_{n=0}^{\infty} (-1)^{n+1} R_1^{n+1} R_2^n H\left(t - \frac{2z+2na_2-2(n+1)a_1}{c_1}\right) \\ +\sum\limits_{n=0}^{\infty} (-1)^n R_1^n R_2^{n+1} H\left(t - \frac{2(n+1)a_2-2na_1-2z}{c_1}\right) \end{array} \right\} \tag{9.27}$$

and after taking the $t=0$ imaging condition, we have:

$$\mathcal{D}(z,t) = \left\{ \begin{array}{ll} -R_1 & \texttt{if } (z = a_1) \\ 0 & \texttt{if } (a_1 < z < a_2) \\ R_2 & \texttt{if } (z = a_2) \end{array} \right. \tag{9.28}$$

Note that in the previous section, i.e., to image above the first reflector at a_1, we obtain the amplitude R_1 when z approach a_1 from above. In this section we image below the first reflector at a_1, the amplitude of the image is $-R_1$ when z approaches a_1 from below, as it should.

9.3 Below the second reflector

$$\begin{aligned} G_0^{DN}(z,z')\big|_{z'=z_g} &= \frac{\left[\nu^{-1}(R_2\lambda - \lambda^{-1}) + R_1\nu(\lambda - R_2\lambda^{-1})\right]\mu + \left[R_1\nu^{-1}(R_2\lambda - \lambda^{-1}) + \nu(\lambda - R_2\lambda^{-1})\right]\mu^{-1}}{2ik_2(1+R_1)(1+R_2)/\rho_2}, \\ \frac{\partial}{\partial z'} G_0^{DN}(z,z')\Big|_{z'=z_g} &= \frac{\left[\nu^{-1}(R_2\lambda - \lambda^{-1}) + R_1\nu(\lambda - R_2\lambda^{-1})\right]\mu - \left[R_1\nu^{-1}(R_2\lambda - \lambda^{-1}) + \nu(\lambda - R_2\lambda^{-1})\right]\mu^{-1}}{2k_2(1+R_1)(1+R_2)/(k\rho_2)}, \end{aligned} \tag{9.29}$$

where $\lambda \equiv e^{ik_2(z-a_2)}$, $\mu \equiv e^{ik(z_g-a_1)}$, and $\nu \equiv e^{ik_1(a_2-a_1)}$.

$$\begin{aligned} D(z,z_s) &= \frac{1}{\rho(z')}\left\{P(z',\omega)\frac{\partial G_0^{DN}(z,z',\omega)}{\partial z'} - G_0^{DN}(z,z',\omega)\frac{\partial P(z',\omega)}{\partial z'}\right\}\Bigg|_{z'=z_g}^{z'=\mathcal{B}} \\ &= \frac{1}{\rho(z')}\left[G_0^{DN}(z,z',\omega)\frac{\partial P(z',\omega)}{\partial z'} - P(z',\omega)\frac{\partial G_0^{DN}(z,z',\omega)}{\partial z'}\right]_{z'=z_g} \\ &= \frac{\rho_2}{2ik_2}e^{ik(a_1-z_s)}\frac{R_1\nu^{-1}(R_2\lambda-\lambda^{-1})+\nu(\lambda-R_2\lambda^{-1})}{(1+R_1)(1+R_2)} \\ &- \frac{\rho_2}{2ik_2}e^{ik(a_1-z_s)}\frac{\nu^{-1}(R_2\lambda-\lambda^{-1})+R_1\nu(\lambda-R_2\lambda^{-1})}{(1+R_1)(1+R_2)}\left\{R_1+(1-R_1^2)\beta\right\} \end{aligned} \tag{9.30}$$

Since $\frac{\rho_2 k}{\rho_0 k_2} = \frac{\rho_2 c_2}{\rho_0 c_0} = \frac{\rho_1 c_1}{\rho_0 c_0}\frac{\rho_2 c_2}{\rho_1 c_1} = \frac{1+R_1}{1-R_1}\frac{1+R_2}{1-R_2}$, the equation above can be simplified as:

$$D(z,z_s) = \frac{\rho_0 e^{ik(a_1-z_s)}/(2ik)}{(1-R_1)(1-R_2)}\left(\begin{array}{l} \left[R_1R_2\nu^{-1}+\nu\right]\lambda \;-\; \left[R_1\nu^{-1}+R_2\nu\right]\lambda^{-1} \\ -\left[R_1R_2\nu^{-1}+R_1^2\nu\right]\lambda \;+\; \left[R_1\nu^{-1}+R_1^2R_2\nu\right]\lambda^{-1} \\ -(1-R_1^2)\lambda\displaystyle\sum_{n=0}^{\infty}(-1)^n\left[R_1^nR_2^{n+2}\nu^{2n+1}+R_1^{n+1}R_2^{n+1}\nu^{2n+3}\right] \\ +(1-R_1^2)\lambda^{-1}\displaystyle\sum_{n=0}^{\infty}(-1)^n\left[R_1^nR_2^{n+1}\nu^{2n+1}+R_1^{n+1}R_2^{n+2}\nu^{2n+3}\right]. \end{array}\right) \tag{9.31}$$

Since

$$\sum_{n=0}^{\infty}(-1)^n\left[R_1^nR_2^{n+2}\nu^{2n+1}+R_1^{n+1}R_2^{n+1}\nu^{2n+3}\right] = R_2^2\nu+(1-R_2^2)\sum_{n=0}^{\infty}(-1)^nR_1^{n+1}R_2^{n+1}\nu^{2n+3}, \tag{9.32}$$

and

$$\sum_{n=0}^{\infty}(-1)^n\left[R_1^nR_2^{n+1}\nu^{2n+1}+R_1^{n+1}R_2^{n+2}\nu^{2n+3}\right] = R_2\nu, \tag{9.33}$$

equation (9.31) can be simplified as follows:

$$
\begin{aligned}
D(z,z_s) &= \frac{\rho_0 e^{ik(a_1-z_s)}(1-R_1^2)\nu}{2ik(1-R_1)(1-R_2)}\left(\lambda - R_2\lambda^{-1} - R_2^2\lambda + R_2\lambda^{-1} - (1-R_2^2)\lambda\sum_{n=0}^{\infty}(-1)^n R_1^{n+1}R_2^{n+1}\nu^{2n+2}\right)\\
&= \frac{\rho_0 e^{ik(a_1-z_s)}(1-R_1^2)(1-R_2^2)}{2ik(1-R_1)(1-R_2)}\lambda\sum_{n=0}^{\infty}(-1)^n R_1^n R_2^n \nu^{2n+1}\\
&= \frac{\rho_0(1+R_1)(1+R_2)}{2ik}e^{ik(a_1-z_s)}e^{ik_2(z-a_2)}\sum_{n=0}^{\infty}(-1)^n R_1^n R_2^n e^{ik_1(2n+1)(a_2-a_1)}.
\end{aligned}
$$

In the derivation above, we rewrite the trivial quantity 1 as the special case of $(-1)^n R_1^n R_2^n \nu^{2n}$ with $n=0$. The expression above is exactly the wave field in the deepest layer: only the down-going wave is present with correct amplitude; the up-going waves cancel with each other as actually happened in the subsurface. And the expression above can be simplified as:

$$
D(z,z_s) = \frac{\rho_0(1+R_1)(1+R_2)}{2ik}e^{ik(a_1-z_s)}e^{ik_1(a_2-a_1)}e^{ik_2(z-a_2)}{}_\gamma
$$

After the downward continuation of the receiver, we can use the Green's theorem to downward continue the source:

$$
\begin{aligned}
G_0^{DN}(z,z')\big|_{z'=z_s} &= \frac{\left[\nu^{-1}(R_2\lambda-\lambda^{-1}) + R_1\nu(\lambda - R_2\lambda^{-1})\right]\xi + \left[R_1\nu^{-1}(R_2\lambda-\lambda^{-1}) + \nu(\lambda-R_2\lambda^{-1})\right]\xi^{-1}}{2ik_2(1+R_1)(1+R_2)/\rho_2},\\
\frac{\partial}{\partial z'}G_0^{DN}(z,z')\Big|_{z'=z_s} &= \frac{\left[\nu^{-1}(R_2\lambda-\lambda^{-1}) + R_1\nu(\lambda - R_2\lambda^{-1})\right]\xi - \left[R_1\nu^{-1}(R_2\lambda-\lambda^{-1}) + \nu(\lambda-R_2\lambda^{-1})\right]\xi^{-1}}{2k_2(1+R_1)(1+R_2)/(k\rho_2)},
\end{aligned}
\tag{9.34}
$$

where $\lambda \equiv e^{ik_2(z-a_2)}$, $\xi \equiv e^{ik(z_s-a_1)}$, and $\nu \equiv e^{ik_1(a_2-a_1)}$.

$$
-\frac{1}{\rho(z_s)}\left(\frac{\partial G_0^{DN}(z,z_s)}{\partial z_s} + ikG_0^{DN}(z,z_s)\right) = \frac{k\rho_2}{k_2\rho_0}\frac{\nu^{-1}(\lambda^{-1}-R_2\lambda) + R_1\nu(R_2\lambda^{-1}-\lambda)}{(1+R_1)(1+R_2)}\xi,
$$

and

$$
\begin{aligned}
-\frac{1}{\rho(z_s)}\left(\frac{\partial G_0^{DN}(z,z_s)}{\partial z_s} + ikG_0^{DN}(z,z_s)\right)D(z,z_s) = \frac{k\rho_2}{k_2\rho_0}&\frac{\nu^{-1}(\lambda^{-1}-R_2\lambda) + R_1\nu(R_2\lambda^{-1}-\lambda)}{(1+R_1)(1+R_2)}e^{ik(z_s-a_1)}\\
&\cdot\frac{\rho_0(1+R_1)(1+R_2)}{2ik}e^{ik(a_1-z_s)}e^{ik_1(a_2-a_1)}e^{ik_2(z-a_2)}{}_\gamma
\end{aligned}
$$

The expression above can be simplified as:

$$\begin{aligned}
E(z,z) &= \frac{\rho_2}{2ik_2} e^{ik_1(a_2-a_1)} e^{ik_2(z-a_2)} \gamma \left\{ \nu^{-1}(\lambda^{-1} - R_2\lambda) + R_1\nu(R_2\lambda^{-1} - \lambda) \right\} \\
&= \frac{\rho_2}{2ik_2} \nu\lambda\gamma \left\{ \nu^{-1}(\lambda^{-1} - R_2\lambda) + R_1\nu(R_2\lambda^{-1} - \lambda) \right\} \\
&= \frac{\rho_2}{2ik_2} \left\{ 1 - R_2\lambda^2 + R_1R_2\nu^2 - R_1\lambda^2\nu^2 \right\} \gamma \\
&= \frac{\rho_2}{2ik_2} \left\{ 1 + R_1R_2\nu^2 - R_2\lambda^2 - R_1\lambda^2\nu^2 \right\} \gamma
\end{aligned}$$

Since: $\left(1 + R_1R_2\nu^2\right)\gamma = \left(1 - R_1R_2\nu^2\right) \sum_{n=0}^{\infty} \left[-R_1R_2\nu^2\right]^n = 1$, and:

$$\begin{aligned}
R_2\lambda^2\gamma = R_2\lambda^2 \sum_{n=0}^{\infty} (-1)^n R_1^n R_2^n \nu^{2n} &= R_2\lambda^2 + R_2\lambda^2 \sum_{n=1}^{\infty} (-1)^n R_1^n R_2^n \nu^{2n} \\
&= R_2\lambda^2 - R_2^2\lambda^2 \sum_{n=1}^{\infty} (-1)^n R_1^n R_2^{n-1} \nu^{2n+2}, \\
R_1\lambda^2\nu^2\gamma = R_1\lambda^2\nu^2 \sum_{n=0}^{\infty} (-1)^n R_1^n R_2^n \nu^{2n} &= \lambda^2 \sum_{n=0}^{\infty} (-1)^n R_1^{n+1} R_2^n \nu^{2n+2}, \\
\left\{ -R_2\lambda^2 - R_1\lambda^2\nu^2 \right\} \gamma = -R_2\lambda^2 - (1 - R_2^2)\lambda^2 \sum_{n=0}^{\infty} (-1)^n R_1^{n+1} R_2^n \nu^{2n+2}&.
\end{aligned}$$

The final downward continuation result can be expressed as:

$$\begin{aligned}
E(z,z) &= \frac{\rho_2}{2ik_2} \left\{ 1 - R_2\lambda^2 - (1 - R_2^2)\lambda^2 \sum_{n=0}^{\infty} (-1)^n R_1^{n+1} R_2^n \nu^{2n+2} \right\} \\
&= \frac{\rho_2}{2ik_2} \left\{ 1 - R_2\lambda^2 + (1 - R_2^2)\lambda^2 \sum_{n=0}^{\infty} (-1)^{n+1} R_1^{n+1} R_2^n \nu^{2n+2} \right\} \\
&= \frac{\rho_2}{2ik_2} \left\{ 1 - R_2 e^{ik_2(2z-2a_2)} + (1 - R_2^2) e^{ik_2(2z-2a_2)} \sum_{n=0}^{\infty} (-1)^{n+1} R_1^{n+1} R_2^n e^{ik_1(2n+2)(a_2-a_1)} \right\}.
\end{aligned}$$

In the results above, $\frac{\rho_2}{2ik_2}$ is the overall amplitude of G_0^+ in the third layer. The first term 1 is the propagation phase of the wave traveling from the source and receiver coincide at depth z. The second term $-R_2 e^{ik_1(2a_2-2a_1)}$ is the reflection from the second reflector at depth a_2 (here it has $-R_2$ as its reflection coefficient since both the source and receiver are located below the reflector).

The third term $(1-R_2^2)e^{ik_1(2a_2-2a_1)}\sum_{n=0}^{\infty}(-1)^{n+1}R_1^{n+1}R_2^n e^{ik_1(2n+2)(a_2-a_1)}$ contains infinite number of internal multiples generated between the first and second reflector.

$$E(z,z,t)=-\frac{\rho_2 c_2}{2}\left\{\begin{array}{l} H(t)-R_2H\left(t-\frac{2z-2a_2}{c_2}\right) \\ +(1-R_2^2)H\left(t-\frac{2z-2a_2}{c_2}-\frac{(2n+2)(a_2-a_1)}{c_1}\right)\end{array}\right\} \tag{9.35}$$

Balancing out the $-\frac{\rho_2 c_2}{2}$ factor, the data after removing the direct wave is denoted as $\mathcal{D}(z,t)\triangleq\frac{-2}{\rho_2 c_2}E(z,z,t)-H(t)$:

$$\mathcal{D}(z,t)=\left\{\begin{array}{l} -R_2H\left(t-\frac{2z-2a_2}{c_2}\right) \\ +(1-R_2^2)H\left(t-\frac{2z-2a_2}{c_2}-\frac{(2n+2)(a_2-a_1)}{c_1}\right)\end{array}\right\} \tag{9.36}$$

and after taking the $t=0$ imaging condition, we have:

$$\mathcal{D}(z,t)=\left\{\begin{array}{ll} -R_2 & \texttt{if } (z=a_2) \\ 0 & \texttt{if } (a_2<z)\end{array}\right. \tag{9.37}$$

Note that in the previous section, i.e., to image between the first and second reflectors, we obtain the amplitude R_2 when z approach a_2 from above. In this section we image below the second reflector at a_2, the amplitude of the image is $-R_2$ when z approaches a_2 from below, as it should.

10 Conclusions

A general and efficient procedure to compute the Green's function with vanishing Dirichlet and Neumann boundary conditions has been derived for a 1D medium of arbitrary complexity, and its effectiveness has been demonstrated with numerical examples that accurately predict the up-going and down-going wave field at depth using only the data on the shallower measurement surface. The density contribution to the Green's theorem and Green's function is accurately studied to better understand its role in imaging. In order to generalize the idea in this paper to a multidimensional earth, a finite-difference scheme is derived and validated by comparison with an analytic benchmark.

Several remarkable properties of the Green's function with double vanishing boundary conditions have been identified:

- The vanishing property of G_0^{DN} for $z>a$ unequivocally states that it is not necessary to know the medium's properties below a target to achieve the target's depth image. This conclusion is also stated in the paper "Finite volume model for migration" by Weglein et al. (2011a).

- G_0^{DN} contains no internal multiple and no source-generated reflections; this property agrees perfectly with not only the reflectionless approximation of WKBJ Green's function, but also with the idea of avoiding reflections and multiples in many current seismic imaging procedures.

We also have reported some very early and very positive news on the first wave theory RTM imaging tests, with a discontinuous reference medium and images that have the correct depth and amplitude (that is, producing the reflection coefficient at the correctly located target) with primaries and multiples in the data. That is an implementation of Weglein et al. (2011a;b) with creative implementation and testing and analysis.

11 Acknowledgments

Jim Mayhan and Jinlong Yang provided the proofreading of the manuscript. The authors would like to thank all M-OSRP members and sponsors. This work has been partially funded by NSFCMG award DMS-0327778 and DOE Basic Energy Sciences Award DE-FG02-05ER15697.

12 Appendix A: Classical Reflection Problem

In this appendix we derive and list the solution of the classical acoustic reflection problem. The medium properties are listed in Table 1. We denote $k = \omega/c_0$, $k_1 = \omega/c_1$, and the incident wave is $e^{ikz'}$. We assume the reflection and transmission waves are $Ae^{-ikz'}$ and $Be^{ik_1z'}$, respectively. In order to have a minimal framework for derivation, the philosophy here is to use the simplest possible form for the incident, reflection, and transmission waves. The complexities caused by flexible reflector depth are transferred to the parameters: A and B.

The boundary condition at the boundary $z' = a$ requires that:

$$\begin{aligned} e^{ika} + Ae^{-ika} &= Be^{ik_1a}, \\ (ik/\rho_0)e^{ika} + (-ik/\rho_0)Ae^{-ika} &= (ik_1/\rho_1)Be^{ik_1a}. \end{aligned} \tag{12.1}$$

The equations above can be simplified as:

$$\begin{aligned} e^{ika} + Ae^{-ika} &= Be^{ik_1a}, \\ e^{ika} - Ae^{-ika} &= \frac{\rho_0 k_1}{\rho_1 k} Be^{ik_1a}. \end{aligned} \tag{12.2}$$

Since $\frac{\rho_0 k_1}{\rho_1 k} = \frac{c_0\rho_0}{c_1\rho_1}$, we have:

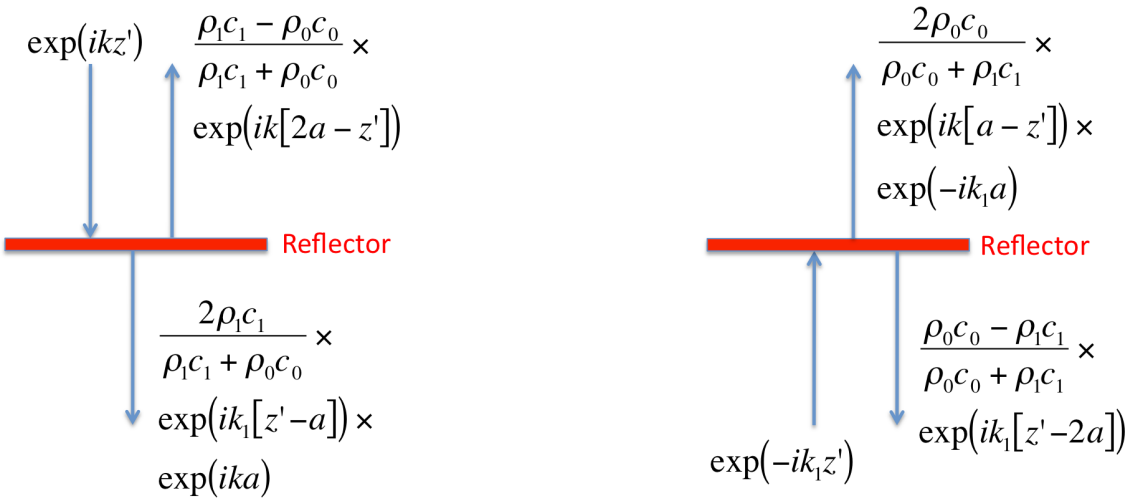

Figure 14: The solution of the two acoustic reflection problems in this appendix. Left: The down-going incident wave from the medium above; right: the up-going incident wave from the medium below.

$$\begin{aligned} e^{ika} + Ae^{-ika} &= Be^{ik_1 a}, \\ e^{ika} - Ae^{-ika} &= \frac{\rho_0 c_0}{\rho_1 c_1} Be^{ik_1 a}. \end{aligned} \tag{12.3}$$

Solving the above equations, we have:

$$\begin{aligned} A &= \frac{c_1\rho_1 - c_0\rho_0}{c_1\rho_1 + c_0\rho_0} e^{ik(2a)} = Re^{ik(2a)}, \\ B &= \frac{2c_1\rho_1}{c_1\rho_1 + c_0\rho_0} e^{i(k-k_1)a} = Te^{i(k-k_1)a}. \end{aligned} \tag{12.4}$$

If the incident wave comes from the second medium: $e^{-ik_1 z'}$, similarly we can assume the reflection wave being of the form $Ae^{ik_1 z'}$ and the transmission wave of the form $Be^{-ikz'}$.

$$\begin{aligned} e^{-ik_1 a} + Ae^{ik_1 a} &= Be^{-ika}, \\ (-ik_1/\rho_1)e^{-ik_1 a} + (ik_1/\rho_1)Ae^{ik_1 a} &= (-ik/\rho_0)Be^{-ika}. \end{aligned} \tag{12.5}$$

After a straightforward simplification we have:

$$
\begin{aligned}
e^{-ik_1 a} + Ae^{ik_1 a} &= Be^{-ika}, \\
e^{-ik_1 a} - Ae^{ik_1 a} &= \frac{k\rho_1}{k_1\rho_0} Be^{-ika}.
\end{aligned}
\tag{12.6}
$$

Remove the ω dependency in $\frac{k\rho_1}{k_1\rho_0}$, to have:

$$
\begin{aligned}
e^{-ik_1 a} + Ae^{ik_1 a} &= Be^{-ika}, \\
e^{-ik_1 a} - Ae^{ik_1 a} &= \frac{\rho_1 c_1}{\rho_0 c_0} Be^{-ika}.
\end{aligned}
\tag{12.7}
$$

The solution of the above equations is:

$$
\begin{aligned}
A &= \frac{c_0\rho_0 - c_1\rho_1}{c_0\rho_0 + c_1\rho_1} e^{-ik_1(2a)} = Re^{-ik_1(2a)}, \\
B &= \frac{2c_0\rho_0}{c_1\rho_1 + c_0\rho_0} e^{i(k-k_1)a} = Te^{i(k-k_1)a}.
\end{aligned}
\tag{12.8}
$$

13 Appendix B: Confirmation that the Green's function (4.10) is the solution of the wave equation with vanishing Dirichlet and Neumann boundary conditions at the deeper boundary

In this case we have: $\mathcal{A} < a < \mathcal{B}$, and the acoustic wave equation is:

$$
\left\{ \rho(z') \frac{\partial}{\partial z'} \left(\frac{\partial}{\rho(z')\partial z'} \right) - \frac{\omega^2}{c^2(z')} \right\} G_0(z, z', \omega) = \delta(z - z'). \tag{13.1}
$$

Here we prove that the boundary conditions at the reflector are satisfied. First is the continuity of pressure. According to equation (4.10), the pressure immediately below the reflector can be obtained by setting z' in the expression for $z' > a$ (i.e., the second case) to a:

$$
G_0(z, a+, \omega) = \rho_1 \frac{e^{ik_1(z-a)} - e^{ik_1(a-z)}}{2ik_1}. \tag{13.2}
$$

while the pressure immediately above the reflector can be obtained by setting z' in the expression for $z' < a$ (i.e., the first case) to a:

$$
G_0(z, a-, \omega) = \frac{\rho_1}{2ik_1} \left\{ \frac{Re^{ik_1(z-a)} - e^{ik_1(a-z)}}{1+R} + \frac{e^{ik_1(z-a)} - Re^{ik_1(a-z)}}{1+R} \right\}. \tag{13.3}
$$

We can simplify the expression above as follows:

$$\begin{aligned} G_0(z,a-,\omega) &= \frac{\rho_1}{2ik_1}\left\{(1-R)e^{ik_1(z-a)} + \frac{-1-R}{1+R}e^{ik_1(a-z)} + \frac{R+R^2}{1+R}e^{ik_1(z-a)}\right\} \\ &= \frac{\rho_1}{2ik_1}\left\{(1-R+R)e^{ik_1(z-a)} - e^{ik_1(a-z)}\right\} \\ &= \frac{\rho_1}{2ik_1}\left\{e^{ik_1(z-a)} - e^{ik_1(a-z)}\right\} \\ &= G_0(z,a+,\omega). \end{aligned} \tag{13.4}$$

On the other hand, the continuity of $\frac{1}{\rho}\frac{\partial G_0^{DN}}{\partial z'}$ across the boundary can be verified in a similar fashion. The value of $\frac{1}{\rho}\frac{\partial G_0^{DN}}{\partial z'}$ immediately below the reflector is:

$$\frac{1}{\rho_1}\left.\frac{\partial G_0(z,z',\omega)}{\partial z'}\right|_{z'=a+} = \frac{-1}{\rho_1}\left\{e^{ik_1(z-a)} + e^{ik_1(a-z)}\right\}. \tag{13.5}$$

while the value of $\frac{1}{\rho}\frac{\partial G_0^{DN}}{\partial z'}$ immediately above the reflector can be obtained by setting z' in the expression for $z' < a$ (i.e., the first case) to a:

$$\frac{1}{\rho_0}\left.\frac{\partial G_0(z,z',\omega)}{\partial z'}\right|_{z'=a-} = \frac{c_1}{\rho_0 c_0}\left\{\frac{Re^{ik_1(z-a)} - e^{ik_1(a-z)}}{1+R} + \frac{Re^{ik_1(a-z)-e^{ik_1(z-a)}}}{1+R}\right\}. \tag{13.6}$$

We can simplify the expression above as follows:

$$\begin{aligned} \frac{1}{\rho_0}\left.\frac{\partial G_0(z,z',\omega)}{\partial z'}\right|_{z'=a-} &= \frac{c_1}{\rho_0 c_0}\left\{(R-1)e^{ik_1(z-a)} + \frac{R-R^2}{1+R}e^{ik_1(z-a)} + \frac{R-1}{1+R}e^{ik_1(a-z)}\right\} \\ &= \frac{c_1}{\rho_0 c_0}\left\{\frac{R-1}{R+1}e^{ik_1(z-a)} + \frac{R-1}{R+1}e^{ik_1(a-z)}\right\} \\ &= \frac{c_1}{\rho_0 c_0}\frac{R-1}{R+1}\left\{e^{ik_1(z-a)} + e^{ik_1(a-z)}\right\} \\ &= \frac{-1}{\rho_1}\left\{e^{ik_1(z-a)} + e^{ik_1(a-z)}\right\} \\ &= \frac{1}{\rho_1}\left.\frac{\partial G_0(z,z',\omega)}{\partial z'}\right|_{z'=a+}. \end{aligned} \tag{13.7}$$

The derivation above takes advantage of the following relations: since $R = \frac{\rho_1 c_1 - \rho_0 c_0}{\rho_1 c_1 + \rho_0 c_0}$, we have:

$$\frac{c_1}{\rho_0 c_0}\frac{R-1}{R+1} = \frac{c_1}{\rho_0 c_0}\frac{\frac{\rho_1 c_1 - \rho_0 c_0}{\rho_1 c_1 + \rho_0 c_0} - 1}{\frac{\rho_1 c_1 - \rho_0 c_0}{\rho_1 c_1 + \rho_0 c_0} + 1} = \frac{c_1}{\rho_0 c_0}\frac{-2\rho_0 c_0}{2\rho_1 c_1} = \frac{-1}{\rho_1}.$$

14 Appendix C: The causal acoustic Green's function used in this report

The analytic solution of the Green's function in equation (2.2) is available if both the velocity $c(z')$ and density $\rho(z')$ fields are constant: i.e., if $c(z') = c_0$ and $\rho(z') = \rho_0$. In this case the term $1/\rho(z') = 1/\rho_0$ becomes a constant and can be moved to the front of the $\partial/\partial z'$ operator, to have:

$$\frac{1}{\rho_0}\left\{\frac{\partial}{\partial z'}\frac{\partial}{\partial z'} + \frac{\omega^2}{c_0^2}\right\} G_0(z, z', \omega) = \delta(z - z').$$

Both terms on the left-hand side of the equation above contain the $\frac{1}{\rho_0}$ factor and the equation can be more succinctly written as:

$$\left\{\frac{\partial}{\partial z'}\frac{\partial}{\partial z'} + \frac{\omega^2}{c_0^2}\right\} G_0(z, z', \omega) = \rho_0\delta(z - z'). \tag{14.1}$$

Note that the equation above is identical to equation (27) of Weglein et al. (2011a), except for the extra density factor ρ_0 on the right-hand side, and the solution for equation (27) of Weglein et al. (2011a) is $\frac{e^{ik(z-z')}}{2ik}$ where $k = \omega/c_0$; our Green's function in equation (14.1) is:

$$G_0(z, z', \omega) = \frac{\rho_0}{2ik}e^{ik|z-z'|}, \tag{14.2}$$

where again, $k = \omega/c_0$.

References

Alford, R. M., K. R. Kelly, and D. M. Boore. "Accuracy of finite-difference modeling of the acoustic wave equation." Geophysics 39 (1974): 834–842.

Baysal, Edip, Dan D. Kosloff, and John W. C. Sherwood. "Reverse time migration." Geophysics 48 (1983): 1514–1524.

Clayton, R. W. and R. H. Stolt. "A Born-WKBJ inversion method for acoustic reflection data." Geophysics 46 (1981): 1559–1567.

Fletcher, R., P. Fowler, P. Kitchenside, and U. Albertin. "Suppressing unwanted internal reflections in prestack reverse-time migration." Geophysics 71 (2006): E79–E82.

Liu, F., G. Zhang, S. A. Morton, and J. P. Leveille. "An optimized wave equation for seismic modeling and reverse time migration." Geophysics 74 (2009): WCA153–WCA158.

Luo, Yi and Gerard T. Schuster. "Bottom-up target-oriented reverse-time datuming." CPS/SEG Geophysics Conference and Exhibition (2004): F55.

Vigh, Denes, E. William Starr, and Jerry Kapoor. "The role of reverse time migration in complex imaging." CSEG RECORDER (June 2009): 20–24.

Weglein, A. B., R. H. Stolt, and J. D. Mayhan. "Reverse-time migration and Green's theorem: Part I — The evolution of concepts, and setting the stage for the new RTM method." Journal of Seismic Exploration 20 (February 2011): 73–90.

Weglein, A. B., R. H. Stolt, and J. D. Mayhan. "Reverse time migration and Green's theorem: Part II — A new and consistent theory that progresses and corrects current RTM concepts and methods." Journal of Seismic Exploration 20 (May 2011): 135–159.

Whitmore, D. N. "Iterative depth imaging by back time propagation." 53^{rd} Annual International Meeting, SEG, Expanded Abstracts. . Society of Exploration Geophysicists, 1983. 382–385.

Short note: Angle constraints on ISS internal-multiple attenuation: The compromise between cost and accuracy

Qiang Fu

April 29, 2013

Abstract

Inverse scattering series (ISS) internal-multiple attenuation is a promising internal-multiple-suppression algorithm. However, an ISS internal-multiple attenuation is extremely calculation intensive, and the demand for huge computation power restricts the implementation of this algorithm on large 3D exploration data sets. Terenghi and Weglein (2012) proposed a method to apply certain angle constraints to reduce the computation cost of ISS internal-multiple attenuation. The essence of the angle constraints is a compromise between the cost of the computation and the accuracy of the result. How many side effects will be introduced by the compromise, and how the trade-offs can be optimized, are the issues of concern. No quantitative test has been done yet to clarify these important concerns. It will be the next step to design a series of tests to reveal the relation between the cost and quality of this method.

1 Introduction

ISS internal-multiple attenuation is a data-driven internal-multiple-suppression algorithm ((Araújo, 1994; Weglein et al., 1997)). The lack of a prerequisite of prior information about the medium through which the seismic wave propagates or the reflectors from which the internal-multiples generate makes the algorithm feasible in areas with complicated geological structure. However, the demand for huge computation time weakens this advantage. Terenghi and Weglein (2012) proposed a method to apply the constants of incident angle and dipping angle to reduce the computation cost of ISS internal-multiple attenuation.

2 Theory

Angle constraints on ISS internal-multiple attenuation consists of three aspects: 1. The inverse scattering series; 2. internal-multiple attenuation by ISS; and 3. The angle constraints on ISS internal-multiple attenuation to reduce computational cost. Weglein et al. (2003) provided a very

comprehensive and detailed review on the inverse scattering series, including the rigorous derivation of the ISS internal-multiple attenuation algorithm.

$$\begin{aligned} b_3(k_g,k_s,q_g+q_s) &= \frac{1}{(2\pi)^2}\int_{-\infty}^{+\infty}\int_{-\infty}^{+\infty} dk_1 e^{-iq_1(\epsilon_g-\epsilon_s)} dk_2 e^{-iq_2(\epsilon_g-\epsilon_s)} \\ &\times \int_{-\infty}^{+\infty} dz_1 e^{i(q_g+q_1)z_1} b_1(k_g,k_1,z_1) \\ &\times \int_{-\infty}^{z_1} dz_2 e^{i(-q_1-q_2)z_2} b_1(k_1,k_2,z_2) \\ &\times \int_{z_2}^{+\infty} dz_3 e^{i(q_2+q_s)z_3} b_1(k_2,k_s,z_3) \end{aligned} \tag{2.1}$$

Equation 2.1 reveals that the ISS multiple attenuation consists of five integrals. Each of them will become a loop in the real implementation. If one can narrow the limit of some of those integrals, the computation will be significantly reduced. This is the reason to introduce angle constraints here. If the relation between the angles (incident angle and dipping angle) and the integral limits (temporal frequency and wavenumbers) can be defined, one can use the distribution of the angles to narrow the integral limits.

Before we begin to discuss this topic further, I should point out one fact explicitly: the angles we mentioned in angle constraints method is not the corresponding angles in the real medium. Because we use one constant reference velocity (c_0) in the derivation of ISS internal-multiple attenuation. Therefore the angles we mentioned in the method is pseudo dipping and incident angles.

Let's start from the time-domain wavefield $P(\mathbf{r_g},\mathbf{r}_s,t)$ on a certain location in the medium $\mathbf{r}_g = \{x_g,y_g,z_g\}$ caused by a point source at $\mathbf{r}_s = \{x_s,y_s,z_s\}$.

In this section, I use Greek letters to denote the horizontal components of the vectors. For instance, $\boldsymbol{\chi}$ is the horizontal component of a location vector $\mathbf{r}$,

$$\boldsymbol{\chi}_s = \{x_s,y_s\},\ \boldsymbol{\chi}_g = \{x_g,y_g\}, \tag{2.2}$$

$$\mathbf{r}_s = \{\boldsymbol{\chi}_s,z_s\},\ \mathbf{r}_g = \{\boldsymbol{\chi}_g,z_g\} \tag{2.3}$$

For simplifying the discussion, one can assume that the sources and receivers are both located on the horizontal free-surface. The seismic exploration data D are the measured wavefield on the surface.

$$D((\boldsymbol{\chi}_g,\boldsymbol{\chi}_s,t) = P(\boldsymbol{\chi}_g,z_g=0,\boldsymbol{\chi}_s,z_s=0,t) \tag{2.4}$$

Let $\mathbf{k}$ be the wavenumber vector, which is the Fourier domain conjugate of the location vector $\mathbf{r}$, and use Greek letters to denote the horizontal components,

$$\mathbf{k}_s = \{k_{sx},k_{sy},k_{sz}\} = \{\boldsymbol{\kappa}_s,q_s\} \tag{2.5}$$

$$\mathbf{k}_g = \{k_{gx},k_{gy},k_{gz}\} = \{\boldsymbol{\kappa}_g,q_g\} \tag{2.6}$$

The data in the Fourier domain can be obtained by the multi-dimensional Fourier transform

$$D(\boldsymbol{\kappa}_g, \boldsymbol{\kappa}_s, \omega) = \int dt d\boldsymbol{\chi}_g d\boldsymbol{\chi}_s D(\boldsymbol{\chi}_g, \boldsymbol{\chi}_s, t) e^{i(\omega t - \boldsymbol{\kappa}_g \boldsymbol{\chi}_g + \boldsymbol{\kappa}_s \boldsymbol{\chi}_s)} \tag{2.7}$$

It is critical to be aware that the vertical wavenumbers (q_s and q_g) are not independent free variables here. They are determined by the combination of horizontal wavenumbers ($\boldsymbol{\kappa}_s$ and $\boldsymbol{\kappa}_g$) temporal frequency (ω).

From the relations

$$|\mathbf{k}_s| = |\{\boldsymbol{\kappa}_s, q_s\}| = \left|\frac{\omega}{c_0}\right| \tag{2.8}$$

$$|\mathbf{k}_g| = |\{\boldsymbol{\kappa}_g, q_g\}| = \left|\frac{\omega}{c_0}\right|, \tag{2.9}$$

it is easy to get $q_s \sim \omega$ and $q_g \sim \omega$ relations for given $\boldsymbol{\kappa}_s$ and $\boldsymbol{\kappa}_g$

$$q_g = -\frac{\omega}{c_0}\sqrt{1 - \frac{c_0^2}{\omega^2}\boldsymbol{\kappa}_g \cdot \boldsymbol{\kappa}_g} \tag{2.10}$$

$$q_s = +\frac{\omega}{c_0}\sqrt{1 - \frac{c_0^2}{\omega^2}\boldsymbol{\kappa}_s \cdot \boldsymbol{\kappa}_s}. \tag{2.11}$$

The signs in equations 2.10 and 2.11 represent the propagation directions of the incoming wave and outgoing wave, respectively.

Figure 1 shows the incident angle γ and dipping angle α of a certain reflector. The image function wavenumbers $\mathbf{k}_m$ and $\mathbf{k}_h$ are defined as the difference and the sum of the source and receiver wavenumbers, respectively. (Stolt and Weglein, 2012) give

$$\mathbf{k}_m = \mathbf{k}_g - \mathbf{k}_s = \{\boldsymbol{\kappa}_g - \boldsymbol{\kappa}_s, q_g - q_s\} \tag{2.12}$$

$$\mathbf{k}_h = \mathbf{k}_g + \mathbf{k}_s = \{\boldsymbol{\kappa}_g + \boldsymbol{\kappa}_s, q_g + q_s\} \tag{2.13}$$

From trigonometry we have the relations

$$|\tan(\alpha)| = \frac{\boldsymbol{\kappa}_m \cdot \boldsymbol{\kappa}_m}{|q_g - q_s|} \tag{2.14}$$

$$\cos(2\gamma) = -\frac{c_0^2}{\omega^2}\mathbf{k}_g \cdot \mathbf{k}_s = -\frac{c_0^2}{\omega^2}(\boldsymbol{\kappa}_s \cdot \boldsymbol{\kappa}_s + q_g q_s), \tag{2.15}$$

which are the relations between the angles and the temporal frequency for the given horizontal wavenumbers $\boldsymbol{\kappa}_s$ and $\boldsymbol{\kappa}_g$. One can calculate the angles from the temporal frequency.

However, the goal is the opposite. The relation we need is from angles to calculate temporal frequency ranges by the angles constants. If the relation is invertible, the goal can be achieved.

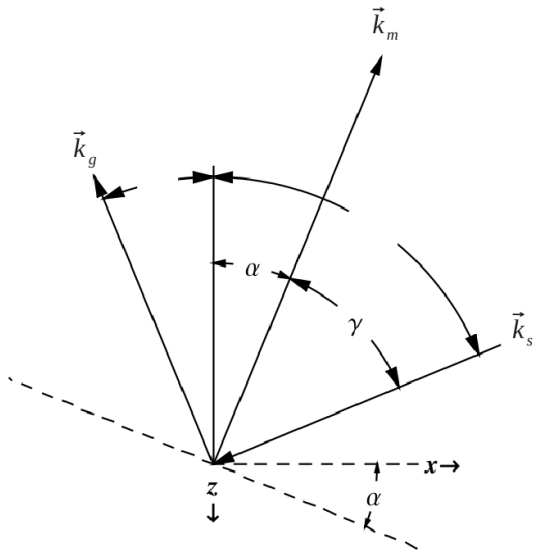

Figure 1: The incident angle and dipping angle of a certain reflector. The dashed line represents a reflector, and $\vec{k_s}$ and $\vec{k_g}$ are the incoming and outgoing wave directions, respectively. α is the incident angle and γ is the dipping angle. Courtesy of Terenghi and Weglein (2012)

$$\frac{\partial \alpha}{\partial \omega} = \frac{|\omega|\,(q_g - q_s)\sqrt{\boldsymbol{\kappa}_m \cdot \boldsymbol{\kappa}_m}}{2q_g q_s\left(c_0^2(\mathbf{k}_g \cdot \mathbf{k}_s) - \omega^2\right)} = \frac{|\omega|\,(q_g - q_s)\sqrt{\boldsymbol{\kappa}_m \cdot \boldsymbol{\kappa}_m}}{2q_g q_s \omega^2(1+\cos(2\gamma)} \tag{2.16}$$

$$\frac{\partial \gamma}{\partial \omega} = \frac{q_g^2 + q_s^2 + 2q_g q_s \cos(2\gamma)}{2q_g q_s \omega\sqrt{1-\cos(2\gamma)}} \tag{2.17}$$

It can be proved that both partial derivatives (equations 2.16 and 2.17) are negative. Therefore the $\alpha{\sim}\omega$ and $\gamma{\sim}\omega$ relations are both monotonic. That means the relations are invertible. One can obtain the temporal frequency ranges from the angle constraints.

For the simplified case here, both sources and receivers are located on the horizontal free-surface ($\epsilon_g = z_g = \epsilon_s = z_s = 0$), and the wavelet of the source is only a spiky δ function ($B(\omega) = 1$), so the ISS internal-multiple-attenuation problem (equation 2.1) becomes

$$\begin{aligned} b_3(\boldsymbol{\kappa}_g, \boldsymbol{\kappa}_s, \omega) \;=\; & \int_{-\infty}^{+\infty}\int_{-\infty}^{+\infty} d\boldsymbol{\kappa}_1 d\boldsymbol{\kappa}_2 \int_{-\infty}^{+\infty} dz_1 e^{i(q_g+q_1)z_1} b_1(\boldsymbol{\kappa}_g, \boldsymbol{\kappa}_1, z_1) \\ & \times \int_{-\infty}^{z_1} dz_2 e^{i(-q_1-q_2)z_2} b_1(\boldsymbol{\kappa}_1, \boldsymbol{\kappa}_2, z_2) \\ & \times \int_{z_2}^{+\infty} dz_3 e^{i(q_2+q_s)z_3} b_1(\boldsymbol{\kappa}_2, \boldsymbol{\kappa}_s, z_3) \end{aligned} \tag{2.18}$$

and all b_1 terms can be calculated from

$$b_1(\boldsymbol{\kappa}_i, \boldsymbol{\kappa}_j, \omega) = iq_i D(\boldsymbol{\kappa}_i, \boldsymbol{\kappa}_j, \omega) \qquad (i, j = g, 1, 2, s) \tag{2.19}$$

As mentioned before, the vertical wavenumbers (q_i) are not independent free variables. For given horizontal wavenumbers ($\boldsymbol{\kappa}$), the vertical wavenumbers (q_i) are dependent on the temporal frequency (ω)

$$q_i = \frac{\omega}{c_0}\sqrt{1 - \frac{c_0^2}{\omega^2}\boldsymbol{\kappa}_i \cdot \boldsymbol{\kappa}_i} \qquad (i, j = g, 1, 2, s). \tag{2.20}$$

Because the vertical wavenumbers (q_i) have to be real numbers, the square root part in equation 2.20 must be non-negative.

$$\frac{\omega^2}{c_0^2} \geq \boldsymbol{\kappa}_i \cdot \boldsymbol{\kappa}_i = |\boldsymbol{\kappa}_i| \qquad (i, j = g, 1, 2, s) \tag{2.21}$$

Because it is shown that the horizontal wavenumbers $\boldsymbol{\kappa}_i$ are determined by the temporal frequency for a given angle, and because the temporal frequency can be calculated from the angles, the integral limit (horizontal wavenumbers $\boldsymbol{\kappa}_i$) can be narrowed by the prior information about the ranges of the angles.

$$\begin{cases} \max(\omega_\gamma^{\min}, \omega_\alpha^{\min}) \leq \omega < \min(\omega_\gamma^{\max}, \omega_\alpha^{\max}) & \omega > 0 \\ \max(-\omega_\gamma^{\max}, -\omega_\alpha^{\max}) < \omega \leq \min(\omega_\gamma^{\min}, \omega_\alpha^{\min}) & \omega < 0 \end{cases} \tag{2.22}$$

3 Future plan

The method that uses angle constraints reduces the computational cost of ISS internal-multiple attenuation, as was shown in previous sections. It is clear that the method is essentially a compromise between cost and quality. Whether adequate computational efficiency can be achieved relative to the quality lost is a key question in deciding whether it is worthwhile to use angle constants to accelerate the speed of ISS internal-multiple attenuation. The answer depends on the relation between the frequency (wavenumbers) reduction in the calculation and the inaccuracy generated by that reduction. No quantitative test has been done yet to clarify this relation. Because of the importance of this question, the next step will be to design a series of tests to reveal the relation between the cost and quality of this method.

4 Acknowledgements

I am grateful to all M-OSRP sponsors for their long-term encouragement and support in this research. Also I would like to thank all members in M-OSRP for the valuable discussions for this paper.

References

Araújo, F. V. Linear and non-linear methods derived from scattering theory: backscattered tomography and internal multiple attenuation. PhD thesis, Universidade Federal da Bahia, 1994.

Stolt, Robert H. and Arthur B. Weglein. Seismic Imaging and Inversion: Volume 1: Application of Linear Inverse Theory. Cambridge University Press, 2012.

Terenghi, P. and A. B. Weglein. "ISS internal multiple attenuation with angle constraints." M-OSRP Annual Report 11 (2012).

Weglein, A. B., F. V. Araújo, P. M. Carvalho, R. H. Stolt, K. H. Matson, R. T. Coates, D. Corrigan, D. J. Foster, S. A. Shaw, and H. Zhang. "Inverse Scattering Series and Seismic Exploration." Inverse Problems (2003): R27–R83.

Weglein, A. B., F. A. Gasparotto, P. M. Carvalho, and R. H. Stolt. "An Inverse-Scattering Series Method for Attenuating Multiples in Seismic Reflection Data." Geophysics 62 (November-December 1997): 1975–1989.

A timely and necessary antidote to in-direct methods and so-called P-wave FWI

Arthur B. Weglein, M-OSRP/Department of Physics/University of Houston

To appear in The Leading Edge September 2013

A central purpose of this paper is to bring an alternative voice, perspective, and understanding to the latest geophysical stampede, technical bubble, and self-proclaimed seismic cure-all, the so-called “Full waveform inversion” or FWI. If you think this is an exaggerated situation or “straw man” issue or argument, I respectfully refer the reader (for one among innumerable pieces of evidence) to the advertisement/announcement of the 2013 SEG Workshop on FWI, 27 April-1 May in Oman, whose opening line is, and I quote, "Full waveform inversion has emerged as the final and ultimate solution to the earth resolution and imaging objective."

Besides representing language, attitude, and a viewpoint that have no place anywhere in science, and, in particular, in exploration seismology, the fact is that the method, as put forth, is from a fundamental and basic-principle point of view (aside from, and well before, any practical considerations and track record of added-value are considered) hardly deserving of the label “inversion,” let alone all the other extreme and unjustified claims and attributes, as being the “deliverance” and the last and final word on the subject.

From a direct-inversion point of view, and for the algorithms that are derived for solving the exact same problem of estimating, for example, the location of velocity anomalies and shallow hazards, and velocity changes at the top and base salt, all the current approaches to so-called full waveform inversion are: (1) always using the wrong data, (2) always using the wrong algorithms, and (3) all too often, using the wrong earth model, as well. Making this clear is one purpose of this article.

The issue being discussed in this paper is not a matter of semantics and is not a labeling/mislabeling issue; it is the substantive issue of what data and what algorithms are called for by direct inversion to achieve certain seismic processing objectives. In particular, we focus here on objectives that rely on the amplitude of reflection data as a function of incident angle to determine changes in, e.g., P-wave velocity, AVO parameters, or so-called FWI.

Another purpose of this paper is to propose and exemplify an alternative and direct inverse solution that actually deserves the label "inversion" and could be useful for those goals and objectives, and perhaps can actually earn, deserve, and warrant a label of FWI, although never as the “ultimate and final solution.” The direct-inversion

approach not only provides a method but also a framework and platform for understanding when it will and will not work. All current so-called FWI methods are indirect model-matching methods, and indirect methods can never provide that capability and clarity. Model-matching run backwards, or solving a forward problem in an inverse sense, resides behind all the current indirect P-wave-only so-called FWI and is never equivalent to a direct inverse solution for any non-linear problem, such as, e.g., target identification or velocity determination/updating, nor does it even represent a fully and completely aligned goal and property of a direct inverse solution.

A third and perhaps most important goal of this paper is to provide a new, comprehensive overview and bridge for these two approaches for those who may be following, applying, and/or considering the current so-called indirect model-matching FWI approach and those proposing, interested in, or providing a road to a direct inverse methodology. We show how these two approaches have the same starting point, and in fact, have the same exact generalized Taylor series expansion for modeling data and for expressing the actual data in terms of a reference model and reference data and the difference between actual and reference properties. The two approaches differ in how they view each of the same terms of that forward series. One view of those individual terms leads to a Taylor series form that does not allow a direct inverse series and that leaves as the only option the running of a forward (linear truncated) series in an inverse sense. That direct inverse series results in an indirect model-matching approach, e.g., as seen in AVO and the so-called FWI methods. Another view and understanding of those individual terms in the forward Taylor series that derives from the fundamental equation of scattering theory (the Lippmann-Schwinger equation) recognizes that the forward Taylor series is a very special class of Taylor series — a geometric series. Further, it is a geometric series for a forward problem, and it has a geometric series for a direct inverse solution. Without understanding and calling upon the scattering-theory equation, that recognition of the forward series as being geometric is not possible, and a direct inverse solution would not be achievable. All of the consequences and differences between the forward model-matching approach leading to methods such as so called FWI and the direct inverse methods, derived from the inverse scattering series, have that simple, accessible, and understandable origin. The details, arguments, and examples behind these three objectives and goals are provided below.

Let’s begin. Seismic processing is an inverse problem, in which measurements on or near the surface of the earth are used to make inferences about the nature of the subsurface that are relevant to the exploration and production of hydrocarbons.

There was a time, not too long in the past, when a discussion of any method for solving inverse or data-processing problems always began with a definition of direct and indirect methods. The latter was deemed the less respectable and the lessor choice

between the two, considered out of desperation and resignation and offered with hesitation and apology. It was associated among “inversionists” with searching and model matching rather than with seeking a direct, clear, and definitive solution through a math-physics analysis.

In our view, that earlier, healthy understanding and respect for the framework and definitiveness of direct inverse methods has largely given way or has been pushed aside, with serious and substantive negative and injurious conceptual and practical consequences. Among the latter manifestations and consequences is the totally mislabeled and ubiquitous phenomenon of so-called “full wave inversion” (FWI) methods. Among FWI references are Brossier et al. (2009), Crase et al. (1990), Gauthier et al. (1986), Nolan and Symes (1997), Pratt (1999), Pratt and Shipp (1999), Sirgue et al. (2010), Symes (2008), Tarantola (1984, 1986), Valenciano et al. (2006), Vigh and Starr (2008), and Zhou et al. (2012).

In this note, we advocate (whenever possible) direct methods for solving processing problems and providing prerequisites. Direct methods offer many conceptual and practical benefits over indirect methods. Advantages of direct methods begin with actually knowing that you are solving the problem that you are interested in solving.

How can you recognize a direct versus an indirect method? Consider the quadratic equation

$$ax^2 + bx + c = 0\,, \tag{1}$$

and the solution

$$x = (-b \pm \sqrt{b^2 - 4ac}) / 2a\,. \tag{2}$$

Equation (2) is a direct solution for the roots of equation (1). On the other hand, if you see a cost function involved in a solution, the solution is indirect. Also, if you see a modeling equation being solved in an inverse sense, or an iteratively linear updating, those are each direct indicators of an indirect solution and a model-matching approach, which too often can start with an incorrect or insufficient modeling equation and a matching of fundamentally inadequate data. The only time that a forward problem solved in an inverse sense can be equivalent to a direct inverse solution is when the direct inverse solution is linear. For example, locating reflectors at depth with a known velocity model is linear, and, hence, e.g., (asymptotic) RTM is a modeling run backwards (i.e., in an inverse sense) to directly determine structure. Another transparent example is given by the forward geometric series

$$S = ar + ar^2 + ar^3 + ... = \frac{ar}{1-r} \qquad when\,|\,r\,|<1 \tag{3}$$

and the inverse

$$\begin{aligned} r &= \frac{S/a}{1+S/a} = S/a - (S/a)^2 + (S/a)^3 ... \\ &= r_1 + r_2 + r_3 + ... \end{aligned} \tag{4}$$

If, rather than these nonlinear relationships among *S*, *a,* and *r*, we instead imagine an exact linear relationship that *S*, *a,* and r might satisfy, e.g.,

$$S = ar \ . \tag{5}$$

then we have the forward problem of solving for *S* given *a* and *r*, and the inverse problem becomes solving for *r* in terms of *S* and *a*. The direct inverse solution *r*=*S*/*a* is equivalent to the forward problem solved in an inverse sense, solving *S*=*ar* for *r* in terms of *S* and *a*. However, if the forward relationship assumed among *S*, *a*, and *r* is a quadratic relationship (an approximate of the actual nonlinear forward problem given by equation (3)), we have

$$S = ar + ar^2 \tag{6}$$

Then, solving the forward problem equation (6) in an inverse sense is a quadratic solution with two roots that can be real or imaginary, whereas the solution to equation (4) is a single real solution for *r*. In place of equation (6), think of the linearized forward Zoeppritz equation for R_{PP} solved in an inverse sense, and the point is clear. This simple and transparent example demonstrates a pitfall of thinking that a direct inversion is equivalent to a forward problem solved in an inverse sense. Another example, pointed out in Weglein et al. (2009), is the direct inverse solution for predicting and removing free-surface and internal multiples, from the inverse-scattering series, where these two distinct algorithms are not only independent of subsurface information, they are also independent of whether we assume the earth is acoustic, elastic, anelastic, heterogeneous, and anisotropic. The multiple-removal algorithms (which are direct and nonlinear) don't change one line of code when you change your mind about the earth model type you want to consider. Can you imagine a model-matching and subtraction method or linear-updating method for predicting and removing multiples, with any cost function, L_1, L_2, L_P, that would be independent of subsurface properties and the type of earth model you are using to generate the synthetic data? It is hard to overstate the significance of this point. The widely recognized benefit to industry from effectively

removing free-surface and internal multiples using algorithms derived from the inverse scattering series, for offshore and onshore plays, never would have occurred if the indirect inversion, model-matching, and iterative updating, and FWI-like thinking, were the approaches pursued for removing multiples.

In general, we look at inversion as a set of tasks: free-surface and internal-multiple removal, depth imaging, and nonlinear AVO. For the purposes of this paper and for discussing FWI, we focus entirely on how the ISS addresses that parameter estimation task in isolation, and as if all other tasks (e.g., multiple removal) had been previously achieved.

Indirect methods such as flat Common-Image Gathers (CIGs) were developed as a response to the inability to directly solve for and adequately provide a velocity model for depth imaging, and those CIGs represent a necessary condition at the image that an accurate velocity would satisfy. Among references for CIGs, we list Anderson et al. (2012), Baumstein et al. (2009), Ben-Hadj-ali et al. (2008, 2009), Biondi and Sava (1999), Biondi and Symes (2004), Brandsberg-Dahl et al. (1999), Chavent and Jacewitz (1995), Fitchner (2011), Guasch et al. (2012), Kapoor et al. (2012), Rickett and Sava (2002), Sava et al. (2005), Sava and Fomel (2003), Sirgue et al. (2009, 2010, 2012), Symes and Carazzone (1991), Tarantola (1987), and Zhang and Biondi (2013). Many wrong velocity models can and will also satisfy a flat-common-image-gather criterion, especially under complex imaging circumstances. Indeed, unquestioned faith in the power of satisfying the flat-CIG criterion can and does contribute to dry-hole drilling. Mathematicians who work on the latter types of CIG problems would better spend their time describing the underlying lack of a necessary and sufficient condition, and the consequences, rather than dressing up and obfuscating the necessary but insufficient condition in fancy, rigorous, and abstract new clothes.

We recognize that the recent surge of interest in estimating changes in velocity is fueled by: (1) the improved ability to produce low-frequency and low-vertical-wavenumber information from new acquisition and improved deghosting; (2) the implicit admission of serious problems with methods to estimate velocity models; e.g., with tomography, iterative flat CIG's searching, and the like; and, of course, (3) the persistent and unacceptable dry-hole drilling rate. Today, for example, we basically remain fixed and without significant progress (at a one-in-ten success rate) in drilling successful exploration wells in the deep-water Gulf of Mexico (Hawthorn (2009), Iledare and Kaiser (2007)).

Indirect methods should only be considered when direct methods are not available or are inadequate, or when you cannot figure out how to solve a problem directly. Indirect methods are often and reasonably employed to allow a channel or an adjustment (a dial) for phenomena and components of reality that are outside and external to the

physics of the system you have chosen and defined. Of course, there always are, and always will be, phenomena outside your assumed and adopted physics and system that must be accommodated and that are ignored at your peril. That's the proper realm and role for indirect methods. Even then, however, they need to be applied judiciously and always with scrutiny of what resides behind cost-function-criteria assumptions. When a direct method to predict the amplitude and phase of free-surface multiples, such as inverse-scattering-series free-surface-multiple removal, includes the obliquity factor, and has the direct satisfaction of prerequisites such as source and receiver deghosting and wavelet estimation, then the better the direct method of providing the prerequisites performs, the better the free-surface demultiple provides the amplitude and phase of the free-surface multiples. If at any stage you decide you can “roll in” obliquity, source and receiver deghosting, and wavelet estimation into a catch-all energy-minimization adaptive subtraction, you run into the serious problem: No matter how much better you achieve a satisfaction of energy minimization, you still have no guarantee that that improved energy minimization aligns with and supports free-surface-multiple removal while preserving primaries. In fact, removal of multiples can increase “energy” (e.g., when you have destructive interference between a primary and a multiple), and it is widely understood that the energy-minimization criteria are today’s greatest impediment to effectively removing free-surface and internal multiples for complex onshore and marine plays. The criteria behind the indirect adaptive step matters. Within the area of free-surface and internal-multiple attenuation, the rush to and overreliance on energy-minimization adaptive subtraction contributes to the inability to effectively and surgically remove multiples at all offsets and without damaging primaries. We discuss that specific issue in a report on seeking adaptive criteria (Weglein 2012 M-OSRP) that serve as an alternative and replacement for energy minimization for free-surface multiple removal. However, the trend of using indirect methods for phenomena and processing goals within the system, and for providing prerequisites within the system, is in general a conceptual and practical mistake. There has been a dangerous and growing tendency to solve everything inside and outside the system by using indirect methods and cost functions. We of course recognize, support, and require ever-faster computers. However, the growth in computational physics, often at the expense of mathematical physics, and the availability of ever-faster computers, encourages the rush to “cost functions” and to searching without thinking, and thus represents a ubiquitous, misguided, and unfortunate trend, with “solutions” that aren’t. When we give up on physics and determinism, we look at statistics and searching, and indirect methods become a “natural” choice and are always readily available, along with their drawbacks and consequences.

A direct method provides a framework of precise data needs, and it delivers a straight-ahead formula that takes in your data and actually solves and explicitly and directly outputs the solution that you seek. Indirect methods can never provide that clarity or

confidence. Model-matching and iterative updating by any fancy name, such as a new “Frechet derivative,” and the so-called “Full Wave Inversion,” are model-matching and are never, ever, equivalent to a direct inversion for the earth's elastic mechanical property changes. The distinction is significant and has both conceptual and mercantile consequences.

Let us present an example of the difference. Let's suppose someone said that you could take a single seismic trace that is a single function of time, and invert simultaneously for velocity and density, each as a function of depth in a 1D earth.

Today, you might reasonably be cautious and concerned because the dimension of the data is less than the overall dimension of the quantities you seek to determine. We have learned as an industry to be dubious in the latter single-trace, solve-for-two-functions-of-depth case. We look skeptically at those who would model-match and pull all kinds of arcane cost functions and generalized inverses together, using different norms and constraints and full-wave predictions of that single trace that can be model-matched with amplitude and phase so that we can call that model-matching scheme “full waveform inversion.” Why can't we solve for density and velocity uniquely from a single trace, since we can certainly model the single trace from knowing the velocity and density as a function of depth? That’s a beginning and an example of thinking that solving a forward problem in an inverse sense is in some way actually solving the inverse problem. What came along in that earlier time, as a response to this question, were direct acoustic inversion methods that said that inverting for velocity and density as functions of depth from a single trace is impossible, or at least that it is impossible to provide the unique and actual velocity and density as a function of depth. That direct-inversion framework convinced many (hopefully most) people that the one-trace-in, two-functions-out approach is not a question or an issue of which indirect algorithm or L_P cost function you are using. It is more basic and stands above algorithm; it's an inadequate-data issue. No algorithm with that single-trace data input should call itself “inversion,” even if that single trace was model-matched and iteratively updated and computed with amplitude and phase and, with too much self-regard, labels itself as “full wave inversion.” We learned to stop running that single trace through search algorithms for velocity and density --- and that lesson was absorbed within our collective psyches in our industry --- for whatever the cost function and local or global minimum you employed. Using the wrong and fundamentally inadequate data closes the book and constitutes the end of the story. Thus, we learned to look for and respect dimension between the data and the sought-after parameters we want to identify. That is a good thing, but it turns out that it's not a good-enough thing. In fact, direct acoustic wavefield inversion for a 1D earth requires all the traces for a given shot record in order to determine one or more parameters (e.g., V_p and density) as a function of depth.

We will show (in a similar way) that the fact that you can solve the forward Zoeppritz equations (or a linear approximate) for a PP reflection coefficient as a function of incident angle and the changes in λ, μ, and ρ across the reflector doesn't imply that you can solve for changes in λ, μ, and ρ in terms of the PP reflection coefficient as a function of angle. A direct inverse for the changes in λ, μ, and ρ demands all multicomponent sources and receivers, or, equivalently, PP, PS, SP, and SS data.

These conditions on data requirements hold for any processing/inverse problem in which the reference or background medium is elastic — e.g., for all amplitude analysis, including AVO and so-called FWI and all ISS multiple removal and imaging with ocean-bottom or onshore acquisition. See Li et al. (2011), Liang et al. (2010), Matson (1997), Matson and Weglein (1998), Weglein et al. (2003), and H. Zhang (2006).

By "inadequate data," we mean something much more basic and fundamental than limitations due to sampling, aperture, and bandwidth. That is, indirect solutions can (and often do) input data that are fundamentally inadequate from a basic and direct inverse perspective and understanding. The indirect methods then search locally and globally around error surfaces with Frechet derivatives and conjugate gradients, and they keep hordes of math, physics, geophysics, and computer scientists busy using giant and super-fast computers looking at outputs and 3D color displays, and being convinced that with all the brainpower and resources that are invested, they are on track and are on their way to solving the problem. What's wrong with linear iterative updating? What's wrong begins with understanding the meaning of a linear inverse. Even in cases in which the data are adequate — e.g., cases with P-wave data and an acoustic inverse model — the algorithms that a direct inverse provides for explicit linear and each nonlinear estimate of changes in P-wave velocity and density, will differ at the very first nonlinear step and at every subsequent step, with the nonlinear iterative linear estimate of these changes in physical properties. The linear, quadratic, cubic, … estimates of physical properties from a direct method are explicit and unique (a generalized Taylor series) and order by order in the data and will not agree with an iterative linear update. Hence, although the iterative linear updating is nonlinear in the data, it does not represent a direct inverse solution. Further, the terms in the direct solution are analytically determined in terms of the first term, whereas iterative linear updating requires generalized inverses, SVD, cost functions, and numerical solutions. They could not be more different. If you had an alternative to the solution of the quadratic equation and it produced different roots from those produced by the direct quadratic formula, equation (2), would you call it "an inverse solution for the roots?" That's the issue, and it's that simple.

For the elastic inverse case, the difference is yet more serious. A direct inverse solution for the P-velocity, V_P, shear velocity, V_S, and density, ρ, and a linear iterative method,

will already differ at the linear step, and that difference and resulting gap grow at each nonlinear step and estimate.

When it comes to directly inverting for changes in elastic properties and density, there are direct and explicit formulas for the linear and nonlinear estimates. The same single unchanged direct inverse ISS set of equations that derived the algorithms for free-surface and internal-multiple removal (and have demonstrated stand-alone capability, see, e.g., Ferreira (2011), Luo et al. (2011), and Weglein et al. (2003, 2011)), have also provided the ISS depth imaging (Weglein et al. 2011, 2012) and direct inversion for earth mechanical properties. In Zhang (2006), we find the first direct nonlinear equations for estimating the changes in elastic properties for a 1D earth.

The mathematical origin of linear inverse theory (and linear iterative inversion) begins with a Taylor series of the recorded data, $D(m)$, from the actual earth. Those data depend on the earth properties characterized by the label m and the synthetic data $D(m_0)$ from an estimate or reference value of those properties that we label, m_0. To relate $D(m)$ and $D(m_0)$, we introduce a Taylor series

$$D(m) = D(m_0) + D'(m_0)\Delta m + \frac{D''(m_0)}{2}\Delta m^2 + \cdots, \tag{7}$$

in which the derivatives are Frechet derivatives. A linearized form of equation (7) is considered

$$D(m) = D(m_0) + D'(m_0)\Delta m_1^1, \tag{8}$$

where the Frechet derivative,

$$D'(m_0) = \frac{D(m_0 + \varepsilon\Delta m) - D(m_0)}{\varepsilon\Delta m} \tag{9}$$

is approximated by a finite-difference approximation involving data at m_0 and data at a nearby model, $m_0+\varepsilon\Delta m$. Δm_1^1 means the first linear estimate of Δm, with the subscript standing for linear and the superscript for the first estimate. The matrix inversion of equation (8) for Δm_1^1 leads to a new approximate $m_0+\Delta m_1^1$, and

$$D(m) - D(m_0 + \Delta m_1^1) = D'(m_0 + \Delta m_1^1)\Delta m_1^2 \tag{10}$$

.

The process is repeated and is the basis of iterative linear inversion. Properties of that process related to convergence to m are spelled out in Blum (1972), page 536, with issues where the constants such as M (in Blum (1972) page 536) that appear in the convergence criteria are unknown.

Another starting point for this type of perturbative approach is from scattering theory, where $D(m)$ relates to the actual Green's function G, and $D(m_0)$ relates to the reference Green's function, G_0 and $V=m-m_0$. The identity among G, G_0, and V is called the Lippmann Schwinger or Scattering Equation (see, e.g., Taylor 1972)

$$G = G_0 + G_0 V G \quad . \tag{11}$$

and an expansion of equation (11) for G in terms of G_0 and V produces

$$G = G_0 + G_0 V G_0 + G_0 V G_0 V G_0 + \cdots \quad . \tag{12}$$

Keys and Weglein (1983) provide the formal association between $D'(m_0)\Delta m$ and $G_0 V G_0$. Equation (7) is a Taylor series in Δm, and as such that series doesn't have an available inverse series. However, since equation (12) (which follows from the scattering equation (11)) is a geometric series in $r=VG_0$ and $a=G_0$, then a geometric series for $S=G-G_0$ in terms of a and r: — $S=ar/(1-r)$ — has an inverse series $r=(S/a)/(1+S/a)$ with terms

$$r_1 = S / a$$

$$r_2 = -(S / a)^2$$

$$r_3 = (S / a)^3$$

$$r_4 = -(S / a)^4$$

...

A unique expansion of VG_0 in orders of measurement values of $(G-G_0)$ is

$$VG_0 = (VG_0)_1 + (VG_0)_2 + \cdots \tag{13}$$

The scattering-theory equation allows that forward series form and the opportunity to find a direct inverse series. Substituting equation (13) into equation (12) and setting the terms of equal order in the data to be equal, we have $D=G_0 V_1 G_0$.

For the elastic equation, V is a matrix and the data are

$$\begin{pmatrix} D^{PP} & D^{PS} \\ D^{SP} & D^{SS} \end{pmatrix} = \begin{pmatrix} G_0^P & 0 \\ 0 & G_0^S \end{pmatrix} \begin{pmatrix} V_1^{PP} & V_1^{PS} \\ V_1^{SP} & V_1^{SS} \end{pmatrix} \begin{pmatrix} G_0^P & 0 \\ 0 & G_0^S \end{pmatrix}$$

$$V_1 = \begin{pmatrix} V_1^{PP} & V_1^{PS} \\ V_1^{SP} & V_1^{SS} \end{pmatrix}$$

$$V = \begin{pmatrix} V^{PP} & V^{PS} \\ V^{SP} & V^{SS} \end{pmatrix}$$

$$V = V_1 + V_2 + \cdots$$

where V_1, V_2 are linear, quadratic contributions to V in terms of the data,

$$D = \begin{pmatrix} D^{PP} & D^{PS} \\ D^{SP} & D^{SS} \end{pmatrix}.$$

The changes in elastic properties and density are contained in $V = \begin{pmatrix} V^{PP} & V^{PS} \\ V^{SP} & V^{SS} \end{pmatrix}$, and that leads to direct and explicit solutions for the changes in mechanical properties in orders of the data, $D = \begin{pmatrix} D^{PP} & D^{PS} \\ D^{SP} & D^{SS} \end{pmatrix}$,

$$\frac{\Delta\lambda}{\lambda} = (\frac{\Delta\lambda}{\lambda})_1 + (\frac{\Delta\lambda}{\lambda})_2 + \cdots$$

$$\frac{\Delta\mu}{\mu} = (\frac{\Delta\mu}{\mu})_1 + (\frac{\Delta\mu}{\mu})_2 + \cdots$$

$$\frac{\Delta\rho}{\rho} = (\frac{\Delta\rho}{\rho})_1 + (\frac{\Delta\rho}{\rho})_2 + \cdots$$

The ability of the forward series to have a direct inverse series derives from (1) the identity among G, G_0, V provided by the scattering equation and then (2) the recognition that the forward series can be viewed as a geometric series for the data, D, in terms of VG_0. The latter derives the direct inverse series for VG_0 in terms of the data.

Viewing the forward problem and series as the Taylor series (7) in terms of Δm doesn't offer a direct inverse series, and hence there is no choice but to solve the forward series in an inverse sense. It is that fact that results in all current AVO and FWI methods being modeling methods that are solved in an inverse sense. Among references that solve a forward problem in an inverse sense in P wave AVO we list Beylkin and Burridge (1990), Boyse and Keller (1986), Burridge et al. (1998), Castagna and Smith (1994), Clayton and Stolt (1981), Foster et al. (2010), Goodway (2010), Goodway et al. (1997),

Shuey (1985), Smith and Gidlow (2000), Stolt (1992), and Stolt and Weglein (1985). The intervention of the explicit relationship among *G*, G_0, and *V* (the scattering equation) in a Taylor series-like form produces a geometric series and a direct inverse solution.

The linear equations are:

$$\begin{pmatrix} \hat{D}^{PP} & \hat{D}^{PS} \\ \hat{D}^{SP} & \hat{D}^{SS} \end{pmatrix} = \begin{pmatrix} \hat{G}_0^P & 0 \\ 0 & \hat{G}_0^S \end{pmatrix} \begin{pmatrix} \hat{V}_1^{PP} & \hat{V}_1^{PS} \\ \hat{V}_1^{SP} & \hat{V}_1^{SS} \end{pmatrix} \begin{pmatrix} \hat{G}_0^P & 0 \\ 0 & \hat{G}_0^S \end{pmatrix} \tag{4.36}$$

$$\hat{D}^{PP} = \hat{G}_0^P \hat{V}_1^{PP} \hat{G}_0^P \tag{4.37}$$

$$\hat{D}^{PS} = \hat{G}_0^P \hat{V}_1^{PS} \hat{G}_0^S \tag{4.38}$$

$$\hat{D}^{SP} = \hat{G}_0^S \hat{V}_1^{SP} \hat{G}_0^P \tag{4.39}$$

$$\hat{D}^{SS} = \hat{G}_0^S \hat{V}_1^{SS} \hat{G}_0^S \tag{4.40}$$

$$\tilde{D}^{PP}\left(k_g, 0; -k_g, 0; \omega\right) = -\frac{1}{4}\left(1 - \frac{k_g^2}{\nu_g^2}\right)\tilde{a}_\rho^{(1)}\left(-2\nu_g\right) - \frac{1}{4}\left(1 + \frac{k_g^2}{\nu_g^2}\right)\tilde{a}_\gamma^{(1)}\left(-2\nu_g\right) + \frac{2k_g^2\beta_0^2}{\left(\nu_g^2 + k_g^2\right)\alpha_0^2}\tilde{a}_\mu^{(1)}\left(-2\nu_g\right) \tag{4.41}$$

$$\tilde{D}^{PS}\left(\nu_g, \eta_g\right) = -\frac{1}{4}\left(\frac{k_g}{\nu_g} + \frac{k_g}{\eta_g}\right)\tilde{a}_\rho^{(1)}\left(-\nu_g - \eta_g\right) - \frac{\beta_0^2}{2\omega^2}k_g\left(\nu_g + \eta_g\right)\left(1 - \frac{k_g^2}{\nu_g\eta_g}\right)\tilde{a}_\mu^{(1)}\left(-\nu_g - \eta_g\right) \tag{4.42}$$

$$\tilde{D}^{SP}\left(\nu_g, \eta_g\right) = \frac{1}{4}\left(\frac{k_g}{\nu_g} + \frac{k_g}{\eta_g}\right)\tilde{a}_\rho^{(1)}\left(-\nu_g - \eta_g\right) + \frac{\beta_0^2}{2\omega^2}k_g\left(\nu_g + \eta_g\right)\left(1 - \frac{k_g^2}{\nu_g\eta_g}\right)\tilde{a}_\mu^{(1)}\left(-\nu_g - \eta_g\right) \tag{4.43}$$

and

$$\tilde{D}^{SS}\left(k_g, \eta_g\right) = \frac{1}{4}\left(1 - \frac{k_g^2}{\eta_g^2}\right)\tilde{a}_\rho^{(1)}\left(-2\eta_g\right) - \left[\frac{\eta_g^2 + k_g^2}{4\eta_g^2} - \frac{2k_g^2}{\eta_g^2 + k_g^2}\right]\tilde{a}_\mu^{(1)}\left(-2\eta_g\right), \tag{4.44}$$

where $a_\gamma^{(1)}$, $a_\mu^{(1)}$, and $a_\rho^{(1)}$ are the linear estimates of the changes in bulk modulus, shear modulus, and density, respectively. The direct quadratic non-linear equations are

$$\begin{pmatrix} \hat{G}_0^P & 0 \\ 0 & \hat{G}_0^S \end{pmatrix}\begin{pmatrix} \hat{V}_2^{PP} & \hat{V}_2^{PS} \\ \hat{V}_2^{SP} & \hat{V}_2^{SS} \end{pmatrix}\begin{pmatrix} \hat{G}_0^P & 0 \\ 0 & \hat{G}_0^S \end{pmatrix}$$
$$= -\begin{pmatrix} \hat{G}_0^P & 0 \\ 0 & \hat{G}_0^S \end{pmatrix}\begin{pmatrix} \hat{V}_1^{PP} & \hat{V}_1^{PS} \\ \hat{V}_1^{SP} & \hat{V}_1^{SS} \end{pmatrix}\begin{pmatrix} \hat{G}_0^P & 0 \\ 0 & \hat{G}_0^S \end{pmatrix}\begin{pmatrix} \hat{V}_1^{PP} & \hat{V}_1^{PS} \\ \hat{V}_1^{SP} & \hat{V}_1^{SS} \end{pmatrix}\begin{pmatrix} \hat{G}_0^P & 0 \\ 0 & \hat{G}_0^s \end{pmatrix}, \quad (4.46)$$

$$\hat{G}_0^P\hat{V}_2^{PP}\hat{G}_0^P = -\hat{G}_0^P\hat{V}_1^{PP}\hat{G}_0^P\hat{V}_1^{PP}\hat{G}_0^P - \hat{G}_0^P\hat{V}_1^{PS}\hat{G}_0^S\hat{V}_1^{SP}\hat{G}_0^P, \quad (4.47)$$

$$\hat{G}_0^P\hat{V}_2^{PS}\hat{G}_0^S = -\hat{G}_0^P\hat{V}_1^{PP}\hat{G}_0^P\hat{V}_1^{PS}\hat{G}_0^S - \hat{G}_0^P\hat{V}_1^{PS}\hat{G}_0^S\hat{V}_1^{SS}\hat{G}_0^S, \quad (4.48)$$

$$\hat{G}_0^S\hat{V}_2^{SP}\hat{G}_0^P = -\hat{G}_0^S\hat{V}_1^{SP}\hat{G}_0^P\hat{V}_1^{PP}\hat{G}_0^P - \hat{G}_0^S\hat{V}_1^{SS}\hat{G}_0^S\hat{V}_1^{SP}\hat{G}_0^P, \quad (4.49)$$

$$\hat{G}_0^S\hat{V}_2^{SS}\hat{G}_0^S = -\hat{G}_0^S\hat{V}_1^{SP}\hat{G}_0^P\hat{V}_1^{PS}\hat{G}_0^S - \hat{G}_0^S\hat{V}_1^{SS}\hat{G}_0^S\hat{V}_1^{SS}\hat{G}_0^S. \quad (4.50)$$

Since $\hat{V}_1^{PP}$ relates to $\hat{D}^{PP}$, $\hat{V}_1^{PS}$ relates to $\hat{D}^{PS}$, and so on, the four components of the data will be coupled in the non-linear elastic inversion. We cannot perform the direct non-linear inversion without knowing all components of the data. Thus, the direct non-linear solution determines the data needed for a direct inverse. That, in turn, defines what a linear estimate means. That is, a linear estimate of a parameter is an estimate of a parameter that is linear in data that can directly invert for that parameter. Since D_{PP}, D_{PS}, D_{SP}, and D_{SS} are needed to determine a_γ, a_μ, and a_ρ directly, a linear estimate for any one of these quantities requires simultaneously solving equations (4.41)-(4.44).

Those direct nonlinear formulas are like the direct solution for the quadratic equation mentioned above and solve directly and nonlinearly for changes in V_p, V_s, and density in a 1D elastic earth. Stolt and Weglein ((2012), Section 7.4, pp. 159-173) present the linear equations for a 3D earth that generalize equations (4.41)-(4.44). Those formulas prescribe precisely what data you need as input, and they dictate how to compute those sought-after mechanical properties. There is no search or cost function, and the unambiguous and unequivocal data needed are full multicomponent data — PP, PS, SP, and SS — for all traces in each of the P and S shot records. The direct algorithm

determines first the data needed and then the appropriate algorithms for using those data to directly compute the sought-after changes in the earth's mechanical properties. Hence, any method that calls itself inversion (let alone full-wave inversion) for determining changes in elastic properties, and in particular the P-wave velocity V_p, and that inputs only P-data, is more off base, misguided, and lost than the methods that sought two or more functions of depth from a single trace. You can model-match P-data until the cows come home, and that takes a lot of computational effort and people with advanced degrees in math and physics computing Frechet derivatives, and requires sophisticated L_P norm cost functions and local or global search engines, so it must be reasonable, scientific, and worthwhile. Why can't we use just PP-data to invert for changes in V_p, V_s, and density, since Zoeppritz says that we can model PP from those quantities, and since we have, using PP-data with angle variation, enough dimension? As I said above, data dimension is good, but not good enough for a direct inversion of those elastic properties. The direct inverse is non-linear. Iterative linear is non-linear. But iterative linear inversion is not in any way equivalent to a direct non-linear inversion. The further evidence that iterative linear inverse is not a direct elastic inverse solution, is that you can iteratively linear invert P wave data. Hence, you can have the fundamentally inadequate data and perform iterative linear updating. That's not possible with a direct inverse method. The framework, data needs, and algorithms provided by direct inversion all matter. If you iteratively linear invert multi-component data, you would not be performing a direct inversion, and your non-linear estimates would not agree with the unique non-linear terms provided by a direct solution. Multi-component data is important, but the direct inverse algorithm of that data is essential. The framework of a direct method helps you understand what will allow things to work in principle, and, equally important, it helps you identify the issue or problem when things don't work. Indirect methods, on the other hand, can never match that definiteness, clarity, and value. When we use just P-wave data with an acoustic or elastic model-matching FWI for shallow-hazard detection or velocity estimation at top salt, and then issues arise, perhaps the framework and requirements described in this note might be items behind a lack of predictive stability and usefulness.

In a paper "Wave theory modeling of P-waves in a heterogeneous elastic medium" (Weglein 2012), a single-channel P-wave formalism is presented as a way to model P-waves in amplitude and phase without needing to model and predict shear waves. This P-only wave-modeling method is intractable as a parameter-estimation inverse procedure, blocked at the first and linear term. That supports the need for all multicomponent data in a direct inverse for estimating changes in the earth's mechanical properties. If one somehow remained insistent that P-data were adequate for a direct elastic inverse, one would have to provide a response to that linear, intractable inverse step. Further, those direct and explicit nonlinear formulas are only

derivable from the direct inverse machinery of the inverse scattering series (please see the references below.)

Using P-wave data with amplitude and phase for an acoustic earth model flies in the face of 40 years of AVO experience, which says that the elastic earth is the minimum realistic earth model for any amplitude-dependent algorithm or processing method. Using P-wave data for an elastic earth model, with algorithms that utilize amplitude and phase, violates the necessary multi-component data needs prescribed by direct inversion of V_p, V_s, and density. Having the adequate data (defined by a direct-inversion framework) is better than not having the necessary and sufficient data and is a good place to start. However, even when one is starting with the indicated multi-component data, the train can still be taken off the track by indirect search and iterative linear-updating algorithms, when direct inverse algorithms are indicated and available. Iterative linear updating of multi-component data is a model-matching indirect method and is never equivalent to a direct inversion of those data.

Some might say in response that P-wave FWI with either an acoustic or elastic medium, followed by use of some search algorithm, represents “an approximation,” and what's wrong with approximations? The answer is precisely that “What IS wrong with the approximation?” If you purposefully or inadvertently ignore (or wish away) the framework and algorithms that a direct solution to the elastic parameter estimation provides, you will never know what you are ignoring and dropping and what your approximation is approximating, nor will you know what value your method actually represents and means, and how you could improve the reliability of your prediction.

In summary, so-called P-wave FWI is something less than advertised and is in general the wrong (acoustic)-earth model, the wrong data, and the wrong method --- but besides that, it has a lot going for it.

In Zhang (2006), the direct elastic inverse was applied to a 4D application and the term beyond linear was able to help distinguish a pressure change from a fluid change. This line of research continued in Xu Li (2011) and H. Liang (2010). This is comparatively illustrated with synthetic log data in Figures 1-6 (from Zhang (2006), pages 95-97).

Epilogue

A direct method to find the route from where you are to where you want to go —- e.g., for a scheduled meeting —- would use MapQuest, while an indirect method would seek and search and stop at every possible location in the city until you arrive somewhere where someone seems to be happy to see you, and you have a toolbox of LP cost functions to define “happy.” A direct solution, in contrast to indirect methods, doesn’t require or ever raise the issue of necessary but insufficient conditions or cost functions,

and it's not a "condition" or property. It's a solution, a construction. Nothing beats that for clarity, efficiency, and effectiveness. The direct MapQuest inversion communication and message to the current indirect P-wave FWI methods is that the latter are searching for the meeting in the wrong city.

The message of this paper is that direct inversion provides a framework, and a set of data requirements and algorithms, that not only have produced a stand-alone capability (with model-type independent algorithms) for removing free-surface and internal multiples, without subsurface information, but also for establishing the requirements for all seismic processing methods that depend on amplitude analysis, such as AVO and so-called FWI. Being frank, we wish these requirements were not the case, because it makes our lives more complicated and difficult — but the conclusions are inescapable. When the framework, data requirements, and direct methods are not satisfied, we have a clear and understandable reason for the resulting failure and for what we might do to provide more reliable and useful predictive capability.

Acknowledgment

I would like to thank the M-OSRP sponsors for their support, and Jim Mayhan, Hong Liang, Di Chang, and Lin Tang for their help in preparing this paper.

References

Anderson, John E., Lijian Tan, and Don Wang. "Time-reversal checkpointing methods for RTM and FWI." *Geophysics* 77, no. 4 (2012): S93-S103.

Baumstein, A., J. E. Anderson, D. L. Hinkley, and J. R. Krebs. "Scaling of the objective function gradient for full wavefield inversion." *79th Annual International Meeting, SEG, Expanded Abstracts,* 2009. 2243–2247.

Beylkin, G., and R. Burridge. "Linearized inverse scattering problem of acoustics and elasticity." *Wave Motion* 12 (1990): 15–22.

Ben-Hadj-ali, H., S. Operto, and J. Vireux. "Velocity model building by 3D frequency-domain, full waveform inversion of wide-aperture seismic data." *Geophysics* 73 (2008): VE101-VE117.

Ben-Hadj-ali, H., S. Operto, and J. Vireux. "Efficient 3D frequency-domain full waveform inversion (FWI) with phase encoding." *71st EAGE Conference & Exhibition,* 2009. P004.

Biondi, B., and P. Sava. "Wave-equation migration velocity analysis." *69th Annual International Meeting, SEG, Expanded Abstracts.* Society of Exploration Geophysicists, 1999. 1723-1726.

Biondi, Biondo, and William W. Symes. “Angle-domain common-image gathers for migration velocity analysis by wavefield-continuation imaging.” *Geophysics* 69 (2004): 1283-1298.

Blum, E. K. *Numerical Analysis and Computation: Theory and Practice.* Reading, Massachusetts: Addison-Wesley Publishing Company, 1972.

Boyse, W. E. and J. B. Keller. “Inverse elastic scattering in three dimensions." *J. Acoust. Soc. Am.* 79 (1986): 215-218.

Brandsberg-Dahl, S., M. de Hoop, and B. Ursin. “Velocity analysis in the common scattering-angle/azimuth domain.” *69th Annual International Meeting, SEG, Expanded Abstracts.* Society of Exploration Geophysicists, 1999. 1715-1718.

Brossier, R., S. Operto, and J. Virieux. “Robust elastic frequency-domain full-waveform inversion using the L1 norm.” *Geophysical Research Letters* 36 (2009): no. 20, L20310.

Burridge, R., M. de Hoop, D. Miller, and C. Spencer. “Multiparameter inversion in anisotropic elastic media.” *Geophysical Journal International* 134 (1998): 757–777.

Castagna, John P. and Steven W. Smith. “Comparison of AVO indicators: A modeling study." *Geophysics* 59 (1994): 1849-1855.

Chavent, G., and C. Jacewitz. “Determination of background velocities by multiple migration fitting.” *Geophysics* 60 (1995): 476–490.

Clayton, R. W. and R. H. Stolt. “A Born-WKBJ inversion method for acoustic reflection data." *Geophysics* 46 (1981): 1559-1567.

Crase, E., A. Pica, M. Noble, J. McDonald, and A. Tarantola. “Robust elastic nonlinear waveform inversion: Application to real data.” *Geophysics* 55 (1990): 527-538.

Ferreira, Andre. Internal multiple removal in offshore Brazil seismic data using the inverse scattering series. Master’s thesis, University of Houston, 2011.

Fitchner, A. *Full seismic waveform modeling and inversion.* Springer-Verlag, 2011.

Foster, Douglas J., Robert G. Keys, and F. David Lane. “Interpretation of AVO anomalies." *Geophysics* 75 no. 5 (2010): 75A3-75A13.

Gauthier, O., A. Tarantola, and J. Virieux. “Two dimensional nonlinear inversion of seismic waveforms.” *Geophysics* 51 (1986): 1387-1403.

Goodway, Bill. “The magic of Lamé." *The Leading Edge* 29 (2010): 1432-1432.

Goodway, Bill, Taiwen Chen, and Jon Downton. “Improved AVO fluid detection and lithology discrimination using Lamé petrophysical parameters; “λρ", “μρ", & “λ/μ fluid stack", from P and S inversions." *67th Annual International Meeting, SEG, Expanded Abstracts.* Society of Exploration Geophysicists, 1997. 183-186.

Guasch, Lluis, Mike Warner, Tenice Nangoo, Jo Morgan, Adrian Umpleby, Ivan Stekl and Nikhil Shah. “Elastic 3D full-waveform inversion.” *82nd Annual International Meeting, SEG, Expanded Abstracts.* Society of Exploration Geophysicists, 2012. 1-5.

Hawthorn, A. “Real Time Sesimic Measurements Whilst Drilling-A Drilling Optimization Measurement for Subsalt Wells." *EAGE Subsalt Imaging Workshop, Cairo, Egypt.* November 2009.

Iledare, O. O. and M. J. Kaiser. Competition and Performance in Oil and Gas Lease Sales and Development in the U.S. Gulf of Mexico OCS Region, 1983-1999. Technical report, U.S. Dept. of the Interior, Minerals Management Service, Gulf of Mexico OCS Region, New Orleans, LA, 2007. OCS Study MMS 2007-034. 106pp.

S. Kapoor, D. Vigh, H. Li and D. Derharoutian. “Full waveform inversion for detailed velocity model building.” *74th Annual Conference and Exhibition, EAGE, Extended Abstracts,* 2012. W011.

Keys, R. G. and A. B. Weglein. “Generalized linear inversion and the first Born theory for acoustic media.” *Journal of Mathematical Physics* 24 (1983) 1444-1449.

Li, X., F. Liu, and A. B. Weglein. “Dealing with the wavelet aspect of the low frequency issue: A synthetic example." *M-OSRP 2010 Annual Meeting*. 2011, 82-89.

Li, Xu. *I. - Multi-parameter depth imaging using the inverse scattering series; II. - Multi-component direct non-linear inversion for elastic earth properties using the inverse scattering series.* PhD thesis, University of Houston, 2011.

Liang, H., A. B. Weglein, and X. Li. “Initial tests for the impact of matching and mismatching between the earth model and the processing model for the ISS imaging and parameter estimation.” *M-OSRP 2009 Annual Meeting.* 2010, 165-180.

Luo, Yi, Panos G. Kelamis, Qiang Fu, Shoudong Huo, Ghada Sindi, Shih-Ying Hsu, and Arthur B. Weglein. “Elimination of land internal multiples based on the inverse scattering series.” *The Leading Edge* 30 (2011): 884–889.

Matson, K. H. *An inverse-scattering series method for attenuating elastic multiples from multi-component land and ocean bottom seismic data.* PhD thesis, University of British Columbia, 1997.

Nolan, C., and W. Symes. “Global solution of a linearized inverse problem for the wave equation.” *Communications on Partial Differential Equations* 22 (1997): 919-952.

Pratt, R. “Seismic waveform inversion in the frequency domain, Part I: Theory and verification in a physical scale model.” *Geophysics* 64 (1999): 888-901.

Pratt, R., and R. Shipp. “Seismic waveform inversion in the frequency domain, Part 2: Fault delineation in sediments using crosshole data.” *Geophysics* 64 (1999): 902–914.

Rickett, J., and P. Sava. “Offset and angle-domain common image-point gathers for shot-profile migration.” *Geophysics* 67 (2002): 883-889.

Sava, P., B. Biondi, and J. Etgen. “Wave-equation migration velocity analysis by focusing diffractions and reflections.” *Geophysics* 70, no. 3 (2005): U19–U27.

Sava, P., and S. Fomel. “Angle-domain common-image gathers by wavefield continuation methods.” *Geophysics* 68 (2003): 1065-1074.

Shuey, R. T. “A simplification of the Zoeppritz equations." *Geophysics* 50 (1985): 609-614.

Sirgue, L., O. I. Barkved, J. P. Van Gestel, O. J. Askim, and J. H. Kommedal. “3D waveform inversion on Valhall wide-azimuth OBC.” *71st Annual Conference and Exhibition, EAGE, Extended Abstracts,* 2009. U038.

Sirgue, L., O. I. Barkved, J. Dellinger, J. Etgen, U. Albertin, and J. H. Kommedal. “Full waveform inversion: the next leap forward in imaging at Valhall.” *First Break* 28 (2010): 65–70.

Sirgue, Laurent, Bertrand Denel and Fuchun Gao. “Challenges and Value of Applying FWI to Depth Imaging Projects.” *74th EAGE Conference and Exhibition incorporating SPE EUROPEC,* 2012.

Smith, George C. and Maurice Gidlow. “A comparison of the fluid factor with λ and μ in AVO analysis." *70th Annual International Meeting, SEG, Expanded Abstracts.* Society of Exploration Geophysicists, 2000. 122-125.

Stolt, R. H. “Seismic inversion revisited." *Geophysical Inversion.* Ed. J. Bee Bednar, L. R. Lines, R. H. Stolt, and A. B. Weglein Proceedings of the Geophysical Inversion Workshop, September 27-29, 1989, Houston, Texas, Society for Industrial and Applied Mathematics, 1992, 3-19.

Stolt, R. H. and A. B. Weglein. “Migration and inversion of seismic data." *Geophysics* 50 (1985): 2458-2472.

Stolt, Robert H. and Arthur B. Weglein. *Seismic Imaging and Inversion, Volume 1.* Cambridge University Press, 2012.

Symes, W. “Migration velocity analysis and waveform inversion.” *Geophysical Prospecting* 56 (2008): 765-790.

Symes, W. W., and J. J. Carazzone. “Velocity inversion by differential semblance optimization.” *Geophysics* 56 (1991): 654–663.

Tarantola, A. “A strategy for nonlinear elastic inversion of seismic reflection data.” *Geophysics* 51 (1986): 1893–1903.

Tarantola, A. *Inverse problem theory: Method for data fitting and model parameter estimation.* Elsevier Science, 1987.

Taylor, John R. *Scattering theory: the quantum theory of nonrelativistic collisions.* John Wiley & Sons, Inc., 1972.

Vigh, D., and E. W. Starr. “3D prestack plane-wave, full-waveform inversion.” *Geophysics* 73, no.5 (2008): VE135–VE144.

Weglein, Arthur B. “Short note: An alternative adaptive subtraction criteria (to energy minimization) for free surface multiple removal." *M-OSRP 2011 Annual Report.* 2012, 375.

Weglein, Arthur B. “Short note: A formalism for (1) modeling the amplitude and phase of pressure waves from a heterogeneous elastic medium and (2) selecting and predicting P-wave events that have only experienced pressure-wave episodes in their history." *M-OSRP 2011 Annual Report.* 2012, 364-3705.

Weglein, Arthur B., Shih-Ying Hsu, Paolo Terenghi, Xu Li, and Robert H. Stolt. “Multiple attenuation: Recent advances and the road ahead (2011).” *The Leading Edge* 30 (2011): 864–875.

Weglein, Arthur B., Fang Liu, Xu Li, Paolo Terenghi, Ed Kragh, James D. Mayhan, Zhiqiang Wang, Joachim Mispel, Lasse Amundsen, Hong Liang, Lin Tang, and Shih-Ying Hsu. “Inverse scattering series direct depth imaging without the velocity model: first field data examples.” *Journal of Seismic Exploration* 21 (2012): 1-28.

Weglein, Arthur B., Haiyan Zhang, Adriana C. Ramirez, Fang Liu, and Jose Eduardo M. Lira. “Clarifying the underlying and fundamental meaning of the approximate linear inversion of seismic data.” *Geophysics* 74, no. 6 (November-December 2009): WCD1–WCD13.

Weglein, A. B. and K. Matson. “Inverse-scattering interval multiple attenuation: an analytic example and subevent interpretation.” *Mathematical Methods in Geophysical Imaging (Proc. SPIE vol. 3453)* ed. S. Hassanzadeh (Bellingham, WA: SPIE) (1998): 1008–1017.

Weglein, A. B., F. V. Araújo, P. M. Carvalho, R. H. Stolt, K. H. Matson, R. T. Coates, D. Corrigan, D. J. Foster, S. A. Shaw, and H. Zhang. “Inverse Scattering Series and Seismic Exploration." *Inverse Problems* 19 (2003): R27-R83.

Weglein, A. B., D. J. Foster, K. H. Matson, S. A. Shaw, P. M. Carvalho, and D. Corrigan. “Predicting the correct spatial location of reflectors without knowing or determining the precise medium and wave velocity: initial concept, algorithm and analytic and numerical example." *Journal of Seismic Exploration* 10 (2002): 367-382.

Valenciano, A., B. Biondi, and A. Guitton. “Target-oriented wave-equation inversion.” *Geophysics* 71, no.4 (2006): A35–A38.

Zhang, Haiyan. *Direct non-linear acoustic and elastic inversion: towards fundamentally new comprehensive and realistic target identification.* PhD thesis, University of Houston, 2006.

Zhang, Y., and B. Biondi. “Moveout-based wave-equation migration velocity analysis.” *Geophysics* 78, no. 2 (2013): U31-U39.

Zhou, Hongbo, Lasse Amundsen, and Guanquan Zhang. “Fundamental Issues in Full Waveform Inversion.” *82nd Annual International Meeting, SEG, Expanded Abstracts.*

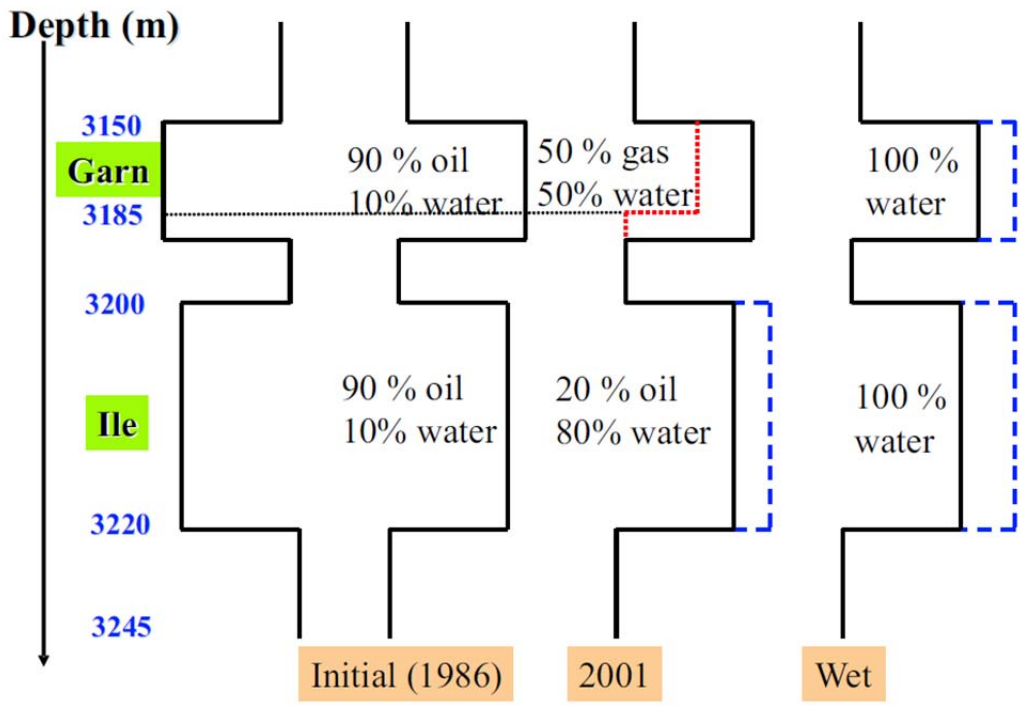

Figure 1. *Schematic of the synthetic well log A-52.*

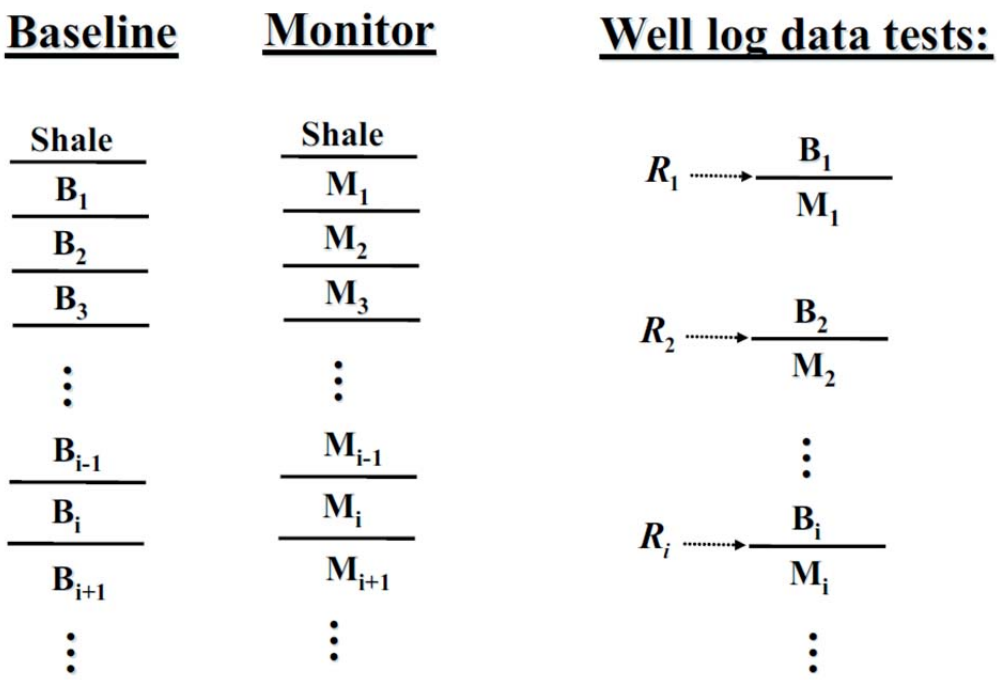

Figure 2. *Schematic of the baseline, monitor and input reflection coefficients.*

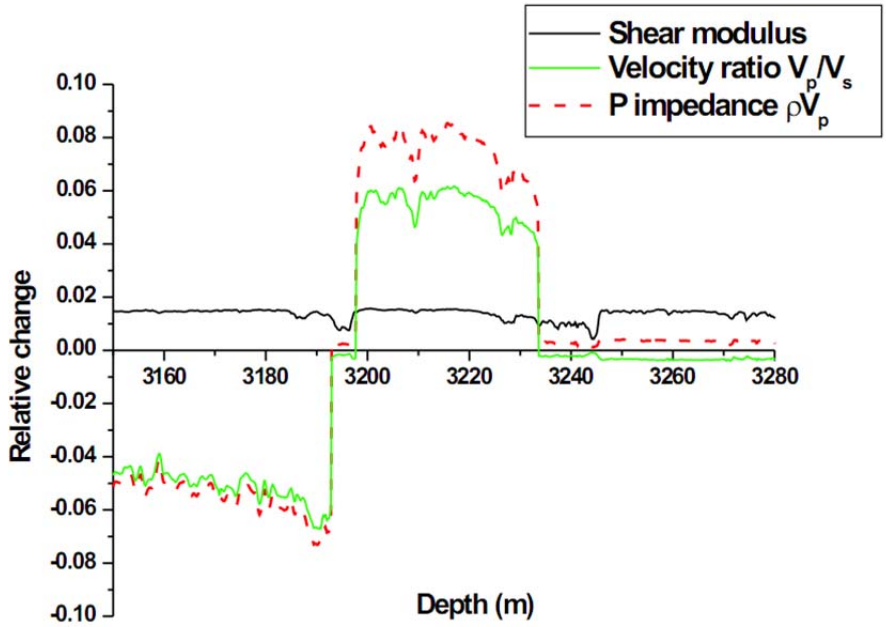

Figure 3. *Comparison of actual changes in shear modulus, P-impedance and velocity ratio Vp/Vs. The baseline is the log data in 1986 and the monitor is the log data in 2001.*

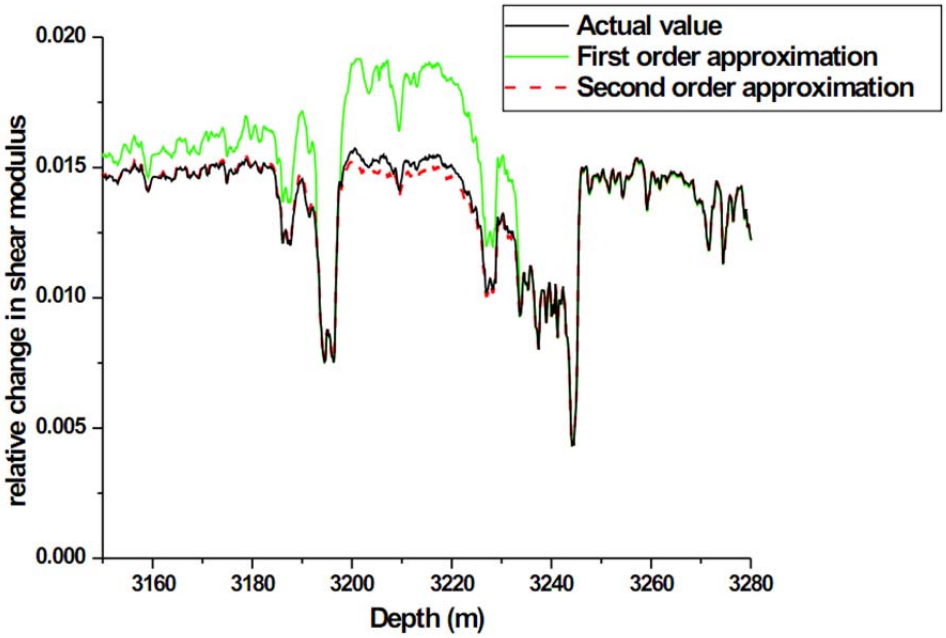

Figure 4. *Comparison of first and second order approximation of relative change in shear modulus. The baseline is the log data in 1986 and the monitor is the log data in 2001.*

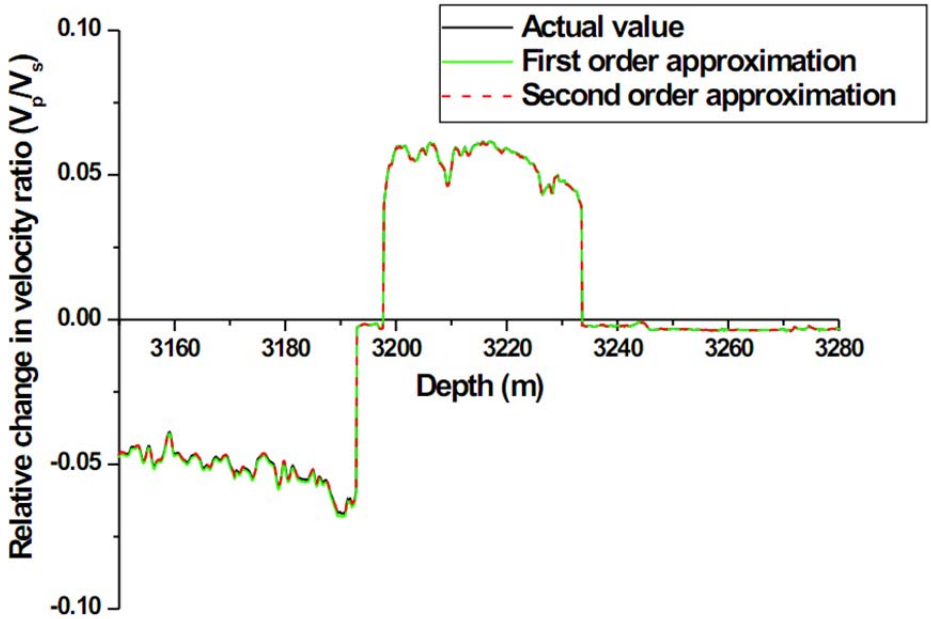

Figure 5. *Comparison of first and second order approximation of relative change in Vp/Vs. The baseline is the log data in 1986 and the monitor is the log data in 2001.*

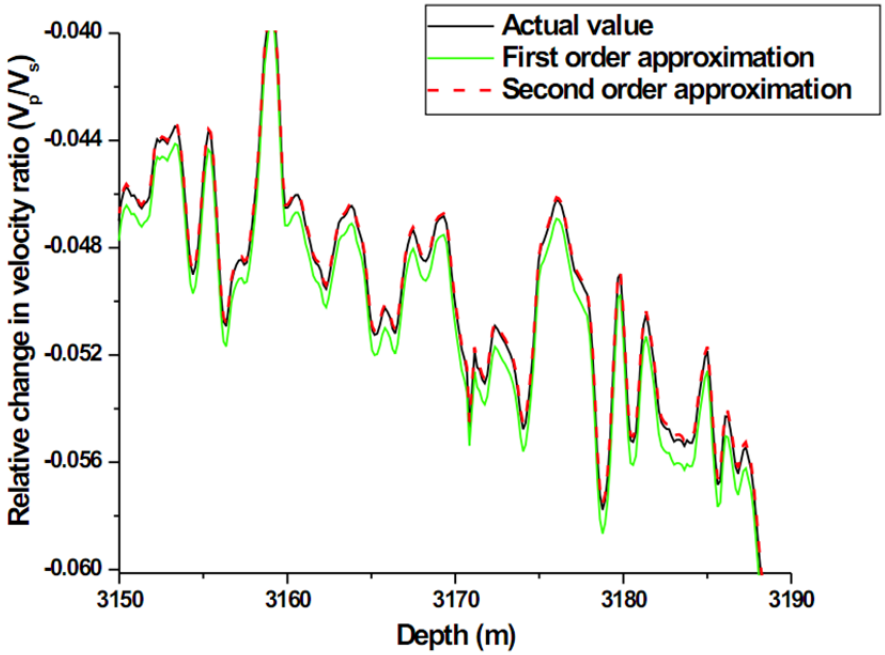

Figure 6. *Zoomed in comparison of first and second order approximation of relative change in Vp/Vs. The baseline is the log data in 1986 and the monitor is the log data in 2001.*

Wavelet estimation and wavefield reconstruction in elastic media, without a subsurface model

Tao Jiang[1], Paolo Terenghi[2], Arthur B Weglein[2]

1:Department of Earth and Atmospheric Sciences, University of Houston, 77004 taojus@gmail.com

2:Department of Physics, University of Houston, 77004, USA

ABSTRACT

The wavelet estimation algorithm in elastic media, which is derived from the displacement wave equation and Green's theorem, is analyzed and then written in component form for direct application. The elastic formulation of Green's theorem provides an algorithm for reconstruction of the direct arrival (or reference wave) and of the scattered field of an elastic seismic experiment, without requiring knowledge of propagation velocities or density. The source wavelet can then be estimated by dividing the reference wave by the analytic Green's dyadic. The input to this algorithm includes the x, y, and z components of the displacement wavefield and their respective spatial derivatives. Initial numerical experiments indicate that: (a) If all the input quantities are available, the reference field is correctly reconstructed below the receivers and the estimated wavelet is precise in phase and amplitude; (b) If only the z-component of the data is available, the wavelet obtained is less accurate in amplitude but is still satisfactory in phase and shape.

Key words: wavelet, elastic media, Green's dyadic tensor

INTRODUCTION

The signature of the source is a fundamental ingredient of many classic problems in exploration seismology. For example, a reliable knowledge of the source signature is required in many data-driven methods that are based on the feedback model (Berkhout and Verschuur, 2005; Verschuur and Berkhout, 2005) and on the inverse scattering series (Araujo et al, 1994; Carvalho and Weglein, 1994; Weglein, et al., 1997; Weglein, et al., 2003) and are used for the removal of free-surface and internal multiples. Within the context of seismic imaging, the source signature (wavelet) is the quantity that most directly determines our ability to obtain highly resolved images of the subsurface. Ultimately, for the purposes of time-lapse analysis and inversion, compensation for the source footprint, and for other characteristics of the particular experimental device being employed, is the key to determination of the indicators and parameters that are sought.

Weglein and Secrest (1990) published a multidimensional, wave-theory method to estimate the source signature directly from seismic recordings, which requires no information on the subsurface. The procedure is based on the Green's theorem and has both an acoustic and an elastic formulation. The elastic approach is based on the elastic formulation of Green's theorem introduced by Pao and Varatharajulu (1976).

In both the acoustic case and the elastic case, the method consists of two steps:

1. Determination of the reference wavefield (the wavefield as it would be if the experiment were carried out in the reference medium), and
2. Extraction of the wavelet through a division by the relevant Green's function.

While acoustic (marine) applications of the Green's theorem have been known for several years and have produced several useful algorithms, such as multiple attenuation (Fokkema and van den Berg, 1993; Amundsen, 2001), wavefield separation, deghosting, and wavelet estimation (Zhang and Weglein, 2005; Zhang and Weglein, 2006; Mayhan et al., 2011), the potential of its elastic counterpart has yet to be carefully analyzed and accomplished. One reason for that disparity certainly resides in the innate complexity of the elastic wave theory, and above all in the large number of measurements a practical experiment would require (12 different types of wavefield measurements).

This paper documents the initial results of an effort to (1) implement in a computer code the elastic wavelet-estimation method published in Weglein and Secrest (1990), (2) evaluate the strictness of the theoretical requirement all of the 12 wavefield measurements, and (3) ultimately, determine whether useful results can be achieved if just the wavefield quantities that are routinely acquired in offshore seismic exploration are available.

Methodology

Green's dyadic for elastic motion equations

The displacement equation of motion in isotropic and homogeneous elastic media is written in the frequency domain as equation 7 in the work of Pao and Varatharajulu (1976), for the case in which only steady-state waves are considered. It is

$$[(\lambda+\mu)\nabla\nabla\cdot+\mu\nabla^2]\vec{u}(\vec{x},\omega)+\rho\omega^2\vec{u}(\vec{x},\omega)=-\rho\vec{f}(\vec{x},\omega)\,. \quad (1)$$

Here, λ and μ are Lamé constants, $\vec{u}$ is the vector displacement field, ρ is density, ω is the circular frequency, and $\vec{f}$ is the body force per unit mass. We can rewrite Eq.1 in such a way that P- and S-wave motions are decoupled, which can only be done under an assumption of isotropy and homogeneity:

$$(\lambda+2\mu)\nabla(\nabla\cdot\vec{u})-\mu\nabla\times(\nabla\times\vec{u})+\rho\omega^2\vec{u}=-\rho\vec{f}, \quad (2)$$

and further,

$$C_p^2\nabla(\nabla\cdot\vec{u})-C_s^2\nabla\times(\nabla\times\vec{u})+\omega^2\vec{u}=-\vec{f}\,, \quad (3)$$

where C_p and C_s are the P- and S-wave velocities, $C_p^2=\sqrt{(\lambda+2\mu)/\rho}$; and $C_s^2=\sqrt{\mu/\rho}$.

Constructed to solve Eq.2, the Green's dyadic satisfies the dyadic equation:

$$[(\lambda+2\mu)\nabla\nabla\cdot-\mu\nabla\times\nabla\times]\overline{\overline{\boldsymbol{G_{mn}}}}(\vec{r},\vec{r}',\omega)+\rho\omega^2\overline{\overline{\boldsymbol{G_{mn}}}}(\vec{r},\vec{r}',\omega)=-\bar{\bar{\boldsymbol{I}}}\delta(\vec{r}-\vec{r}') \quad (4)$$

where $\bar{\bar{\boldsymbol{I}}}$ is the unit dyadic $\begin{bmatrix} 1 & & \\ & 1 & \\ & & 1 \end{bmatrix}$. The Cartesian index $m, n = 1,2\ or\ 3$, which represents the direction in the Cartesian coordinate system. $\overline{\overline{\boldsymbol{G_{mn}}}}$ is the dyadic Green's displacement tensor, which describes the **n**th-component vector-displacement field at observation point $\vec{r}$ caused by the **m**th-component of the source at point $\vec{r}'$, and $\delta(\vec{r} - \vec{r}')$ is the 3D Dirac delta function: $\int \delta(\vec{r} - \vec{r}')f(\vec{r})d\vec{r} = f(\vec{r} = \vec{r}')$.

The solution of the elastic wave equation 2 is the vector displacement field $\vec{u}$, which can be written using Green's dyadic in the frequency domain:

$$u_n(\vec{r}, \omega) = \iiint_{\infty} G_{mn}(\vec{r}, \vec{r}', \omega)[-\rho f_m(\vec{r}', \omega)]\mathrm{d}\vec{r}'. \quad (5)$$

Following Morse and Feshbach (1953), we can construct the Green's dyadic $\overline{\overline{\boldsymbol{G_{mn}}}}$ as the sum of a P-wave term and an S-wave term, as follows:

$$\overline{\overline{\boldsymbol{G_{mn}}}} = \overline{\overline{\boldsymbol{G_p}}} + \overline{\overline{\boldsymbol{G_s}}} \quad , \quad (6)$$

where $\overline{\overline{\boldsymbol{G_p}}}$ and $\overline{\overline{\boldsymbol{G_s}}}$ satisfy the following two equations, respectively:

$$(\lambda + 2\mu)\nabla\nabla \cdot \overline{\overline{\boldsymbol{G_p}}}(\vec{r}, \vec{r}', \omega) + \rho\omega^2\overline{\overline{\boldsymbol{G_p}}}(\vec{r}, \vec{r}', \omega) = -\bar{\bar{\boldsymbol{I}}}_{\boldsymbol{p}}\delta(\vec{r} - \vec{r}') \quad (7a)$$

and

$$-\mu\nabla \times \nabla \times \overline{\overline{\boldsymbol{G_s}}}(\vec{r}, \vec{r}', \omega) + \rho\omega^2\overline{\overline{\boldsymbol{G_s}}}(\vec{r}, \vec{r}', \omega) = -\bar{\bar{\boldsymbol{I}}}_{\boldsymbol{s}}\delta(\vec{r} - \vec{r}') \ , \quad (7b)$$

where $\overline{\overline{\boldsymbol{I}}} = \overline{\overline{\boldsymbol{I}}}_{\boldsymbol{p}} + \overline{\overline{\boldsymbol{I}}}_{\boldsymbol{s}}$, and the delta function contains two components, which means that both a P-wave and an S-wave are generated by the point source.

In Eq. 7a, $\overline{\overline{\boldsymbol{G_p}}}$ is made to generate only a P-wave; thus $-\mu\nabla\times\nabla\times\overline{\overline{\boldsymbol{G_p}}} = 0$. Also, in Eq. 7b, $\overline{\overline{\boldsymbol{G_s}}}$ is made to generate only an S-wave; thus $(\lambda+2\mu)\nabla\nabla\cdot\overline{\overline{\boldsymbol{G_s}}} = 0$, so that the P- wave and S-wave are decoupled. The full wave equation 4 is the sum of P-wave equation 7a and S-wave equation 7b.This decoupling of P- and S-waves only exists in isotropic and homogeneous media in which the stiffness tensor has just two independent components: λ and μ.

Using the identities: $\nabla\times(\nabla a) = 0$ for any scalar field a and $\nabla\cdot\left(\nabla\times\vec{b}\right) = 0$ for any vector field $\vec{b}$, we can construct the forms of $\overline{\overline{\boldsymbol{G_p}}}$ and $\overline{\overline{\boldsymbol{G_s}}}$ from the basic Green's function g_p and $g_s$of the scalar wave equation for vector wave equations:

$$\overline{\overline{\boldsymbol{G_p}}}(\vec{r},\vec{r}',\omega) = \frac{1}{(\lambda+2\mu)}\frac{1}{k_p^2}\left[\nabla g_p\nabla' - \overline{\overline{\boldsymbol{I}}}_{\boldsymbol{p}}\delta(\vec{r}-\vec{r}')\right]$$

$$= \frac{1}{\rho C_p^2}\left[\frac{1}{k_p^2}\sum_{m,n=1}^{3}\hat{\boldsymbol{e}}_{\boldsymbol{m}}\hat{\boldsymbol{e}}_{\boldsymbol{n}}\frac{\partial}{\partial x_m}\frac{\partial}{\partial x_n'}g_p - \frac{1}{k_p^2}\overline{\overline{\boldsymbol{I}}}_{\boldsymbol{p}}\delta(\vec{r}-\vec{r}')\right] \qquad (8a)$$

and

$$\overline{\overline{\boldsymbol{G_s}}}(\vec{r},\vec{r}',\omega) = \frac{1}{\mu}\frac{1}{k_s^2}\left[\nabla\times\left(\overline{\overline{\boldsymbol{I}}}g_s\right)\times\nabla' - \overline{\overline{\boldsymbol{I}}}_{\boldsymbol{p}}\delta(\vec{r}-\vec{r}')\right]$$

$$= \frac{1}{\rho C_s^2}\left[-\frac{1}{k_s^2}\sum_{m,n=1}^{3}\hat{\boldsymbol{e}}_{\boldsymbol{m}}\hat{\boldsymbol{e}}_{\boldsymbol{n}}\frac{\partial}{\partial x_m}\frac{\partial}{\partial x_n'}g_s - \frac{1}{k_s^2}\overline{\overline{\boldsymbol{I}}}\nabla^2 g_s - \frac{1}{k_s^2}\overline{\overline{\boldsymbol{I}}}_{\boldsymbol{s}}\delta(\vec{r}-\vec{r}')\right] \quad . \qquad (8b)$$

Here k_p and k_s are the wavenumbers of P-waves and S-waves, respectively, and g_p and g_s are Green's functions that satisfy $(\nabla^2 + k^2)g_{p,s} = -\delta$.

For a 3D medium, they can be shown to be (P.1433, Morse and Feshback, 1953):

$$g_{p,s} = \frac{e^{ik_{p,s}r}}{4\pi r} \quad . \tag{9}$$

For those field points not at the source ($\vec{r} \neq \vec{r}'$), the deltas in 8a and 8b evaluate to zero: $\bar{\bar{\boldsymbol{I}}}\delta = \bar{\bar{\boldsymbol{I}}}_{\boldsymbol{p}}\delta = \bar{\bar{\boldsymbol{I}}}_{\boldsymbol{s}}\delta = 0$.

Also, because $\nabla^2 g_s = -k^2 g_s - \delta$; $\frac{1}{C_p^2}\frac{1}{k_p^2} = \frac{1}{C_s^2}\frac{1}{k_s^2} = \frac{1}{\omega^2}$; and $\frac{\partial}{\partial x_n} = -\frac{\partial}{\partial x_n'}$, the Green's dyadic is written as:

$$\overline{\overline{\boldsymbol{G_{mn}}}} = \overline{\overline{\boldsymbol{G_p}}} + \overline{\overline{\boldsymbol{G_s}}} = \frac{1}{4\pi\rho\omega^2}\left[\delta_{mn}k_s^2\frac{exp(ik_s r)}{r} - \frac{\partial}{\partial x_m}\frac{\partial}{\partial x_n}\left(\frac{exp(ik_p r)}{r} - \frac{exp(ik_s r)}{r}\right)\right]. \tag{10}$$

Figure 1 shows the wavefields generated by convolving a Ricker wavelet with the analytic forms $\overline{\overline{\boldsymbol{G_{mn}}}}$, $\overline{\overline{\boldsymbol{G_p}}}$, and $\overline{\overline{\boldsymbol{G_s}}}$ to demonstrate the effectiveness and accuracy of this type of expression of Green's dyadic tensor. The P- and S-wavefields are decoupled using $\overline{\overline{\boldsymbol{G_p}}}$ and $\overline{\overline{\boldsymbol{G_s}}}$, as expected. $\overline{\overline{\boldsymbol{G_{mn}}}}$'s form will be used for $\overline{\overline{\boldsymbol{G_0}}}$ as the reference Green's function later. It can be seen that the horizontal components of the wavefield associated with $\overline{\overline{\boldsymbol{G_p}}}$ exhibit the characteristic polarity change while they are moving from one side of the source to the other. Similar behavior can be observed for $\overline{\overline{\boldsymbol{G_s}}}$.

Algorithm of wavefield extinction in elastic media

The extinction theorem (Weglein and Secrest, 1990) is

$$\rho c_p^2 \oint_S \left[\left(\overline{\overline{\boldsymbol{G_0}}}(r,r')\cdot\hat{n}'\right)\left(\nabla'\cdot\boldsymbol{u}(r',r_s)\right)-\left(\nabla'\cdot\overline{\overline{\boldsymbol{G_0}}}\right)(\boldsymbol{u}\cdot\hat{n}')\right]ds'$$

$$-\rho c_s^2 \oint_S \left[\overline{\overline{\boldsymbol{G_0}}}\cdot(\hat{n}'\times\nabla'\times\boldsymbol{u})+\left(\nabla'\times\overline{\overline{\boldsymbol{G_0}}}\right)\cdot(\hat{n}'\times\boldsymbol{u})\right]ds'$$

$$=\begin{cases} reference\ field, & r\ in\ V\ (or\ below\ receivers) \\ scattered\ field, & r\ out\ V\ (or\ above\ receivers) \end{cases}, \qquad (11)$$

where r_s is the source location, r' is receiver location and the integral variable, and r is the evaluation location where the reconstructed field is calculated. The term $\hat{n}'$ is the unit vector pointing outwards and normal to the surface, and it describes how the Green's theorem can be utilized to selectively isolate certain portions of the seismic wavefield without knowing the properties of the actual earth.

As shown in Figure 2, a surface integral over S surrounding volume V is calculated to reconstruct the reference field when the evaluation point r is chosen inside V, or to reconstruct the scattered field when the evaluation point r is chosen outside V. The volume V surrounded by S is the hemisphere extending to infinity and bounded by the receiver plane at the top. When the hemisphere extends to infinity, we can see from Eq.10 that the Green's dyadic on its surface approaches 0, therefore the surface integral over S reduces to the surface integral only over the receiver plane S_0. In this case, the directional vector $\hat{n}' = [0,0,-1]$, thus Eq.11 can be simplified as Eq.11a:

$$\rho c_p^2 \int\limits_{S0} \left\{ \begin{bmatrix} -G_{13} \\ -G_{23} \\ -G_{33} \end{bmatrix} \left(u_{1,1'} + u_{2,2'} + u_{3,3'}\right) - \begin{bmatrix} G_{11,1'} + G_{12,2'} + G_{13,3'} \\ G_{21,1'} + G_{22,2'} + G_{23,3'} \\ G_{31,1'} + G_{32,2'} + G_{33,3'} \end{bmatrix} (-u_3) \right\} dx'dy'$$

$$-\rho c_s^2 \int\limits_{S0} \left[\boldsymbol{G_{mn}} \cdot \begin{bmatrix} u_{1,3'} - u_{3,1'} \\ u_{2,3'} - u_{3,2'} \\ 0 \end{bmatrix} + (\nabla' \times \boldsymbol{G_{mn}}) \cdot \begin{bmatrix} u_2 \\ -u_1 \\ 0 \end{bmatrix} \right] dx'y'$$

$$= \begin{cases} reference\ field, & r\ in\ V\ (or\ below\ receivers) \\ scattered\ field, & r\ out\ V\ (or\ above\ receivers) \end{cases} . \qquad (11a)$$

Finally, we can obtain the wavefield-extinction algorithm in vector component form:

$$\rho c_p^2 \int\limits_{S0} \begin{bmatrix} -G_{13}\left(u_{1,1'} + u_{2,2'} + u_{3,3'}\right) + \left(G_{11,1'} + G_{12,2'} + G_{13,3'}\right)u_3 \\ -G_{23}\left(u_{1,1'} + u_{2,2'} + u_{3,3'}\right) + \left(G_{21,1'} + G_{22,2'} + G_{23,3'}\right)u_3 \\ -G_{33}\left(u_{1,1'} + u_{2,2'} + u_{3,3'}\right) + \left(G_{31,1'} + G_{32,2'} + G_{33,3'}\right)u_3 \end{bmatrix} dx'dy'$$

$$-\rho c_s^2 \int\limits_{S0} \begin{bmatrix} G_{11}\left(u_{1,3'} - u_{3,1'}\right) + G_{12}\left(u_{2,3'} - u_{3,2'}\right) + \left(G_{22,3'} - G_{32,2'}\right)u_1 + \left(G_{31,2'} - G_{21,3'}\right)u_2 \\ G_{21}\left(u_{1,3'} - u_{3,1'}\right) + G_{22}\left(u_{2,3'} - u_{3,2'}\right) + \left(G_{32,1'} - G_{12,3'}\right)u_1 + \left(G_{11,3'} - G_{31,1'}\right)u_2 \\ G_{31}\left(u_{1,3'} - u_{3,1'}\right) + G_{32}\left(u_{2,3'} - u_{3,2'}\right) + \left(G_{12,2'} - G_{22,1'}\right)u_1 + \left(G_{21,1'} - G_{11,2'}\right)u_2 \end{bmatrix} dx'y'$$

$$= \begin{cases} reference\ field, & r\ in\ V\ (or\ below\ receivers) \\ scattered\ field, & r\ out\ V\ (or\ above\ receivers) \end{cases} \qquad (11b)$$

The indices 1,2,3 indicate the x,y,z axes, respectively. The index after the comma indicates the direction that is taken by the spatial derivative with respect to, for example, $u_{1,2'} = \frac{\partial U_x}{\partial y'}$. All the derivatives are over the components x_i' of the integration variable r' on the receiver plane. Notice that here Green's dyadic $\overline{\overline{\boldsymbol{G_0}}}(r, r')$ is a function of r and r', and the displacement field $\boldsymbol{u}(r', r_s)$ is a function of r' and r_s.

Both the extinction and wavelet extraction algorithms require knowledge of a reference medium, which defines $\boldsymbol{G_0}$. The reference medium is defined as the simplest

medium that agrees with the actual earth at and near the locations where the field and its derivatives are measured. In marine seismic exploration, its properties are readily identified with those of seawater. Consequently, the reference medium can largely be considered to be acoustic and homogeneous, and the algorithm can be simply evaluated using analytical methods.

Onshore, determination of the reference (elastic) medium may certainly be more difficult. However, at the early stage of this research, we choose not to address that problem directly: within the rest of this document the reference medium is assumed to be a homogeneous elastic half space with known properties (Vp, Vs,ρ).

Wavelet estimation using the wavefield extinction algorithm in elastic media

When r is chosen inside V (Fig.2) or below receivers (Fig.3, left side), Eq.11b can be used to calculate the reference wavefield at r, as if the wave had gone through the reference medium without scattering. In the reference medium, the vector wavefield of 3-component displacement can also be written as the product of a wavelet (source signature) and the Green's dyadic tensor,

$$A(\omega, r_s)G_0(r, r_s) = U_{ref}(r, r_s). \tag{12}$$

The power of the extinction theorem is that the simplest reference medium can be chosen as long as it agrees with the real medium where the fields and their derivatives are measured. Therefore, the Green's dyadic solution of a whole-space isotropic

homogeneous medium Eq.10 can be chosen as the value of Green's tensor in a reference medium.

Next, if the nature of the body force at the source is known, the wavelet estimation algorithm can be directly obtained from Eq.11b. From here onwards, we make an assumption that the source wavelet only acts along the z-direction. In other words, it is a directional force applied at the source point in the vertical direction. Therefore the z-component of the reference field equals the product of the wavelet and the reference Green's dyadic component G_{33}. Under that assumption, the algorithm of vertical wavelet estimation in elastic media can be written as:

$$A(\omega) = \frac{1}{G_{33}(r, r_s)} \left\{ \rho c_p^2 \int_S \left[-G_{33}\left(u_{1,1'} + u_{2,2'} + u_{3,3'}\right) + \left(G_{31,1'} + G_{32,2'} + G_{33,3'}\right) u_3 \right] ds' \right.$$

$$\left. -\rho c_s^2 \int_S \left[-G_{11} u_{3,1'} - G_{12} u_{3,2'} + G_{13}\left(u_{1,1'} + u_{2,2'}\right) + \left(G_{12,2'} - G_{22,1'}\right) u_1 + \left(G_{21,1'} - G_{11,2'}\right) u_2 \right] ds' \right\} \tag{13}$$

The RHS of Eq.13 inside the brace is the z-component of the surface integral in Eq.11b. The Cartesian indices 1,2,3 indicate the x,y,z axes, respectively. The index after the comma indicates the direction that is taken by the spatial derivative with respect to. for instance, $U_{1,2} = \frac{\partial U_x}{\partial y}$. The wavelet will be obtained from this algorithm.

If the volume force is along a direction other than z, a circular symmetry rule can always be used to change the indices (1->2->3->1) in all the terms in Eq.13, to obtain an

expression that is a suitable algorithm for wavelet estimation in the desired source direction.

DESIGN AND RESULTS OF NUMERICAL TESTS

Three different tests have been designed to check the accuracy and potential of the algorithm in different circumstances. The model is an isotropic and homogeneous elastic medium without a free surface above and without scattering. The common parameters used in these tests are listed in Table 1.

From Figure 2 we know already that the surface integral in the algorithm of Eq.13 can be approximated as the integral over the receiver plane S_{xy} topping the volume V. The source is located at $(1000m, 1000m, 50m)$, 150m above the receivers. The receivers are in the plane S_{xy} at a depth of $200m$. Evaluation of Eq 13 is performed at a depth of 100m for tests above receivers, and at a depth of 300m for tests below receivers. In both cases, the evaluation is performed in the vertical plane containing the source. To compare with the reference field for all offsets, we output the reconstructed field of all 201 evaluation points at the same depth along the line y=1000m. The reference fields are also calculated with the analytic Green's dyadic. Figure 3 shows the experimental configurations for tests above and below the receivers. At each single evaluation point (black circle in Figure 3), the surface integral over S can output the reconstructed fields. Therefore it is possible to obtain an arbitrary number of estimated wavelets. Averaging the wavelet from all estimations will significantly increase the accuracy and reduce the numerical noise.

The data sets we choose for these early tests are generated from the product of the Green's dyadic $G_{mn}(r', r_s)$ and the source wavelet $A(\omega)$, which the algorithm will try to recover, on the basis of the assumption that the initial pulse was given by a force in the z-direction.

In the same way as above, except this time using $G_{mn}(r, r_s)$ instead of $G_{mn}(r', r_s)$, we also generate a "reference" dataset to be compared with the outcome of the braced expression in Eq.13. The profiles of the reference displacement fields at a depth of 300m are shown in the left column of Figure 1.

Test 1: full data, full Green's dyadic

In the first test, we input all the required data, which are 12 fields ($U_i \; and \; U_{i,j}; i, j = 1,2,3$), including all the components of the displacement field and all three spatial derivatives of each. The full analytic Green's dyadic is used. The test parameters are identical to those listed in Table 1.

Eq.11 suggests that when we are evaluating below the receivers, the reconstructed fields are equal to the reference wavefields, which is shown in the left column of Figure 1, and when we are evaluating above the receivers, the reconstructed fields are equal to the scattered wavefields, which is zero because our homogeneous model doesn't have any scattering. Let's find out by outputting the surface integral for 201 evaluation points along one line.

Figure 4 shows the resulting traces reconstructed below the receivers, in which each trace is the one estimated from the surface integral for one evaluation point. In theory, the reconstructed fields below the receivers should be equal to the reference fields, as shown in the left column of Figure 1. After comparing the two sets of figures, we can state that the arrivals of the P-wave and the S-wave are precisely the same in amplitude, phase, and time. Some noise can be seen near the boundaries. There are several reasons to consider. First, this test only calculates the surface integral in a finite area, and the numerical grids are very sparse, so truncation at the edge of receivers will cause noise. Second, we notice that the integral is calculated in the frequency domain, so a short FFT length can also cause this kind of aliasing error. This error is very small in amplitude compared with that of the wave arrivals, so its effect can be neglected when we estimate the wavelet. Averaging over many estimation results will further reduce the effects of this error.

Now we have the reconstructed reference wavefields, so that from Eq.13 we can divide the reference fields by the Green's dyadic in the reference media to obtain the wavelet. The wavelet used to generate our data is shown in Figure 5a. The wavelet estimated from the reconstruction below the receivers is shown in Figure 5b.

Table 2 presents the real wavelet and the estimated wavelet, side by side, for every time sample. It clearly shows that the similarity between the estimated wavelet and the real wavelet is higher than 97.6% from the 20th sample to the 41st sample. The

amplitude of the wavelet beyond this range is very small and can be considered to be zero. The algorithm of Eq.13 works very well in this situation.

Next, let's reconstruct the field above the receivers. A zero field is expected because the scattered field in our model is zero. The evaluation points are at a depth of 100m, and all the other parameters remain the same as the case below the receivers. The x- and z-components of displacement fields for reconstruction above the receivers are shown in Figure 6.

From Figure 6, it is obvious that the main wavefields vanish. The residue is the same boundary error as is shown in Figure 4. The amplitude of the residue in Figure 6 is identical to that in Figure 4. Therefore it can be neglected for the same reason.

The estimated wavelet above the receivers is given in Figure 7. Notice that the maximum amplitude of the estimation above the receivers falls into the order of 10^{-4}, so that the estimation is negligible when displayed beside the estimation below the receivers. This amount of error is expected when we analyze the error around boundaries.

To further understand how the surface integral vanishes above and accumulates below receivers, we display the integrand function for one estimation point for both cases. In Figure 8, the integrand function is shown for evaluation point $(1400,1000,300)$, below the receivers.

In Figure 9, the integrand function is shown for evaluation point $(1400,1000,100)$, above the receivers. The polarity reversal of integrand functions is indicated by arrows. After summing the integrand functions for all receivers, we can see that the surface integral accumulates below receivers and vanishes above receivers. In both cases, the cross-terms will cancel in the surface integral.

Test 2: only z-component data, full Green's dyadic

There are many restrictions for this application on real data, and one of the most non-negligible problems is that usually we don't have sufficient data from our geophones. Generally speaking, the z-component data and their derivatives are fairly easy to get. Before taking the step into real data, we want to know how this algorithm does with insufficient data input, in particular with $U_3, U_{3,1}, U_{3,2}, U_{3,3}$.

In this test, we input only the z-component of the displacement field and its three spatial derivatives into our algorithm. For several reasons, we only are interested in the result for the case below the receivers. Reason 1 is that in real onshore applications, there is no wave in the air above the receivers. Reason 2 is that the cancelation is not expected to happen if we don't provide all the required data, which is easier to understand if we look at Eq.13: the first surface integral has 2 missing terms out of 6, and the second surface integral has 6 missing terms out of 8. Although it sounds fishy, we really want to extract some useful information with only the z-component data.

The reconstructed fields below the receiver using only z-component data and the full Green's dyadic are shown in Figure 10. Figure 10 shows a worse result than that in Figure 4. The result has some additional waves between the P- and S-waves, because the cross-terms can't be canceled without all the required data in test 2. We can guess that the averaging may help us to extract some information about the wavelet. Then we display the estimated wavelet in Figure 11.

The wavelet in Figure 11 looks promising. It has the right phase, and is only a little off the correct shape and amplitude. The averaging may reduce the error from a single estimation and make the final result better. Now let's check the wavelet estimated from a single evaluation point, as is shown in Figure 12. From Figure 12, the error spike exists at the side bands of the wavelet, mainly caused by the cross-terms that can't be canceled.

Test 3: only z-component data, P-wave Green's dyadic Gp

It seems that the cross-terms cause a major problem. To the reader's knowledge, the cross-terms are the multiplication of the P-wave (or S-wave) Green's dyadic and the S-wave (or P-wave) displacement field's derivatives, or alternatively, the multiplication of the P-wave (S-wave) Green's dyadic's derivatives and the S-wave (P-wave) displacement field. Since we only use z-component data, the input near the source wavefield is mainly contributed by the P-wave. We choose to switch the S-wave part off in the Green's dyadic and use only the P-wave Green's dyadic in test 3, which is described in Eq.8 and Figure 1.

In this test, we still use 4 data sets ($U_3, U_{3,1}, U_{3,2}, U_{3,3}$) as input data. The only difference between test 2 and test 3 is the choice of Green's dyadic. All the other parameters are the same as those in Table 1.

The reconstructed fields below the receiver using only z-component data and P-wave Green's dyadic are shown in Figure 13.

The reconstructed field using the P-wave Green's dyadic is very close to the reference field shown in the middle column of Figure 1. The low-frequency noise in the center is caused by the rapid change of the P-wave Green's dyadic in the frequency domain. The amplitude of the noise is negligible compared with the main wavefields.

The wavelet estimated from averaging the 201 estimations is given in Figure 14, and the wavelet from a single estimation at (1400, 1000, 30) is given in Figure 15.

When we use the P-wave Green's dyadic in conjunction with the insufficient z-component data, the single estimation result in Figure 15 doesn't have more noise than the averaging in Figure 14. The overall results are very satisfactory, if we acknowledge that 2 terms in the first integral are not taken into account. After comparing it with the original wavelet, we observe that the wavelet estimation in test 3 keeps the exact phase, a very similar shape, and a lower than actual amplitude compared with the real wavelet.

Attention should be paid in this type of calculation. We altered Green's dyadic to a P-wave-only form, which violates the basic assumption that the reference field should agree with the real medium where the data and the derivatives are measured. The

result doesn't show a large error for this very simple model without any scattering. However, we suspect that it may cause trouble when we deal with a more complicated model that has more reflectors. The reason we could not test that is because very limited data can be obtained from the 12 components (3 displacements, each with 3 spatial derivatives). If the example had a reflector, the results would be less favorable for an acoustic reference and single-component data. Thus, further investigation is needed to evaluate the performance of this method in the case of limited data.

CONCLUSIONS

In this paper, we first provide an algorithm for estimating a wavelet in elastic media, without prior subsurface information in a form that can be directly applied. Then we analyze the characteristics of the Green's dyadic in the situation of decoupled P- and S-wave Green's dyadics in elastic media.

We designed three numerical experiments to test the algorithm for different purposes. The first is to test the accuracy and correctness of the algorithm, in which we use all 12 data sets and the full Green's dyadic. The second one is to test the usefulness of the algorithm when we input the insufficient data that are usually provided from almost all the existing geophones. The third one is to attempt to improve the result from the second test.

We conclude from all the results of the three tests:

This Green's theorem-based wavelet-estimation algorithm is proved to be correct and shows its effectiveness, accuracy, and robustness. When fed all the required data, it can yield a nearly perfect estimated wavelet.

The most exciting performance aspect of this algorithm is that it can make good use of all the existing z-component-only data and can calculate good wavelet estimates that have the correct phase, a very similar shape, and a lower-than-actual amplitude. The reason for the reduced amplitude is that the data in a large offset don't contain all the energy found in the z-component, and the horizontal components are not input into this algorithm. Thus, it can only give results on the basis of what is input. To summarize, the closer the input data are to the requirements of the algorithm, the better the results are that can be obtained. We should be careful when we use the P-wave Green's dyadic instead of the full wave. The testing shows that the P-wave Green's dyadic is safe to use in homogeneous media, but the result of acoustic-reference and single-component data would be less favorable for a model with more reflectors.

ACKNOWLEDGEMENT

This paper would not have been possible without the valuable discussion within M-OSRP group of the University of Houston.

REFERENCES

Amundsen, L., 2001, Elimination of free-surface related multiples without need of the source wavelet. Geophysics 66, 327–341.

Araújo, F., A. Weglein, P. Carvalho, and R. Stolt, 1994, Inverse scattering series for multiple attenuation: An example with surface and internal multiples, 64th Annual International Meeting, SEG, Expanded Abstracts, 1039–1041.

Berkhout, A. J. and D. J. Verschuur, 2005, Removal of internal multiples with the common-focus-point (CFP) approach: Part 1 — Explanation of the theory: Geophysics, 70, no. 3, V45–V60, doi:10.1190/1.1925753.

Carvalho, P. and A. Weglein, 1994, Wavelet estimation for surface multiple attenuation using a simulated annealing algorithm: 64th Annual International Meeting, SEG, Expanded Abstracts, 1481–1484.

Fokkema, J. T. and P.M. van den Berg 1993, Seismic Applications of Acoustic Reciprocity, Elsevier, ISBN 0444890440.

Hsu, S. Y., E. Otnes, and A. C. Ramirez, 2010, Quasi-Monte Carlo integration for the inverse scattering internal multiple attenuation algorithm, SEG Expanded Abstracts 29, 3462.

Morse and Feshbach, 1953, Methods of Theoretical Physics, Cambridge University Press.

Pao, Y. H. and V. Varatharajulu, 1976, Huygens' Principle, radiation conditions, and integral formulas for the scattering of elastic waves, Journal of the Acoustical Society of America, Vol. 59, No. 6.

Verschuur, D. J. and A. J. Berkhout, 2005, Removal of internal multiples with the common-focus-point (CFP) approach: Part 2—Application strategies and data examples: Geophysics, 70, no. 3, V61–V72, doi:10.1190/1.1925754.

Weglein, A. and B. G. Secrest, 1990, Wavelet estimation for a multidimensional acoustic or elastic earth, Geophysics, Vol. 55, No. 7.

Weglein, A., F. Araújo, P. Carvalho, and R. Stolt, 1997, An inverse-scattering series method for attenuating multiples in seismic reflection data, Geophysics, 62, no. 6, 1975–1989, doi:10.1190/1.1444298.

Weglein, A., F. Araújo, P. Carvalho, R. Stolt, K. Matson, R. Coates, D. Corrigan, D. Foster, S. Shaw and H. Zhang, 2003, " Inverse scattering series and seismic exploration," Inverse Problems, Institute of Physics Publishing.

Table 1 Parameters in the numerical tests for wavelet estimation in elastic media.

C_p	1500 m/s	Source	Peak	120ms; or 31st sample
C_s	1000 m/s		Dominant f	20Hz
Density ρ	1 g/cm^3	Receiver	Number	201 inline and crossline
Sampling	4ms		Interval	dx=dy=10m
Trace length	512	Evaluation	Location	Above or below receiver
Recording time	2.048sec		Profile	201points in y=1000m

Table 2 Comparison of the original wavelet used to generate the data and the wavelet estimated from the Green's theorem-based elastic wavelet estimation algorithm.

Sample No.	Real value	Estimation	Sample No.	Real value	Estimation	Sample No.	Real value	Estimation
1	-2.31E-23	3.38E-05	21	-2.10E-02	-2.11E-02	41	-2.10E-02	-2.05E-02
2	-8.94E-22	9.59E-06	22	-5.54E-02	-5.54E-02	42	-6.85E-03	-6.40E-03
3	-3.05E-20	-4.44E-06	23	-0.12436	-0.12441	43	-1.93E-03	-1.60E-03
4	-9.15E-19	1.80E-05	24	-0.23496	-0.23501	44	-4.70E-04	-3.32E-04
5	-2.41E-17	5.75E-05	25	-0.3651	-0.36514	45	-9.98E-05	-1.38E-04
6	-5.58E-16	7.20E-05	26	-0.44493	-0.44497	46	-1.84E-05	-1.72E-04
7	-1.13E-14	4.92E-05	27	-0.37173	-0.37177	47	-2.97E-06	-1.95E-04
8	-2.03E-13	1.81E-05	28	-7.76E-02	-7.76E-02	48	-4.19E-07	-1.75E-04
9	-3.18E-12	6.36E-06	29	0.38423	0.3842	49	-5.17E-08	-1.39E-04
10	-4.37E-11	5.13E-06	30	0.82019	0.820162	50	-5.58E-09	-1.22E-04
11	-5.27E-10	-9.98E-06	31	1	0.999976	51	-5.27E-10	-1.43E-04
12	-5.58E-09	-3.30E-05	32	0.82019	0.820172	52	-4.37E-11	-1.94E-04
13	-5.17E-08	-2.23E-05	33	0.38423	0.384215	53	-3.18E-12	-2.45E-04
14	-4.19E-07	5.08E-05	34	-7.76E-02	-7.76E-02	54	-2.03E-13	-2.70E-04
15	-2.97E-06	1.59E-04	35	-0.37173	-0.37173	55	-1.13E-14	-2.61E-04
16	-1.84E-05	2.28E-04	36	-0.44493	-0.44491	56	-5.58E-16	-2.29E-04
17	-9.98E-05	1.55E-04	37	-0.3651	-0.36502	57	-2.41E-17	-1.87E-04
18	-4.70E-04	-2.81E-04	38	-0.23496	-0.23481	58	-9.15E-19	-1.43E-04
19	-1.93E-03	-1.84E-03	39	-0.12436	-0.12409	59	-3.05E-20	-1.07E-04
20	-6.85E-03	-6.84E-03	40	-5.54E-02	-5.50E-02	60	-8.94E-22	-8.06E-05

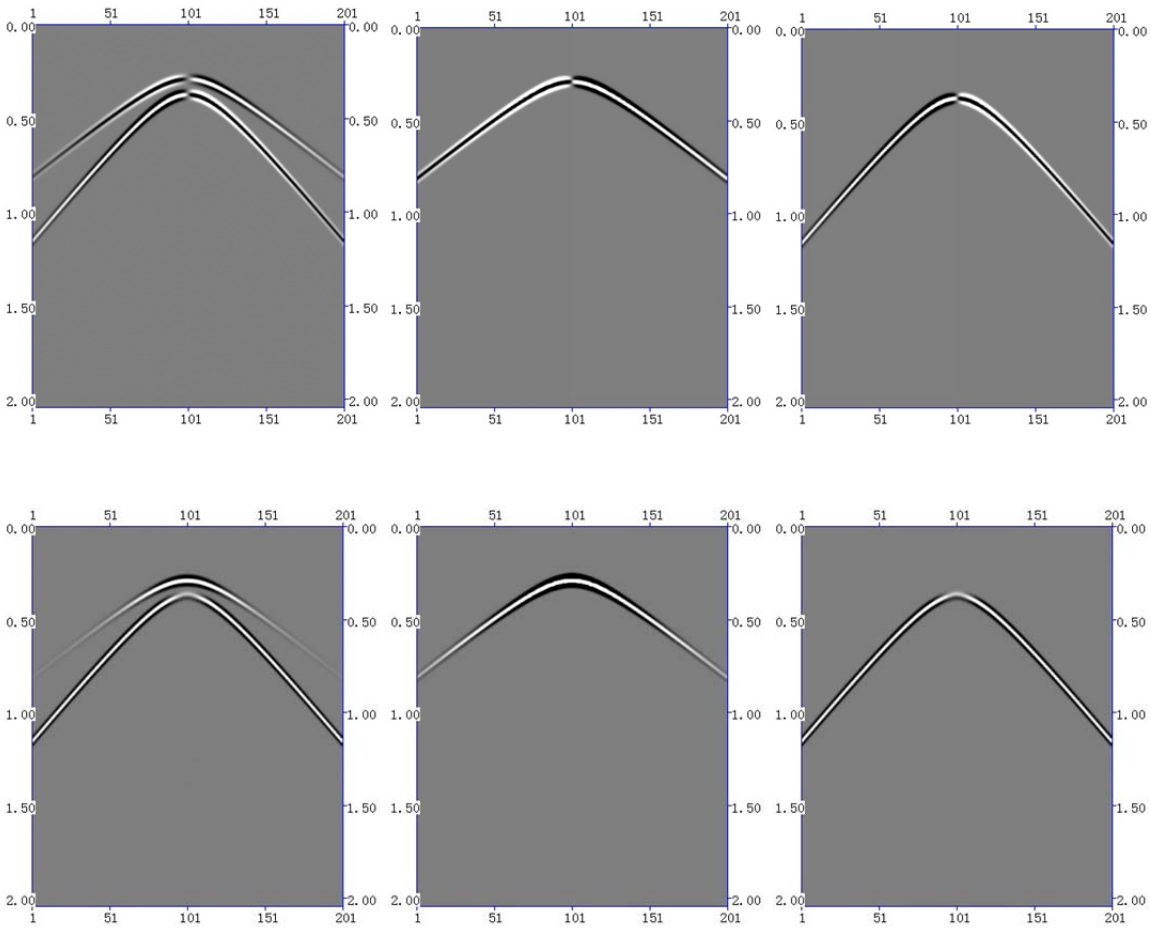

Figure 1 The displacement fields generated by analytic Green's dyadic. The left column is from the full Green's dyadic, including P- and S-wave terms. tThe middle column is from the P-wave term of Green's dyadic, and the right column is from S-wave term of Green's dyadic. The x-components of displacement fields are the upper ones, and the z-components are the lower ones. The lateral axis is the receiver number, and the vertical axis is the time (in seconds). The source is a Ricker wavelet in the z-direction with a peak at 120ms in the center of the x-y plane, at a depth of 50m. The receivers are at a depth

of 300m. The receiver distance is 10m. $C_p = 1500ms^{-1}; C_s = 1000ms^{-1}$. The white color indicates positive amplitude and the black color is negative amplitude.

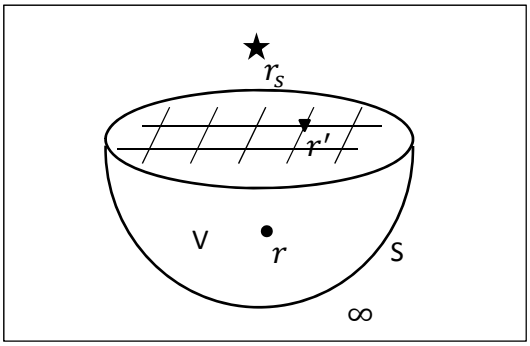

Figure 2 Sketch of the geometry of the reconstruction equation using Green's theorem in elastic media.

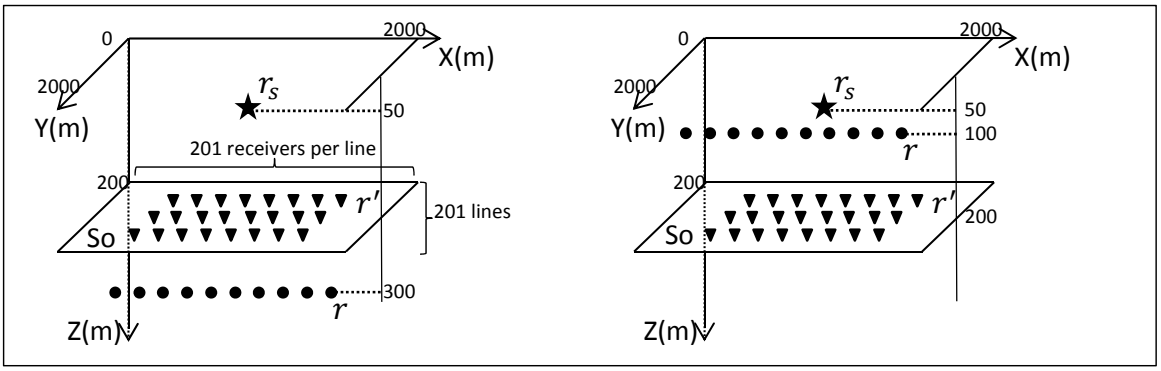

Figure 3 The sketches of experimental configurations for tests above (see right panel) and below receivers (see left panel) S_0. The star indicates the source location at a depth of 50m; triangles indicate receivers at a depth of 200m; black circles indicate evaluation points at a depth 300m (below) or 100m (above) the receivers and along y=1000.

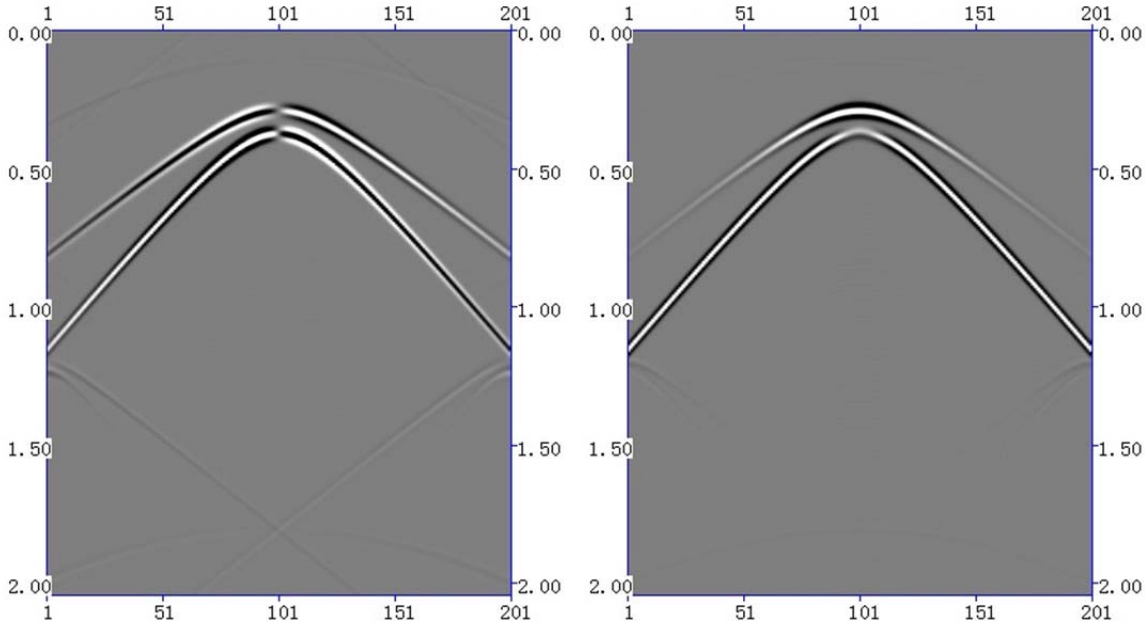

Figure 4 The wavefields reconstructed below the receivers by the wavelet estimation algorithm in elastic media. The left side is the x-component of displacement fields, and the right side is the z-component. All 12 required data sets and the full Green's dyadic are used.

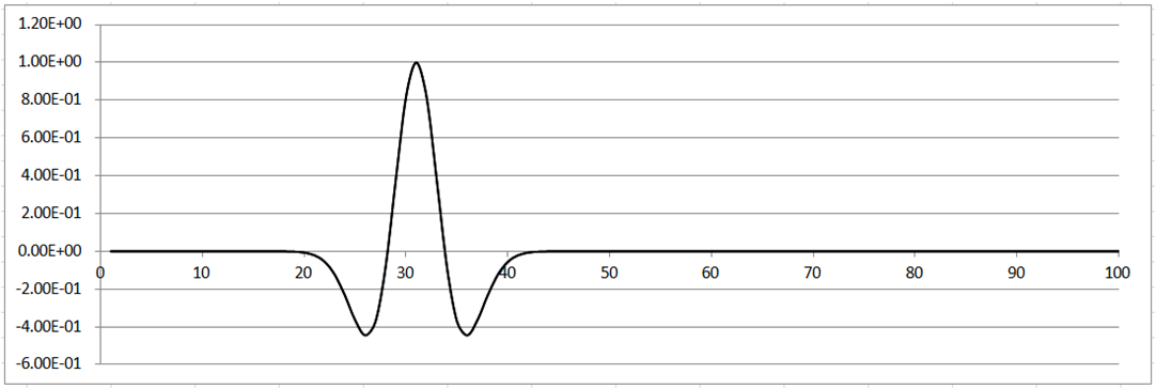

Figure 5a The wavelet used to generate the data in our experiments. It's a Ricker wavelet with the peak at the 31st sample, or 120ms, a dominant frequency of 20Hz, and the peak amplitude of 1.

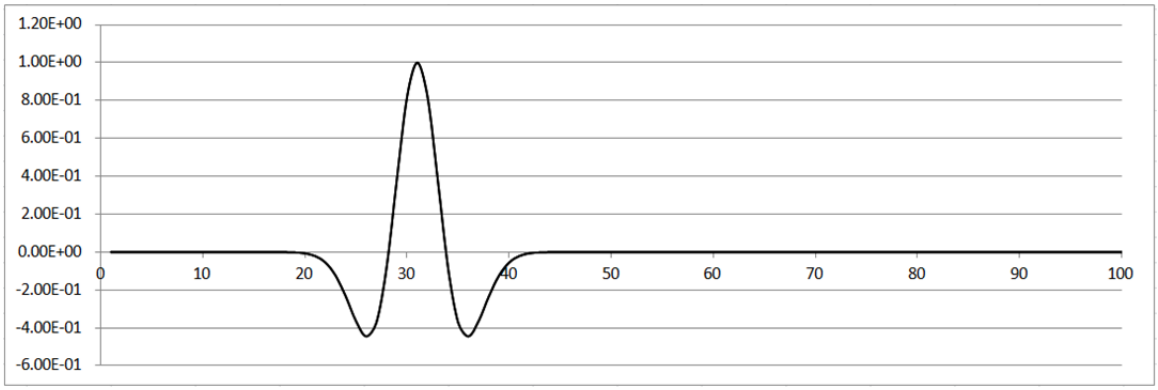

Figure 5b The wavelet estimated when evaluation points are below receivers. All required data are used. The full Green's dyadic is used to generate the data and estimate the wavelet. The wavelet is the average value of 201 estimations along the line y=1000.

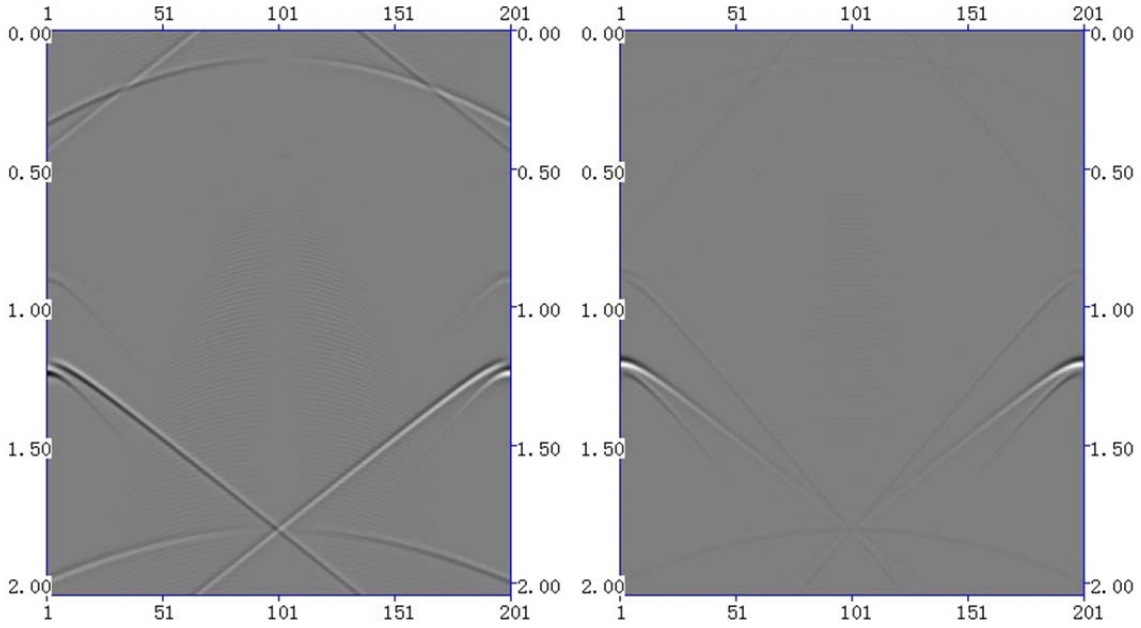

Figure 6 The wavefields reconstructed above the receivers by the wavelet estimation algorithm in elastic media. The left side is the x-component of displacement fields, and the right side is the z-component. All 12 required data sets and the full Green's dyadic are used.

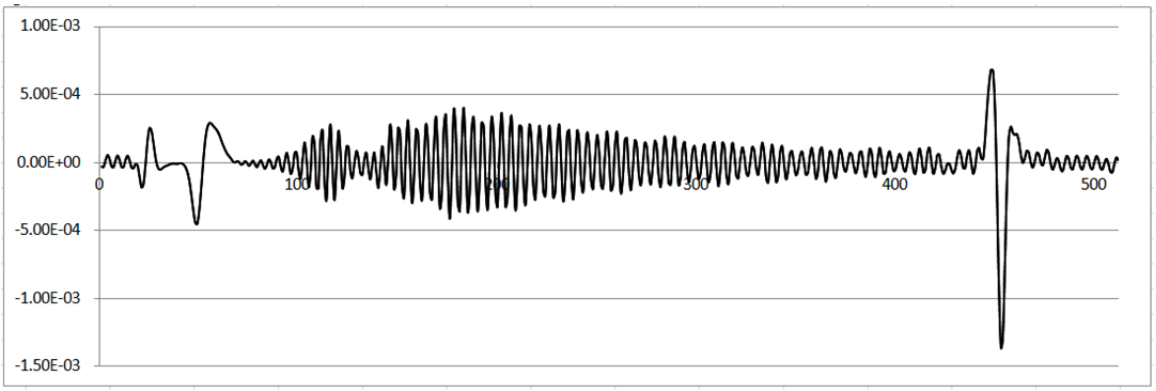

Figure 7 The wavelet estimated when evaluation points are below receivers. All required data are used. The full Green's dyadic is used to generate the data and estimate the wavelet. The wavelet is the average value of 201 estimations along the line y=1000.

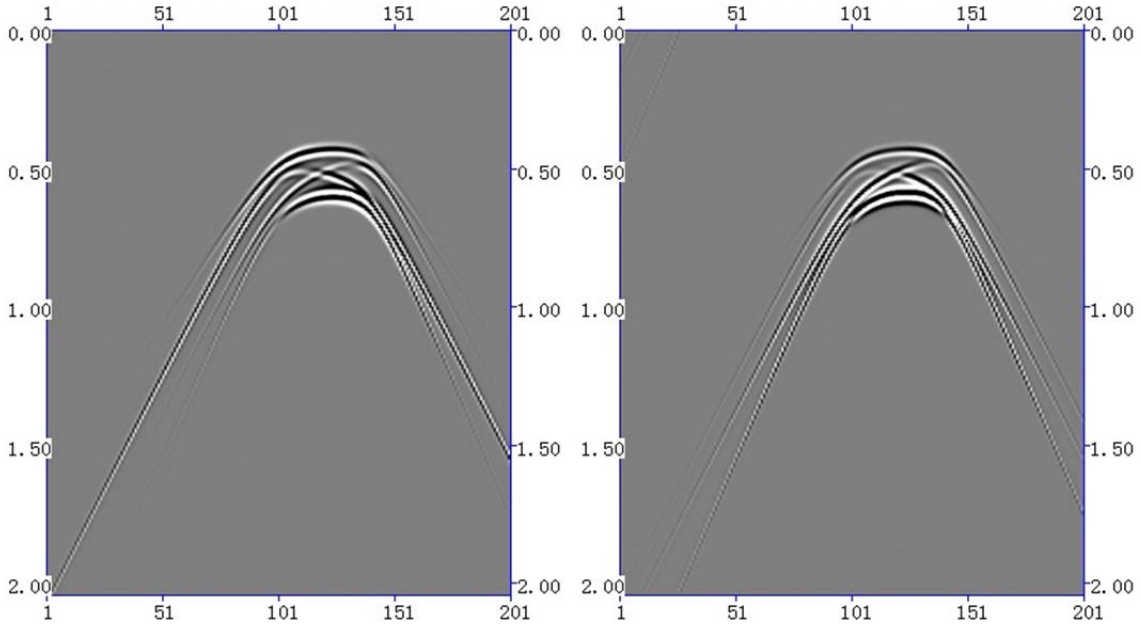

Figure 8 The integrand functions for one estimation point$(1400,1000,300)$, which is below the receivers. The left side is the x-component, and the right side is the z-component. All required 12 data sets and the full Green's dyadic are used.

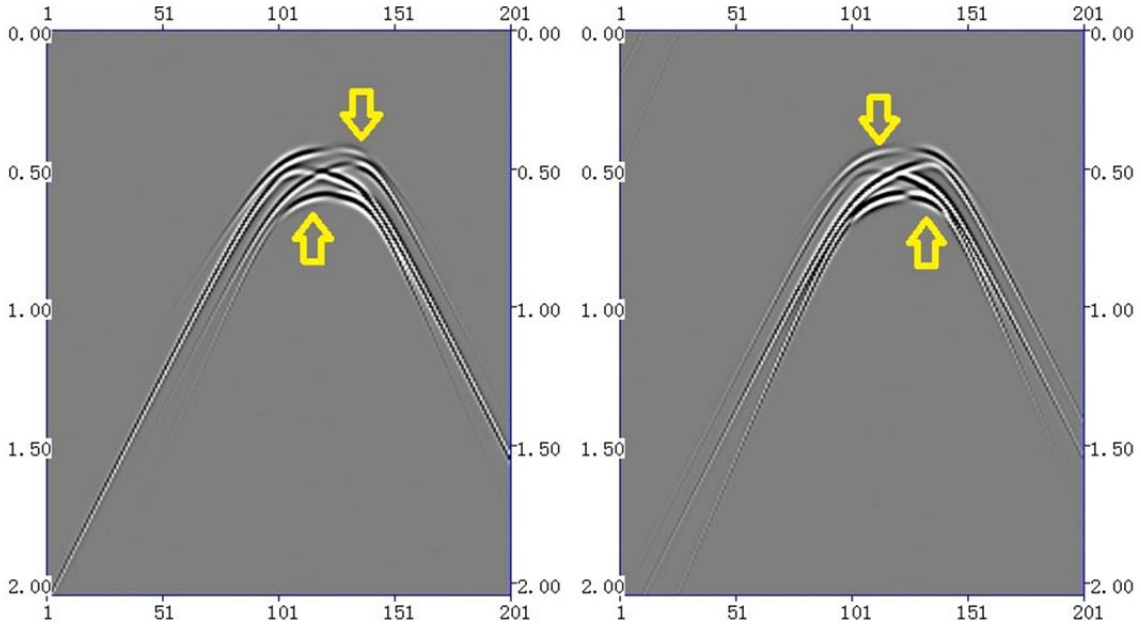

Figure 9 The integrand functions for one estimation point$(1400,1000,100)$, which is above the receivers. The left side is the x-component, and the right side is the z-component. The arrow indicates where the polarity reversal occurs compared with the integrand functions below the receivers. All 12required data sets and the full Green's dyadic are used.

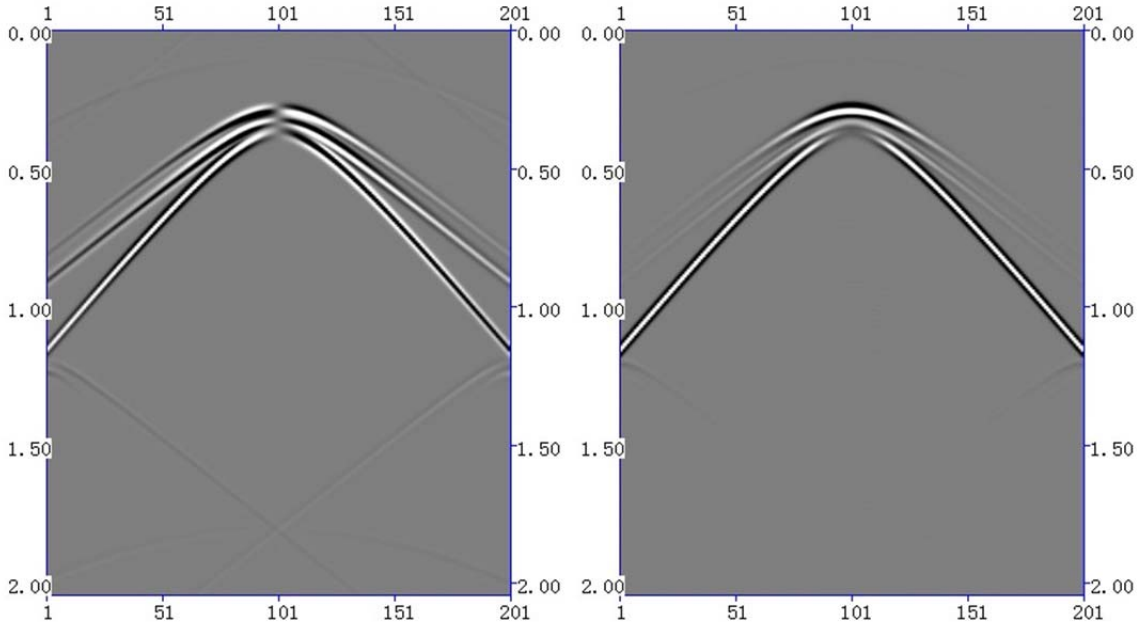

Figure 10 The wavefields reconstructed below the receivers by the wavelet estimation algorithm in elastic media. The left side is the x-component of displacement fields, and the right side is the z-component. Four data sets of z-components and the full Green's dyadic are used.

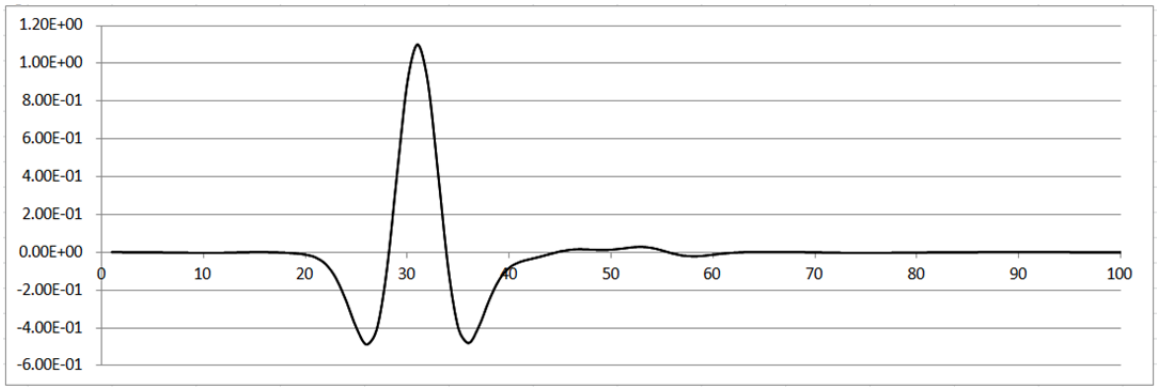

Figure 11 The wavelet estimated when evaluation points are below the receivers. $U_3, U_{3,1}, U_{3,2}, U_{3,3}$ are used as input data. The full Green's dyadic is used to generate the data and estimate the wavelet. The wavelet is the average value of 201 estimations along the line y=1000.

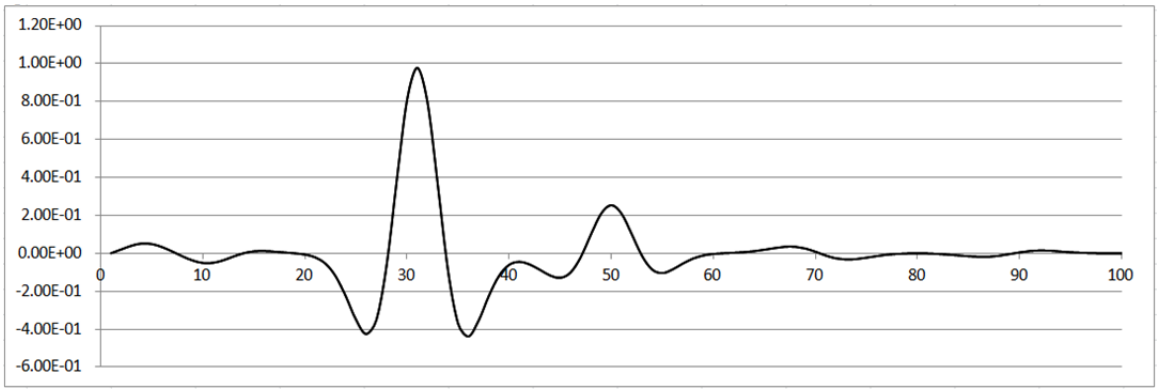

Figure 12 The wavelet estimated when evaluation points are below the receivers. $U_3, U_{3,1}, U_{3,2}, U_{3,3}$ are used as input data. The full Green's dyadic is used to generate the data and estimate the wavelet. The wavelet is the value for one estimation at the point (1400, 1000, 300).

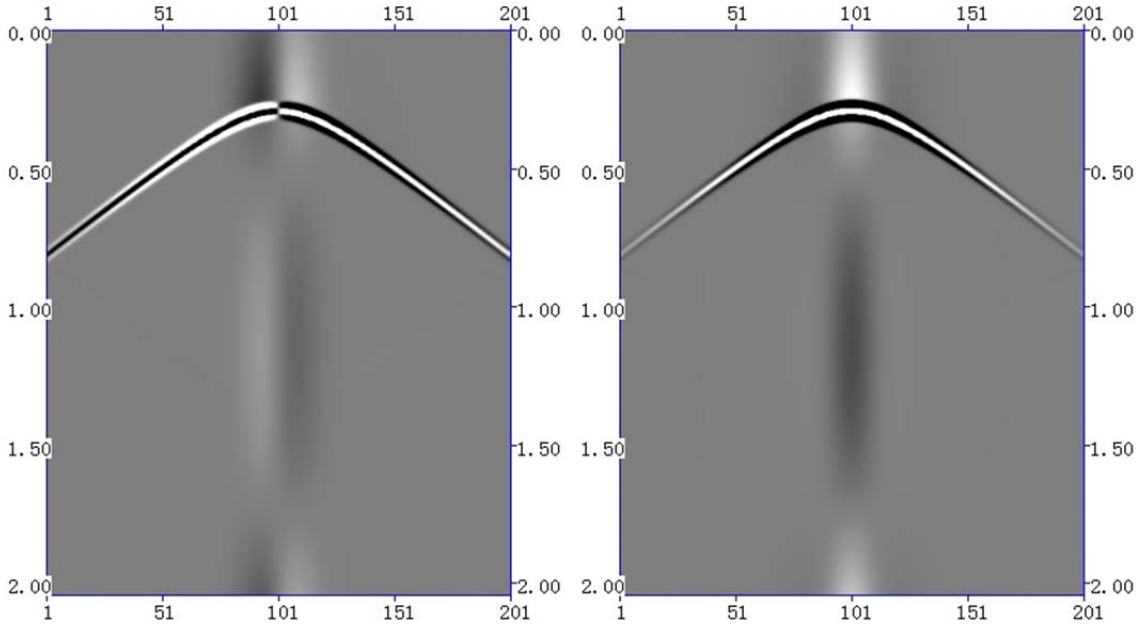

Figure 13 The wavefields reconstructed below the receivers by the wavelet estimation algorithm in elastic media. The left side is the x-component of displacement fields, and the right side is the z-component. Four data sets of z-components and the P-wave Green's dyadic are used.

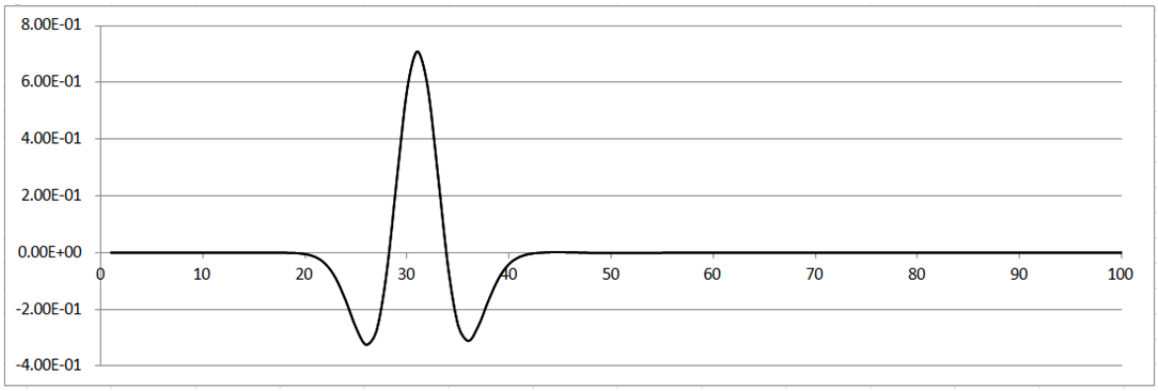

Figure 14 The wavelet estimated when evaluation points are below the receivers. $U_3, U_{3,1}, U_{3,2}, U_{3,3}$ are used as input data. The P-wave Green's dyadic is used to generate the data and estimate the wavelet. The wavelet is the average value of 201 estimations along the line y=1000.

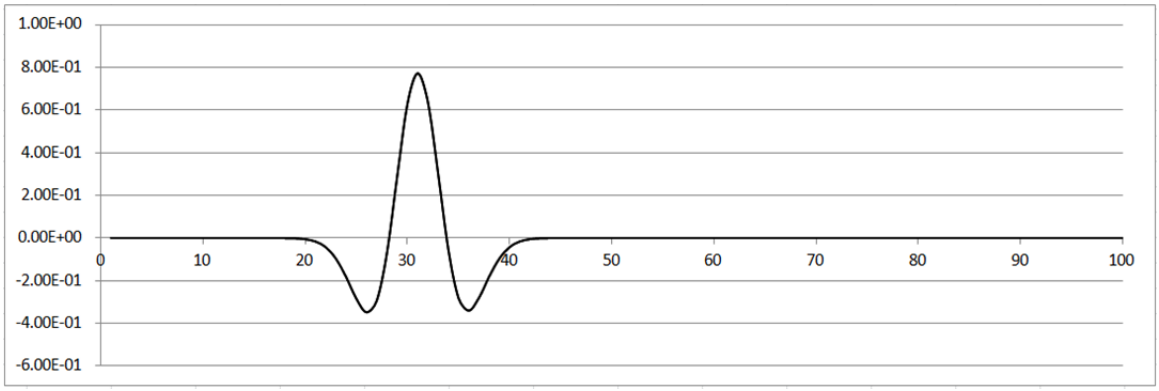

Figure 15 The wavelet estimated when evaluation points are below the receivers. $U_3, U_{3,1}, U_{3,2}, U_{3,3}$ are used as input data. The P-wave Green's dyadic is used to generate the data and estimate the wavelet. The wavelet is the value for one estimation at the point (1400, 1000, 300).

Time saving method based on angular quantities applied to an internal multiple attenuation algorithm: fundamental concept, development and numerical analysis.

Hichem Ayadi, Arthur B. Weglein, M-OSRP, University of Houston.*

SUMMARY

The Inverse Scattering Series (ISS) is a direct inversion method for a multidimensional acoustic, elastic and anelastic earth. It communicates that all inversion processing goals are able to be achieved directly and without any subsurface information. This task is reached through a task-specific subseries of the ISS. Using primaries in the data as subevents of the first-order internal multiples, the leading-order attenuator can predict the time of all the first-order internal multiples and is able to attenuate them.

However, the ISS internal multiple attenuation algorithm can be a computationally demanding method specially in a complex earth. By using an approach that is based on two angular quantities and that was proposed in Terenghi et al. (2012), the cost of the algorithm can be controlled. The idea is to use the two angles as key-control parameters, by limiting their variation, to disregard some calculated contributions of the algorithm that are negligible. Moreover, the range of integration can be chosen as a compromise of the required degree of accuracy and the computational time saving.

This time-saving approach is presented in this paper and applied to the ISS internal multiple attenuation algorithm. Through a numerical analysis, the relationship between accuracy and performance is examined and discussed.

INTRODUCTION

Araújo et al. (1994) and Weglein et al. (1997) have proposed the ISS internal multiple attenuation algorithm. It is a leading order contribution towards the elimination of first order internal multiples. The algorithm is based on the construction of an internal multiple attenuator coming from a subseries of the ISS. It has received positive attention for stand-alone capability for attenuating first-order internal multiples in marine and off-shore plays.

Terenghi et al. (2012) introduced two angular quantities that can be used as a key-control of the computational cost of the ISS leading order internal multiple attenuation algorithm. The two angles, the dip angle and the incidence angle, are related to the wavefield variables in the f-k domain. Therefore, control of this angles can be key to our ability to control the time loop of the algorithm. In this paper, we will discuss how the computational cost can relate to the accuracy to the internal multiples prediction. In other words, is it possible to reduce the computational time of the ISS internal multiple attenuation algorithm without affecting its efficiency?

In the first part of this paper, a description of the internal multiple attenuation algorithm will be provided. Then, the angle constraints method will be develloped and applied to the ISS internal multiple attenuation algorithm. Finally, a numerical analysis will be shown in order to discuss the relation between the accuracy and efficiency of the algorithm, and this key-control parameters.

THE INVERSE SCATTERING SERIES INTERNAL MULTIPLE ATTENUATION ALGORITHM

In seismic processing, many methods make assumptions and require subsurface information. However sometimes these assumptions could be difficult or impossible to satisfy in a complex world. The Inverse Scattering Series states that all processing objectives can be achieved directly and without any subsurface information.

The Inverse Scattering Series is based on scattering theory which is a form of a perturbation analysis. It describes how a scattered wavefield (the difference between the actual wavefield and the reference wavefield) relates to the perturbation (the difference between the actual medium and the reference medium).

The forward scattering series construction starts with the differential equations governing wave propagation in the media:

$$LG = \delta(r - r_s), \tag{1}$$

$$L_0 G_0 = \delta(r - r_s). \tag{2}$$

With L and L_0 the actual and the reference differential operators. And G and G_0 are the actual and reference Green's functions. We define the scattered field as $\psi_s = G - G_0$ and the pertubation as $V = L_0 - L$.

The Lippmann-Schwinger equation relates G, G_0 and V:

$$G = G_0 + G_0 V G \tag{3}$$

Substituing iteratively the Lippmann-Schwinger equation into itself gives the forward scattering series:

$$\begin{aligned} \psi_s &= G_0 V G_0 + G_0 V G_0 V G_0 + G_0 V G_0 V G_0 V G_0 + ... \\ &= (\psi_1) + (\psi_2) + (\psi_3) + ..., \end{aligned} \tag{4}$$

Where, (ψ_n) is the portion of the scattered wavefield that is the nth order in V. The measured values of ψ_s are the data D.

The pertubation V can also be expanded as a series,

$$V = V_1 + V_2 + V_3 + ... \tag{5}$$

Substituing V into the forward scattering series, and evaluating the scattered field on the measurement surface results in the inverse scattering series:

$$(\psi_s)_m = (G_0 V_1 G_0)_m \tag{6}$$

$$0 = (G_0 V_2 G_0)_m + (G_0 V_1 G_0 V_1 G_0)_m \tag{7}$$

$$\begin{aligned} 0 = {} & (G_0 V_3 G_0)_m + (G_0 V_2 G_0 V_1 G_0)_m + \\ & (G_0 V_1 G_0 V_2 G_0)_m + (G_0 V_1 G_0 V_1 G_0 V_1 G_0)_m \end{aligned} \tag{8}$$

...

Internal multiple attenuation algorithm with angle constraints

The Inverse Scattering Series internal multiple attenuation concept is based on the analogy between the forward and the inverse series. The forward series could generate primaries and internal multiples through the action of G_0 on the perturbation V, while, the inverse series can achieve a full inversion of V by using G_0 and the measured data. The way that G_0 acts on the pertubation to construst the internal multiples suggests the way to remove them. In the forward series the first-order internal multiples have their leading-order contribution from the third term: $G_0VG_0VG_0VG_0$. This suggests that the leading-order attenuator of internal multiples can be find in the third term in the inverse series equation (8). In Weglein et al. (1997), a subseries that attenuates internal multiples was identified and separated from the entire inverse scattering series.

The ISS internal multiple attenuation algorithm is a subseries of the inverse scattering series. The algorithm begins with the input data $D(k_g,k_s,\omega)$ which is the data in the ω temporal frequency deghosted and with free-surface multiple removed. This means that they are only primaries and internal multiples in the data. With k_s, k_g are the source and receiver horizontal wavenumber. Then, let define $b_1(k_g,k_s,\omega)$ which correspond to an uncollapsed f-k migration of effective incident plane-wave data as

$$b_1(k_g,k_s,\omega) = (-2iq_s)D(k_g,k_s,\omega) \tag{9}$$

where $q_s = sgn(\omega)\sqrt{(\frac{\omega}{c_0})^2 - k_s}$ is the source vertical wavenumber and c_0 the reference velocity. The second term in the algorithm is the leading-order attenuator b_3, which attenuates all the first-order internal multiples. The leading-order attenuator for a 2D earth is given by,

$$\begin{aligned} b_3(k_s,k_g,\omega) \quad &= \tfrac{1}{(2\pi)^2}\int_{-\infty}^{+\infty}dk_1\int_{-\infty}^{+\infty}dk_2 e^{-iq_1(z_g-z_s)}e^{-iq_2(z_g-z_s)} \\ &\times \int_{-\infty}^{+\infty}dz_1 b_1(k_g,k_1,z_1)e^{i(q_g+q_1)z_1} \\ &\times \int_{-\infty}^{z_1-\varepsilon}dz_2 b_1(k_1,k_2,z_2)e^{-i(q_1+q_2)z_2} \\ &\times \int_{z_2+\varepsilon}^{+\infty}dz_3 b_1(k_2,k_s,z_3)e^{i(q_2+q_s)z_3} \end{aligned} \tag{10}$$

where z_1, z_2 and z_3 are the pseudo-depths. ε is a small positive parameter chosen in order to make sure that $z_1 > z_2$ and $z_3 > z_2$ are satisfied.
Finally, using the input data and the leading-order attenuator of the first-order internal multiples, the data with the first-order internal multiples attenuated is given by

$$D(k_g,k_s,\omega) + D_3(k_g,k_s,\omega) \tag{11}$$

with $D_3(k_g,k_s,\omega) = (-2iq_s)^{-1}b_3(k_g,k_s,\omega)$.

COMPUTATIONAL COST SAVING METHOD : ANGLE CONSTRAINTS.

Terenghi et al. (2012) discuss about two angular quantities that can be used in order to reduce the computational cost of any algorithm defined in source and receiver transformed domain. The idea is to construct key-control parameters that allow to disregard some part of the calculus that is insignificant during the computation. In other words, use this key-paramters to optimize some intervals of calculus in the algorithm. The approach used is based on certain angular quantities in order to control the cost of the algorithm.

Stolt and Weglein (2012) define the image function wavenumber as a difference between the receiver and source-side wavenumbers

$$\vec{k_m} = \vec{k_g} - \vec{k_s} = (\vec{\kappa_g} - \vec{\kappa_g}, q_g - q_s) \tag{12}$$

With $\vec{\kappa_s}$ and $\vec{\kappa_s}$ the horizontal component of the source and receiver wavenumbers. These definitions allow the construc-

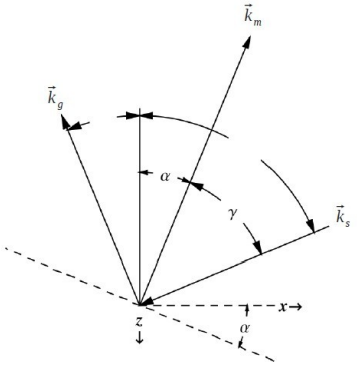

Figure 1: Plane waves at an interface in the subsurface. α is the angle between $\vec{k_m}$ and the vertical component. γ is the angle between $\vec{k_m}$ and $\vec{k_g}$ or $\vec{k_s}$. Figure from Terenghi et al. (2012).

tion of two angles α and γ (cf. Figure 1): α the dip angle corresponds to the angle between the surface and the horizontal component. γ the incident angle is the angle between the image function wavenumber and the source (or receiver) side wavenumber. Using simple trigonometry, α and γ can be related to the field quantities in the f-k domain:

$$\alpha = tan^{-1}\left(\frac{\sqrt{\vec{\kappa_m}.\vec{\kappa_m}}}{|\,q_g - q_s\,|}\right) \tag{13}$$

$$\gamma = \frac{1}{2}\left(-\frac{c_0^2}{\omega^2}(\vec{\kappa_g}.\vec{\kappa_s} + q_g q_s)\right) \tag{14}$$

The dependence of α and γ on the temporal frequency is carried by the occurrences of the vertical wavenumber q. Moreover, the relationship between α, γ and ω is monotonic. This means that at fixed values of $\vec{\kappa_s}$ and $\vec{\kappa_g}$ any given value of ω univocally identifies angles α and γ. Then, increasing the temporal frequencies in the data maps to decreasing values of the reflection dip and the aperture angle. At set value of $\vec{\kappa_s}$ and $\vec{\kappa_s}$, it is possible to conclude that any desired finite angle-domain interval maps to a similar finite frequency domain interval. This may be used in order to decrease the number of loop. Indeed, looking at the eqs (10), b_3 have - in 2D - two integrations over the wavenumber component. Therefore, it is possible to constrain the algorithm within a range of angular quantities,

$$\alpha_{min} \leq \alpha \leq \alpha_{max} \tag{15}$$

$$\gamma_{min} \leq \gamma \leq \gamma_{max} \tag{16}$$

Using the α/γ and ω monotonic relationship, the total frequency interval can also be constrained,

$$max(\omega_{\gamma}^{min}, \omega_{\alpha}^{min}) \leq \omega \leq min(\omega_{\gamma}^{max}, \omega_{\alpha}^{max}) \tag{17}$$

Then, the reduction of the total frequency interval allows to reduce the interval of integration of b_3, which means reducing the number of loop.

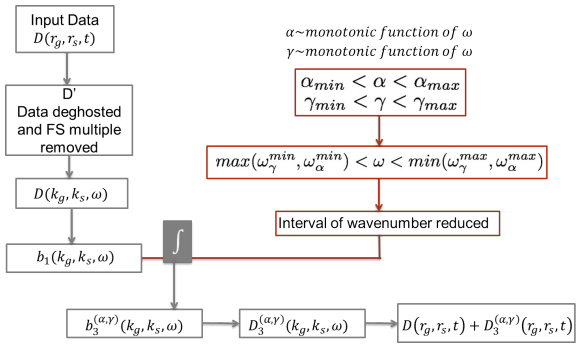

Figure 2: Process of the ISS internal multiple attenuation with angle constraints.

Figure 2 recapitulates in a graph the ISS internal multiple algorithm with angle constraints.
In the next section, a numerical analysis continues and illustrates the discussion, in which the efficiency and accuracy of the angle constraints method applied to the ISS internal multiple attenuation algorithm is discussed.

NUMERICAL ANALYSIS

The model considered in this numerical analysis is a three layer earth at depth : $z = 1000$m, 1300m and 1700m. The source shot ($z = 910$ and $x = 6086$) is recorded by 928 receivers. In Figure 3 is the shot gather with primaries (green arrow) and internal multiples.

In the Figure 4, is the internal multiple prediction using the ISS internal multiple attenuation algorithm. All the first-order internal multiple are predicted. The model is in 1D; consequently just one angle (the incident angle γ) can be used as a key-control parameter. The analysis made in 1D for γ can be extended to α by analogy.
The Figure 5 illustrates the internal multiple prediction that uses angle constraints, as shown in Figure 2, for different γ_{max}. Also, for the same γ_{max} the percentage of time saved is listed in the Table 1.

γ_{max}	15°	20°	25°
Percentage time saved	67 %	57 %	50 %

Table 1: Time saved (in %) for the different γ_{max} studied.

A first interpretation would be that we do not need to compute for a full open γ-angle (90° degree by definition) to obtain an

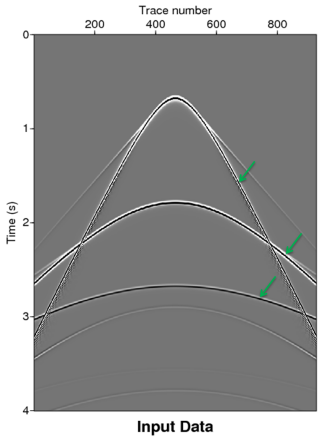

Figure 3: Shot gather recorded. The three primaries resulting from the three layers-reflectors are shown by the green arrows.

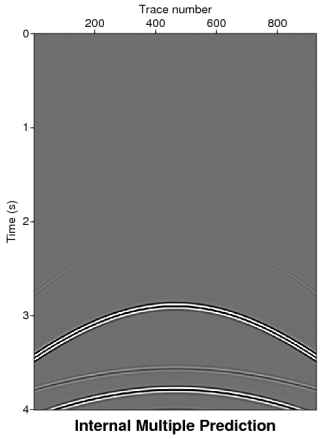

Figure 4: Prediction of all the first-order internal multiples.

accurate prediction of the internal multiples. Notice that a prediction with a full open angle corresponds to an internal multiple prediction without any angle constraints. Even so, with reduction to a certain angle (γ_{limite}), the prediction of the internal multiples is degraded.
For one trace number (750), is plotted in the Figure 6 the amplitude for different γ_{max} and compared with the amplitude for a full open γ-angle. In the Figure 5, the prediction of the internal multiples for $\gamma_{max} = 20°$ seems to be the same as $\gamma_{max} = 25°$ and Figure 4. If we look more precisely to the amplitude, we can notice that it had been affected. The amplitude for $\gamma_{max} = 20°$ do not overlap with the amplitude for $\gamma_{max} = 90°$ contrary to $\gamma_{max} = 25°$.
If we look at the shape (cf. Figure 7), the same interpretation can be made. For $\gamma_{max} = 25°$ the shape matches with an usual internal multiple prediction (full open γ-angle). Bellow this incident angle, the shape do not match which means that the prediction can not be considered accurate.

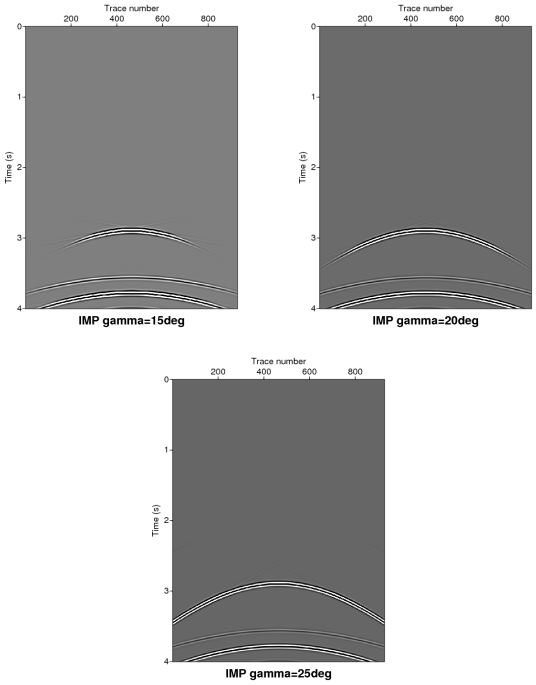

Figure 5: Internal multiple prediction for different angles of γ: $\gamma_{max} = 15°$, $\gamma_{max} = 20°$ and $\gamma_{max} = 25°$.

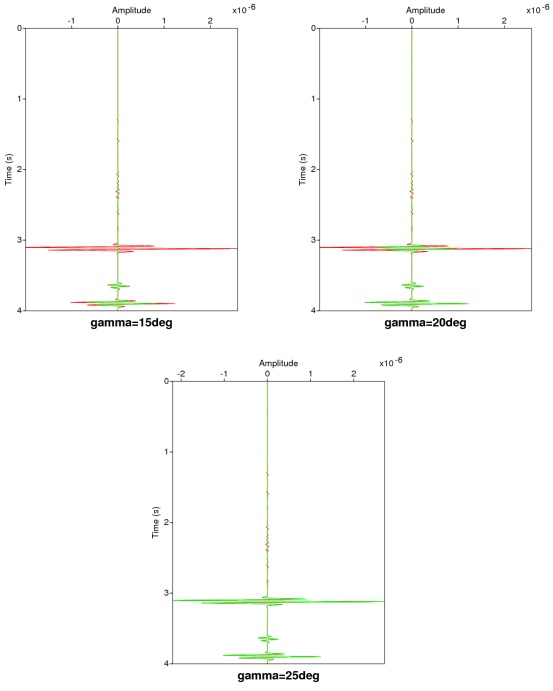

Figure 6: Comparaison of the amplitude for a full open γ-angle (red) and for different γ_{max} (green).

DISCUSION AND CONCLUSION

Terenghi et al. (2012) have introduced a time saving method:

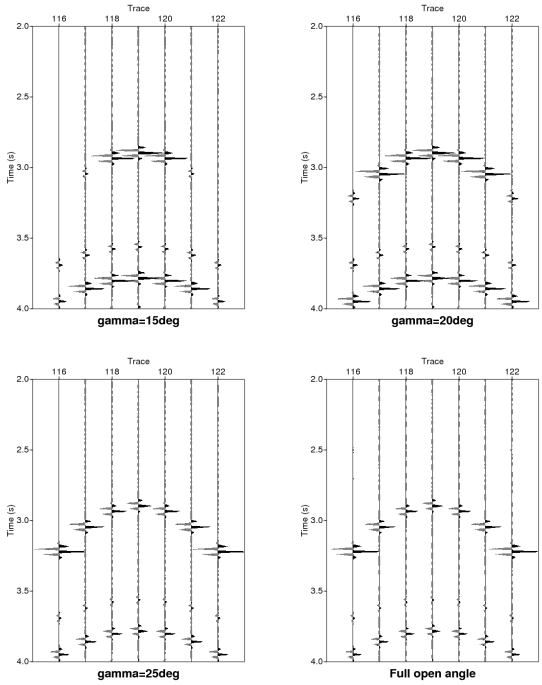

Figure 7: Wiggle plot for $\gamma_{max} = 15°$, $\gamma_{max} = 20°$, $\gamma_{max} = 25°$ and full open γ-angle. Source at trace number 119.

the angle constraints. Looking at the procedure (cf. Figure 2), it is undeniable that applied to an algorithm defined in source and receiver transformed domain like the ISS internal multiple attenuation, this approach can reduce considerably the computational cost of the algorithm. Studying the impact of this key-control method in the algorithm, it appears that a compromise between the time saved and the accuracy of the internal multiple prediction has to be made. Indeed, above a certain "angle limit" the internal multiple prediction stays accurate and precise. Below, the internal multiples are still predicted at the right time but with an approximate amplitude. Thus, the angle constraints is a trade-off tool between accuracy and cost of the algorithm. In other words, the ISS internal multiple algorithm will have its computational time reduced according to the degree of accuracy required by the user. The next step will be to identify this two angles using the input data in order to be able to define the constraint limits.

ACKNOWLEDGEMENTS

First, we would like to express our appreciation to Total E&P USA for establishing the research scholar position for the first author in M-OSRP. Also, we would like to thank all the sponsors for their support. We thank all the member of the M-OSRP group and specially Hong Liang, Chao Ma and Wilbert Herrera for the different rewarding discussions. A special acknowledgement to Paolo Terenghi for his avant-gardism and his contribution that inspired this work.

REFERENCES

Weglein, A. B., F. V. Araújo, P. M. Carvalho, R. H. Stolt, K. H. Matson, R. T. Coates, D. Corrigan, D. J. Foster, S. A. Shaw, and H. Zhang. "Inverse Scattering Series and Seismic Exploration." *Inverse Problems* (2003): R27–R83.

Araújo, F. V., A.B. Weglein, P.M. Carvalho and R.M. Stolt. "Inverse scattering series for multiple attenuation: An example with surface and internal multiples" *SEG Technical Program Expanded Abstract* (1994): 1039-1041.

Stolt, Robert H. and Arthur B. Weglein. "Seismic Imaging and Inversion : Volume 1: Application of Linear Inverse Theory." *Cambridge, United Kingdom: Cambridge University Press* (2012).

Weglein, A.B.,F.A. Gasparotto, P.M. Carvalho and R.M. Stolt. " An inverse-scattering series method for attenuating multiples in seismic reflection data." *Geophysics* (1997): 1975-1989.

Weglein, A.B., S. Hsu, P. Terenghi, X. Li and R.M. Stolt. "Multiple attenuation : Recent advances and the road ahead 2011." *The Leading Edge* (2011): 864-875.

Terenghi P. and A.B. Weglein "ISS internal multiple attenuation with angle constraints" *Annual report* (2012): R242–R266.

Eliminating first-order internal multiples with downward reflection at the shallowest interface: theory and initial examples

Wilberth Herrera and Arthur B. Weglein, M-OSRP, University of Houston

SUMMARY

The Inverse Scattering Series (ISS) is capable of directly achieving all processing objectives through specific-task subseries and without any subsurface information. In this work a subseries of the ISS is isolated, with the specific task of removing internal multiples of first-order, with downward reflection at the shallowest reflector. The algorithm predicts both the phase and exact amplitude of the internal multiples and does not modify any primary; therefore the internal multiples are removed surgically. This algorithm may be relevant and provide added value when one of the internal multiples under discussion is interfering destructively with (or is proximal to) a primary, and the attenuation of the internal multiple provided by previous algorithms is not adequate for the clean removal of the multiple and not touching the primary. To show how the elimination subseries proposed in this work deals with this challenging situation, an analytic example with three interfaces is included, with one of the relevant first-order internal multiples interfering destructively with the primary generated at the third reflector. We show in particular how the interfering internal multiple is eliminated with no damage to the amplitude or the phase of the primary, as is expected from a method for surgical removal of internal multiples.

INTRODUCTION

Using the ISS and the concept of specific-task subseries, a multidimensional direct algorithm was derived in Araújo (1994), Araújo et al. (1994) and Weglein et al. (1997), to predict and attenuate internal multiples present in the data of a seismic experiment. Prediction methods are followed by the energy-minimization adaptive subtraction to try to accommodate all shortcomings in the prediction. However, there are situations in which the energy-minimization adaptive subtraction technique is not suitable anymore, and the attenuation of internal multiples is not enough for a correct interpretation of the seismic data. An example of this challenging situation for the oil industry can arise when an internal multiple is interfering destructively with (or is proximal to) a primary associated to a target e.g. subsalt targets. This situation is often present in onshore exploration, but it can also happen offshore. While the energy-minimization adaptive subtraction technique is of value for isolated multiples, in this case it might also affect the primary interfering with the internal multiple.

Therefore, it is important to develop new algorithms with enhanced capabilities. In response to this need, Ramírez and Weglein (2005) and Ramírez (2007) discuss early ideas for moving attenuation of internal multiples towards elimination through higher order terms in the ISS. Those ideas and concepts are here progressed and developed leading to a subseries which surgically removes at the same time all internal multiples of first-order having their single downward reflection generated at the shallowest reflector (we will refer to those events as internal multiples generated at the shallowest reflector/interface).

As with any other subseries from the ISS previously isolated, this algorithm requires no subsurface information. We also illustrate how to use this subseries in a three-interface analytic model, to surgically remove the first-order internal multiple generated at the shallowest interface and with both upward reflections generated at the second reflector. The parameters of the model are chosen to allow the internal multiple to interfere destructively with the primary generated at the third reflector.

REVIEW OF THE LEADING-ORDER ATTENUATOR

The Inverse Scattering Series (ISS) is a direct inversion method which can in principle determine, in seismic applications, subsurface properties of the earth using only the measured data D in a seismic experiment, and a Green's function for a chosen reference medium. Unfortunately, with no a priori information of the subsurface of the earth, the convergence is highly restricted (Carvalho 1992).

However, specific-task subseries with different objectives in the chain of data processing can be isolated, and have better convergence properties than the entire ISS. In regard of internal multiples, a subseries was isolated in Araújo (1994) and Weglein et al. (1997), with the specific task of the attenuation of internal multiples of all orders (the order of an internal multiple is defined as the number of downward reflections it experiences anywhere during its travel time. See Figure 1).

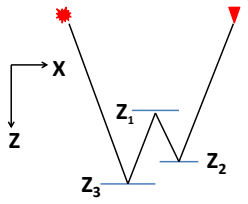

Figure 1: First-order internal multiple: we say, based on the position where reflections occur, that the interfaces generating a first-order internal multiple are in a "lower-higher-lower" configuration.

This Internal Multiple Attenuation Subseries (IMAS) requires that 1) the data D have been deghosted, 2) the reference wave field and free-surface multiples have also been removed from the data and 3) the source wavelet has been deconvolved. The first term of this subseries is the result of the uncollapsed Stolt's migration of the data using the water speed, c_0. The second

term, conveniently named the *leading-order attenuator*, attenuates all first-order internal multiples at a single step and is of third-order in the measured data.

It turns out that the elimination subseries isolated in this work shares with the IMAS the first two terms, i.e., the data migrated at water speed and the leading-order attenuator. However, both subseries differ from each other for higher-order terms. Hence, we review here the leading-order attenuator, and in the next section we explain how to isolate the higher-order contributions to the elimination subseries.

We will restrict our discussion to a 1D earth with data generated by waves at normal incidence. In this case, the analytic expression for the leading-order attenuator is (Weglein et al. 2003)

$$b_3(k) = \int_{-\infty}^{\infty} dz e^{ikz} b_1(z) \int_{-\infty}^{z-\varepsilon} dz' e^{-ikz'} b_1(z') \times$$

$$\int_{z'+\varepsilon}^{\infty} dz'' e^{ikz''} b_1(z''), \qquad (1)$$

where ε is a small and positive parameter introduced to ensure the characteristic "lower-higher-lower" configuration for first-order internal multiples, and to avoid configurations including contributions from the self-interactions, which are defined by the conditions $z'' = z'$ and $z' = z$ in eq. (1). Also, the input $b_1(z)$ of the leading-order attenuator is the first term of the subseries, i.e., the deghosted data migrated at water speed using uncollapsed Stolt's migration. The subindexes in $b_1(k)$ and $b_3(k)$ mean that they are of first-order and third-order respectively in the data.

In the following, we will restrict to the 1D model shown in Figure 2, where Z_i denotes the depth of the i-th. reflector for $i = 1,2,3$.

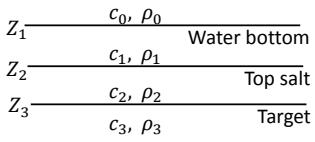

Figure 2: A 1D earth model, with three interfaces. The first interface, with depth Z_1 is the water bottom. The second interface, with depth Z_2, can be identified with the top salt and the third interface, with depth Z_3, can be identified with the target.

We consider data made of primaries and internal multiples created by spike-waves at normal incidence: $D(t) = R_1\delta(t-t_1) + R_2'\delta(t-t_2) + R_3'\delta(t-t_3) + IM$, with $R_2' = T_{01}R_2T_{10}$, $R_3' = T_{01}T_{12}R_2T_{21}T_{10}$. Also t_i is the travel time of the primary associated with the interface with depth Z_i, R_i is the reflection coefficient experienced by a wave when upward reflected at the interface with depth Z_i, and T_{ij} represents the transmission coefficient experienced by a wave traveling from the acoustic medium with parameters (c_i, ρ_i) to the acoustic medium with parameters (c_j, ρ_j).

In this case, the input of the leading-order attenuator, eq. (1), becomes:

$$b_1(z) = R_1\delta(z-z_1) + R_2'\delta(z-z_2) + R_3'\delta(z-z_3) + \cdots, \quad (2)$$

where $z_i = c_0 t_i/2$ is the position of the reflector with depth Z_i, after Stolt's uncollapsed migration*. The z_i are usually referred to as *pseudodepths*, and we say that eq. (2) is in the *pseudodepth* domain.

Although the input data of the leading-order attenuator, eq. (2), includes primaries and internal multiples, we only consider the effect of the primaries. Initial steps towards the inclusion of internal multiples are addressed in Ma and Weglein (2012) and Liang and Weglein (2012). In the time domain the result for the evaluation of eq. (1), using eq. (2) is (See Weglein et al. 2003)

$$b_3(t) = -T_{01}T_{10} * (IM)_{j=1} + \cdots, \qquad (3)$$

where $(IM)_{j=1}$ is the sum of the contributions to the data of all first-order internal multiples generated at the shallowest reflector of the model:

$$(IM)_{j=1} = -T_{01}R_2R_1R_2T_{10}\delta(t-(2t_2-t_1))$$

$$-2T_{01}R_2R_1T_{21}R_3T_{12}T_{10}\delta(t-(t_2+t_3-t_1))$$

$$-T_{01}T_{12}^2R_3R_1R_3T_{21}^2\delta(t-(2t_3-t_1)). \qquad (4)$$

Consider now the contribution of the data and the leading-order attenuator $b_3(t)$ to the IMAS:

$$b_1(t) + b_3(t) = P + [1 - T_{01}T_{10}](IM)_{j=1} + \cdots, \qquad (5)$$

where P stands for primaries. As $0 < T_{01}T_{10} < 1$, it follows from (5) that the amplitude contribution of $(IM)_{j=1}$ is reduced by an amount $T_{01}T_{10}$ with respect to their contribution previous to the addition of $b_3(t)$. $T_{01}T_{10}$ is referred as *attenuator factor*. An analogous situation is present for the internal multiple with downward reflection at the second reflector. However, in the present work we will only need the effects of $b_3(t)$ on $(IM)_{j=1}$.

THE ELIMINATION SUBSERIES

In the past section we showed, using the model of Figure 2, how the leading-order attenuator decreases the amplitude contribution for first-order internal multiples generated at the shallowest interface, by an amount of $T_{01}T_{10}$. This means that to promote this attenuation to an elimination, the contribution of higher-order terms from the elimination subseries need to

*For normal incidence of a spike-wave, the relation between $D(t)$ and $b_1(z)$ is as follows: 1) Fourier transform $D(t)$, 2) write the result, $D(\omega)$, in terms of $z_i = c_0 t_i/2$ and the vertical wavenumber $k = 2\omega/c_0$ to end with a function $D(k)$ and 3) define $b_1(z) \equiv \mathscr{F}^{-1}[D(k)]$ where $\mathscr{F}^{-1}$ denotes the inverse Fourier transform

move this attenuator factor to the unity: when those higher-order contributions are added to the initial attenuation provided by $b_3(t)$, the predicted amplitude will exactly match $(IM)_{j=1}$. Hence, the collective contribution of the terms in the elimination subseries will remove $(IM)_{j=1}$ from the data.

To isolate terms from the ISS with the right contributions, it is convenient to express 1 in terms of R_1. For this purpose the following geometric series expansion is useful:

$$1 = \frac{T_{01}T_{10}}{T_{01}T_{10}} = \frac{T_{01}T_{10}}{(1-R_1^2)} = T_{01}T_{10}(1+R_1^2+R_1^4+\cdots). \quad (6)$$

Notice that after distributing the product on the right hand side of eq. (6), the first term is the initial attenuation provided by the leading-order attenuator. Therefore, the remaining terms are the amplitude contribution required from higher-order terms, in any subseries claiming to promote the attenuation to elimination. We will focus in isolating the term with attenuation factor $T_{01}T_{10}*R_1^2$, the second term on the right hand side of eq. (6). We also want to predict the exact travel time of the internal multiples, i.e., we are looking for a term with contribution equal to $T_{01}T_{10}*R_1^2*(IM)_{j=1}$.

Upon inspection of the ISS, we arrive to:

$$b_5^{(IM)_{j=1}}(k) \equiv \int_{-\infty}^{\infty} dz e^{ikz} b_1(z) \int_{-\infty}^{z-\varepsilon} dz' e^{-ikz'} F[b_1(z')] \times \int_{z'+\varepsilon}^{\infty} dz'' e^{ikz''} b_1(z''). \quad (7)$$

$F[b_1(z')]$ is given by

$$F[b_1(z')] = \mathscr{F}^{-1}\left[\int_{-\infty}^{\infty} dz e^{ikz} b_1(z) \int_{z-\varepsilon}^{z+\varepsilon} dz_1 e^{-ikz_1} b_1(z_1) \times \int_{z_1-\varepsilon}^{z_1+\varepsilon} dz_2 e^{ikz_2} b_1(z_2)\right], \quad (8)$$

where $\mathscr{F}^{-1}$ means inverse Fourier transform, and the subindex in $b_5^{(IM)_{j=1}}$ means that it is of fifth-order in the data. The ε is applied in this context to include the self-interactions $z_2 = z_1$ and $z_1 = z$, rather than to avoid them, as is the case for the leading-order attenuator.

Upon evaluation of eqs. (7) and (8) using the primaries in eq. (2), the result in the time domain includes the expected contribution, plus additional terms which contribute to further attenuation of (presumably they also start the elimination of) other first-order internal multiples: $b_5^{(IM)_{j=1}}(t) = -T_{01}T_{10} * R_1^2 * (IM)_{j=1} + \cdots$.

Consider now the sum of the data, the leading-order attenuator and $b_5^{(IM)_{j=1}}$:

$$b_1(t) + b_3(t) + b_5^{(IM)_{j=1}}(t) = P + [1 - T_{01}T_{10}(1+R_1^2)](IM)_{j=1} + \cdots. \quad (9)$$

Eq. (9) makes evident that in this case the attenuation factor $T_{01}T_{10}$ is changed to $T_{01}T_{10}(1+R_1^2)$. This attenuation contains the first and second terms of the geometric series on the right hand side of eq. (6). Hence, the expression proposed for $b_5^{(IM)_{j=1}}$ in eqs. (7) and (8) correctly reproduces the required amplitude contribution to move the attenuation of $(IM)_{j=1}$ a step closer to elimination.

Higher-order contributions for the elimination subseries are analogous to eq. (7) but with an appropriate $F[b_1(z')]$, e.g. the function $F[b_1(z')]$ for the term following $b_5^{(IM)_{j=1}}$, denoted $b_7^{(IM)_{j=1}}$, and with contribution $T_{01}T_{10} * R_1^4 * (IM)_{j=1}$ is

$$F[b_1(z')] = \mathscr{F}^{-1}\left[\int_{-\infty}^{\infty} dz e^{ikz} b_1(z) \int_{z-\varepsilon}^{z+\varepsilon} dz_1 e^{-ikz_1} b_1(z_1) \times \int_{z_1-\varepsilon}^{z_1+\varepsilon} dz_2 e^{ikz_2} b_1(z_2) \int_{z_2-\varepsilon}^{z_2+\varepsilon} dz_3 e^{-ikz_3} b_1(z_3) \times \int_{z_3-\varepsilon}^{z_3+\varepsilon} dz_4 e^{ikz_4} b_1(z_4)\right]. \quad (10)$$

Following this line of thinking, further contributions to the elimination of $(IM)_{j=1}$ can be isolated to get the elimination subseries:

$$b^{(IM)_{j=1}}(t) = b_1(t) + b_3(t) + b_5^{(IM)_{j=1}}(t) + b_7^{(IM)_{j=1}}(t) + \cdots. \quad (11)$$

We can use as many terms as we need, in order to achieve a desired degree of accuracy in the prediction of an internal multiple (of first-order and generated at the shallowest reflector).

APPLICATION OF THE ELIMINATION SUBSERIES TO AN ANALYTIC MODEL

In this section we will use an analytic model in which an internal multiple of first-order is interfering destructively with a primary. This is to show the usefulness of the eliminator subseries by surgically removing the internal multiple.

The analytic model we will focus is the three-interface model of Figure 2, with specific values for the acoustic parameters assigned as $(1500m/s, 1000kg/m^3)$, $(2280m/s, 1000kg/m^3)$, $(9000m/s, 1700kg/m^3)$ and $(9900, 1578kg/m^3)$ for (c_0, ρ_0), (c_1, ρ_1), (c_2, ρ_2) and (c_3, ρ_3) respectively. The Primary created at the interface with depth Z_i is denoted P_i. First-order internal multiples are denoted as IM_{ijk} with j indicating the reflector in which the downward reflection is generated; i and k indicate the reflectors where the first and second upward reflections are generated respectively.

The interfering events are the primary P_3 and the internal multiple IM_{212}, whose common travel time is 2.2947s. The amplitudes for P_3 and IM_{212} are 0.0045 and -0.1084 respectively. A trace is shown in Figure 3, from which the amplitude of the combined event $P_3 + IM_{212}$ can be read as -0.1039: the polarity is opposite to that of the primary.

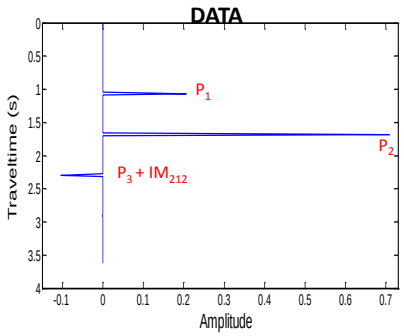

Figure 3: Data of the model. This data includes primaries and the relevant internal multiples of first order.

Next is the application of $b_3(t)$ to attenuate internal multiples of first-order. For the interfering event the amplitude after the action of $b_3(t)$ is -0.0001 and hence the amplitude attenuation is not enough to change the polarity of the interfering event. This might lead to assign to the primary an incorrect polarity.

From the above paragraph it is evident that improvement in the predicted amplitude for IM_{212} is necessary. This is possible if we include further terms from the elimination subseries isolated in the previous section. This is shown in Figure 4, in which the effect of the third term, $b_5^{(IM)_{j=1}}(t)$, has been included in addition to $b_3(t)$.

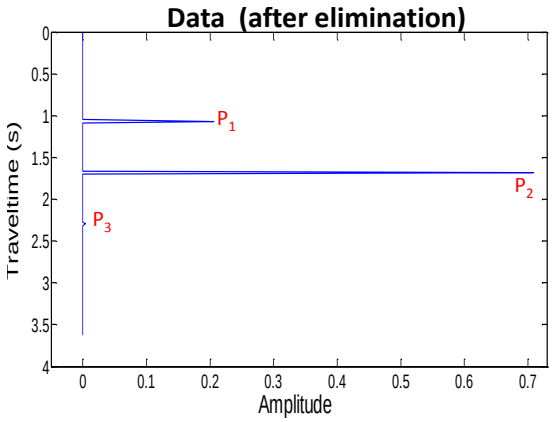

Figure 4: Data after the action of both, the leading-order attenuator and $b_5^{(IM)_{j=1}}(t)$.

The primary P_3 is now with its original amplitude and polarity, 0.0045, which means that the interfering internal multiple has been removed. However, for more complex models the convergence can be slower, and more terms might be needed. Also, from Figure 4, it can be noticed that neither the travel times nor the amplitudes of the primaries P_1 and P_2 are changed, as expected from a method for surgical removal of internal multiples.

DISCUSSION AND CONCLUSIONS

We have isolated from the ISS a subseries whose task is to eliminate first-order internal multiples generated at the shallowest interface, and also attenuates internal multiples from all deeper reflectors. This elimination subseries predicts the phase and the exact amplitude of the internal multiples and does not modify any primary. Therefore, the surgical removal of such internal multiples is achieved.

We have also applied the eliminator subseries to an analytic example with three interfaces. The configuration is set up to produce an internal multiple (with downward reflection at the shallowest reflector) interfering destructively with the primary generated at the third reflector, in a way that the leading-order attenuator is not enough to let the primary show up in the data with its correct polarity. We show how the action of the third-order and fifth-order contributions of the algorithm remove the interfering internal multiple, making the primary to appear in the trace with its original amplitude and polarity. In practice however, it is not possible to know a priori the number of terms that are necessary to eliminate the interfering internal multiple. The recipe is to apply to the data one term at a time until no change is noticed in the primary. Although higher-order terms will imply an increased computational cost (more integrals need to be calculated), if the interfering primary is suspected to be the target, then the investment might be worthwhile, as a situation involving a drilling or no drilling decision might be involved and processing costs pale compared to drilling dry holes.

Interfering events are common in onshore exploration, but they may also occur offshore. Therefore, the algorithm in this work may provide added value in those challenging geologic configurations in which techniques such as the energy-minimization adaptive subtraction fails.

Further research in this topic includes extending the method beyond the normal incidence assumption of the present work, and to derive the corresponding multidimensional version of the subseries presented here. Additionally, current challenges in exploration seismology might also require the removal of other internal multiples of first-order, generated beneath the shallowest reflector. Hence, a more generalresearch goal is to isolate a subseries, with the specific task of the elimination of first-order internal multiples generated at all reflectors.

ACKNOWLEDGMENTS

We want to thank Paolo Terenghi, Chao Ma and Hong Liang for useful discussions during the realization of this work. We thank the M-OSRP sponsors for their encouragement and their support.

REFERENCES

Araújo, F. V., 1994, Linear and non-linear methods derived from scattering theory: backscattering tomography and internal-multiple attenuation.: PhD thesis, Universidade Federal da Bahía, Brazil. (In Portuguese).

Araújo, F. V., W. A. B., C. P. M., and S. R. H., 1994, Inverse scattering series for multiple attenuation: an example with surface and internal multiples, *in* 64th Ann. Int. SEG Mtg, Expanded Abstracts: Soc. Expl. Geophys., 1039–41.

Carvalho, P. M., 1992, Free-surface multiple reflection elimination method based on nonlinear inversion of seismic data: PhD thesis, Universidade Federal da Bahia. (In Portuguese).

Liang, H., and A. B. Weglein, 2012, A further general modification of the leading order iss attenuator of first order internal multiples to accommodate primaries and internal multiples when an arbitrary number of reflectors generate the data: theory, development, and examples: M-OSRP 2012 Annual Meeting, 148–166.

Ma, C., and A. B. Weglein, 2012, Modifying the leading-order iss attenuator of first-order internal multiples to accomodate primaries and internal multiples: fundamental concept and theory, development, and examples exemplified when three reflectors generate the data: M-OSRP 2012 Annual Meeting, 133–147.

Ramírez, A. C., 2007, I. - inverse scattering subseries for removal of internal multiples and depth imaging primaries; ii. - green's theorem as the foundation of interferometry and guiding new practical methods and applications: PhD thesis, University of Houston.

Ramírez, A. C., and A. B. Weglein, 2005, An inverse scattering internal multiple elimination method: Beyond attenuation, a new algorithm and initial tests, *in* 75st Annual International Meeting, SEG, Expanded Abstracts: Soc. Expl. Geophys.

Weglein, A. B., F. V. Araújo, P. M. Carvalho, R. H. Stolt, K. H. Matson, R. T. Coates, D. Corrigan, D. J. Foster, S. A. Shaw, and H. Zhang, 2003, Inverse scattering series and seismic exploration: Inverse Problems, **19**, R27–R83.

Weglein, A. B., F. A. Gasparotto, P. M. Carvalho, and R. H. Stolt, 1997, An inverse-scattering series method for attenuating multiples in seismic reflection data: Geophysics, **62**, 1975–1989.

General theory for accommodating primaries and multiples in internal multiple algorithm: analysis and numerical tests

Hong Liang, Chao Ma and Arthur B. Weglein, M-OSRP/Physics Dept./University of Houston*

SUMMARY

The inverse scattering series (ISS) predicts internal multiples directly and without subsurface information. This is achieved through a task-specific subseries within the overall ISS. The ISS leading-order attenuator of first-order internal multiple is the leading-order term in the subseries that contributes to the removal of first-order internal multiples. It has shown stand-alone capabilities for internal multiple prediction/attenuation for both marine and on-shore plays. The basic idea behind the leading-order attenuator is that all the events in the data are treated as subevents and combined nonlinearly (three data sets are involved), and among all the combinations first-order internal multiples can be predicted by the combination that has all subevents correspond to primaries. However, the entire data set, consisting of primaries and internal multiples, enters the algorithm. When internal multiples in the data themselves act as subevents, the leading-order attenuator produces not only first-order internal multiples, but also higher-order internal multiples and, at times, spurious events. The latter have been observed in the tests of Fu et al. (2010) and Luo et al. (2011). Weglein et al. (2011) have noted this and suggest that the resolution of the problem would reside in other terms of the ISS. Ma et al. (2012) describes the initial occurrence of the circumstance under which spurious event arises, and explains how to address that issue. This abstract extends the analysis in Ma et al. (2012) to more complex circumstances, and provide a description of the general arrival of spurious events. In this abstract we show how the ISS anticipates the issue due to spurious events and provides the response.

INTRODUCTION

The inverse scattering series can achieve all processing objectives directly and without subsurface information. Compared to the ISS free-surface multiple removal methods where the location and the properties of the free surface responsible for free-surface multiples are well-defined, the ISS internal multiple method does not require information concerning the properties of the Earth where internal multiples have experienced a shallowest downward reflection. It is data-driven and predicts internal multiples at all depths at once.

The ISS internal multiple attenuation algorithm was first proposed by Araújo et al. (1994) and Weglein et al. (1997). This algorithm is applicable for towed-streamer field data, land data, and ocean bottom data (Matson and Weglein, 1996; Matson, 1997) and can accommodate internal multiples with converted wave phases (Coates and Weglein, 1996). Ramírez and Weglein (2005) and Ramírez (2007) discuss early ideas to extend the attenuation algorithm towards an elimination method. The ISS internal multiple algorithm has shown encouraging results and differential added value when compared to other internal multiple methods (Fu et al., 2010; Hsu et al., 2011; Terenghi et al., 2011; Weglein et al., 2011; Luo et al., 2011; Kelamis et al., 2013).

Early analysis of the ISS leading-order attenuator focused on the performance of internal multiples prediction by using subevents that correspond to primaries. However, the input data contain both primaries and internal multiples and all events in the data will be treated as subevents. Under some circumstances treating internal multiples as subevents in the leading-order internal multiple algorithm can lead to spurious events. We show that spurious events can occur when more than two reflectors are involved in the data being processed, and explain how terms further in the ISS address and remove those spurious events. Following the suggestion of Weglein et al. (2011) Ma et al. (2012) derives the modified ISS internal multiple algorithm addressing the spurious event arising from the second of the three integrals of the ISS leading-order attenuator in a three-reflector medium. This paper evaluates that algorithm using numerical examples, and also extends the algorithm to a medium with a large number of reflectors.

THE LEADING-ORDER ISS INTERNAL MULTIPLE ATTENUATION ALGORITHM

The ISS internal multiple attenuation algorithm is a subseries of the inverse scattering series. The first term in the algorithm is the deghosted input data D from which the reference wavefield and free-surface multiples have been removed and source wavelet has been deconvolved. The second term in the algorithm is the leading-order attenuator of first-order internal multiples which attenuates first-order internal multiples (the order of an internal multiple is defined by the total number of downward reflections). The leading-order attenuator in a 2D earth is given by Araújo et al. (1994) and Weglein et al. (1997). For a 1D earth and a normal incidence wave the equation reduces to

$$b_3^{PPP}(k) = b_3(k) = \int_{-\infty}^{\infty} dz_1 e^{ikz_1} b_1(z_1) \int_{-\infty}^{z_1-\varepsilon} dz_2 e^{-ikz_2} b_1(z_2) \int_{z_2+\varepsilon}^{\infty} dz_3 e^{ikz_3} b_1(z_3), \quad (1)$$

where the deghosted data, $D(t)$, for an incident spike wave, satisfy $D(\omega) = b_1(2\omega/c_0)$, and where $b_1(z) = \int_{-\infty}^{\infty} e^{-ikz} b_1(k) dk$, $k = 2\omega/c_0$ is the vertical wavenumber, and $b_1(z)$ corresponds to an uncollapsed FK migration of an normal incident spike plane-wave data. For non-spike data, there is an obliquity factor in the relations between the data D and b_1 in the frequency domain (see Page R64 and R65 in Weglein et al. (2003)). Here, we introduce a new notation b_3^{PPP} where the superscript ("P" represents primary) indicates which events in the data input in each of the three integrals that

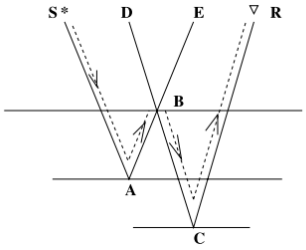

Figure 1: An internal multiple (dashed line) constructed by the "lower-higher-lower" pattern of three primary subevents (solid line). Figure adapted from Weglein et al. (2003).

we are focusing on towards the overall purpose of removing first-order internal multiples. The data with first-order internal multiples attenuated are

$$D(t)+D_3(t), \tag{2}$$

where $D_3(t)$ is the inverse Fourier transform of $D_3(\omega)$ and $D_3(\omega)=b_3(k)$ for an incident spike wave. Weglein and Matson (1998) showed that this algorithm can be interpreted using the subevent concept (see Figure 1).

THE GENERAL OUTPUT OF THE LEADING-ORDER ATTENUATOR WHEN AN INTERNAL MULTIPLE IS TREATED AS A SUBEVENT BY THE ALGORITHM

Early analysis focused exclusively on the performance of the algorithm for b_3 for the events in the data that correspond to primaries. However, seismic data contain not only primary events but also internal multiples. Zhang and Shaw (2010) have shown that higher-order internal multiples can be predicted by the leading-order attenuator using internal multiples as subevents in a two-interface example. However, the situation is considerably more complicated when the data from three or more reflectors are considered. In the latter case, spurious events can be predicted whose traveltimes do not correspond to an event in the data. In this section, we illustrate in a 1D earth the specific conditions under which the spurious events are produced by the leading-order attenuator using one internal multiple subevent.

An internal multiple subevent in the second integral in b_3

In Ma et al. (2012) it is shown that in a medium with three reflectors, and when an internal multiple acts as a subevent in the second of the three integrals (in equation 1) a spurious event can be produced. In this section, we interpret this diagrammatically using Figure 2 (pseudo-depth is determined by the water speed image, $b_1(z)$). An internal multiple has each of its downward reflections between two upward reflections. Then, in the diagrammatic representation of an internal multiple (Figure 2(a)) a higher red circle with a "-" sign should have lower blue circles with "+" signs on both side. However, in Figure 2(c) each of the two red circles has only one lower blue circle on one side, and one higher blue circle on the other side. Thus, this predicted event is neither an

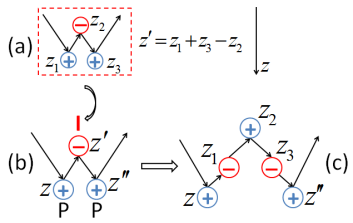

Figure 2: Diagrammatic illustration of the generation of a spurious event. (a) The diagram of a first-order internal multiple. The sign "+" ("-") means upward (downward) reflection or the pseudo-depth is added (subtracted). (b) Three subevents used by b_3: a primary ("P") with pseudo-depth z, an internal multiple ("I") with pseudo-depth z', and a primary with pseudo-depth z'', with $z'<z,z''$. (c) The produced spurious event with pseudo-depth $(z+z''-(z_1+z_3-z_2))$.

internal multiple, nor a primary. The spurious event described here is generated by the leading-order attenuator using an internal multiple subevent in the second integral. The way it is generated suggests the way it can be removed. For the removal of this type of spurious events, substituting b_3 for the second b_1 in equation 1 leads to equation 3. The subevent combination of "primary–predicted internal multiple–primary" in equation 3 can be used to attenuate the spurious event. We examine one of the fifth order terms ($G_0V_1G_0V_3G_0V_1G_0$) that satisfies the required Figure 2(c) geometry. The derivation and analytical examples are shown in Ma et al. (2012).

$$b_5^{PIP}(k)=\int_{-\infty}^{\infty}dz_1e^{ikz_1}b_1(z_1)\int_{-\infty}^{z_1-\varepsilon}dz_2e^{-ikz_2}b_3(z_2)\int_{z_2+\varepsilon}^{\infty}dz_3e^{ikz_3}b_1(z_3) \tag{3}$$

The output of the new ISS internal multiple algorithm for this three reflectors case is

$$D(t)+D_3(t)+D_5^{PIP}(t), \tag{4}$$

where $D_5^{PIP}(t)$ is the inverse Fourier transform of $D_5^{PIP}(\omega)$ and $D_5^{PIP}(\omega)=b_5^{PIP}(k)$ for spike data. The original algorithm (equation 2) attenuates the first-order internal multiples and preserve primaries but can also output spurious events. The modified algorithm in equation 4 provides the benefit of the original algorithm while addressing issues due to spurious events.

An internal multiple subevent in either of the outer integrals in b_3

The problem is yet more complicated when a first-order internal multiple subevent is in either of the outer integrals. As shown in the left panel of Figure 3, when an internal multiple with pseudo-depth z'' is in the rightmost integral ($z,z''>z'$), we have $z''=(z_1+z_3-z_2)>z'$ (this lower-higher-lower relationship in pseudo depth domain is required by b_3, and if it is not satisfied this kind of subevent combination will not occur in b_3). In such a case, there are several possible relations between z_1,z_2,z_3 and z', which are as follows:

- As shown by the first item in Figure 3, when $z_1 > z'$, the predicted event has the same pseudo-depth as a second order internal multiple. Its subevent construction is shown in Figure 4(a), and this occurs in a medium with number of reflectors $N \geq 2$.
- The second item in Figure 3 shows that when $z_1 = z'$, the predicted event has the same pseudo-depth as a first-order internal multiple. Figure 4(b) describes its subevent construction, which only happens in a medium with $N \geq 3$.
- The third item in Figure 3 shows that a spurious event is produced with $z_1 < z'$ and $z_3 < z'$ (the red circle at z' has only one lower blue circle on one side). Its subevent construction is illustrated by Figure 4(c). This type of spurious event can only be generated in a medium with $N \geq 4$.

Using the same logic and analysis as the previous section, we propose another method to address this type of spurious events by replacing the third b_1 in equation 1 with b_3, and the new term is shown in equation 5. Since this type of spurious event could be produced by the leading order attenuator using a first-order internal multiple subevent in either of the outer integrals (these two cases are equivalent), there is a leading coefficient 2 in the equation 5. This term is also identified from a portion of the fifth order term in the ISS (from the term $G_0V_1G_0V_1G_0V_3G_0$).

$$b_5^{PPI}(k) = 2\int_{-\infty}^{\infty} dz_1 e^{ikz_1} b_1(z_1) \int_{-\infty}^{z_1-\varepsilon} dz_2 e^{-ikz_2} b_1(z_2) \int_{z_2+\varepsilon}^{\infty} dz_3 e^{ikz_3} b_3(z_3) \tag{5}$$

The new ISS internal multiple algorithm for this case with more than three reflectors is

$$D_1(t) + D_3(t) + D_5^{PIP}(t) + D_5^{PPI}(t). \tag{6}$$

where $D_5^{PPI}(t)$ is the Fourier transform of $D_5^{PPI}(\omega)$ and $D_5^{PPI}(\omega) = b_5^{PIP}(k)$ for an incident spike wave. This modified general algorithm in equation 6 retains the strengths of the original algorithm while addressing issues due to spurious events.

NUMERICAL EXAMPLES

In this section, we will compute and analyze the new terms for one dimensional, three reflector models. The spurious event would be produced when the internal multiple subevent is in the second of the three integrals. Thus, only the term in equation 3 will be tested in this section. In the previous section, the input data are assumed to be source wavelet. If the data are generated by using a source wavelet, then we have $D(\omega) = A(\omega)b_1(2\omega/c_0)$, and hence, $D_3(\omega) = A(\omega)b_3(\omega/c_0)$, and $D_5^{PIP}(\omega) = A(\omega)b_5^{PIP}(\omega/c_0)$.

Figure 5(a) shows a 1D normal-incidence trace, which includes three primaries and all internal multiples. Figure 5(b) shows the comparison of the actual internal multiples in the

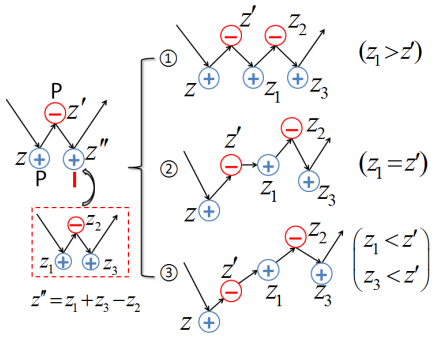

Figure 3: Diagrammatic illustration of predicted events when an internal multiple subevent is in either of the outer integrals.

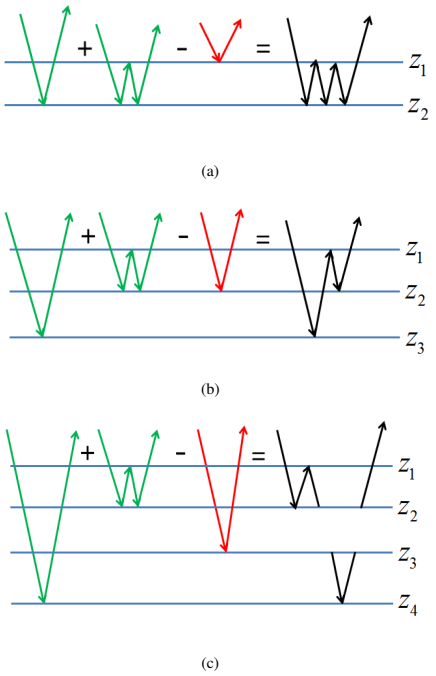

Figure 4: Events generated by the leading-order attenuator using an internal multiple subevent in either of the outer integrals: (a) a second order internal multiple, (b) a first order internal multiple, and (c) a spurious event, $2z_2 - z_1 > z_3$.

data and the events produced by the leading-order attenuator. From the results we can see that by treating both primaries and internal multiples as subevents the leading-order attenuator can predict first-order and higher-order internal multiples, as well as the spurious event (pointed by the green arrow). Figure 5(c) shows the comparison of the spurious event generated by the leading-order attenuator and the one predicted by the higher-order term. By adding D_5^{PIP} to D_3 the spurious event is well attenuated and the internal multiple prediction is almost unchanged, as shown in Figure 6. From Figure 6 we can conclude that the modified algorithm in equation 4 provides the benefit of original algorithm (equation 2) while addressing the limitation due to spurious events.

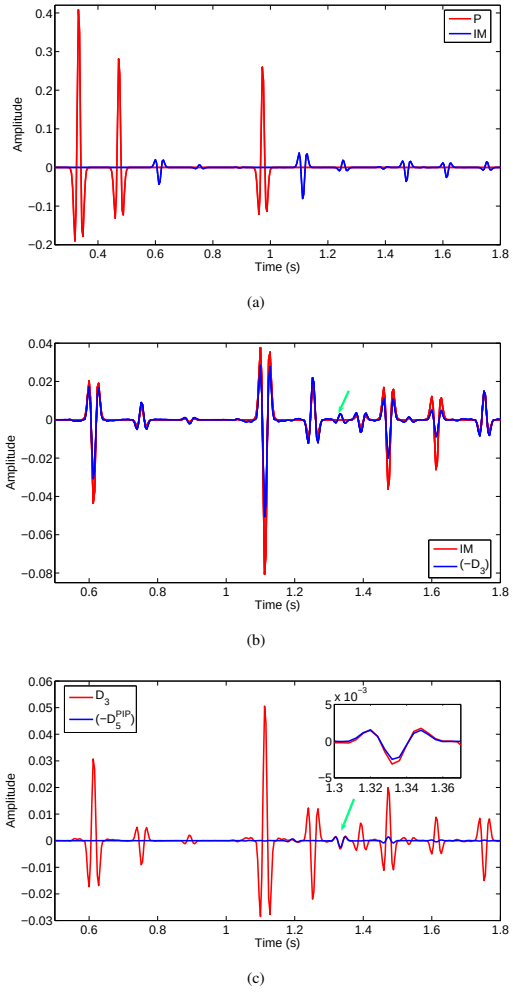

Figure 5: (a) An input trace, including primaries (red) and all internal multiples (blue); (b) Actual internal multiples in the data (red), and events predicted by the ISS leading-order attenuator (blue) including predicted internal multiples and the spurious event (pointed by the green arrow); (c) comparison of the actual spurious event in D_3 and the predicted one in $(-D_5^{PIP})$ (pointed by the green arrow and and the close-up shown in the upper right box).

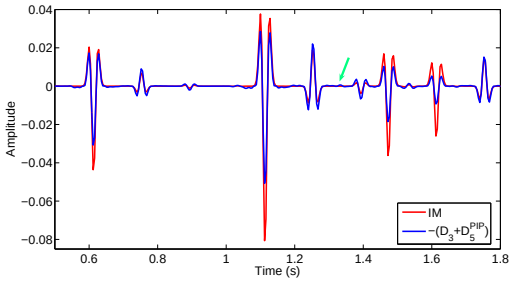

Figure 6: Actual internal multiples in the data (red) and the ones predicted by the modified algorithm (represented by $-(D_3+D_5^{PIP})$). Green arrow points to the spurious events.

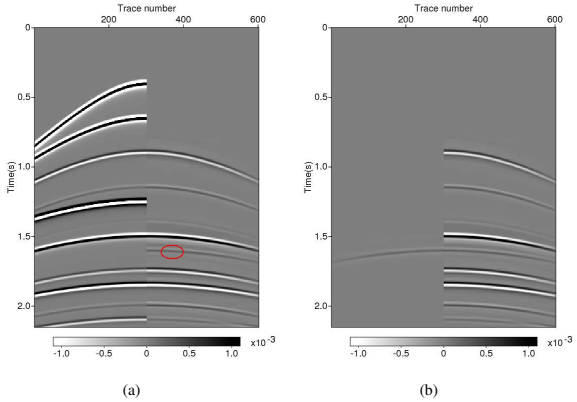

Figure 7: (a) The left are the input data (the first, second and fifth events are primaries), and the right are the events produced by b_3 (the spurious event is marked by the red circle); (b) The right are the events produced by b_3, and the left is the spurious event predicted by b_5^{PIP}.

The modified algorithm 4 can be also extended to 2D experiment in a 1D earth. Figure 7(a) shows a shot gather on the left, and on the right are the events predicted by the leading-order attenuator, in which the red circle mark the generated spurious event. In Figure 7(b), the right are still the events predicted by the leading-order attenuator, while the left shows the spurious event predicted by the higher-order term.

CONCLUSIONS

While the ISS leading-order attenuator has demonstrated its capability for internal multiple removal, it has strengths and limitations as implied by "leading order" and "attenuator".The modified algorithm presented in this paper and Ma et al. (2012) addresses a shortcoming of the current leading-order ISS internal multiple attenuation algorithm that are observed in the examples of Fu et al. (2010) and Luo et al. (2011). Spurious events can be a particular problem if they are proximal to or interfere with primaries or multiples. If you suspect that this is the case, then the algorithm of this paper can remove the spurious event. The modified ISS internal multiple attenuation algorithm retains the benefit of the original algorithm while addressing one of its shortcomings. It now accommodates both primaries and internal multiples in the input data.

ACKNOWLEDGMENTS

We are grateful to all M-OSRP sponsors for their support of this research. Special thanks to Paolo Terenghi for assistance, Jim Mayhan for helpful comments and suggestions.

REFERENCES

Araújo, F. V., A. B. Weglein, P. M. Carvalho, and R. H. Stolt, 1994, Inverse scattering series for multiple attenuation: An example with surface and internal multiples: SEG Technical Program Expanded Abstracts, 1039–1041.

Coates, R. T., and A. B. Weglein, 1996, Internal multiple attenuation using inverse scattering: Results from prestack 1 & 2D acoustic and elastic synthetics: SEG Technical Program Expanded Abstracts, 1522–1525.

Fu, Q., Y. Luo, G. K. Panos, S. Huo, G. Sindi, S. Hsu, and A. B. Weglein, 2010, The inverse scattering series approach towards the elimination of land internal multiples: SEG Technical Program Expanded Abstracts, 3456–3461.

Hsu, S., P. Terenghi, and A. B. Weglein, 2011, The properties of the inverse scattering series internal multiple attenuation algorithm: Analysis and evaluation on synthetic data with lateral variations, choosing reference velocity and examining its sensitivity to near surface properties: Mission-Oriented Seismic Research Program (M-OSRP), Annual Report, 16–28.

Kelamis, P. G., Y. Luo, and A. Weglein, 2013, Strategies of land internal multiple elimination based on Inverse Scattering Series: Presented at the 6th International Petroleum Technology Conference.

Luo, Y., P. G. Kelamis, Q. Fu, S. Huo, G. Sindi, S. Hsu, and A. B. Weglein, 2011, Elimination of land internal multiples based on the inverse scattering series: The Leading Edge, 884–889.

Ma, C., H. Liang, and A. B. Weglein, 2012, Modifying the leading order iss attenuator of first-order internal multiples to accommodate primaries and internal multiples: fundamental concept and theory, development, and examples exemplified when three reflectors generate the data: M-OSRP 2011 Annual meeting.

Matson, K. H., 1997, An inverse-scattering series method for attenuating elastic multiples from multi-component land and ocean bottom seismic data: PhD thesis, University of British Columbia.

Matson, K. H., and A. B. Weglein, 1996, Removal of elastic interface multiples from land and ocean bottom data using inverse scattering: SEG Technical Program Expanded Abstract, 1526–1530.

Ramírez, A. C., 2007, I.-inverse scattering subseries for removal of internal multiples and depth imaging primaries; ii.-green's theorem as the foundation of interferometry and guiding new practical methods and applications: PhD thesis, University of Houston.

Ramírez, A. C., and A. B. Weglein, 2005, An inverse scattering internal multiple elimination method: beyond attenuation, a new algorithm and initial test: SEG Technical Program Expanded Abstracts, 2115–2118.

Terenghi, P., S. Hsu, A. B. Weglein, and X. Li, 2011, Exemplifying the specific properties of the inverse scattering series internal-multiple attenuation method that reside behind its capability for complex onshore and marine multiples: The Leading Edge, 876–882.

Weglein, A. B., F. V. Araújo, P. M. Carvalho, R. H. Stolt, K. H. Matson, R. T. Coates, D. Corrigan, D. J. Foster, S. A. Shaw, and H. Zhang, 2003, Inverse scattering series and seismic exploration: Inverse Problems, R27–R83.

Weglein, A. B., F. A. Gasparotto, P. M. Carvalho, and R. H. Stolt, 1997, An inverse-scattering series method for attenuating multiples in seismic reflection data: Geophysics, 1975–1989.

Weglein, A. B., S. Hsu, P. Terenghi, X. Li, and R. Stolt, 2011, Multiple attenuation: Recent advances and the road ahead 2011: The Leading Edge, 864–875.

Weglein, A. B., and K. H. Matson, 1998, Inverse scattering internal multiple attenuation: an analytic example and subevent interpretation: Mathematical Methods in Geophysical Imaging V, 108–117.

Zhang, H., and S. Shaw, 2010, 1-D analytical analysis of higher order internal multiples predicted via the inverse scattering series based algorithm: SEG Technical Program Expanded Abstracts, 3493–3498.

Accommodating primaries and multiples in internal multiple algorithm: initial concept and data tests

Chao Ma, Hong Liang and Arthur B. Weglein, M-OSRP/Physics Dept./University of Houston*

SUMMARY

The Inverse Scattering Series (ISS) is a comprehensive framework for achieving seismic data processing goals without requiring subsurface information. Distinct isolated task-specific subseries can accomplish free surface multiple removal, internal multiple removal, depth imaging and inversion of primaries. The current leading-order internal multiple attenuation algorithm derived from ISS can predict all first-order internal multiples with the correct time and an approximate, well understood amplitude, at all depths at once. It has shown unmatched capability on complex synthetic and onshore data compared with other methods (e.g., Fu et al. (2010); Luo et al. (2011); Ferreira (2011)). However, in Weglein et al. (2011), there are issues pointed out (e.g., spurious prediction) and circumstances have been identified when those issues are significant. It was also pointed out the limitation is only for the current leading-order algorithm, not for the entire inverse scattering series. This paper provides details for the simplest circumstance under which spurious prediction arises, and how to locate higher-order terms within ISS to address that issue. The companion and complementary paper (Liang et al., 2012) provides a description of the general arrival of spurious events when using the current leading-order algorithm under more complicated/complex circumstances and how the ISS provides the response. The new algorithm maintains the strength of the current leading-order algorithm and, in addition, provides added value to address a limitation of the leading-order algorithm that arises when primaries and multiples enter the algorithm.

INTRODUCTION

In seismic exploration, primaries are events that have experienced only one upward reflection while multiples are events that have experienced multiple upward reflections. Multiples that have at least one downward reflection at the free surface (air-water or air-land) are free surface multiples. Multiples that have experienced all their downward reflections below the free surface are internal multiples. The order of an internal multiple depends on the number of downward reflections it has experienced. For example, the first-order internal multiples have only one downward reflection (dashed line in Figure 1). The primaries-only assumption in seismic data analysis requires multiple removal. The methods for removing multiples are classified as separation and wavefield prediction (e.g.,Weglein (1999) and Weglein et al. (2011)). The separation methods sought a characteristic to distinguish primaries from multiples, while the early wavefield prediction methods first modeled and then subtracted multiples. Each of these approaches have earned their place in the seismic toolbox. However, as seismic exploration moves toward more complex areas, these methods have limitations due to their assumptions and the requirements for subsurface information. The ISS free surface multiple removal algorithm (Carvalho and Weglein, 1994; Weglein et al., 1997) and internal multiple attenuation algorithm (Araújo et al., 1994; Weglein et al., 1997) starts by avoiding the assumptions of the earlier methods, e.g., they are completely multi dimensional and have no requirements for subsurface information. There are both separation and wavefield prediction ingredients in the ISS multiple removal methods and they can be viewed as a next step in the development of separation and wavefield prediction methods (Weglein et al., 2011).

The current algorithm to attenuate first-order internal multiple derived from ISS is called leading-order internal multiple attenuation algorithm. The "leading-order" means it **begins** the work of removing first-order internal multiples, i.e., it predicts all first-order internal multiples at all depths at once with the correct time and an approximate, well understood amplitude. Because it is only a leading-order algorithm, limitations can occur (Weglein et al., 2011). Spurious events can be generated when there are three or more than three significant internal multiple generators. However, an analysis indicates that the spurious prediction can be addressed by including more terms into the current leading-order algorithm. This paper will analyze the simplest case where limitation of the current leading-order algorithm can occur and show how higher-order can be isolated to address that limitation.

AN OVERVIEW OF THE ISS LEADING-ORDER INTERNAL MULTIPLE ATTENUATION ALGORITHM

The leading-order contribution to constructing a class of multiples in the forward series suggests the leading-order contribution for their removal in the inverse series (Weglein et al., 2003). A subseries that focuses on internal multiple removal can be isolated from the inverse series. The ISS internal multiple attenuation algorithm starts with the input data, $D(x_g,x_s,t)$ with the wavelet deconvolved, ghosts and free surface multiples removed. The leading-order prediction of the first-order internal multiples, in a 2D earth is,

$$\begin{aligned} b_3(k_g,k_s,\omega) = \frac{1}{(2\pi)^2}\int_{-\infty}^{\infty}dk_1\int_{-\infty}^{\infty}dk_2 e^{-iq_1(z_g-z_s)}e^{iq_2(z_g-z_s)} \\ \times\int_{-\infty}^{\infty}dz_1 b_1(k_g,k_1,z_1)e^{i(q_g+q_1)z_1} \\ \times\int_{-\infty}^{z_1-\varepsilon}dz_2 b_1(k_1,k_2,z_2)e^{-i(q_1+q_2)z_2} \\ \times\int_{z_2+\varepsilon}^{\infty}dz_3 b_1(k_2,k_s,z_3)e^{i(q_2+q_s)z_3}, \end{aligned} \quad (1)$$

where $D(k_g,k_s,\omega)$ is the Fourier transform of $D(x_g,x_s,t)$, ω is temporal frequency, k_s and k_g are the horizontal wavenumbers for the source and receiver coordinates, respectively; q_g and q_s are the vertical source and receiver wavenumbers defined by

$q_i = sgn(\omega)\sqrt{\frac{\omega^2}{c_0^2} - k_i^2}$ for $i = (g,s)$; z_s and z_g are source and receiver depths; and z_j ($j = 1,2,3$) represents the pseudo-depth using reference velocity migration. The quantity $b_1(k_g,k_s,z)$ corresponds to an uncollapsed migration (Weglein et al., 1997) of effective plane-wave incident data, and $b_1(k_g,k_s,q_g+q_s) = -2iq_sD(k_g,k_s,\omega)$.

With the input data and the leading-order prediction of the first-order internal multiples, we can obtain the data with the first-order internal multiples attenuated, given by

$$D(k_g,k_s,\omega) + D_3(k_g,k_s,\omega), \tag{2}$$

where $D_3(k_g,k_s,\omega) = (-2iq_s)^{-1}b_3(k_g,k_s,q_g+q_s)$.

For a 1D earth and a normal incident plane wave, equation 1 reduces to

$$b_3(k) = \int_{-\infty}^{\infty} dz_1 e^{ikz_1} b_1(z_1) \int_{-\infty}^{z_1-\varepsilon} dz_2 e^{-ikz_2} b_1(z_2) \times \int_{z_2+\varepsilon}^{\infty} dz_3 e^{ikz_3} b_1(z_3). \tag{3}$$

The leading-order ISS internal multiple attenuation algorithm for the first-order internal multiples in a 1D earth and an normal incident plane wave is

$$b_1 + b_3. \tag{4}$$

Note that the $(-2iq_s)$ factor is not needed here. However, for an incident wave which is not a plane wave, the output of the ISS leading-order removal of the first-order internal multiples needs the $(-2iq_s)$ factor to take b to D as in equation 2.

The portion of the third term of the ISS that predicts the first-order internal multiple attenuation is isolated by requiring the "lower(A)-higher(B)-lower(C)" relationship in pseudo-depth domain as shown in Figure 1. Figure 1 only shows the case where primaries act as subevents predicting first-order internal multiples. Notice that the input data contain both primaries and internal multiples and there are circumtances, shown in the next section, where the "lower-higher-lower" template would produce spurious events when one of the subevents is an internal multiple. However, these spurious events are fully anticipated and removed by other higher order terms in the inverse series.

A LIMITATION OF CURRENT LEADING-ORDER INTERNAL MULTIPLE ATTENUATION ALGORITHM ARISING IN A THREE-REFLECTOR MODEL

Zhang and Shaw (2010) analytically show that higher-order internal multiples, e.g., second-order internal multiples can be generated when internal multiples act as subevents in the case where there are two reflectors. In this paper, we use a three reflector example as a simplest circumstance to analyze when/where the spurious prediction can occur.

In a three reflector model (Figure 2), data due to an impulsive incident spike wave $\delta(t-\frac{z}{c})$ are

$$D(t) = R_1\delta(t-t_1) + R_2'\delta(t-t_2) + R_3'\delta(t-t_3) + R_4'\delta(t-(2t_2-t_1)), \tag{5}$$

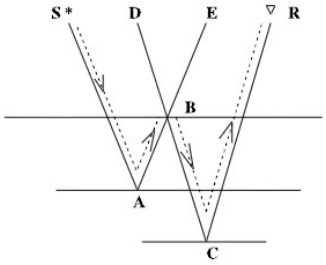

Figure 1: Combination of subevents for the first-order internal multiple (dashed line), $(SABE)_{time} + (DBCR)_{time} - (DBE)_{time} = (SABCR)_{time}$, figure adapted from Weglein et al. (2003). The capitalized letters stand for a primary or an internal multiple.

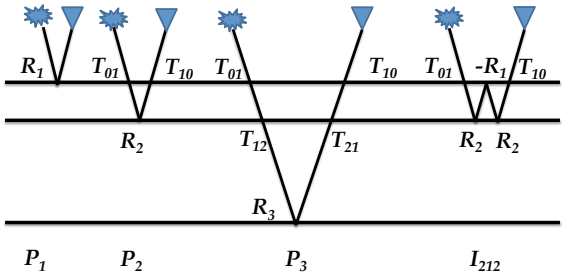

Figure 2: Three primaries and one internal multiple in a three-reflector model.

where $R_2' = T_{01}R_2T_{10}$, $R_3' = T_{01}T_{12}R_3T_{21}T_{10}$, $R_4' = T_{01}R_2(-R_1)R_2T_{10}$, and t_i, R_i are two way times and reflection coefficients from the ith reflector, respectively. T_{ij} is the transmission coefficient between the ith and jth reflector.

Given this data, we find from equation 3 that

$$\begin{aligned} &b_3(t) = \\ &R_1(R_2')^2\delta(t-(2t_2-t_1)) + 2R_1R_2'R_3'\delta(t-(t_2+t_3-t_1)) \\ &+R_1(R_3')^2\delta(t-(2t_3-t_1)) + R_2(R_3')^2\delta(t-(2t_3-t_2)) \\ &+2R_1R_2'R_4'\delta(t-(3t_3-2t_1)) + R_2'(R_4')^2\delta(t-(3t_3-2t_2)) \\ &+2R_1R_3'R_4'\delta(t-(t_3+2t_2-2t_1)) + R_1(R_4')^2\delta(t-(4t_2-3t_1)) \\ &+2R_2'R_3'R_4'\delta(t-(t_3+t_2-t_1)) + (R_3')^2R_4'\delta(t-(2t_3-(2t_2-t_1))). \end{aligned} \tag{6}$$

We have assumed the travel time of the internal multiple is less than that of the third primary in deriving equation 6. An analysis of the traveltimes of these events shows that each of them corresponds to an internal multiple with the exception of the last event $(R_3')^2R_4'\delta(t-(2t_3-(2t_2-t_1)))$, which is a spurious event prediction.

The data entering this algorithm include both primaries and internal multiples, i.e., $b_1 = P + I$, where P stands for primaries, and I stands for internal multiples. It follows from

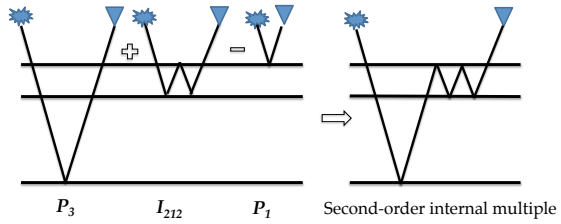

Figure 3: Subevent diagram for the prediction of a second-order internal multiple. This corresponds to $R_1R_3'R_4'\delta(t-(t_3+2t_2-2t_1))$ in equation 6.

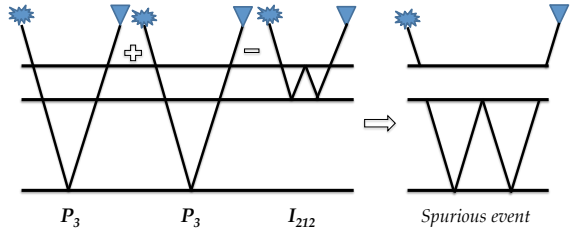

Figure 4: Subevent diagram for the prediction of a spurious event. This corresponds to $(R_3')^2R_4'\delta(t-(2t_3-(2t_2-t_1)))$ in equation 6.

equation 3 that

$$\begin{aligned} b_3 &= b_1 * b_1 * b_1 \\ &= (P+I)(P+I)(P+I) \\ &= PPP+PPI+PIP+IPP+PII+IPI+IIP+III, \end{aligned}$$

where $*$ stands for the nonlinear interaction between the data. Notice that we use the above expression to categorize different possible subevents combinations, it is not specifying which events acting as subevents.

A more detailed analysis shows that in equation 6, first-order internal multiples are predicted in the case of primaries entering the three integrands and acting as subevents (*PPP*), higher-order multiples are predicted in the case of an internal multiple entering the innermost and/or outermost integrand (*PPI*, *IPP*, or *IPI*), and the spurious event is predicted in the case of an internal multiple entering the middle integrand (*PIP*).

Extending the diagrammatic illustrations in Zhang and Shaw (2010), Figure 3 and Figure 4 illustrate the generation of a second-order internal multiple and a spurious event in this three reflector example, respectively.

It can be shown that in the cases where there are more than three internal multiple generators, additional spurious events can be generated by *PPI* or *IPP* combinations (Liang et al., 2012).

A NEW HIGHER-ORDER ISS CONTRIBUTION TO ADDRESS THE SPURIOUS PREDICTION OF THE LEADING-ORDER TERM

The way for the ISS method to reach seismic data processing goals, e.g., removing multiples and imaging, is through collective works from different terms that share the same objective. For example, terms that can remove internal multiples are grouped together, in which each term achieves what the order of that term enables it to achieve towards the ultimate goal. There are certain issues that a term of a given order can address, and other issues that require aid from higher order terms. Here, the leading-order term is able to attenuate all the first-order internal multiples at all depths, and the removal of spurious events generated by this leading-order term requires aid from higher-order terms within ISS. Following the suggestions in Weglein et al. (2011), we show how to isolate higher-order term that help to remove spurious prediction generated by the leading-order term.

To isolate the higher-order term, we first analyze the generation of a spurious event. The left part of Figure 5 shows the generation of a spurious event when an internal multiple acts as a middle subevent, the higher-order term must produce a negative of that spurious prediction to address it. With that in mind, we isolate the higher-order term from a portion of fifth-order term in inverse series, i.e., $(G_0^dV_1'G_0^dV_3'G_0^dV_1'G_0^d)_m$.

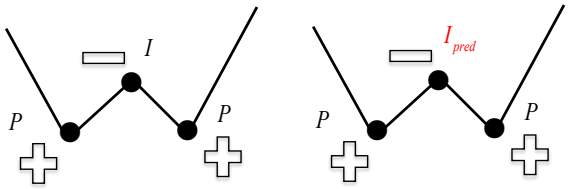

Figure 5: The left part shows the "lower-higher-lower" template of the current leading-order algorithm when the three subevents are "primary-internal multiple-primary"; the right part shows the higher-order term to address the spurious prediction in which the predicted internal multiple acts as a middle subevent. "+" and "-" sign indicate addition and subtraction of phase term for three subevents.

In one dimension, the higher-order term is,

$$\begin{aligned} b_5^{PIP}(k) = \int_{-\infty}^{\infty} dz_1 e^{ikz_1} b_1(z_1) \int_{-\infty}^{z_1-\varepsilon} dz_2 e^{-ikz_2} b_3(z_2) \\ \times \int_{z_2+\varepsilon}^{\infty} dz_3 e^{ikz_3} b_1(z_3), \end{aligned} \tag{7}$$

where $b_1(z)$ is an uncollapsed migration and $b_3(z)$ is the first-order attenuator. The superscript, *PIP* indicates that this higher-order term, b_5^{PIP} is included to address the spurious prediction generated by primary-internal multiple-primary subevent combination.

Equation 7 and equation 3 together provide a new ISS intenral multiple attenuation algorithm for a 1D earth,

$$D_1(t)+D_3(t)+D_5^{PIP}(t), \tag{8}$$

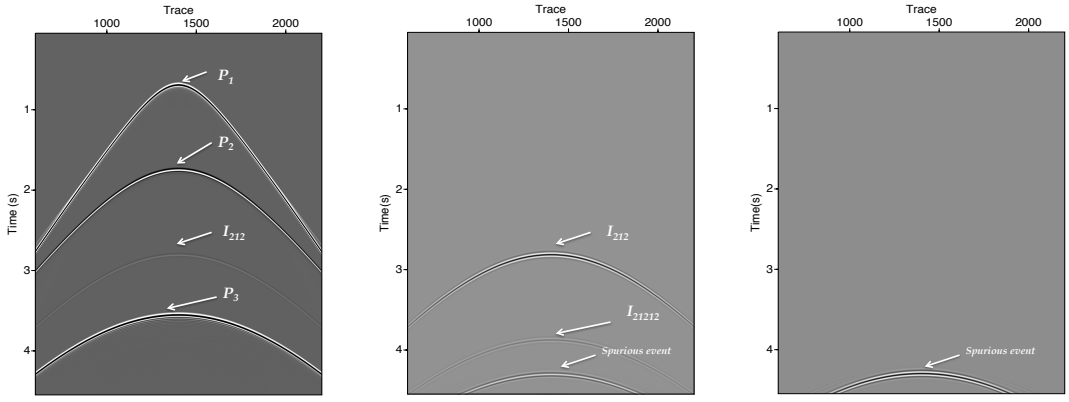

Figure 6: (a): the input data; (b) internal multiple prediction of the current leading-order algorithm; (c) prediction of higher-order modification to address spurious prediction.

Where, in 1D case, $D_5^{PIP} = b_5^{PIP}$.

We use the same analytic example (Figure 2) to test the new algorithm. Substituting $D(t)$ in equation 5 and b_3 in equation 6 into equation 7 produces a term, $R_1(R_2')^2(R_3')^2\delta(t-(2t_3-(2t_2-t_1)))$. Substitution of $R_2' = T_{01}R_2T_{10}$ leads to

$$(T_{01}T_{10})^2R_1(R_2)^2(R_3')^2\delta(t-(2t_3-(2t_2-t_1))).$$

The spurious event in b_3 is

$$(-T_{01}T_{10})R_1(R_2)^2(R_3')^2\delta(t-(2t_3-(2t_2-t_1))).$$

Hence, the introduced higher-order term can effectively address the spurious prediction in the current leading-order algorithm.

We present a synthetic example in 1.5D to test the higher-order modification. The model parameters we use to generate the test data are shown as follows, $V_1 = 1500m/s, \rho_1 = 1.0g/cm^3, d_1 = 500m; V_2 = 1700m/s, \rho_2 = 1.8g/cm^3, d_2 = 900m; V_3 = 1550m/s, \rho_3 = 1.0g/cm^3, d_3 = 1530m; V_4 = 5000m/s, \rho_4 = 4.0g/cm^3$.

The data, $D(t)$ are shown in Figure 6 (a). The first, second and fourth event are three primaries, P_1, P_2, P_3, from three reflectors, respectively; the third event is a first-order internal multiple, I_{212}, generated by the first two reflectors. Internal multiple predictions using the current leading-order algorithm, $D_3(t)$ are shown in Figure 6 (b). Both internal multiples (first-order I_{212} and second-order I_{21212}) and a spurious event are generated. The result of higher-order modification, $D_5^{PIP}(t)$ is shown in Figure 6 (c). The introduced term, $D_5^{PIP}(t)$ can address the spurious prediction.

It is worth pointing out that the current leading-order internal multiple attenuation algorithm is sufficient and adequate when the there are two significant internal multiple generator, e.g., in deep water of Gulf of Mexico where the water bottom and top salt are two main internal multiple generators. When there exist more than two significant internal multiple generators and the amplitude of an internal multiple is comparable with that of a deeper primary, e.g., in Middle East where there are strong near-surface internal multiple generators, the current leading-order algorithm can produce significant spurious prediction, higher-order modification needs to be included to address the spurious prediction.

DISCUSSION AND CONCLUSION

In this paper, we provide both (1) a detailed analysis for the simplest circumstance under which significant spurious events can be generated by the current leading-order internal multiple attenuation algorithm and (2) a higher-order term that is selected from inverse scattering series to address that spurious prediction. The simpler case shown in this paper provides an initial analysis and helps to understand the more complicated and more realistic case shown in Liang et al. (2012). The ISS can remove all internal multiples without subsurface information and also remove spurious events that arise from using a complex data in a leading-order algorithm.

To conclude, the new higher-order algorithm in this paper provides added value to the current leading-order ISS internal multiple attenuation algorithm, it retains the strength of the original leading-order algorithm while addressing a limitation in the latter.

ACKNOWLEDGMENTS

We thank M-OSRP sponsors for their support of this research. The authors would like to thank Wilberth Herrera, Jim Mayhan, and Paolo Terenghi for reviewing.

REFERENCES

Araújo, F. V., A. B. Weglein, P. M. Carvalho, and R. H. Stolt, 1994, Inverse scattering series for multiple attenuation: An example with surface and internal multiples: SEG Technical Program Expanded Abstracts, 1039–1041.

Carvalho, P., and A. B. Weglein, 1994, Wavelet estimation for surface multiple attenuation using a simulated annealing algorithm: SEG Technical Program Expanded Abstracts, 1481–1484.

Ferreira, A. S., 2011, Internal multiple removal in offshore brazil seismic data using the inverse scattering series: Master's thesis, University of Houston.

Fu, Q., Y. Luo, P. Kelamix, S. Huo, G. Sindi, S.-Y. Hsu, and A. B. Weglein, 2010, The inverse scattering series approach towards the elimination of land internal multiples: SEG Expanded Abstracts, 3456–3461.

Liang, H., C. Ma, and A. B. Weglein, 2012, A further general modification of the leading order iss attenuator of first order internal multiples to accommodate primaries and internal multiples when an arbitrary number of reflectors generate the data: theory, development, and examples: M-OSRP Annual Report, 148–166.

Luo, Y., P. G. Kelamis, Q. Fu, S. Huo, G. Sindi, S.-Y. Hsu, and A. B. Weglein, 2011, Elimination of land internal multiples based on the inverse scattering series: The Leading Edge, 884–889.

Weglein, A. B., 1999, Multiple attenuation: an overview of recent advances and the road ahead (1999): The Leading Edge, 40–44.

Weglein, A. B., F. V. Araújo, P. M. Carvalho, R. H. Stolt, K. H. Matson, R. T. Coates, D. Corrigan, D. J. Foster, S. A. Shaw, and H. Zhang, 2003, Inverse scattering series and seismic exploration: Inverse Problems, R27–R83.

Weglein, A. B., F. A. Gasparotto, P. M. Carvalho, and R. H. Stolt, 1997, An inverse-scattering series method for attenuating multiples in seismic reflection data: Geophysics, **62**, 1975–1989.

Weglein, A. B., S.-Y. Hsu, P. Terenghi, X. Li, and R. H. Stolt, 2011, Multiple attenuation: Recent advances and the road ahead (2011): The Leading Edge, 864–875.

Zhang, H., and S. Shaw, 2010, 1-d analytical analysis of higher order internal multiples predicted via the inverse scattering series based algorithm: SEG Expanded Abstracts, **29**, 3493–3498.

GEOPHYSICS, VOL. 78, NO. 2 (MARCH-APRIL 2013); P. WA77–WA89, 12 FIGS., 3 TABLES.
10.1190/GEO2012-0295.1

First application of Green's theorem-derived source and receiver deghosting on deep-water Gulf of Mexico synthetic (SEAM) and field data

James D. Mayhan[1] and Arthur B. Weglein[1]

ABSTRACT

Deghosting benefits traditional seismic processing and is a prerequisite to all inverse-scattering-series based processing. The freedom of choosing a convenient reference medium (and associated Green's function) means Green's theorem offers a flexible framework for deriving useful algorithms including deghosting. Among advantages over traditional deghosting methods are: (1) no need for Fourier transforms over receivers and sources, and (2) can accommodate a horizontal or non-horizontal measurement surface, the latter of particular interest for ocean bottom and onshore applications. The theory of Green's theorem-derived deghosting is presented, and its first application on deep-water Gulf of Mexico synthetic (SEAM) and field data is reported. The source and receiver deghosting algorithms work with positive and encouraging results.

INTRODUCTION

Deghosting is a long-standing problem (see, e.g., Robinson and Treitel, 2008) and benefits traditional seismic processing and all inverse-scattering-series (ISS) based processing. The benefits of deghosting include the following: (1) removing the downward component of the recorded pressure wavefield (receiver deghosting) enhances seismic resolution by removing ghost notches and boosting low frequencies, (2) deghosting is a prerequisite for many processing algorithms including multiple elimination (ISS free-surface multiples, ISS internal multiples, and surface-related-multiple elimination), and (3) model-matching full-wave inversion (FWI) benefits from enhanced low-frequency data.

Although ISS methods are independent of subsurface velocity (and in fact of all subsurface properties), they make certain assumptions about their input data. Weglein et al. (2003) describe how every ISS isolated-task subseries requires (1) the removal of the reference wavefield, (2) an estimate of the source signature and radiation pattern, and (3) source and receiver deghosting, and how the ISS has a nonlinear dependence on these preprocessing steps. The fact that the ISS is nonlinear places a higher premium on preprocessing requirements. An error in the input to a linear process creates a linear error in its output, but the same linear error in ISS input creates a combination of linear, quadratic, cubic, etc., errors in its output. The non-linear model matching FWI would share that interest.

The freedom of choosing a convenient reference medium (and associated Green's function) means Green's theorem offers a flexible framework for deriving useful algorithms. Green's theorem methods can be categorized as wavefield prediction or wavefield separation. To predict the wavefield anywhere in a volume V, Green's theorem based wavefield prediction has the traditional need for (a) wavefield measurements on the boundary S enclosing V and (b) a knowledge of the medium throughout V. Examples of wavefield prediction based on Green's theorem include Schneider (1978), Clayton and Stolt (1981), Stolt and Weglein (2012), and reverse-time migration (Weglein et al., 2011a, 2011b). In contrast, Green's theorem-based wavefield separation only assumes separate sources inside and outside V, and nothing about the character of those sources is called for or needed. Within wavefield separation, different applications (e.g., wavelet estimation and deghosting) call for different choices of reference media and sources. Examples of wavefield separation based on Green's theorem include source-wavelet estimation (Weglein and Secrest, 1990) and deghosting (Weglein et al., 2002; Zhang and Weglein, 2005, 2006; Zhang, 2007). In Green's theorem wavefield separation methods, evaluating the surface integral at a point inside V provides the contribution to the total field at a point inside V due to sources outside V, without needing or determining the nature or properties of any of the actual (active or passive) sources inside or outside V. Hence, Green's theorem-derived wavefield separation preprocessing steps (e.g., for wavelet

Manuscript received by the Editor 28 July 2012; revised manuscript received 18 December 2012; published online 20 March 2013.
[1]University of Houston, M-OSRP, Houston, Texas, USA. E-mail: jdmayhan@uh.edu; aweglein@uh.edu.

estimation and deghosting) are consistent with subsequent ISS processing methods that also do not assume knowledge of or require subsurface information. The Green's theorem wavefield prediction and wavefield separation methods are multidimensional and work in the $(\mathbf{r}, \omega)$ or $(\mathbf{r}, t)$ data spaces (and, hence, are simple to apply to irregularly spaced data).

Green's theorem-derived deghosting was developed in a series of papers (Weglein et al., 2002; Zhang and Weglein, 2005, 2006; Zhang, 2007) and has characteristics not shared by previous methods. For example, there is no need for Fourier transforms over receivers and sources, and it can accommodate a horizontal or non-horizontal measurement surface. In Mayhan et al. (2011), we reported the first use of Green's theorem-derived receiver deghosting on deep-water Gulf of Mexico synthetic (SEAM) and field data; in Mayhan et al. (2012), we reported the first use of Green's theorem-derived source deghosting on the same data; and in this paper we provide more detail on the algorithms used.

A brief aside on our terminology. (1) The total wavefield P measured by the hydrophones is considered as the sum of a reference wavefield P_0 (which for a homogeneous whole-space reference medium (used in Green's theorem deghosting) is a direct wave from source to receiver) and the scattered wavefield P_s (which is $P - P_0$). (2) Ghosts begin their propagation moving upward from the source (source ghosts) or end their propagation moving downward to the receiver (receiver ghosts) or both (source/receiver ghosts) and have at least one upward reflection from the earth.

After the reference wavefield and all ghosts have been removed, multiples and primaries are defined. (3) Free-surface multiples have at least one downward reflection from the air/water boundary and more than one upward reflection from the earth. (An nth order free-surface multiple has n downward reflections from the air/water boundary.) (4) Internal multiples have no downward reflections from the air/water boundary, more than one upward reflection from the earth, and at least one downward reflection from below the free surface. (An nth order internal multiple has n downward reflections from any reflector(s) below the free surface.) (5) Primaries have only one upward reflection from the earth. These marine events are summarized in Figure 1.

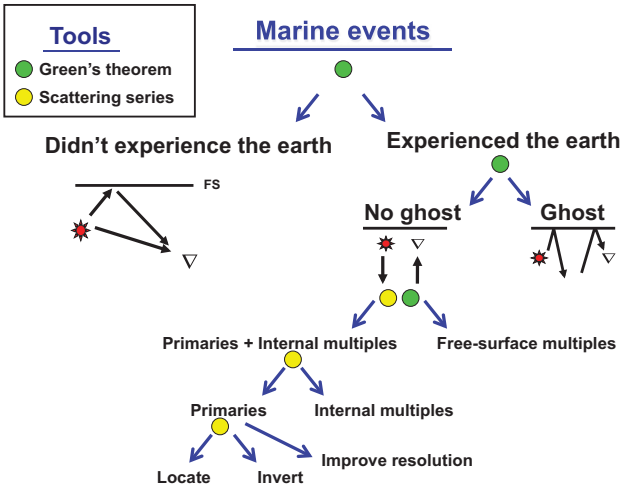

Figure 1. Classification of marine events and how they are processed.

The source- and receiver-deghosting steps described below essentially follow the method described and exemplified in pages 33–39 of Zhang (2007). The difference is that for each shot we choose to input dual measurements of P and $\partial P/\partial z$ along the towed streamer, whereas Zhang chose to use the source wavelet and P along the cable for his numerical examples. (The theory in Zhang [2007] covers both cases.) The advantages of having the wavefield P and its normal derivative along the towed streamer are (1) to allow deghosting for an arbitrary source distribution without needing to know or to determine the source, and (2) for increased stability in the vicinity of notches. Using measurements at two depths (or G_0^{DD} as described below) introduces a more depth-sensitive denominator.

THEORY

Receiver deghosting

Green's theorem derived-preprocessing is based on a perturbation approach where the actual problem and medium are considered as composed of a reference medium plus "sources." The latter arise as source terms in the differential equation that describes the wave propagation in the actual medium. A reference medium (and its associated Green's function) is chosen to facilitate solving the problem at hand, and the perturbations are represented as source terms necessary to write the actual propagation in terms of a reference medium source term picture. Within that general reference medium and source term framework, Green's theorem-derived preprocessing is remarkably wide ranging. For example, Figure 2 shows the configuration chosen for Green's theorem-derived deghosting. For deghosting, a reference medium that consists of a whole-space of water requires three source terms: a source that corresponds to air and begins above the air-water boundary, the air guns in the water column, and a source that corresponds to earth and begins below the water-earth boundary. Choosing a hemispherical surface of integration bounded below by the measurement surface, and the prediction or observation point inside the surface of integration

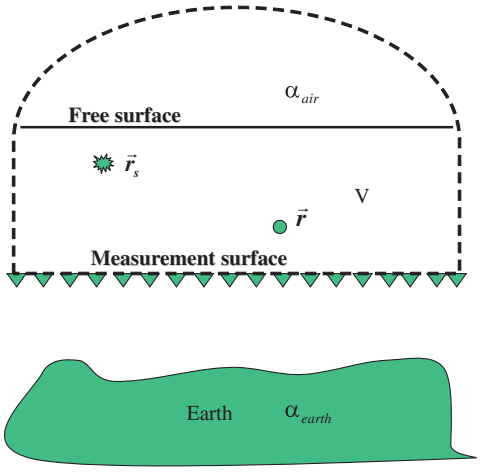

Figure 2. Configuration for Green's theorem-derived deghosting (Zhang [2007] Figure 2.10). α_{air} and α_{earth} are perturbations, the differences between the actual medium (half-space of air, water, half-space of earth) and the reference medium (whole-space of water). The closed surface S of integration is the measurement surface plus the dashed line. $\mathbf{r}$ in the figure corresponds to $\mathbf{r}_g'$ in equation 2.

gives receiver-deghosted data, P'_R (as explained in Appendix A). A different choice of a reference medium (a half-space of air and a half-space of water, separated by an air/water boundary) with two source terms, is useful for separating the reference wave P_0=$P_0^d + P_0^{FS}$and $P_s = P - P_0$. The prediction or observation point outside or inside the surface of integration, gives wavefield separation, in which the total wavefield P is separated into the reference wavefield P_0 (prediction or observation point outside) or the scattered wavefield P_s (prediction or observation point inside).

Green's theorem-derived deghosting (receiver and source) is based on Weglein et al. (2002), Zhang and Weglein (2005, 2006), and Zhang (2007). Depending on the marine experiment, we have the following options for receiver deghosting. (1) If we have P measurements only, we can use a derived variation of Green's theorem (equation 3), a "double Dirichlet" Green's function (equation 7 or 8), and an estimate of the source wavelet to predict P and $\partial P/\partial z$ above the towed streamer(s). Then we can use the derived variation of Green's theorem, a "whole-space" Green's function (equation 1), and the predicted P and $\partial P/\partial z$ to predict receiver-deghosted P'_R above the input P and $\partial P/\partial z$. (2) If we have a dual-sensor towed streamer or over/under towed streamers, we can use the derived variation of Green's theorem and a whole-space Green's function to directly predict receiver-deghosted P'_R above the towed streamer(s). The theory of case (2) assumes measurement of the pressure wavefield P and its normal derivative $\partial P/\partial n \equiv \nabla P(\mathbf{r}, \mathbf{r}_s, \omega) \cdot \hat{\mathbf{n}}$ where $\mathbf{r}$ is the receiver location, $\mathbf{r}_s$ is the source location, and $\hat{\mathbf{n}}$ is the unit normal to the measurement surface (pointing away from the enclosed volume V).

The reference medium is chosen to be a whole-space of water (where a causal solution exists for the acoustic wave equation in 3D). In the $(\mathbf{r}, \omega)$ domain, the causal whole-space Green's function is

$$G_0(\mathbf{r}, \mathbf{r}'_g, \omega) = G_0^d = \begin{cases} -(1/4\pi)\exp(ikR_+)/R_+ & \text{in 3D} \\ -(i/4)H_0^{(1)}(kR_+) & \text{in 2D} \end{cases} \tag{1}$$

where $\mathbf{r}'_g$ is the observation or prediction location, $k = \omega/c_0$, c_0 is the wave speed in the reference medium, $R_+ = |\mathbf{r} - \mathbf{r}'_g|$, and $H_0^{(1)}$ is the zeroth-order Hankel function of the first kind (Morse and Feshbach [1953], § 7.2). The observation or prediction point is chosen between the air/water boundary and the measurement surface, i.e., inside the volume V bounded by the closed surface of integration consisting of the measurement surface and the dashed line in Figure 2. For a discussion of why the causal whole-space Green's function exhibits the forms in equation 1, please see chapter 7 in Morse and Feshbach (1953).

The configuration in Figure 2, the derived variation of Green's theorem, and the acoustic wave equations for P and G_0^d combine to give the key equation,

$$P'_R(\mathbf{r}'_g, \mathbf{r}_s, \omega) = \oint_S dS\, \hat{\mathbf{n}} \cdot [P(\mathbf{r}, \mathbf{r}_s, \omega)\nabla G_0^d(\mathbf{r}, \mathbf{r}'_g, \omega) - G_0^d(\mathbf{r}, \mathbf{r}'_g, \omega)\nabla P(\mathbf{r}, \mathbf{r}_s, \omega)], \tag{2}$$

where S is the closed surface consisting of the measurement surface and the dashed line in Figure 2, and $\hat{\mathbf{n}}$ is the unit normal to S (pointing away from the enclosed volume V). The source location, $\mathbf{r}_s$, and observation or prediction point, $\mathbf{r}'_g$, are inside the volume V. Extending the radius of the hemisphere to infinity, invoking the Sommerfeld radiation condition, and assuming a horizontal measurement surface, the integral over the closed surface becomes an integral over the measurement surface (Weglein et al. [2002] equation 5),

$$P'_R(\mathbf{r}'_g, \mathbf{r}_s, \omega) = \int_{m.s.} dS \left[P(\mathbf{r}, \mathbf{r}_s, \omega) \frac{\partial}{\partial z} G_0^d(\mathbf{r}, \mathbf{r}'_g, \omega) - G_0^d(\mathbf{r}, \mathbf{r}'_g, \omega) \frac{\partial}{\partial z} P(\mathbf{r}, \mathbf{r}_s, \omega) \right]. \tag{3}$$

The algorithm in equation 3 lends itself to application in a marine single-shot experiment. If the predicted cable is above the towed cable and below the shots, equation 3 identifies and attenuates downgoing waves at the predicted cable (as shown in Appendix A). Receiver ghosts, source/receiver ghosts, the direct wave, and the direct wave's reflection at the air/water boundary are removed.

Green's theorem derived receiver deghosting can be compared with a conventional $P + V_z$ sum method of deghosting (Amundsen, 1993; Robertsson and Kragh, 2002; Kragh et al., 2004). For a 3D point source and given a 1D earth and horizontal acquisition and adequate sampling to allow a Fourier transform from space to wavenumber, the two algorithms are equivalent. But these givens can be an issue. In addition, the application of the $P + V_z$ sum, under certain circumstances, brings other assumptions. For example, a 1D layered earth is assumed and dense sampling is needed to support its inverse Hankel transform (Amundsen [1993], p. 1336). The latter is often considered the current industry standard deghosting method. In contrast, the Green's theorem deghosting algorithm (1) can accommodate a 1D, 2D, or 3D earth and (2) stays in coordinate space. Within these assumptions, $P + V_z$ can be derived from Green's theorem as shown in Appendix B. The derivation follows in the tradition of Corrigan et al. (1991), Amundsen (1993), Weglein and Amundsen (2003); Weglein et al. (personal communication, 2013). This derivation, which to our knowledge has not been

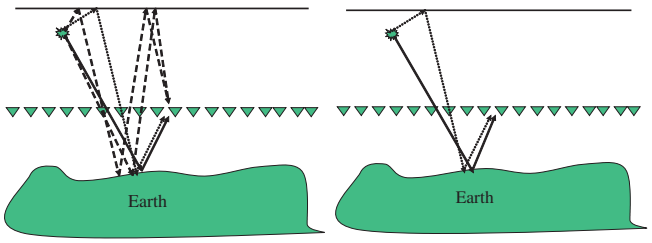

Figure 3. Input (left), receiver deghosted (right) (Zhang [2007] Figure 2.14).

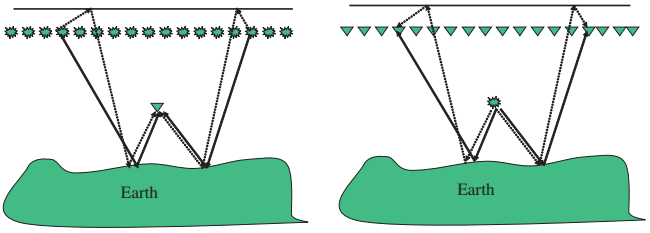

Figure 4. CSG to CRG (left), exchange coordinates (right) (Zhang [2007] Figure 2.15–2.16).

published before, shows that deghosting in the wavenumber-frequency domain is a special case of the more general deghosting in the space-frequency domain derived from Green's theorem.

Source deghosting

We have shown how Green's theorem can be applied to select the portion of the seismic wavefield that is upgoing at a field position above the cable. The algorithm uses data from a single shot gather and the receiver coordinate as the integration variable. This section shows how the theory can be similarly applied for source deghosting, where the portion of the wavefield that is downgoing at the source is sought. Depending on the marine experiment, we have the following options for source deghosting. (1) If we have a collection of single source experiments, we can use the derived variation of Green's theorem (equation 3), a double Dirichlet Green's function (equation 7 or 8), and receiver-deghosted data P'_R to predict new P'_R and $\partial P'_R/\partial z$ above the receiver-deghosted data. Then we can use the derived variation of Green's theorem, a whole-space Green's function (equation 1), and the predicted P'_R and $\partial P'_R/\partial z$ to predict source and receiver-deghosted P'_{SR} above the input P'_R and $\partial P'_R/\partial z$. (2) If we have over/under shots, we can use the derived variation of Green's theorem (equation 4), a whole-space Green's function, and receiver-deghosted data P'_R to directly predict source and receiver-deghosted P'_{SR} above the receiver-deghosted data. An application of reciprocity to the entire set of shot records allows the original receiver-ghost removal to become a source-ghost removal. Then a second application of the derived variation of Green's theorem over receivers results in source- and receiver-deghosted data. An experiment with over/under receivers and over/under sources can be receiver deghosted and source deghosted by a double application of the derived variation of Green's theorem (part of Weglein et al., 2002).

Green's theorem-derived source deghosting begins with source-receiver reciprocity. We interpolate shots so that the distance between shots is the same as the inline distance between receivers, assign "station numbers" to shots and receivers relative to a grid fixed in space, use the station numbers to re-sort the sail line from common-shot gathers (CSGs) to common-receiver gathers (CRGs), and exchange the locations of the shots and receivers. Source ghosts upgoing at the shots are now receiver ghosts downgoing at the "receivers," and a second application of equation 3 will remove them. This can be seen in Figures 3 and 4. In Figure 3, the left panel shows the recorded data (for simplicity, only primaries and their ghosts are shown), and the right panel shows receiver-deghosted data (the receiver ghosts and source/receiver ghosts have been attenuated leaving primaries and their source ghosts). In the left panel of Figure 4, CSGs have been sorted to produce CRGs, and in the right panel shot and receiver locations have been exchanged. The configuration in panel (d) looks like that in panel (a), so a second application of equation 3 will remove the source ghosts.

If the experiment has over/under shots, the integral analogous to equation 3 is

$$P'_{SR}(\mathbf{r}'_g,\mathbf{r}'_s,\omega)=\int_{\text{sources}} dS\,\hat{\mathbf{n}}\cdot[P'_R(\mathbf{r}'_g,\mathbf{r},\omega)\nabla G_0^+(\mathbf{r},\mathbf{r}'_s,\omega) - G_0^+(\mathbf{r},\mathbf{r}'_s,\omega)\nabla P'_R(\mathbf{r}'_g,\mathbf{r},\omega)]. \quad (4)$$

With single shot experiments, the next step in Green's theorem-derived source deghosting predicts a dual-sensor cable. Now (following Zhang (2007)) use a double Dirichlet Green's function G_0^{DD} to predict a dual-sensor cable above the receiver-deghosted cable. G_0^{DD} is constructed to vanish on the air/water boundary and the measurement surface (Morse and Feshbach [1953], p. 812ff; Osen et al., 1998; Tan, 1999; Zhang [2007], p. 20ff). In the $(\mathbf{r},\omega)$ domain, Green's theorem now takes the form

$$P'_R(\mathbf{r}''_g,\mathbf{r}_s,\omega)=\int_{m.s.} dS'_g P'_R(\mathbf{r}'_g,\mathbf{r}_s,\omega)\frac{\partial G_0^{DD}}{\partial z_g{}'}(\mathbf{r}'_g,\mathbf{r}''_g,\omega)|_{z'_g=m.s.} \quad (5)$$

$$\frac{\partial P'_R}{\partial z''_g}(\mathbf{r}''_g,\mathbf{r}_s,\omega)=\int_{m.s.} dS'_g P'_R(\mathbf{r}'_g,\mathbf{r}_s,\omega)\frac{\partial^2 G_0^{DD}}{\partial z'_g\partial z''_g}(\mathbf{r}'_g,\mathbf{r}''_g,\omega)|_{z'_g=m.s.} \quad (6)$$

where $\mathbf{r}''_g$ is the observation or prediction point, $\mathbf{r}_s$ is the shot location, $\mathbf{r}'_g$ is the receiver location on the receiver-deghosted cable, and

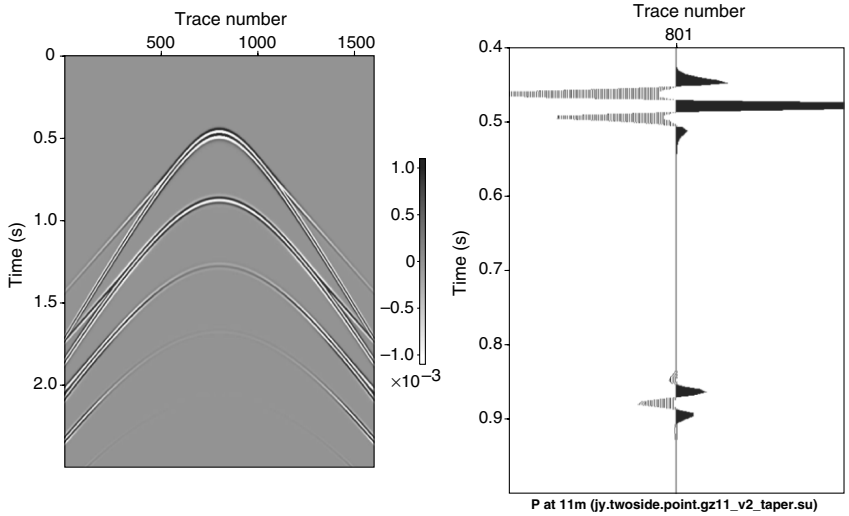

Figure 5. Flat-layer model: P_s at 11 m. The first event is the water bottom primary and its ghosts, and the second event is the first free surface multiple and its ghosts. The right panel shows the zero-offset trace (801 of 1601). More detail is given in Table C-1 in Appendix C.

differentiating equation 5 with respect to the observation or prediction coordinate z_g'' derives equation 6. P_R' is the result of receiver deghosting and source-receiver reciprocity. For a single source experiment, source and receiver deghosting is achieved (with over/under receivers) first using equation 3 and then substituting equations 5 and 6 in equation 4.

In 2D the analytic form of the double Dirichlet Green's function G_0^{DD} in the $(\mathbf{r}, \omega)$ domain is

$$G_0^{DD}(\mathbf{r}_g', \mathbf{r}_g'', \omega) = -\frac{1}{b}\sum_{n=1}^{\infty}\frac{1}{\sqrt{\beta}}\exp\left(-\sqrt{\beta}|x_g' - x_g''|\right) \times \sin\left(\frac{n\pi}{b}z_g'\right)\sin\left(\frac{n\pi}{b}z_g''\right) \quad (7)$$

where (x_g'', z_g'') are the observation or prediction coordinates, (x_g', z_g') are the receiver coordinates on the receiver-deghosted cable, the air/water boundary is at $z_g' = 0$, the input (receiver-deghosted) cable is at $z_g{}' = b$, and we assume $\beta \equiv (n\pi/b)^2 - k^2 > 0$ (Osen et al., 1998; Tan, 1999). In 3D,

$$G_0^{DD}(\mathbf{r}_g'', \mathbf{r}_g', \omega) = \frac{2\pi i}{b}\sum_{n=1}^{\infty}H_0^{(1)}(\gamma\rho)\sin\left(\frac{n\pi}{b}z_g'\right)\sin\left(\frac{n\pi}{b}z_g''\right) \quad (8)$$

where $\gamma = i\sqrt{\beta}$ and $\rho = \sqrt{(x_g'' - x_g')^2 + (y_g'' - y_g')^2}$ (Osen et al., 1998). For a discussion as to why G_0^{DD} has these forms, please see p. 820 in Morse and Feshbach (1953). For purposes of numeric evaluation, the Hankel function with imaginary argument is replaced by a hyperbolic Bessel function with real argument (Morse and Feshbach [1953], p. 1323).

The following simple analysis shows that for separating up and down waves using two measurements at one depth can be more stable than two measurements at two different depths. Using P measured at two depths introduces a depth sensitive denominator. Under perfect conditions the two methods are equivalent, but under practical conditions they are not. For example,

$$P = A\ \exp(ikz) + B\ \exp(-ikz) \quad (9)$$

$$P(0) = A + B \quad (10)$$

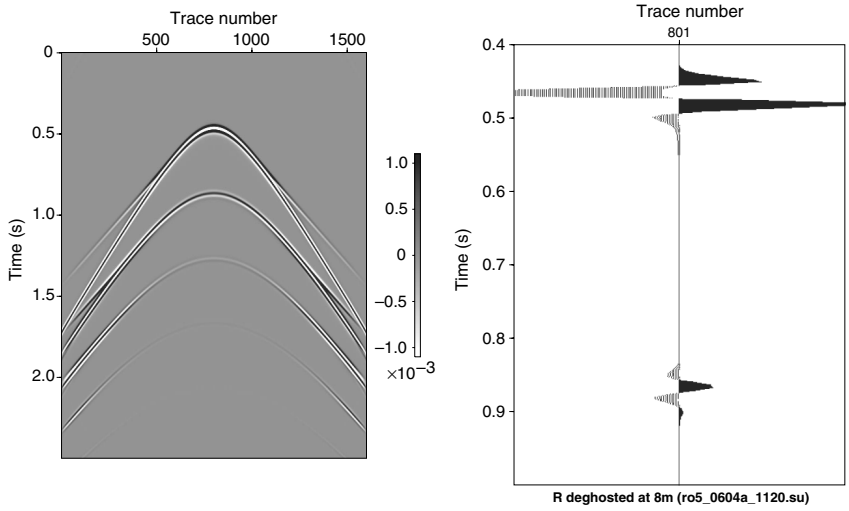

Figure 6. Flat-layer model: Receiver deghosted P_s at 8 m. Note that the receiver and source-receiver ghosts have been attenuated. The right panel shows the zero-offset trace (801 of 1601).

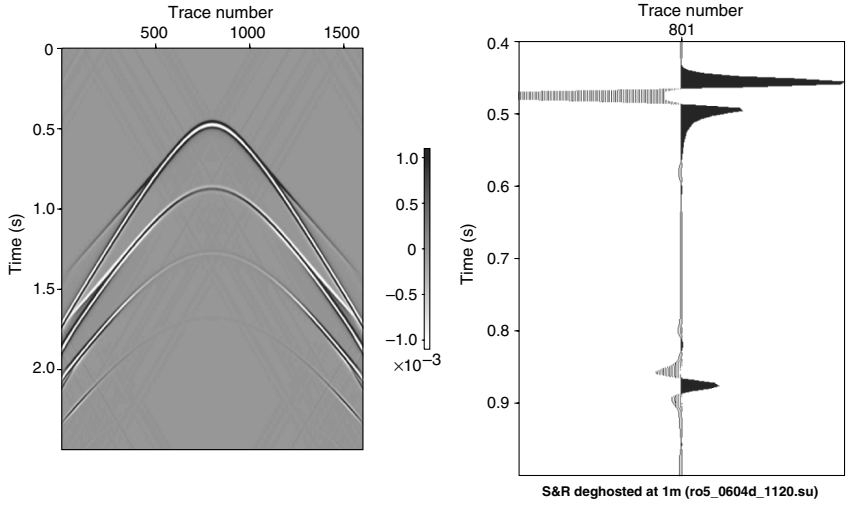

Figure 7. Flat-layer model: Source and receiver deghosted P_s at 1 m. Note that the source ghosts have been attenuated. The right panel shows the zero-offset trace (801 of 1601).

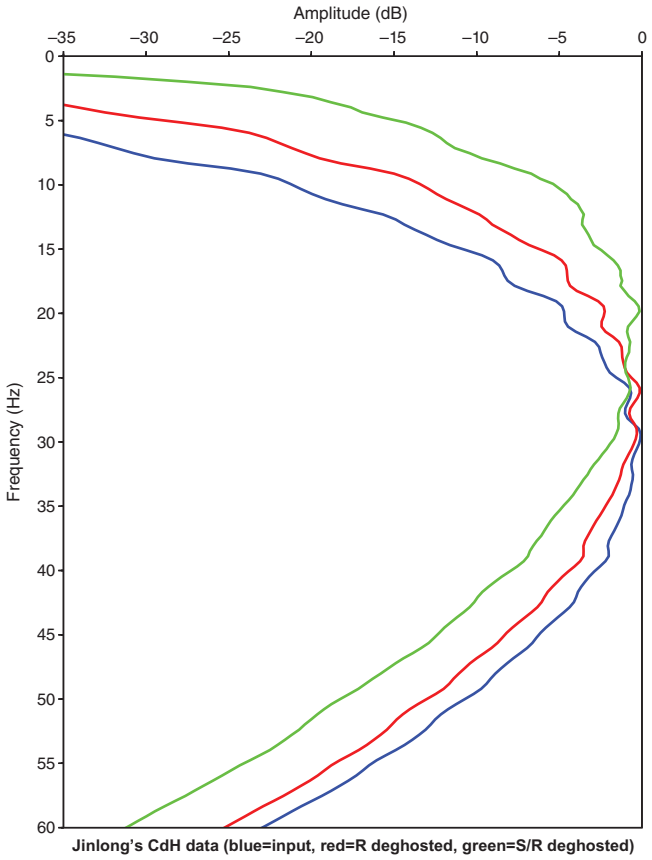

Figure 8. Flat-layer model data, spectrum of the zero-offset trace (801 of 1601): blue = input, red = receiver deghosted, green = source and receiver deghosted. Note the shift of the spectrum toward lower frequencies. Also note that source and receiver deghosting (green) has a larger effect that receiver deghosting (red). Receiver deghosting results from one application of the algorithm to measured data, whereas source and receiver deghosting results from three applications: receiver deghosting, wavefield prediction (of the receiver deghosted data at a point above the cable), and source deghosting.

$$\frac{dP}{dz}(0) = ik(A - B) \tag{11}$$

$$A = \frac{dP/dz(0) + ikP(0)}{2ik} \tag{12}$$

$$B = \frac{dP/dz(0) - ikP(0)}{-2ik} \tag{13}$$

is stable. However, measurements at two depths or G_0^{DD} (the latter comes from $G_0 = 0$ at two depths) gives

$$P(0) = A + B \tag{14}$$

$$P(a) = A\ \exp\ (ika) + B\ \exp(-ika) \tag{15}$$

$$A = \frac{P(0)\exp(-ika) - P(a)}{-2i\ \sin(ka)} \tag{16}$$

$$B = \frac{P(0)\exp(ika) - P(a)}{2i\ \sin(ka)} \tag{17}$$

which is sensitive in the vicinity of ghost notches (where $ka = n\pi$). If our interest is away from ghost notches, one-source experiments will be fine for source and receiver deghosting, whereas if our interest includes the ghost notches, two-source experiments can provide more stability for source-side deghosting. The appropriate method depends on bandwidth and depth of sources and receivers. If our sources and receivers are at the ocean bottom, ghost notches come up early and double sources would be indicated. This also impacts receiver deghosting using measurements at two depths because of sensitivity to ghost notches. The alternative method of receiver deghosting using the source wavelet $A(\omega)$, P along the cable, and the double Dirichlet Green's function G_0^{DD} allows receiver deghosting without the need for measurements at two depths, but G_0^{DD} uses information at two different depths and hence

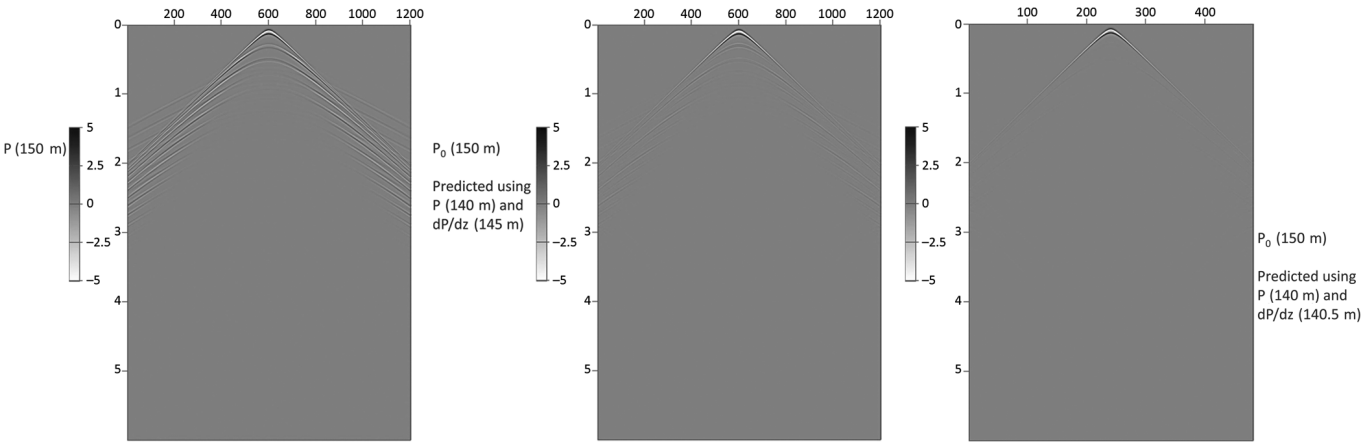

Figure 9. P at 150 m (left panel), P_0 at 150 m using 10 m between over/under cables (middle panel), P_0 at 150 m using 1 m between over/under cables (right panel). Note the "leakage" of P_s in the middle panel and the absence of visible "leakage" of P_s in the right panel.

may have stability issues compared to two measurements at one depth.

Code

The implementation of the above theory is done in a straightforward manner. The Green's theorem-derived algorithm computes the surface integral in equation 3. The method requires as input two wave fields, the pressure measurements P and their normal derivatives $\partial P/\partial z$. Measuring the latter requires a dual-sensor cable or over/under cables. The programs use data in the Seismic Unix (SU) format and integrate with all native SU programs.

RESULTS

Example: Flat-layer model

Figure 5 shows synthetic data produced using Cagniard-de Hoop code and a flat-layer model. (More detail on the input data is given in Tables C-1, C-2, and C-3 in Appendix C.) The first event is the

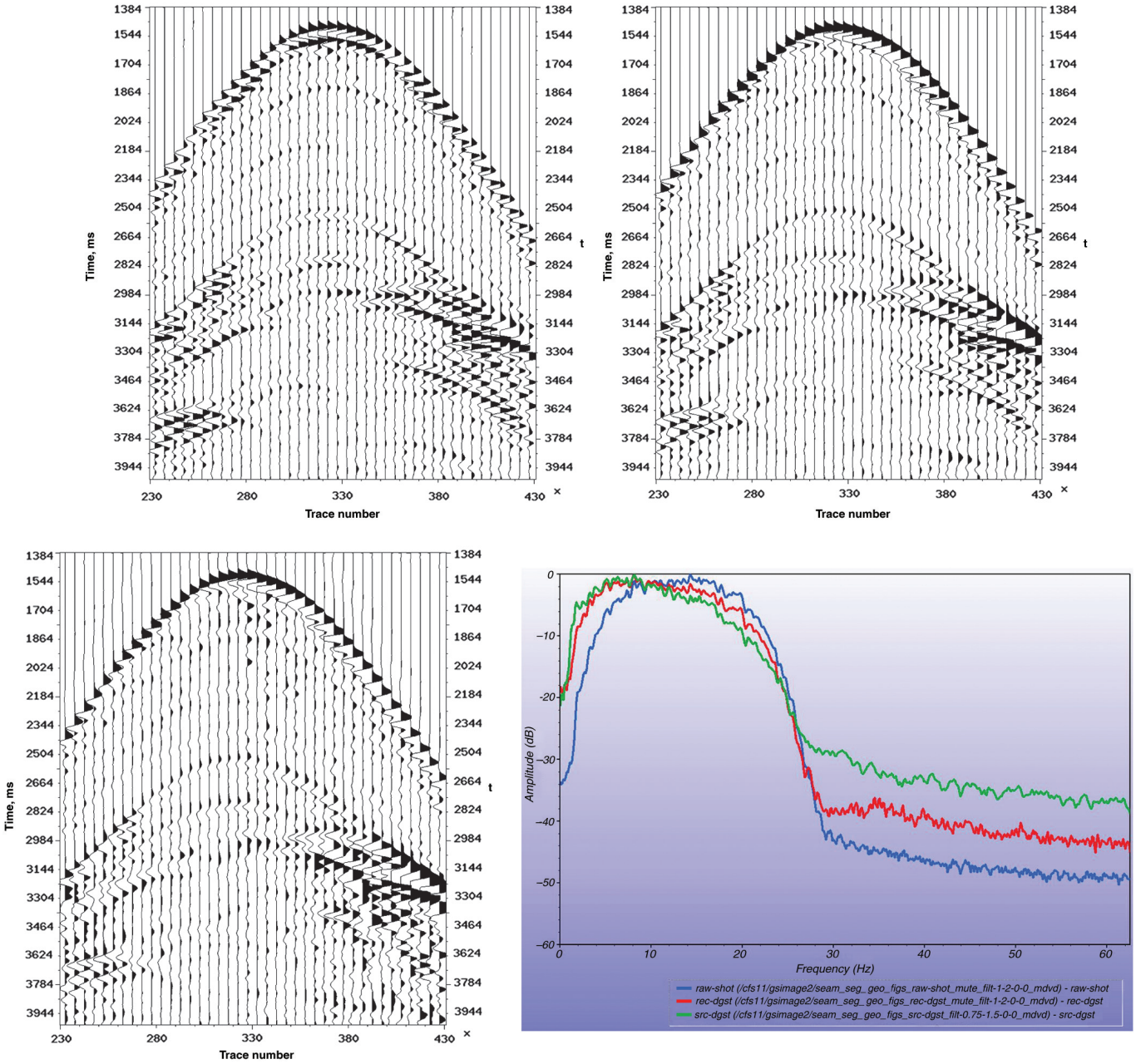

Figure 10. SEAM data, shot 131,373: recorded data at 17 m (top left), receiver deghosted at 10 m (top right), source and receiver deghosted at 10 m (bottom left). Note the collapsed wavelets in the top right and bottom left panels. Frequency spectra (bottom right): red = P at 17 m, blue = receiver deghosted at 10 m, green = source and receiver deghosted at 10 m. The spectrum uses a window of 201 traces (232–432) by 0.6 s (1.4–2.0). The first source notch is at 44 Hz which lies above the source frequency range (1–30 Hz). Note the shift of the spectrum toward lower frequencies (which may be of interest to FWI).

water-bottom primary and its source ghost, receiver ghost, and source/receiver ghost, and the second event is the first free-surface multiple and its three ghosts. Figure 6 shows Green's theorem-derived output computed using equation 3. Comparing Figures 5 and 6 shows that the receiver ghost and source/receiver ghost associated with the primary and first free-surface multiple have been attenuated. Figure 7 shows the result of source deghosting. Comparing Figures 6 and 7 shows that the source ghost has been attenuated for the first event (the water-bottom primary) and the second event (the first free-surface multiple). Deghosting also boosts low frequencies as seen in Figure 8.

Does the quality of deghosting depend on the distance between the over/under cables? Tang (L. Tang, 2013, personal communication) has used the same algorithm and a similar flat-layer model to study how a particular wavefield separation (into the reference and scattered fields) depends on this (and other) parameters. She concluded, "The estimated results get better when the over/under cables are closer to each other, i.e., P and dP/dz are approximately located at the same depth." Her results are shown in Figure 9. Robertsson and Kragh (2002) report the same result, where their upper "cable" is the air/water boundary. It is expected that the quality of deghosting is also a function of the distance between the over/under cables.

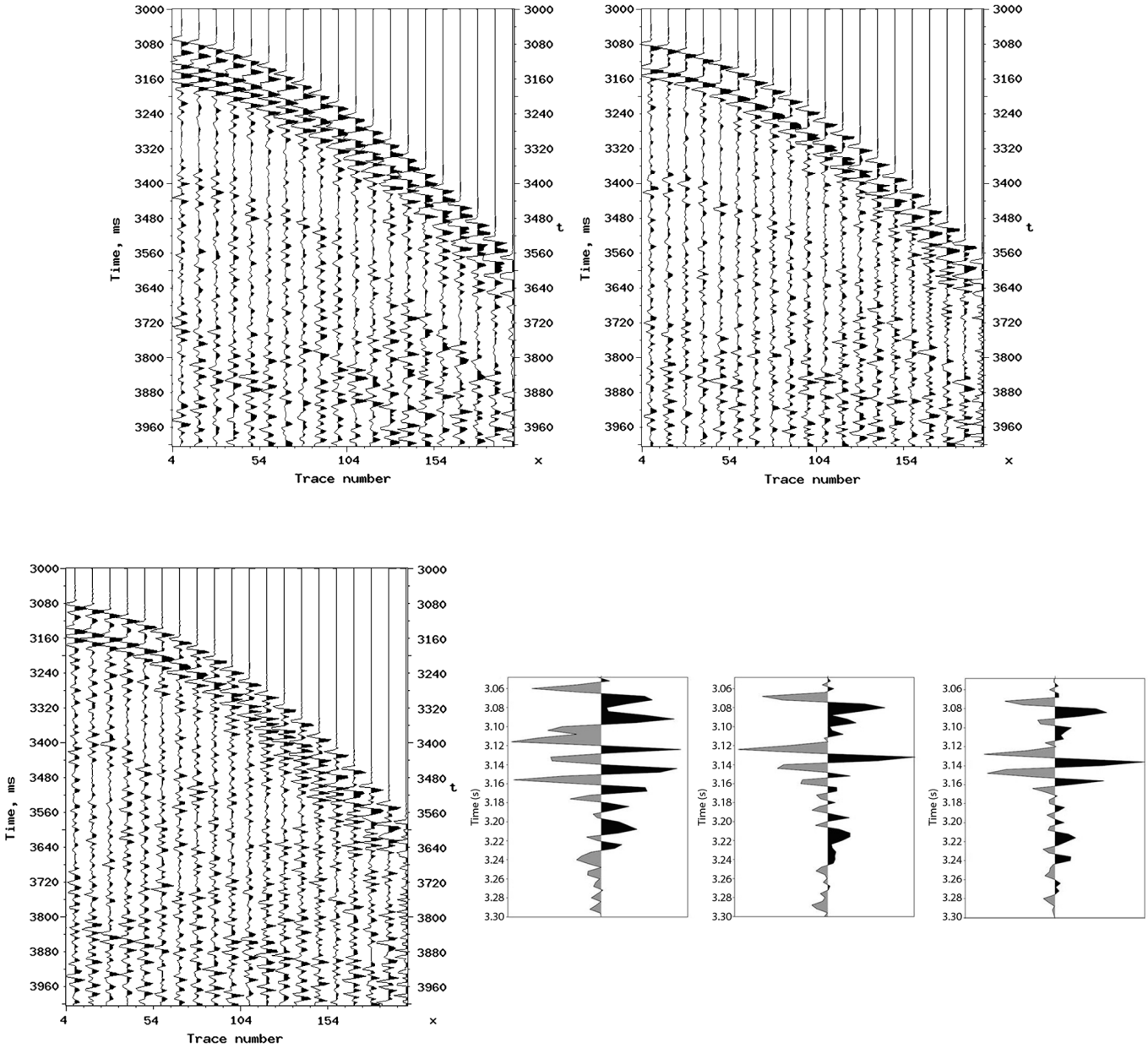

Figure 11. Field data: hydrophones at 22–25 m (top left), receiver deghosted at 10.5 m (top right), source and receiver deghosted at 8 m (bottom left). Note the collapsed wavelets in the top right and bottom left panels. Closeup of trace 5 in each of the above panels (bottom right). Note the gradual recovery of the shape of the wavelet: by receiver deghosting (middle trace) then by source and receiver deghosting (right trace). Input data courtesy of PGS.

Example: SEAM

Green's theorem-derived deghosting was applied to the SEAM data set generated based on a deep-water Gulf of Mexico earth model (SEG Advanced Modeling Corporation [SEAM], 2011). We used the special SEAM classic data set modeled to simulate dual-sensor acquisition by recording the pressure wavefield at two different depths, 15 and 17 m, respectively. This dual-sensor data consisted of nine sail lines for an equivalent wide-azimuth towed-streamer survey. The source interval is 150 × 150 m, whereas the receiver interval is 30 m in inline and crossline directions. (More detail about this data is given in Table C-2 in Appendix C.) Given the low frequency of the data (less than 30 Hz) and the source and receiver depths of 15 and 17 m, the ghost reflections are not as separable as in the previous flat layer model with deeper sources and receivers. In this shallower source and receiver situation, successful deghosting would correspond to a change in the wavelet shape. The top left panel of Figure 10 shows SEAM input, the top right panel shows receiver-deghosted output computed by the Green's theorem approach, and the bottom left panel shows source and receiver-deghosted output also computed by the Green's theorem approach. In the top right and bottom left panels of Figure 10, note the collapsed wavelet. In the bottom right panel of Figure 10, note the shift of the amplitude spectrum toward low frequencies. Deghosting reduces amplitude between notches, where constructive interference occurs between waves propagating upward and waves propagating downward. In this data, notches occur at $f = nc_0/(2z)$, i.e., at multiples of 50 Hz. Because the source energy is in frequencies less than 30 Hz, deghosting is manifested by the frequency shift.

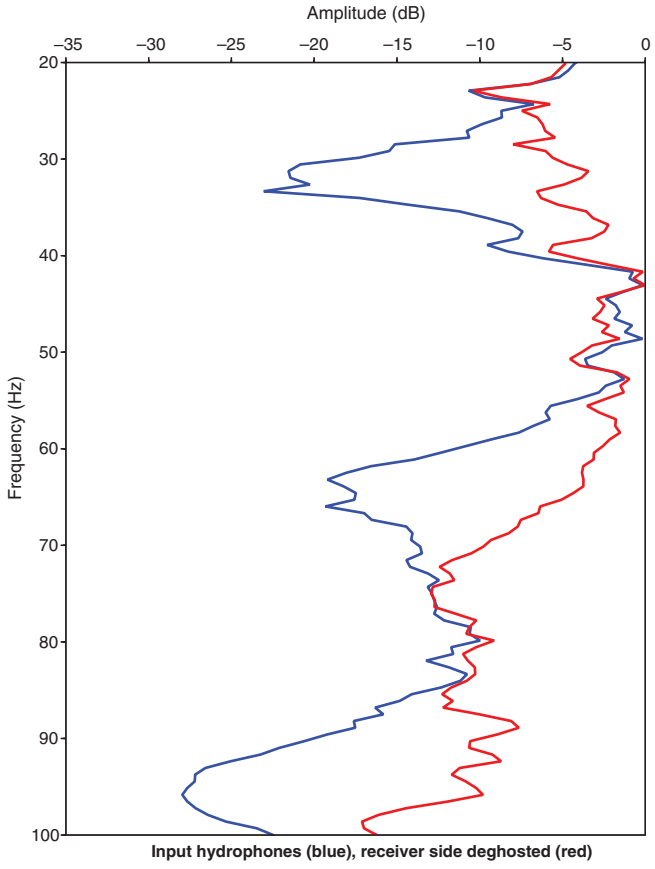

Figure 12. Field data: muted hydrophones (blue), receiver deghosted (red). The receiver notches around 30, 60, and 90 Hz have been filled in. Input data courtesy of PGS.

Example: Field data

Green's theorem-derived deghosting was also applied to a field survey from the deep-water Gulf of Mexico. The data were acquired using dual-sensor streamers comprised of hydrophones and vertical geophones. (More detail about this data is given in Table C-3 in Appendix C.) The vertical geophones measure V_z, whereas Green's theorem-
derived algorithms require dP/dz. It can be shown (from the equation of motion for a fluid, see Appendix D) that the required conversion is $dP/dz = i\omega\rho V_z$, where ρ is the density of the reference medium (sea water). The top left panel in Figure 11 shows a close up of an input shot record whereas the top right panel displays the same traces after receiver deghosting and the bottom left panel displays the same traces after source and receiver deghosting. Note the collapsed wavelet in the output images. This is also demonstrated in Figure 12, which compares the amplitude spectra before and after receiver deghosting. As expected, the deghosting solution successfully removed the notches from the spectrum that are associated with the receiver ghost. In the bottom right panel in Figure 11, note the gradual recovery of the shape of the wavelet: first by receiver deghosting (middle trace) and then by source and receiver deghosting (right trace).

DISCUSSION

In deep water, the particular form of Green's theorem-derived algorithm that was applied works as well as a conventional $P + V_z$ sum. It does so without the need for a Hankel transform from coordinate space to wavenumber domain, thus avoiding the difficulty of sufficient sampling needed to support the inverse Hankel transform (Amundsen [1993], p. 1336). There are two categories of advantages in using Green's theorem: (1) avoiding demands of transforms when the measurement is on a horizontal surface, and (2) when the acquisition is not confined to a horizontal measurement surface, which precludes the use of transforms. Evaluating the advantages of the Green's theorem-derived algorithm requires side by side testing of the two algorithms as the water becomes shallower, the water bottom becomes less flat, and full 3D acquisition is used.

CONCLUSIONS

The message for the prospector or seismic processor seeking the bottom line and user-guide for seeking to source and receiver deghost marine towed streamer and ocean bottom data is as follows: (1) away from notches, a single streamer of pressure data, and an estimate of the source signature can achieve receiver deghosting, and a set of single shot records can then achieve source deghosting, and (2) if deghosting is requiring for a frequency range that includes the notches (as can occur for high-frequency towed streamer acquisition and will occur with ocean-bottom data), then we advocate measurements of the pressure and its normal derivative along a cable for receiver deghosting and a set of dual over-under source experiments to achieve source deghosting. We have implemented and tested Green's theorem-derived source and receiver deghosting for the first time on deep-water Gulf of Mexico synthetic (SEAM)

and field data. These tests indicate that the algorithm works with positive and encouraging results. The Green's theorem derived deghosting algorithms provide a unique and comprehensive framework and methodology for understanding and addressing each of these cases.

ACKNOWLEDGMENTS

We are grateful to the M-OSRP sponsors for their support of this research and the three anonymous reviewers for their constructive comments, which enhanced the clarity of this paper. The first author is also grateful to ExxonMobil and PGS for internships and Nizar Chemingui (PGS), Paolo Terenghi (M-OSRP now PGS), and the second author for mentoring.

APPENDIX A

RECEIVER DEGHOSTING: SUPPLEMENTAL THEORY

Following Weglein et al. (2002) and Chapter 2 of Zhang (2007), to separate upward-moving and downward-moving waves, we define the following (see Figure 2):

1) a reference medium consisting of a whole-space of water with wavespeed c_0,
2) a perturbation $\alpha_{\text{air}}(\mathbf{r})$ that is the difference between the reference medium (water) and the upper part (air) of the actual medium, defined by $1/c^2_{\text{air}} = 1/c^2_{\text{water}}(1-\alpha_{\text{air}})$,
3) a perturbation $\alpha_{\text{earth}}(\mathbf{r})$ that is the difference between the reference medium (water) and the lower part (earth) of the actual medium, defined by $1/c^2_{\text{earth}} = 1/c^2_{\text{water}}(1-\alpha_{\text{earth}})$,
4) V is a volume bounded above by an upper hemisphere and below by the measurement surface,
5) a surface (air-water interface) above the measurement surface (i.e., inside V),
6) a source at $\mathbf{r}_s$ above the measurement surface (again inside V),
7) a causal whole-space Green's function $G_0^+(\mathbf{r},\mathbf{r}'_g,\omega)$ in the reference medium,
8) $k_0 = \omega/c_0$,
9) the prediction/observation point $\mathbf{r}'_g \in V$ lying below the source $\mathbf{r}_s$ and above the measurement surface, and
10) S as the hemisphere's surface.

For two wavefields P and G_0^+, Green's theorem becomes

$$\oint_S \mathrm{d}S\,\mathbf{n}\cdot[P(\mathbf{r},\mathbf{r}_s,\omega)\nabla G_0^+(\mathbf{r},\mathbf{r}'_g,\omega) - G_0^+(\mathbf{r},\mathbf{r}'_g,\omega)\nabla P(\mathbf{r},\mathbf{r}_s,\omega)] = \int_V \mathrm{d}\mathbf{r}[P(\mathbf{r},\mathbf{r}_s,\omega)\nabla^2 G_0^+(\mathbf{r},\mathbf{r}'_g,\omega) - G_0^+(\mathbf{r},\mathbf{r}'_g,\omega)\nabla^2 P(\mathbf{r},\mathbf{r}_s,\omega)]. \quad \text{(A-1)}$$

Substituting the partial differential equations for the pressure wavefield P and causal whole-space Green's function G_0^+

$$(\nabla^2 + k_0^2)P(\mathbf{r},\mathbf{r}_s,\omega) = A(\omega)\delta(\mathbf{r}-\mathbf{r}_s) + k_0^2(\alpha_{\text{air}}+\alpha_{\text{earth}})P \quad \text{(A-2)}$$

$$(\nabla^2 + k_0^2)G_0^+(\mathbf{r},\mathbf{r}'_g,\omega) = \delta(\mathbf{r}-\mathbf{r}'_g) \quad \text{(A-3)}$$

into the right hand side of equation A-1 gives

$$\begin{aligned}&\int_V \mathrm{d}\mathbf{r}\{P(\mathbf{r},\mathbf{r}_s,\omega)[-k_0^2 G_0^+ + \delta(\mathbf{r}-\mathbf{r}'_g)] - G_0^+(\mathbf{r},\mathbf{r}'_g,\omega)[-k_0^2 P \\ &+ A(\omega)\delta(\mathbf{r}-\mathbf{r}_s) + k_0^2(\alpha_{\text{air}}+\alpha_{\text{earth}})P]\} \\ &= \int_V \mathrm{d}\mathbf{r}\{P(\mathbf{r},\mathbf{r}_s,\omega)\delta(\mathbf{r}-\mathbf{r}'_g) - P(\mathbf{r},\mathbf{r}_s,\omega)k_0^2 G_0^+(\mathbf{r},\mathbf{r}'_g,\omega) \\ &+ G_0^+(\mathbf{r},\mathbf{r}'_g,\omega)k_0^2 P(\mathbf{r},\mathbf{r}_s,\omega) \\ &- k_0^2[\alpha_{\text{air}}(\mathbf{r})+\alpha_{\text{earth}}(\mathbf{r})]P(\mathbf{r},\mathbf{r}_s,\omega)G_0^+(\mathbf{r},\mathbf{r}'_g,\omega) \\ &- A(\omega)\delta(\mathbf{r}-\mathbf{r}_s)G_0^+(\mathbf{r},\mathbf{r}'_g,\omega)\}. \end{aligned} \quad \text{(A-4)}$$

The first term gives $P(\mathbf{r}'_g,\mathbf{r}_s,\omega)$ because the prediction/observation point $\mathbf{r}'_g$ is between the measurement surface and air-water surface, i.e., $\in V$. The cross terms $-P(\mathbf{r},\mathbf{r}_s,\omega)k_0^2 G_0^+(\mathbf{r},\mathbf{r}'_g,\omega) + G_0^+(\mathbf{r},\mathbf{r}'_g,\omega)k_0^2 P(\mathbf{r},\mathbf{r}_s,\omega)$ cancel. (This cancellation occurs in the frequency domain but not in the time domain.) $\alpha_{\text{earth}}(\mathbf{r}) = 0$ because the volume integral doesn't contain α_{earth}. The last term gives $A(\omega)G_0^+(\mathbf{r}_s,\mathbf{r}'_g,\omega)$ because the source (air guns) is between the measurement surface and air-water surface, i.e., within the volume V. Substituting these four results into equation A-4 gives for the left member of A-4

$$P(\mathbf{r}'_g,\mathbf{r}_s,\omega) - \int_V d\mathbf{r}\,k_0^2\alpha_{air}(\mathbf{r})P(\mathbf{r},\mathbf{r}_s,\omega)G_0^+(\mathbf{r},\mathbf{r}'_g,\omega) - A(\omega)G_0^+(\mathbf{r}_s,\mathbf{r}'_g,\omega). \quad \text{(A-5)}$$

Using the symmetry of the Green's function ($G_0^+(\mathbf{r}_s,\mathbf{r}'_g,\omega) = G_0^+(\mathbf{r}'_g,\mathbf{r}_s,\omega)$) and collecting terms gives

$$\oint_S \mathbf{n}\,\mathrm{d}S\cdot[P(\mathbf{r},\mathbf{r}_s,\omega)\nabla G_0^+(\mathbf{r},\mathbf{r}'_g,\omega) - G_0^+(\mathbf{r},\mathbf{r}'_g,\omega)\nabla P(\mathbf{r},\mathbf{r}_s,\omega)] = P(\mathbf{r}'_g,\mathbf{r}_s,\omega) - \int_V \mathrm{d}\mathbf{r}\,G_0^+(\mathbf{r},\mathbf{r}'_g,\omega)k_0^2\alpha_{air}(\mathbf{r})P(\mathbf{r},\mathbf{r}_s,\omega) - A(\omega)G_0^+(\mathbf{r}'_g,\mathbf{r}_s,\omega). \quad \text{(A-6)}$$

The physical meaning of equation A-6 is that the total wavefield at $\mathbf{r}'_g$ can be separated into three parts. There are three spatially distributed sources causing the wavefield P. From the extinction theorem/Green's theorem, the left side of equation A-6 is the contribution to the field at $\mathbf{r}'_g$ due to sources outside V. There is one source outside V, $\rho_{\text{earth}} = k^2\alpha_{\text{earth}}P$. The contribution it makes at $\mathbf{r}'_g$ is $\int G_0^+\rho_{\text{earth}}$ and upgoing. The two other sources ($\rho_{\text{air}} = k^2\alpha_{\text{air}}P$ and $\rho_{\text{air guns}}$) produce a down field at $\mathbf{r}'_g$, since $\mathbf{r}'_g$ is below $\mathbf{r}_s$.

Letting the radius of the hemisphere go to ∞, the Sommerfeld radiation condition gives

$$\int_{m.s.} \mathrm{d}S\mathbf{n}\cdot[P(\mathbf{r},\mathbf{r}_s,\omega)\nabla G_0^+(\mathbf{r},\mathbf{r}'_g,\omega) - G_0^+(\mathbf{r},\mathbf{r}'_g,\omega)\nabla P(\mathbf{r},\mathbf{r}_s,\omega)] = P'_R(\mathbf{r}'_g,\mathbf{r}_s,\omega), \quad \text{(A-7)}$$

where $P(\mathbf{r},\mathbf{r}_s,\omega)$ and $\nabla P(\mathbf{r},\mathbf{r}_s,\omega)\cdot\hat{\mathbf{n}}$ are respectively the hydrophone measurements and normal derivatives (in the frequency domain), and G_0^+ is the causal whole-space Green's function for a homogeneous acoustic medium with water speed.

APPENDIX B

DERIVATION OF CONVENTIONAL $P + V_z$ SUM FROM GREEN'S THEOREM

A conventional $P + V_z$ sum receiver deghosts by decomposing P into an upgoing wavefield, P^{up}, and a downgoing wavefield, P^{down}, using

$$\left.\begin{matrix} P^{\text{up}} \\ P^{\text{down}} \end{matrix}\right\} = \frac{1}{2}(\tilde{P} \mp \frac{\rho\,\omega}{k_z}\tilde{V}_z), \tag{B-1}$$

where $\tilde{P}, \tilde{V}_z$ are plane waves and $k_z = \sqrt{(\omega/c_0)^2 - k_x^2 - k_y^2}$. Equation B-1 is equation 1 in Klüver et al. (2009), which is equation 17 in Amundsen (1993). The latter assumes a half-space of air, a water column, and a 1D layered earth.

Substituting the (acoustic) partial differential equations for the pressure wavefield $P(\mathbf{r}', \omega)$ and Green's function $G_0(\mathbf{r}, \mathbf{r}', \omega)$ into Green's second identity gives

$$\begin{aligned}\int_V d\mathbf{r}' P(\mathbf{r}', \mathbf{r}_s, \omega)\delta(\mathbf{r}' - \mathbf{r}) &= \int_V d\mathbf{r}' \rho(\mathbf{r}', \mathbf{r}_s, \omega) G_0(\mathbf{r}, \mathbf{r}', \omega) \\ &+ \oint_S dS' \hat{\mathbf{n}}' \cdot [P(\mathbf{r}', \mathbf{r}_s, \omega)\nabla' G_0(\mathbf{r}, \mathbf{r}', \omega) \\ &- G_0(\mathbf{r}, \mathbf{r}', \omega)\nabla' P(\mathbf{r}', \mathbf{r}_s, \omega)].\end{aligned} \tag{B-2}$$

See, e.g., Weglein et al. (2002) and Chapter 2 of Zhang (2007). For deghosting, use the configuration shown in Figure 2, i.e., choose

1) $\rho(\mathbf{r}', \mathbf{r}_s, \omega) = A(\omega)\delta(\mathbf{r}' - \mathbf{r}_s) + k^2[\alpha_{\text{air}}(\mathbf{r}') + \alpha_{\text{earth}}(\mathbf{r}')]P(\mathbf{r}', \mathbf{r}_s, \omega)$,
2) V is a volume bounded above by an upper hemisphere and below by the measurement surface,
3) $\mathbf{r}$ above the measurement surface and below the air/water boundary (i.e., $\in V$), and
4) G_0 a whole-space causal Green's function G_0^+.

We can start with Appendix A, equation A-7

$$\begin{aligned}P_R'(\mathbf{r}, \mathbf{r}_s, \omega) = \int_{m.s.} dS' \hat{\mathbf{n}}' \cdot [&P(\mathbf{r}', \mathbf{r}_s, \omega)\nabla' G_0^+(\mathbf{r}, \mathbf{r}', \omega) \\ &- G_0^+(\mathbf{r}, \mathbf{r}', \omega)\nabla' P(\mathbf{r}', \mathbf{r}_s, \omega)].\end{aligned} \tag{B-3}$$

For simplicity assume 2D, and equation B-3 becomes

$$\begin{aligned}P_R'(x, z, x_s, z_s, \omega) = \int_{m.s.} dx' \\ \times \left[P(x', z', x_s, z_s, \omega)\frac{\partial G_0^+}{\partial z'}(x, z, x', z', \omega)\right. \\ \left. - G_0^+(x, z, x', z', \omega)\frac{\partial P}{\partial z'}(x', z', x_s, z_s, \omega)\right].\end{aligned} \tag{B-4}$$

Fourier transform equation B-4 with respect to x,

$$\begin{aligned}\int dx\, \exp(ik_x x) P_R'(x, z, x_s, z_s, \omega) = \int dx\, \exp(ik_x x) \\ \times \int_{m.s.} dx' \left[P(x', z', x_s, z_s, \omega)\frac{\partial G_0^+}{\partial z'}(x, z, x', z', \omega)\right. \\ \left. - G_0^+(x, z, x', z', \omega)\frac{\partial P}{\partial z'}(x', z', x_s, z_s, \omega)\right].\end{aligned} \tag{B-5}$$

The left side of equation B-5 becomes $\tilde{P}_R'(k_x, z, x_s, z_s, \omega)$. Substitute the bilinear form of the Green's function into the right hand side of equation B-5,

$$\begin{aligned}&\int dx\, \exp(ik_x x) \\ &\times \int_{m.s.} dx' \left\{ P(x', z', x_s, z_s, \omega)\frac{\partial}{\partial z'}\right. \\ &\times \left[\frac{1}{2\pi}\int dk_x' \frac{\exp(-ik_x'(x - x'))\exp(ik_z'(z' - z))}{2ik_z'}\right] \\ &- \frac{1}{2\pi}\int dk_x' \frac{\exp(-ik_x'(x - x'))\exp(ik_z'(z' - z))}{2ik_z'}\frac{\partial P}{\partial z'} \\ &\left.\times (x', z', x_s, z_s, \omega)\right\},\end{aligned} \tag{B-6}$$

where $k_z' = \sqrt{(\omega/c_0)^2 - k_x'^2}$. Substitute $\mu = \mathbf{r} - \mathbf{r}'$ in equation B-6,

$$\begin{aligned}&\int_{m.s.} dx' \int d\mu_x\, \exp[ik_x(\mu_x + x')]\left[P(x', z', x_s, z_s, \omega)\right. \\ &\times \frac{1}{2\pi}\int dk_x' \frac{\exp(-ik_x'\mu_x)\exp(-ik_z'\mu_z)}{2ik_z'}(-ik_z')(-1) \\ &\left. - \frac{1}{2\pi}\int dk_x' \frac{\exp(-ik_x'\mu_x)\exp(-ik_z'\mu_z)}{2ik_z'}\frac{\partial P}{\partial z'}(x', z', x_s, z_s, \omega)\right] \\ &= \frac{1}{2\pi}\int_{m.s.} dx' \int d\mu_x \exp[ik_x(\mu_x + x')]\left[P(x', z', x_s, z_s, \omega)\right. \\ &\times \int dk_x' \exp(-ik_x'\mu_x) ik_z' \\ &\left. - \int dk_x' \exp(-ik_x'\mu_x)\frac{\partial P}{\partial z'}(x', z', x_s, z_s, \omega)\right]\frac{\exp(-ik_z'\mu_z)}{2ik_z'} \\ &= \frac{1}{2\pi}\int dk_x' \frac{\exp(-ik_z'\mu_z)}{2ik_z'}\int d\mu_x\, \exp(-i(k_x' - k_x)\mu_x) \\ &\times \left[ik_z'\int_{m.s.} dx'\, \exp(ik_x x')P(x', z', x_s, z_s, \omega)\right. \\ &\left. - \int dx' \exp(ik_x x')\frac{\partial P}{\partial z'}(x', z', x_s, z_s, \omega)\right].\end{aligned} \tag{B-7}$$

In equation B-7, the integral over $d\mu_x$ gives a Dirac delta, $2\pi\delta(k_x' - k_x)$, the integral over dx' is a Fourier transform of the pressure wavefield and gives $\tilde{P}(k_x, z', x_s, z_s, \omega)$, and the vertical derivative of the pressure wavefield is $i\omega\rho\, V_z(x', z', x_s, z_s, \omega)$. (The latter relationship is derived in Appendix D.) The integral of dx' over the measurement surface allows a Fourier transform because, in the derivation of equation B-3, we took the radius of the hemisphere to infinity. We now have (for the right side of equation B-5),

$$\begin{aligned}\frac{1}{2\pi}\int dk_x' \frac{\exp(-ik_z'\mu_z)}{2ik_z'}2\pi\delta(k_x' - k_x)\left[ik_z'\tilde{P}(k_x, z', x_s, z_s, \omega)\right. \\ \left. - i\omega\rho\int dx' \exp(ik_x x')V_z(x', z', x_s, z_s, \omega)\right].\end{aligned} \tag{B-8}$$

In equation B-8, the integral over dx' is a Fourier transform of the vertical velocity field and gives $\tilde{V}_z(k_x, z', x_s, z_s, \omega)$. Using $k_z'^2 = \omega^2/c_0^2 - k_x'^2$ and $k_z^2 = \omega^2/c_0^2 - k_x^2$, equation B-8 can be rewritten as

$$\int dk_x' \,\delta(k_x' - k_x)\frac{\exp(-ik_z'\mu_z)}{2ik_z'}[ik_z'\tilde{P}(k_x, z', x_s, z_s, \omega) - i\omega\rho\,\tilde{V}_z(k_x, z', x_s, z_s, \omega)]$$
$$= \frac{\exp(-ik_z'\mu_z)}{2ik_z'}[ik_z'\tilde{P}(k_x, z', x_s, z_s, \omega) - i\omega\rho\,\tilde{V}_z(k_x, z', x_s, z_s, \omega)]. \quad \text{(B-9)}$$

Collecting terms gives

$$\tilde{P}_R'(k_x, z, x_s, z_s, \omega) = \frac{\exp(-ik_z'\mu_z)}{2ik_z'}(ik_z) \times \left[\tilde{P}(k_x, z', x_s, z_s, \omega) - \frac{\omega\rho}{k_z}\tilde{V}_z(k_x, z', x_s, z_s, \omega)\right]$$
$$= -\frac{1}{2}\exp[ik_z'(z' - z)]\left[\tilde{P}(k_x, z', x_s, z_s, \omega) - \frac{\omega\rho}{k_z}\tilde{V}_z(k_x, z', x_s, z_s, \omega)\right]. \quad \text{(B-10)}$$

In the last equation, the phase factor $\exp(ik_z'(z' - z))$ takes the one-way wavefield $\tilde{P}_R'$ from the cable depth z' to the predicted (deghosted) depth z. This demonstrates that the Green's theorem deghosting reduces to the Fourier form equation B-10 under conditions which allow the steps in this demonstration. The standard practice deghosting $P - V_z$ algorithm today is a version of B-10 that accommodates a 3D point source, but assumes the earth is 1D. Equations B-3 and B-10 allow the lifting of the 1D assumption, and in addition B-3 doesn't require a horizontal measurement surface.

APPENDIX C

INPUT DATA

Table C-1. Synthetic data: Flat-layer-model data created using Cagniard-de Hoop code.

Parameter	Value
Number of shots	1
Number of channels per shot	1601
Number of samples per trace	625
Time sampling	4 ms
Record length	2.5 s
Shot interval	n.a.
Group interval	3 m
Shortest offset	0 m
Gun depth	7 m
Streamer depth	9 and 11 m

Air/water boundary, water depth 300 m, 1D constant velocity acoustic earth ($c = 2250$ m/s)
$\partial P/\partial z \simeq (P(11\text{ m}) - P(9\text{ m}))/2$ m
This data was created by Jinlong Yang using code written by Jingfeng Zhang (now at BP).

Table C-2. Synthetic data: SEAM deep-water Gulf of Mexico model.

Parameter	Value
Number of shots	9×267
Number of channels per shot	661×661
Number of samples per trace	2001
Time sampling	8 ms
Record length	16 s
Shot interval	150 m
Group interval	30 m
Shortest offset	0 m
Gun depth	15 m
Streamer depth	15 and 17 m

Air/water boundary, variable water depth, 3D variable density acoustic earth
3D source, frequency of source: 1–30 Hz
Distance between towed streamers: 30 m
$\partial P/\partial z \simeq (P(17\text{ m}) - P(15\text{ m}))/2$ m
Reviewer 2 pointed out that "The numerical approximation of the vertical derivative using a finite difference approach is subject to considerable error when a distance $dz = 2$ m is used. In other words, the pressure data have a much higher accuracy than the pressure derivative data when computed this way."

Table C-3. Field data: Deep-water Gulf of Mexico.

Parameter	Value
Number of shots	2451
Number of channels per shot	960
Number of samples per trace	3585
Time sampling	4 ms
Record length	14.34 s
Shot interval	32 m
Group interval	12.5 m
Shortest offset	112 m
Gun depth	9 m
Streamer depth	25 m

Data courtesy of PGS
Dual-sensor towed streamer
$\partial P/\partial z = i\omega\rho V_z$, where ρ is the density of the reference medium (seawater)

APPENDIX D

QUICK DERIVATION OF $\partial P/\partial z = i\omega\rho V_z$

1) Newton's second law of motion: $\mathbf{F} = m d\mathbf{V}/dt$
2) Consider a unit volume in a fluid: $\mathbf{F} = \rho\, d\mathbf{V}/dt$
3) Fourier transform: $\mathbf{F} = \rho(-i\omega\mathbf{V})$
4) Force in a fluid is the pressure gradient: $\mathbf{F} = -\nabla P = \rho(-i\omega\mathbf{V})$
5) Rewriting: $\nabla P = i\omega\rho\,\mathbf{V}$
6) The z-component is the desired result.

REFERENCES

Amundsen, L., 1993, Wavenumber-based filtering of marine point-source data: Geophysics, **58**, 1335–1348, doi: 10.1190/1.1443516.

Clayton, R. W., and R. H. Stolt, 1981, A Born-WKBJ inversion method for acoustic reflection data: Geophysics, **46**, 1559–1567, doi: 10.1190/1.1441162.

Corrigan, D., A. B. Weglein, and D. D. Thompson, 1991, Method and apparatus for seismic survey including using vertical gradient estimation to separate downgoing seismic wavefields: U. S. Patent number 5,051,961.

Klüver, T., P. Aaron, D. Carlson, A. Day, and R. van Borselen, 2009, A robust strategy for processing 3D dual-sensor towed streamer data: 79th Annual International Meeting, SEG, Expanded Abstracts, 3088–3092.

Kragh, E., J. O. A. Robertsson, R. Laws, L. Amundsen, T. Røsten, T. Davies, K. Zerouk, and A. Strudley, 2004, Rough sea deghosting using wave heights derived from low frequency pressure recordings — A case study: 66th Annual International Conference and Exhibition, EAGE.

Mayhan, J. D., P. Terenghi, A. B. Weglein, and N. Chemingui, 2011, Green's theorem derived methods for preprocessing seismic data when the pressure P and its normal derivative are measured: 81st Annual International Meeting, SEG, Expanded Abstracts, 2722–2726.

Mayhan, J. D., A. B. Weglein, and P. Terenghi, 2012, First application of Green's theorem derived source and receiver deghosting on deep water Gulf of Mexico synthetic (SEAM) and field data: 82nd Annual International Meeting, SEG, Expanded Abstracts, doi: 10.1190/segam2012-0855.1.

Morse, P. M., and H. Feshbach, 1953, Methods of theoretical physics: McGraw-Hill Book Co.

Osen, A., B. G. Secrest, L. Amundsen, and A. Reitan, 1998, Wavelet estimation from marine pressure measurements: Geophysics, **63**, 2108–2119, doi: 10.1190/1.1444504.

Robertsson, J. O. A., and E. Kragh, 2002, Rough-sea deghosting using a single streamer and a pressure gradient approximation: Geophysics, **67**, 2005–2011, doi: 10.1190/1.1527100.

Robinson, E. A., and S. Treitel, 2008, Digital imaging and deconvolution: The ABCs of seismic exploration and processing: SEG.

Schneider, W. A., 1978, Integral formulation for migration in two and three dimensions: Geophysics, **43**, 49–76, doi: 10.1190/1.1440828.

SEG Advanced Modeling Corporation (SEAM), 2011, The SEG advanced model: Technical report, SEG, (http://www.seg.org/resources/research/seam).

Stolt, R. H., and A. B. Weglein, 2012, Seismic imaging and inversion, **1**, Cambridge University Press.

Tan, T. H., 1999, Wavelet spectrum estimation: Geophysics, **64**, 1836–1846, doi: 10.1190/1.1444689.

Weglein, A. B., and L. Amundsen, 2003, Short note: G_0^{D0} and G_0^d integral equations relationships; the triangle relation is intact: M-OSRP 2002 Annual Report, 32–35.

Weglein, A. B., F. V. Araújo, P. M. Carvalho, R. H. Stolt, K. H. Matson, R. T. Coates, D. Corrigan, D. J. Foster, S. A. Shaw, and H. Zhang, 2003, Inverse scattering series and seismic exploration: Inverse Problems, **19**, R27–R83, doi: 10.1088/0266-5611/19/6/R01.

Weglein, A. B., and B. G. Secrest, 1990, Wavelet estimation for a multidimensional acoustic earth model: Geophysics, **55**, 902–913, doi: 10.1190/1.1442905.

Weglein, A. B., S. A. Shaw, K. H. Matson, J. L. Sheiman, R. H. Stolt, T. H. Tan, A. Osen, G. P. Correa, K. A. Innanen, Z. Guo, and J. Zhang, 2002, New approaches to deghosting towed-streamer and ocean-bottom pressure measurements: 72nd Annual International Meeting, SEG, Expanded Abstracts, 1016–1019.

Weglein, A. B., R. H. Stolt, and J. D. Mayhan, 2011a, Reverse-time migration and Green's theorem: Part I — The evolution of concepts, and setting the stage for the new RTM method: Journal of Seismic Exploration, **20**, 73–90.

Weglein, A. B., R. H. Stolt, and J. D. Mayhan, 2011b, Reverse time migration and Green's theorem: Part II — A new and consistent theory that progresses and corrects current RTM concepts and methods: Journal of Seismic Exploration, **20**, 135–159.

Zhang, J., 2007, Wave theory based data preparation for inverse scattering multiple removal, depth imaging and parameter estimation: Analysis and numerical tests of Green's theorem deghosting theory: Ph.D. thesis, University of Houston.

Zhang, J., and A. B. Weglein, 2005, Extinction theorem deghosting method using towed streamer pressure data: analysis of the receiver array effect on deghosting and subsequent free surface multiple removal: 75th Annual International Meeting, SEG, Expanded Abstracts, 2095–2098.

Zhang, J., and A. B. Weglein, 2006, Application of extinction theorem deghosting method on ocean bottom data: 76th Annual International Meeting, SEG, Expanded Abstracts, 2674–2678.

Using Green's theorem to satisfy data requirements of multiple removal methods: The impact of acquisition design

Lin Tang, James D. Mayhan, Jinlong Yang, and Arthur B. Weglein, M-OSRP, University of Houston*

SUMMARY

The freedom of choosing a convenient reference medium means Green's theorem offers a flexible framework for deriving a number of useful algorithms. Methods that can be derived from Green's theorem include: separation of reference and scattered wavefields ($P = P_0 + P_s$), wavelet estimation, and ghost removal. Green's theorem preprocessing methods are fully consistent with the inverse scattering series (ISS) isolated task subseries processing because Green's theorem wave separation methods are multidimensional and make no assumptions about the earth. The ISS multiple removal algorithms require their input data to be deghosted and to have an estimate of the wavelet. We discuss the effect of acquisition design on Green's theorem for predicting P_0 and P_s and for deghosting.

INTRODUCTION

Preprocessing of seismic data, including removal of reference waves, wavelet estimation, and removal of ghosts, is very important in seismic data processing. The reference wave does not experience reflection from the earth, which is our ultimate objective, so it should be removed before subsequent analysis. Seismic data are affected by both the acquisition signature and the properties of the earth. Thus, we need to identify and remove the wavelet's contribution from the seismic data (Weglein and Secrest (1990)). Deghosting will remove the down-going wave from the scattered wave and will enhance the low-frequency content of the data (Mayhan et al., 2011, 2012; Mayhan and Weglein, 2013). These are the prerequisites of the following steps of multiple removal and depth imaging in the Inverse Scattering Series (ISS) algorithm (Weglein et al. (2003)). All three of these processing steps can be achieved by using Green's theorem. In Weglein and Secrest (1990), wave separation and wavelet estimation by using Green's theorem are discussed. By performing an integral along the measurement surface, we can predict the reference wave or the scattered wave, depending on the choice of observation point. Green's theorem can work in multiple dimensions and is especially effective in the case of interfering events, compared with other methods such as simply muting the direct wave from the data, which can lead to the loss of long offset wave information. By the way, the thing we call a wavelet is the factor that separates what we are measuring P_0 vs. a Green's function G_0 and hence includes the source signature and the instrument response, that we could call the acquisition wavelet. In the methods described below, the factor $A(\omega)$ is actually the acquisition wavelet.

In this paper we focus on preparing the data for the subsequent multiple removal steps, including removing reference wave, estimating wavelet and deghosting. The effect of acquisition design on wave separation when using an over/under cable is discussed. The necessity of deghosting for free surface multiple removal will be shown.

THEORY

In scattering theory, we treat the actual medium as a combination of an unperturbed medium, called the reference medium, and a perturbation. Correspondingly, the total measured wavefield P is the summation of the reference wave P_0 and the scattered wave P_s. P_0 does not experience the earth, which is our interest, thus we need to remove it before further processing and analysis. In the marine environment, for the purpose of separating P_0 and P_s, we choose as the reference medium a half-space of water plus a half space of air. Overlaying the reference medium are two sources, the air guns and the earth, which create the measured wavefield P, where $P = P_0 + P_s$. Combining the wave equations for P_0 and the corresponding Green's function G_0 in the reference medium and Green's second identity, we can have the equations for Green's theorem wave separation. When choosing the observation point below the measurement surface, we have the reference wave

$$P_0(\mathbf{r},\mathbf{r_s},\omega) = \int_{m.s.} dS\hat{\mathbf{n}}\cdot \left[P(\mathbf{r}',\mathbf{r_s},\omega)\nabla' G_0(\mathbf{r}',\mathbf{r},\omega) - G_0(\mathbf{r}',\mathbf{r},\omega)\nabla' P(\mathbf{r}',\mathbf{r_s},\omega)\right]. \quad (1)$$

In addition, using the information of reference wave P_0, we can solve for the wavelet

$$A(\omega) = \frac{P_0(\mathbf{r},\mathbf{r_s},\omega)}{G_0(\mathbf{r},\mathbf{r_s},\omega)}. \quad (2)$$

When choosing the observation above the cable, Green's theorem will give us the scattered wave P_s,

$$P_s(\mathbf{r},\mathbf{r_s},\omega) = \int_{m.s.} dS\hat{\mathbf{n}}\cdot \left[P(\mathbf{r}',\mathbf{r_s},\omega)\nabla' G_0(\mathbf{r}',\mathbf{r},\omega) - G_0(\mathbf{r}',\mathbf{r},\omega)\nabla' P(\mathbf{r}',\mathbf{r_s},\omega)\right]. \quad (3)$$

From the above equations, we can see that given the wavefield P and its normal derivative P_n on the measurement surface, we can easily calculate the reference wave P_0 and the scattered wave P_s, depending on the observation point we choose. In other words, the reference wave and the scattered wave are separated by using Green's theorem.

Green's theorem receiver deghosting is carried out via

$$P'_R(\mathbf{r}'_g,\mathbf{r}_s,\omega) = \int_{\text{m.s.}} dS\,\hat{\mathbf{n}}\cdot [P(\mathbf{r},\mathbf{r}_s,\omega)\nabla G_0^+(\mathbf{r},\mathbf{r}'_g,\omega) - G_0^+(\mathbf{r},\mathbf{r}'_g,\omega)\nabla P(\mathbf{r},\mathbf{r}_s,\omega)], \quad (4)$$

where $P(\mathbf{r},\mathbf{r}_s,\omega)$ is the measured pressure wavefield, $G_0^+(\mathbf{r},\mathbf{r}'_g,\omega)$ is a whole space, causal Green's function, $\mathbf{r}_s$ is the source location, $\mathbf{r}$ is a receiver location, $\mathbf{r}'_g$ is the prediction point, and the integration is over the measurement surface for a common shot gather (Weglein et al., 2002; Zhang and Weglein, 2005, 2006; Zhang, 2007). The input (measurements of P and its normal derivative) requires over/under cables. Similarly, Green's theorem source deghosting uses

$$P'_{SR}(\mathbf{r}'_g,\mathbf{r}'_s,\omega)=\int_{\text{sources}} dS\hat{\mathbf{n}}\cdot$$
$$[P'_R(\mathbf{r}'_g,\mathbf{r},\omega)\nabla G_0^+(\mathbf{r},\mathbf{r}'_s,\omega)-G_0^+(\mathbf{r},\mathbf{r}'_s,\omega)\nabla P'_R(\mathbf{r}'_g,\mathbf{r},\omega)], \quad (5)$$

where the input (P'_R and its normal derivative) requires over/under sources, and the integration is for a common receiver gather. If we have a single cable measuring P and we can estimate the isotropic wavelet $A(\omega)$, we can receiver deghost by first computing

$$P'(\mathbf{r}'_g,\mathbf{r}_s,\omega)=A(\omega)G_0^{DD}(\mathbf{r}'_g,\mathbf{r}_s,\omega)+$$
$$\int_{\text{m.s.}} dS\hat{\mathbf{n}}\cdot P(\mathbf{r},\mathbf{r}_s,\omega)\nabla G_0^{DD}(\mathbf{r},\mathbf{r}'_g,\omega) \quad (6)$$
$$\frac{\partial P'}{\partial z'_g}(\mathbf{r}'_g,\mathbf{r}_s,\omega)=A(\omega)\frac{\partial G_0^{DD}}{\partial z'_g}(\mathbf{r}'_g,\mathbf{r}_s,\omega)+$$
$$\int_{\text{m.s.}} dS\hat{\mathbf{n}}\cdot P(\mathbf{r},\mathbf{r}_s,\omega)\nabla\frac{\partial G_0^{DD}}{\partial z'_g}(\mathbf{r},\mathbf{r}'_g,\omega). \quad (7)$$

Equation 7 is the derivative of equation 6, and G_0^{DD} is a "double Dirichlet" Green's function constructed to vanish on both the free surface and measurement surface (Osen et al., 1998; Tan, 1999). In this case, the outputs of equations 6 and 7 are the inputs to equation 4. Similarly, in the absence of over/under sources, source deghosting is accomplished by substituting the output of equation 4 into equations 6 and 7 (but without the terms containing the wavelet), then their outputs become the inputs to equation 5.

THE EFFECT OF ACQUISITION DESIGN

Green's theorem requires the wavefield P and its normal derivative P_n on the measurement surface as the input. In marine exploration, an over/under cable has been used to obtain data at two depths. Here we study some practical issues when performing Green's theorem for wave separation using over/under cable acquisition.

The depth difference between the cables

Since the wavefield P is the recorded data, the normal derivative needs to be calculated in the case of a geophone in the marine environment. When using an over/under cable, an easy way to calculate the normal derivative is to subtract the data of the upper cable from the data of the lower cable and then divide by their depth difference, i.e.,

$$\frac{dP(\frac{z_1+z_2}{2})}{dz}=\frac{P(z_2)-P(z_1)}{z_2-z_1}. \quad (8)$$

As the above equation shows, the normal derivative of P is at the depth $(z_1+z_2)/2$, rather than at z_1 or z_2, where wavefield P is measured. This mismatch may affect the wave separation results.

In our synthetic tests using the reflectivity method, we first used a 1D acoustic model with the source at 5m and two cables, one at a depth of 45m and one at 50m. (The cables were placed unrealistically deep to better illustrate the results.) Thus the two cables are separated by 5m. Using Green's theorem, the scattered wave P_s is predicted at 20m, and P_0 is predicted at 80m, as shown in Figure 1. Next, we reduced the depth difference between the two cables to 1m (one cable at 49m, the other at 50m), and in that case Green's theorem gives the predicted P_s at 20m and P_0 at 80m as shown in Figure 2. (The cables were placed unrealistically close again to better illustrate the results.) From these two results, we can clearly see that when the depth difference is 5m, as in Figure 1, there are several residuals left in both cases of P_0 and P_s, while in Figure 2, the predicted results are clean. This indicates that reducing the difference in cable depths can significantly increase the accuracy of wave separation results, since the depth of P_n now better matches with the depth of P in the Green's theorem integral.

The depth of the predicted wave

Other factors may affect the estimated results. The actual experiment shows that the choice of the predicted cable depth can change the quality of the result. Figure 3 shows the choice of different depths when predicting the scattered wave P_s. Here we define the depth difference between the predicted cable and the measurement surface as $\triangle z$. We also define the interval between traces as $\triangle x$. As we can see, the predicted result has many residuals when $\triangle z$ is very small compared with $\triangle x$. Only when $\triangle z$ is at least half of $\triangle x$ are the predicted results acceptable. Likewise, Figure 4 shows the predicted results of P_0 at different depths. We again got the similar conclusion that only when the depth difference between the predicted cable and the actual cable is larger than 1/2 of the interval between traces, does the predicted direct wave have few residuals.

DEGHOSTING SEAM DATA

We applied Green's theorem to the SEAM data set generated based on a deepwater Gulf of Mexico earth model (The SEG Advanced Modeling Corporation (SEAM), 2011). We used the special SEAM classic data set modeled to simulate dual sensor acquisition by recording the pressure wavefield at two different depths, 15 and 17m respectively. This dual sensor data consisted of nine sail lines for an equivalent wide azimuth towed streamer survey. Given the low frequency of the data (less than 30Hz) and the source and receiver depths of 15m and 17m, the ghost reflections overlap/interfere with non-ghost events, and successful deghosting would correspond to a change in the wavelet shape. The result is shown in Figure 5. In the right panel, we see there is no source notch to fill; the first source notch is at 44Hz which lies above the source frequency range (1–30Hz).

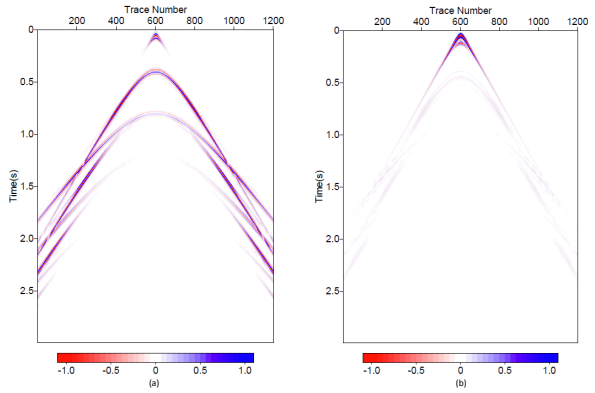

Figure 1: *Using an over/under cable with a 5m depth difference. (a) P_s predicted at 20m, (b) P_0 predicted at 80m.*

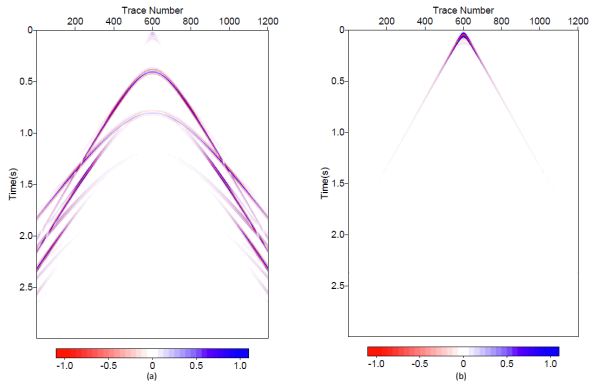

Figure 2: *Using an over/under cable with a 1m depth difference. (a) P_s predicted at 20m, (b) P_0 predicted at 80m.*

FREE SURFACE MULTIPLE REMOVAL

ISS free-surface multiple elimination method has the ability to predict accurately the phase and amplitude of multiples if its pre-requisites (wavelet and deghosted data) are satisfied. Figures 6(a) and 6(b) are the input data with and without ghosts, respectively. Inputting them into ISS free-surface multiple elimination algorithm, Figures 6(c) and 6(d) are their corresponding free-surface multiple predictions. After subtracting from the input data, Figures 6(e) and 6(f) show the results after free-surface multiple removal. If the input data are not deghosted, ISS free-surface multiple removal method can predict the exact phase but only approximate amplitude of multiples. After deghosting, we can see that all free-surface multiples are predicted exactly and through a simple subtraction; they are all well eliminated and most importantly primaries are not touched, as shown in Figure 6(f).

CONCLUSIONS

The ISS multiple removal algorithms require their input data to be deghosted and to have an estimate of the wavelet, each of which can be accomplished with distinct forms of Green's the-

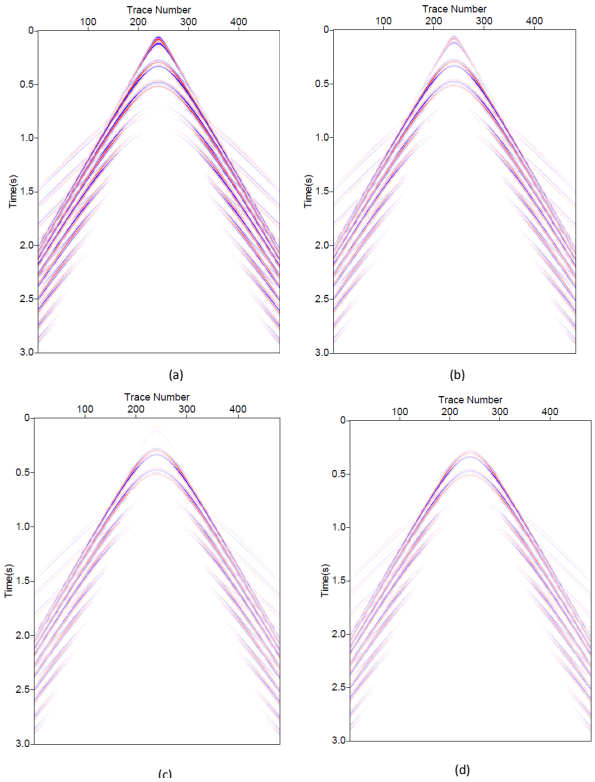

Figure 3: *Predicted P_s when: (a) $\triangle z$ =1/8 $\triangle x$, (b) $\triangle z$ =1/4 $\triangle x$, (c) 1$\triangle z$ =1/2 $\triangle x$, and (d)$\triangle z$ = $\triangle x$.*

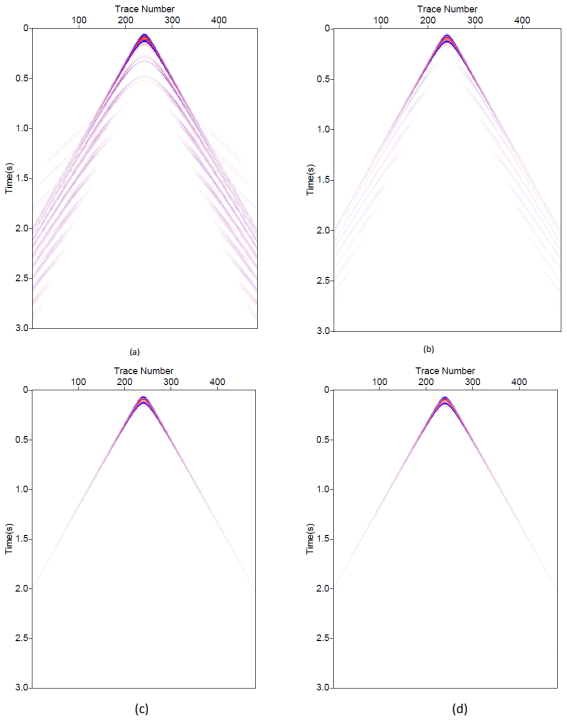

Figure 4: *Predicted P_0 when: (a) $\triangle z$ =1/8 $\triangle x$, (b) $\triangle z$ =1/4 $\triangle x$, (c) 1$\triangle z$ =1/2 $\triangle x$, and (d)$\triangle z$ = $\triangle x$.*

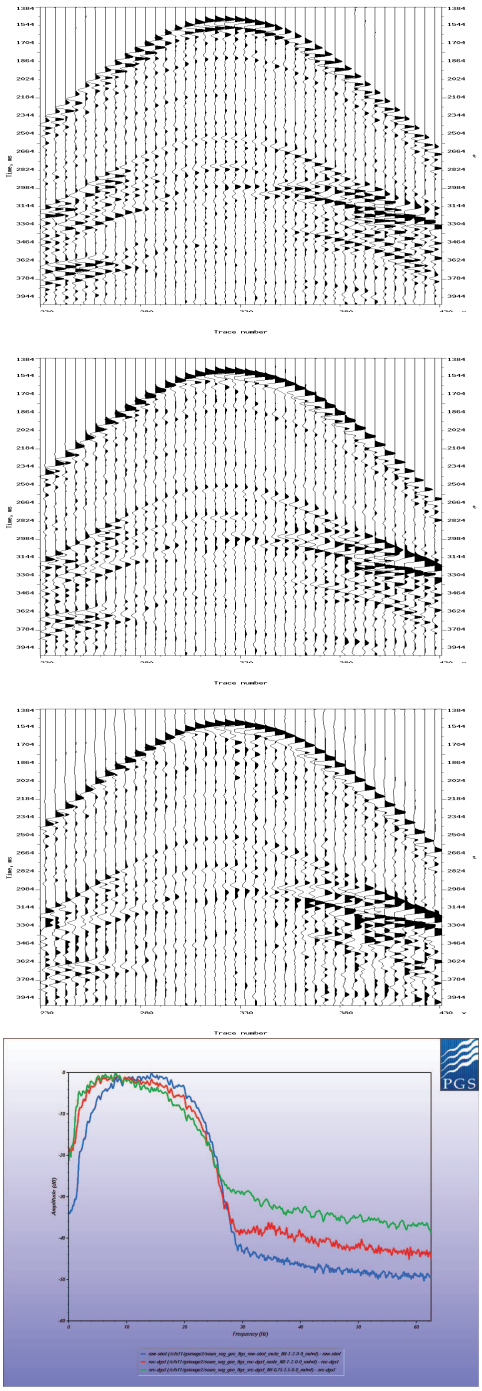

Figure 5: *SEAM data, shot 131373: recorded data at 17m (top panel), receiver deghosted at 10m (second panel), source and receiver deghosted at 10m (third panel). Note the collapsed wavelets in the second and third panels. Frequency spectra (bottom panel): red=P at 17m, blue=receiver deghosted at 10m, green=source and receiver deghosted at 10m. The spectrum uses a window of 201 traces (232-432) by 0.6s (1.4-2.0). The first source notch is at 44Hz which lies above the source frequency range (1–30Hz). Note the shift of the spectrum towards lower frequencies (which may be of interest to FWI).*

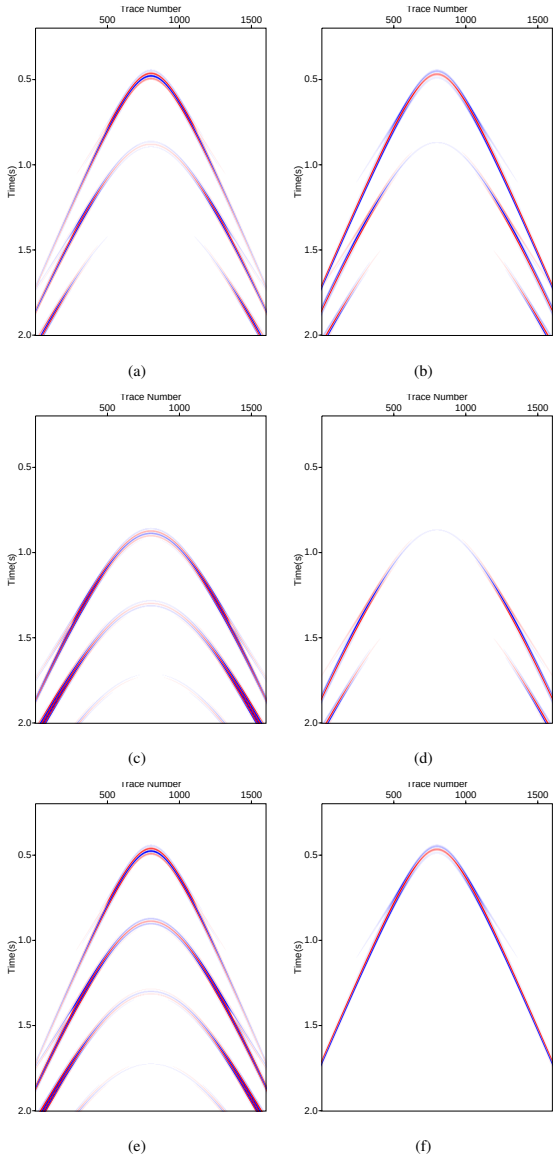

Figure 6: (a)&(b) Input data with and without ghosts; (c)&(d) corresponding free-surface multiple prediction; (e)&(f) After free-surface multiple removal through a simple subtraction.

orem. The effects of (1) the difference in the depth between the over cable and the under cable, and (2) the choice of the location of the predicted reference wave or scattered wave relative to the cable are studied. The tests show that to get useful wave separation results, the depth difference between the two cables should be quite small, and we choose to predict the wave at least 1/2 $\triangle x$ from the cable. The importance of deghosting before free surface multiple removal is also shown.

ACKNOWLEDGMENTS

We thank the M-OSRP sponsors for their support of this research. The second author also thanks PGS for permission to use SEAM data and Nizar Chemingui (PGS) for internships.

REFERENCES

Mayhan, J. D., P. Terenghi, A. B. Weglein, and N. Chemingui, 2011, Green's theorem derived methods for preprocessing seismic data when the pressure P and its normal derivative are measured: 81st Annual International Meeting, SEG, Expanded Abstracts, Society of Exploration Geophysicists, 2722–2726. (Ranked by SEG "in the top 31 papers presented at the San Antonio meeting").

Mayhan, J. D., and A. B. Weglein, 2013, First application of Green's theorem-derived source and receiver deghosting on deep-water Gulf of Mexico synthetic (SEAM) and field data: Geophysics, **78**, WA77–WA89.

Mayhan, J. D., A. B. Weglein, and P. Terenghi, 2012, First application of Green's theorem derived source and receiver deghosting on deep water Gulf of Mexico synthetic (SEAM) and field data, *in* 82nd Annual International Meeting, SEG, Expanded Abstracts: Society of Exploration Geophysicists, 1–5.

Osen, A., B. G. Secrest, and L. Amundsen, 1998, Wavelet estimation from marine pressure measurements: Geophysics, **63**, 2108–2119.

Tan, T. H., 1999, Wavelet spectrum estimation: Geophysics, **64**, 1836–1846.

The SEG Advanced Modeling Corporation (SEAM), 2011, The SEG Advanced Model: Technical report, Society of Exploration Geophysicists. (`http://www.seg.org/resources/research/seam`).

Weglein, A. B., F. V. Araújo, P. M. Carvalho, R. H. Stolt, K. H. Matson, R. T. Coates, D. Corrigan, D. J. Foster, S. A. Shaw, and H. Zhang, 2003, Inverse scattering series and seismic exploration: Inverse Problems, R27–R83.

Weglein, A. B., and B. G. Secrest, 1990, Wavelet estimation for a multidimensional acoustic earth model: Geophysics, **55**, 902–913.

Weglein, A. B., S. A. Shaw, K. H. Matson, J. L. Sheiman, R. H. Solt, T. H. Tan, A. Osen, G. P. Correa, K. A. Innanen, Z. Guo, and J. Zhang, 2002, New approaches to deghosting towed-streamer and ocean-bottem pressure measurements: 72nd Annual International Meeting, SEG, Expanded Abstracts, 1016–1019.

Zhang, J., 2007, Wave theory based data preparation for inverse scattering multiple removal, depth imaging and parameter estimation: analysis and numerical tests of Green's theorem deghosting theory: PhD thesis, University of Houston.

Zhang, J., and A. B. Weglein, 2005, Extinction theorem deghosting method using towed streamer pressure data: analysis of the receiver array effect on deghosting and subsequent free surface multiple removal, *in* 75th Annual International Meeting, SEG, Expanded Abstracts: Society of Exploration Geophysicists, **24**, 2095–2098.

———, 2006, Application of extinction theorem deghosting method on ocean bottom data, *in* 76th Annual International Meeting, SEG, Expanded Abstracts: Society of Exploration Geophysicists, **25**, 2674–2678.

The multiple attenuation toolbox: Progress, challenges and open issues

Arthur B. Weglein, M-OSRP/Physics Dept./University of Houston

SUMMARY

This paper describes recent progress in attenuating free surface and internal multiples for marine and on-shore plays. While there is much to celebrate within the multiple attenuation toolbox, with recent progress and improved capability, there are also significant fundamental open issues and practical challenges that remain to be addressed.

INTRODUCTION

Multiple removal is a longstanding problem in exploration seismology. Although methods for removing multiples have advanced and have become more effective, the concomitant industry trend toward more complex exploration areas and difficult plays has at times outpaced advances in multiple-attenuation capability. The topic of multiples, and the need for developing ever more effective methods for their removal, remains high in terms of industry interest, priority and research investment.

We advocate a tool-box approach and orientation for understanding: (1) overall multiple attenuation capability, and (2) the place and role that each method within the toolbox plays within the spectrum of different capabilities and responses, and (3) how to choose the method that's a best match for the user's application and objective. In this paper, we present a status report on the multiple attenuation toolbox and the open and prioritized issues yet to be addressed.

THE MULTIPLE ATTENUATION TOOLBOX

Among the current methods within the multiple attenuation toolbox, we will focus on: (1) Radon transform, (2) DELPHI feedback methods, and (3) the inverse scattering series approach. These methods were chosen because they each represent different assumptions and knowledge of subsurface properties, and the reflectors that have generated the multiples.

As we move from Radon, to feedback, to inverse scattering series (for free surface and internal multiples), the need for subsurface information and user intervention decreases and the commensurate cost increases. The cost-effective and appropriate choice depends on the complexity of the geology, the data, and your processing objective. If one can well estimate the velocity of primaries and there is sufficient moveout between primaries and multiples then Radon methods are often the indicated choice (Foster and Mosher, 1992; Trad et al., 2002, 2003; Nowak and Imhof, 2006; Abbad et al., 2011). If the free surface multiples are isolated (and temporally distinct from primaries) the SRME (from DELPHI) plus Radon followed by adaptive subtraction is an effective strategy. The DELPHI approach to internal multiple attenuation (Berkhout and Palthe, 1980; Berkhout and Verschuur, 1997; Berkhout, 1999; Berkhout and Verschuur, 2005b,a; Kelamis and Verschuur, 2000; Kelamis et al., 2002, 2006b, 2008; Luo et al., 2007; Verschuur et al., 1992) requires some information about the generators of internal multiples and will be a cost-effective choice when that criteria can be satisfied. The inverse scattering series (ISS) for free surface multiples predicts the amplitude and phase of free surface multiples at all offsets, doesn't require a Radon transform or adaptive subtraction and can eliminate the multiple in the presence of proximal or interfering events (Carvalho et al., 1992; Weglein et al., 2003). The latter is more costly than: (1) Radon, and (2) SRME (DELPHI) combined with Radon followed by adaptive subtraction, but can be the cost effective choice when the surgical removal of free surface multiples that are proximal to primaries or other multiples of different orders is the goal. Inverse scattering series methods for removing internal multiples (see, e.g., Araújo et al. (1994); Weglein et al. (2003)) require no subsurface information or interpretive intervention, cost more than Radon or feedback loop methods, but are the appropriate and indicated choice under the most complex and daunting geologic and data conditions, and when one is interested in predicting the amplitude and phase of multiples at all offsets. The latter elimination provides the surgical removal of multiples without injuring primaries. Choosing the appropriate tool for the specific exploration play and application is how we advocate using the current capability within the multiple attenuation toolbox. In fact, if your data set and prospect objectives can be accommodated by Radon, then it would be contraindicated to use a method that is more than necessary and will not provide a return on the added investment. Progress and future advances in capability will add to (and facilitate) the choices within the toolbox and broaden the circumstances under which multiples can be effectively removed without damaging primaries. The expanded and enhanced toolbox empowers those interested in paying more to access more capability to have that opportunity. Advances in computer capability always mitigate the cost factor. The use of different methods within the toolbox has varied over time, as industry trends and portfolio move from the readily accessible to the more complex and challenging plays.

OFFSHORE AND ONSHORE MULTIPLE REMOVAL: PROGRESS AND OPEN ISSUES

In offshore exploration, the industry trend to explore in deep water, with even a flat horizontal water bottom and a 1D subsurface, immediately caused many traditional and useful signal processing/statistical-based multiple-removal methods to bump up against their assumptions, break down, and to fail. The confluence of (1) high drilling costs in deepwater plays, (2) specific deepwater challenges (e.g., shallow subsea hazards), (3) the need to develop fields with fewer wells, (4) the complex and rapidly laterally varying overburden and boundaries/target and (5) the record of drilling dry holes, drives the need for greater capability for removing marine free-surface and internal multiples, as well as improving methods of imag-

ing.

Marine field data tests have demonstrated that under complex data and subsurface conditions that the ISS methods demonstrate their mettle and delivery. The ISS algorithms were recently employed on offshore Brazil data in Ferreira (2011) (see Figure 2). One of the conclusions of the latter study with Petrobras was "no other method was able to show similar effectiveness in attenuating the internal multiples generated by the salt layers".

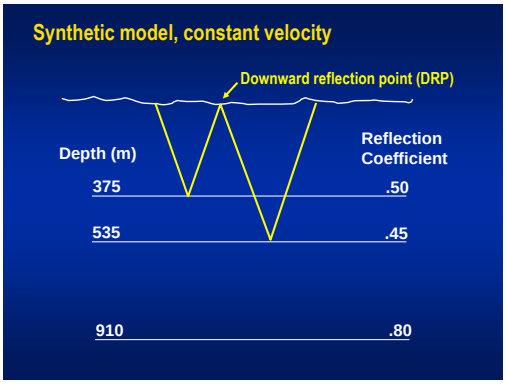

(a)

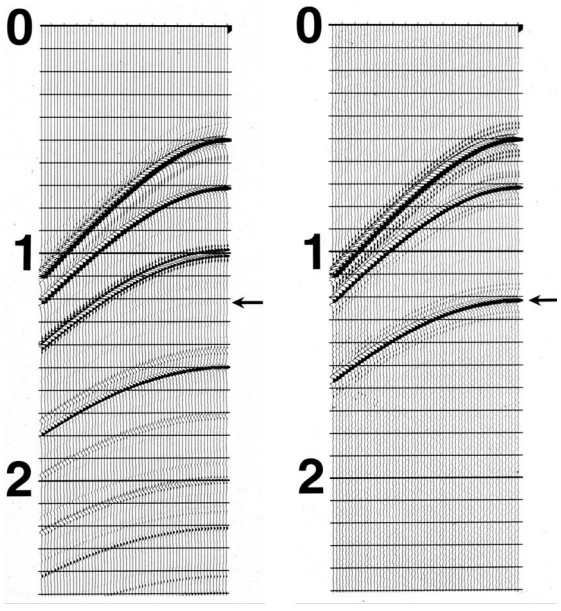

(b) (c)

Figure 1: Hidden reflector example: (a) Synthetic Model; (b) Shot record; (c) Shot record after an accurate amplitude and phase prediction of free surface multiple elimination. This example shows that the ISS free surface algorithm doesn't require a residual Radon or adaptive step. Note that the energy minimization criteria fails in this example. (Example provided courtesy of Bill Dragoset.)

Moving onshore, the estimation and removal of land internal multiples can make the toughest marine-multiple problem pale in comparison. The presence of proximal and interfering pri-

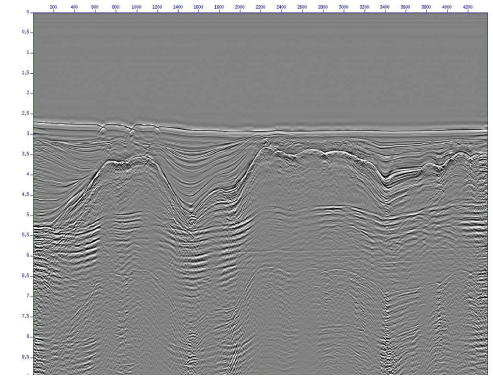

(a)

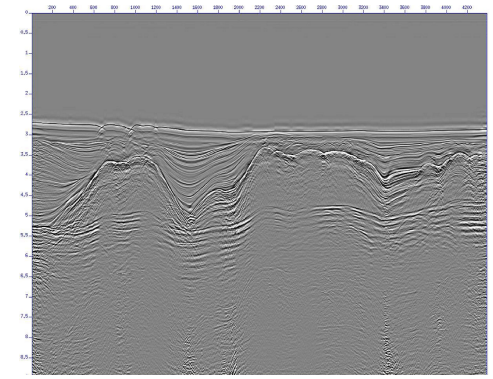

(b)

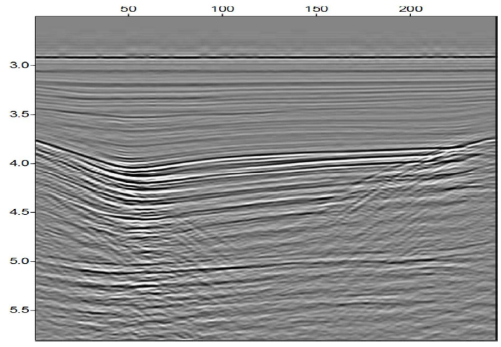

(c)

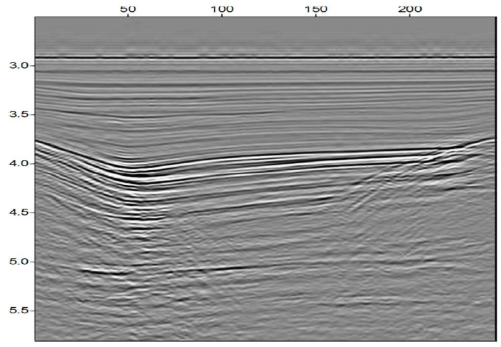

(d)

Figure 2: Stack before (a) and after (b) free surface multiple removal; common offset sections before (c) and after (d) internal multiple attenuation (Ferreira, 2011).

maries and internal multiples of different orders can occur in marine situations, but their frequent occurrence for land internal multiples raises the priority and interest in both the amplitude and phase fidelity of prediction. Developing an alternative to energy-minimizing-based adaptive subtraction techniques is also a priority and pressing need. For example, in Kelamis et al. (2006a), Fu et al. (2010), Luo et al. (2011), Weglein et al. (2011), and Kelamis et al. (2013), the basic cause of the land multiple-removal challenge in Saudi Arabia is identified as a series of complex, thin layers encountered in the near surface.

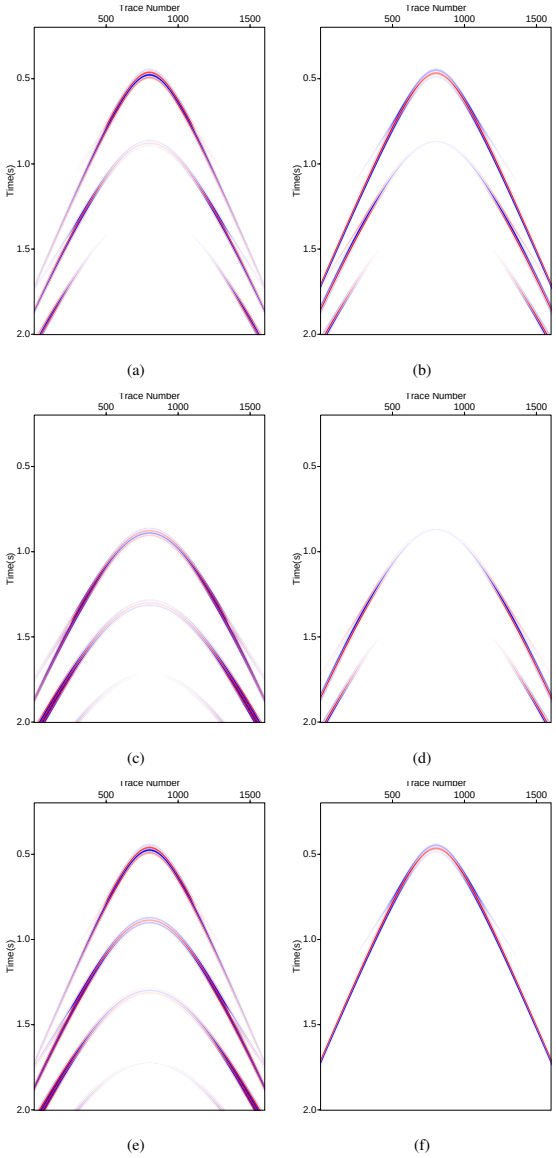

Figure 3: The left column is data and processing with ghosts in the data , and the right column is data and processing with ghosts removed. (a) and (b) are input data, (c) and (d) are free surface multiple predictions, and (e) and (f) after free surface multiple removal through a simple subtraction. Comparing (e) and (f) shows the residual if we do not remove ghosts.

Fu et al. (2010) concluded that "Their (ISS internal multiple algorithm) performance was demonstrated with complex synthetic and challenging land field data sets with encouraging results, where other internal multiple suppression methods were unable to demonstrate similar effectiveness."

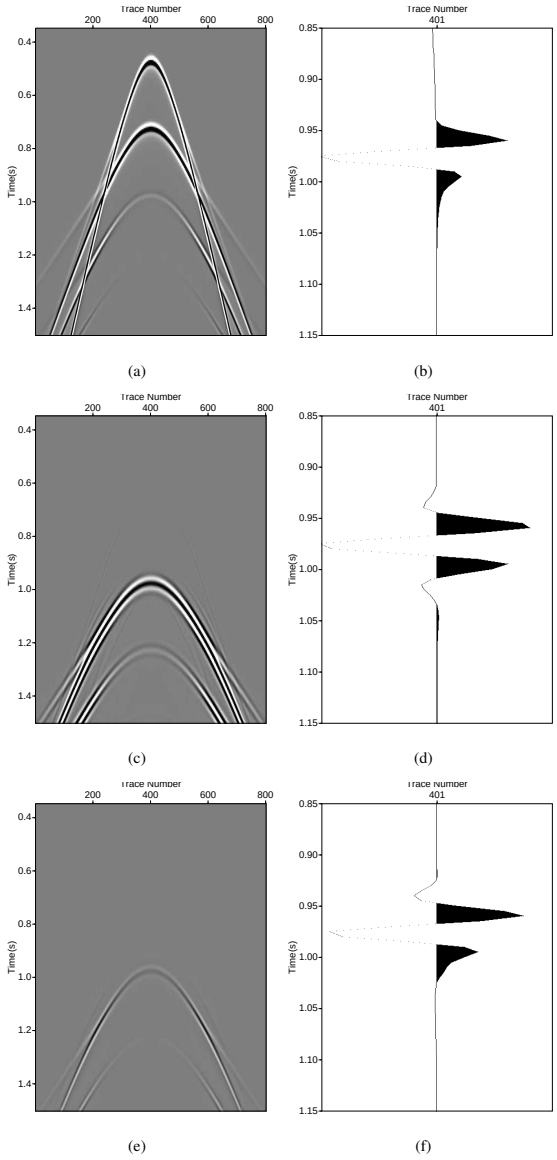

Figure 4: In the left column, (a) is the input data set (two primaries and first-order internal multiple), (c) is the internal multiple prediction without deconvolving the wavelet, and (e) is the internal multiple prediction with deconvolution of the wavelet. The right hand column shows only the first-order internal multiple (corresponding zero-offset traces). We see that removing the wavelet moves both the amplitude and shape of the predicted first-order internal multiple to the actual.

In general, strong reflectors at any depths are significant sources of internal multiples, especially where geologic bodies with different seismic properties are in contact. Typical examples are alternating sequences of sedimentary rocks, salt layers, basaltic layers or coal seams, which can give rise to short-period internal multiples.

PREDICTION AND SUBTRACTION

Multiple removal is often described as a two-step procedure: prediction and subtraction. The subtraction step is meant to try to compensate for any algorithmic compromises, or real world conditions, outside the physical framework behind the prediction. In multiple-removal applications, the subtraction step frequently takes the form of energy-minimizing adaptive subtraction. The idea is that a section of data (or some temporally local portion of data) without multiples has less energy than the data with multiples. One often hears that the problem with multiple attenuation is not the prediction but the subtraction. In fact, the real problem is excessive reliance on the adaptive subtraction to solve too many problems, with an energy-minimizing criteria that can be invalid or fail with proximal or overlapping events. The breakdown of the energy-minimization adaptive subtraction criteria itself can occur precisely when the underlying physics behind, e.g., high-end inverse scattering series multiple prediction (that it is intended to serve) will have its greatest strength and will undermine rather than enhance the prediction. (Please see Figure 1.) Statistics based non-energy minimization adaptive subtraction approaches are presented in Liu and Dragoset (2013) and Kaplan and Innanen (2008). The latter reports showed encouraging results. Weglein (2012) presents a non-energy minimization adaptive criteria that is derived from, and aligned with, the properties of the free surface algorithm. We would encourage further research and development of fundamentally new adaptive criteria to address this outstanding and high priority issue.

Progress to take the algorithm for internal multiple attenuation towards elimination is reported in W. Herrera (Herrera et al., 2013) and Y. Zou (Zou et al., 2013). The latter work developed ideas first suggested in Ramírez and Weglein (2009). When there are two or more internal multiple generators, the leading order internal multiple attenuator can generate spurious events. C. Ma (Ma et al., 2013) and H. Liang (Liang et al., 2013) have provided algorithms with all the advantages of the leading order attenuator but without the artifacts.

P. Terenghi (Terenghi et al., 2012) developed and H. Ayadi (Ayadi et al., 2013) tested a method that mitigates the computational challenge of 3D ISS internal multiple attenuation. Musil and Kostov (2008) describe a 2.5D free surface multiple elimination algorithm. Extending the latter technique to internal multiples would be worthwhile.

PREREQUISITES

The currently most effective multiple attenuation methods require a reasonable source signature and deghosting, and Green's theorem methods have been developed for that purpose (see Zhang and Weglein (2005); Zhang and Weglein (2006); and Mayhan et al. (2011)).

We cite references here that demonstrate the impact of Green's theorem deghosting on free surface multiple elimination (Figure 3), and the wavelet deconvolution on internal multiple prediction (Figure 4) (Yang et al., 2013). L. Amundsen (Amundsen, 1993; Ikelle and Amundsen, 2005) pioneered P+Vz deghosting, and J. Zhang (Weglein et al., 2002; Zhang and Weglein, 2005, 2006; Zhang, 2007) pioneered and J. Mayhan (Mayhan et al., 2011, 2012; Mayhan and Weglein, 2013) developed Green's theorem deghosting algorithms. Advances in acquisition (e.g., dual sensor or over/under cables) have allowed these Green's theorem methods and subsequent processing to reach their potential.

SUMMARY

The toolbox approach views the collection of available methods for attenuating multiples and recognizes that each method has strengths and limitations and, for a given prospect and play, that one chooses the appropriate method from a cost-effectiveness perspective. It is always important to keep in mind that in the broader perspective and ultimate consideration within the cost-effectiveness calculation and driver, that the cost of seismic processing is dwarfed by the cost saving from avoiding drilling dry holes.

There is a documented shift and trend in the changing relative emphasis of, e.g., Radon, Feedback, and Inverse Scattering Series methods that is attributable and closely tied to the trend and changes in the exploration and production strategies, interests and portfolios of petroleum producers and companies that provide services. Those same influences and factors determine the priority of open issues and the pressing need to address them.

ACKNOWLEDGEMENT

We thank the M-OSRP sponsors for their encouragement and support. For the offshore Brazil field data tests (Ferreira, 2011), we thank R. A. Rosa Fernandes and his group at Petrobras, for their outstanding assistance, expertise and support in the processing and analysis of the data. P. Terenghi is thanked for his guidance and mentoring of that project within M-OSRP. I would like to thank Hong Liang, Jim Mayhan, Lin Tang, and Jinlong Yang for their assistance with this manuscript.

REFERENCES

Abbad, B., B. Ursin, and M. J. Porsani, 2011, A fast, modified parabolic Radon transform: Geophysics, **76**, V11–V24.

Amundsen, L., 1993, Wavenumber-based filtering of marine point-source data: Geophysics, **58**, 1335–1348.

Araújo, F. V., A. B. Weglein, P. M. Carvalho, and R. H. Stolt, 1994, Inverse scattering series for multiple attenuation: An example with surface and internal multiples: 64th Annual International Meeting, SEG, Expanded Abstracts, Society of Exploration Geophysicists, 1039–1041.

Ayadi, H., and A. B. Weglein, 2013, Inverse scattering series internal multiple attenuation and angle constraints: fundamental concept, development and numerical analysis when three reflectors generate the data: M-OSRP 2012 Annual Meeting, TBD.

Berkhout, A. J., 1999, Multiple removal based on the feedback model: The leading Edge, 127–131.

Berkhout, A. J., and D. W. V. W. Palthe, 1980, Migration in the presence of noise: Geophysical Prospecting, **28**, 372.

Berkhout, A. J., and D. J. Verschuur, 1997, Estimation of multiple scattering by iterative inversion, part i: Theoretical considerations: Geophysics, 1586–1595.

———, 2005a, Multiple removal and wavelet deconvolution in the inverse data space: SEG Technical Program Expanded Abstracts, 2684–2688.

———, 2005b, Removal of internal multiples with the common-focus-point (cfp) approach: Part 1 explanation of the theory: Geophysics, V45–V60.

Carvalho, P. M., A. B. Weglein, and R. H. Stolt, 1992, Nonlinear inverse scattering for multiple suppression: Application to real data. Part i: 62nd Annual International Meeting, SEG, Expanded Abstracts, Society of Exploration Geophysicists, 1093–1095.

Ferreira, A., 2011, Internal multiple removal in offshore Brazil seismic data using the inverse scattering series: Master's thesis, University of Houston.

Foster, D. J., and C. C. Mosher, 1992, Suppression of multiple reflections using the Radon transform: Geophysics.

Fu, Q., Y. Luo, P. G. Kelamis, S. Huo, G. Sindi, S.-Y. Hsu, and A. B. Weglein, 2010, The inverse scattering series approach towards the elimination of land internal multiples: 80th Annual International Meeting, SEG, Expanded Abstracts, Society of Exploration Geophysicists, 3456–3461.

Herrera, W., C. Ma, H. Liang, and A. B. Weglein, 2013, An inverse scattering elimination subseries for first-order internal multiples with downward reflection at the shallowest interface: M-OSRP 2012 Annual Meeting, TBD.

Ikelle, L. T., and L. Amundsen, 2005, Introduction to petroleum seismology (investigations in geophysics no. 12): Society of Exploration Geophysicists.

Kaplan, S. T., and K. A. Innanen, 2008, Adaptive separation of free-surface multiples through independent component analysis: Geophysics, **73**, V29–V36.

Kelamis, P., W. Zhu, K. Rufaii, and Y. Luo, 2006a, Land multiple attenuation-The future is bright: 76th Annual International Meeting, SEG, Expanded Abstracts, Society of Exploration Geophysicists, 26992703.

Kelamis, P. G., Y. Luo, and A. Weglein, 2013, Strategies of land internal multiple elimination based on Inverse Scattering Series: Presented at the Technical Session 21: Recent Development in Seismic Imaging/Processing, International Petroleum Technology Conference, Beijing, China.

Kelamis, P. G., Y. Luo, W. Zhu, and K. O. Al-Rufaii, 2008, Two pragmatic approaches for attenuation of land multiples: 70th EAGE.

Kelamis, P. G., and D. J. Verschuur, 2000, Surface-related multiple elimination on land seismic data strategies via case studies: Geophysics, 719–734.

Kelamis, P. G., E. Verschuur, K. E. Erickson, R. L. Clark, and R. M. Burnstad, 2002, Data-driven internal multiple attenuation applications and issues on land data: SEG Technical Program Expanded Abstracts, 2035–2038.

Kelamis, P. G., K. O. R. W. Zhu, and Y. Luo, 2006b, Land multiple attenuation-the future is bright: SEG Technical Program Expanded Abstracts, 2699–2703.

Liang, H., and A. Weglein, 2013, Source wavelet effects on the ISS internal-multiple leading-order-attenuation algorithm and its higher-order modification: M-OSRP 2012 Annual Meeting, TBD.

Liu, K.-H., and W. H. Dragoset, 2013, Blind source separation of seismic signals based on information maximization: Geophysics. (accepted for publication in Geophysics).

Luo, Y., P. G. Kelamis, Q. Fu, S. Huo, G. Sindi, S.-Y. Hsu, and A. B. Weglein, 2011, Elimination of land internal multiples based on the inverse scattering series: The Leading Edge, **30**, 884–889.

Luo, Y., W. Zhu, and P. G. Kelamis, 2007, Internal multiple reduction in inverse-data domain: SEG Technical Program Expanded Abstracts, 2485–2489.

Ma, C., and A. B. Weglein, 2013, One-dimensional analytic analysis of the effects of including internal multiples as part of input into the leading-order inverse scattering series (ISS) internal-multiple attenuation algorithm: comparison between free-surface and internal-multiple cases: M-OSRP 2012 Annual Meeting, TBD.

Mayhan, J. D., P. Terenghi, A. B. Weglein, and N. Chemingui, 2011, Green's theorem derived methods for preprocessing seismic data when the pressure P and its normal derivative are measured: 81st Annual International Meeting, SEG, Expanded Abstracts, Society of Exploration Geophysicists, 2722–2726.

Mayhan, J. D., and A. B. Weglein, 2013, First application of Green's theorem-derived source and receiver deghosting on deep-water Gulf of Mexico synthetic (SEAM) and field data: Geophysics, **78**, WA77–WA89.

Mayhan, J. D., A. B. Weglein, and P. Terenghi, 2012, First application of Green's theorem derived source and receiver deghosting on deep water Gulf of Mexico synthetic (SEAM) and field data: 82nd Annual International Meeting, SEG, Expanded Abstracts, Society of Exploration Geophysicists, 1–5.

Musil, M., and C. Kostov, 2008, A 2.5D method for removal of free-surface-related seismic events: Presented at the 70th EAGE Conference & Exhibition.

Nowak, E. J., and M. G. Imhof, 2006, Amplitude preservation of Radon-based multiple-removal filters: Geophysics, **71**, V123–V126.

Ramírez, A. C., and A. B. Weglein, 2009, Green's theorem as a comprehensive framework for data reconstruction, regularization, wavefield separation, seismic interferometry, and wavelet estimation: A tutorial: Geophysics, **74**, W35–W62.

Terenghi, P., and A. B. Weglein, 2012, ISS internal multiple attenuation with angle constraints: M-OSRP 2011 Annual Meeting, 242–266.

Trad, D., T. Ulrych, and M. Sacchi, 2003, Latest views of the sparse Radon transform: Geophysics, 386–399.

Trad, D. O., T. J. Ulrych, and M. D. Sacchi, 2002, Accurate interpolation with high-resolution time-variant Radon transforms: Geophysics, 644–656.

Verschuur, D. J., A. J. Berkhout, and C. P. A. Wapenaar, 1992, Adaptive surface-related multiple elimination: Geophysics, 1166–1177.

Weglein, A. B., 2012, Short note: An alternative adaptive subtraction criteria (to energy minimization) for free surface multiple removal: M-OSRP 2011 Annual Report, 375.

Weglein, A. B., F. V. Araújo, P. M. Carvalho, R. H. Stolt, K. H. Matson, R. T. Coates, D. Corrigan, D. J. Foster, S. A. Shaw, and H. Zhang, 2003, Inverse scattering series and seismic exploration: Inverse Problems, **19**, R27–R83.

Weglein, A. B., S.-Y. Hsu, P. Terenghi, X. Li, and R. H. Stolt, 2011, Multiple attenuation: Recent advances and the road ahead (2011): The Leading Edge, **30**, 864–875.

Weglein, A. B., S. A. Shaw, K. H. Matson, J. L. Sheiman, R. H. Stolt, T. H. Tan, A. Osen, G. P. Correa, K. A. Innanen, Z. Guo, and J. Zhang, 2002, New approaches to deghosting towed-streamer and ocean-bottom pressure measurements: 72nd Annual International Meeting, SEG, Expanded Abstracts, Society of Exploration Geophysicists, 2114–2117.

Yang, J., L. Tang, J. D. Mayhan, and A. B. Weglein, 2013, Using Green's theorem to satisfy input requirements of ISS multiple removal algorithms: 83rd Annual International Meeting, SEG, Expanded Abstracts, Society of Exploration Geophysicists, TBD. (Submitted April 3, 2013).

Zhang, J., 2007, Wave theory based data preparation for inverse scattering multiple removal, depth imaging and parameter estimation: analysis and numerical tests of Green's theorem deghosting theory: PhD thesis, University of Houston.

Zhang, J., and A. B. Weglein, 2005, Extinction theorem deghosting method using towed streamer pressure data: analysis of the receiver array effect on deghosting and subsequent free surface multiple removal: 75th Annual International Meeting, SEG, Expanded Abstracts, Society of Exploration Geophysicists, 2095–2098.

———, 2006, Application of extinction theorem deghosting method on ocean bottom data: 76th Annual International Meeting, SEG, Expanded Abstracts, Society of Exploration Geophysicists, 2674–2678.

Zou, Y., and A. B. Weglein, 2013, Internal multiple removal: an amplitude correction equation for internal-multiple attenuator (1D normal incidence): M-OSRP 2012 Annual Meeting, TBD.

INVERSE SCATTERING SERIES DIRECT DEPTH IMAGING WITHOUT THE VELOCITY MODEL: FIRST FIELD DATA EXAMPLES

ARTHUR B. WEGLEIN[1], FANG LIU[1], XU LI[1], PAOLO TERENGHI[1], ED KRAGH[2], JAMES D. MAYHAN[1], ZHIQIANG WANG[1], JOACHIM MISPEL[3], LASSE AMUNDSEN[3], HONG LIANG[1], LIN TANG[1] and SHIH-YING HSU[1]

[1] *M-OSRP, University of Houston, 617 Science & Research Bldg. 1, Houston, TX 77004, U.S.A.*
[2] *SCR/Schlumberger, Schlumberger Cambridge Research Center High Cross, Madingley Road, Cambridge CB3 0EL, U.K.*
[3] *Statoil ASA, Statoil Forskningssenter, Arkitekt Ebbells veg 10, 7053 Ranheim, Norway.*

(Received September 3, 2011; revised version accepted November 24, 2011)

ABSTRACT

Weglein, A.B., Liu, F., Li, X., Terenghi, P., Kragh, E., Mayhan, J.D., Wang, Z., Mispel, J., Amundsen, L., Liang, H., Tang, L. and Hsu, S.-Y., 2012. Inverse scattering series direct depth imaging without the velocity model: First field data examples. *Journal of Seismic Exploration*, 21: 1-28.

In Weglein et al. (2010) an update and status report were provided on the progress on the inverse scattering series (ISS) direct depth imaging without the velocity model. In that article, results on synthetics with sufficient realism indicated that field data tests were warranted. This paper documents those first field data tests. These first early tests are encouraging and indicate that ISS direct depth imaging on field data is possible. Each member of a set of three distinct data or algorithmic conditions and requirements are identified and shown to be necessary for inverse scattering direct depth imaging, without a velocity model, to be effective and to produce the accurate structural configuration of reflectors and interfaces in the subsurface. Taken together, that set represents both necessary and sufficient conditions. In addition, for ISS imaging, the CIG flatness condition is a necessary and sufficient indication that an accurate depth image has been reached. The latter property is in contrast to conventional velocity dependent imaging methods where common image gather (CIG) flatness is a necessary but not a sufficient condition that a correct depth image has been achieved. The next steps, and open issues, on the road between viable and providing relevant and differential added value to the seismic tool-box are described and discussed.

KEY WORDS: imaging, migration, inverse scattering series, field data, velocity, CIG flatness.

0963-0651/12/$5.00

INTRODUCTION/BACKGROUND

For the purposes of this paper, an accurate depth image means a correct spatial location and configuration of interfaces/reflectors in the earth. All currently applied direct depth imaging methods and indirect imaging concepts firmly believe that depth and velocity are inextricably linked. That cornerstone of all current imaging means that any direct imaging method requires an accurate velocity model to produce an accurate image in depth.

DIRECT AND INDIRECT METHODS FOR IMAGING AND/OR INVERSION ARE NOT EQUIVALENT

It is essential to understand the significance of the term 'direct' in 'direct depth imaging'. Given an accurate velocity model (with an appropriate imaging method that can accurately backpropagate in space, or time, down through the velocity model), all current leading-edge imaging methods (e.g., Kirchhoff, FK, Beam and RTM) are able to directly output the depth (the actual spatial configuration) of reflectors. Within the framework of RTM methods, which assume an accurate velocity model, a recent set of papers (Weglein et al., 2011b, and Weglein et al., 2011c), advanced RTM concepts and methods, to address fundamental issues and shortcomings within current RTM practice, including the removal of the need for Perfectly Matched Layers (PML) and issues associated with that approach.

Indirect imaging methods (e.g., examining move-out trajectories and seeking flat common image gathers (CIG), Common Focus Point (CFP), Common Reflection Surface (CRS) and 'path integral' approaches) seek to satisfy a property or condition that an image with an accurate velocity would satisfy. Those properties are necessary conditions, but not sufficient, and hence satisfying the indirect proxy for an adequate velocity model is not equivalent to knowing the velocity and direct depth imaging. Therefore, satisfying these indirect criteria is no guarantee, and can lead to the correct depth or to any one of a set of incorrect depths. The latter truth is rarely (if ever) spoken and even rarer to find mentioned or exemplified in print. Most importantly, these indirect approaches fervently believe that a direct depth imaging method would require and demand a velocity model, and that there is absolutely no way around it, and that depth and velocity are innately linked and coupled on a very basic and fundamental level. That thinking is clear, and 100% correct within the framework of current imaging concepts and methods. However, that conventional mainstream thinking is limited from another broader perspective, and is superseded by the new broader framework for imaging provided by the inverse scattering series (ISS). Amundsen et al. (2005, 2006, 2008) have developed direct inversion methods for 1D acoustic and elastic media. The ISS is the only

direct inversion for both a 1D and a multi-dimensional acoustic, elastic and anelastic earth.

In addition to being direct and applicable for a multi-dimensional earth, the ISS (Weglein et al., 2003) is further unique in allowing for all processing objectives (including multiple removal, depth imaging, target identification, and Q compensation) to be achieved directly and without subsurface information.

In the same 'direct' sense that current imaging methods can directly output the spatial configuration of reflectors with a velocity model, ISS imaging algorithms can directly output the correct spatial configuration without the velocity model. It is the only method with that potential and capability.

Within the tool-box of multiple removal methods, the ISS internal multiple method is the only algorithm that predicts the removal of all internal multiples directly, and without subsurface information. The latter claim of ISS multiple removal capability was once highly controversial, incredulous and widely considered impossible. However, now it's not only understood to be possible, it has been documented and reported to have stand-alone capability in comparison with all other internal multiple methods (see, e.g., Luo et al., 2011). There is one set of unchanged ISS equations that at once communicates that all multiples can be removed, and all primaries can be accurately depth imaged - directly and without any subsurface information, including velocity. If one believes that it is impossible to directly depth image without the velocity using the ISS, then one is forced to also believe that it is impossible to remove internal multiples without subsurface information. They come from the exact same set of equations and logic.

The ISS subseries for direct depth imaging communicates that depth and velocity are not inextricably and fundamentally linked. The ISS provides a new superseding theory that views the current velocity-depth relationship and framework as a special limiting case, as quantum mechanics and relativity view classical physics as limiting and special cases, within a new comprehensive and broader platform and framework. The new broader ISS framework for imaging reduces to current imaging algorithms when the velocity model is adequate, a property that a superseding theory must satisfy, and most amazingly it determines automatically on its own for any particular data set, or portion of a data set (and a given velocity model and migration algorithm), whether the new framework is needed, or whether the current conventional imaging framework and a given velocity model is in any individual case accurate and will suffice. The new imaging framework determines if its services, that is, whether the terms beyond the first term (the first and linear term in ISS imaging corresponds to current linear conventional imaging) are needed and will be called upon, and if it determines a response in the affirmative, then and only then, will it activate the new ISS imaging framework terms and call them into action. That need or

no-need, yes or no ISS imaging decision is made unambiguously and automatically in the first term within the ISS imaging series after the conventional linear image, and a 'no-need' determination not only shuts down the first non-linear term but all subsequent terms in the imaging series at any specific well-located image in the linear conventional migration. How does it know if it's an adequately or an inadequately located image? The guess would be that some criteria is being used by ISS imaging to determine 'wellness' of the image, since we are so oriented to that 'indirect' criteria orientation and religion (e.g., CIG flatness or iterative updating with an objective function and search engine). There is no 'indirect' criteria being employed in any ISS application, rather the directness within the ISS is the driver, and it doesn't provide merely perturbation theory, where some initial estimate is perturbed and updated, but rather purposeful perturbation theory, with 'direct' and 'purposeful' being the key and coupled concepts and the central and essential point. The 'directness' in ISS is what makes each term have a purpose, and identifiable within specific tasks towards inversion, and those terms within the ISS imaging series determine first if their purpose is needed at some location within a conventional migrated image before they act. Direct inversion, provided in the form of a series (perturbation), inexorably leads to purposeful perturbation theory, where each and every term has a unique and specific purpose and role, that can in turn be associated with isolated tasks - within the overall goal of inversion. That's in contrast with indirect methods, e.g., typical iterative linear or other indirect updating and search engine schemes, the latter more often based on mathematics and optimization, on 'all or nothing' thinking, typically settling for the latter. In some circles indirect methods have even defined themselves as the only definition and meaning of inversion as 'datafitting'. The consequences of ignoring the distinction between direct and indirect methods are tremendously significant. From a direct inversion perspective, for determining changes in earth mechanical properties, the so-called 'full wave inversion' methods today are inverting the wrong and fundamentally inadequate P to P data, with wrong algorithms, and with a wrong earth model. Would we today ignore the insights, lessons and the direct solution offered by $x = [-b \pm \sqrt{(b^2 - 4ac)} / 2a]$ for the quadratic equation, $ax^2 + bx + c = 0$ in favor of minimizing and searching various norms of $\| ax^2 + bx + c \|$? The latter is precisely what we are too often pursuing in the field of 'inversion' for changes in Earth mechanical properties. The indirect methods seem based on lack of hope or awareness of direct methods, and depend on big expensive, fast computers - and therefore have the affectation and imprimatur of being modern, computational and 'scientific', but too frequently are merely old ideas dressed up in abstract, rigorous and obfuscating mathematical language (for details and implications see, e.g., Weglein et al., 2009).

All current leading edge migration methods, such as, Beam, Kirchhoff and RTM, are linear. The ISS direct depth imaging without the velocity algorithm is a non-linear relationship between data and the wavefield at depth.

ISS TASK SPECIFIC SUBSERIES FOR MULTIPLE REMOVAL, DEPTH IMAGING AND DIRECT NON-LINEAR AVO

Each and every term and portion of any term within the ISS is computed directly in terms of data. All tasks associated with inversion (e.g., multiple removal, depth imaging, nonlinear direct AVO, and Q compensation) are each contained within the series. Hence, these individual tasks are each achievable directly in terms of data, and without subsurface information. Every seismic processing objective is carried out as an isolated task subseries of the ISS, and operates without subsurface information, by involving distinct non-linear communication of the recorded seismic data. Only the ISS communicates that all seismic objectives can be achieved in basically the same way that free surface multiples are removed. The free surface and internal multiple removal subseries have not only been shown to be viable but have also demonstrated added value and stand alone capability for predicting the amplitude and phase of multiples (see, e.g., Luo et al., 2011; Matson et al., 1999; Weglein and Dragoset, 2005; Fu et al., 2010), in particular, demonstrated under complex marine and on-shore circumstances. In this paper, we examine for the first time the issue of ISS depth imaging viability on field data. All conventional direct depth imaging methods only require knowledge of the velocity model to determine the spatial locations of reflectors. Hence, the ISS direct depth imaging subseries project began by assuming that only the velocity was variable and unknown. While all processing tasks are realizable directly and without subsurface information, all tasks are not equally simple or easy for the inverse series to achieve. For example, for different task specific subseries: one term eliminates each order of free surface multiple, while one term attenuates each order of internal multiple, furthermore, a series can locate reflectors beneath a small difference between actual and reference velocity, and another more inclusive imaging series can deliver the same structure determination effectiveness for larger contrasts in velocity. To-date the evolution and status of ISS imaging algorithms involves greater inclusiveness of ISS imaging terms and types of terms, and capability, but is not close to all of the ISS terms and capability that reside within the ISS. The issue is when a certain degree or state of ISS imaging capture will provide a tool box contribution with differential added-value in comparison to current imaging methods that require a velocity model.

The initial ISS imaging series (Weglein et al., 2002, Shaw et al., 2004, Innanen, 2004) were labeled LOIS for leading order imaging series. That evolved into a higher order cascaded series in closed form developed by Fang Liu (2006) and labeled as HOIS. All of that early development assumed that the only variable and unknown subsurface property was acoustic P wave velocity.

Figs. 1-8 illustrate the ISS imaging results for an earth in which only velocity varies. The algorithms are described in Liu (2006); Liu et al. (2005);

Zhang et al. (2007). The higher order imaging series (HOIS) methods pioneered in Liu and Weglein (2009) developed for velocity only varying media, are multi-dimensional ISS imaging algorithms that address imaging challenges that also exist in a one dimensional subsurface. Fang Liu's HOIS method was extended to HOIS+LE by Wang and Weglein (2011) to incorporate the imaging challenges addressed by HOIS, and in addition to accommodate certain imaging challenges that exclusively arise in a multi-dimensional laterally varying subsurface. The latter higher order imaging series plus laterally exclusive algorithm uses the acronym HOIS+LE. The progression of that velocity only varying subsurface ISS direct depth imaging capability, without the velocity model (HOIS and HOIS+LE) capability is shown in Figs. 1-8, for the fault shadow zone and pre-salt examples. HOIS and HOIS+LE contain higher order imaging terms for large contrasts and duration of those differences, imaging terms extracted from within the ISS. As mentioned above, these algorithms represent increasing capability, but are not containing all orders or all imaging terms for either a one-dimensional or multi-dimensional subsurface. More capability will be included in future algorithms. However, the HOIS and HOIS+LE algorithms are direct, require no velocity model building and updating, are closed form and both are lightning fast. The cost to run the HOIS and HOIS+LE algorithms is roughly 30% more than the single water speed FK Stolt migration. The single water speed migration is the costliest part of the ISS algorithm. It's essentially free, and that's amazing. The imaging results in Figs. 1-8 would be impressive for a conventional method that spent much time and effort to find the velocity from the data with a velocity analysis and then to image through it, that would take

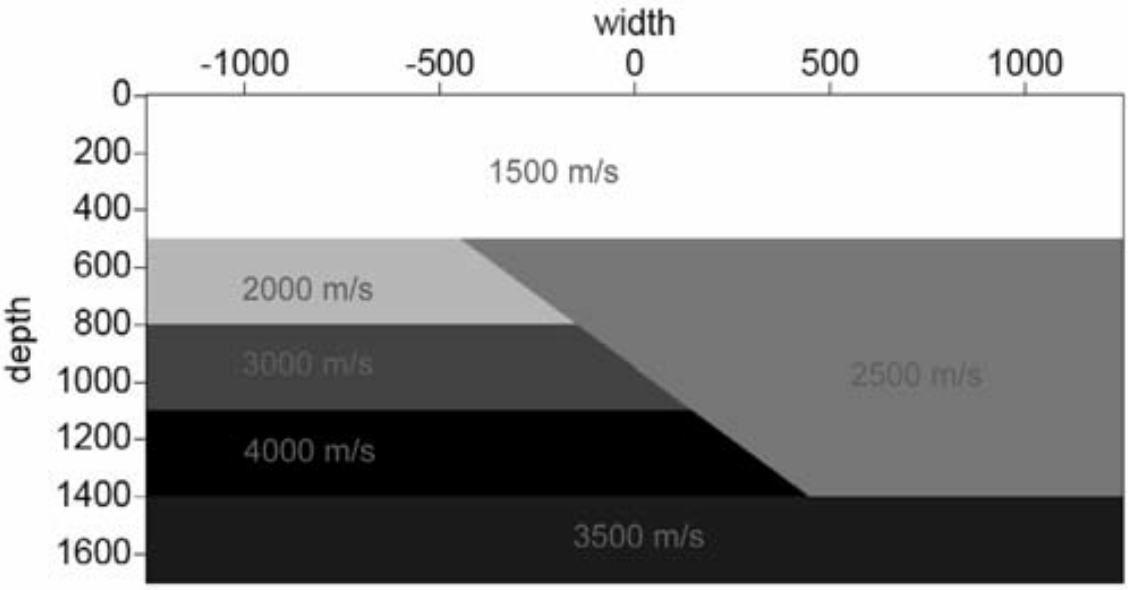

Fig. 1. The fault shadow zone model. Not to scale.

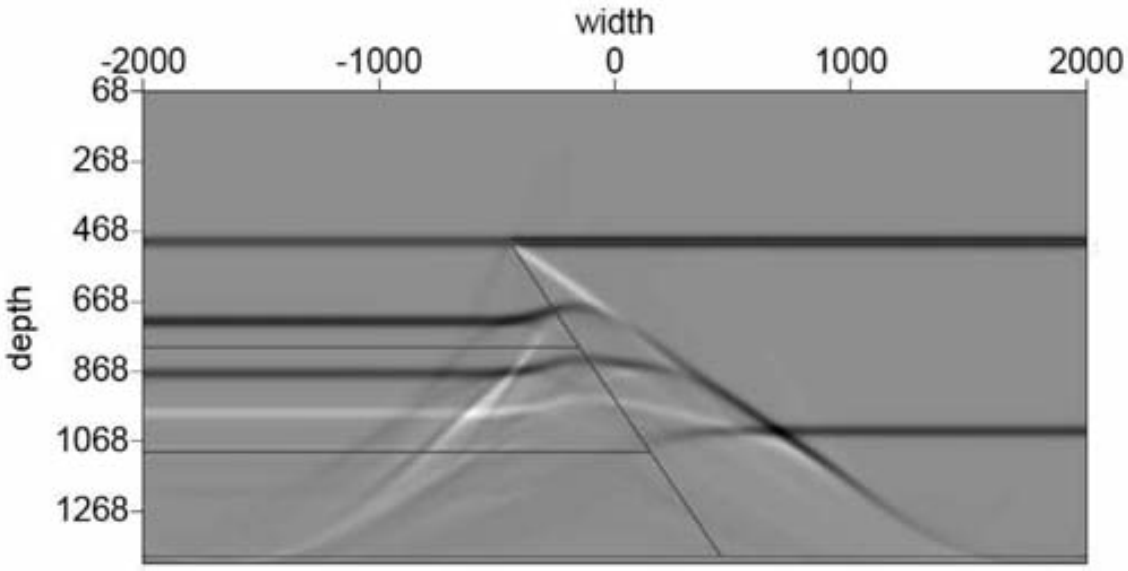

Fig. 2. The water speed pre-stack FK Stolt migration for the data from the fault shadow model (Liu and Weglein, 2009).

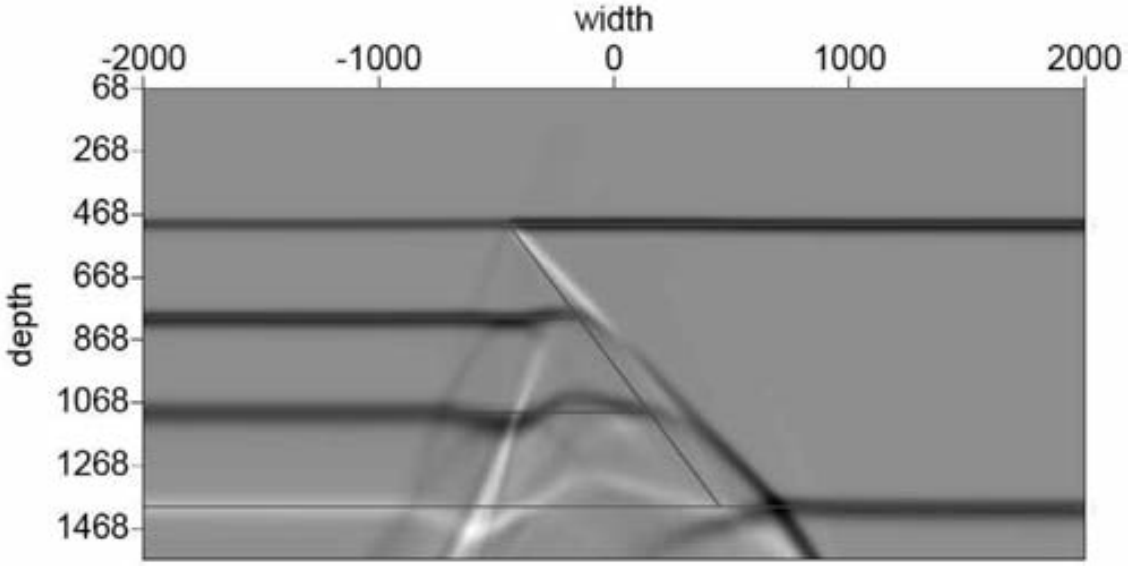

Fig. 3. Fault model - HOIS (Liu and Weglein, 2009).

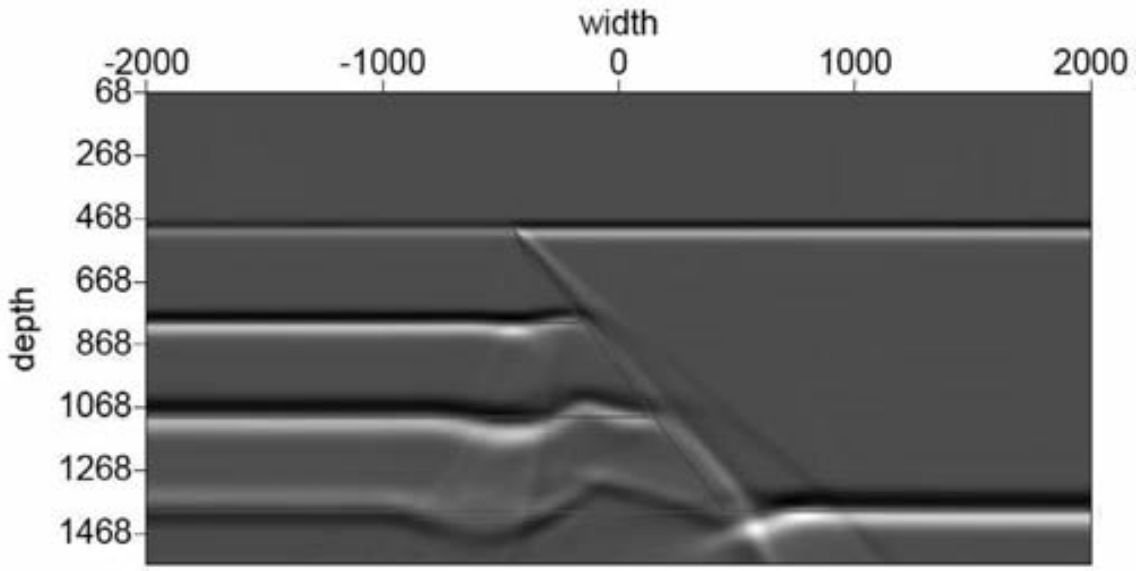

Fig. 4. Fault model HOIS+LE (Wang and Weglein, 2011).

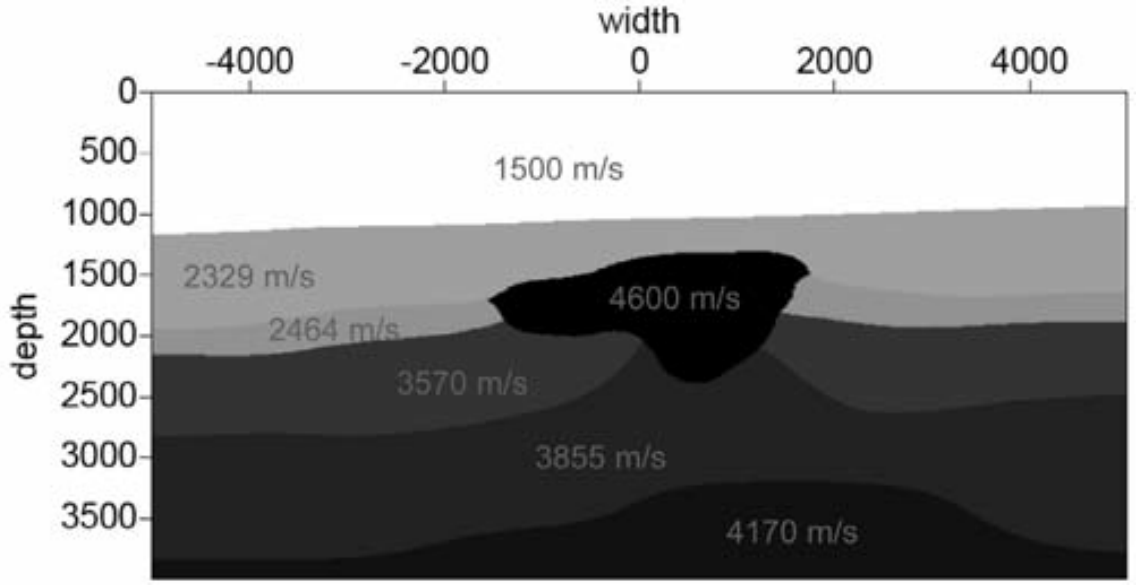

Fig. 5. Salt model.

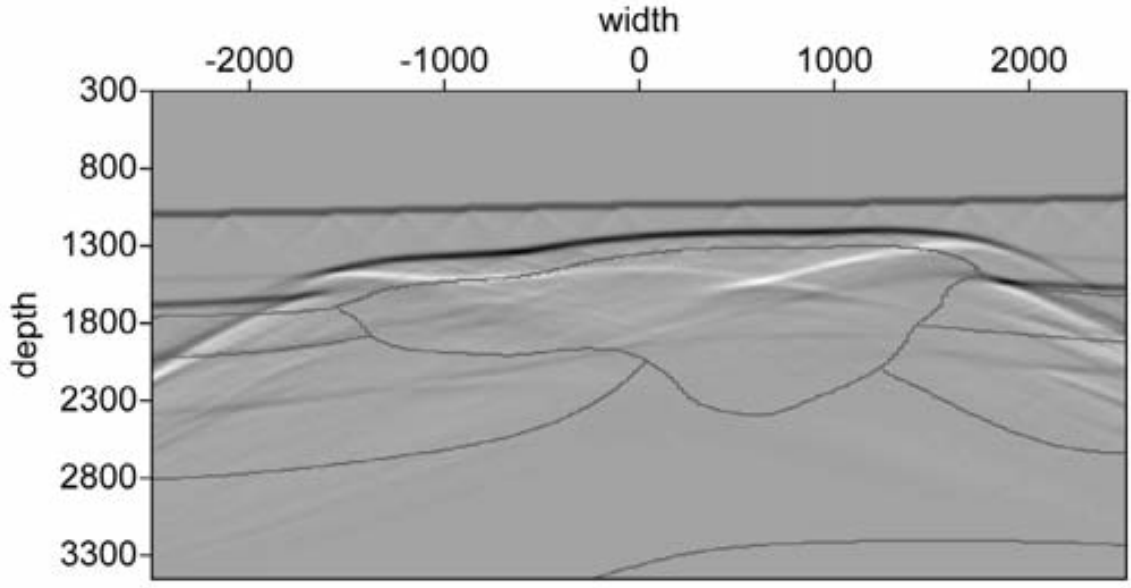

Fig. 6. Salt model water speed migration.

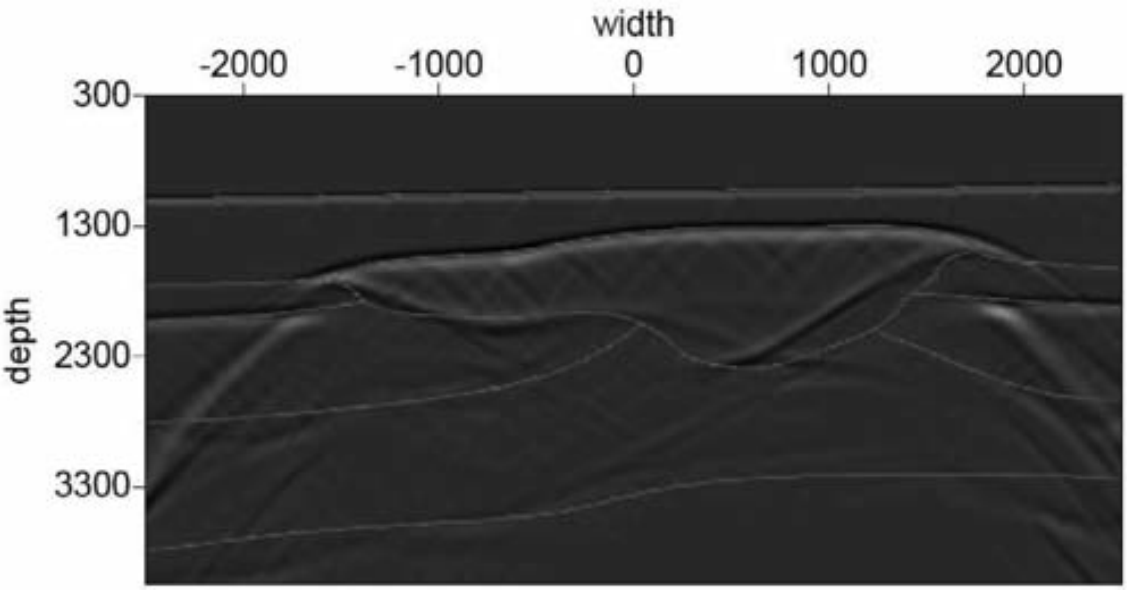

Fig. 7. Salt model - HOIS (Liu, 2006).

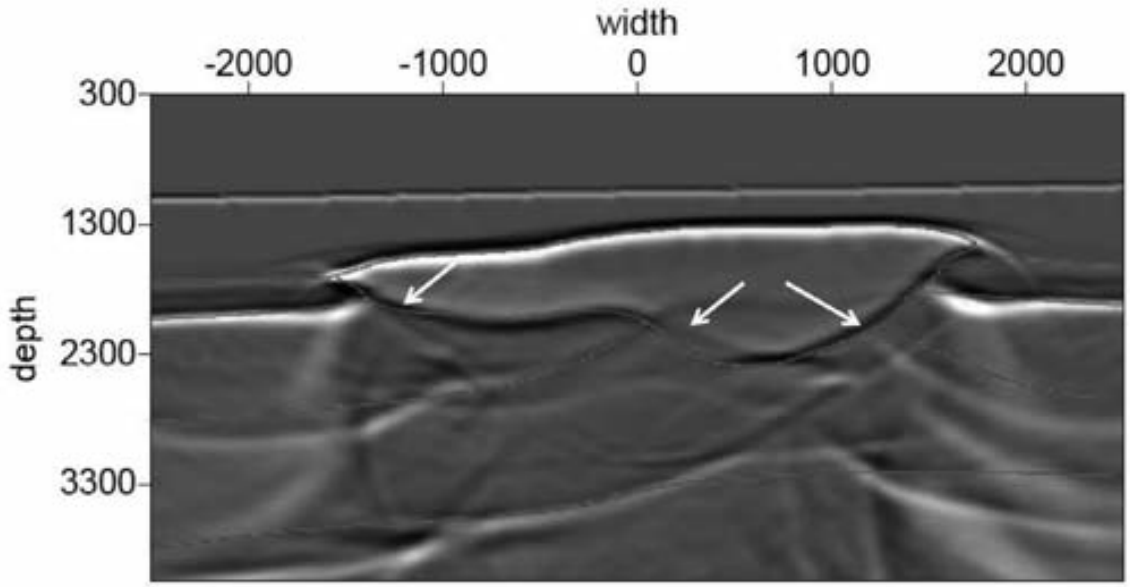

Fig. 8. Salt model - HOIS+LE (Wang and Weglein, 2011).

orders of magnitude longer to approximate the velocity and to migrate and image. These examples and algorithms exemplify the tremendous potential, promise and power that reside within the ISS for direct depth imaging without a velocity model, although these two specific algorithms (HOIS and HOIS+LE) are merely the tip of the iceberg in terms of capturing ISS imaging terms and capability. They represent progress within an important front (assuming that only velocity varies in the subsurface) in the ISS depth imaging campaign.

Imaging methods that require the velocity use only the phase of the data to determine depth. In contrast, all ISS tasks achieve their goals without subsurface information by using both the amplitude and phase of the events in seismic data.

MODEL TYPE AND ISS DEPTH IMAGING

The distinct ISS free surface and internal multiple attenuation subseries are model-type independent (see Weglein et al., 2003). That means those algorithms are completely unchanged if the earth is assumed to be an acoustic, elastic or anelastic medium. The ISS direct depth imaging subseries project has not reached a stage of development where a model-type independent ISS depth imaging algorithm is available. Therefore, at this time, the issue of ISS depth imaging and the assumed earth model-type needs to be considered in developing, evaluating and applying these techniques.

When we assume an acoustic earth model and, furthermore, that mechanical property changes in the medium are only due to velocity changes (and not density changes), then each reflection corresponds to a change in velocity at the reflector. For the latter earth model, if in addition the ISS imaging algorithm assumes (as we assume in this paper) that the reference velocity everywhere is constant and equal to the wave speed above the first and shallowest reflector, then ISS imaging will require (and the ISS depth imaging automatically provides and arranges) that all reflections above every initially mislocated reflector to be included and involved in the ISS depth imaging algorithm's input and action to correctly place the initially misplaced reference velocity imaged reflector.

However, if the medium allows changes in both velocity and density (as can and often does occur in the real earth), then the situation for ISS depth imaging is considerably more complicated both in theory and practice. To understand what gives rise to this new complexity, in a world where we assume that velocity and density can both vary, we will consider a specific example in such a medium, where the velocity is actually constant, and throughout the volume is equal to the constant reference velocity. The reflections in this example are then only caused by density variations. Then the constant reference velocity migration will accurately locate each reflector in this actual velocity equals reference velocity case. There is no need for ISS imaging beyond the first ISS term corresponding to reference velocity migration. Therefore density only reflections do not enter ISS depth imaging algorithms. The latter statement assumes that the objective of depth imaging is simply to locate reflectors and nothing more. Hence, we conclude that for an earth where both density and velocity can vary, that all reflections shallower than a given mislocated reflector are no longer necessarily involved through ISS imaging in aiding a mislocated deeper reflector. If the shallower reflection corresponds to either a velocity change, or to a velocity and density change, then that reflection enters the assistance package to aid the deeper mislocated reflector, but if the shallower reflection corresponds to only a density change, it doesn't enter that ISS depth imaging aid package. That's one of several new issues for a velocity and density varying earth that doesn't exist in a world where velocity is the only parameter that can vary. Further, if an ISS depth imaging algorithm that was derived from the ISS for an earth model where velocity is the only variable that can change, and the data that is input into the algorithm comes from a model where velocity and density can both vary, then initially well-located reflectors can be moved to an incorrect location and erroneously located images will not be corrected. However, there is no need to despair, because the multi-parameter acoustic or elastic ISS imaging, from the moment the multi-parameter ISS is written down, are immediately aware of this new issue that it needs to address, and automatically removes density only reflections from the ISS imaging algorithms, without knowing or determining the velocity and density configuration in the earth. Hence, the consequence of using all of the information in seismic primary

events (amplitude and phase) in ISS depth imaging without the velocity model, ultimately results in the need for ISS depth imaging to preclude density only reflections. The angle dependence of the amplitude of events is used by ISS imaging to preclude density only reflections.

THE EXCLUSION OF DENSITY ONLY REFLECTIONS IS APPROPRIATE FOR ISS MIGRATION FOR STRUCTURE BUT WOULD BE INCLUDED IF MIGRATION-INVERSION IS THE ISS GOAL

The exclusion of density only reflections would be inappropriate if the isolated task was designed to provide both a depth image plus an angle dependent reflection coefficient at those depth images, the latter for the purposes of migration-inversion. The ISS depth imaging in an acoustic earth where the P-wave velocity V_P and density (and for an elastic earth with P-wave velocity V_P, shear wave velocity V_S and density) can all vary and all are initially (and remain, completely) unknown, was formulated in Weglein et al. (2008) to retain the strength of a velocity only earth with a single imaging output, as a generalized reflectivity, while the exclusion of density only reflections is extracted from the strength of the multi-parameter ISS machinery. The results were summarized in Weglein et al. (2010).

THE IMPACT OF DATA LIMITATIONS ON ISS SUBSERIES

Table 1 summarizes the dependence/sensitivity of different ISS subseries on seismic bandwidth. As the latter table indicates, there is an increased dependency as we progress from the ISS free surface multiple case (where the subseries works one frequency at a time, and has absolutely no concern about bandlimited data) to the depth imaging subseries where the absence of low frequency in the data can have a deleterious effect on the ability of the ISS to move from the original linear incorrect depth image to the correct depth.

Table 1. The degree to which each ISS task specific subseries depends on the temporal frequency content of the data.

Specific subseries	Dependence on temporal frequency content of the data
Free surface multiple	None
Internal multiple	Very mild
Depth imaging	Some

THE CONDITIONS/ISSUES/REQUIREMENTS THAT NEED TO BE ADDRESSED FOR ISS DEPTH IMAGING ALGORITHMS TO BE EFFECTIVE ON FIELD DATA AND TO PROVIDE ACCURATE SPATIAL CONFIGURATIONS OF REFLECTORS IN THE SUBSURFACE

There are several absolute conditions, requirements and issues that need to be satisfied or addressed, respectively - in order for the current approach to ISS direct depth imaging without a velocity model to provide an effective and accurate spatial configuration of reflectors and interfaces in the earth. Those issues are: (1) sensitivity to (and interest in) low frequency/low vertical wavenumbers in the data; (2) assuming the appropriate earth model type and number of spatial dimensions in deriving the ISS imaging algorithm; (3) within a given and appropriate earth model type, the inclusion of sufficient imaging terms from the inverse scattering series, to address all shortcomings and problems from using as the first step a single constant velocity migration. Among items the ISS must accommodate, and address are: (I) how different is the actual velocity from the reference value, and the extent, duration, width of the layer, or over what region is that difference occurring; (II) how many parameters are assumed to be unknown in the appropriate model-type - the larger the number of unknown parameters in the model type, the harder the series has to work (that is, more ISS imaging terms have to be included) for the same contrast and duration of differences, in comparison with how hard the imaging series has to work for a single parameter changing model with comparable difference values and duration. The CIG flatness criteria is a necessary and sufficient condition that these conditions (1) and (3) have been satisfied and with an appropriate model type (condition 2) that the direct ISS imaging has produced the correct depth.

In the examples below, we will isolate and separately examine each of these issues. The order that we will follow is: first assume that there is no low frequency issue, and no model type matching issue between the model used to generate the data and the model used for processing the data, that is, the model behind the ISS imaging algorithm. In that first example, we examine the consequence of including or not including sufficient ISS imaging terms, in the ISS imaging algorithm to match and address the contrast in properties between actual and reference, and the duration of those differences. Fig. 9 shows two different ISS imaging results for a layered model. The first is LOIS (Leading Order Imaging Series, see, e.g, Shaw et al., 2004 extended to the multi-parameter case Weglein et al., 2008) and the second is HOIS (Higher Order Imaging Series, see e.g., Liu et al., 2005 also extended to the multi-parameter case Weglein et al., 2008) where LOIS has fewer types of terms and imaging capability in comparison to HOIS. The fact that HOIS is adequate inclusion of imaging terms (and LOIS is not) for this particular example's contrast and duration of differences between reference and actual velocity, is indicated by HOIS predicting the correct depth and having a flat

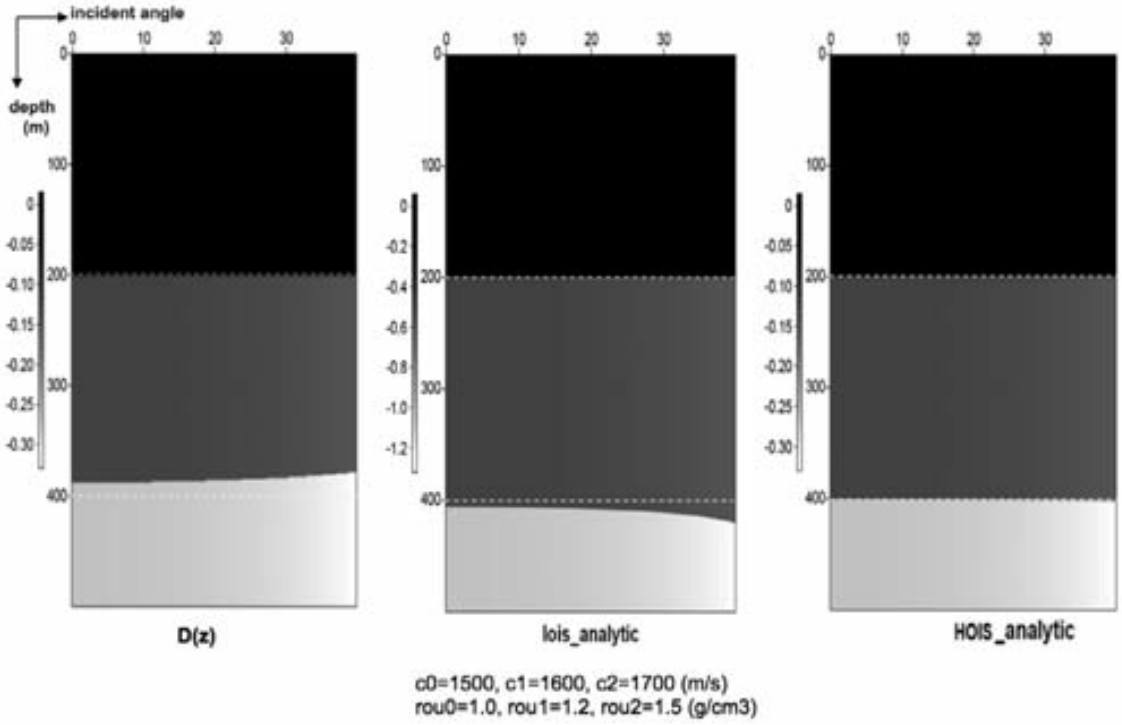

Fig. 9. Left: input FK-migrated data in pseudodepth domain. Center: LOIS result. Right: HOIS result. These figures demonstrate that with more capture, i.e., inclusion of more imaging terms, HOIS imaged the reflectors to their correct depth location, whereas LOIS did not.

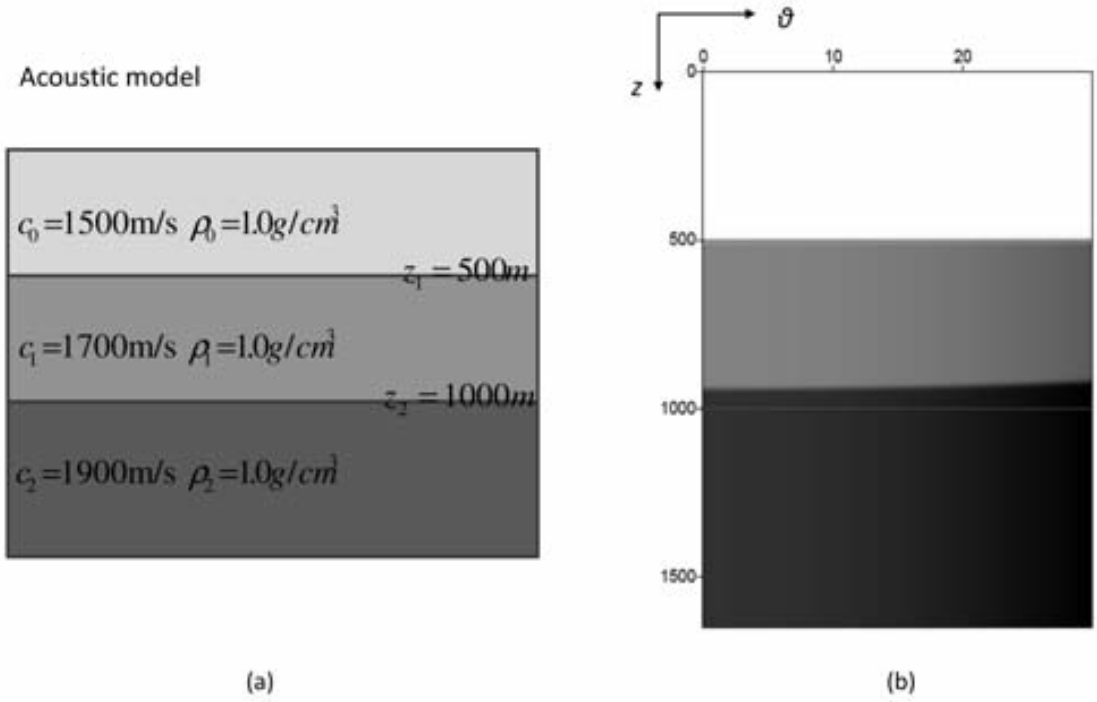

Fig. 10. (a) shows the acoustic model we are testing for evaluating the dependence of ISS on seismic bandwidth. (b) is the water speed FK Stolt migration, the red lines represent the true location of the reflectors.

CIG (Common Image Gather) where the latter only occurs when the correct depth is predicted. Hence, within a given model type and with adequate low frequency (see Figs. 12-14 for the assumed source signature spectrum, with the inclusion of significant low frequency), for ISS imaging to be effective requires adequate inclusion of imaging terms to match the contrasts and durations between actual and reference properties. The LOIS images have a move-out pattern indicating inadequate capture/inclusion of ISS imaging terms. However,the ISS imaging results with HOIS outputs common image gather flatness at the correct depth and indicates that the latter capture of imaging terms matches the contrasts and duration in the data. CIG flatness indicates adequate capture of ISS imaging terms. Hence, within a given model type and adequate low frequency content, the CIG moving and flatness output is a necessary and sufficient condition that this direct ISS depth imaging is working and the spatial configuration of the image is accurate.

All LOIS terms are also within HOIS, plus additional higher order imaging terms to address larger contrasts and duration than LOIS can accommodate. While HOIS is higher order than LOIS, it is not all orders, even for a 1D earth, nor does it accommodate imaging issues and challenges which exclusively exist in a laterally varying earth, for example, like diffractions (see, e.g., Wang and Weglein, 2011).

The second case: assume that the model-type between data generation and processing, that is, the model behind the ISS imaging algorithm, is a match, and that adequate capture is within the ISS imaging algorithm to address and accommodate the contrasts and duration. Now compare the results with adequate (see Fig. 11(a)) and decimated low frequency data, the latter with a sine squared taper (see Fig. 11(b)).

The results are shown in Fig. 11 where the former has adequate low frequency, and the latter has low frequency decimated. With low frequency tapered the result of ISS imaging is severely damaged, becoming equivalent to the original and erroneous water speed FK Stolt migration (see Fig. 10(b)). In Fig. 11(c) a source signature regularization has been applied which first removes the original wavelet and replaces it by a Gaussian. The source regularization of the low frequency tapered data allows the ISS depth imaging to become as effective as when the low frequency content was originally adequate. The ISS imaging results comparing adequate low frequency data, tapered low frequency data, and source signature regularized data are shown in Figs. 11(a), 11(b) and 11(c), respectively. The tapered data is a more severe and daunting test, than often occurs with field data, where some low frequency is present. The absolute shutdown of ISS imaging in the tapered data case, is a bit too severe a conclusion for field data, where some low and zero frequency in the data brings some small ISS effectiveness, where once again it is significantly enhanced by

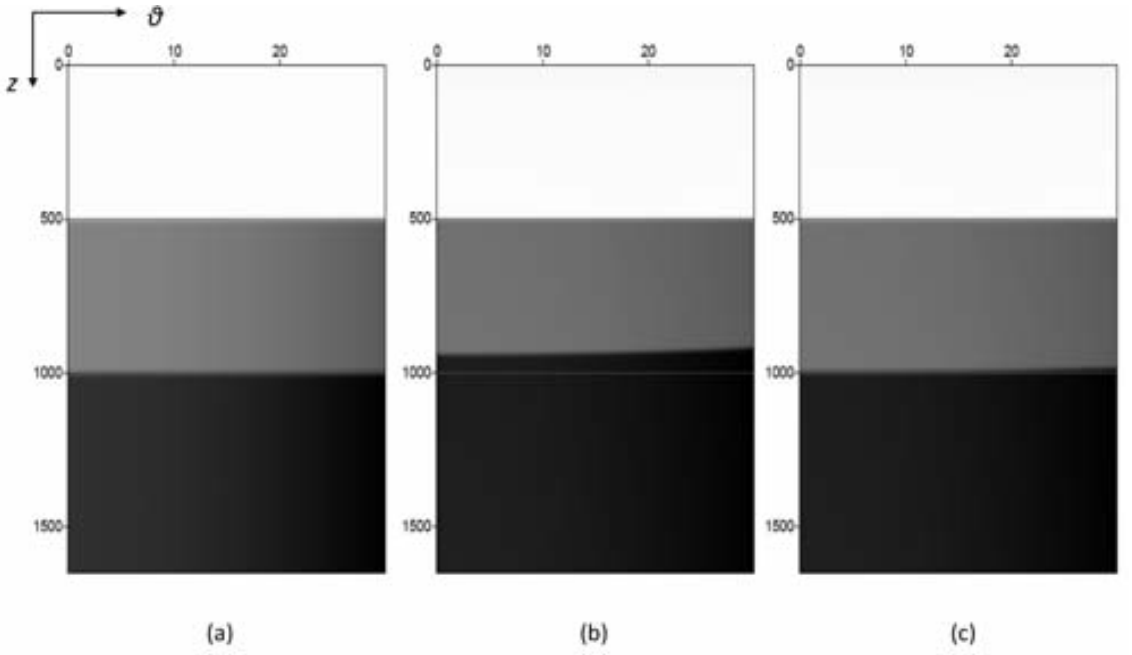

Fig. 11. This figure illustrates the imaging result for a velocity varying only earth model. (a) shows ISS imaging with data which has low frequency information. (b) shows ISS imaging with band-limited data. (c) shows the imaging result with the regularization being applied. This ISS imaging bandwidth issue is documented in Shaw (2005).

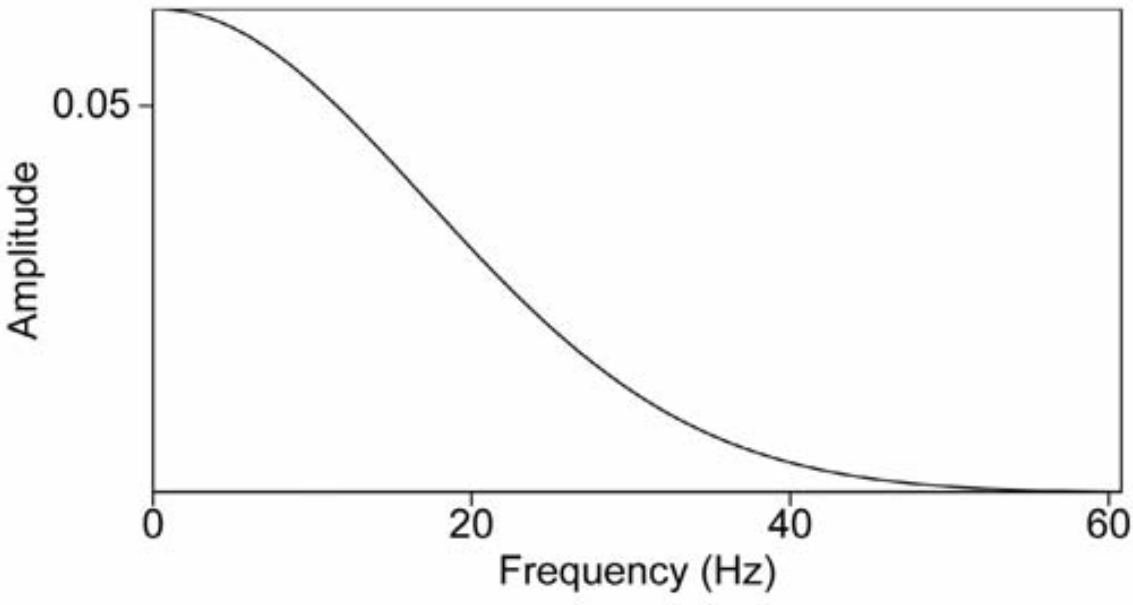

Fig. 12. Spectrum of data with low frequency.

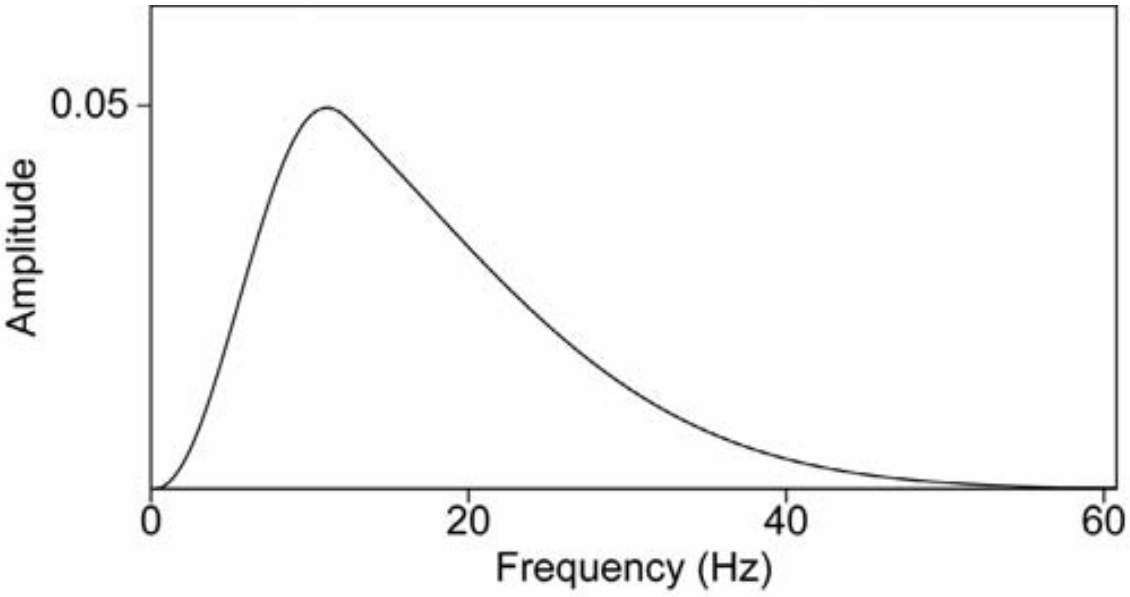

Fig. 13. Spectrum of data with diminished low frequency.

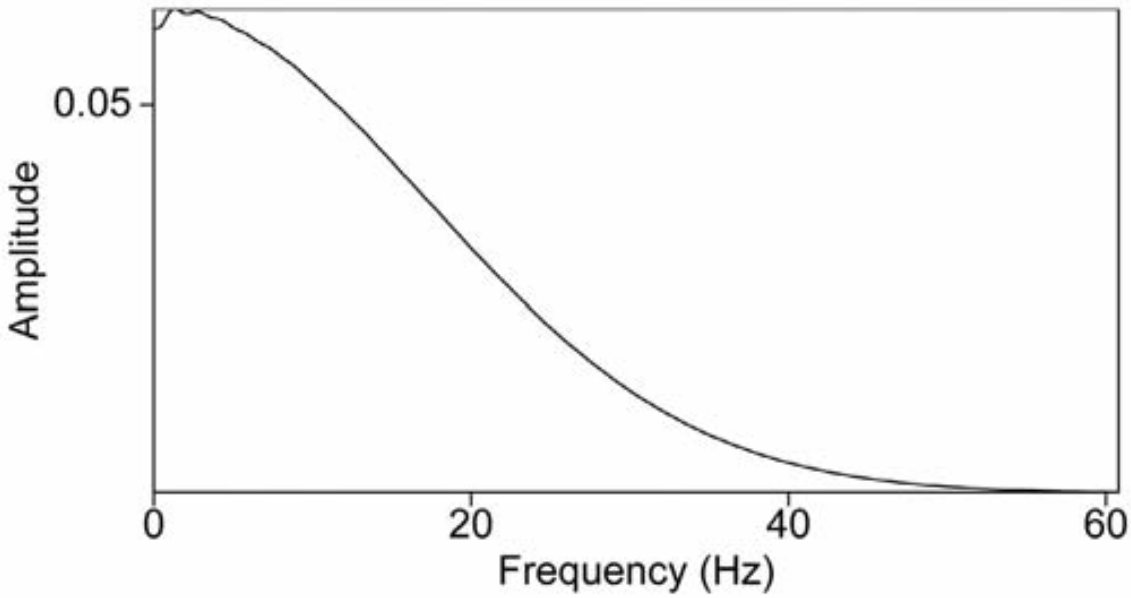

Fig. 14. Spectrum of regularized data.

the regularization. Hence, within a model type match, and adequate imaging term capture, the moved and flat CIG condition is a necessary and sufficient condition that the critical low frequency issue has been addressed. The high bar and demand on the source regularization in this synthetic example is a very positive and encouraging note and message.

Finally, we examine the case where a source signature regularization is needed and has been applied, and while the particular ISS imaging algorithm has adequate capture for a simpler earth model type, it is inadequate for a more

complicated earth model. In that case the data is generated using the more complicated earth model (more 'complicated' means more earth mechanical properties/parameters can vary) but the ISS imaging algorithm corresponds to the simpler model type. We will examine this for the case where the data is generated by a model where velocity and density both vary, but the ISS imaging algorithm assumes that only the velocity varies. That situation is illustrated in Figs. 15 and 16 where: (1) the model, (2) the water speed FK Stolt migration and (3) the velocity only varying ISS imaging algorithm result are shown. The flat CIG result indicates the ISS depth imaging result would produce the accurate depth if the data had come from a velocity only model, and that within the latter model, that effective source regularization and adequate and appropriate capture of ISS imaging terms had taken place. Hence, a flat CIG is a necessary and sufficient condition that source regularization and adequate imaging capability within a model type has been achieved. If the model type is appropriate for the data being imaged then depth will be produced. If the model

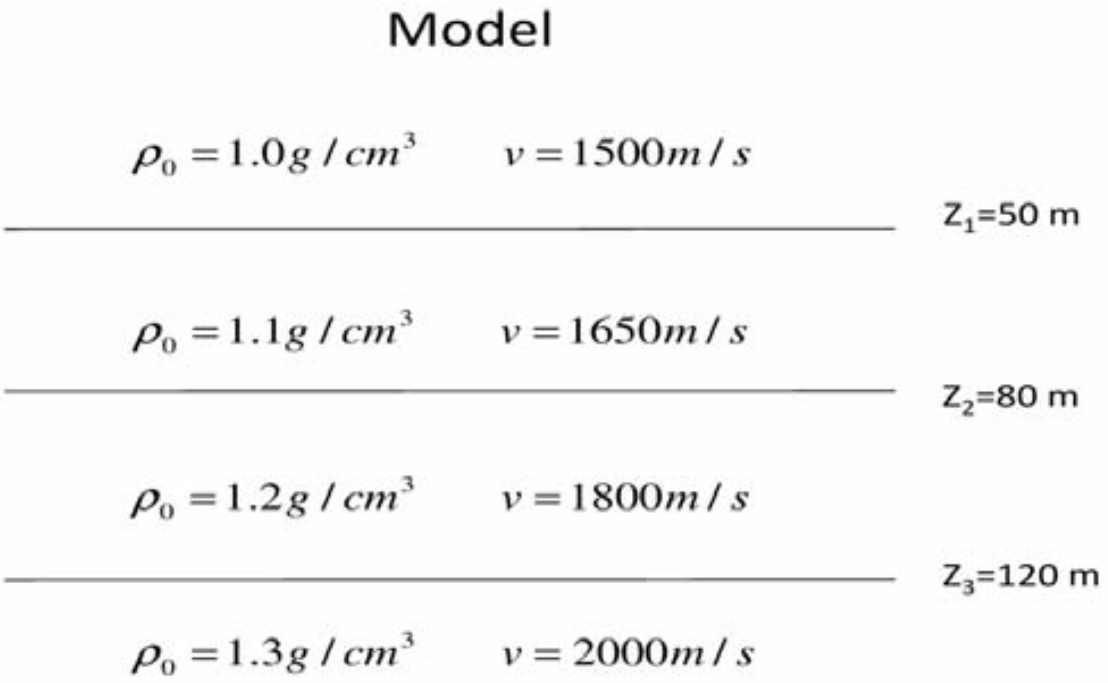

Fig. 15. An acoustic model with both velocity and density variations.

type used in the imaging is not a match with the model of the data, then CIG flatness would indicate that a critical source regularization is effective and that either the depth is being output or depth in a parallel and less complicated world is being accurately predicted. Flat CIG indicates that the critical source signature regularization is working. If you did not adequately source signature regularize and capture imaging terms for a velocity only world, then images would neither move nor flatten from the water speed migration result.

Under the latter circumstances, and as long as the low vertical wave-number sensitivity is addressed then, if: (1) the data comes from an earth where both velocity and density actually vary, (2) the ISS imaging algorithm, that will be used, was derived assuming that only the velocity in the Earth varies, and (3) the ISS imaging algorithm's ISS capture of imaging terms is adequate to correctly locate reflectors in depth if the data had been derived from a velocity only earth model, then the ISS imaging will produce flat common image gathers at the correct depth for a velocity only varying earth but at the incorrect location for an earth model type where velocity and density are both variable. Hence, if you assume a less complete model than is represented by the actual earth, then the ISS imaging output for the less complete model with flat common image gathers indicates it has addressed: (1) the low vertical wave-number issue and (2) adequate capture to produce the correct depth if the

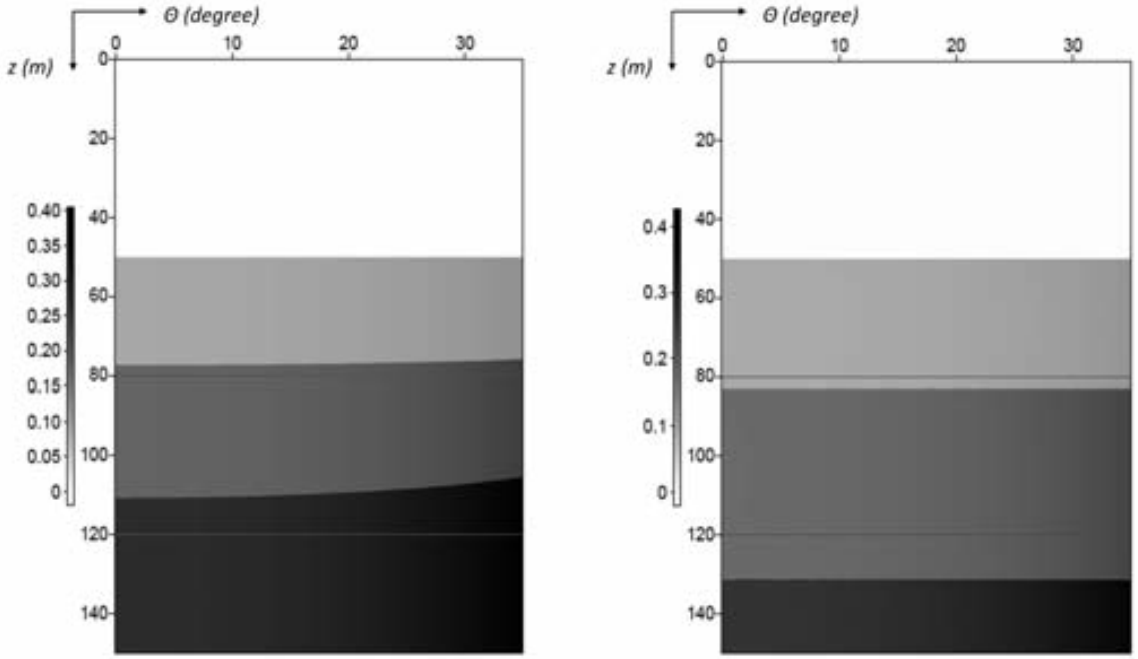

Fig. 16. (a) shows the input data generated from the geological model in Fig. 15. (b) shows ISS imaging results with velocity-only formulism. Red lines indicate the true depth of the reflectors.

lesser model type were adequate. That is behind the base-line ISS depth imaging testing of field data in this paper, and the conclusion that ISS direct depth imaging is viable. Figs. 15-16 demonstrate this idea, by having the actual model correspond to a velocity and density Earth while the ISS imaging assumes that only the velocity is varying. Note the ISS imaging flat CIG in Fig. 16(b).

There are many other issues that need to be taken into consideration in developing practical ISS depth imaging algorithms. Among these issues are: (1) within an appropriate earth model type, whether the necessary number and types of terms from the inverse series have been included to match the imaging challenge due to the difference between the actual and reference velocity, and the duration of that difference; and (2) whether the density only reflections have been excluded from the ISS depth imaging algorithm. All of these issues need to be addressed to have the ISS depth imaging algorithm produce an accurate depth section. When these requirements are met the ISS image moves until it stops, and when it stops it's there. The move-out becomes flat and the imaging series directly produces a flat common image gather (CIG) at the correct depth. In contrast to all current imaging methods where CIG flatness is a necessary but not a sufficient condition for depth imaging accuracy, the CIG flatness is a by-product of ISS imaging, and a necessary and sufficient indication that depth has been found. It's a direct depth finding machine, and when it stops it is done. With ISS imaging CIG flatness is an indication that a direct method is done, not an indirect proxy for velocity used to find the depth, where for the latter conventional use it is necessary but not sufficient for depth location. Within the current ISS imaging formulation, the overriding requirement and number one issue for field data application of ISS depth imaging is being able to address the sensitivity to missing low frequency components in the data (or more accurately, low vertical wave number). If that low frequency sensitivity is not addressed, then gathering or not gathering appropriate and necessary ISS imaging terms or excluding density only reflections will not matter, and will be of no practical consequence. Hence, addressing the bandwidth issue for ISS imaging is the number one priority, the make or break issue for field data application, viability and delivery of its promise of high impact differential added value. A regularization scheme has been developed in Liu et al. (2010) to directly address that low frequency challenge. A key purpose of this paper is to examine whether this regularization method will allow the ISS imaging algorithms to be effective and work on field data. Therefore, with this first field data examination, we relax all of the other requirements for ISS depth imaging and consider the field data as though it were generated by a velocity only varying earth. Within that parallel world where only velocity varies, the ISS depth imaging will need to address the band-limited nature of field data, and also will require having enough ISS imaging terms (within an acoustic velocity only varying subsurface assumption) to be effective for accurately locating reflectors.

The three requirements or conditions of: (1) source signature regularization, (2) adequate algorithmic ISS capture, and (3) appropriate earth model type between data generation and data processing, taken together represent a set of necessary and sufficient conditions that ISS imaging requires to be effective and working. A flat CIG is a necessary and sufficient condition that indicates ISS depth imaging effectiveness within an appropriate earth model type.

KRISTIN FIELD DATA ISS IMAGING

A similar approach is followed for a CMP gather selected from the Kristin data set (Fig. 17, Majdanski et al., 2010). Fig. 20(a) shows a water-speed migration of the data in Fig. 17, while Fig. 20(b) shows the ISS imaging result after regularization. Event 1 is the water bottom primary, event 2 is the sub-water bottom primary, event 3 is the internal multiple between event 1 and 2 and event 4 is the third primary. Event 4, the third primary has a non-flat move-out with a water speed migration. It turns out that event 1, the water-bottom primary, represents a density change but no velocity change. That was deduced by: (1) assuming that the shear velocity was probably close to zero at the water bottom, and hence an acoustic model would be adequate, (2) examining the angle dependence of the data at the water bottom, (3) the angle independence of that water bottom reflection indicates that density changed but not velocity, and (4) that $\alpha_1 - \beta_1$, is the difference between linear estimates of bulk modulus and density (and corresponds to the linear estimate to the change in acoustic velocity), and is zero when the reflection has no velocity change. In acoustics, if the linear estimate of the change in velocity is zero, then the actual change in velocity is zero. Velocity is the only acoustic parameter that exhibits that property. Fig. 21 shows the water bottom has no change in acoustic velocity.

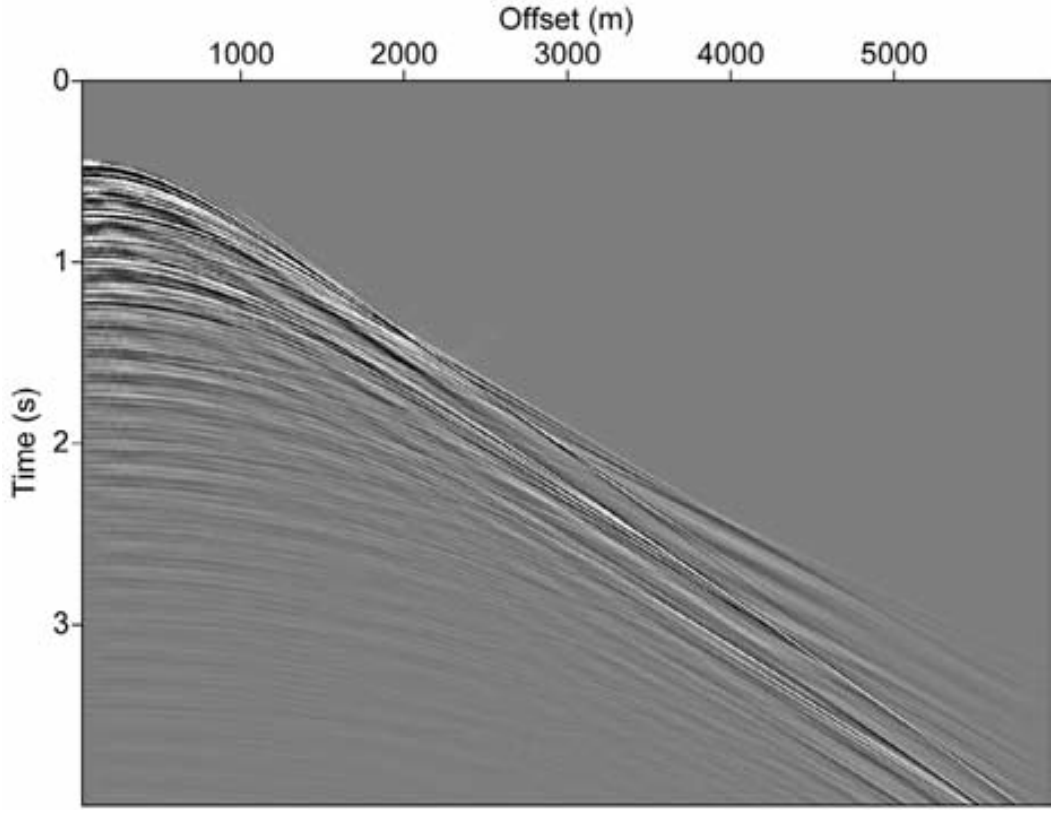

Fig. 17. The CMP gather tested from Kristin data.

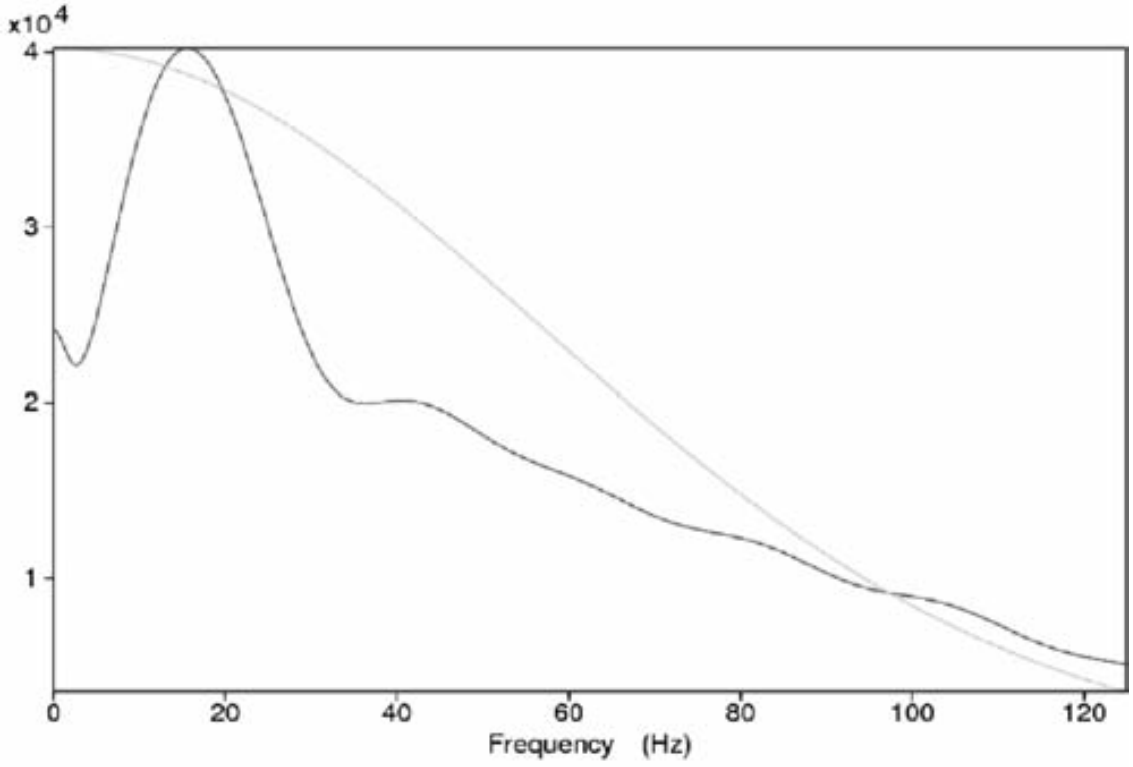

Fig. 18. Source signature regularization analysis. Amplitude spectrum of original wavelet (in red) and the target wavelet we wish to have (in green). We scale the spectrum of the target wavelet [exp $(-\omega^2/a^2)$, where $a = 80\pi$] to be of the same magnitude as that of the original wavelet for easy comparison.

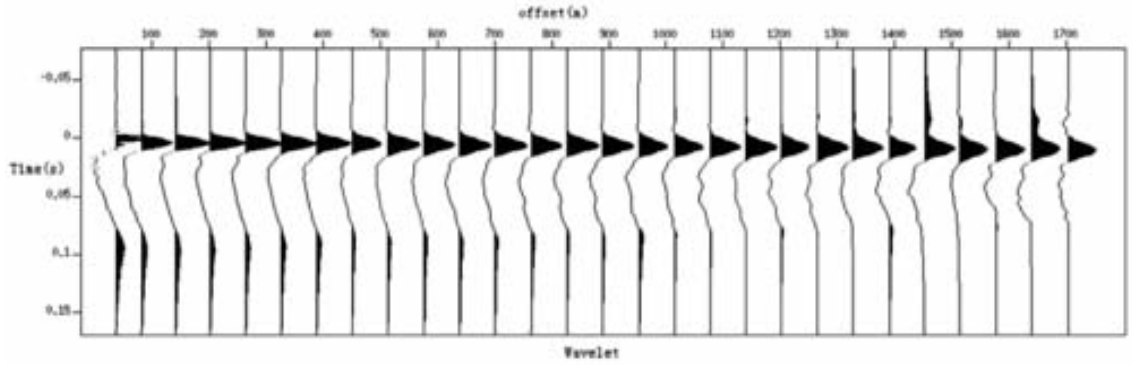

Fig. 19. Wavelet A(t), cable II (source at depth 7 m and receivers at depth 18 m).

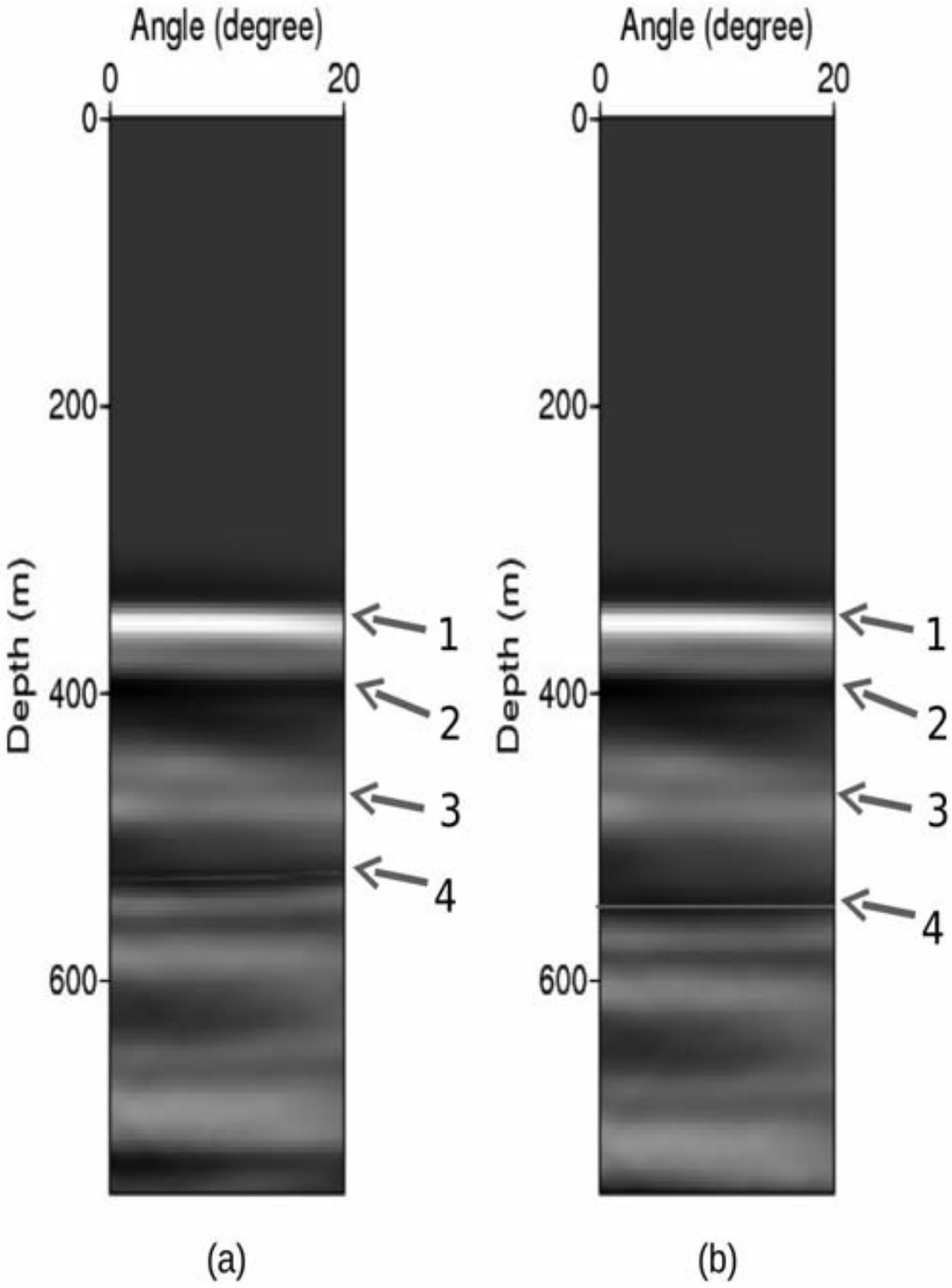

Fig. 20. For the Kristin data test: (a) shows water speed migration. The red line indicates water speed migration image for event 4. (b) shows ISS imaging result. The red line shows ISS image for event 4.

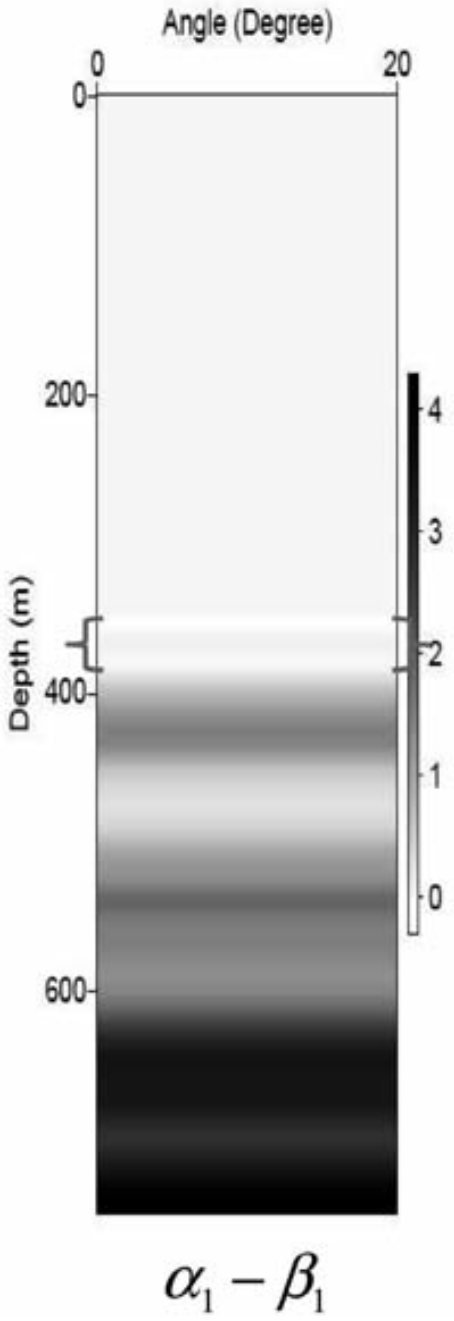

Fig. 21. Kristin data ISS depth imaging result.

Hence, the layer below the water-bottom has the same acoustic velocity as water. Further, the first order internal multiple (event 3) in that first sub-water-bottom layer also has a water-speed move-out. Hence, events 1, 2, and 3 all have flat CIGs with a water-speed FK Stolt migration (Fig. 22). Event 4 has move-out due to a velocity change at the base of the first sub-water-bottom layer. With a regularized ISS depth imaging the result for the image of event 4 is a shifted and flat CIG output. Hence, the ISS depth imaging is working on the very shallow sub-sea-bottom portion of the Kristin data set

within the context of a velocity only varying earth. The shifted ISS image and flat CIG of event 4, the third primary, indicates that bandwidth issues have been addressed, and sufficient capture of ISS imaging terms are within the ISS imaging algorithm. If for this field data set and ISS depth imaging test, either one of these conditions (addressing bandwidth sensitivity and adequate inclusion of ISS imaging terms) were a remaining and outstanding issue, then event 4 would not have moved and produced a flat CIG. The success of this test is thus defined. The next steps are to apply the regularized ISS depth imaging to an acoustic variable velocity and density model for the very shallow and sub-water-bottom reflectors, and a P-wave velocity V_P, shear wave velocity V_S and density varying elastic earth model for the deeper reflectors, to preclude density only reflections, and for outputting actual depth. If the second reflector corresponds to only a velocity change then Fig. 20(b) represents the correct depth of the first, second and third reflectors, the latter corresponding to event 4, directly and without knowing, needing or determining the velocity change across the second reflector.

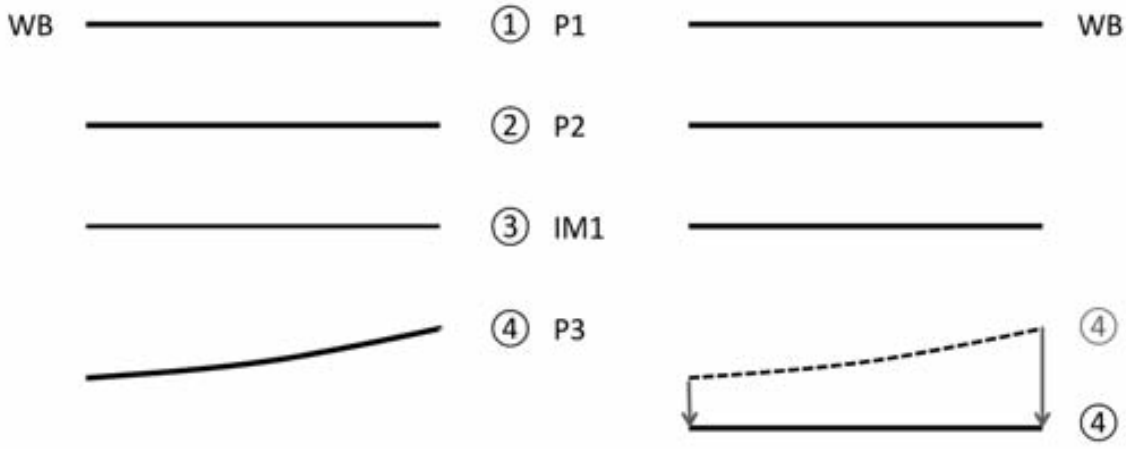

Fig. 22. This figure summarizes the results of the initial ISS depth imaging tests on the very shallow, near ocean bottom section of the Kristin data.

THE PLAN FORWARD

In the entire line of papers and theses within the history of the ISS imaging project, Weglein et al. (2002); Shaw et al. (2004); Liu (2006); Wang and Weglein (2011) there is an assumption (which for a simple two reflector/single layer example, and a chosen constant reference velocity equal

to the actual velocity above the shallower reflector) that the perturbation or difference between the actual and reference properties, and the linear estimate of that perturbation, are both 'box-like' in character. For this simple example, the linear estimate (using the reference velocity to migrate) is a box whose upper surface is at the correct depth and the lower is at the incorrect depth. Within this box-like formulation, defining imaging as locating the edges of the box (reflectors) and hence, structure, the ISS then has to correct the original box into a box whose upper and lower end are both at the correct depth. That change requires the ISS imaging to create a box that takes the mislocated original lower interface and adds a box to bring it to the correct depth. Box construction places a high burden on low vertical wave-numbers. In hindsight, that box-like formulation was not the most strategic, frugal, and well-considered way to correct mislocated images at depth. Constructing boxes when only the location of edges is of interest is paying too high a price for the sought after boundary location output. Staying closer to the data space and away from model space is the key. We plan to recast all ISS imaging methods as we move forward, in terms of moving mislocated data-like 'spikes', and that new formulation will provide a set of theoretical and practical benefits for ISS imaging efficacy that are being formulated and examined at this time. We are also examining reducing the burden of capturing adequate ISS imaging terms in an elastic earth, where the P-wave velocity, shear wave velocity and density are variable and unknown and remain unknown. We are exploring the possibility of reducing the number of independent parameters through either empirical relationships, e.g., using Garner-Garner or Greenburg-Castagna, or effective media (e.g., the optical potential). The combination of: (1) moving spikes (images) rather than boxes, and (2) reducing the elastic parameters to one effective parameter will expedite the promise and delivery of, e.g., Figs. 4 and 8 to field data.

The M-OSRP imaging research team (working in cooperation with our sponsors) is engaged in moving from the current news and report that demonstrates field data viability for ISS imaging to providing added value. The ultimate goal is to have ISS imaging match the efficacy that ISS free surface and internal multiple removal have provided for the removal of coherent noise, i.e., multiples (see, e.g., Weglein et al., 2011a), and to extend that capability for extracting information from signal (the collection of all primaries).

CONCLUSIONS

In this paper, we have shown that the ISS depth imaging algorithm can address the most serious practical limitation/challenge field data will place on ISS depth imaging: that is, limitations in seismic bandwidth. With this accomplished, the further steps to extend these tests to variable density and velocity acoustic and elastic media are achievable, and realizing that is within

the sphere of issues we can influence and make happen. The most significant difference and potential obstacle between synthetic data tests and field data for developing and delivering ISS depth imaging has been addressed.

ACKNOWLEDGMENT

We thank Professor Tadeusz Ulrych for his excellent suggestions and insightful comments in his review of this paper. We thank all the sponsors of M-OSRP for their support and encouragement. We have been partially funded by and are grateful for NSFCMG award DMS-0327778 and DOE Basic Sciences award DE-FG02-05ER15697. M-OSRP would like to thank Statoil ASA, Petoro, ExxonMobil, Eni, Total, and Schlumberger/WesternGeco for granting access to the Kristin data and special thanks to Ed Kragh (Schlumberger Cambridge Research), Joachim Mispel (Statoil ASA), Mariusz Majdanski (Schlumberger Cambridge Research), Mark Thompson, and Einar Otnes for their assistance and cooperation.

REFERENCES

Amundsen, L., Reitan, A., Arntsen, B. and Ursin, B., 2006. Acoustic nonlinear amplitude versus angle inversion and data-driven depth imaging in stratified media derived from inverse scattering approximations. Inverse Problems, 22: 1921.

Amundsen, L., Reitan, A., Arntsen, B. and Ursin, B., 2008. Elastic nonlinear amplitude versus angle inversion and data-driven depth imaging in stratified media derived from inverse scattering approximations. Inverse Problems, 24: 045006.

Amundsen, L., Reitan, A., Helgesen, H.K. and Arntsen, B., 2005. Data-driven inversion/depth imaging derived from approximations to one-dimensional inverse acoustic scattering. Inverse Problems, 21: 1823-1850.

Fu, Q., Luo, Y., Kelamis, P.G., Huo, S., Sindi, G., Hsu, S.-Y. and Weglein, A.B., 2010. The inverse scattering series approach towards the elimination of land internal multiples. Expanded Abstr., 80th Ann. Internat. SEG Mtg., Denver: 3456-3461.

Innanen, K.A., 2004. Methods for the treatment of acoustic and absorptive/dispersive wave field measurements. Ph.D. thesis, University of British Columbia.

Liu, F., 2006. Multi-dimensional depth imaging without an adequate velocity model. Ph.D. thesis, University of Houston.

Liu, F., Li, X. and Weglein, A.B., 2010. Addressing innate data limitations in ISS imaging algorithms: distinct data regularization methods to address different types of data limitations, to facilitate and allow specific ISS imaging steps and goals. 2010 M-OSRP Ann. Rep., 50-81.

Liu, F. and Weglein, A.B., 2009. Inverse scattering series velocity dependent imaging in laterally varying media: analysis of transcendental integrals in the mathematics of multidimensional imaging. 2008 M-OSRP Ann. Mtg.

Liu, F., Weglein, A.B., Nita, B.G. and Innanen, K.A., 2005. Inverse scattering series for vertically and laterally varying media: application to velocity independent depth imaging. M-OSRP Ann. Rep., 4.

Luo, Y., Kelamis, P.G., Fu, Q., Huo, S., Sindi, G., Hsu, S.-Y. and Weglein, A.B., 2011. Elimination of land internal multiples based on the inverse scattering series. The Leading Edge, 30: 884-889.

Majdanski, M., Kostov, C., Kragh, E., Moore, I., Thompson, M. and Mispel, J., 2010. Field data results of elimination of free-surface-related events for marine over/under streamer data. Extended Abstr., EAGE Conf., Barcelona.

Matson, K.H., Corrigan, D.C., Weglein, A.B., Young, C.Y. and Carvalho, P.M., 1999. Inverse scattering internal multiple attenuation: results from complex synthetic and field data examples. Expanded Abstr., 69th Ann. Internat. SEG Mtg., Houston: 1060-1063.

Shaw, S.A., 2005. An Inverse Scattering Series Algorithm for Depth Imaging of Reflection Data from a Layered Acoustic Medium with an Unknown Velocity Model. Ph.D. thesis, University of Houston.

Shaw, S.A., Weglein, A.B., Foster, D.J., Matson, K.H. and Keys, R.G., 2004. Isolation of a leading order depth imaging series and analysis of its convergence properties. J. Seismic Explor., 13: 157-195.

Wang, Z. and Weglein, A.B., 2011. An investigation of ISS imaging algorithms beyond HOIS, to begin to address exclusively laterally varying imaging challenges. M-OSRP 2010 Ann. Mtg., 105-114.

Weglein, A.B., Araújo, F.V., Carvalho, P.M., Stolt, R.H., Matson, K.H., Coates, R.T., Corrigan, D., Foster, D.J., Shaw, S.A. and Zhang, H., 2003. Inverse scattering series and seismic exploration. Inverse Problems, 19: R27-R83.

Weglein, A.B. and Dragoset, W.H., 2005. Multiple Attenuation (Geophysics Reprint No. 24). SEG, Tulsa, OK.

Weglein, A.B., Foster, D.J., Matson, K.H., Shaw, S.A., Carvalho, P.M. and Corrigan, D., 2002. Predicting the correct spatial location of reflectors without knowing or determining the precise medium and wave velocity: initial concept, algorithm and analytic and numerical example. J. Seismic Explor., 10: 367-382.

Weglein, A.B., Hsu, S., Terenghi, P., Li, X. and Stolt, R.H., 2011a. Multiple attenuation: Recent advances and the road ahead (2011). The Leading Edge, 30: 864-875.

Weglein, A.B., Liu, F., Wang, Z., Li, X. and Liang, H., 2010. The inverse scattering series depth imaging algorithms: development, tests and progress towards field data application. Expanded Abstr., 80th Ann. Internat. SEG Mtg., Denver: 4133-4138.

Weglein, A.B., Ramírez, A.C., Innanen, K.A., Liu, F., Lira, J.E. and Jiang, S., 2008. The underlying unity of distinct processing algorithms for: (1) the removal of free surface and internal multiples, (2) Q compensation (without Q), (3) depth imaging, and (4) nonlinear AVO, that derive from the inverse scattering series. Expanded Abstr., 78th Ann. Internat. SEG Mtg., Las Vegas: 2481-2486.

Weglein, A.B., Stolt, R.H. and Mayhan, J.D., 2011b. Reverse-time migration and Green's theorem: Part I - the evolution of concepts, and setting the stage for the new RTM method. J. Seismic Explor., 20: 73-90.

Weglein, A.B., Stolt, R.H. and Mayhan, J.D., 2011c. Reverse time migration and Green's theorem: Part II - a new and consistent theory that progresses and corrects current RTM concepts and methods. J. Seismic Explor., 20: 135-159.

Weglein, A.B., Zhang, H., Ramírez, A.C., Liu, F. and Lira, J.E.M., 2009. Clarifying the underlying and fundamental meaning of the approximate linear inversion of seismic data. Geophysics, 74: WCD1-WCD13.

Zhang, J., Liu, F., Innanen, K. and Weglein, A.B., 2007. Comprehending and analyzing the leading order and higher order imaging closed forms derived from inverse scattering series. 2006 M-OSRP Ann. Rep.: 149-159.

First field data examples of inverse scattering series direct depth imaging without the velocity model

Arthur B. Weglein[*], *Fang Liu*[*], *Xu Li*[*], *Paolo Terenghi*[*], *Ed Kragh*[†], *James D. Mayhan*[*], *Zhiqiang Wang*[*], *Joachim Mispel*[‡], *Lasse Amundsen*[‡], *Hong Liang*[*], *Lin Tang*[*], *and Shih-Ying Hsu*[*], *M-OSRP/Physics Dept./UH*[*], *SCR/Schlumberger*[†], *and Statoil ASA*[‡]

Summary

In Weglein et al. (2010) an update and status report were provided on the progress on the inverse scattering series (ISS) direct depth imaging without the velocity model.

In that report, results on synthetics with sufficient realism indicated that field data tests were warranted. This paper documents those first field data tests. These first early tests are encouraging and indicate that ISS direct depth imaging on field data is possible. The next steps on the road between viable and providing relevant and differential added value to the seismic tool-box are described and discussed.

Introduction / Background

All currently applied direct depth imaging methods and indirect imaging concepts firmly believe that depth and velocity are inextricably linked. That cornerstone of all current imaging means that any direct imaging method requires an accurate velocity model to produce an accurate image in depth.

It is essential to understand the significance of the term 'direct' in 'direct depth imaging'. Given an accurate velocity model, all current leading-edge imaging methods (e.g., Kirchhoff, FK, Beam and RTM) are able to directly output the depth (the actual spatial configuration) of reflectors.

Indirect imaging methods (e.g., flat common image gathers, differential moveout, CFP, CRS and 'path integral' approaches) seek to satisfy a property or condition that an image with an accurate velocity would satisfy. Those properties are necessary conditions, but not sufficient, and hence satisfying the indirect proxy for an adequate velocity model is not equivalent to knowing the velocity and direct depth imaging. Hence, satisfying these indirect criteria is no guarantee, and can lead to the correct depth or to any one of a set of incorrect depths. The latter truth is rarely (if ever) spoken and even rarer to find mentioned in print. Most importantly, these indirect approaches fervently believe that a direct depth imaging method would require and demand a velocity model, and that there is absolutely no way around it, and that depth and velocity are inextricably connected. That thinking is clear, and 100% correct within the framework of current imaging concepts and methods.

However, that thinking is superseded by the new broader framework for imaging provided by the ISS.

Amundsen et al. 2005, 2006, 2008 have developed direct inversion methods for 1D acoustic and elastic media. The ISS is the only direct inversion for both a 1D and a multi-D acoustic, elastic and anelastic earth.

In addition to being direct and applicable and applied for a multi-D earth, the ISS (Weglein et al. (2003)) allows for all processing objectives (including multiple removal and depth imaging) to be achieved directly and without subsurface information.

In the same 'direct' sense, that current imaging methods can directly output the spatial configuration of reflectors with a velocity model, ISS imaging algorithms can directly output the correct spatial configuration without the velocity model. It is the only method with that capability.

The ISS subseries for direct depth imaging communicates that depth and velocity are not inextricably linked.

The ISS provides a new superseding theory that views the current velocity-depth relationship and framework as a special limiting case, as quantum mechanics and relativity view classical physics as a limiting and special case, within a new comprehensive and broader platform and framework.

The new broader framework for imaging reduces to current imaging algorithms when the velocity model is adequate, and most amazingly it determines on its own for any particular data set, or portion of a data set, whether the new framework is needed, or whether the current conventional imaging framework will suffice. The new imaging framework determines if its services are called upon, and then and only then, will it activate the new ISS imaging framework terms and call them into action.

All current leading edge migration methods, such as, beam, Kirchhoff and RTM, are linear. In contrast, the ISS direct depth imaging without the velocity algorithm is a non-linear relationship between data and the wavefield at depth.

ISS task specific subseries for multiple removal, depth imaging and direct non-linear AVO

Each and every term and portion of any term within the ISS is computed directly in terms of data. All tasks associated with inversion (e.g., multiple removal, depth imaging, non-linear direct AVO, and Q compensation) are each contained within the series. Hence, these individual tasks are each achievable directly in terms of data, without subsurface information. Every seismic processing objective is carried out as a subseries of

DOI http://dx.doi.org/10.1190/segam2012-0850.1

the ISS, and operates without subsurface information, by involving distinct non-linear communication of the recorded seismic data. Only the ISS communicates that all seismic objectives can be achieved in basically the same way that free surface multiples are removed.

The free surface and internal multiple removal subseries have not only been shown to be viable but have also demonstrated added value and stand alone capability for predicting the amplitude and phase of multiples (See, e.g., Luo et al. 2011; Weglein and Dragoset 2005; Fu et al. 2010), in particular, demonstrated under complex marine and on-shore circumstances. In this paper, we examine for the first time the issue of ISS depth imaging viability on field data.

All conventional imaging methods require knowledge of the velocity model to determine the spatial locations of reflectors. Hence, the ISS series project began by assuming that only the velocity was variable and unknown. Figures 1-3 illustrate the ISS imaging results for an earth in which only velocity varies. The algorithms are described in Liu (2006); Liu et al. (2005); Zhang et al. (2007).

Imaging methods that require the velocity use only the phase of the data to determine depth. In contrast, all ISS tasks achieve their goals without subsurface information by using both the amplitude and phase of seismic data. The latter difference requires the exclusion of events from imaging subseries that do not relate to or contribute towards the task of depth imaging. Reflections that correspond to density only changes must be precluded from exclusively depth imaging tasks. The ISS depth imaging in an acoustic earth where V_p and density (and for an elastic earth with V_p, V_s and density), can all vary and all are initially (and remain, completely) unknown was formulated and the results were summarized in Weglein et al. (2010).

The impact of data limitations on ISS subseries

Table 1 summarizes the dependence/sensitivity of different ISS subseries on seismic bandwidth. As the latter table indicates, there is an increased dependency as we progress from the ISS free surface multiple case to the depth imaging subseries where (in the current "box-moving" formulation) the absence of low frequency in the data can have a deleterious effect on the ability of the ISS to move from the original linear incorrect depth image to the correct depth.

There are many other issues that need to be taken into consideration in developing practical ISS depth imaging algorithms. Among these issues are: (1) have the appropriate number and types of terms from the inverse series been included to match the imaging challenge due to the difference between the actual and reference velocity, and the duration of that difference; and (2) have the density only reflections been excluded from the ISS depth imaging algorithm. All of these issues need to be addressed to have the ISS depth imaging algorithm produce an accurate depth section. The moveout becomes flat and the imaging series directly produces a flat common image gather (CIG) at the correct depth.

In contrast to all current imaging methods where CIG flatness is a necessary but not a sufficient condition for depth imaging accuracy, the CIG flatness is a by-product of ISS imaging, and a necessary and sufficient indication that depth has been found. It's a direct depth finding machine, and when it stops it is done. With ISS imaging CIG flatness is an indication that a direct method is done, not an in-direct proxy for velocity used to find the depth, where for the latter conventional use it is necessary but not sufficient for depth location.

The overriding requirement and number one issue for field data application of ISS depth imaging is being able to address the sensitivity to missing low frequency components in the data (or low vertical wave number). If that low frequency sensitivity is not addressed, then gathering or not gathering appropriate and necessary ISS imaging terms or excluding density only reflections will not matter, and will be of no practical consequence. Hence, addressing the bandwidth issue for ISS imaging is the number one priority, the make or break issue for field data application, viability and delivery of its promise of high impact differential added value. A regularization scheme has been developed in Liu and Weglein (2009) to directly address that low frequency challenge. The purpose of this paper is to examine whether this regularization method will allow the ISS imaging algorithms to be effective and work on field data. Therefore, with this first field data examination, we relax all of the other requirements for ISS depth imaging and consider the field data as though it were generated by a velocity only varying earth. Within that parallel world where only velocity varies, the ISS depth imaging will need to address the band-limited nature of field data, and also will require having enough ISS imaging terms (within an acoustic velocity only varying subsurface assumption) to be effective for accurately locating reflectors.

In Figure 4, we present an acoustic model with no density variations and the water speed migration for the data from that model. Figure 5 (a) shows the inverse scattering imaging series ideal result, with full band-width data. In (b), the data has been altered by a sine squared taper up to $10Hz$ which damped the low frequency information and the ISS imaging without regularization is ineffective. In (c), with the regularization applied, the ISS depth imaging successfully corrects the data move-out and reveals the correct depth.

A similar approach is followed for a CMP gather selected from the Kristin data-set (Figure 7, Majdanski et al. (2010)). Figure 8 (a) shows a water-speed migration of the data in Figure 7, while Figure 8 (b) shows the ISS imaging result after regularization.

Event 1 is the water bottom primary, event 2 is the subwater bottom primary, event 3 is the internal multiple between event 1 and 2 and event 4 is a third primary. Event 4, the third primary has a moveout with a water

DOI http://dx.doi.org/10.1190/segam2012-0850.1

speed migration.

It turns out that event 1, the water-bottom primary, represents a density change but no velocity change. Hence, the layer below the water-bottom has the same acoustic velocity as water. Further, the first order internal multiple (event 3) in that first sub-water-bottom layer also has a water-speed move out. Hence, events 1, 2, and 3 all have flat CIGs with a water-speed FK Stolt migration (Figure 6). Event 4 has move-out due to a velocity change at the base of the first sub-water-bottom reflector.

With a regularized ISS depth imaging the result for the image of event 4 is a shifted and CIG flat output. Hence, the ISS depth imaging is working on the very shallow subsea-bottom portion of the Kristin data set within the context of a velocity only varying earth. The shifted ISS image and flat CIG of event 4, the third primary, indicates that bandwidth issues have been addressed, and sufficient capture of ISS imaging terms are within the ISS imaging algorithm. If for this field data set and ISS depth imaging test, either one of these conditions (addressing bandwidth sensitivity and adequate inclusion of ISS imaging terms) were a remaining and outstanding issue, then event 4 would not have moved and produced a flat CIG. The success of this test is thus defined. A more detailed and comprehensive analysis behind the logic and conclusions of this paper will appear in Weglein et al. (2012). The next steps are to apply the regularized ISS depth imaging to an acoustic variable velocity and density model for the very shallow and sub-water-bottom reflectors, and a Vp, Vs and density varying elastic earth model for the deeper reflectors, to preclude density only reflections, and for outputting actual depth. The M-OSRP imaging research team is engaged in moving from the current news and report that demonstrates field data viability for ISS imaging to providing added value. The ultimate goal is to have ISS imaging match the efficacy that ISS free surface and internal multiple removal have provided for the removal of coherent noise, and to extend that capability for extracting information from signal (the collection of all primaries).

Conclusions

In this paper, we have shown that the ISS depth imaging algorithm can address the most serious practical limitation/challenge field data will place on ISS depth imaging: that is, limitations in seismic bandwidth. With this accomplished, the further steps to extend these tests to variable density and velocity acoustic and elastic media are achievable, and realizing that is within the sphere of issues we can influence and make happen. The most significant difference between synthetic data and field data for ISS depth imaging has been examined and addressed.

Acknowledgment

We thank all the sponsors of M-OSRP for their support and encouragement. We have been partially funded by and are grateful for NSFCMG award DMS-0327778 and DOE Basic Sciences award DE-FG02-05ER15697. The M-OSRP group would like to thank Statoil ASA and Schlumberger/WesternGeco for granting access to the Kristin data and Mark Thompson, Mariusz Majdanski and Einar Otnes for their assistance and cooperation.

Figures

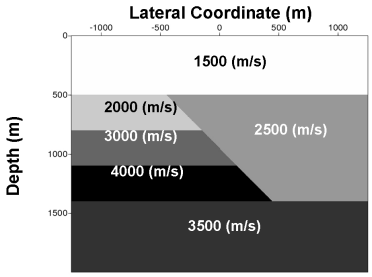

Fig. 1: The fault shadow zone model.

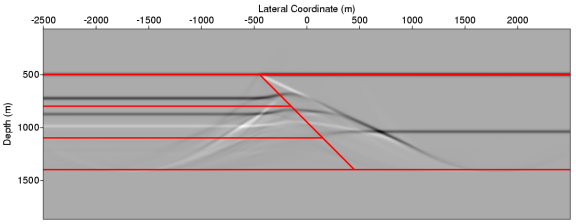

Fig. 2: The water speed pre-stack FK Stolt migration for the data from the fault shadow model.

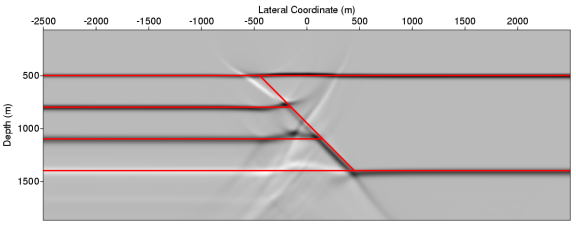

Fig. 3: The inverse scattering series image (with partial capture of ISS imaging capability) for the fault shadow model.

DOI http://dx.doi.org/10.1190/segam2012-0850.1

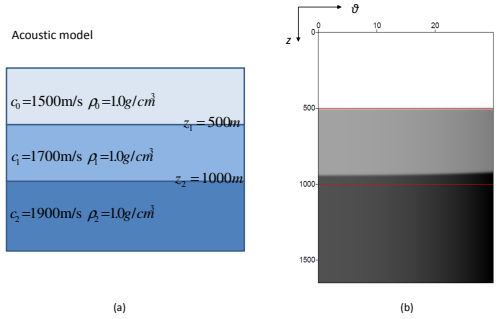

Fig. 4: Figure (a) shows the acoustic model we are testing for evaluating the dependence of ISS on seismic bandwidth. Figure (b) is the water speed FK Stolt migration, the red lines represent the true location of the reflectors.

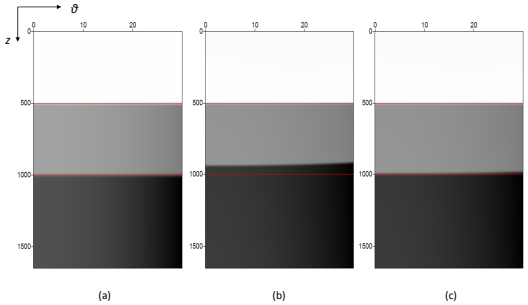

Fig. 5: This figure illustrates the imaging result for a velocity varying only earth model. Figure (a) shows ISS imaging with data which has low frequency information. Figure (b) shows ISS imaging with band-limited data. Figure (c) shows the imaging result with the regularization being applied. This ISS imaging bandwidth issue is documented in Shaw (2005).

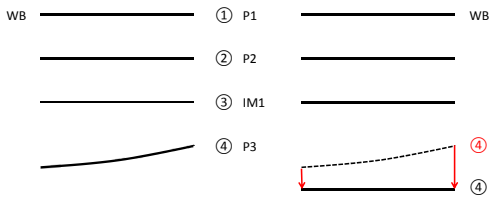

Fig. 6: This figure summarizes the results of the initial ISS depth imaging tests on the very shallow, near ocean bottom section of the Kristin data.

Dependence on temporal frequency content of the data	Specific subseries
None	Free surface multiple
Very mild	Internal mulitple
Some	Depth imaging

Table 1: This table shows the dependence of ISS specific subseries on temporal frequency content of the data.

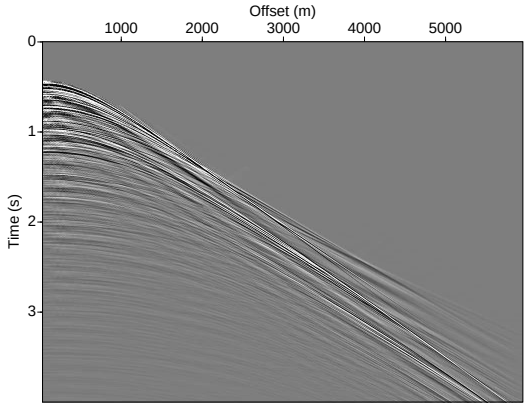

Fig. 7: The CMP gather we tested from Kristin data.

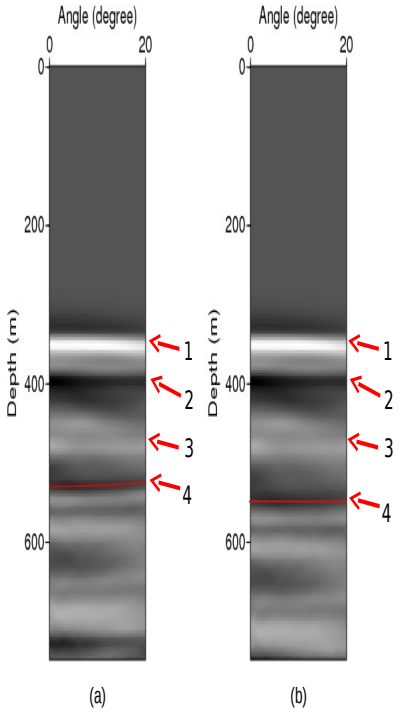

Fig. 8: For the Kristin data test: Figure (a) shows water speed migration. The red line indicate water speed migration image for event 4. Figure (b) shows ISS imaging result. The red line shows ISS image for event 4.

SEG Las Vegas 2012 Annual Meeting
DOI http://dx.doi.org/10.1190/segam2012-0850.1

http://dx.doi.org/10.1190/segam2012-0850.1

EDITED REFERENCES

Note: This reference list is a copy-edited version of the reference list submitted by the author. Reference lists for the 2012 SEG Technical Program Expanded Abstracts have been copy edited so that references provided with the online metadata for each paper will achieve a high degree of linking to cited sources that appear on the Web.

REFERENCES

Amundsen, L., A. Reitan, B. Arntsen, and B. Ursin, 2006, Acoustic nonlinear amplitude versus angle inversion and data-driven depth imaging in stratified media derived from inverse scattering approximations: Inverse Problems, **22**, 1921–1945.

Amundsen, L., A. Reitan, B. Arntsen, and B. Ursin, 2008, Elastic nonlinear amplitude versus angle inversion and data-driven depth imaging in stratified media derived from inverse scattering approximations: Inverse Problems, **24**, 045006, doi:10.1088/0266-5611/24/4/045006.

Amundsen, L., A. Reitan, H. K. Helgesen, and B. Arntsen, 2005, Data-driven inversion/depth imaging derived from approximations to one-dimensional inverse acoustic scattering: Inverse Problems, **21**, 1823–1850.

Fu, Q., Y. Luo, P. G. Kelamis, S. Huo, G. Sindi, S.-Y. Hsu, and A. B. Weglein, 2010, The inverse scattering series approach towards the elimination of land internal multiples: 80th Annual International Meeting, SEG, Expanded Abstracts, 3456–3461.

Liu, F., 2006, Multi-dimensional depth imaging without an adequate velocity model: Ph.D. dissertation, University of Houston.

Liu, F., and A. B. Weglein, 2009, Addressing the bandlimited nature of seismic source and rapid lateral variations of the earth: Source regularization and cascaded imaging operator: Mission-Oriented Seismic Research Program (M-OSRP) 2008 Annual Report, 72–117.

Liu, F., A. B. Weglein, B. G. Nita, and K. A. Innanen, 2005, Inverse scattering series for vertically and laterally varying media: Application to velocity independent depth imaging: Mission-Oriented Seismic Research Program (M-OSRP) 2004 Annual Report, 176–263.

Luo, Y., P. G. Kelamis, Q. Fu, S. Huo, G. Sindi, S.-Y. Hsu, and A. B. Weglein, 2011, Elimination of land internal multiples based on the inverse scattering series: The Leading Edge, **30**, 884–889.

Majdanski, M., C. Kostov, E. Kragh, I. Moore, M. Thompson, and J. Mispel, 2010, Field data results of elimination of free-surface-related events for marine over/under streamer data: 72nd Conference and Exhibition, EAGE, Extended Abstracts, B017.

Shaw, S. A., 2005, An inverse scattering series algorithm for depth imaging of reflection data from a layered acoustic medium with an unknown velocity model: Ph.D. dissertation, University of Houston.

Weglein, A. B., F. V. Araujo, P. M. Carvalho, R. H. Stolt, K. H. Matson, R. T. Coates, D. Corrigan, D. J. Foster, S. A. Shaw, and H. Zhang, 2003, Inverse scattering series and seismic exploration: Inverse Problems, **19**, R27–R83.

Weglein, A. B., and W. H. Dragoset, 2005, Multiple attenuation: SEG.

Weglein, A. B., F. Liu, X. Li, P. Terenghi, E. Kragh, J. D. Mayhan, Z. Wang, J. Mispel, L. Amundsen, H. Liang, L. Tang, and S.-Y. Hsu, 2012, Inverse scattering series direct depth imaging without the velocity model: First field data examples: Journal of Seismic Exploration, **21**, 1–28.

Accommodating the source (and receiver) array in free-surface multiple elimination algorithm: impact on interfering or proximal primaries and multiples

Jinlong Yang, James D. Mayhan, Lin Tang and Arthur B. Weglein, M-OSRP, University of Houston*

SUMMARY

Free-surface multiple elimination (FSME) algorithm (Carvalho, 1992; Weglein et al., 1997) is modified and extended to accommodate a source (and receiver) array with a radiation pattern. That accommodation can provide added value compared to previous methods that assumed a single point source (air-gun) for the fidelity of amplitude and phase prediction of free surface multiples at all offsets. For the source-array data, if all prerequisites are provided, the new algorithm has the theoretical capability of predicting the exact phase and amplitude of multiples, and in principle removing them through a simple subtraction. Green's theorem method can provide all its data requirements: (1) removing the reference wavefield, (2) estimation of source wavelet and radiation pattern, and (3) source and receiver deghosting. Green's theorem method is consistent with the new FSME algorithm. They are both multidimensional and do not require any subsurface information. The new FSME algorithm is tested on a 1D acoustic model, and the results indicate that the new algorithm enhances the multiple prediction when the data and experiment are caused by an array rather than a single air-gun.

INTRODUCTION

In marine seismic exploration, multiple removal is a classic long-standing problem. Various methods (e.g., Carvalho, 1992; Verschuur et al., 1992; Weglein et al., 1997, 2003; Berkhout and Verschuur, 1999; Dragoset et al., 2008) have been developed to either attenuate or eliminate free-surface multiples, and each method has different assumptions, advantages, and limitations. Among these methods, the inverse scattering series (ISS) FSME method (Carvalho, 1992; Weglein et al., 1997) does not need any subsurface information, which is a big advantage, especially under conditions of complex geology. The ISS method predicts the free-surface multiples accurately, while the feedback-loop method (Verschuur et al., 1992) only provides approximate predictions because it ignores the obliquity factor and retains the source-side ghost. Therefore, the ISS method can remove the free-surface multiples through a simple subtraction, and most importantly it preserves primary energy (e.g., Carvalho, 1992; Araújo, 1994; Weglein et al., 1997), while the feedback-loop method has to remove the multiples adaptively using certain criteria (energy minimization, for example). The energy minimization criterion works well when there are no overlapping or proximal primaries and multiples in the input data. If primaries and multiples are overlapping and destructively interfering, the energy minimization criterion can be invalid or fail and the adaptive subtraction will not work very well.

To predict free-surface multiples precisely, the ISS method has certain data requirements: (1) removal of the reference wavefield, (2) an estimation of the source wavelet and radiation pattern, and (3) source and receiver deghosting. Green's theorem wave separation methods that are consistent with the ISS method have been applied to provide these three criteria, since they are both multidimensional wave theoretic preprocessing methods and do not need any subsurface information. Green's theorem methods offer a flexible framework for deriving a number of useful algorithms due to the freedom of choosing a reference medium. When choosing air-water as the reference medium, the reference wavefield and the scattered wavefield can be seperated, and the source wavelet and radiation pattern can be estimated (Weglein and Secrest, 1990; Weglein et al., 2002). When choosing the whole space of water as the reference medium, the ghosts can be removed. Green's theorem methods have been pioneered by J. Zhang (Weglein et al., 2002; Zhang and Weglein, 2005, 2006; Zhang, 2007) and developed by J. Mayhan (Mayhan et al., 2011, 2012; Mayhan and Weglein, 2013). If all the prerequisites are provided, Zhang (2007) has shown that the ISS FSME algorithm can predict free-surface multiples accurately for a point-source data and remove them from the data without the need of adaptive subtraction.

However, for source-array data, the ISS FSME algorithm is not sufficient because this method assumes a single point source. In other words, the source has no variation of amplitude or phase with take-off angle. Nevertheless, in towed marine acquisition, a source array is commonly used to increase the power of the source, broaden the bandwidth, and cancel the random noise. The source array exhibits directivity in take-off angle (Loveridge et al., 1984). That directivity is an issue for AVO analysis and removing or attenuating multiples. In seismic processing, it is essential that we characterize the source (and receiver) array's effect on any seismic processing methods. Therefore, to improve the accuracy of the predicted multiples, the ISS FSME algorithm is extended by accommodating a source array. That accommodation can enhance the fidelity of amplitude and phase prediction of free surface multiples at all offsets.

THEORY

The ISS FSME algorithm is a fully data-driven algorithm and does not require any subsurface information. It has the ability to accurately predict the free-surface multiples order-by-order and then remove them through a simple subtraction. The ISS FSME algorithm for an isotropic point source in a 2D case is given by (Carvalho, 1992; Weglein et al., 1997, 2003):

$$D'_n(k_g,k_s,\omega) = \frac{1}{i\pi A(\omega)}\int dk D'_1(k_g,k,\omega) q e^{iq(\varepsilon_g+\varepsilon_s)} D'_{n-1}(k,k_s,\omega), \quad (1)$$

where k_g, k_s and ω represent the Fourier conjugates of receiver, source, and time, respectively. ε_g and ε_s are the receivers' and sources' depth below the free surface, respectively. The obliquity factor q is given by $q = sgn(\omega)\sqrt{\omega^2/c_0^2 - k^2}$, and c_0 is the reference velocity. The FSME algorithm only requires the source signature $A(\omega)$ and source and receiver side deghosted data $D_1'(k_g,k,\omega)$ as its input. The free-surface multiples are predicted order-by-order and then added together give the deghosted and free-surface demultipled data $D'(k_g,k_s,\omega) = \sum_{n=1}^{\infty} D_n'(k_g,k_s,\omega)$.

For source-array data, the ISS FSME algorithm can only predict multiples approximately. To incorporate the source array, the FSME algorithm is extended from a single point source to a source array with a radiation pattern, as follows:

$$D_n'(k_g,k_s,\omega) = \frac{1}{i\pi}\int \frac{dk}{\rho(k,q,\omega)} D_1'(k_g,k,\omega) q e^{iq(\varepsilon_g+\varepsilon_s)} D_{n-1}'(k,k_s,\omega), \quad (2)$$

where $\rho(k,q,\omega)$ is the projection of source signature in the f-k domain and $k^2+q^2 = \omega^2/c_0^2$. The projection of source signature $\rho(k,q,\omega)$ can be directly achieved from the reference wavefield that is separated from the measured data by using Green's theorem method (Weglein and Secrest, 1990) by choosing air-water as its reference medium.

The key point is to obtain the projection of source signature $\rho(k,q,\omega)$ from the reference wavefield. We assume that the source array is invariant from one shot to the next. In other words, the geometry or the distribution of the source array remains for each shot. The direct reference wavefield P_0^d for a 2D case can be expressed as an integral of the direct reference Green's function G_0^d over all air-guns in an array,

$$P_0^d(x,z,x_s,z_s,\omega) = \int dx'dz' \rho(x',z',\omega) G_0^d(x,z,x'+x_s,z'+z_s,\omega), \quad (3)$$

where (x,z) and (x_s,z_s) are the prediction point and source point, respectively. (x',z') is the distribution of the source with respect to the source locator (x_s,z_s). Using the bilinear form of Green's function and Fourier transforming over x, we obtain the relationship between ρ and P_0^d as

$$P_0^d(k,z,x_s,z_s,\omega) = \rho(k,q,\omega)\frac{e^{iq|z-z_s|}}{2iq} e^{ikx}. \quad (4)$$

Since $k^2+q^2 = \omega^2/c_0^2$, q is not a free variable, hence, we can not obtain $\rho(x,z,\omega)$ in space-frequency domain by taking an inverse Fourier transform on $\rho(k,q,\omega)$. However, the projection of the source signature $\rho(k,q,\omega)$ can always be achieved directly from the direct reference wavefield P_0^d in the f-k domain, where the variable k or q represent the amplitude variations of the source signature with angles. Ikelle et al. (1997) also proposed a similar quantity $A(k,\omega)$, the inverse source wavelet, and solved it indirectly using the energy minimization criterion.

Substituting the projection of the source signature $\rho(k,q,\omega)$ into the inverse scattering free-surface removal subseries, the new FSME algorithm (equation 2) can be derived (Yang and Weglein, 2012). The new algorithm accommodates a source (and receiver) array and can provide added value for the fidelity of amplitude and phase prediction of free surface multiples at all offsets. The new FSME algorithm is fully multi-dimensional and does not require any subsurface information. Therefore, it is consistent with Green's theorem methods that provide all the data requirements. The new FSME algorithm (equation 2) is also consistent with the previous FSME algorithm (equation 1) when the source array reduces to a point source.

NUMERICAL TESTS

In this section, we will show numerical tests of the free-surface multiple removal for the source-array data with overlapping or interfering primaries and multiples. The numerical tests are based on a 1D acoustic model with varying velocity and constant density, as shown in Figure 1. The model has one

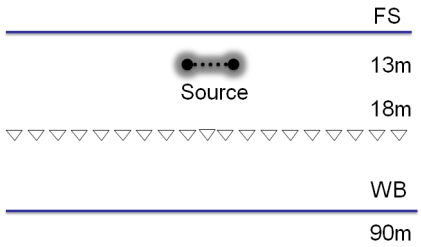

Figure 1: One-dimensional acoustic constant-density medium.

shallow reflector at 90m, hence, the primary is interfering and overlapping with the free-surface multiples. The depths of the source and receiver are 13m and 18m, respectively. Using the Cagniard-de Hoop method, the synthetic data are generated by a source array (Figure 2) that contains nine air-guns in one line with 24m range. The advantage of the Cagniard-de Hoop

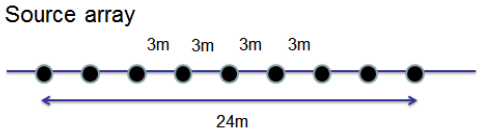

Figure 2: Source array with nine air-guns.

method is that we can accurately calculate any specific event we are interested in, so that we can compare it with the results predicted by the FSME algorithm. Here, we assume that the source array only varies laterally with identical source signatures, but the assumption is not necessary in the ISS FSME theory.

The tests are organized as follows: We first preprocess the generated source-array data using Green's theorem methods. After data preprocessing, we input the data into the previous FSME (equation 1) and the new FSME (equation 2) algorithms to predict and remove free-surface multiples and compare their results.

Data preprocessing by using Green's theorem methods

Figure 3(a) illustrates the data set generated by a source array with nine air-guns using the Cagniard-de Hoop method.

For simplicity, only the primary and the first-order free-surface multiple and their corresponding ghosts are generated. As we discussed above, Green's theorem methods are consistent with the new FSME method, because they are multidimensional and do not require any subsurface information. Furthermore, Green's theorem methods do not care about the source distribution, hence, the source-array data can be preprocessed by Green's theorem methods to satisfy the data requirement of the FSME algorithm. When choosing the air-water as the reference medium, Green's theorem wave separation method separates the total wavefield P (Figure 3(a)) into two parts: the reference wavefield P_0 (Figure 3(b)) and the scattered wavefield P_s (Figure 4(a)). After wave separation, Green's the-

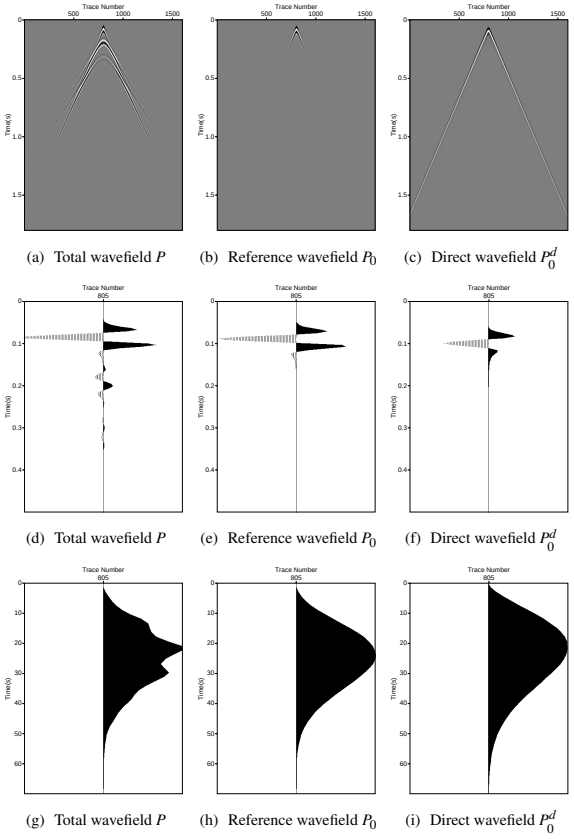

(a) Total wavefield P (b) Reference wavefield P_0 (c) Direct wavefield P_0^d

(d) Total wavefield P (e) Reference wavefield P_0 (f) Direct wavefield P_0^d

(g) Total wavefield P (h) Reference wavefield P_0 (i) Direct wavefield P_0^d

Figure 3: Wave separation and deghosting

orem deghosting method is needed to deghost the reference wavefield and the scattered wavefield by choosing the whole space of water as its reference medium. Figure 3(c) shows the direct reference wavefield P_0^d by deghosting the reference wavefield P_0. It can be seen that most of far offset energies are recovered. Figures 3(d), 3(e), and 3(f) represent the wiggle plots of the zero-offset traces. We can see that the reference wavefield is separated and its ghost is removed very well. From the spectra plots, we can see that the low frequency information is boosted, as shown in Figures 3(g), 3(h), and 3(i). Figures 4(b) and 4(c) illustrate the scattered wavefield P_s after removing the receiver-side ghosts and source & receiver ghosts, respectively. Figures 4(d), 4(e), and 4(f) are the wiggle plots of the zero-offset traces and Figures 4(g), 4(h), and 4(i) are their corresponding spectra plots. The notch at $c_0/2d = 1500/(2*18) \approx 42Hz$ is removed after receiver side deghosting. Both receiver side deghosting and source side deghosting recover more low frequency information and do not touch the primary.

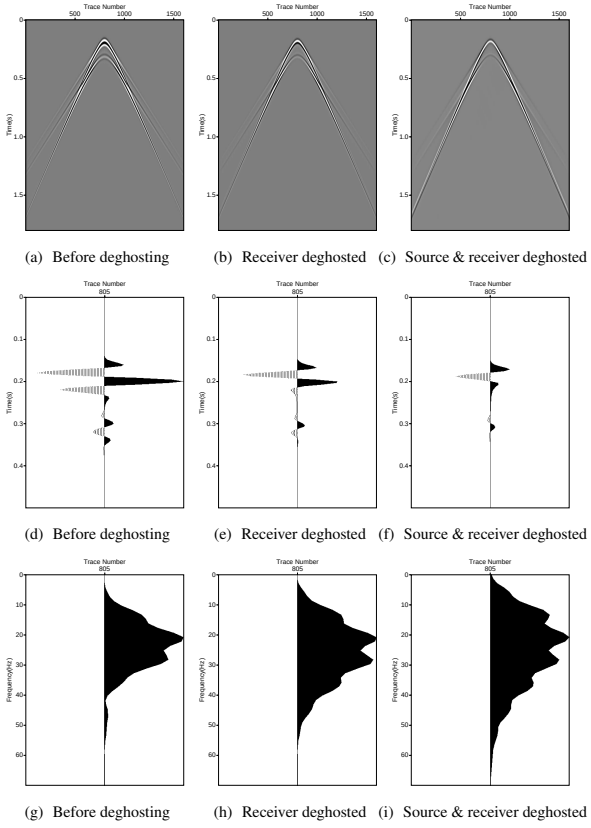

(a) Before deghosting (b) Receiver deghosted (c) Source & receiver deghosted

(d) Before deghosting (e) Receiver deghosted (f) Source & receiver deghosted

(g) Before deghosting (h) Receiver deghosted (i) Source & receiver deghosted

Figure 4: Deghosting the scattered wavefield

Free-surface multiple removal

With all data requirements satisfied, we input them into the previous FSME (equation 1) and the new FSME (equation 2) algorithms to predict and remove free-surface multiples and compare their results. The source and receiver side deghosted data (Figure 4(c)) are reploted in Figure 5(a) to show more details. Figure 5(b) is its corresponding wiggle plot for a small window (times from 1.0s to 1.4s and traces from 1330 to 1420); we can see that the primary and the first-order free-surface multiple are overlapping when the offset exceeds approximately 1000m. Furthermore, in Figure 5(b) it can be seen that they are destructively overlapping. Therefore, the adaptive subtraction method can be invalid or fail for this kind of situation, because the method is based on the energy minimization criterion, which assumes that the energy of the data will be minimized after the multiples are removed. However, in this case, the energy increases after removal of the multiples.

First, we apply the previous FSME algorithm (equation 1) to predict free-surface multiples. It predicts phase accurately but an approximate amplitude. After removing the free-surface multiple, Figure 5(c) shows that most multiples are removed,

but there are still some residual multiples. Whether this result is valuable or not depends on the objective. If the amplitude is not critical, then this method is sufficient. For cases like AVO analysis and inversion, in which amplitude is important, such residual multiples could produce errors in the prediction.

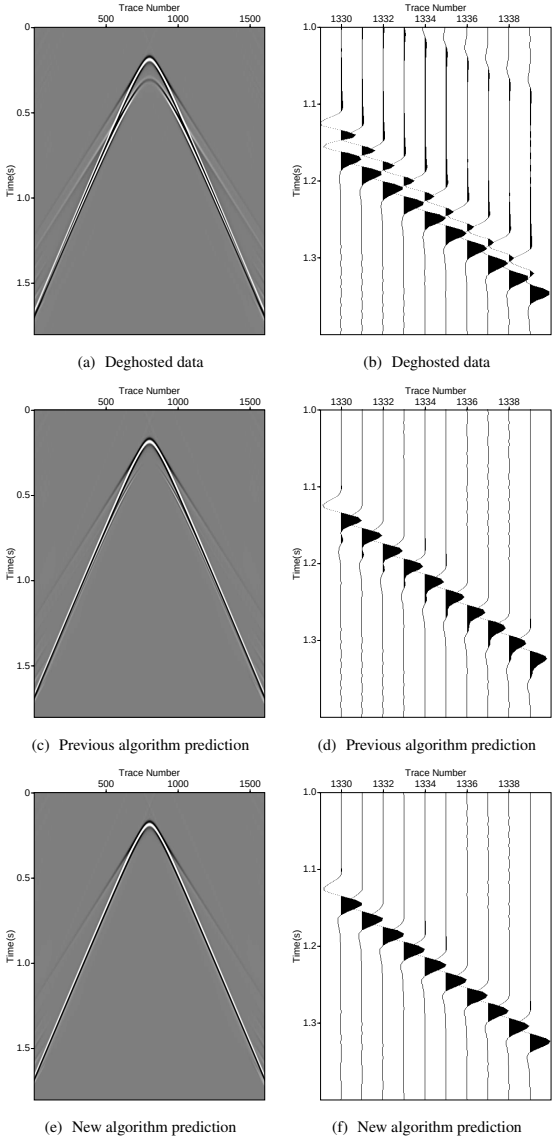

(a) Deghosted data (b) Deghosted data

(c) Previous algorithm prediction (d) Previous algorithm prediction

(e) New algorithm prediction (f) New algorithm prediction

Figure 5: The left column are the input data and after free-surface multiple removal using the previous and new FSME algorithms. The right column are their corresponding wiggle plots for a small window (times from 1.0s to 1.4s and traces from 1330 to 1420).

Next, the new FSME algorithm (Equation 2) is used to predict free-surface multiples. It can predict both amplitude and phase accurately for the source-array data at all offsets. After a simple subtraction, all the multiples are eliminated completely, as shown in Figure 5(e). Therefore, the new FSME algorithm works very well for the source-array data that have interfering events. Comparing Figures 5(f) and 5(d), we can see that the primary is still affected by the residual multiple in Figure 5(d), while in Figure 5(f), the primary remains untouched as the original primary. Figure 6 illustrates the detail of comparison for one trace at offset $= 1800m$. After removing

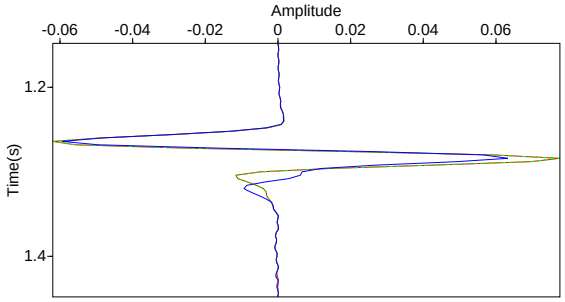

Figure 6: Red: the original primary in the input data; Blue: after multiple removal using the previous FSME algorithm; Green dash: after multiple removal using the new FSME algorithm.

free-surface multiple using the new algorithm, the primary is the same as the original one in the input data, while using the previous algorithm, the primary (Figure 5(d)) is a little weaker than the original primary, and this amplitude error will seriously affect AVO analysis.

CONCLUSIONS

A new FSME algorithm is proposed and tested on source-array data that have interfering primaries and multiples. The new FMSR algorithm accommodates a source (and receiver) array and can provide added value compared to previous methods for the fidelity of amplitude and phase prediction of free surface multiples at all offsets. If all prerequisites are provided, the new FSME algorithm, in principle, has the ability to predict free-surface multiples precisely, and removing them through a simple subtraction. All prerequisites can be achieved using Green's theorem methods by choosing different reference media. The new FSME algorithm is consistent with Green's theorem methods. They are both multidimensional and do not need any subsurface information. The numerical tests show that for source-array data, the previous isotropic source FSME algorithm can only predict phase accurately but amplitude approximately. This amplitude error can seriously affect the prediction results, such as AVO analysis and inversion, when a multiple intersects a primary. The new FSME algorithm could accommodate array data and eliminate free-surface multiples without damaging primaries.

ACKNOWLEDGMENTS

We are grateful to the M-OSRP sponsors for their encouragement and support.

REFERENCES

Araújo, F. V., 1994, Linear and non-linear methods derived from scattering theory: backscattered tomography and internal multiple attenuation: PhD thesis, Universidade Federal da Bahia.

Berkhout, A. J., and D. J. Verschuur, 1999, Removal of internal multiples: 69th SEG Annual International Meeting, 1334–1337.

Carvalho, P. M., 1992, Free-surface multiple reflection elimination method based on nonlinear inversion of seismic data: PhD thesis, Universidade Federal da Bahia.

Dragoset, B., I. Moore, M. Yu, and W. Zhao, 2008, Removal of internal multiples: 78th SEG Annual International Meeting, 2426–2430.

Ikelle, L. T., G. Roberts, and A. B. Weglein, 1997, Source signature estimation based on the removal of the first-order multiples: Geophysics, **62**, 1904–1920.

Loveridge, M. M., G. E. Parkes, L. Hatton, and M. H. Worthington, 1984, Effects of marine source array directivity on seismic data and source signature deconvolution: First Break, **2**, 16–22.

Mayhan, J. D., P. Terenghi, A. B. Weglein, and N. Chemingui, 2011, Green's theorem derived methods for preprocessing seismic data when the pressure P and its normal derivative are measured: 81st Annual International Meeting, SEG, Expanded Abstracts, Society of Exploration Geophysicists, 2722–2726. (Ranked by SEG "in the top 31 papers presented at the San Antonio meeting").

Mayhan, J. D., and A. B. Weglein, 2013, First application of Green's theorem-derived source and receiver deghosting on deep-water Gulf of Mexico synthetic (SEAM) and field data: Geophysics, **78**, WA77–WA89.

Mayhan, J. D., A. B. Weglein, and P. Terenghi, 2012, First application of Green's theorem derived source and receiver deghosting on deep water Gulf of Mexico synthetic (SEAM) and field data, *in* 82nd Annual International Meeting, SEG, Expanded Abstracts: Society of Exploration Geophysicists, 1–5.

Verschuur, D. J., A. J. Berkhout, and C. P. Wapenaar, 1992, Adaptive surface-related multiple elimination: Geophysics, **57**, 1166–1177.

Weglein, A. B., F. V. Araújo, P. M. Carvalho, R. H. Stolt, K. H. Matson, R. T. Coates, D. Corrigan, D. J. Foster, S. A. Shaw, and H. Zhang, 2003, Inverse scattering series and seismic exploration: Inverse Problems, R27–R83.

Weglein, A. B., F. A. Gasparotto, P. M. Carvalho, and R. H. Stolt, 1997, An inverse-scattering series method for attenuating multiples in seismic reflection data: Geophysics, **62**, 1975–1989.

Weglein, A. B., and B. G. Secrest, 1990, Wavelet estimation for a multidimensional acoustic earth model: Geophysics, **55**, 902–913.

Weglein, A. B., S. A. Shaw, K. H. Matson, J. L. Sheiman, R. H. Solt, T. H. Tan, A. Osen, G. P. Correa, K. A. Innanen, Z. Guo, and J. Zhang, 2002, New approaches to deghosting towed-streamer and ocean-bottem pressure measurements: 72nd Annual International Meeting, SEG, Expanded Abstracts, 1016–1019.

Yang, J., and A. B. Weglein, 2012, Incorporating source and receiver arrays in the inverse scattering series free-surface multiple elimination algorithm: theory and examples that demonstrate impact: MOSRP Annual Report, **1**, 114–132.

Zhang, J., 2007, Wave theory based data preparation for inverse scattering multiple removal, depth imaging and parameter estimation: analysis and numerical tests of green's theorem deghosting theory: PhD thesis, University of Houston.

Zhang, J., and A. B. Weglein, 2005, Extinction theorem deghosting method using towed streamer pressure data: Analysis of the receiver array effect on deghosting and subsequent free surface multiple removal: SEG/Houston 2005 Annual Meeting, 2095–2100.

———, 2006, Application of extinction theorem deghosting method on ocean bottom data: SEG/Houston 2006 Annual Meeting, 2674–2678.

A new method to eliminate first order internal multiples for a normal incidence plane wave on a 1D earth

Yanglei Zou, Arthur B. Weglein, M-OSRP/Physics Dept./University of Houston

SUMMARY

A new method to remove internal multiples has been derived under 1D normal incidence. This new method is a step further from the inverse scattering series(ISS) internal-multiple attenuator(IMA) to an eliminator under 1D normal incidence. In the procedure of the method, it constructs the reflection coefficients in order to remove the extra transmission coefficients of the events and then constructs a new function based on the reflection coefficients. This method may be relevant and provide value when primaries and internal multiples interfere with each other in both on-shore and off-shore data under near 1D circumstances. This method does not seek higher order terms in the ISS to construct an algorithm that eliminate first order internal multiples generated by all reflectors.

INTRODUCTION

The inverse scattering series(ISS) allows specific seismic processing objectives, such as free-surface-multiple removal and internal-multiple removal to be achieved directly in terms of data, without any subsurface estimation of the earths properties.

For internal-multiple removal, the Inverse Scattering Series Internal-Multiple Attenuator(IMA) can predict correct time and well-understood amplitude for all internal multiples without any subsurface information. The IMA can remove internal multiples more effectively by using energy minimization adaptive subtraction (EMAS). However, events may interfere with each other in both on-shore and off-shore seismic data. In these cases, the EMAS criteria may fail. For example, when a primary destructively interferes with an internal multiple and the real energy of the primary is greater than the interfering event, the EMAS will not only remove the internal multiple but also touch the primary. The EMAS criteria is to remove one event in the interfering events and obtain the minimum data energy. However, in this example, the criteria fails as the real primary has greater energy.

Predicting the correct amplitude of the internal multiples is an effective way of avoiding the limitations of EMAS. W.Herrera and A.B.Weglein(2012) and has derived a subseries that can eliminate all first order internal multiples generated at the shallowest reflector and can further attenuate deeper internal multiples. The present work is a step further from the IMA to an eliminator under 1D normal incidence. The method is derived based on the analytic expressions of the data under 1D normal incidence. And in the procedure of the method, it determines the reflection coefficients in order to remove the extra transmission coefficients of the events and constructing a new function based on the reflection coefficients. This method may be relevant and provide value when primaries and internal multiples destructively interfering with each other in 1D normal incidence data.

INTERNAL MULTIPLE ATTENUATOR(IMA) AND ATTENUATION FACTOR(AF) UNDER 1D NORMAL INCIDENCE

The 1D normal incidence version of IMA given by Araújo (1994) Weglein et al. (1997) is presented as follows:

$$b_3^{IM}(k) = \int_{-\infty}^{\infty} dz e^{ikz} b_1(z) \int_{-\infty}^{z-\varepsilon_2} dz' e^{-ikz'} b_1(z') \times \int_{z'+\varepsilon_1}^{\infty} dz'' e^{ikz''} b_1(z''). \quad (1)$$

To demonstrate the mechanism of the internal multiple attenuation algorithm and to examine its properties, Weglein et al. (2003) considered the simplest two-layer model that can produce an internal multiple. For this model, the reflection data caused by an impulsive incident wave $\delta(t-\frac{z}{c})$ is:

$$D'(t) = R_1\delta(t-t_1) + T_{01}R_2T_{10}\delta(t-t_2) + \cdots \quad (2)$$

where t_1, t_2 and R_1, R_2 are the two way times and reflection coefficients from the two reflectors,respectively; and T_{01} and T_{10} are the coefficients of transmission between model layers 0 and 1 and 1 and 0, respectively.

$$D'(\omega) = R_1 e^{i\omega t_1} + T_{01}R_2T_{10}e^{i\omega t_2} + \cdots . \quad (3)$$

where$D'(\omega)$ is the temporal Fourier transform of $D'(t)$. Make a water speed migration with:$z_1 = \frac{c_0 t_1}{2}$ $z_2 = \frac{c_0 t_2}{2}$.

The input data can now be expressed in terms of $k = k_z$, z_1 and z_2:

$$b(k) = R_1 e^{ikz_1} + T_{01}R_2T_{10}e^{ikz_2} + \cdots \quad (4)$$

The date is now ready for the internal multiple algorithm. Substituting $b(k)$ into the algorithm, we derive the prediction in the time domain:

$$b_3 t = R_1R_2^2T_{01}^2T_{10}^2\delta(t-(2t_2-t_1)) \quad (5)$$

From the example it is easy to compute the actual first order internal multiple precisely:

$$-R_1R_2^2T_{01}T_{10}\delta(t-(2t_2-t_1)) \quad (6)$$

Therefore, the time prediction is precise, and the amplitude of the prediction has an extra power of $T_{01}T_{10}$ which is called the Attenuation Factor(AF), thus defining exactly the difference between the attenuation represented by b_3 and elimination.

To derive a general formula for the amplitude prediction of the algorithm, A.C.Ramírez and A.B.Weglein (2005) analyzed a model with n layers and respective velocities C_n, n is an integer. By using the definitions $R_1 = R_1'$, $R_N' = R_N\prod_{i=1}^{N-1}(T_{i-1,i}T_{i,i-1})$

and Einsteins summation, the reflection data from a normal incident spike wave we obtain the following:

$$D(t) = R'_n \delta(t - t_n) + internal\ multiples \tag{7}$$

The generalized prediction of the attenuator is obtained by the following:

$$b_3^{IM}(k) = R'_i R'_j R'_k e^{ikz_i} e^{ikz_j} e^{ikz_k} \tag{8}$$

which in the time domain becomes

$$b_3^{IM}(k) = R'_i R'_j R'_k \delta(t - (t_i + t_k - t_j)) \tag{9}$$

By evaluating Equation (9) for different values of i, j and k the amplitude prediction of first order internal multiples is obtained and can be generalized for any amount of layers in a 1D model. Compared with the real amplitude of internal multiples in the data, we can obtain the AF(Figure 1 shows an example of the Attenuation Factor).

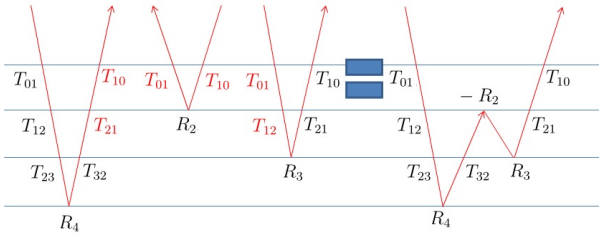

Figure 1: an example of the Attenuation Factor of a first order internal multiple generated at the second reflector. The red terms in this figure show the extra transmission coefficients. The Attenuation Factor in this example is $AF_2 = (T_{01}T_{10})^2 T_{12}T_{21}$

The attenuation factor, AF_j, in the prediction of internal multiples is given by the following:

$$AF_j = \begin{cases} T_{0,1}T_{1,0} & (j=1) \\ \prod_{i=1}^{N-1} (T_{i-1,i}^2 T_{i,i-1}^2) T_{j,j-1} T_{j-1,j} & (1 < j < J) \end{cases} \tag{10}$$

The attenuation factor AF_j can also be performed by using reflection coefficients:

$$AF_j = \begin{cases} 1 - R_1^2 & (j=1) \\ (1-R_1^2)^2 (1-R_2^2)^2 \cdots (1-R_{j-1}^2)^2 (1-R_j^2) & (1 < j < J) \end{cases} \tag{11}$$

The subscript j represents the generating reflector, and J is the total number of interfaces in the model. The interfaces are numbered starting with the shallowest location.

A NEW IDEA TO ELIMINATE INTERNAL MULTIPLES UNDER 1D NORMAL INCIDENCE

The discussion above demonstrates that all first order internal multiples generated at the same reflector have the same AF. In order to predict correct amplitude of first order internal multiples directly in terms of data, a new term in the second integral of IMA can be developed to remove the AF and make the function an eliminator. The function must be developed from

$$b_3^{IM}(k) = \int_{-\infty}^{\infty} dz e^{ikz} b_1(z) \int_{-\infty}^{z-\varepsilon_2} dz' e^{-ikz'} b_1(z') \times \int_{z'+\varepsilon_1}^{\infty} dz'' e^{ikz''} b_1(z'') \tag{12}$$

to

$$b_E^{IM}(k) = \int_{-\infty}^{\infty} dz e^{ikz} b_1(z) \int_{-\infty}^{z-\varepsilon_2} dz' e^{-ikz'} F[b_1(z')] \times \int_{z'+\varepsilon_1}^{\infty} dz'' e^{ikz''} b_1(z'') \tag{13}$$

For the 1D normal incidence, $b_1(z)$ is the water speed migration of the data. It is expressed as follows:

$$\begin{aligned} b_1(z) =& R_1\delta(z-z_1) + R'_2\delta(z-z_2) + R'_3\delta(z-z_3) + \cdots \\ &+ R'_n\delta(z-z_n) + \cdots \end{aligned} \tag{14}$$

The $F[b_1(z)]$ should have the form as the following:

$$\begin{aligned} F[b_1(z')] =& \frac{R_1}{AF_{j=1}}\delta(z'-z_1) + \frac{R'_2}{AF_{j=2}}\delta(z'-z_2) + \cdots \\ &+ \frac{R'_n}{AF_{j=n}}\delta(z'-z_n) + \cdots \\ =& \frac{R_1\delta(z'-z_1)}{1-R_1^2} + \frac{R'_2\delta(z'-z_2)}{(1-R_1^2)^2(1-R_2^2)} + \cdots \\ &+ \frac{R'_n\delta(z'-z_n)}{(1-R_1^2)^2(1-R_2^2)^2\cdots(1-R_{n-1}^2)^2(1-R_n^2)} \\ &+ \cdots \end{aligned} \tag{15}$$

By using reverse engineering,Y.Zou(2013) derived the $F[b_1(z)]$ directly in terms of data:

$$F[b_1(z)] = \lim_{\varepsilon' \to 0} \frac{c(z)\int_{z-\varepsilon}^{z+\varepsilon} c(z'')dz''}{\int_{z-\varepsilon}^{z+\varepsilon} b_1(z')dz'\{1 - [\int_{z-\varepsilon}^{z+\varepsilon} c(z'')dz'']^2\} + \varepsilon'} \tag{16}$$

$$c(z) = \frac{b_1(z)}{1 - \int_{-\infty}^{z-\varepsilon} dz' b_1(z') \int_{z'-\varepsilon}^{z'+\varepsilon} dz'' c(z'')} \tag{17}$$

To derive the $F[b_1(z)]$ function from $b_1(z)$, c(z) must first be solved in equation (17). Thereafter, c(z) is integrated into Equation (16). And take $F[b_1(z)]$ into equation (13), we will get the new equation.

First type of equation approximation

Equation (17) is an integral equation:

$$c(z) = \frac{b_1(z)}{1 - \int_{-\infty}^{z-\varepsilon} dz' b_1(z') \int_{z'-\varepsilon}^{z'+\varepsilon} dz'' c(z'')}$$

Generally, this kind of equation does not have analytical solutions; hence, an approximation must be made for equation

(17). The simplest approximation is presented as follows:

$$\begin{aligned} c(z)_{1T} =& \frac{b_1(z)}{1-\int_{-\infty}^{z-\varepsilon} dz' b_1(z') \int_{z'-\varepsilon}^{z'+\varepsilon} dz'' c(z'')} \\ \approx& \frac{b_1(z)}{1-0} \\ \approx& b_1(z) \end{aligned} \tag{18}$$

Integrate $c(z)_{1T}$ into equation (16). And take $F[b_1(z)]$ into equation (13), we will get the first type of equation approximation. It can be shown that this first kind approximation can predict correct amplitude for all first order internal multiples generated at the shallowest reflector and can further attenuate deeper internal multiples.

Second type of equation approximation

A more accurate approximation is presented as follows:

$$\begin{aligned} c(z)_{2T} =& \frac{b_1(z)}{1-\int_{-\infty}^{z-\varepsilon} dz' b_1(z') \int_{z'-\varepsilon}^{z'+\varepsilon} dz'' c(z'')} \\ \approx& \frac{b_1(z)}{1-\int_{-\infty}^{z-\varepsilon} dz' b_1(z') \int_{z'-\varepsilon}^{z'+\varepsilon} dz'' b_1(z'')} \end{aligned} \tag{19}$$

Integrate $c(z)_{2T}$ into Equation (16). And take $F[b_1(z)]$ into equation (13), we will get the second type of equation approximation. This type of approximation can predict the correct amplitude for all first order internal multiples generated at the shallowest and next shallowest reflectors and can further attenuate deeper internal multiples.

And we can again replace the c(z) in the denominator by equation(19) to get a better approximation, for 1D normal incidence data, all these three approximations are presented as follows:

$$\begin{aligned} c(z)_{1T} =& R_1\delta(z-z_1) + R_2'\delta(z-z_2) + R_3'\delta(z-z_3) \\ &+ R_4'\delta(z-z_4) + \cdots \end{aligned} \tag{20}$$

$$\begin{aligned} c(z)_{2T} =& R_1\delta(z-z_1) + \frac{R_2'}{1-R_1^2}\delta(z-z_2) + \frac{R_3'}{1-R_1^2-R_2'^2}\delta(z-z_2) \\ &+ \frac{R_4'}{1-R_1^2-R_2'^2-R_3'^2}\delta(z-z_4) + \cdots \\ =& R_1\delta(z-z_1) + R_2\delta(z-z_2) + \frac{R_3'}{1-R_1^2-R_2'^2}\delta(z-z_2) \\ &+ \frac{R_4'}{1-R_1^2-R_2'^2-R_3'^2}\delta(z-z_4) + \cdots \end{aligned} \tag{21}$$

$$\begin{aligned} c(z)_{3T} =& R_1\delta(z-z_1) + R_2\delta(z-z_2) + \frac{R_3'}{1-R_1^2-R_2'\frac{R_2'}{1-R_1^2}}\delta(z-z_3) \\ &+ \frac{R_4'}{1-R_1^2-R_2'\frac{R_2'}{1-R_1^2}-R_3'\frac{R_3'}{1-R_1^2-R_2'^2}}\delta(z-z_4) + \cdots \\ =& R_1\delta(z-z_1) + R_2\delta(z-z_2) + R_3\delta(z-z_3) \\ &+ \frac{R_4'}{1-R_1^2-R_2'\frac{R_2'}{1-R_1^2}-R_3'\frac{R_3'}{1-R_1^2-R_2'^2}}\delta(z-z_4) + \cdots \end{aligned} \tag{22}$$

We can see the first event has correct amplitude in $c(z)_{1T}$, the first two events have correct amplitude in $c(z)_{2T}$ and the first three events have correct amplitude in $c(z)_{3T}$. In those equations, the reflection coefficients of first several layers have been correctly constructed and reflection coefficients of deeper layers have been better constructed. That means in the procedure, the reflection coefficients have been constructed in order to remove extra transmission coefficients from the middle integral.

Only primaries are considered as the input in deriving all these equations. However, for these two types of approximations, the conclusion is still valid when we consider real data which contains both primaries and internal multiples as input. By using these approximations to predict the amplitude of internal multiples generated at the shallowest and next shallowest reflectors, in $F[b_1(z)]$, only the part of the data preceding the second primary is used. Considering that the internal multiples do not arrive prior to the second primary, that part of the data remains the same when only primaries or both primaries and internal multiples are considered.

NUMERICAL EXAMPLES

This section presents a numerical example that shows the result of the original IMA and the two types of equation approximation of the new equation.

Figure 2 and 3 show the model used in this study and the 1D normal incidence input data, respectively. We will do following comparison of the part of the data in the red rectangular shown in figure 3.

The output of IMA in Figure 4 clearly shows that all multiples are predicted with the correct time and approximate amplitude. Figure 5, which displays the first type of equation approximation of the new function, shows that all internal multiples with a downward reflection at the shallowest reflector (IM_{212},IM_{312} and IM_{213})are removed. And in Figure 6,we can see all internal multiples generated at the shallowest and the next shallowest reflectors (IM_{212},IM_{312},IM_{213} and IM_{323}) are removed by the second type of equation approximation.

In the figure 4,5 and 6:

P_3 is the Third primary. IM_{212},IM_{213},IM_{312} are internal multiples with a downward reflection at the shallowest reflector.The three numbers in the subscript refer to the historical number of reflectors in the internal multiples. For example, IM_{212} is a first order internal multiple with two upward reflection at the second reflector and a downward reflection at the first(shallowest) reflector. IM_{323} is a internal multiple with a downward reflection at the next shallowest reflector. The spurious event is an false event generated by IM_{212},P_3 and IM_{212}, which exist in every figure. (A method for removing the spurious events have been discovered by Ma et al. (2012) Liang et al. (2012)).

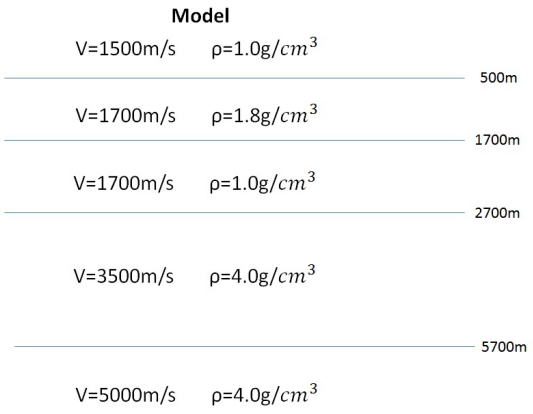

Figure 2: Model

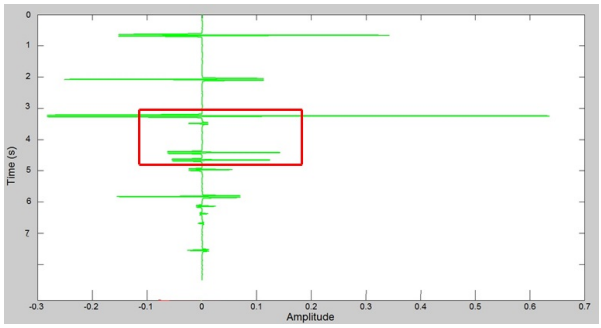

Figure 3: Input data(1D normal incidence)

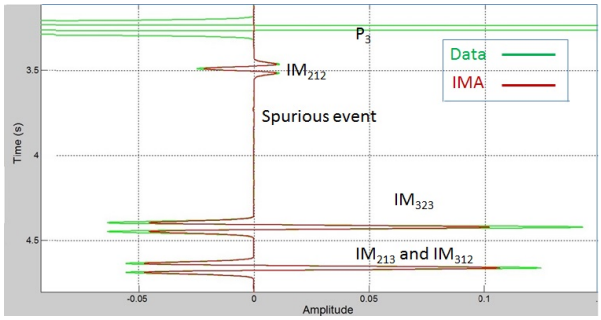

Figure 4: Output of the ISS-IMA

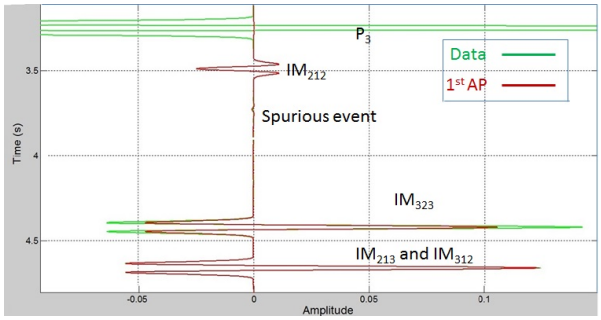

Figure 5: Output of the first type of equation approximation

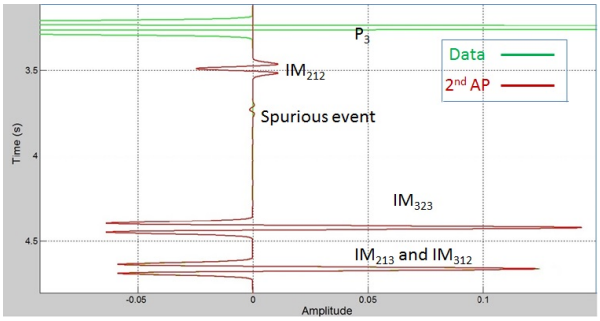

Figure 6: Output of the second type of equation approximation

CONCLUSION

1.A new method to remove internal multiples has been derived under 1D normal incidence. In the procedure of the method, it constructs the reflection coefficients in order to remove the extra transmission coefficients and then constructs a new function based on the reflection coefficients.

2.Two different types of equation approximation are also presented: (1) The first type of equation approximation can predict the correct amplitude of all first order internal multiples generated at the shallowest reflector. (2)The second type of equation approximation can predict the correct amplitude of all first order internal multiples generated at the shallowest and next shallowest reflectors. Depending on the goals, different types of approximation can be made, and we can achieve each specific goal by using the corresponding equation approximations. In practise, the elimination (not attenuation) method of internal multiples may be relevant and provide value when primaries and internal multiples interfere with each other in both on-shore and off-shore data under near 1D circumstances.

3.This equation and its approximations:
(a)not generate any more events than IMA.
(c)not touch primaries.

ACKNOWLEDGMENTS

We are grateful to all M-OSRP sponsors for long-term encouragement and support in this research. We would like to thank all our colleagues for the help of finishing this abstract and valuable discussions in this research program.

REFERENCES

A.C.Ramírez, and A.B.Weglein, 2005, Progressing the analysis of the phase and amplitude prediction properties of the inverse scattering internal multiple attenuation algorithm.: J. of Seismic Expl., **13**, 283–301.

Araújo, F. V., 1994, Linear and non-linear methods derived from scattering theory: backscattered tomography and internal multiple attenuation: PhD thesis, Universidade Federal da Bahia.

Liang, H., C. Ma, and A. B. Weglein, 2012, A further general modification of the leading order iss attenuator of first order internal multiples to accommodate primaries and internal multiples when an arbitrary number of reflectors generate the data: theory, development, and examples: Mission Oriented Seismic Research Program Annual Report, 148–165.

Ma, C., H. Liang, and A. B.Weglein, 2012, Modifying the leading order iss attenuator of first-order internal multiples to accommodate primaries and internal multiples: fundamental concept andtheory, development, and examples exemplified when three reflectors generatethe data: Mission Oriented Seismic Research Program Annual Report, 133–147.

Weglein, A. B., F. V. Araújo, P. M. Carvalho, R. H. Stolt, K. H. Matson, R. T. Coates, D. Corrigan, D. J. Foster, S. A. Shaw, and H. Zhang, 2003, Inverse scattering series and seismic exploration: Inverse Problems, R27–R83.

Weglein, A. B., F. A. Gasparotto, P. M. Carvalho, and R. H. Stolt, 1997, An inverse-scattering series method for attenuating multiples in seismic reflection data: Geophysics, **62**, 1975–1989.